# SGP South – Groundwater Assessment

## Response to EA Amendment 20250319 Information Request

Prepared for:


Prepared by:


INTERA Incorporated

JULY, 2025

# Executive Summary

Arrow Energy (Arrow) is seeking to amend Environmental Approval EA0001613 for its Surat Gas Project (SGP) South operations, in part to remove condition Water 1B, which restricts the location of coal seam gas (CSG) production wells within 10 km of Lot 40 DY85.

This document provides:

1. An assessment of the potential influence of five CSG wells, proposed to be located within 10 km of the centre of Lot 40 DY85 near the boundary of petroleum lease (PL) 493, on the movement of contaminants associated with the historical underground coal gasification (UCG) activities on Lot 40 DY85.
2. A response to groundwater-related actions 9, 10, and 11 in the EA0001613 information request issued by the Department of Environment, Technology, Science and Innovation (DETSI) on 11 June 2025.

The groundwater assessment was performed using numerical groundwater flow, contaminant transport, and particle tracking modelling, based on the most recent Field Development Plan (FDP) for PL253 and PL493 with an ensemble history-matched dataset. Predictive modelling scenarios were conducted for a period of 200 years to assess and quantify the potential incremental influence of the five CSG wells on the migration of contaminants from Lot 40 DY85. Scenario 1 includes abstraction from the five wells located near the south-western boundary of PL493 (exist within 10 km of Lot 40 DY85), as well as abstraction from all CSG wells not operated by Arrow Energy, the 55 wells within PL253 (associated with the approved Arrow Energy EA0001401 PL253 Stage 1 activities), and the 28 wells located within PL493. Scenario 2 excludes the five wells but includes all other abstraction wells incorporated in the Scenario 1.

The modelling results indicate that the median year for hydraulic gradient reversal in the Macalister coal seam at Lot 40 DY85 is late 2025, with some reversals occurring as late as 2035. The vertical gradient between the Springbok Sandstone and the Macalister coal seam remains consistently downward in all model realisations, with no reversals observed throughout the simulation period. The maximum particle migration distance from the Lot 40 DY85 boundary was 2,432 m across both scenarios.

Naphthalene is predicted to deplete earlier than benzene, with mean depletion years of 2027–2028 in the Springbok Sandstone and 2021 in the Macalister coal seam, consistent between scenarios. Early depletion (P5) was observed as early as 2018–2020, while later depletion estimates (P95) extended to 2040 in the Springbok and 2032 in the Macalister. Benzene showed longer persistence, with mean depletion projected around 2042–2043 in the Springbok and 2032 in the Macalister. P5 values for benzene ranged from 2026–2032, and P95 values extended to 2049 in the Springbok and 2045 in the Macalister.

The results from the assessment showed that pumping from the five CSG wells near the boundary of PL493 would have a minimal impact on the movement of contaminants from Lot 40 DY85 towards existing receptors. The simulated drawdown and associated flow fields demonstrate that the proposed five CSG wells do not induce hydraulic gradients that would increase the risk of contaminant migration, suggesting that the operation of these five wells under the current FDP wouldn't have any impact on the migration of contaminants residing within Lot 40 DY85. The assessment also showed that contaminants will attenuate before groundwater flows out of Lot 40

DY85, posing a negligible to small risk of off-site migration, and particle tracking shows that no on-site particles reach off-site receptors during the simulation period.

The results of predictive modelling scenarios indicated no significant difference in simulated contaminant concentrations between Scenario 1 and Scenario 2. This suggests that the five CSG wells near the PL493 boundary would have minimal impact on contaminant migration from Lot 40 DY85.

The following is a summary of the responses to the relevant EA0001613 information requests items.

## Item 9

Item 9 requests a groundwater assessment to understand the risks associated with the historical underground coal gasification activities on Lot 40 DY85. Responses to the specific actions under Item 9 are summarised as follows:

**Action 9(a)**

The potential influences and risks related to Lot 40 DY85 are associated with contaminants within the collapsed coal gasifier mobilising in the groundwater and flowing out of Lot 40 DY85 towards existing receptors. The potential for movement of contaminants out of the site is controlled by the timing of the reversal of the current inward hydraulic gradients to outward and the timing of the complete degradation of the contaminants of concern (COCs) in the groundwater. Risks are also associated with the probability of contaminants in the groundwater reaching any known existing receptors.

These risks were evaluated using a quantitative uncertainty analysis (UA) on a numerical groundwater flow model incorporating contaminant transport and particle tracking. The robust UA with an ensemble approach generated probabilistic results that allow for a quantitative evaluation of these risks. The results indicate that contamination will attenuate before hydraulic gradients recover and groundwater flows out of Lot 40 DY85, with a negligible to small risk of some contamination migrating out of the Lot 40 DY85. The particle tracking results, which are conservative and do not include attenuation of the contaminants, did not produce any model realisations that resulted in on-site particles reaching any off-site receptors within 200 years. The contaminant transport modelling indicates that all contaminants will completely attenuate by 2049 (i.e., within 24 years) with 95% confidence, which indicates that a 200-year predictive period is highly conservative. The groundwater monitoring results confirm the contaminant transport modelling outcome, demonstrating that benzene and naphthalene concentrations in the majority of monitoring bores — including Department of Resources (DOR) and Arrow bores screened within the Springbok Sandstone, Macalister Seam Package, and Wambo Seam Package — have been either below the limit of reporting (LOR) or showing an overall declining trend, with recent concentrations approaching or falling below the LOR (1 µg/L) and investigation limits. The modelling outcome along with groundwater monitoring results therefore conclude an extremely low risk of contamination migrating beyond Lot 40 DY85.

**Action 9(b)**

Justifications for relevant model inputs, including the model grid, boundary conditions, CSG well completion intervals and abstraction schedules, contaminant source and distribution, and contaminant attenuation processes, are presented in this section of the report. An acceptable and unbiased outcome in the model results was ensured by the following safeguards:

1. The base model was constructed on the leading established conceptualisation of the site.
2. A highly parameterised uncertainty quantification (and calibration) with a broad prior parameter uncertainty was used.
3. Only three iterations in the calibration/history matching were implemented to protect against bias and variance corruption resulting from defects in the conceptual model.
4. The history matching process was conducted using different types of data to avoid the bias that can result from relying on a single data type during calibration.
5. A prior-data conflict assessment was conducted, which indicated the potential presence of structural components within the system that are not currently captured in the numerical model or its underlying conceptual framework.
6. Finally, the effect of bias on decision-critical forecasts is expected to be minimised due to the comparative (i.e., relative) nature of the predictions; that is, predictions of changes and incremental influences (e.g., differences between simulations, times for gradient reversals) rather than predictions of absolute vales (e.g., hydraulic head distributions).

**Action 9(c)**

Studies have shown that neglecting dual-phase flow in modelling CSG depressurisation can lead to significant overestimation of pressure drawdowns, as demonstrated by comparisons of single-phase and multiphase models (Moore et al., 2013, 2015). This study showed that gas desorption reduces water permeability and displaces water from cleats, both of which limit drawdown propagation. OGIA (2021) addressed this in their regional impact assessments using a hybrid approach that approximates dual-phase effects within a modified single-phase model.

While the current model omits dual-phase flow, this is considered acceptable for predicting the contaminant migration from a former UCG site, as the overestimated drawdowns offer conservative forecasts—assuming accurate parameterisation and extraction rates.

History matching based on single-phase assumptions, however, can introduce bias, particularly due to the presence of gas reducing hydraulic conductivity, consistent with observed slow groundwater recovery. CSIRO (2023) warned that such fitting may underestimate hydraulic conductivity, leading to non-conservative predictions of contaminant movement. The current modelling addresses this by using time-varying, spatially localised hydraulic properties that can adjust downward, thereby mimicking gas-phase effects and minimising bias beyond the UCG site. Although absolute forecasts may still carry some bias, the comparative scenario analysis remains robust.

## Item 10

Item 10 requests clarification of the limitations and uncertainties associated with the modelling presented to support the SGP South Groundwater Assessment. It also requests a comparison of recharge and conceptualised and/or modelled rates in the SGP South Groundwater Assessment model with those used in the Office of Groundwater Impact Assessment OGIA (2019, 2021) models. Summaries of the specific responses are provided below.

**Action 10(a)**

<u>Limited data points resulting in simplification of contours and flow direction</u>

Groundwater contours and flow directions are not direct inputs to the models; rather, they are simulated based on the model inputs and history matching to observed data. The models are therefore simulating plausible flow directions and head distributions based on physical processes.

Groundwater quality being highly variable spatially

The spatial variability of the groundwater quality data was incorporated into the model using geostatistics to generate stochastic distributions of initial contaminant concentrations. This resulted in a set of 200 different concentration distributions representing realistic ranges of COC distributions, which were then used to run the ensemble of history matching simulations. This method ensures that the variability of groundwater is captured and constrained by all available data.

Reservoir pressure variations as a result of venting and issues as a result of kill water introduced at some bores

Safeguards were applied to analyse and exclude data that likely represent conditions affected by venting-related pressure changes and introduction of kill water. The groundwater monitoring data were reviewed by the third-party contractor, and the data that likely represent conditions affected by venting-related pressure changes and the introduction of kill water were then excluded from history matching to avoid biasing the history matching with inappropriate values. In addition, various data types were used in history matching to minimise the risk of history-matching and making predictions based on inconsistent datasets.

**Action 10(b)**

Recharge rates applied to the SGP South Groundwater Assessment model were assigned based on values from the OGIA (2019, 2021) model, with +-50% range for the UA ensembles. These rates are therefore consistent with those applied in the OGIA model.

Flow rate estimates for the Macalister coal seam, generated using the current model, were compared with those from the OGIA model, based on hydraulic gradients and ranges of input parameters (i.e., hydraulic conductivities and specific yields). The results indicate that the average modelled flow velocities at the same location near Lot 40 DY85 are nearly identical between the two models. The review indicated that the OGIA model assumed a single homogeneous specific yield for the entire Macalister coal seam layer, while the INTERA model assumed a range of specific yield values that encompass the OGIA value and range over two orders of magnitude. The results of this review therefore indicate that the INTERA and OGIA models have similar resultant flow velocities and that the INTERA model has ranges of input values that better represent ranges of flow velocities in the groundwater.

## Item 11

Item 11 requests additional information about model results. Summaries of the specific responses are as follows.

The year in which the hydraulic gradient at Lot 40 DY85 inverts

Model results indicate gradient reversal could occur as early 2025 and as late as 2035. There is no demonstrable difference between the results for the Scenario 1 (with the five CSG wells near the boundary of PL493) and Scenario 2 (excluding the five CSG wells near the boundary of PL493).

The vertical gradient between Springbok Sandstone and WCM Macalister

The vertical gradient between the Springbok Sandstone and the Macalister coal seam of the Walloon Coal Measures (WCM) varies throughout each model simulation; however, the modelled gradient remains downward for all realisations and for both CSG well scenarios.

The maximum particle migration distance from the boundary of Lot 40 DY85 over the simulation period

The maximum particle migration distance from boundary Lot 40 DY85 is 2,432 m and 2,425 m for Scenario 1 and Scenario 2, respectively.

The particle locations at the end of the simulation period

Maps showing the maximum extent of particle locations at the end of the model simulation period are included in Section 2.3.2.4 below.

Forecasted contaminant concentrations around Lot 40 DY85

Contaminant concentrations will vary with time as the contaminant plume degrades. The ensemble approach results in over 150 realisations with varying predicted contamination concentration fields.

Predictive contaminant transport modelling results indicate that there is no significant difference in the simulated contaminant concentrations between Scenario 1 and Scenario 2, suggesting that the five CSG wells near the boundary of PL493 would have a minimal impact on contaminant migration from Lot 40 DY85.

Predictive year at which the hydrocarbon plume would deplete

The model UA approach results in a range of predictive years for plume depletion, presented as P5, P50 (mean), and P95 probabilities of plume attenuation by a given year. Since benzene attenuation takes slightly longer than naphthalene, benzene values are used to characterise the overall contaminant plume.

The P50 and P95 probabilities for the year of contaminant plume attenuation in the Springbok Sandstone and Macalister coal seam are summarised below.

Benzene in Springbok Sandstone is forecast to attenuate completely between 2032 and 2049, based on the 95% confidence interval. The ensemble's mean forecast year is 2042 for Scenario 1 and 2043 for Scenario 2.

In the Macalister coal seam, benzene is forecast to attenuate completely between 2026 and 2045. The mean forecast year for complete degradation of benzene is 2032 for both Scenario 1 and Scenario 2.

**Conclusion**

Based on the model results and the responses to the actions requested in EA0001613, it is concluded that Condition Water 1B is no longer required to protect groundwater or environmental values. Removal of this condition will enable Arrow to optimise CSG well placement without increasing the potential for adverse groundwater impacts associated with historical UCG activities on Lot 40 DY85.

# Table of Contents



# List of Appendices

# List of Figures

# List of Tables

# Acronyms

| | |
|---|---|
| µg/L | Micrograms per liter |
| INTERA | INTERA Geosciences Pty Ltd |
| BTEX | Benzene, toluene, ethylbenzene, xylene |
| CMA | Cumulative Management Area |
| COC | Contaminants of concern |
| CSG | Coal seam gas |
| DETSI | Department of the Environment, Tourism, Science and Innovation |
| DOR | Department of Resources |
| FDP | Field Development Plan |
| km | Kilometre |
| LOR | Limit of reporting |
| OGIA | Office of Groundwater Impact Assessment |
| PL | Petroleum lease |
| SGP | Surat Gas Project |
| UA | Uncertainty Analysis |
| UCG | Underground coal gasification |
| UWIR | Underground water impact report |
| WCM | Walloon Coal Measures |
| WEL | MODFLOW well boundary package |

# 1.0 SGP South Groundwater Assessment

## 1.1 Introduction

INTERA Geosciences Pty Ltd (INTERA) was commissioned by Arrow Energy to develop numerical groundwater flow, contaminant transport, and particle tracking models, and to conduct scenario testing based on the recently developed groundwater flow and transport model (INTERA, 2024). This work supports the EA0001613 Amendment for Arrow's SGP South operations, specifically to facilitate the removal of condition Water 1B, which restricts the placement of coal seam gas (CSG) production wells within 10 km of Lot 40 DY85. The main objective of the scenario testing is to investigate and quantify the potential impact of five wells, located near the south-western boundary of PL493, on the migration of contaminants from Lot 40 DY85.

The general approach involves running two model scenarios:

- The first scenario includes abstraction from the five wells located near the south-western boundary of PL493 (exist within 10 km of Lot 40 DY85), as well as abstraction from all CSG wells not operated by Arrow Energy, the 55 wells within PL253 (associated with the approved Arrow Energy EA0001401 PL253 Stage 1 activities), and the 28 wells located within PL493. The above-mentioned 55 wells were updated for this scenario with revised extraction rates and operation years to reflect Arrow's current Field Development Plan (FDP) for PL253.
- The second scenario excludes the five wells but includes all other abstraction wells incorporated in the first scenario.

The differences between the results of each scenario were then evaluated to quantify the incremental impact of the five wells on contaminant migration from Lot 40 DY85.

The outcome of model scenarios was then used to respond to the groundwater-related items in the EA0001613 Information Request issued by DETSI on 11 June 2025. The specific responses are included in Section 2 of this report.

## 1.2 CSG Wells and Scenarios

The model scenarios include a set of CSG wells divided into following groups:

- All non-Arrow CSG wells.
- The updated 55 wells from the approved Arrow Energy PL253 stage 1 activities (hereafter referred to as the "55 wells").
- The 28 wells in PL493 (hereafter referred to as the "Blue Circle Wells").
- The 5 wells in PL493 near the south-west boundary within 10 km of Lot 40 DY85 (hereafter referred to as the "5 Red Circle Wells"). These wells are proposed to be drilled on two pads.

Figure 1-1 shows the location of all the Arrow CSG wells, including the two drill pads that will accommodate the 5 Red Circle Wells. Figure 1-2 displays a zoomed-in view of the 5 Red Circle Wells.

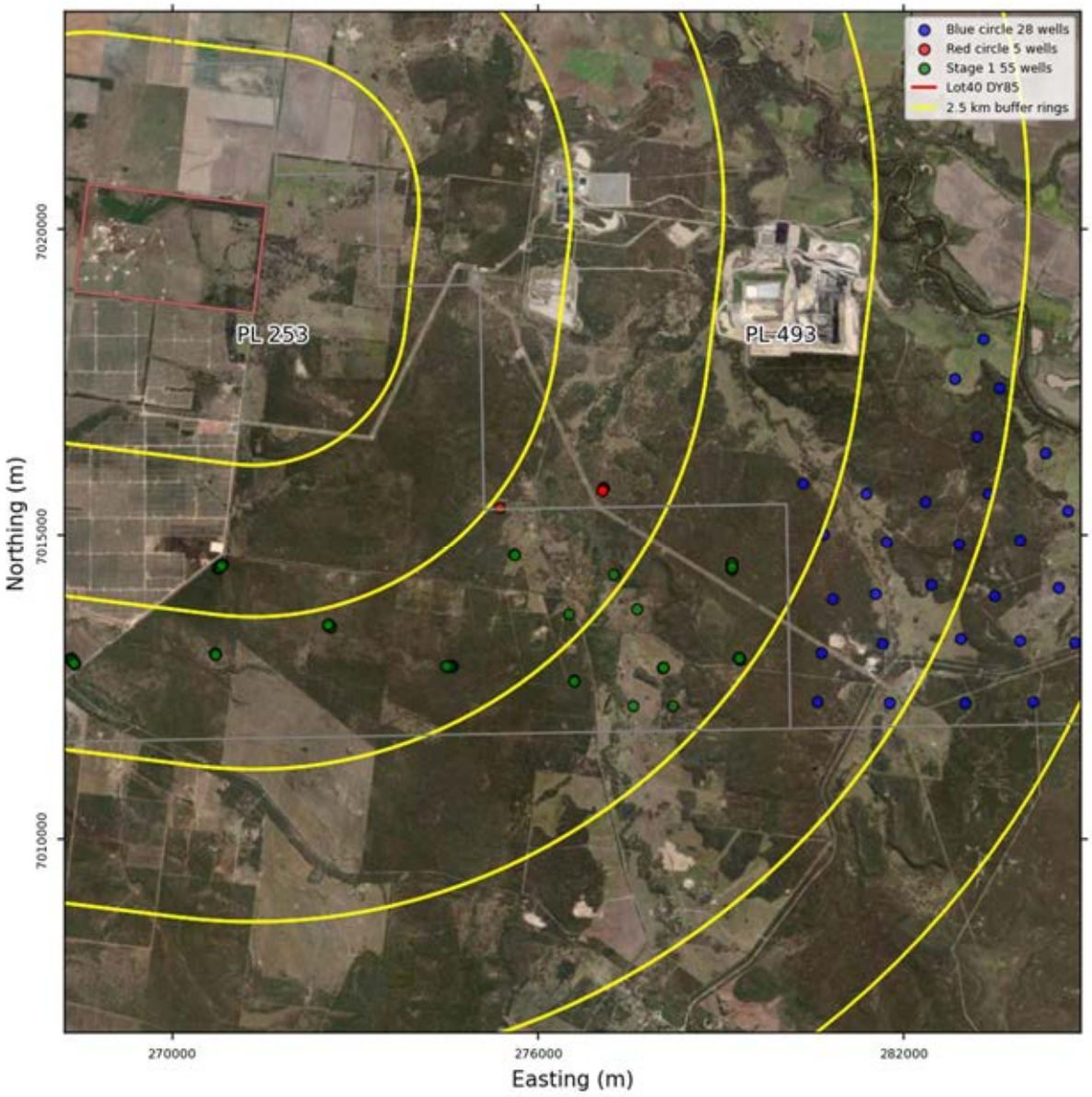


Figure 1-1 – Map of the updated CSG wells (both Arrow and non-Arrow) and the boundary of the PLs, including PL253 and PL493. Yellow lines indicate 2.5km concentric buffers from Lot 40 DY85.


Figure 1-2 – Map of the 5 Red Circle Wells and the boundary of the PL253 and PL493.

The CSG wells are planned to be completed with the top of the screen within either the Wambo, Argyle, Kogan, or Macalister coal seams, and the bottom of the screen within the Condamine coal seam for all wells. Table 1-1 provides a number of wells with screens planned to be completed within specific formation intervals. Detailed completion interval for each CSG well is provided in Appendix A.

Table 1-1 – Number of wells allocated to different screen intervals.

| Screen Interval (coal seam from – to) | Number of wells |
|---|---|
| Macalister - Condamine | 35 |
| Kogan - Condamine | 41 |
| Wambo - Condamine | 8 |
| Argyle - Condamine | 4 |
| **Total Wells** | **88** |

The simulated scenarios, described below, differ based on whether the 5 Red Circle Wells are included or excluded. These five wells are located near the southern boundary of PL493 within 10 km of Lot 40 DY85, as explained above.

### 1.2.1 Model Scenario Descriptions

Developed based on the history-matched Arrow's PL253 numerical model (Section 1.3.1), scenario 1 includes all the wells listed in Section 1.2. This scenario, therefore, includes the following wells:

- Non-Arrow CSG wells.
- 55 wells
- 28 Blue Circle Wells
- 5 Red Circle Wells

Scenario 2 is the same as Scenario 1 except that the 5 Red Circle Wells are excluded. This scenario, therefore, includes the following wells:

- Non-Arrow CSG wells.
- 55 wells
- 28 Blue Circle Wells

Figure 1-3 shows the pumping rates over time for Scenarios 1 and 2, and for the 5 Red Circle Wells. The operation of the wells is planned to start in 2028, reaching full capacity between 2029 and 2032, with a combined peak extraction rate of approximately 9,729 $m^3/d$, inclusive of the 5 Red Circle Wells. The 5 Red Circle Wells are expected to commence operation in 2030 with a combined rate of up to 1,133 $m^3/d$.

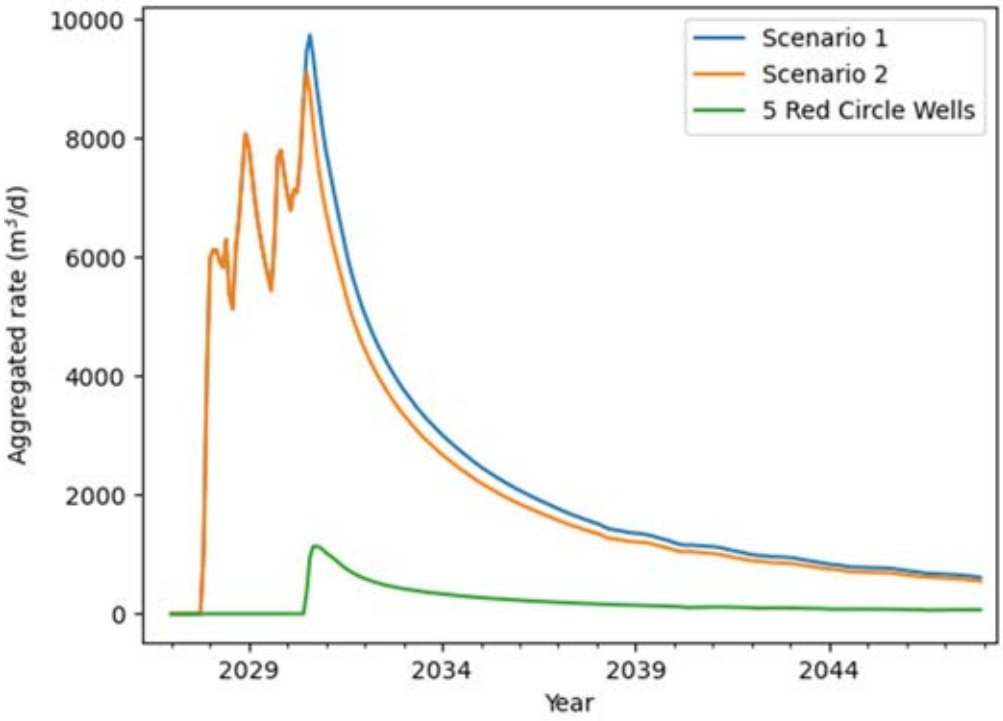


Figure 1-3 – Time series of the allocated pumping rates for scenarios 1 and 2.

## 1.3 Methodology

The predictive model scenarios described earlier were developed using Arrow's PL253 numerical model (INTERA, 2024), history-matched to data up to September 2024. Arrow PL253 numerical model is summarised in Section 1.3.1, with full details available in INTERA (2024) (see Appendix B, Section 3).

For predictive model scenarios, a total of 120 realisations were used and updated with the current FDP (updated pumping rates and schedules for 55 wells, Blue Circle Wells, and 5 Red Circle Wells described in Section 1.2) to simulate the effects of the 5 Red Circle Wells. Arrow's updated pumping rates and schedules were incorporated into the predictive models using the WEL package, following the same approach as the Arrow's PL253 numerical model. Wells were assigned to target layers based on the well information presented in Appendix A. For deviated wells, a linear trajectory between the top and the bottom grid cells was calculated and assigned to all intersecting grid cells.

Extraction rates from existing (pilot) and proposed Arrow CSG wells were distributed across screened layers using a transmissivity weighted approach to ensure that the volume extracted per layer was proportional to the relative hydraulic conductivity and thickness.

### 1.3.1 Arrow PL253 – Numerical Model Summary

The Arrow PL253 model (INTERA, 2024), which simulates groundwater flow and contaminant transport processes, was developed using MODFLOW 6 and is presented in the Consolidated Modelling Report (Appendix B). Figure 1-4 shows the model domain, the CSG wells (both Arrow and non-Arrow), the PLs, and the 2.5 km concentric buffer zones around Lot 40 DY85.

The Arrow PL253 model is a three-dimensional (3D) numerical model based on OGIA (2021) and AGE (2020), but its layers were updated using bore log data supplied by Arrow, resulting in an expansion to a total of 18 layers. Additional details about the Arrow PL253 model layers is provided in Section 3.1.2 of Appendix B.

The model employs a quadtree unstructured grid enabling local refinement in areas of interest, such as the Lot40 DY 85 (referred as Lot40) and the Hopeland pilot-test site. It was opted to switch from a Voronoi mesh, which was used in the previous model (AGE, 2020), to a quadtree grid as this facilitates a fully scripted workflow and removes the reliance on proprietary software. The quadtree grid was generated using the opensource software GRIDGEN (Lien et al, 2017). The vertical discretization of the Arrow PL253 model is implemented for 18 model layers explained in the previous paragraph. Additional details about the Arrow PL253 model grid are in Section 3.1.3 of Appendix B.

The model boundary conditions incorporate bore pumping rates and schedules as provided by Arrow. Non-Arrow CSG extraction rates were based on the most recent generation of regional cumulative impact assessment modelling as presented in OGIA (2021). External boundary conditions applied at the edges of the model domain were also derived from OGIA (2021). Model boundary conditions are described in more detail in Section 3.1.4 of Appendix B.

The model incorporates estimates of source terms for contaminants within the coal gasifiers. These source terms – including contaminant source concentrations and estimated degradation rates – were based on contaminant concentrations' ranges identified in nearby wells. These concentrations were then used to develop stochastic realisations of source distributions, which were incorporated

into the model simulations to evaluate the overall risk of contaminant migration out of Lot 40 DY85. The ranges of source terms were compared with historical and recent contaminant concentration data provided by Arrow, as well as with the data from a similar coal gasification plant reported in the literature (EHS Support, 2014; WMV Environmental Pty Ltd, 2014; and Mallett, 2018) and were found to be consistent with these data. The contaminant source terms are discussed in more detail in Section 2.1.3.1 in this report. Additional details about the contaminant source terms are in Section 4.3.1.2 of Appendix B.

History matching in the Arrow PL253 model was conducted using groundwater level time series, vertical head differences, and contaminant concentration time series for benzene and naphthalene. A highly parameterised approach was applied for history matching over the period from January 2000 to December 2024 using data available up to September 2024. Additional details about history matching and calibration of the Arrow PL253 model are in Section 3.2 and Section 4.3.2 of Appendix B.

The model simulates groundwater head and the distribution of contaminants – i.e., benzene and naphthalene concentrations – considering mechanical dispersion, molecular diffusion, natural attenuation (sorption and biodegradation / decay), and dual domain mass transfer processes continuously occurring within the subsurface. Additional details about the contaminant transport modelling functions in the Arrow PL253 model are in Section 4.3.1 of Appendix B.

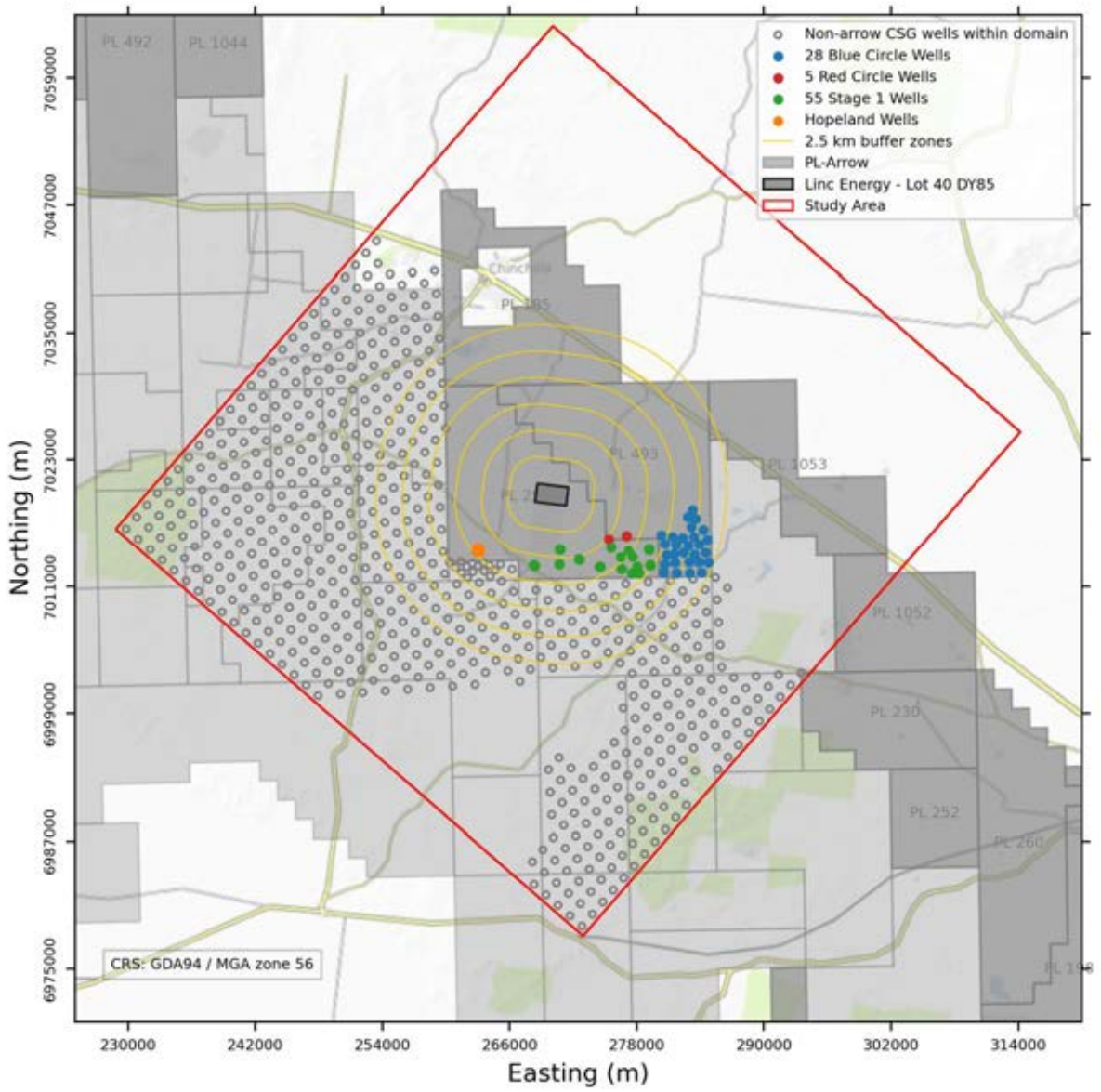


Figure 1-4 – Map of study area (model domain), PLs, Lot 40 DY85 boundaries and CSG wells. Yellow lines indicate concentric 2.5 km buffer zones from Lot 40 DY85.

## 1.4 Impact Assessment

The goal of this assessment is to understand the impact of the 5 Red Circle Wells on the migration of contaminants – i.e., benzene and naphthalene – from Lot 40 DY85. This analysis focuses on the incremental impact of these wells on hydraulic gradient reversal within Lot 40 DY85, including the timing of potential contaminant migration beyond its boundary, the effect on contaminant attenuation, the extent of residual contamination at the time of reversal, and ultimately, the overall extent of contaminant transport.

The following section presents the results from the simulation of Scenarios 1 and 2, focusing on the relative effect from the 5 Red Circle wells on:

- Gradient reversal difference between scenarios 1 and 2.

- Contaminant attenuation difference between scenario 1 and 2.
- Particle migration from Lot 40 DY85 difference between scenario 1 and 2.

### 1.4.1 Gradient reversal difference between scenarios

Figure 1-5 shows the year in which gradient reversal occurs for the simulated scenarios. The mean year of gradient reversal for both Scenarios 1 and 2 is 2025, with the maximum year being 2035. Almost no difference is observed between scenarios, indicating that the proposed abstraction from the 5 Red Circle Wells is expected to have a negligible impact on the rate of recovery and reversal of the gradient in and around Lot 40 DY85.

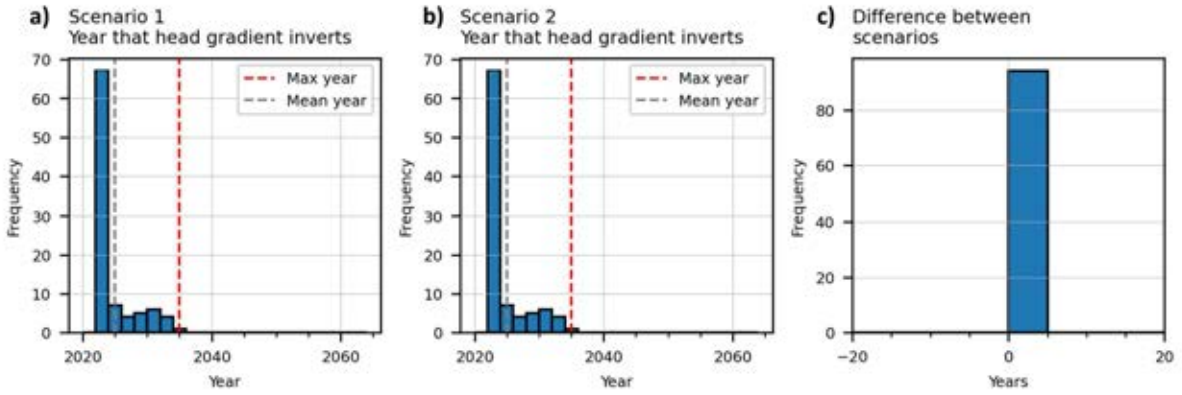


Figure 1-5 - Gradient reversal histograms for (a) Scenario 1, (b) Scenario 2, and (c) the difference in years between the two scenarios.

### 1.4.2 Drawdown differences between scenarios

Drawdowns from Scenario 1 were subtracted from those in Scenario 2 to calculate incremental drawdowns associated with the 5 Red Circle Wells. Maps showing the modelled absolute heads in the Springbok Sandstone for Scenario 1 (Figure 1-6) and Scenario 2 (Figure 1-7) indicate very little difference in heads due to these wells. The map of incremental drawdowns for the Springbok Sandstone (Figure 1-8) shows that drawdowns induced by the five Red Circle Wells are less than one meter throughout the model domain.

Similarly, maps of modelled absolute heads in the Macalister coal seam layer for Scenario 1 (Figure 1-9) and Scenario 2 (Figure 1-10) show minimal differences, with a maximum incremental drawdown of approximately 4.5 m (Figure 1-11).

For the Condamine coal seam layer, maps for Scenario 1 (Figure 1-12) and Scenario 2 (Figure 1-13) indicate minor but visible differences in heads, with a maximum incremental drawdown of about 27 m across the model domain (Figure 1-14).

Overall, these results indicate that the five Red Circle Wells will have minimal impact on future drawdowns in the Springbok Sandstone and Macalister formations across the model domain.

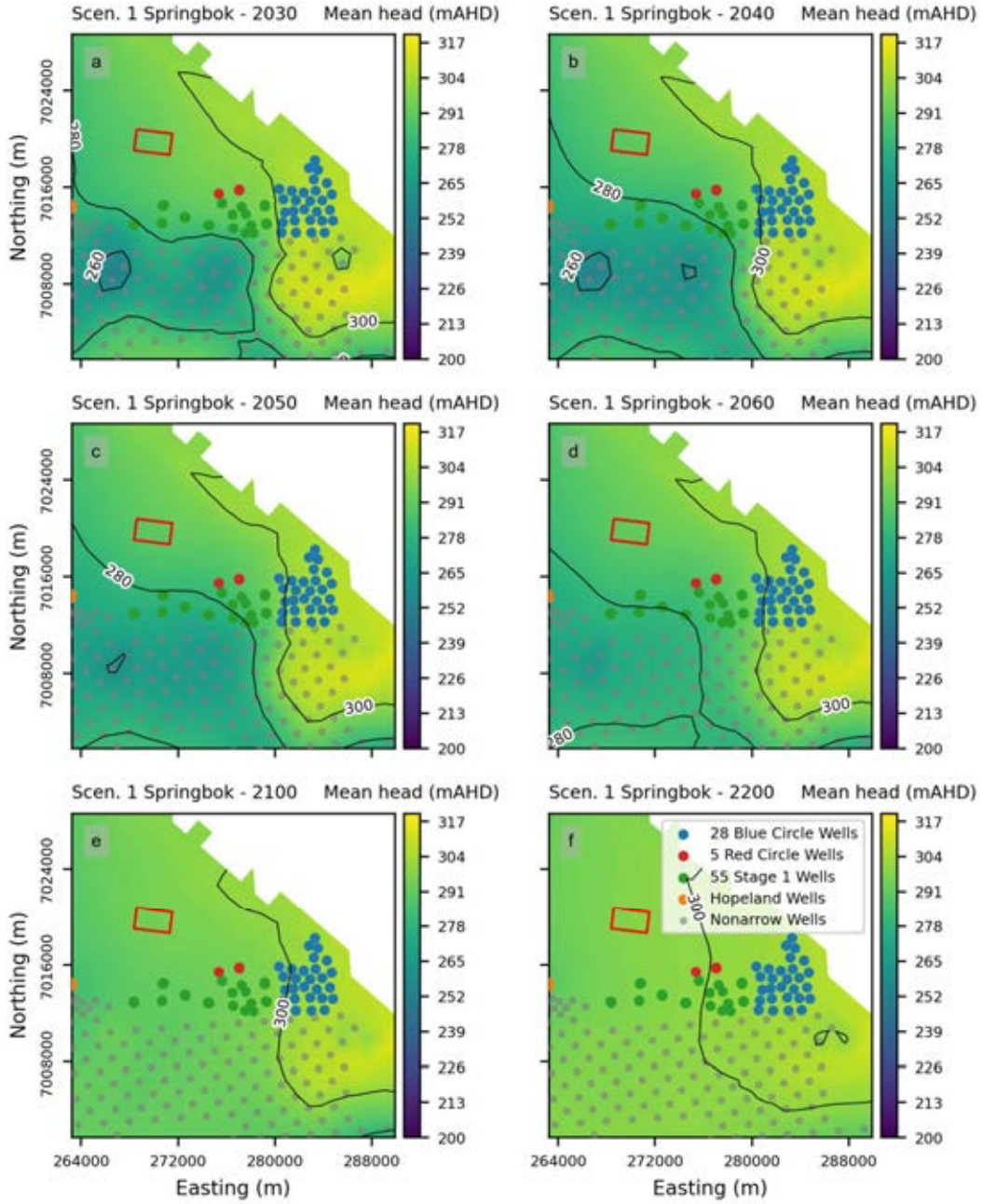


Figure 1-6 – Maps showing the average ensemble heads for Scenario 1 in Springbok Sandstone model layer associated with the 5 Red Circle Wells for model years 2030, 2040, 2050, 2060, 2100, and 2200. The red rectangle indicates the location of Lot 40 DY85.

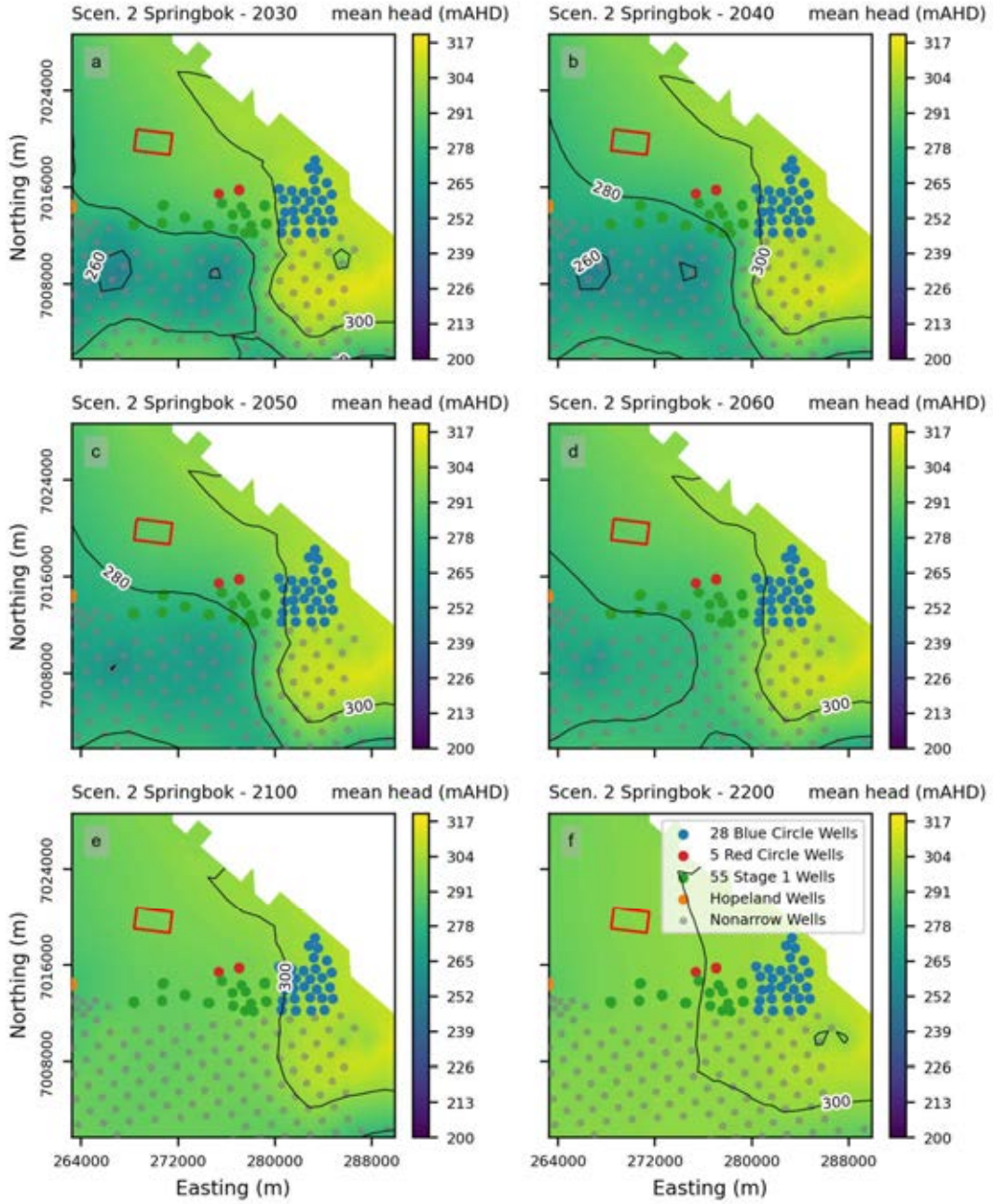


Figure 1-7 – Maps showing the average ensemble heads for Scenario 2 in Springbok Sandstone model layer associated with the 5 Red Circle Wells for model years 2030, 2040, 2050, 2060, 2100, and 2200. The red rectangle indicates the location of Lot 40 DY85.

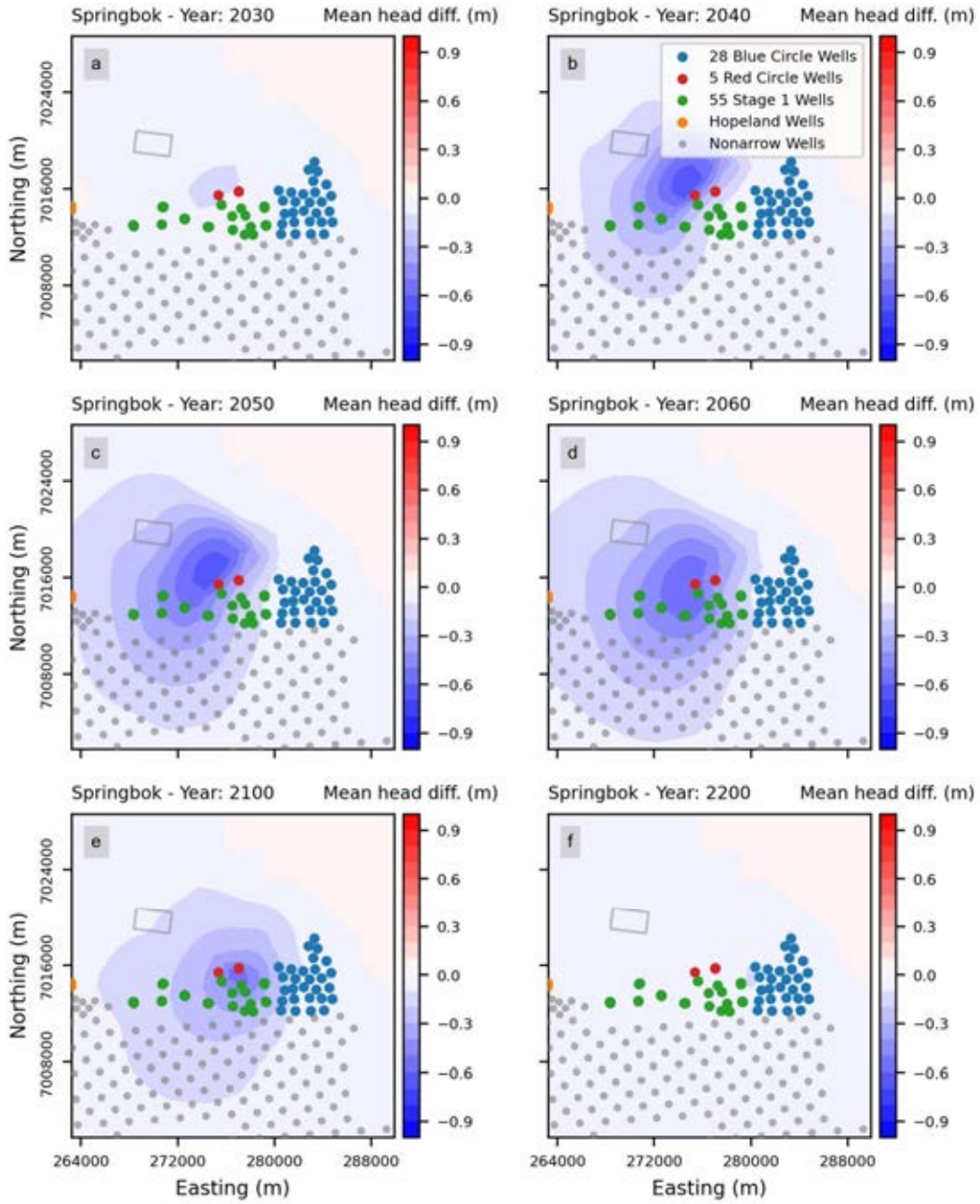


Figure 1-8 – Maps showing incremental drawdowns in the Springbok Sandstone model layer associated with the 5 Red Circle Wells for model years 2030, 2040, 2050, 2060, 2100, and 2200. The grey rectangle indicates the location of Lot 40 DY85.

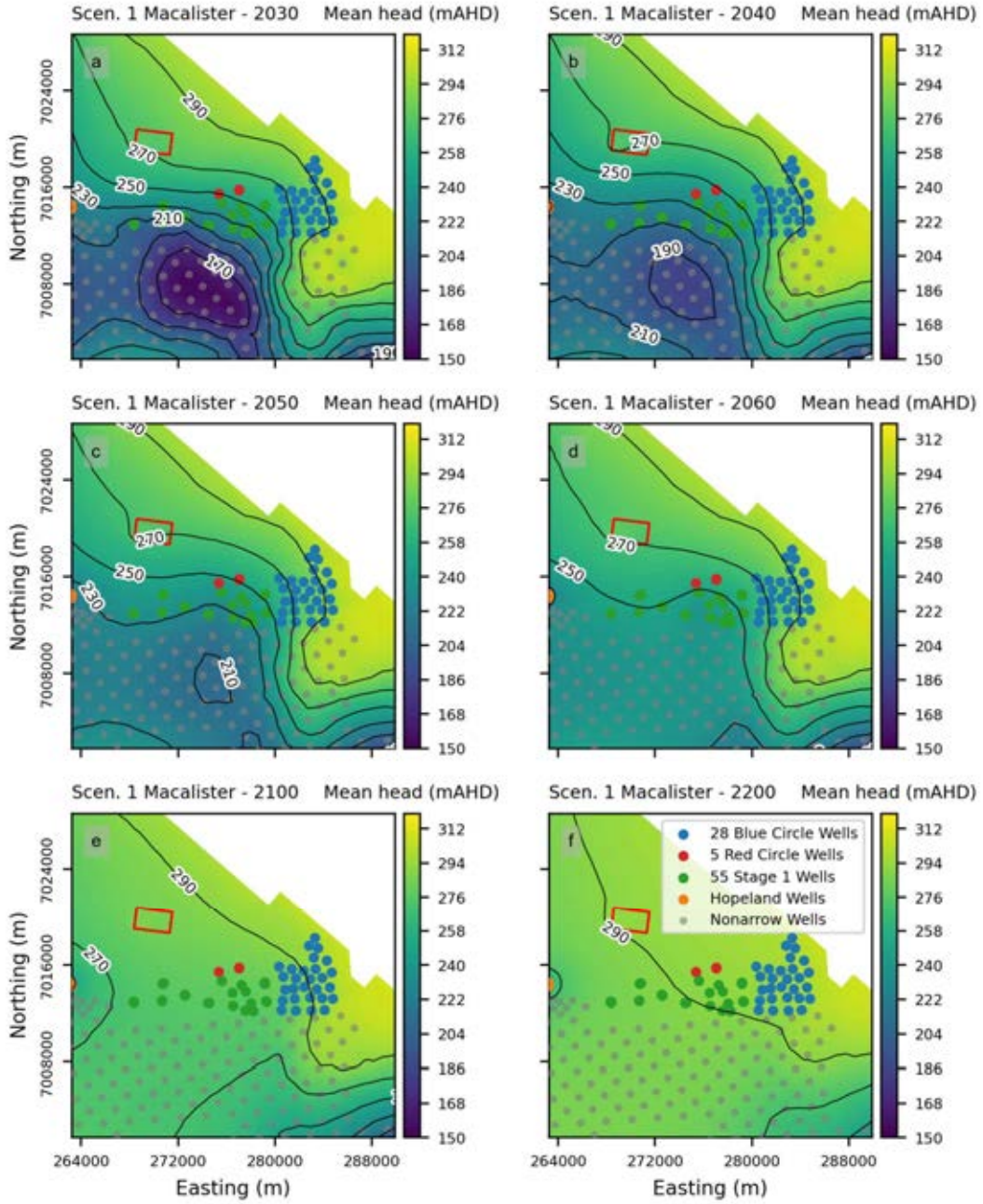


Figure 1-9 – Maps showing the average ensemble heads for Scenario 1 in Macalister coal seam model layer associated with the 5 Red Circle Wells for model years 2030, 2040, 2050, 2060, 2100, and 2200. The red rectangle indicates the location of Lot 40 DY85.

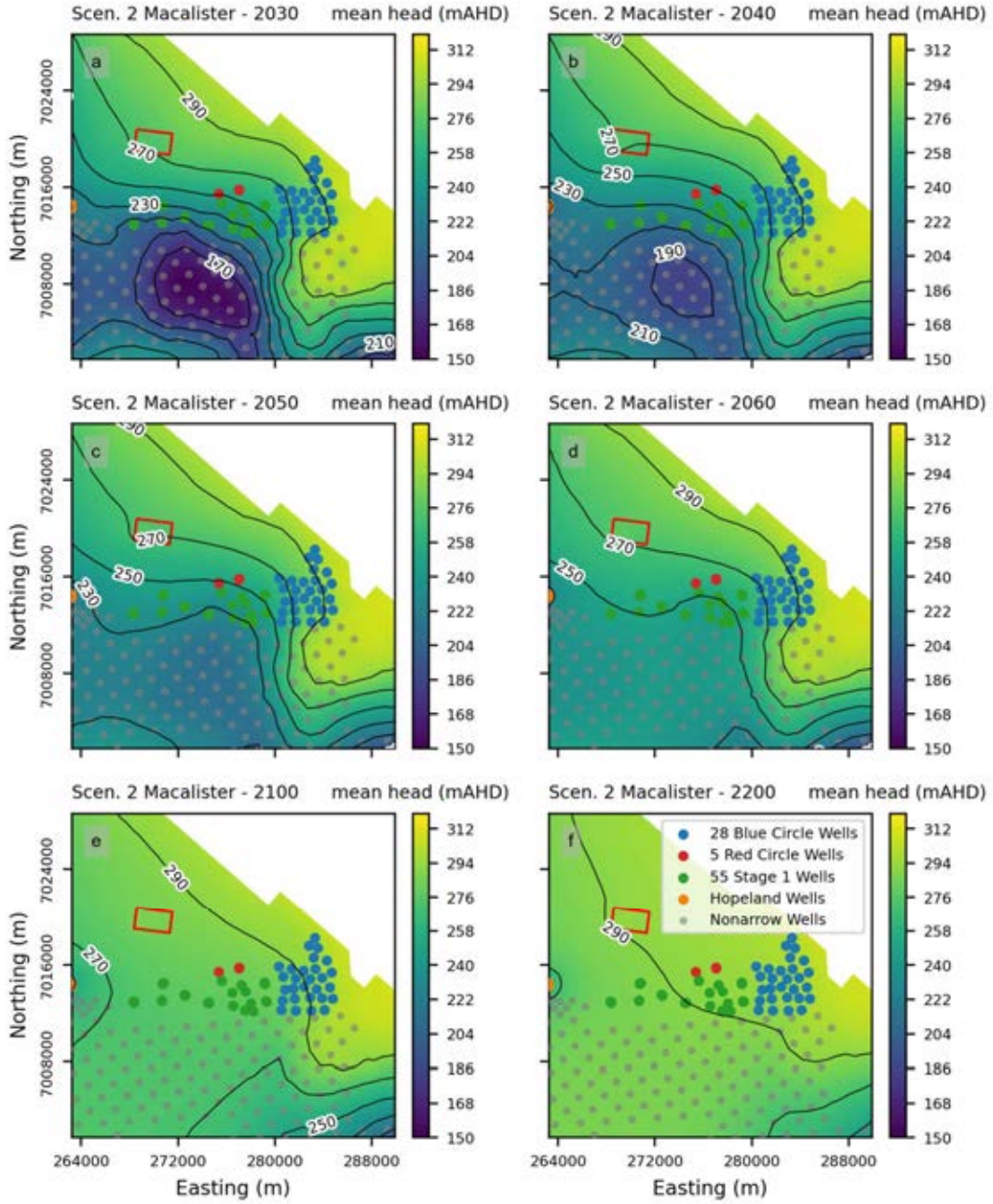


Figure 1-10 – Maps showing the average ensemble heads for Scenario 2 in Macalister coal seam model layer associated with the 5 Red Circle Wells for model years 2030, 2040, 2050, 2060, 2100, and 2200. The red rectangle indicates the location of Lot 40 DY85.

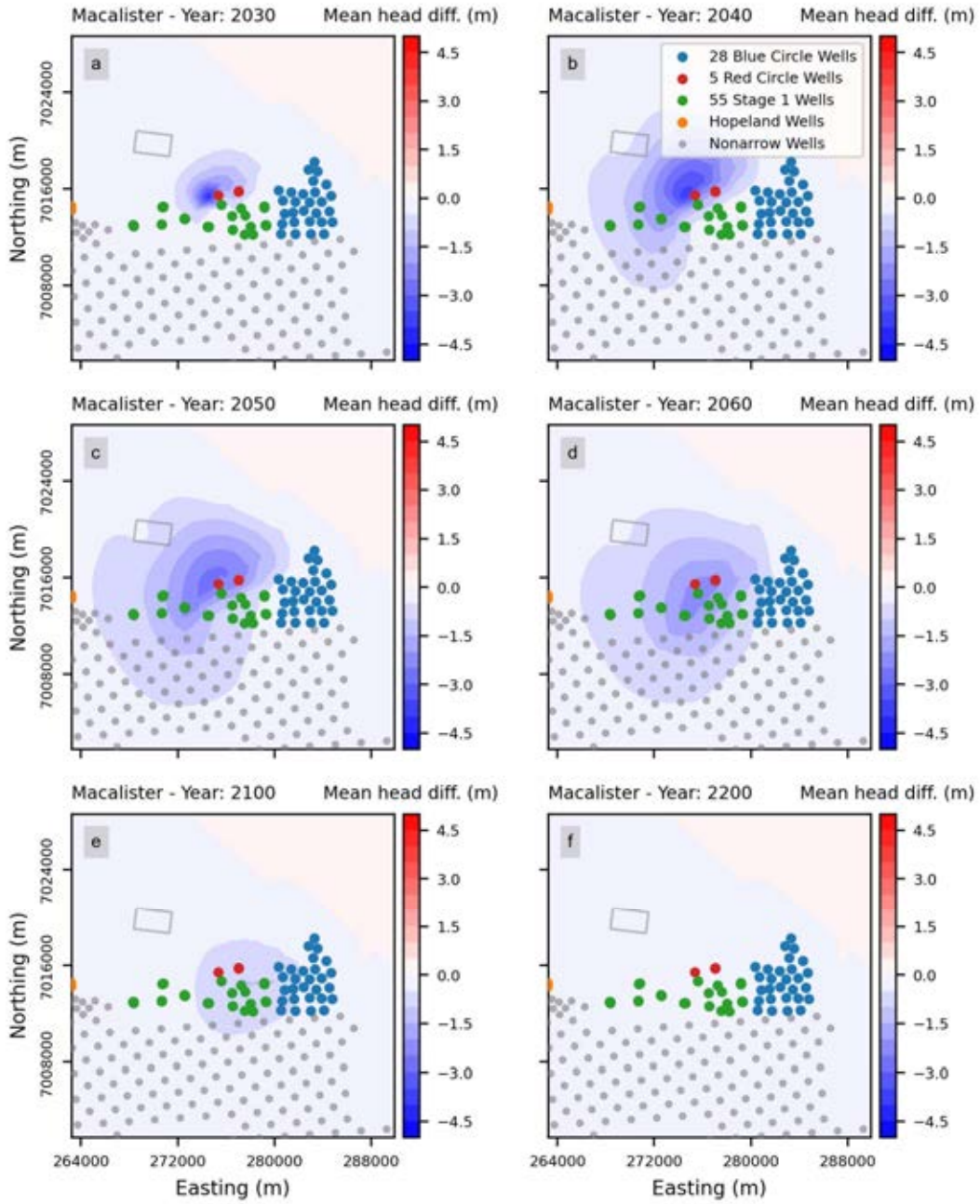


Figure 1-11 – Maps showing incremental drawdowns in the Macalister coal seam model layer associated with the 5 Red Circle Wells for model years 2030, 2040, 2050, 2060, 2100, and 2200. The grey rectangle indicates the location of Lot 40 DY85.

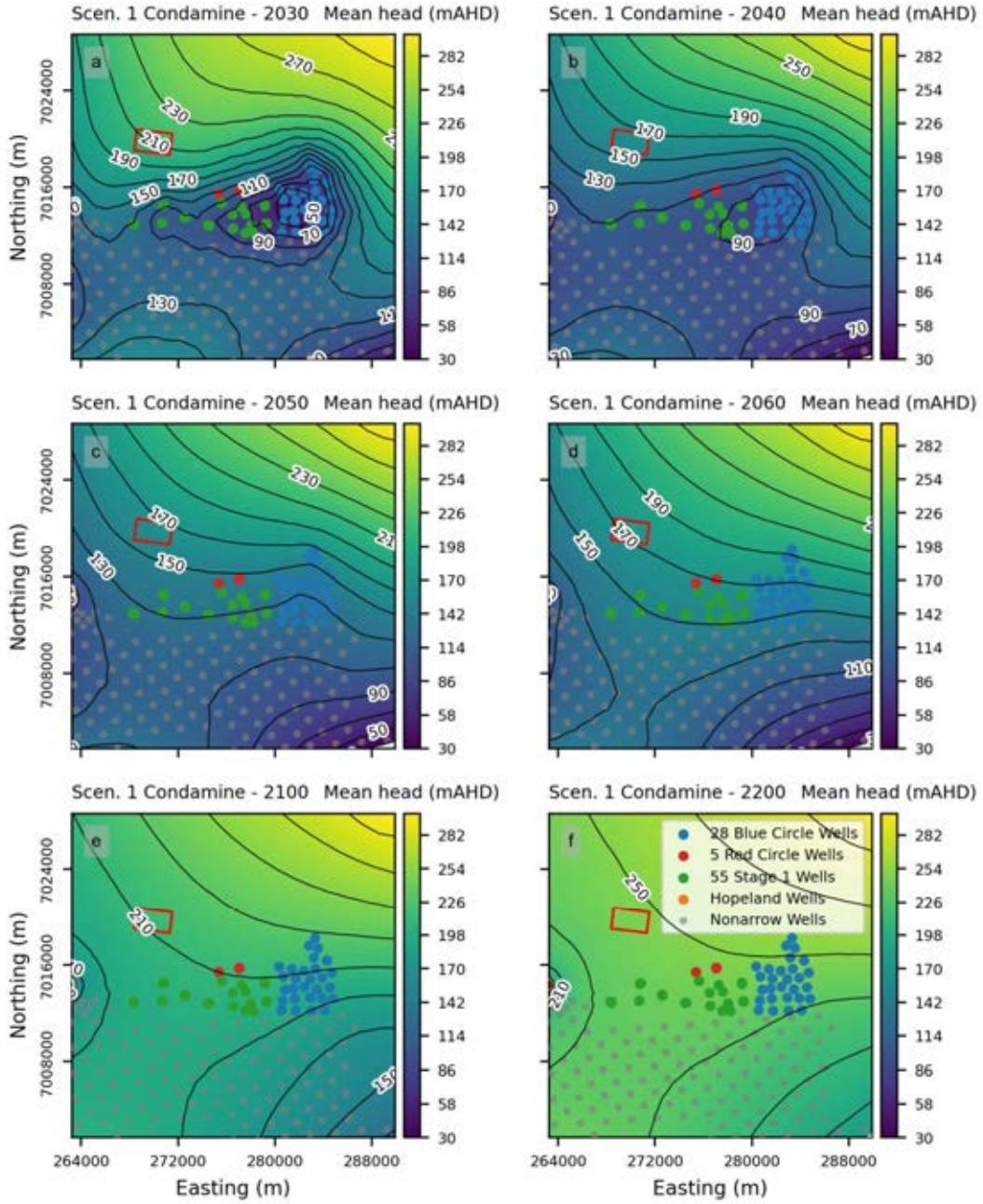


Figure 1-12 – Maps showing the average ensemble heads for Scenario 1 in Condamine coal seam model layer associated with the 5 Red Circle Wells for model years 2030, 2040, 2050, 2060, 2100, and 2200. The red rectangle indicates the location of Lot 40 DY85.

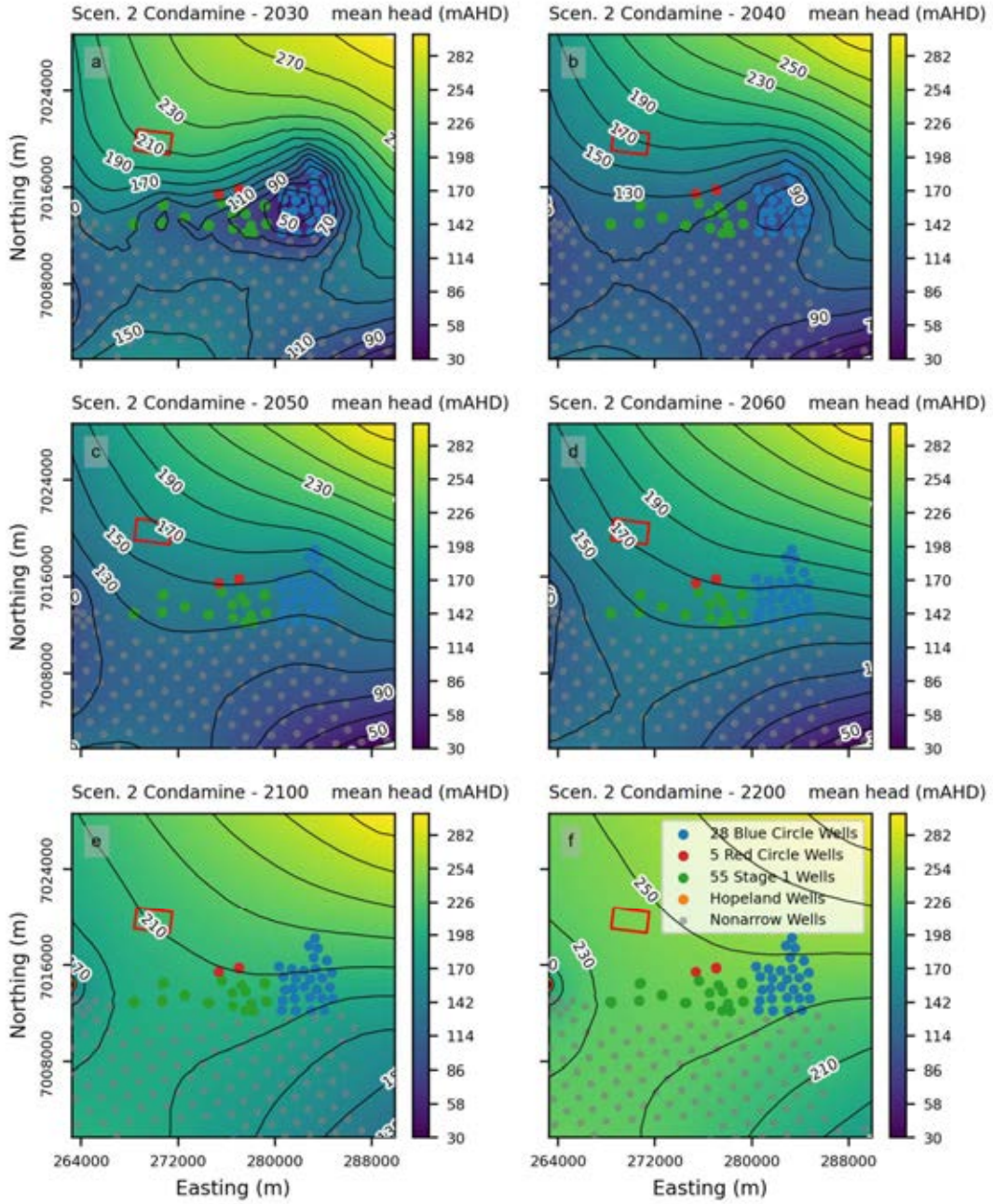


Figure 1-13 – Maps showing the average ensemble heads for Scenario 2 in Condamine coal seam model layer associated with the 5 Red Circle Wells for model years 2030, 2040, 2050, 2060, 2100, and 2200. The red rectangle indicates the location of Lot 40 DY85.

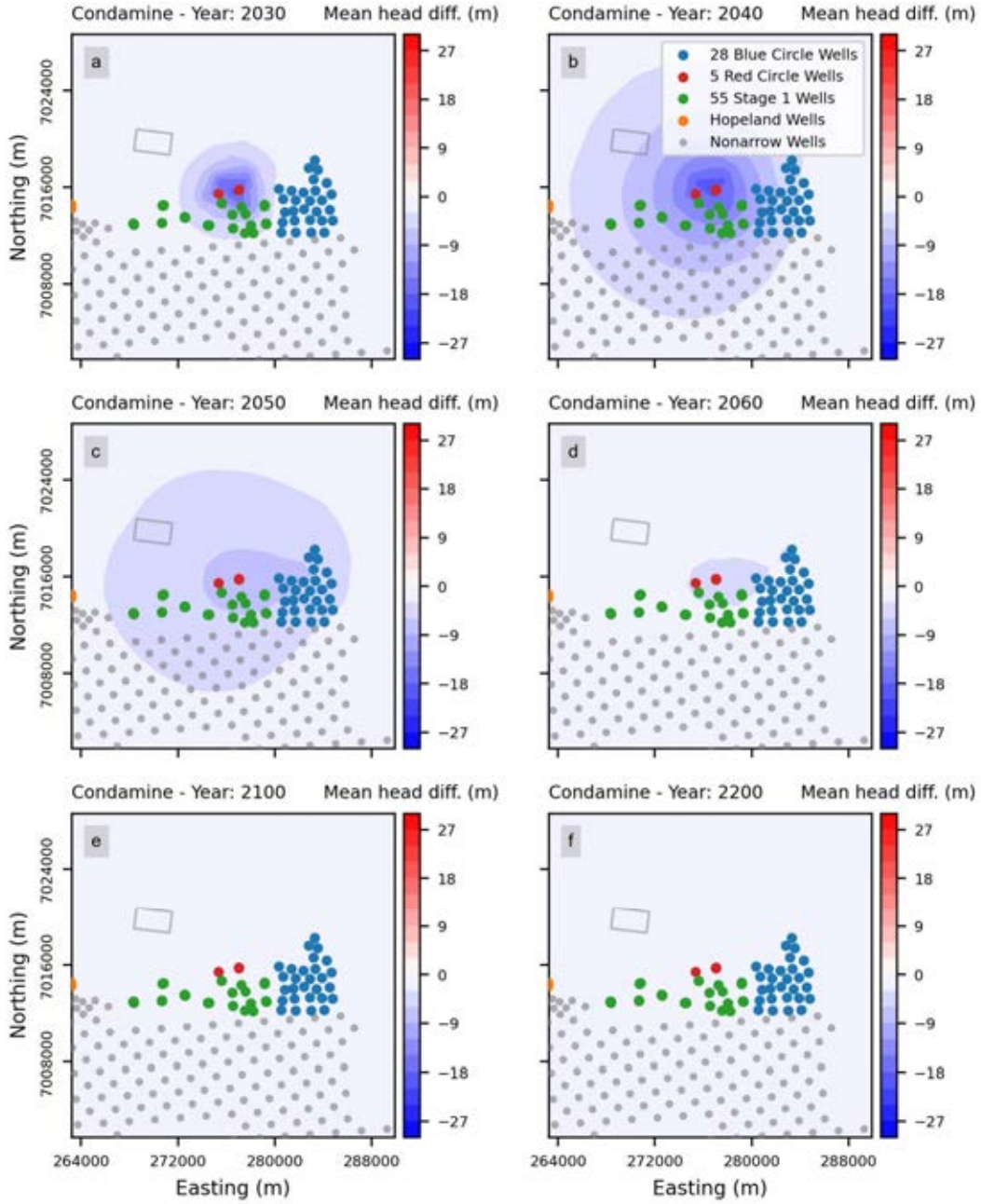


Figure 1-14 – Maps showing incremental drawdowns in the Condamine coal seam model layer associated with the 5 Red Circle Wells for model years 2030, 2040, 2050, 2060, 2100, and 2200. The grey rectangle indicates the location of Lot 40 DY85.

### 1.4.3 Contaminant attenuation difference between scenarios

Modelled mean contaminant distributions throughout the predictive period for each of the predictive scenarios, using benzene and naphthalene concentrations as representative constituents, were plotted on similar maps of the study area. To assess the impact of the five Red Circle Wells, the modelled concentrations in each cell for Scenario 2 were subtracted from those for Scenario 1, resulting in maps showing the incremental differences in concentration distributions attributable to these wells.

### 1.4.3.1 Benzene

Modelled mean benzene concentrations in the Springbok Sandstone (Figure 1-15 and Figure 1-16) and the Macalister coal seam (Figure 1-18 and Figure 1-19) show complete attenuation between model years 2030 and 2080 for both scenarios. Differences in concentrations between Scenario 1 and Scenario 2 (Figure 1-17 and Figure 1-20) are minimal, with values less than 1E-04 µg/L across all model years.

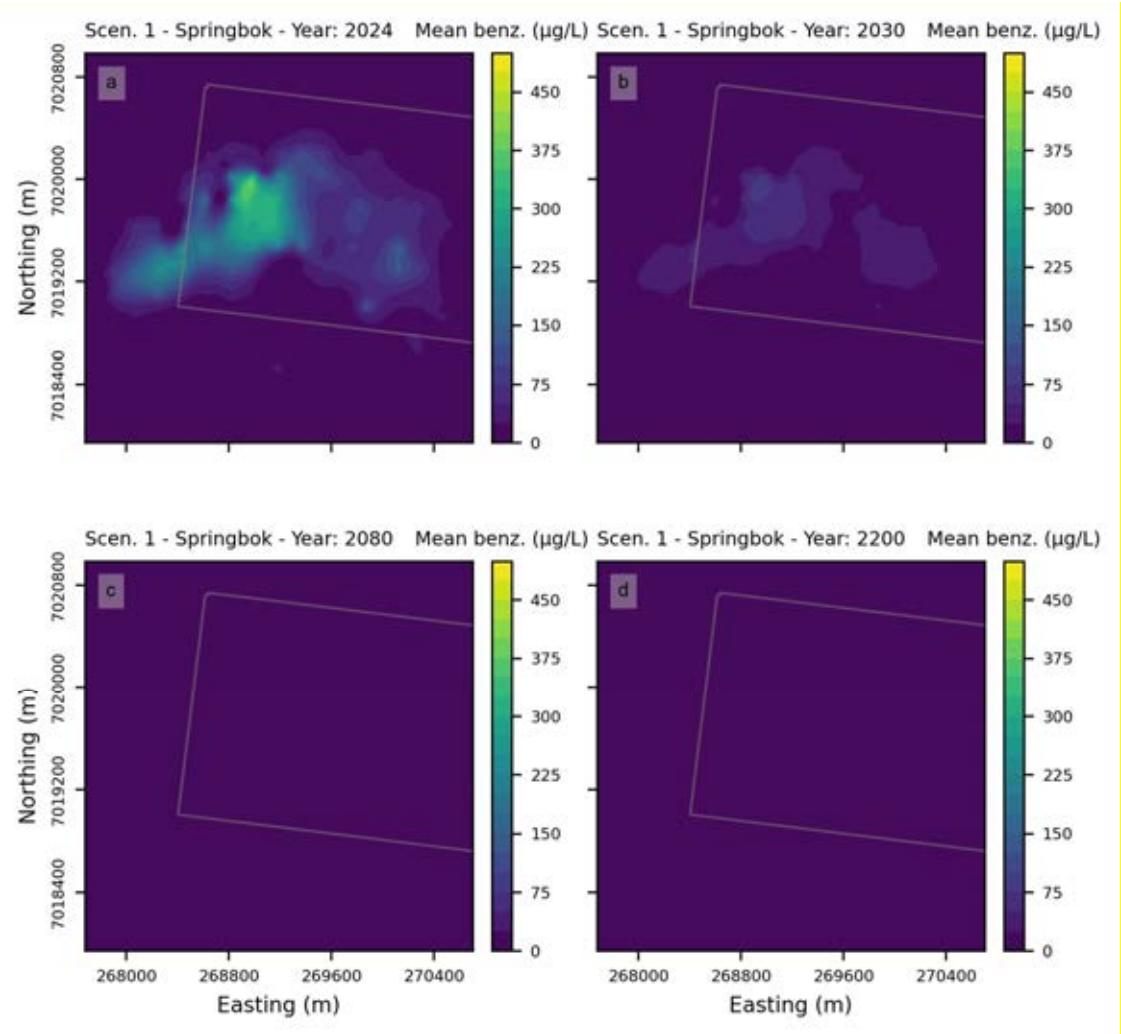


Figure 1-15 – Maps showing the average ensemble concentration of benzene for Scenario 1 in Springbok Sandstone model layer associated with the 5 Red Circle Wells for model years 2024, 2030, 2080, 2200.

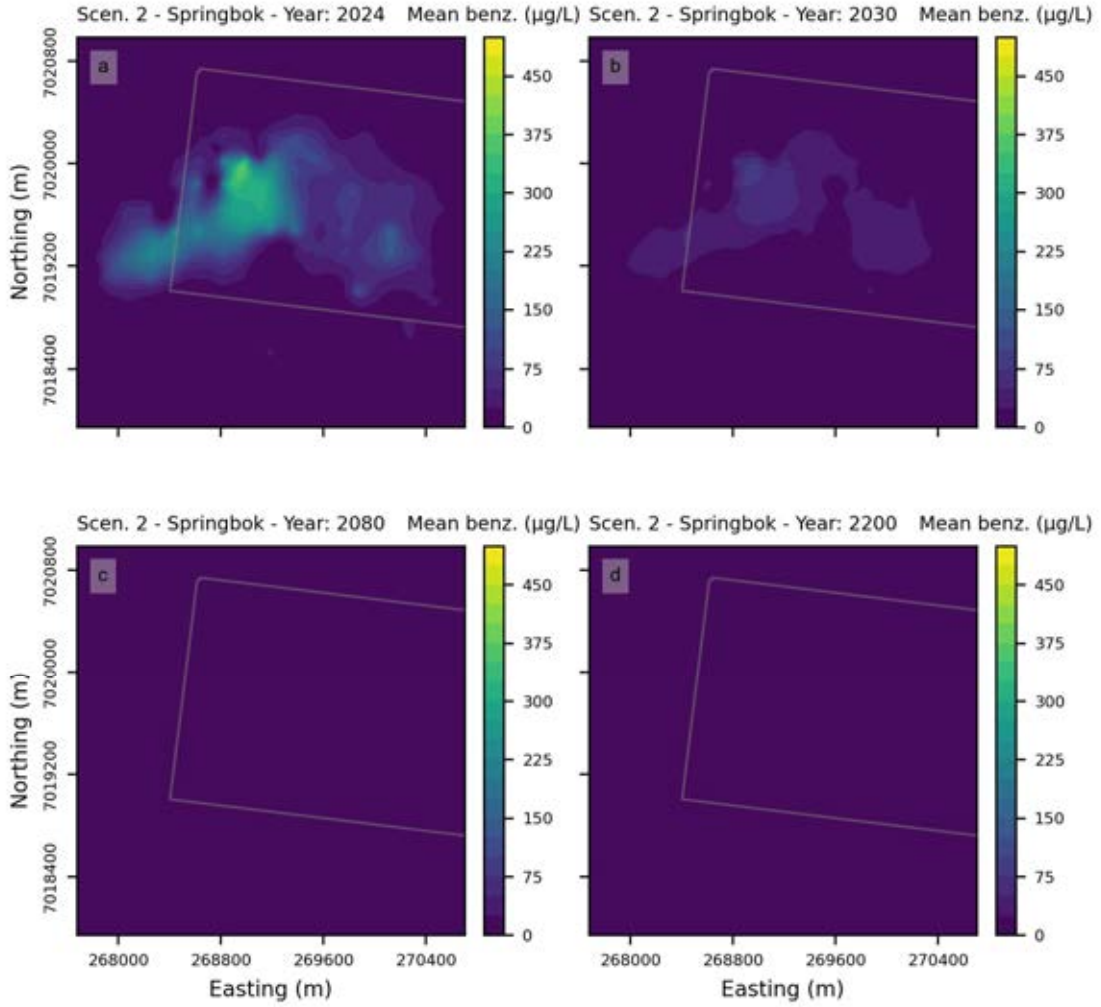


Figure 1-16 – Maps showing the average ensemble concentration of benzene for Scenario 2 in Springbok Sandstone model layer associated with the 5 Red Circle Wells for model years 2024, 2030, 2080, 2200.

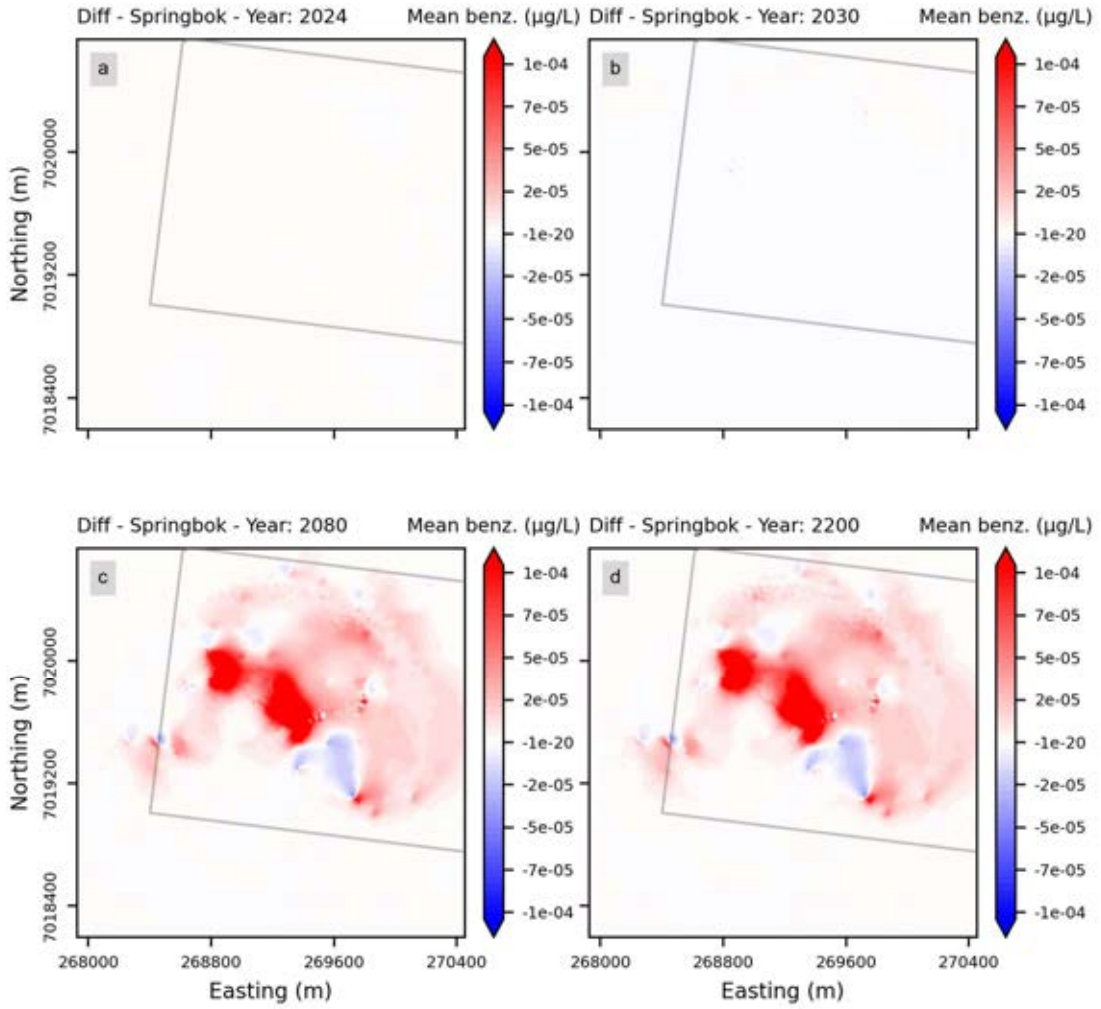


Figure 1-17 – Maps showing the average difference in benzene between scenarios 1 and 2 for Springbok Sandstone model layer associated with the 5 Red Circle Wells for model years 2024, 2030, 2080, 2200.

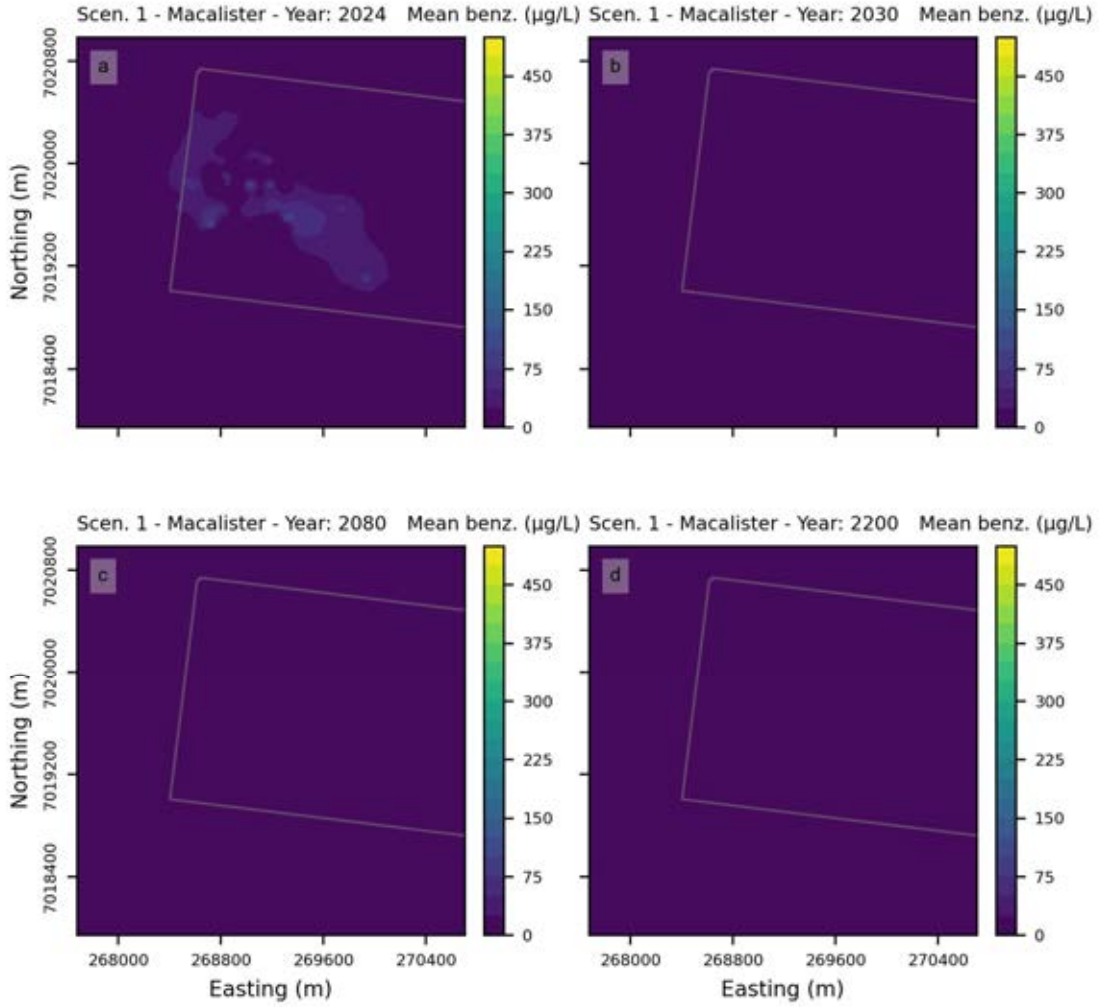


Figure 1-18 – Maps showing the average ensemble concentration of benzene for Scenario 1 in Macalister coal seam model layer associated with the 5 Red Circle Wells for model years 2024, 2030, 2080, 2200.

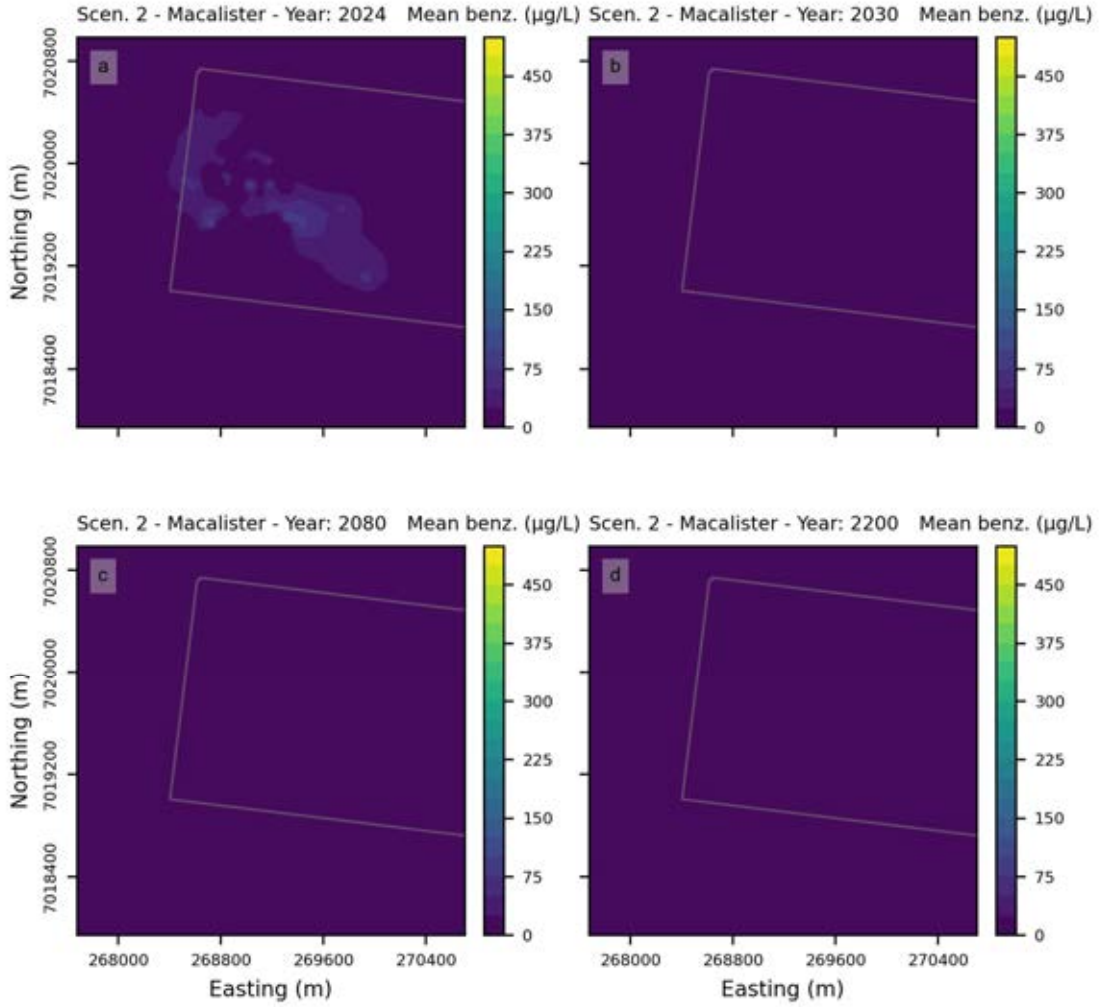


Figure 1-19 – Maps showing the average ensemble concentration of benzene for Scenario 2 in Macalister coal seam model layer associated with the 5 Red Circle Wells for model years 2024, 2030, 2080, 2200.

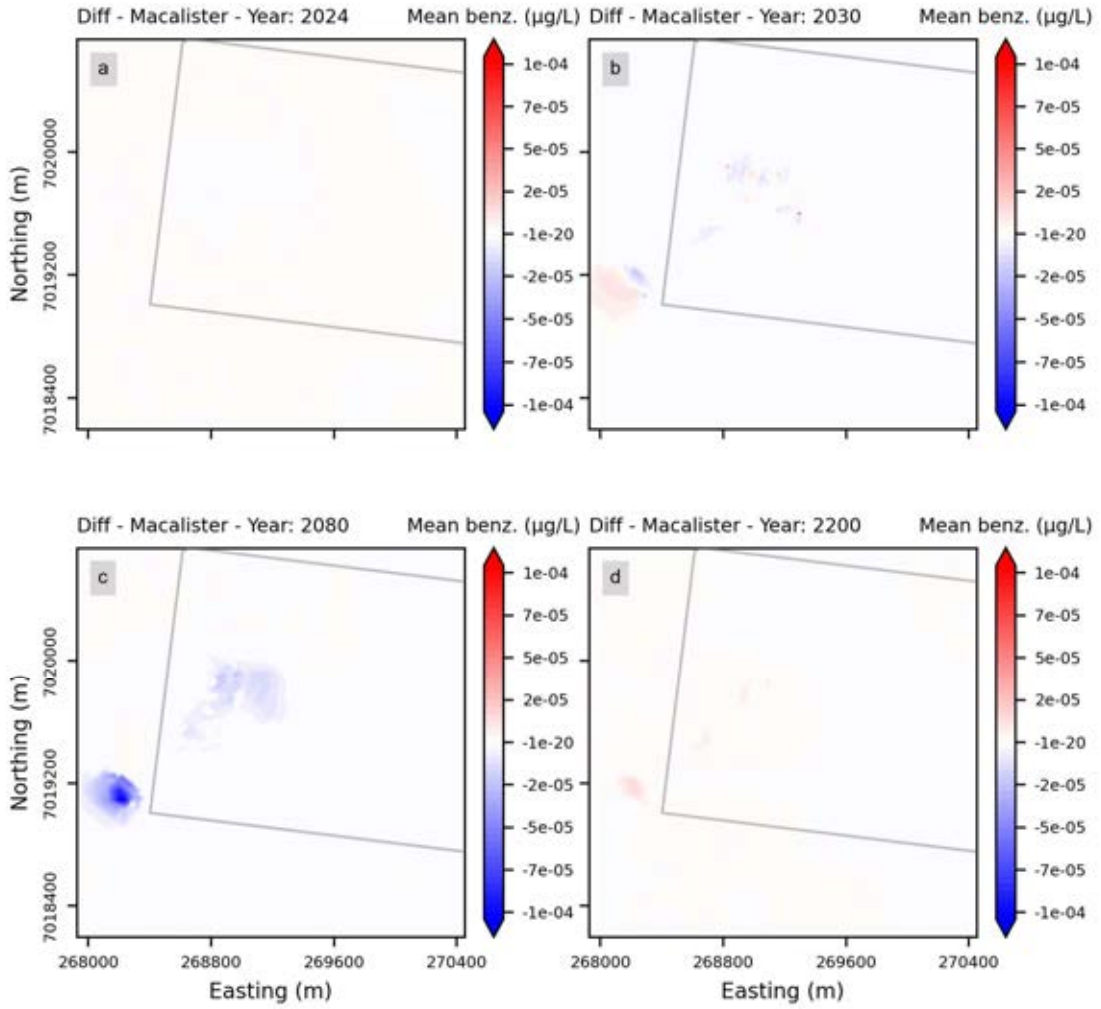


Figure 1-20 – Maps showing the average difference in benzene between scenarios 1 and 2 for Macalister coal seam model layer associated with the 5 Red Circle Wells for model years 2024, 2030, 2080, 2200.

Figure 1-21 presents histograms showing the model year in which 99% of cells achieve benzene concentrations below 1 µg/L for both the Springbok Sandstone and Macalister coal seam under Scenarios 1 and 2. The histograms indicate a very small difference in the time between the two model scenarios for both model layers (see Figure 1-21e and f), supporting the conclusion that the 5 Red Circle Wells have a minimal impact on benzene distribution and attenuation in the models.

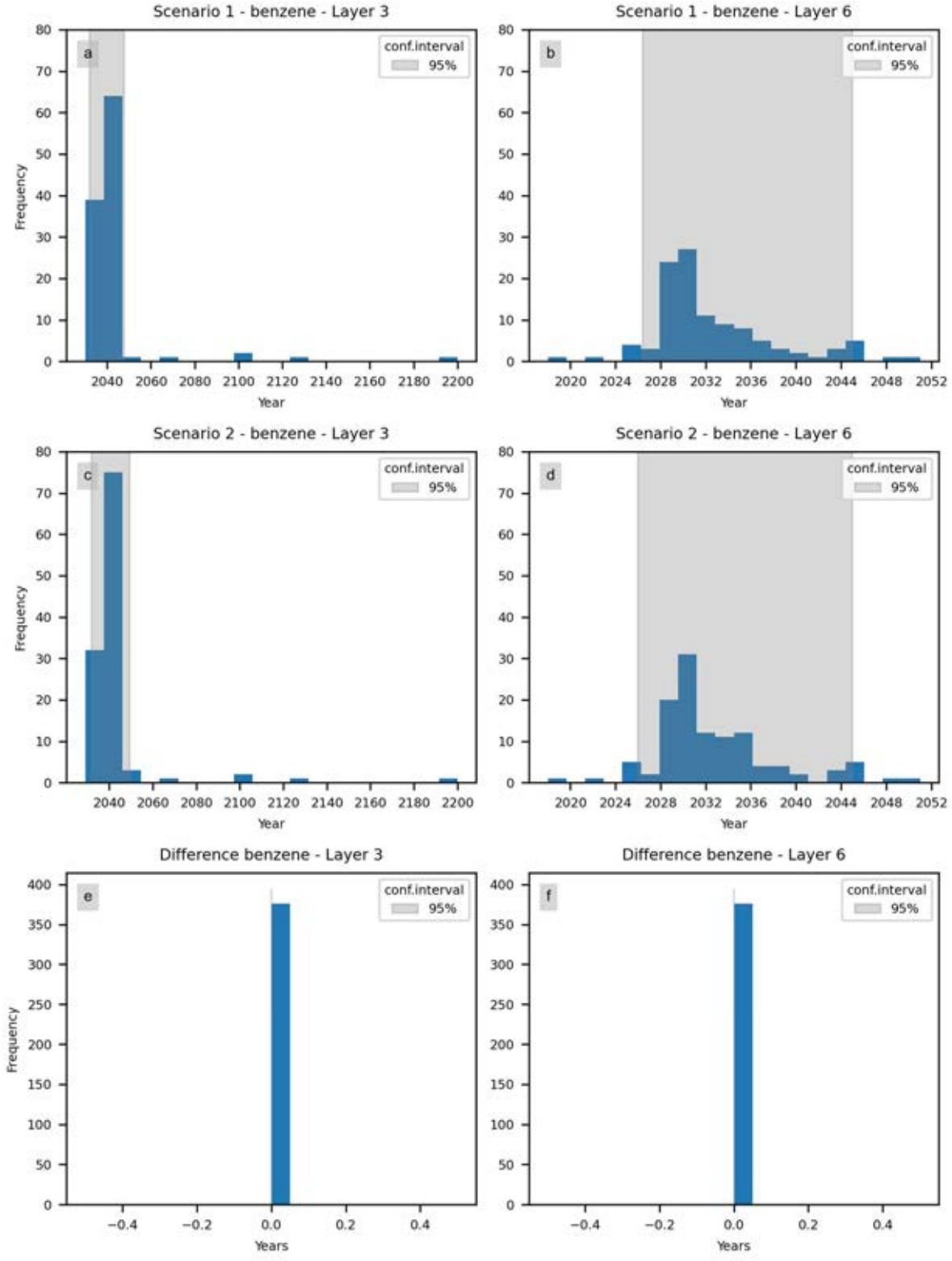


Figure 1-21 – Histograms showing the model year in which 99% of cells achieved benzene concentrations below the LOR (1 µg/L) in layers 3 and 6 (Springbok Sandstone and Macalister coal seam) for Scenario 1 (a and b) and Scenario 2 (c and d). Subplots (e) and (f) present the differences between the two scenarios.

### 1.4.3.2 Naphthalene

Modelled mean concentrations of naphthalene in both the Springbok Sandstone (Figure 1-22 and Figure 1-23) and the Macalister coal seam (Figure 1-25 and Figure 1-26) show complete attenuation outside Lot 40 between model years 2030 and 2080 for both scenarios. Differences in concentrations between Scenario 1 and Scenario 2 (Figure 1-24 and Figure 1-27) are minimal, with values less than 1E-02 µg/L across all model years.

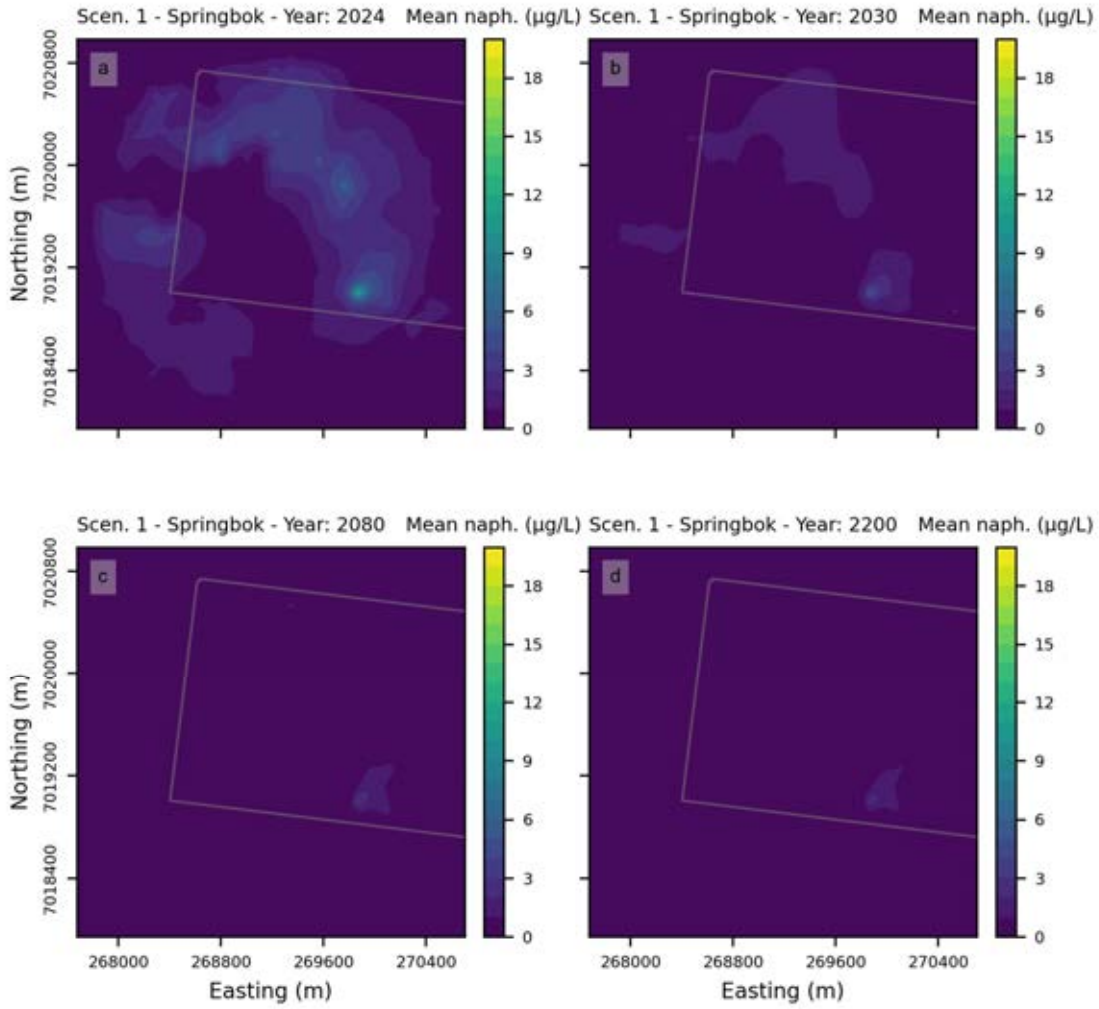


Figure 1-22 - Maps showing the average ensemble concentration of naphthalene for Scenario 1 in Springbok Sandstone model layer associated with the 5 Red Circle Wells for model years 2024, 2030, 2080, 2200.

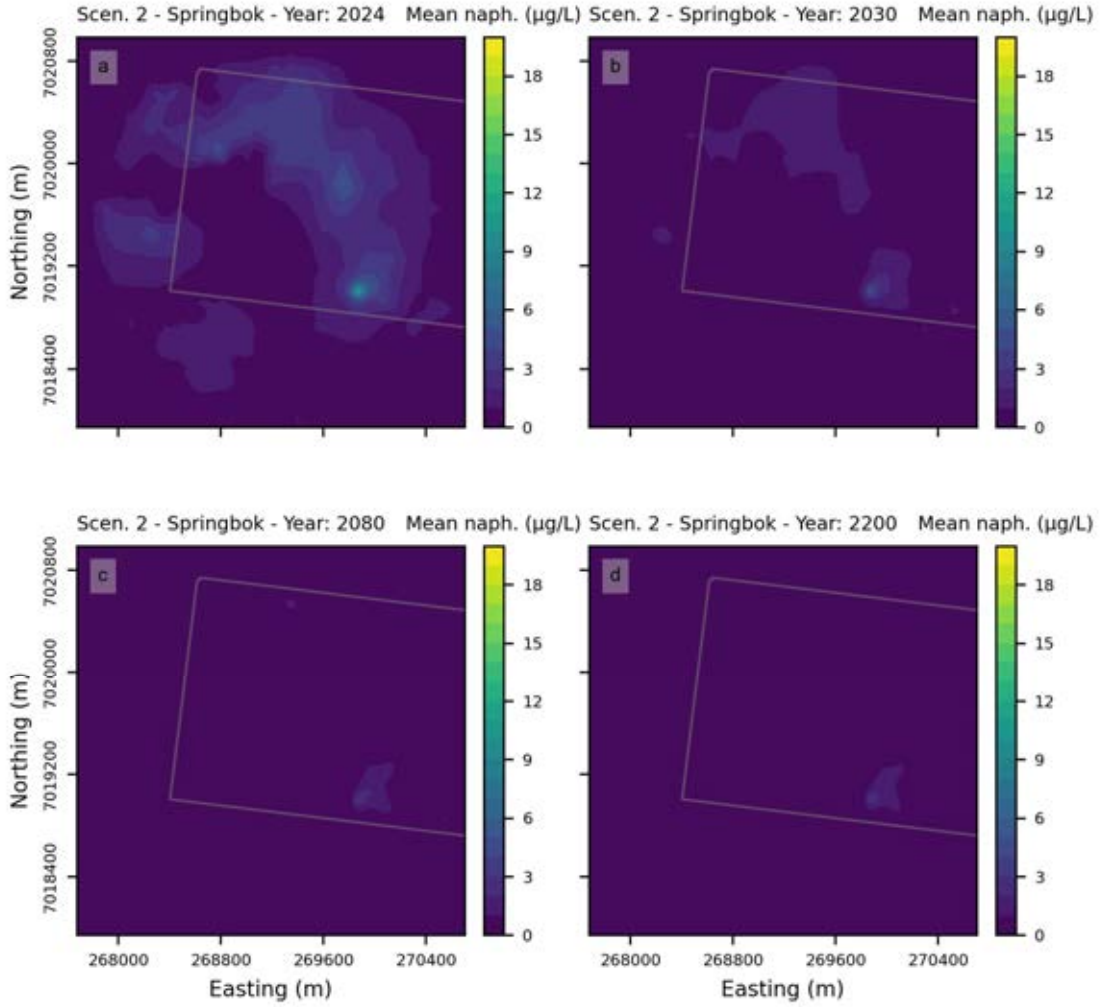


Figure 1-23 - Maps showing the average ensemble concentration of naphthalene for Scenario 2 in Springbok Sandstone model layer associated with the 5 Red Circle Wells for model years 2024, 2030, 2080, 2200.

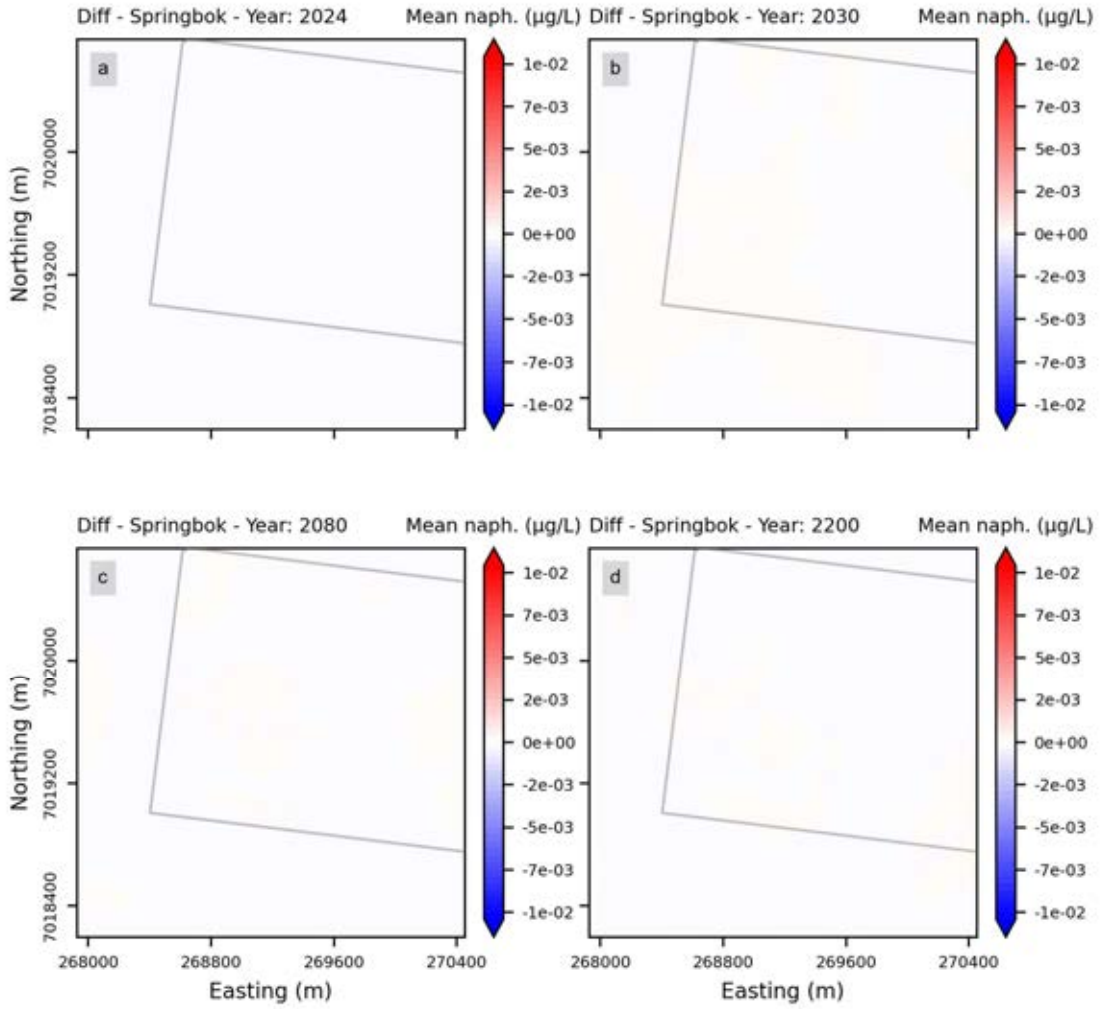


Figure 1-24 - Maps showing the average difference in naphthalene between scenarios 1 and 2 for Springbok Sandstone model layer associated with the 5 Red Circle Wells for model years 2024, 2030, 2080, 2200.

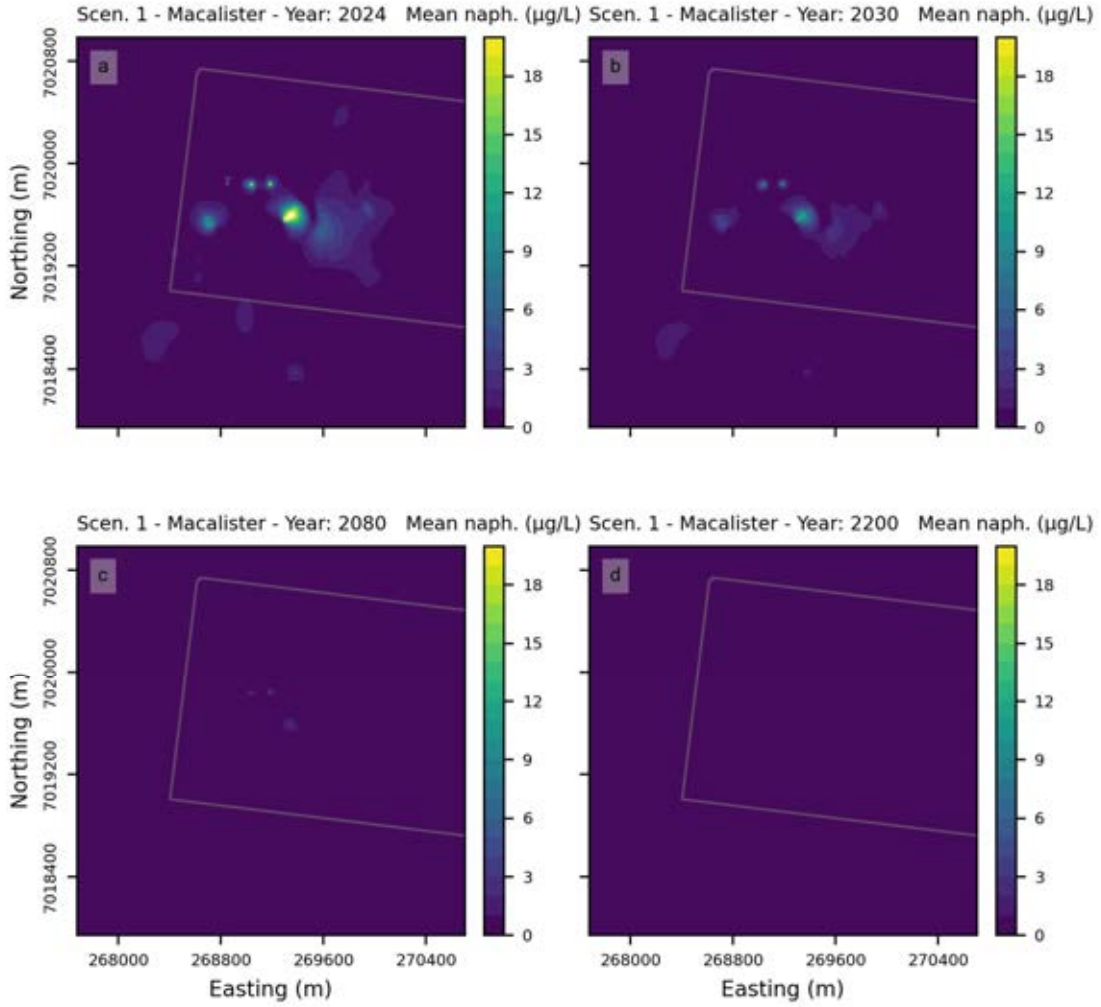


Figure 1-25 - Maps showing the average ensemble concentration of naphthalene for Scenario 1 in Macalister coal seam model layer associated with the 5 Red Circle Wells for model years 2024, 2030, 2080, 2200.

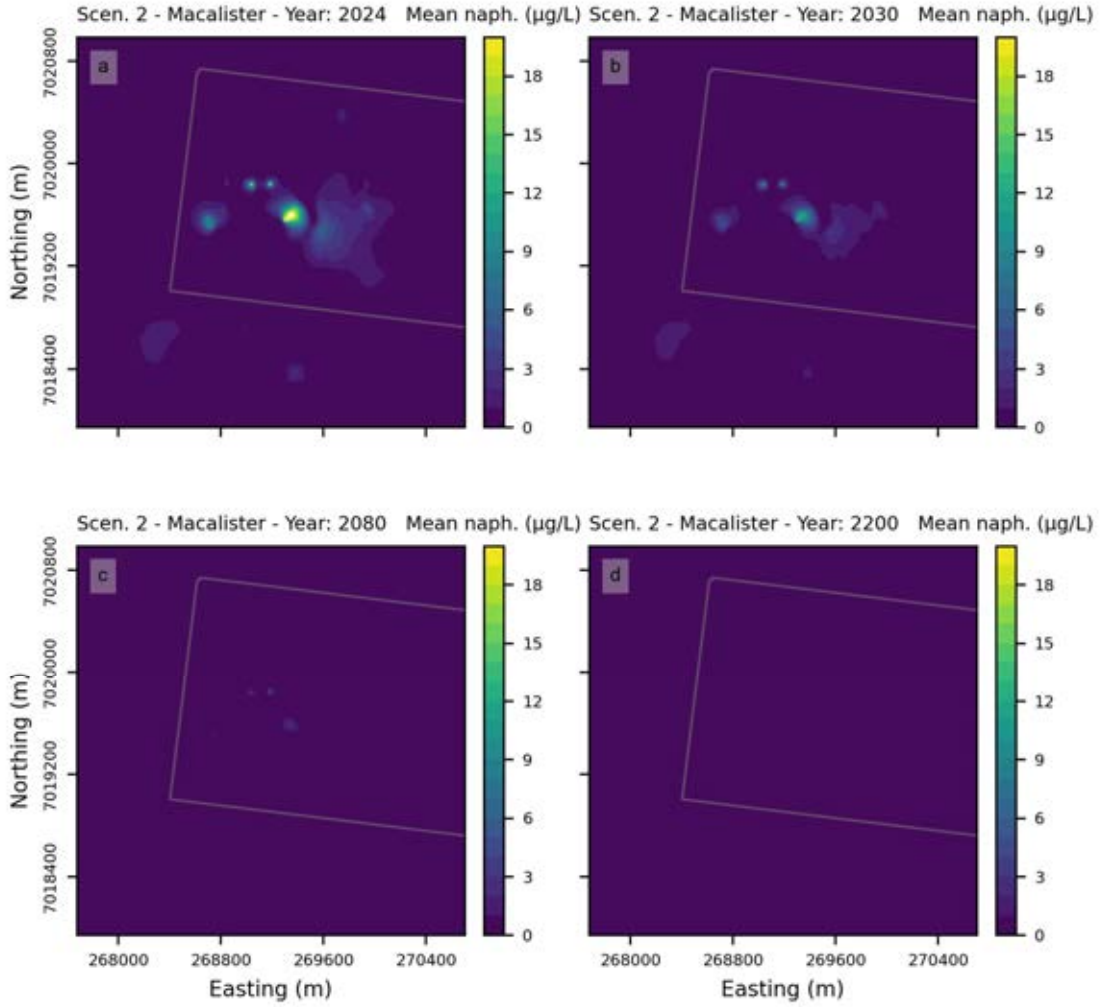


Figure 1-26 – Maps showing the average ensemble concentration of naphthalene for Scenario 2 in Macalister coal seam model layer associated with the 5 Red Circle Wells for model years 2024, 2030, 2080, 2200.

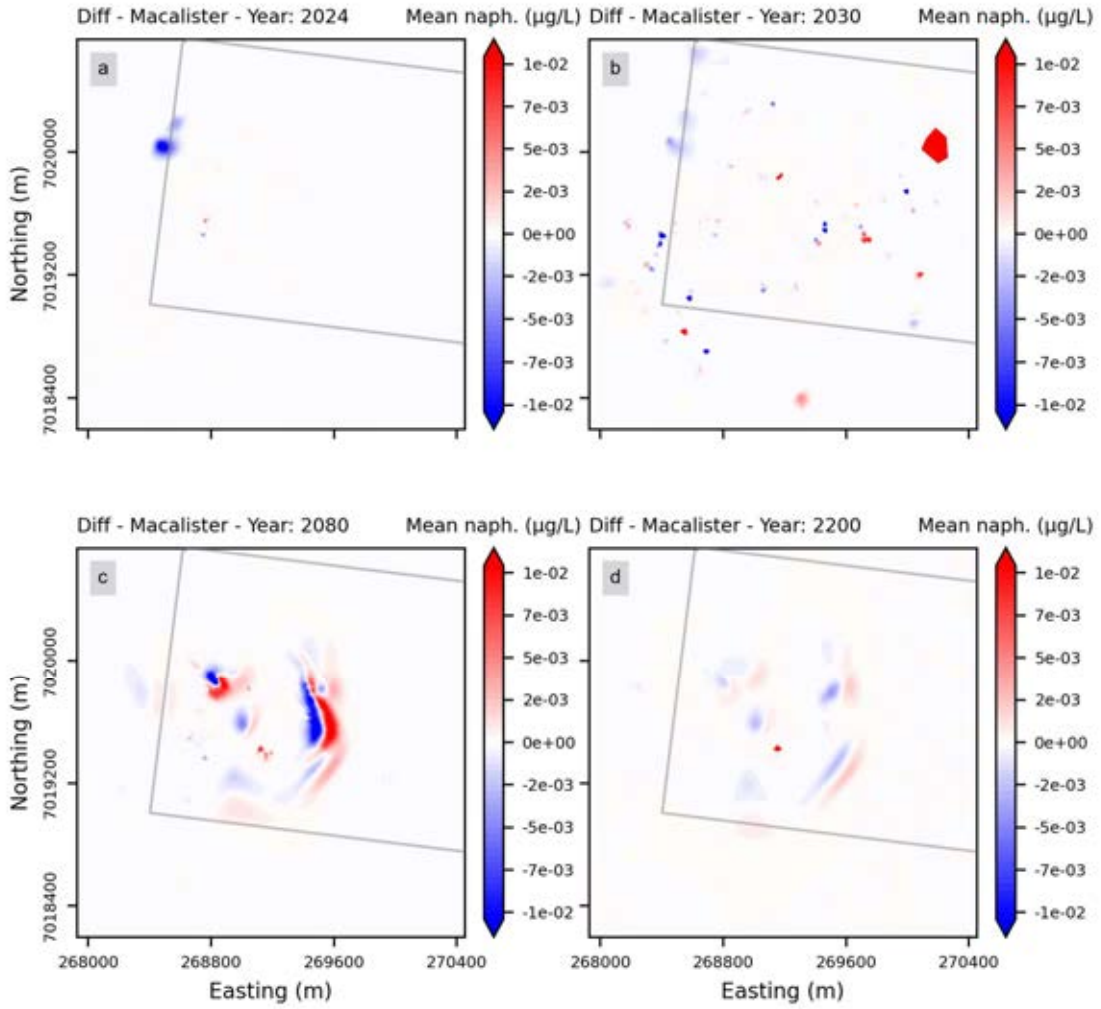


Figure 1-27 – Maps showing the average difference in naphthalene between scenarios 1 and 2 for Macalister coal seam model layer associated with the 5 Red Circle Wells for model years 2024, 2030, 2080, 2200.

Figure 1-28 presents histograms showing the model year at which 99% of the model cells achieve naphthalene concentrations below 1 µg/L for the Springbok Sandstone and Macalister coal seam for both Scenarios 1 and 2. The histograms indicate a very small difference in the time between the two model scenarios for both model layers (see Figure 1-28e and 1-28f), supporting the conclusion that the 5 Red Circle Wells have a minimal impact on naphthalene distribution and attenuation in the models.

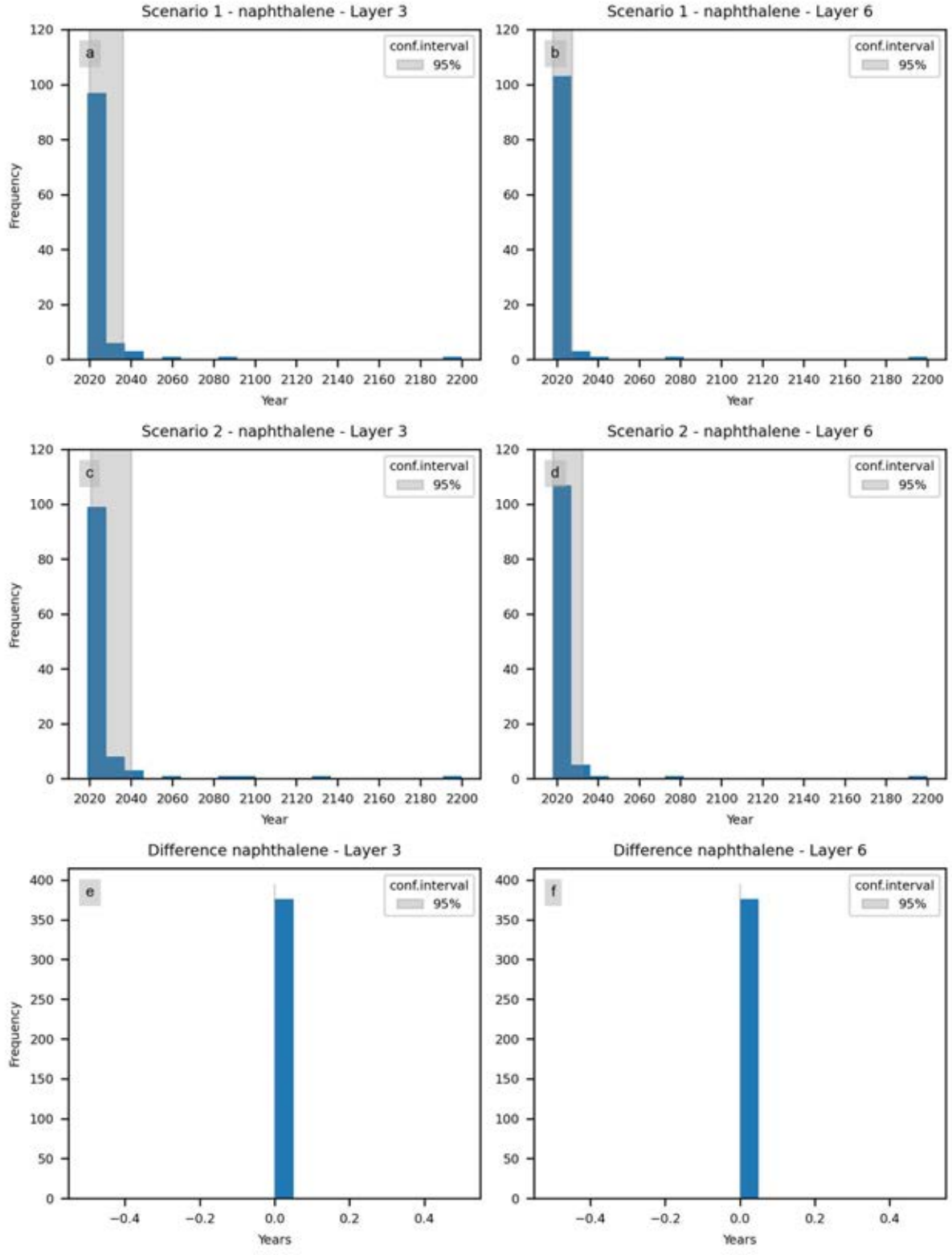


Figure 1-28 – Histograms showing the year when 99% of model cells reached naphthalene concentrations below the limit of reporting (LOR, 1 µg/L) in layers 3 and 6 (Springbok Sandstone and WCM Macalister coal seam) are presented for Scenario 1 (a and b) and Scenario 2 (c and d). Subplots (e) and (f) display the differences between the two scenarios.

The concentration differences reported in Figure 1-17, Figure 1-20, Figure 1-24, and Figure 1-27 are several orders of magnitude below the investigation and reporting limits for benzene or naphthalene in water (typically 1 µg/L). These results indicate that the 5 Red Circle Wells have no impact on the distribution or attenuation of contaminants in the Springbok Sandstone or Macalister coal seam.

### 1.4.4 Particle migration

Particle tracking was applied to the predictive models as a proxy for non-reactive solute transport to evaluate the maximum potential extent of contaminant migration. Particles were placed in the gasifiers and on the boundary of Lot 40 DY85 at the commencement of the simulation period. This method enables the identification of areas that contaminants could potentially reach over time in the absence of natural attenuation or degradation processes, thus providing a conservative (or worst case) scenario for contaminant travel.

Figure 1-29 displays the probability that a grid cell contains at least one particle at the end of the simulation period under Scenario 1, while Figure 1-30 Figure 1-shows the same under Scenario 2. In these maps, coloured areas indicate regions with a non-zero probability of groundwater flow from the site, whereas uncoloured areas represent locations with zero probability of particle arrival (i.e., groundwater flow from site).

Figure 1-31 shows the difference in particle arrival probability between Scenario 1 and Scenario 2. As indicated, excluding the 5 Red Circle Wells in Scenario 2 results in probability differences of less than 0.04 for all model years, which indicates that the 5 Red Circle Wells would not significantly alter the spatial extent or direction of particle movement originating from Lot 40 DY85. In other words, the simulated migration pattern was largely unaffected by the presence or absence of the Red Circle Wells, suggesting they would not contribute to the expansion of the contamination plume under the simulated conditions.

Summary statistics for particle movement distances under Scenarios 1 and 2 are presented in Table 1-2. The differences in average and maximum distances are less than 0.3 m and 0.4 m, respectively. These results support the conclusion that the 5 Red Circle Wells have a minimal impact on the extent of the simulated contaminant plume.

**Table 1-2 - Summary statistics of simulated particle distances from Lot40 boundary for both scenarios over the entire simulated period for all parameter realisations in the posterior ensemble.**

| Particle Source | Scenario | Distance from Lot40 boundary* (m) | | |
|---|---|---|---|---|
| | | min | average | Max |
| Monitoring bores | Scenario 1 | -875.9 | -278.3 | 2421.4 |
| | Scenario 2 | -875.9 | -278.3 | 2424.5 |
| Lot40 boundary | Scenario 1 | -875.9 | 24.9 | 2431.8 |
| | Scenario 2 | -876 | 24.6 | 2418.1 |
| Gasifiers | Scenario 1 | -876 | -422.6 | 1045.4 |
| | Scenario 2 | -876 | -422.5 | 1045.8 |

** Negative distances indicate particles migrating toward Lot 40 DY85, while positive distances represent particles migrating away from Lot 40 DY85.*

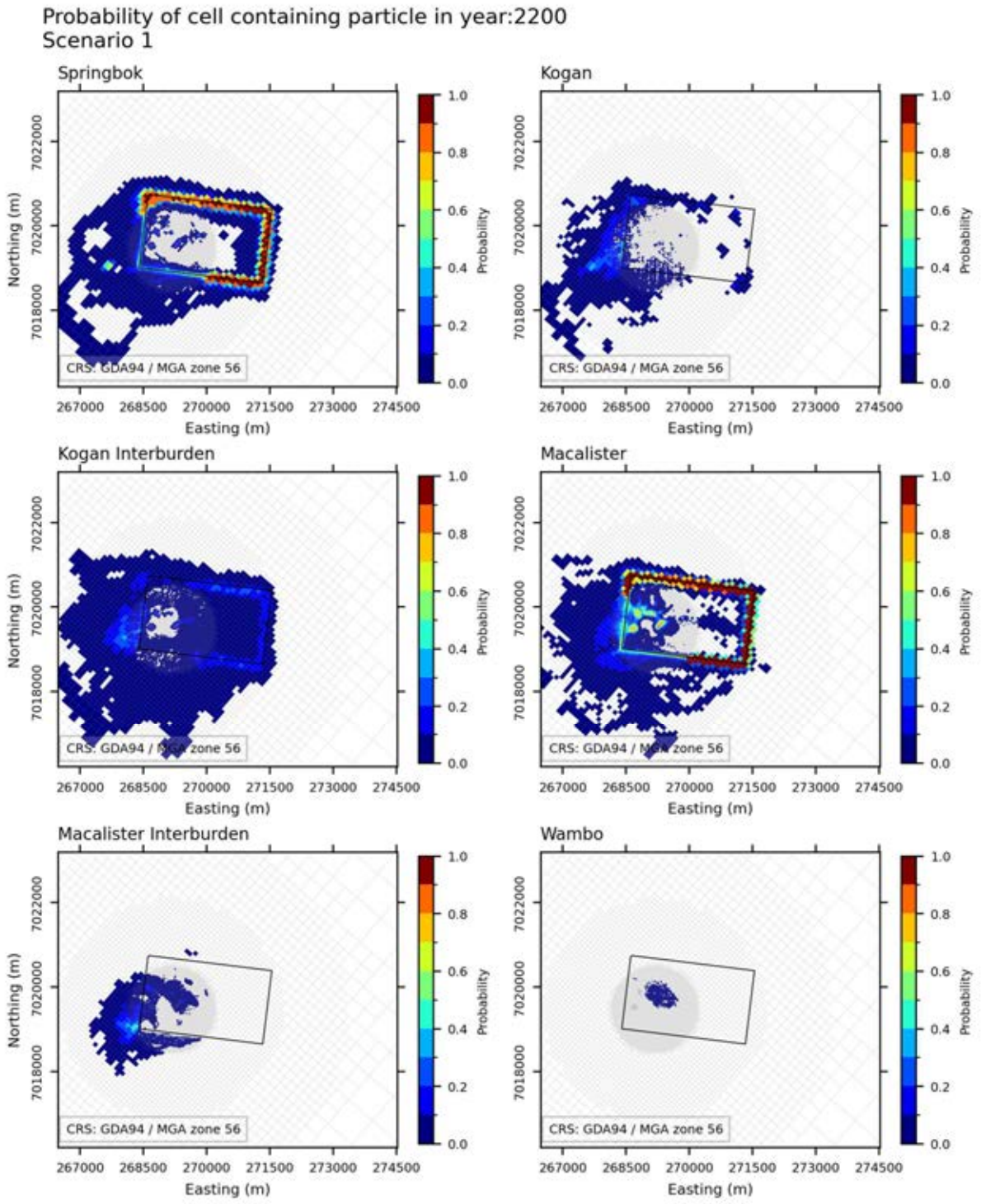


Figure 1-29 – Map of probability of a particle reaching any given location within the map area for Scenario 1. Map is also showing Lot 40 DY 85 (rectangle in centre of each plot).

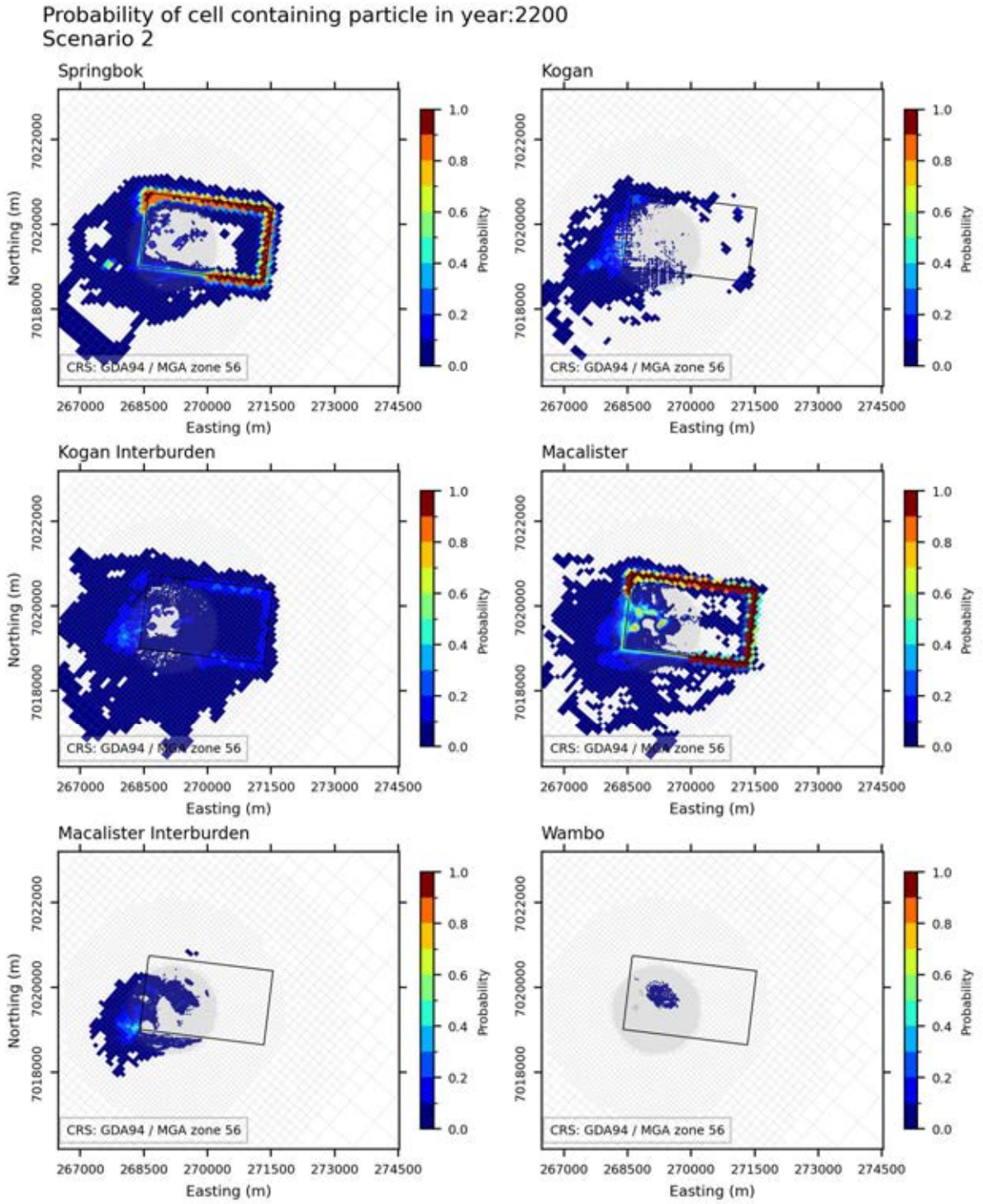


Figure 1-30 – Map of probability of a particle reaching any given location within the map area for Scenario 2. Map is also showing Lot 40 DY 85 (rectangle in centre of each plot).

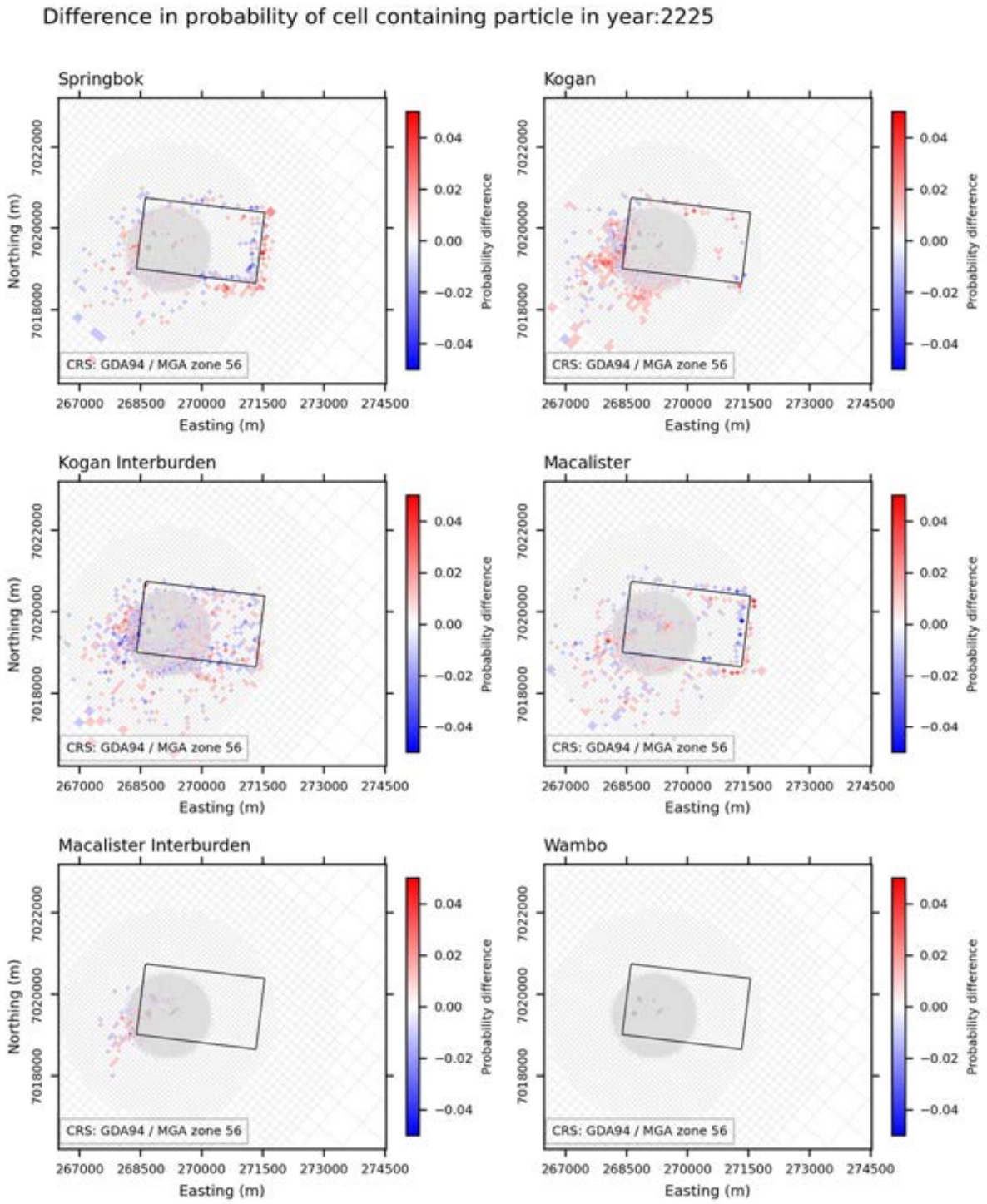


Figure 1-31 – Map of the difference in probability of a grid cell containing at least one particle between Scenario 1 and 2. Map is also showing Lot 40 DY85 (rectangle in centre of each plot).

## 1.5 Conclusions

Results from the simulated ensemble showed that the 5 Red Circle Wells are expected to have a minimal impact on the migration of the contaminants beyond Lot 40 DY85. This is due to:

(1) Their minimal influence on reversing the hydraulic gradient from inwards to outwards inside the Lot 40 DY85.
(2) Their minor impact on delaying the natural attenuation of benzene and naphthalene.
(3) Their negligible effect on increasing the travel distance of particles, which serves as a proxy for a conservative case (i.e., no natural attenuation processes and no mechanical dispersion).

# 2.0 Response to Information Request EA0001613

## 2.1 Item – Action 9

### 2.1.1 DETSI Requirement – Item 9

From EA Amendment 20250319 Information Request EA0001613:

*To support the proposed amendments to water conditions in this application, a groundwater assessment, including modelling, is required to understand the extent of risks on EA0001613 associated with the historical underground coal gasification (UCG) activities on Lot 40 DY85.*

*Action 9*

*a) Provide an in-depth assessment, including groundwater modelling, that identifies potential influences and risks associated with Lot 40 DY85 on the land and activities subject to EA0001613.*

*b) Provide supporting information that justifies the relevant inputs for the groundwater modelling and what process was applied to confirm an acceptable and unbiased outcome to the modelling results.*

*c) Prove a discussion with evidence on how reservoir pressure has been considered and accounted for in the model to determine groundwater flow direction at Lot 40 DY85.*

### 2.1.2 Response to Action 9 (a)

In general, the evaluation of the risks associated with Lot 40 DY85 involves assessing the potential overall impacts of the operation and identifying and evaluating the potential receptors of those impacts.

The potential impacts associated with Lot 40 DY85 are related to the probability of contaminants from the coal gasifiers mobilising in groundwater and migrating beyond the Lot 40 DY85 boundary.

Current water levels throughout the Lot 40 DY85 are depressed due to the operation of the coal gasifiers in 2013. These lowered water levels have created downward and inward hydraulic gradients within Lot 40 DY85. Since 2013, water levels have been gradually recovering within Lot 40 DY85 and are expected to eventually rise to a point where groundwater will begin to flow outward from Lot 40 DY85 (AECOM, 2018; INTERA, 2024).

Potential impacts associated with Lot 40 DY85 are also influenced by the degradation rates of each contaminant of concern (COC) and the time required to achieve complete attenuation at the site. Therefore, evaluating the risk of groundwater contamination migrating from Lot 40 DY85 depends on predictions of when the hydraulic gradient will reverse, the subsequent future horizontal and vertical gradients and related flow directions, as well as the timing of degradation of the COCs. These hydrogeologic factors – specifically, the timing of the hydraulic gradient reversal and the timing of complete degradation of the COCs – were evaluated here using numerical groundwater flow and contaminant transport models. These models were run using multiple realisations to quantify uncertainty and directly evaluate the risks associated with specific predictions of interest. For this assessment, the specific predictions of interest are the timing of the reversal from inward to outward hydraulic gradient as it determines when contamination in the coal gasifiers may start to

migrate beyond Lot 40 DY85, and the timing of the complete attenuation of the COCs in the groundwater.

The model used to evaluate the timing of the hydraulic gradient reversal is the multi-layer transient numerical groundwater flow model described in Section 1.3.1 of this document. A highly parameterised uncertainty analysis (UA), with a broad prior parameter uncertainty, was applied to the groundwater flow modelling to identify ranges of model parameter ensembles that satisfy the history-matching requirements. A more detailed justification of the model inputs and setup is provided in the response to Action 9 (b) (Section 2.1.3). The CSG well pumping scenarios used to evaluate these predictions of interest are presented in Section 1.0 (as Scenarios 1 and 2). As discussed in the response to Action 11, the large number of predictive ensembles resulted in reversal years spanning from 2025 to 2035. The models also indicate that the vertical hydraulic gradient between the Macalister coal seam (which hosts the collapsed coal gasifiers) and the overlying Springbok Sandstone remains downward in all model realisations.

Benzene and Naphthalene were selected as representative COCs for the contaminant transport modelling. Benzene, a known carcinogen, is the most mobile of the BTEX (benzene, toluene, ethylbenzene, and xylene) compounds, having the highest solubility in water and the lowest adsorption potential (Odermatt, 1994), while naphthalene is the most water-soluble Polycyclic Aromatic Hydrocarbon (PAH) (Bayard et al, 2020). Benzene and naphthalene also have the highest concentrations in the chemical data compared to the rest of the BTEX and PAH compounds respectively and were also adopted in previous modelling of the site (AGE, 2023). Furthermore, benzene has been shown to degrade more slowly than the rest of the BTEXN compounds (Prommer et al., 2003), making it a good indicator for the extent of contaminated groundwater.

The groundwater flow model includes a transport routine that determines predictive probabilities for the year in which each contaminant will be completely depleted. Model results indicate that naphthalene is expected to achieve complete attenuation with 95% confidence by 2040 in the Springbok Sandstone and by 2032 in the Macalister coal seam. For benzene, the model predicts the complete attenuation with 95% confidence by 2049 in the Springbok Sandstone and by 2045 in the Macalister coal seam. When these results are compared to the mean and range of predicted years for the reversal of the hydraulic gradient of flow model, the contaminant transport simulations indicate some overlap between the timing of gradient reversal and complete contaminant depletion. This suggests a negligible to small risk of contaminants migrating out of Lot 40 DY85. The risk of future impacts from contamination are further reduced by the fact that significant attenuation of benzene and naphthalene contamination has already been observed in monitoring data from the Springbok Sandstone and Macalister coal seam formations (Figure 2-1).

Groundwater monitoring results (Figure 2-1) confirm the contaminant transport modelling outcome, showing that benzene and naphthalene concentrations in most monitoring bores – including DOR and Arrow bores screened within the Springbok Sandstone, Macalister Seam Package, and Wambo Seam Package – are either below the limit of reporting (1 µg/L) or exhibit a declining trend. Recent concentrations are approaching or falling below both the LOR and investigation limits. Together, these results indicate an extremely low risk of contamination migrating beyond Lot 40 DY85.

Risks are also associated with the probability of contaminants reaching any known existing receptors (see Figure 2-2). This probability was evaluated by applying particle tracking applied to the ensemble of groundwater flow model results. As shown in Figure 2-3, particle tracking over a 200-year period indicates very little movement to the east, northeast, and southeast with some off-site displacement

to the south and southwest. Importantly, the nearest known receptor – a water supply bore located east of the Lot 40 DY85 – lies outside the areas impacted by particles' movement.

To summarise:

- The overall risk of contaminant migration from Lot 40 DY85 was assessed using a quantitative UA of a numerical groundwater flow model incorporating contaminant transport and particle tracking.
- One hundred and twenty (120) model realisations were used in the UA to determine the probabilities of contaminant movement within and beyond Lot 40 DY85. This robust probabilistic approach, rather than relying on a single calibrated deterministic groundwater model, enabled a quantitative evaluation of the risks of contaminant migration from Lot 40 DY85.
- Results from the mean realisation of the flow model, in conjunction with outputs from the contaminant transport model, indicate that contamination will completely attenuate before hydraulic gradients recover and groundwater begins to flow out of the Lot 40 DY85. However, the overall UA revealed a broad range of timing for hydraulic gradient reversal, with approximately 30 realisations showing groundwater outflow occurring before complete attenuation of the contaminants. These findings suggest a negligible to low risk of some contamination migrating off-site before it fully degrades.
- The set of particle-tracking realisations, which are conservative and do not account for any attenuation, showed no instances of on-site particles reaching any off-site receptors within 200 years. The transport modelling predicts complete contaminant attenuation by 2049 (within 24 years) with 95% confidence, making the 200-year predictive particle tracking period highly conservative. Notably, significant attenuation of the contamination has already been observed at the site.
- The overall modelling results – showing a negligible to small risk of contamination leaving the site combined with the extremely low probability of particle tracks reaching any receptor – suggest a low risk of any contamination impacting any known receptors.

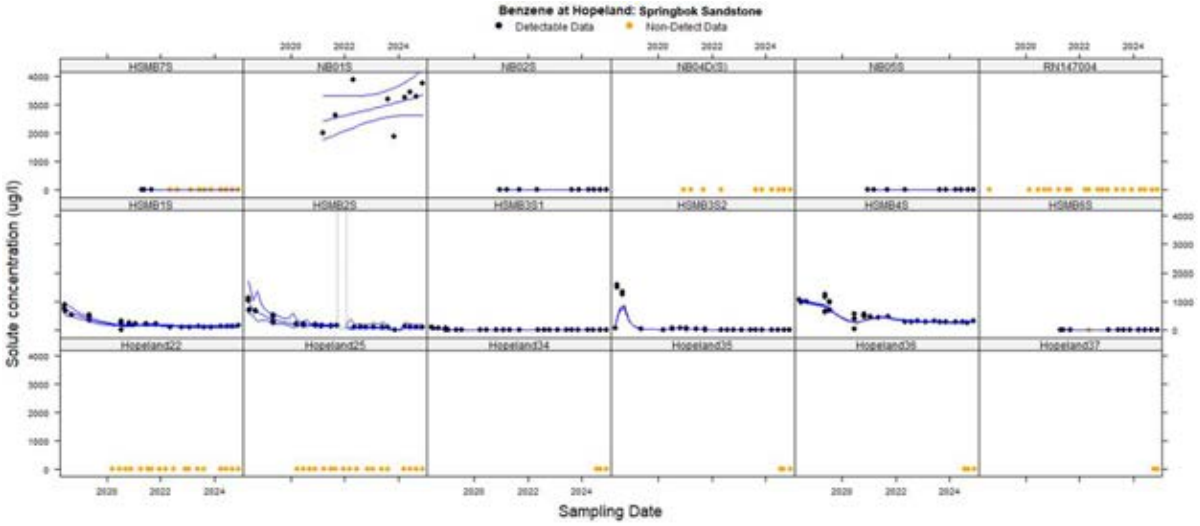

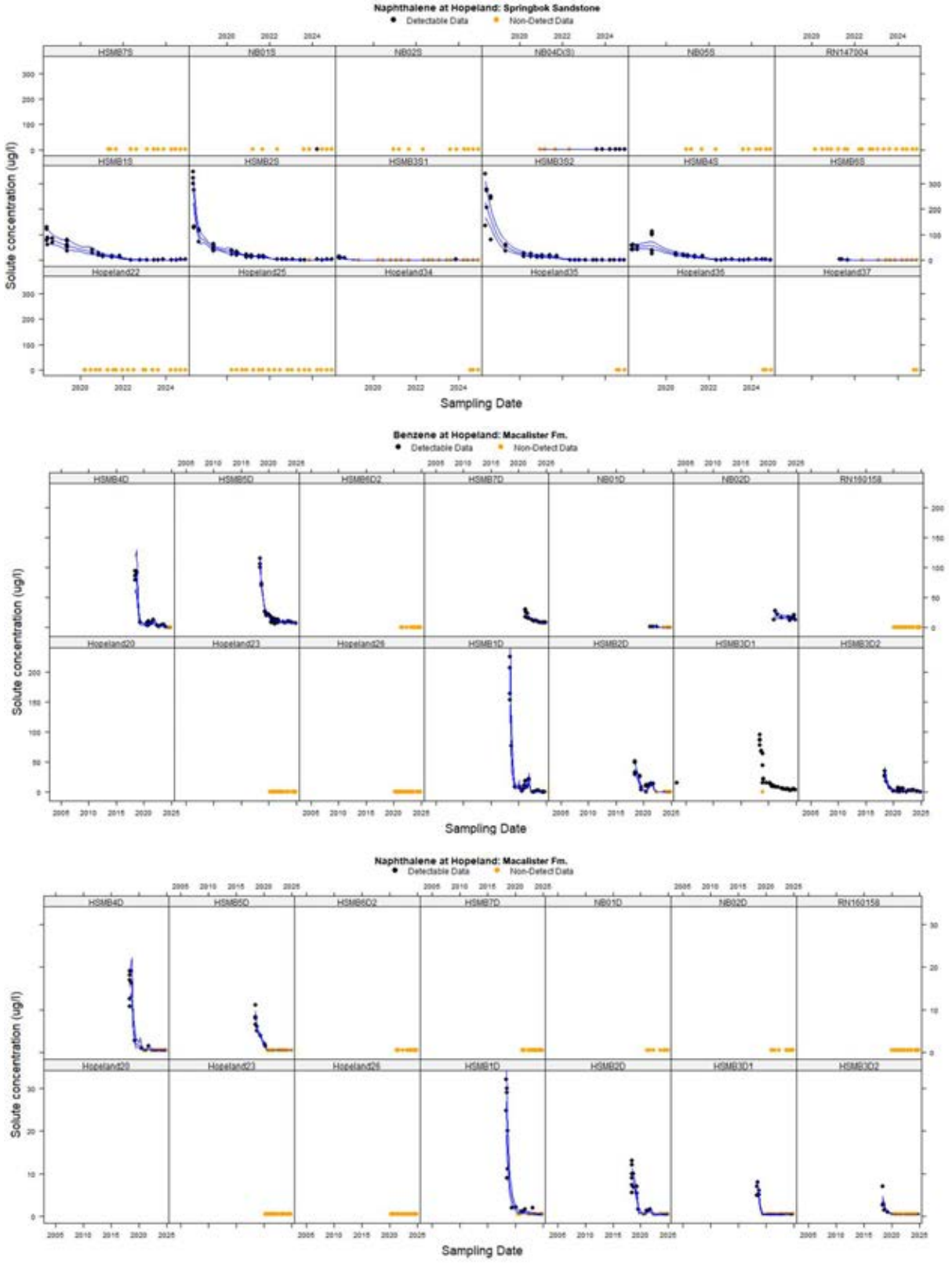


Figure 2-1 – Time-series of benzene and naphthalene concentrations in monitoring bores in the Springbok Sandstone and Macalister coal seam.

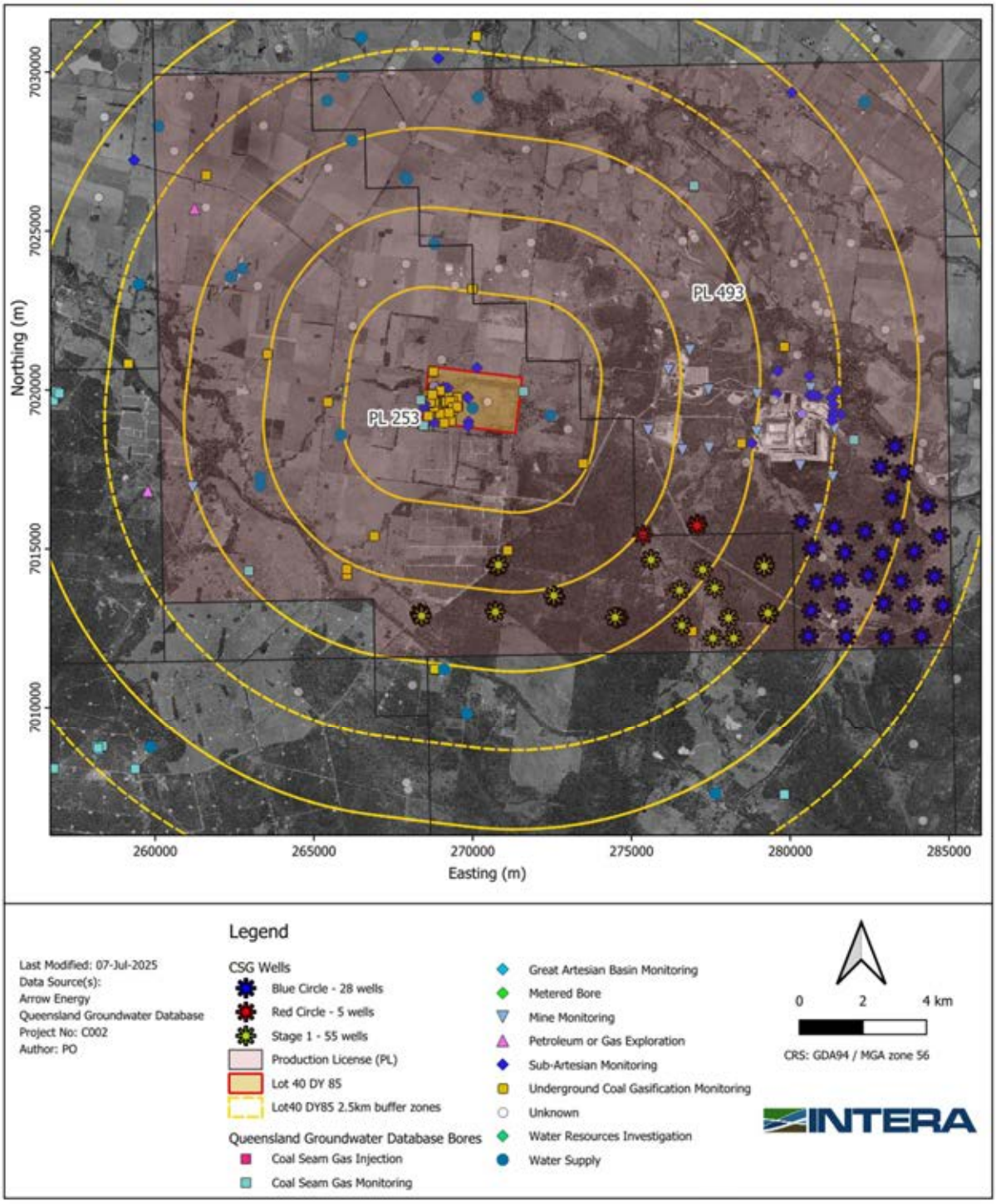


Figure 2-2 – Map showing the location of Lot 40 DY85, a set of 2.5 km buffer zones around the Lot 40 DY85, and existing known bores. The blue circles ("Water Supply") are the primary known receptors within the project area. The red stars show the locations of the pads containing the 5 red circle wells.

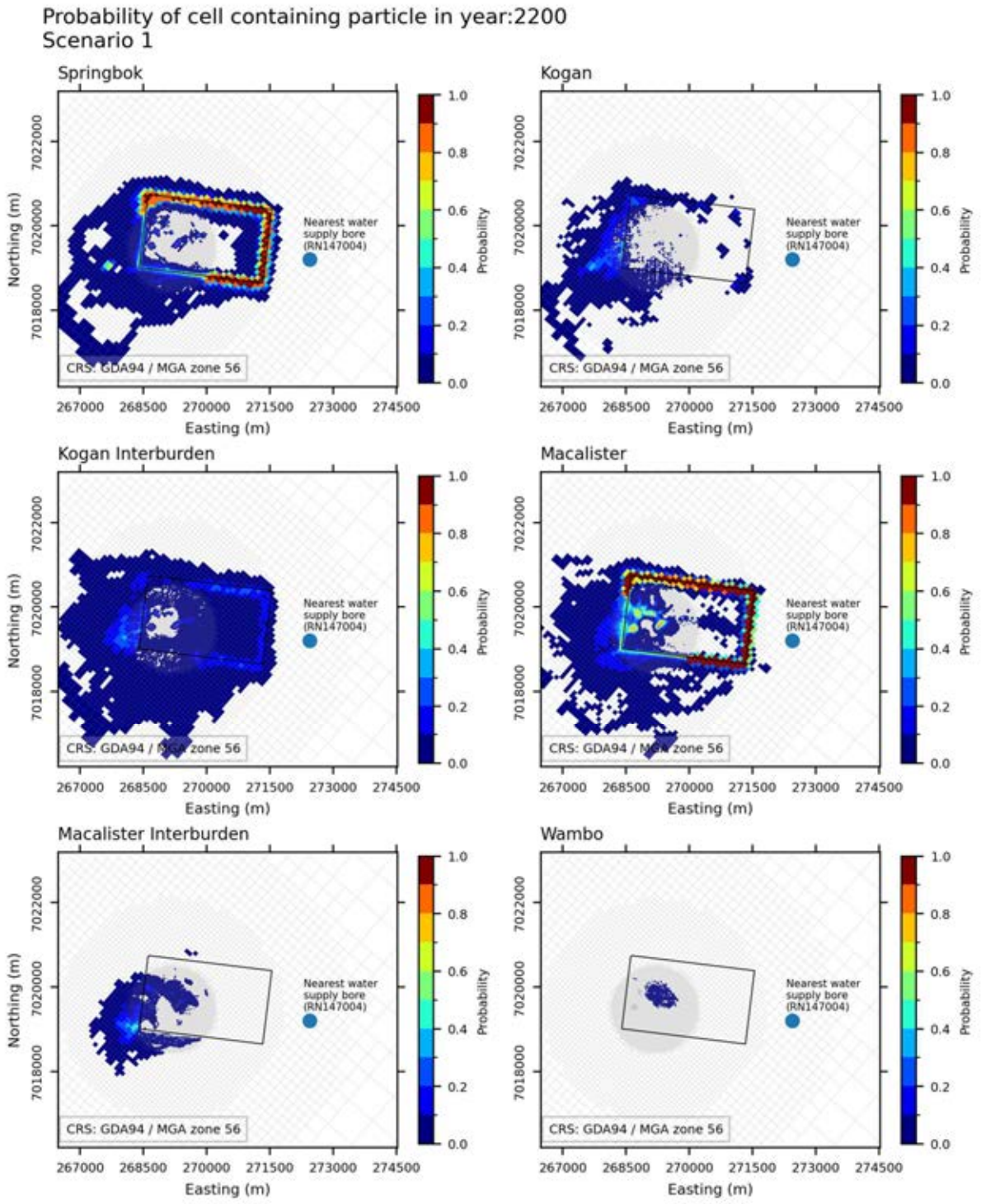


Figure 2-3 – Map of probability of a particle reaching any given location within the map area for Scenario 1. Map is also showing Lot 40 DY85 (rectangle in centre of each plot) and the nearest water supply bore (blue dot). The nearest bore to the southwest (see Figure 2-2) is located about 750 m west of the western boundary of each plot.

## 2.1.3 Response to Action 9 (b)

### 2.1.3.1 Supporting information that justifies the relevant inputs for model

All the relevant inputs for the groundwater flow and transport models were sourced from the PL253 Conceptual Model presented in the Consolidated Modelling Report (INTERA, 2024; see Appendix B), which was in turn based on AGE (2023) and OGIA's models (OGIA, 2016, 2019, 2021). The following section presents a summary of the relevant inputs, for more details please refer to Section 3 in Appendix B.

1. Model Grid and Stratigraphy

Based on previous work (INTERA, 2024), a quadtree unstructured grid was employed in the groundwater flow and transport models to enable local refinement in areas of interest such as the Lot 40 DY85 and the Hopeland pilot-test site. It was generated using the open-source software GRIDGEN (Lien et al, 2017). The model grid was updated from Arrow's earlier models (AGE, 2023) by switching from a Voronoi mesh to a quadtree grid, facilitating a fully scripted workflow and eliminating reliance on proprietary software.

The model stratigraphy was also updated using local geological data supplied by the Arrow development team and cross-checked against OGIA information. For instance, bore logs from Lot 40 DY85 confirmed the presence of certain coal seam interburdens described by OGIA (2016).

Please refer to Section 3.1.3 in INTERA, 2024 (Appendix B) for more information.

2. External Boundary Conditions

General Head Boundaries (GHB) were applied along the model's external boundaries. GHBs are assigned using time-varying heads extracted from OGIA (2021) groundwater model to account for regional CSG activities. Please refer to Section 3.1.4 in INTERA, 2024 for more information.

3. CSG wells operated by Arrow

Rates of water extraction and the locations of the future CSG wells and Hopeland pilot wells were provided by Arrow. The wells included in the scenarios for this assessment are described in Section 1 of this document.

4. CSG wells not operated by Arrow

Locations and extraction rates for existing and proposed non-Arrow CSG wells within the model domain were derived from the OGIA (2021) model.

5. Contaminant source

There is limited published information on the mass and distribution of the contaminant source at the site; however, Arrow provided an extensive dataset of COC concentrations from groundwater samples collected by Arrow and DETSI from monitoring bores near the source area. These monitoring data were used to establish stochastic realisations of the initial groundwater concentration field at and around the site, with the ranges of values based on the monitoring data and a multiplier of 1.5 applied to the highest observed concentration.

The actual contaminant source is assumed to exist in a non-aqueous phase within the coal gasifier area and is simulated using a mass loading rate (i.e., a rate at which contaminant mass is added to the groundwater) calibrated to match the distributions of contaminant concentrations identified in

the monitoring bores. The initial source concentration ranges used in the model calibration runs encompass all the monitoring data provided by Arrow, as well as concentration ranges reported at a similar coal gasification pilot site (EHS Support, 2014; WMV Environmental Pty Ltd, 2014; and Mallett, 2018). For the model calibration and predictive model runs the natural depletion of the contaminant source over time was simulated using source depletion rate functions (i.e., functions that controls the rate at which contaminants attenuate in the groundwater) that were approximated from literature values (Prommer, 2003; Grathwohl, 2011) for NAPL dissolution into groundwater and were incorporated into the history-matching process, allowing them to be informed by monitoring data from nearby bores. This ensures that the contaminant source depletion rates are consistent with Arrow's recent monitoring data from bores located near the gasifiers. A linear depletion was assumed for the mass loading rate at the contaminant source, consistent with observations from experimental and modelling studies of hydrocarbon source depletion, as presented in Grathwohl (2011).

Additional details can be found in section 4.3.1 and 4.3.2 in the Consolidated Modelling Report (INTERA, 2024; see Appendix B).

6. Initial contaminant distribution

The initial contaminant distribution at the site is based on a substantial dataset from a moderate number of unevenly distributed wells. Due to the spatial heterogeneity of contamination and the associated high degree of uncertainty, a statistical approach was used to generate different equally possible maps of initial contaminant concentration. Each map was generated using different assumptions about how concentrations vary over distance and direction, represented by spatially varying variograms that capture expected spatial patterns in the data. By varying the variogram parameters, the modelling encompassed a wide range of realistic scenarios. These maps were further constrained using concentration data from 2018 to 2020, resulting in a set of 200 different initial distributions of benzene and naphthalene concentrations that honour both the observed data and the conceptual understanding that higher concentrations are present within the gasifiers due to the presence of the contaminant source.

Additional details can be found in section 4.3.1 and 4.3.2 in the Consolidated Modelling Report (INTERA, 2024; see Appendix B).

7. Sorption

A linear sorption approach was adopted with a partition coefficient ($K_d$) defined as:

$$K_d = K_{oc}\, F_{oc} \quad (1)$$

Where $K_{oc}$ corresponds to the organic carbon-water partition coefficient and $F_{oc}$ denotes the fraction of organic carbon in the aquifer material. Initial values and upper and lower bounds of $K_{oc}$ were obtained from the published literature (Table 2-1) and values of $F_{oc}$ were estimated to have a mean of 35% for coal seam layers and 10% for non-coal seam layers, as per CSIRO (2023) advice. Nonetheless, a non-linear sorption model was tested and found to behave similarly to the linear model at higher aqueous concentrations, where most of the variability occurs. Given this similarity and considering that the linear model improved numerical tractability and ensemble convergence, the linear sorption approach was deemed sensible.

Details can be found in section 4.3.1 and 4.3.2 in the Consolidated Modelling Report (INTERA, 2024; see Appendix B).

Table 2-1 - $K_{oc}$ Values (see Section 7 in Appendix B for complete references)

| Components | Koc (L/kg) | Koc ($m^3$/kg) | Source |
|---|---|---|---|
| Naphthalene | 830 | 0.83 | Kishi et al., (1990) |
| | 843 | 0.84 | Vowles and Mantoura (1987) |
| | 871 | 0.87 | Karickhoff (1981) |
| | 907 | 0.91 | Stauffer and MacIntyre (1986) |
| | 912 | 0.91 | Hodson and Williams (1988) |
| | 960 | 0.96 | Southworth and Keller (1986) |
| | 1000 | 1 | Southworth and Keller (1986) |
| | 1000 | 1 | Kan and Tomson (1990) |
| | 1096 | 1.1 | McCarthy and Jiminez (1985) |
| | 1161 | 1.16 | Lokke (1984) |
| | 1290 | 1.29 | Rippen et al., (1982) |
| | 1300 | 1.3 | Karickhoff et al., (1979) |
| | 1333 | 1.33 | Karickhoff (1982) |
| | 1400 | 1.4 | Podoll et al., (1989) |
| | 1413 | 1.41 | Szabo et al., (1990a) |
| | 1440 | 1.44 | Rippen et al., (1982) |
| | 1445 | 1.45 | Szabo et al., (1990a) |
| | 1610 | 1.61 | Rippen et al., (1982) |
| | 1861 | 1.86 | Barrett et al., (1994) |
| | 1950 | 1.95 | Wood et al., (1990) |
| Benzene | 31 | 0.03 | Chiou et al., (1983) |
| | 38 | 0.04 | Seip et al., (1986) |
| | 44 | 0.04 | Seip et al., (1986) |
| | 49 | 0.05 | Abdul et al., (1987) |
| | 54 | 0.05 | Seip et al., (1986) |
| | 60 | 0.06 | Karickhoff (1981) |
| | 63 | 0.06 | Piwoni and Banerjee (1989) |
| | 66 | 0.07 | Szabo et al., (1990a) |
| | 74 | 0.07 | Szabo et al., (1990a) |
| | 83 | 0.08 | Karickhoff et al., (1979) |
| | 92 | 0.09 | Rogers et al., (1980) |
| | 100 | 0.1 | Rogers et al., (1980) |

8. Decay (degradation)

Biologically mediated degradation (biodegradation) is one of the dominant processes that reduces the aqueous concentration of hydrocarbons, especially in the absence of groundwater stresses (Prommer et al., 2003). In the current model, biodegradation is represented using a first-order decay function. A first-order decay model is the most common kinetic degradation approach applied for organic compounds in non-reactive contaminant transport studies (Bekins et al., 1998). The decay constant values used in this model were primarily sourced from Suarez and Rifai (1999), which provides a comprehensive compilation of experimental data from several in situ, field, and laboratory studies.

Details can be found in sections 4.3.1 and 4.3.2 of the Consolidated Modelling Report (INTERA, 2024; see Appendix B).

#### 2.1.3.2 Process applied to confirm an acceptable and unbiased outcome

To ensure an acceptable and unbiased outcome in the modelling results, a number of safeguards have been implemented to:

1. Minimise bias, and
2. Express parametric and conceptual uncertainty while using a single conceptual model to develop the numerical model.

These safeguards are:

1. The base model was constructed on the leading established conceptualisation of the site (AECOM, 2018; Arrow, 2020, 2021; AGE, 2020; GHD, 2019).

2. The highly parameterised uncertainty quantification (and calibration) with a broad prior parameter uncertainty was employed. This explores a considerable portion of parameter space and allows for capturing variations within the conceptual model.

3. Only three iterations in the calibration / history matching were implemented. This helps prevent bias and variance corruption that can result from defects in the conceptual model (acknowledging that the conceptual model—and its numerical representation—will always be defective at some scale).

4. The history matching process was conducted using different data types – including absolute groundwater heads, vertical head differences, and concentrations of naphthalene and benzene – to minimise bias that can arise from calibrating to a single data type.

5. A prior-data conflict assessment was conducted, indicating the potential presence of structural components within the system that are not currently captured in the numerical model or its underlying conceptual framework.

6. The ultimate purpose of the model is to compare the effect of the 5 CSG wells, and due to the comparative (i.e., relative) nature of the predictions, the effect of bias on decision-critical forecasts is expected to be minimised.

### 2.1.4 Response to Action 9 (c)

Studies have suggested that neglecting dual-phase flow can result in an overestimation of the impact of CSG depressurisation (Herckenrath et al. 2015; Moore et al. 2013; Moore et al. 2015). Moore et al. (2013, 2015) conducted an extensive study on the flow conditions near a semi-synthetic coal bed methane extraction well-field. They compared the pressures computed by a conventional single-phase groundwater flow model with those computed by a multiphase reservoir simulator. The study revealed that the drawdowns computed by a single-phase groundwater flow model can significantly exceed those computed by a multiphase reservoir model, both near extraction well-fields and at considerable distances from them. Moore et al., (2013, 2015) identified two main reasons for the overestimation of pressure drawdown by a standard groundwater model.

Firstly, as gas desorbs from the coal matrix due to coal seam depressurisation, it reduces the relative permeability of the water phase in the cleat system, where fluid flow occurs. This reduction in water

phase permeability impedes the outward propagation of the extraction-induced cone of depressurisation.

Secondly, gas displaces water from the coal. Even in areas of low coal porosity, the volume of water released by gas generation in cleats significantly exceeds that released from elastic storage, further mitigating the transient outward propagation of extraction-induced drawdown.

To account for these effects in regional impact modelling, some studies (e.g., Herckenrath et al. 2015) implemented a hybrid approach where the above effects are approximated in a modified single-phase groundwater flow model designed for regional scale impact assessment.

The current groundwater model does not include dual-phase flow effects. From a predictive standpoint, this is not of significant concern, but with some caveats. The predictions of interest for this study are related to the migration of contaminants from the former UCG site. Should it occur, movement away from the site will be induced by drawdown resulting from neighbouring CSG operations.

As discussed above, drawdown simulated by a single-phase model is likely to be overestimated. Thus, from a contaminant transport perspective, a single-phase model should provide conservative forecasts of contaminants' migration distances. This assumes that (1) the parameters used in the single-phase model accurately represent the real-world system, and (2) the simulated extraction rates from CSG wells reflect actual rates.

However, history matching a single-phase models' parameters against measured drawdown influenced by dual-phase processes carries the risk of inducing bias. As noted in the conceptualisation report (AECOM, 2018), there is a possibility of a gas phase at the former UCG site. This could lead to a lower effective hydraulic conductivity, consistent with the slow groundwater levels recovery observed in monitoring bores (Herckenrath et al. 2015).

In their review of previous modelling efforts for the site, CSIRO (2023) noted that attempting to fit drawdown recovery at the former UCG site may have led to an underestimation of calibrated hydraulic conductivity values. From a predictive perspective, this could result in unconservative predictions of contaminant migration off-site.

In the history matching conducted for the current groundwater modelling, this issue is partially addressed by decoupling the calibrated hydraulic properties before and after operation of the UCG site. Pressure recovery at the former UCG site is controlled locally through time-varying hydraulic properties. Unlike previous modelling efforts (e.g., AGE, 2023), these time-varying properties are allowed to both decrease and increase relative to their original values. These parameters can emulate the effect of lower hydraulic conductivity (and storage) caused by the presence of a gas phase. Propensity for bias to be introduced to hydraulic properties beyond the site is thus reduced. Constraining the spatial extent of potential bias is further ensured using distance-based localisation.

History matched parameters should thus reflect the effective hydraulic properties during the period when recovery data were collected. However, they do not allow for any subsequent changes such as those caused by ongoing re-adsorption of the gas phase. Consequently, flow and transport beyond the affected area should be less susceptible to bias.

Since the modelling conducted here focuses on comparative analysis between field development plans, any bias is expected to have minimal impact on decision-critical forecasts. While absolute predictions of recovery at the site may be subject to bias—and thus affect estimates of contaminant

migration timing and distance—the relative differences between scenarios are unlikely to be influenced.

## 2.2 Item – Action 10

### 2.2.1 DETSI Requirement – Item 10

From EA Amendment 20250319 Information Request EA0001613:

*The following issues may impact the monitoring of groundwater levels and quality and determining groundwater flow directions and trends at Lot 40 DY85:*

- *limited data points resulting in simplification of contours and flow direction*
- *groundwater quality being highly variable spatially*
- *reservoir pressure variations as a result of venting*
- *issues as a result of kill water introduced at some bores*

*Additionally, DETSI requires a complete understanding of the limitations of the groundwater modelling, to understand any uncertainty in the influence of the gasifiers on groundwater levels and reservoir pressure flow patterns, and conversely the risk of migration off-site.*

*Action 10*

*a) Relevant to the required groundwater modelling and results, provide an assessment with details on any limitations and uncertainty associated with the abovementioned issues and how these have been addressed.*

*b) Where relevant, such as for reported recharge rates, provide a comparison with OGIA conceptualised and/or modelled rates to support values applied in the groundwater modelling.*

### 2.2.2 Response to Action 10 (a)

#### 2.2.2.1 Limited data points resulting in simplification of contours and flow direction

We acknowledge that the limited number of groundwater level monitoring points can affect the detail and accuracy of interpreted contours and inferred flow directions when visualised from data.

It is important to note, however, that groundwater levels contours are not direct inputs to the model. Instead, the model simulates heads based on hydrogeological properties, boundary conditions, and observed data. The initial steady-state model provides a physically consistent starting point, followed by changes in the hydrogeological properties due to the gasifier operation and water abstraction from bores in and around the project site. The model was history matched against observed data, and where data were sparse, care was taken to avoid overfitting. Therefore, while the interpretation of contours is limited by data availability, this does not compromise the ability to simulate plausible flow directions based on physical processes.

#### 2.2.2.2 Groundwater quality being highly variable spatially

To incorporate this into the model, a statistical method was used to generate different possible maps (i.e., spatial distributions) of the initial contaminant concentration. Each map was based on a different set of assumptions about how concentrations vary over distance and direction, represented through spatially varying variograms describing the expected spatial patterns in the

data. By varying the variogram parameters, the modelling captured a broad range of realistic scenarios. These maps were then constrained using concentration data from Arrow and conceptual assumptions. This process resulted in a set of 200 different spatial distributions of concentration showing different distributions of benzene and naphthalene, that simultaneously honour the real concentration data and conceptual assumptions (e.g., elevated concentrations near gasifiers and low concentrations outside Lot 40 DY85). These 200 maps were used to run the ensemble of simulations for history matching with data up September 2024. This methodology ensures that the variability of groundwater quality is captured and constrained with all data available from Arrow as well as data from a similar UCG site as presented in the literature (EHS Support, 2014; WMV Environmental Pty Ltd, 2014; and Mallett, 2018).

#### 2.2.2.3 Reservoir pressure variations as a result of venting and issues as a result of kill water introduced at some bores

The groundwater monitoring data were reviewed by the third-party contractor, and the data that likely represent conditions affected by venting-related pressure changes and the introduction of kill water were then excluded from history matching to avoid biasing the history matching with inappropriate values. Where possible, data were amended to prevent mixing measurements from venting and non-venting events within the same time series. In cases where this separation was not feasible, and to minimise potential bias associated with the presence of kill water in the measurement data, the following safeguards were applied:

- **Conflicting data were excluded**: If a sudden jump in the data (possibly caused by venting) could not be explained by the model realisations, those data points were excluded from the history-matching process to avoid introducing bias.
- **Multiple data types were used in history matching, including**:
    - Absolute heads
    - Vertical head differences
    - Benzene and naphthalene concentrations

Incorporating different data types into the history-matching process helped minimise the risk of making predictions based on mixed or inconsistent datasets.

### 2.2.3 Response to Action 10 (b)

Recharge rates were sourced from the OGIA (2019, 2021) and AGE (2020) models. Initial recharge rates were 3.5, 1.0 and 0.2 mm/year for the Condamine Alluvium, Gubberamunda Sandstone and Westbourne Formation, respectively. These recharge rates were allowed to vary within the ensemble by +-50%. The recharge ranges and their comparison with OGIA (2019, 2021) values are shown in Table 2-2.

Table 2-2 – Recharge values and comparison with OGIA values.

| Formation | Min. (mm/yr) | Max. (mm/yr) | Mean (mm/yr) | Calibrated OGIA value (mm/yr) |
|---|---|---|---|---|
| Condamine Alluvium / Gubberamunda Sandstone | 1.75 | 4.5 | 3.5 | 3.5 for Condamine<br>3 for Gubberamunda |
| Westbourne Formation | 0.1 | 0.3 | 0.2 | 0.2 |

In the present work, the estimate of modelled flow rates in a relevant layer (the Macalister coal seam) were compared with that of the OGIA (2021) model at a common location based on ranges of input parameters (hydraulic conductivity, specific yield) and modelled hydraulic gradients in the same model year (2017). Flow velocities (*v*) were calculated using the following:

$$v = {}^{Ki}/_{S_y} \quad (2)$$

where:

v = flow velocity (m/d)

k = hydraulic conductivity (m/d)

i = hydraulic gradient (-)

$S_y$ = specific yield (-)

These estimated modelled flow rates were then directly compared to show consistency between the two models.

Figure 2-4 shows modelled hydraulic heads in OGIA (2019) model layer 13 (equivalent to the Macalister coal seam) for model year 2017 in the final calibrated model. The contour interval is 25 meters. The hydraulic gradient (i) at a location about 3 km west-northwest of Lot 40 DY85 (short black line on Figure 2-4) is calculated as a drop in head (DH) of 75 m over a length (DL) of 850 m, or I = 0.088. Hydraulic conductivity (K) distributions for the model ensembles as indicated in Figure 2-5 indicate values ranging from about 0.001 m/d to 0.01 m/d with a low standard deviation. The model assumed a consistent specific yield ($S_y$) of 0.01 for the entire model layer.

Figure 2-6 shows modelled hydraulic heads in layer 6 (equivalent to the Macalister coal seam) of the present model for year 2017 from the median realisation in the final calibrated ensemble. The contour interval is 20 meters. The hydraulic gradient (i) at a location about 3 km west-northwest of Lot 40 DY85 (short blue line on Figure 2-6) is calculated as a drop in head (DH) of 80 m over a length (DL) of 850 m, or I = 0.094. Hydraulic conductivity (K) distributions in model layer 6 determined for all the history-matched model ensembles range from about 0.0039 m/d to 0.095 m/d with a low standard deviation. Specific yield ($S_y$) distributions in model layer 6 determined for all the history-matched model ensembles range from 0.0019 to 0.1 with a median of 0.059.

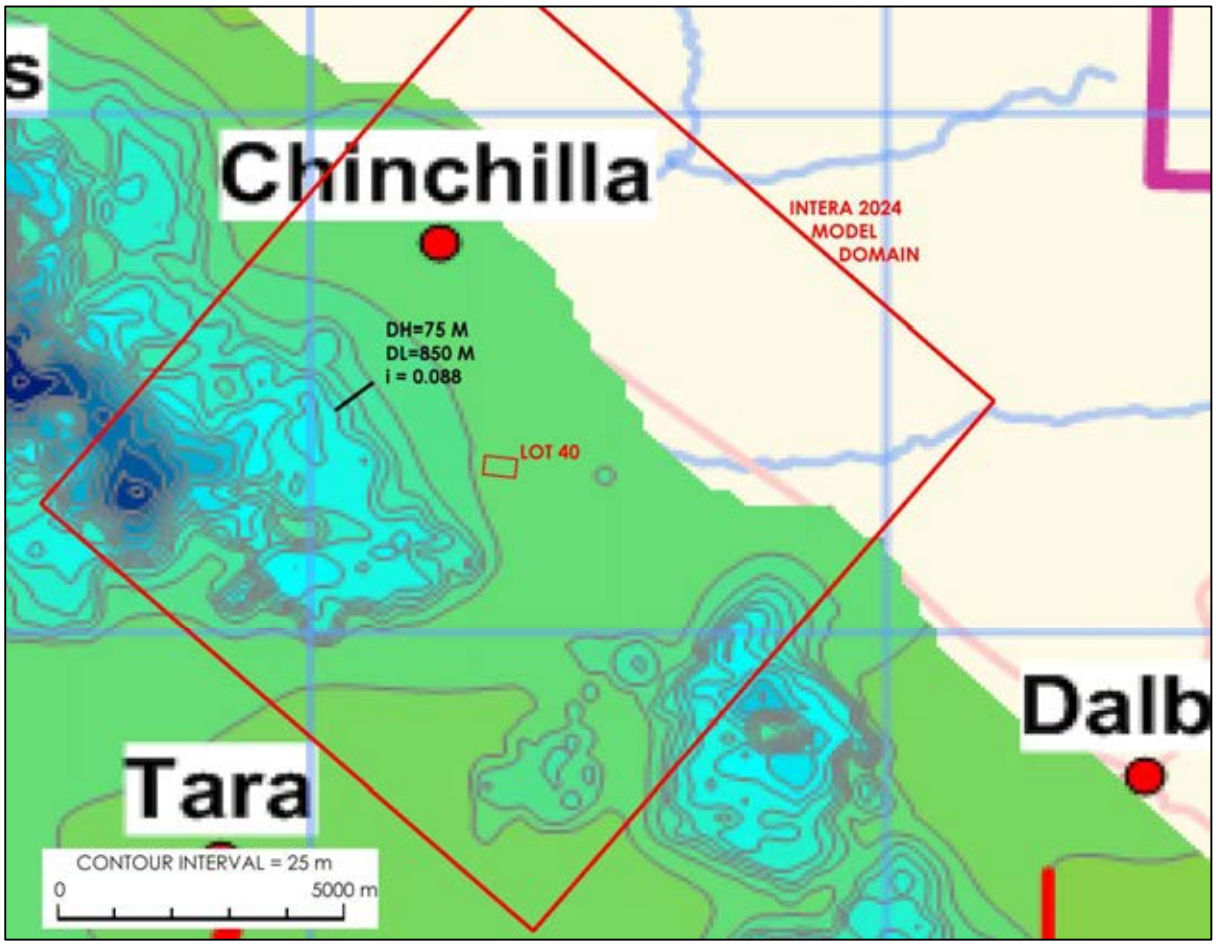


Figure 2-4 – Calibrated groundwater level contours in model layer 13 at the end of model year 2017 (from OGIA, 2019). The black line located northwest of Lot 40 DY85 is the line used for the hydraulic gradient calculation.

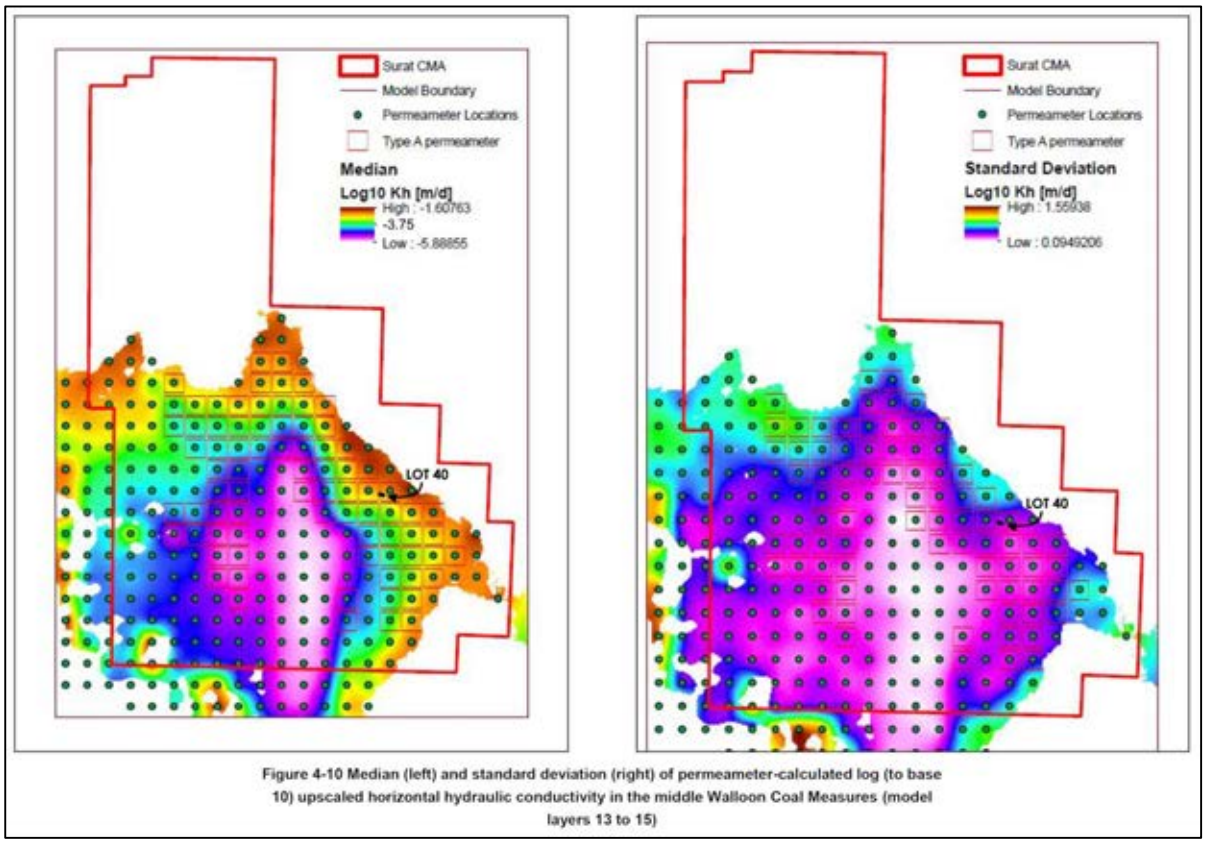


Figure 2-5 – Median (left) and standard deviation (right) of permeameter-calculated log (to base 10) upscaled horizontal hydraulic conductivity in the middle Walloon Coal Measures (model layers 13 to 15). From OGIA, 2019.

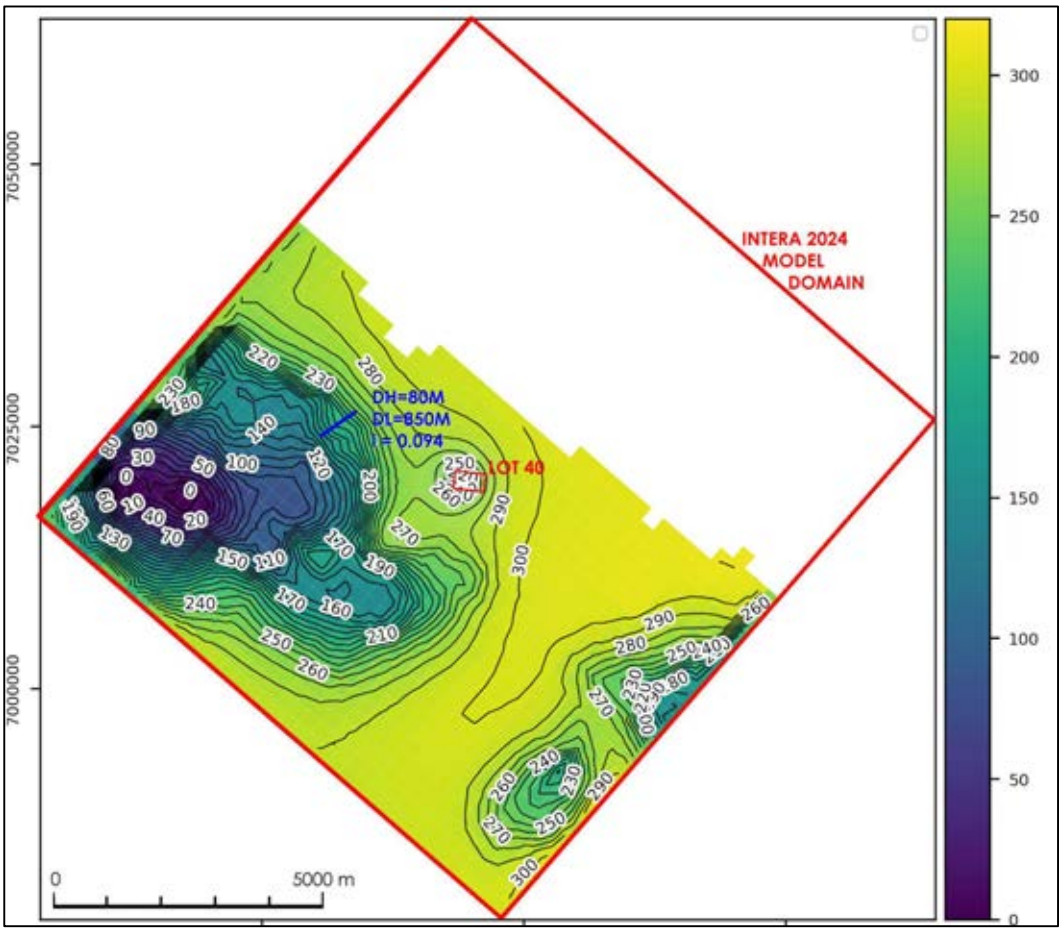


**Figure 2-6 – Calibrated groundwater level contours in model layer 6 at the end of model year 2017 (INTERA, 2024). The blue line located northwest of Lot 40 DY85 is the line used for the hydraulic gradient calculation.**

A summary of all input values with the resulting ranges of flow velocities is provided in Table 2-3. The results indicate that the average modelled flow velocities at the same location near Lot 40 DY85 are nearly identical between the two models. As shown in Table 2-3, the model review indicated that the OGIA model assumed a single homogeneous specific yield for the entire Macalister coal seam layer, while the INTERA model assumed a range of specific yield values that encompass the OGIA value within a range of over two orders of magnitude. The results of this review, therefore, indicate that the INTERA and OGIA models have similar resultant flow velocities and that the INTERA model has ranges of input values that better represent ranges of flow velocities in the groundwater.

**Table 2-3 – Parameter comparison between OGIA and the INTERA model**

| Parameter | OGIA model | INTERA model | Units |
|---|---|---|---|
| Hydraulic Gradient | 0.088 | 0.094 | - |
| Sy (low) | 0.01 | 0.0019 | - |
| Sy (mean) | | 0.059 | - |
| Sy (high) | | 0.1 | - |
| K (low) | 0.001 | 0.0039 | m/d |
| K (mean) | 0.005 | 0.029 | m/d |
| K (high) | 0.01 | 0.095 | m/d |

| Parameter | OGIA model | INTERA model | Units |
|---|---|---|---|
| Flow Velocity (low) | 0.009 | 0.004 | m/d |
| **Flow Velocity (mean)** | **0.044** | **0.046** | **m/d** |
| Flow Velocity (high) | 0.088 | 4.706 | m/d |

## 2.3 Item – Action 11

### 2.3.1 DETSI Requirement – Item 11

From EA Amendment 20250319 Information Request EA0001613:

*If available, provide the following additional information:*

- *The year in which the hydraulic gradient at Lot 40 DY85 inverts;*
- *The vertical gradient between Springbok Sandstone and WCM Macalister;*
- *The maximum particle migration distance from the boundary of Lot 40 DY85 over the simulation period;*
- *The particle locations at the end of the simulation period;*
- *Forecasted contaminant concentrations around Lot 40 DY85;*
- *Predictive year at which the hydrocarbon plume would deplete.*

*Additionally provide the latest monitoring results report Arrow has completed for the historic UCG site.*

### 2.3.2 Response to Action 11

#### 2.3.2.1 The year in which the hydraulic gradient at Lot 40 DY85 inverts

According to the simulated ensemble, the average time at which the gradient in the Lot 40 DY85 reverses (late 2025) is the same for Scenario 1 (5 Red Circle Wells Active) and Scenario 2 (5 Red Circle Wells Excluded). However, some realisations show gradient reversal as soon as the start of 2025 and as late as 2035.

#### 2.3.2.2 The vertical gradient between Springbok Sandstone and WCM Macalister

Figure 2-7 presents the vertical head differences between Macalister coal seam and Springbok Sandstone layers within Lot 40 DY85 for Scenario 1, Scenario 2, and the difference between both scenarios. It is important to note that the vertical gradient in both scenarios—and across all realisations—remains consistently greater than zero. This indicates that the modelled vertical gradient is downwards (i.e., from the Springbok Sandstone to the Macalister coal seam) in all realisations, with no reversal in gradient direction during the simulation period. There's no difference between the two scenarios.

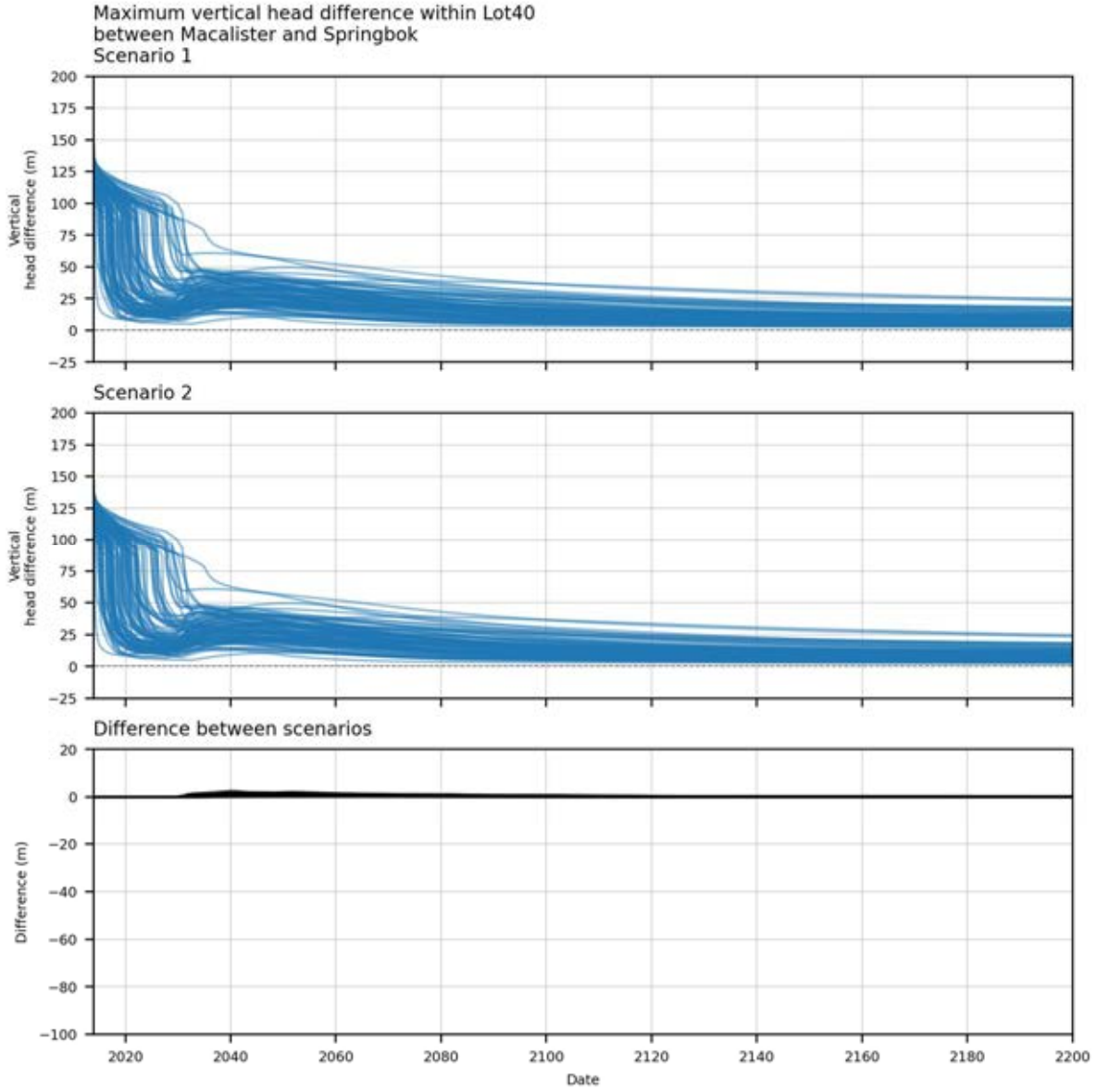


Figure 2-7 – Vertical head differences between Macalister coal seam and Springbok Sandstone layers within Lot 40 DY85 for the (top) Scenario 1, (middle) Scenario 2 and (bottom) the difference between both scenarios.

#### 2.3.2.3 The maximum particle migration distance from the boundary of Lot 40 DY85 over the simulation period

Table 1-2 present summary statistics for particle movement distances under Scenarios 1 and 2. As indicated in Section 1.4.4, the maximum particle migration distance from the Lot 40 DY85 boundary was 2,432 m and 2,425 m for Scenarios 1 and 2, respectively, with almost no difference between the two scenarios.

#### 2.3.2.4 The particle locations at the end of the simulation period

Figure 2-8 presents the particle locations over the simulation period for the realisation that produced the longest particle travel distance for Scenario 1.

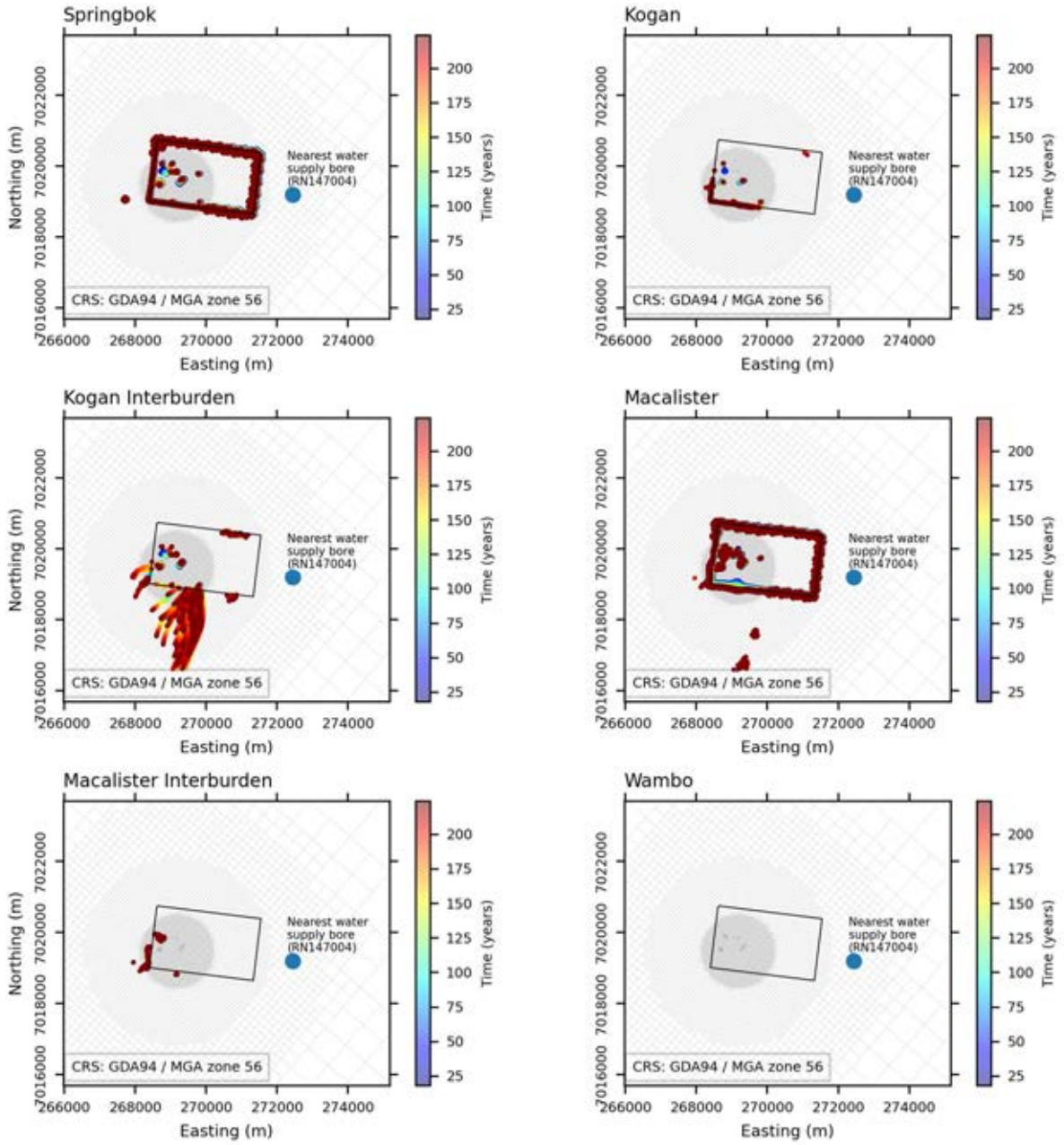


Figure 2-8 – Particle locations over the simulated period for the realisation (within scenario 1) that depicted the longest travel distance.

### 2.3.2.5 Forecasted contaminant concentrations around Lot 40 DY85

Benzene and naphthalene concentrations' maps are presented in Section 1.4.3. These maps show the mean ensembles concentrations for the Springbok Sandstone and Macalister coal seam for each scenario. Snapshots are provided for the years 2024, 2030, 2080 and 2200.

### 2.3.2.6 Predictive year at which the hydrocarbon plume would deplete

Table 2-4 summarises the model-predicted years when naphthalene and benzene concentrations are expected to completely attenuate (defined as the year when more than 99% of grid cells have concentrations below 1 µg/L). The contaminant transport models were evaluated using a UA with a

large ensemble of input parameters. As such, results are presented for P5, P50 (mean), and P95 probabilities rather than individual values. As shown in Table 2-4, naphthalene achieves complete attenuation faster than benzene; therefore, attenuation of benzene concentrations is used to characterise the overall depletion of the hydrocarbon plume.

From the simulated predictive ensemble, the following conclusions can be drawn:

- Benzene in Springbok Sandstone is predicted to attenuate completely between 2032 and 2049, based on 95% confidence interval. The mean predicted year across the ensemble is 2042 and 2043 for Scenario 1 and Scenario 2, respectively, indicating practically no difference between the scenarios.
- Benzene in Macalister coal seam is predicted to achieve complete attenuation between 2026 and 2045, based on the 95% confidence interval. The mean predicted year of the ensemble is 2032 for both Scenario 1 and Scenario 2, indicating practically no difference between scenarios.
- Naphthalene in Springbok Sandstone is predicted to attenuate completely between 2020 and 2040, based on the 95% confidence interval. The mean predicted year of the ensemble is 2027 and 2028 for Scenario 1 and Scenario 2, respectively, indicating practically no difference between scenarios.
- Naphthalene in Macalister coal seam is predicted to achieve complete attenuation between 2018 and 2032, based on the 95% confidence interval. The mean predicted year of the ensemble is 2021 for both Scenario 1 and Scenario 2, implying practically no difference between scenarios.

**Table 2-4 - Summary of predicted years to achieve contaminant depletion.**

| Compound | Statistics | Springbok Sandstone | | Macalister Coal Seam | |
|---|---|---|---|---|---|
| | | Scenario 1 | Scenario 2 | Scenario 1 | Scenario 2 |
| Naphthalene | P5 | 2020 | 2020 | 2018 | 2018 |
| | Mean | 2027 | 2028 | 2021 | 2021 |
| | P95 | 2036 | 2040 | 2027 | 2032 |
| Benzene | P5 | 2032 | 2032 | 2026 | 2026 |
| | Mean | 2042 | 2043 | 2032 | 2032 |
| | P95 | 2047 | 2049 | 2045 | 2045 |

# 3.0 Conclusions

Arrow Energy (Arrow) is seeking to amend Environmental Approval EA0001613 for its Surat Gas Project (SGP) South operations, including the removal of Condition Water 1B, which restricts the location of coal seam gas (CSG) production wells within 10 km of Lot 40 DY85.

The groundwater assessment was conducted to: (1) evaluate the potential influence of five CSG wells proposed within 10 km of the centre of Lot 40 DY85, near the boundary of petroleum lease (PL) 493, on the movement of contaminants from historical underground coal gasification (UCG) activities at Lot 40 DY85; and (2) address groundwater-related actions 9, 10, and 11 from the EA0001613 information request issued by the Department of Environment, Technology, Science and Innovation (DETSI) on 11 June 2025.

The assessment was based on numerical groundwater flow, contaminant transport, and particle tracking modelling using the most recent Field Development Plan (FDP) for PL253 and PL493, along with an ensemble history-matched dataset. Predictive modelling scenarios were run over a 200-year period to assess the potential incremental impact of the five CSG wells on contaminant migration from Lot 40 DY85. Scenario 1 included abstraction from the five proposed wells near the southwestern boundary of PL493 (within 10 km of Lot 40 DY85), as well as from all non-Arrow-operated CSG wells, the 55 wells within PL253 (associated with EA0001401 approval), and the 28 wells within PL493. Scenario 2 excluded the five proposed wells but included all other wells from Scenario 1.

The modelling indicated that the median year for hydraulic gradient reversal in the Macalister coal seam at Lot 40 DY85 is late 2025, with reversals occurring as late as 2035. The vertical gradient between the Springbok Sandstone and the Macalister coal seam remains downward in all model realisations, with no reversal observed over the simulation period. The maximum particle migration distance from the Lot 40 DY85 boundary was 2,432 m across all model realisations.

Naphthalene was predicted to deplete earlier than benzene, with mean depletion years of 2027–2028 in the Springbok Sandstone and 2021 in the Macalister coal seam, consistent across both scenarios. Early depletion (P5) was predicted as early as 2018–2020, while later estimates (P95) extended to 2040 in the Springbok and 2032 in the Macalister. Benzene showed greater persistence, with mean depletion predicted around 2042–2043 in the Springbok and 2032 in the Macalister. P5 values for benzene ranged from 2026–2032, while P95 extended to 2049 in the Springbok and 2045 in the Macalister.

Overall, the assessment concluded that pumping from the five CSG wells near PL493 has minimal impact on contaminant migration from Lot 40 DY85. The wells do not induce hydraulic gradients that increase the risk of contaminant movement, and contaminants are expected to attenuate before leaving the site, posing a negligible to low risk of off-site migration.

Based on the modelling results and the responses to the actions requested in EA0001613, it is concluded that Condition Water 1B is no longer necessary to protect groundwater or environmental values. Its removal would allow Arrow to optimise the placement of CSG wells without increasing the risk of adverse groundwater impacts related to historical UCG activities at Lot 40 DY85.

# 4.0 References

AECOM, 2018. Conceptual Site Model – Hopeland Site. Prepared for Department of Environment and Science by AECOM Australia Pty Ltd. 12th September 2018.

AGE, 2020. Production Licensing Modelling Support prepared for Arrow Energy by Australasian Groundwater and Environmental Consultants Pty Ltd. June 2020.

AGE, 2023. PL 253 Environmental Approval Amendment Support – Contaminant transport validation – Addendum to AGE (2022) by Australasian Groundwater and Environmental Consultants Pty Ltd. 19th January 2023.

Arrow, 2020. PL253 Conceptual model –2020 Update. Technical Note, Surat Gas Project.

Arrow, 2021. Groundwater Characteristics Monitoring Plan.

Bayard, R., Barna, L., Mahjoub, B., and Gourdon, R., 2020. Influence of the presence of PAHs and coal tar on naphthalene sorption in soils, Journal of Contaminant Hydrology, Volume 46, Issues 1–2, pp. 61-80. https://doi.org/10.1016/S0169-7722(00)00125-X.

Bekins B, A., Warren E., Godsy E, M., 1998. A comparison of zero-order, first-order and Monod biotransformation models. Ground Water 36, 261-268.

EHS Support, 2014. BWC UCG Site Investigation Report J14002; confidential report from WMV Environmental Pty Ltd to Carbon Energy Limited, Pittsburgh, USA *as reported in* Mallett, C.W., 2018. Environmental controls for underground coal gasification; Proceedings of the Institution of Mechanical Engineers, Part A: Journal of Power and Energy; v. 232 (1), https://doi.org/10.1177/0957650917723733

Grathwohl, P. (2011). Fate and transport of organic compounds in (to) the subsurface environment. In B. Xing, N. Senesi, & P. M. Huang (Eds.), Biophysico-chemical processes of anthropogenic organic compounds in environmental systems (Chapter 8). Wiley.

GHD, 2019. Arrow Hopeland Groundwater Study Groundwater Modelling Report – PL253.

Herckenrath, D., Doherty, J. and Panday, S., 2015. Incorporating the effect of gas in modelling the impact of CBM extraction on regional groundwater systems, Journal of Hydrology, vol. 523, pp. 587–601.

INTERA, 2024. PL253 – Conceptual Site, Groundwater Flow, Contaminant Transport and Predictive Modelling: Consolidated Report; contract report prepared for Arrow Energy by INTERA Geosciences Pty Ltd.

Moore, C.R., Doherty, J.E., Howell, S., Erriah, L., de Verteuil, D., Cui, T., 2013. Challenges for upscaling hydraulic properties and processes in the coal seam gas context, CSIRO.

Moore, C.R., Doherty, J., Howell, S., Erriah, L., 2015. Some Challenges Posed by Coal Bed Methane Regional Assessment Modeling. Groundwater 53, 737–747. https://doi.org/10.1111/gwat.12276

Lien, J.M., Liu, G., and Langevin, C.D., 2017. GRIDGEN version 1.0.02 -- A computer program for generating unstructured finite-volume grids: U.S. Geological Survey Software Release, 06 January 2017. http://dx.doi.org/10.5066/F79G5JXV

Odermatt, J.R., 1994. Natural chromatographic separation of benzene, toluene, ethylbenzene and xylenes (BTEX compounds) in a gasoline contaminated ground water aquifer. Organic Geochemistry, Volume 21, Issues 10–11, pp. 1141-1150. https://doi.org/10.1016/0146-6380(94)90076-0.

OGIA, 2016. Hydrogeological Conceptualisation Report for the Surat Cumulative Management Area. OGIA, Department of Natural Resources and Mines.

OGIA, 2019. Groundwater Modelling Report. Surat Cumulative Management Area.

OGIA, 2021. Modelling of cumulative groundwater impacts in the Surat CMA: approach and methods. Version 1.0.

Prommer, H., Davis G.B., Barry D.A., Miller C.T., 2003. Modelling the Fate of Petroleum Hydrocarbons in Groundwater. Proceedings of the Fifth National Workshop on the Assessment of Site Contamination.

# APPENDIX A

# Updated CSG Wells

| Well name | Coal seam formation top | Coal seam formation bottom | Group |
|---|---|---|---|
| Wyalla 36 | Wambo | Condamine | Blue circle 28 wells |
| Wyalla 30 | Wambo | Condamine | Blue circle 28 wells |
| Wyalla 42 | Wambo | Condamine | Blue circle 28 wells |
| Wyalla 39 | Wambo | Condamine | Blue circle 28 wells |
| Wyalla 26 | Wambo | Condamine | Blue circle 28 wells |
| Wyalla 43 | Wambo | Condamine | Blue circle 28 wells |
| Wyalla 28 | Wambo | Condamine | Blue circle 28 wells |
| Wyalla 40 | Wambo | Condamine | Blue circle 28 wells |
| Wyalla 47 | Wambo | Condamine | Blue circle 28 wells |
| Wyalla 21 | Wambo | Condamine | Blue circle 28 wells |
| Wyalla 25 | Wambo | Condamine | Blue circle 28 wells |
| Wyalla 46 | Wambo | Condamine | Blue circle 28 wells |
| Wyalla 23 | Wambo | Condamine | Blue circle 28 wells |
| Wyalla 38 | Wambo | Condamine | Blue circle 28 wells |
| Wyalla 41 | Wambo | Condamine | Blue circle 28 wells |
| Wyalla 24 | Wambo | Condamine | Blue circle 28 wells |
| Wyalla 37 | Wambo | Condamine | Blue circle 28 wells |
| Wyalla 29 | Wambo | Condamine | Blue circle 28 wells |
| Wyalla 27 | Wambo | Condamine | Blue circle 28 wells |
| Wyalla 35 | Argyle | Condamine | Blue circle 28 wells |
| Wyalla 45 | Wambo | Condamine | Blue circle 28 wells |
| Wyalla 33 | Wambo | Condamine | Blue circle 28 wells |
| Wyalla 31 | Argyle | Condamine | Blue circle 28 wells |
| Wyalla 32 | Argyle | Condamine | Blue circle 28 wells |
| Wyalla 44 | Wambo | Condamine | Blue circle 28 wells |
| Wyalla 22 | Wambo | Condamine | Blue circle 28 wells |
| Wyalla 34 | Wambo | Condamine | Blue circle 28 wells |
| Wyalla 49 | Argyle | Condamine | Blue circle 28 wells |
| Wyalla 107 | Macalister | Condamine | Red circle 5 wells |
| Wyalla 104 | Wambo | Condamine | Red circle 5 wells |
| Wyalla 103 | Wambo | Condamine | Red circle 5 wells |
| Wyalla 102 | Wambo | Condamine | Red circle 5 wells |
| Wyalla 101 | Wambo | Condamine | Red circle 5 wells |
| Hopeland 402 | Macalister | Condamine | Stage 1 55 wells |
| Hopeland 484 | Macalister | Condamine | Stage 1 55 wells |
| Hopeland 148 | Wambo | Condamine | Stage 1 55 wells |
| Hopeland 121 | Kogan | Condamine | Stage 1 55 wells |
| Hopeland 405 | Macalister | Condamine | Stage 1 55 wells |
| Hopeland 142 | Wambo | Condamine | Stage 1 55 wells |
| Hopeland 482 | Macalister | Condamine | Stage 1 55 wells |

| Well name | Coal seam formation top | Coal seam formation bottom | Group |
|---|---|---|---|
| Hopeland 132 | Macalister | Condamine | Stage 1 55 wells |
| Hopeland 166 | Macalister | Condamine | Stage 1 55 wells |
| Hopeland 125 | Kogan | Condamine | Stage 1 55 wells |
| Hopeland 418 | Macalister | Condamine | Stage 1 55 wells |
| Hopeland 411 | Macalister | Condamine | Stage 1 55 wells |
| Hopeland 144 | Wambo | Condamine | Stage 1 55 wells |
| Hopeland 126 | Kogan | Condamine | Stage 1 55 wells |
| Hopeland 416 | Macalister | Condamine | Stage 1 55 wells |
| Hopeland 157 | Macalister | Condamine | Stage 1 55 wells |
| Hopeland 403 | Macalister | Condamine | Stage 1 55 wells |
| Hopeland 412 | Macalister | Condamine | Stage 1 55 wells |
| Hopeland 145 | Wambo | Condamine | Stage 1 55 wells |
| Hopeland 147 | Wambo | Condamine | Stage 1 55 wells |
| Hopeland 171 | Macalister | Condamine | Stage 1 55 wells |
| Hopeland 158 | Macalister | Condamine | Stage 1 55 wells |
| Hopeland 107 | Macalister | Condamine | Stage 1 55 wells |
| Hopeland 131 | Macalister | Condamine | Stage 1 55 wells |
| Hopeland 153 | Macalister | Condamine | Stage 1 55 wells |
| Hopeland 414 | Macalister | Condamine | Stage 1 55 wells |
| Hopeland 133 | Macalister | Condamine | Stage 1 55 wells |
| Hopeland 123 | Kogan | Condamine | Stage 1 55 wells |
| Hopeland 401 | Macalister | Condamine | Stage 1 55 wells |
| Hopeland 167 | Macalister | Condamine | Stage 1 55 wells |
| Hopeland 152 | Macalister | Condamine | Stage 1 55 wells |
| Hopeland 156 | Macalister | Condamine | Stage 1 55 wells |
| Hopeland 415 | Macalister | Condamine | Stage 1 55 wells |
| Hopeland 106 | Macalister | Condamine | Stage 1 55 wells |
| Hopeland 174 | Macalister | Condamine | Stage 1 55 wells |
| Hopeland 146 | Wambo | Condamine | Stage 1 55 wells |
| Hopeland 165 | Macalister | Condamine | Stage 1 55 wells |
| Hopeland 122 | Kogan | Condamine | Stage 1 55 wells |
| Hopeland 128 | Kogan | Condamine | Stage 1 55 wells |
| Hopeland 483 | Macalister | Condamine | Stage 1 55 wells |
| Hopeland 124 | Kogan | Condamine | Stage 1 55 wells |
| Hopeland 417 | Macalister | Condamine | Stage 1 55 wells |
| Hopeland 404 | Macalister | Condamine | Stage 1 55 wells |
| Hopeland 143 | Wambo | Condamine | Stage 1 55 wells |
| Hopeland 481 | Macalister | Condamine | Stage 1 55 wells |
| Hopeland 127 | Kogan | Condamine | Stage 1 55 wells |
| Hopeland 172 | Macalister | Condamine | Stage 1 55 wells |
| Hopeland 175 | Macalister | Condamine | Stage 1 55 wells |
| Hopeland 155 | Macalister | Condamine | Stage 1 55 wells |

| Well name | Coal seam formation top | Coal seam formation bottom | Group |
|---|---|---|---|
| Hopeland 170 | Macalister | Condamine | Stage 1 55 wells |
| Hopeland 173 | Macalister | Condamine | Stage 1 55 wells |
| Hopeland 413 | Macalister | Condamine | Stage 1 55 wells |
| Hopeland 154 | Macalister | Condamine | Stage 1 55 wells |
| Hopeland 406 | Macalister | Condamine | Stage 1 55 wells |
| Hopeland 151 | Macalister | Condamine | Stage 1 55 wells |

# Appendix B

REPORT

# PL253 – Conceptual Site, Groundwater Flow, Contaminant Transport and Predictive Modelling

## Consolidated Report

## Hopeland, QLD

**Prepared for:**

Arrow Energy Pty Ltd
39/111 Eagle St,
Brisbane, QLD 4000

**Prepared by:**

INTERA Incorporated
166/580 Hay Street
Perth, WA 6000

November 28, 2024

# Executive Summary

**Introduction**

Arrow Energy Pty Ltd (Arrow) plans to extract coal seam gas on production licence 253 (PL253). The licence covers the former Linc Energy underground coal gasification (UCG) site, where groundwater contains residual hydrocarbon contamination. The Department of Environment and Sciences (DES) has authorised an Environmental Authority EA0001401 (EA) for an initial 55 production wells in PL253. To address the EA comments on previous modelling conducted on PL253, Arrow has requested INTERA to 1) update conceptual site model, 2) based on updated conceptual site model, develop the groundwater flow model and conduct history matching, 3) implement uncertainty analysis, 4) conduct particle tracking and contaminant transport modelling, 5) undertake predictive analysis, and (6) conduct impact assessment.

A numerical groundwater model was developed, expanding on the previous modelling efforts of GHD (2019) and AGE (2020 and 2023). The overarching goal is to assess the impacts of the proposed CSG operations at PL253 on groundwater flow and contaminant migration from the former Linc Energy site at Lot40 DY85. The present work, therefore, aims to fulfill this goal using particle tracking and contaminant transport modelling based on updated groundwater flow model.

**Site Conceptual Model**

A site conceptual model of the PL253 and surrounding tenements (including PL493 and PL185) was updated based on previous work from AGE (2023) and GHD (2019), prior to development of the groundwater flow and transport models. The site conceptualisation includes the geologic framework and mapping of the hydrostratigraphic units with focus in the geometry and continuity of the layers. In addition, an analysis of groundwater levels trends and the latest distribution of groundwater heads was conducted using available monitoring bores data. Noteworthy, bores in Springbok and WCM Macalister have depicted a recovery in pressure since cessation of the UCG operation, especially in Lot40 DY85. Since then, groundwater levels have remained stable with some exceptions in Lot40 DY85.

The groundwater quality data were analysed using groundwater sampling data which dates to 2024. Major ions were analysed to identify water type and BTEXN compounds (benzene, toluene, ethylbenzene, xylenes and naphthalene) constituting the main organic contaminants in the site. Springbok depicts higher concentrations of benzene and naphthalene than WCM Macalister. Broadly speaking, BTEXN concentrations have decreased between 2020 to date due to migration of the contaminants and/or natural attenuation. However, bores like NB02D have depicted a stable concentration of BTEXN compounds like benzene.

Finally, the risk to downstream groundwater users is assessed to be minimal in the near to medium future due to the existing level of depressurisation within the Walloon Coal Measures. The likelihood of contaminants moving vertically into other geological layers is also low because the pressure in this formation (Walloon Coal Measures) is lower than both the overlying and the underlying units (refer to Chapter 2.3.3). Furthermore, there is no indication of vertical fractures at the gasifiers' locations, although fractures have been noted in the broader Lot40 DY85.

**Groundwater Flow Model**

A single-phase groundwater flow model was developed in MODFLOW6, updating an existing MODFLOW-USG model (AGE, 2023). The grid was also updated which includes refined discretisation at Lot40 DY 85. Additionally, the model layers were updated with bore log data supplied by Arrow.

External boundary conditions, as well as non-Arrow CSG extraction rates were updated from the most recent generation of regional cumulative impact assessment modelling (OGIA, 2021).

Boundary conditions were applied to simulate the (1) former UCG gasifier operations and their impacts, (2) CSG production wells (Arrow and non-Arrow) and Hopeland pilot-test wells, (3) external boundary conditions arising from regional CSG activities, and (4) recharge. The operation of UCG gasifiers is understood to have caused depressurisation through water/gas removal and changes in hydraulic properties due to the combustion process. The former was simulated using the drain (DRN) package, and the latter with time-varying hydraulic properties.

History matching involves changing model parameters until outputs from a group of models reproduce observed, measured data. The aim is to find combinations of a model's uncertain attributes that minimise the difference between simulated and the observed data. History matching was undertaken using the Iterative Ensemble Smoother (IES) method implemented in PEST++. This method enables efficient solutions to high-dimensional inverse problems, as well as calibration-constrained non-linear uncertainty analysis.

Targets for history matching of the groundwater flow model included groundwater level time-series and the vertical head differences observed between bores screened across various hydrostratigraphic units. Additional observations of "soft data" were included as constraints to preclude parameters which result in unrealistic behaviour.

Parameterised model features included hydraulic properties and boundary conditions. These include static and time-varying hydraulic properties, as well as external boundary conditions, well extraction rates and properties of the UCG gasifiers. Pilot points are employed for spatially varying parameters to enable incorporation of subsurface heterogeneity.

A posterior parameter ensemble with 159 realisations was obtained through history matching. Each of these adequately represent measured data and soft constraints. Comparison between measured and simulated time-series of hydraulic heads in bores around Lot40 were well reproduced. Statistical model benchmarks run over the entire posterior simulated ensemble indicated that the ensemble of models performed well. For all realisations, values of root mean square error (RMSE) for hydraulic heads observations below 10% were achieved.

**Particle Tracking and Contaminant Transport Modelling**

Two approaches (particle tracking and contaminant transport modelling) were considered to assess the impact of the proposed field development on migration of contaminants within PL253, in particular around and within Lot40 DY85.

First, the particle tracking model was used to assess potential contaminant flow paths without including natural attenuation processes, effectively simulating the centre of the plume of a conservative tracer.

A contaminant transport model was then developed based on the groundwater flow numerical model. Unlike particle tracking model, the contaminant transport model includes, mechanical dispersion, molecular diffusion, as well as natural attenuation (sorption and biodegradation/decay), and dual domain mass transfer processes continuously occurring within subsurface and have a profound impact on migration and attenuation of the existing contaminants. Benzene and naphthalene were selected as the simulated compounds, as the more recalcitrant contaminants of the BTEXN family. Conditioning of the groundwater quality data was conducted to characterise the initial contaminant distribution and its uncertainty.

The posterior parameter ensemble of 159 realisations obtained from the groundwater flow model was used as a prior parameter ensemble for the contaminant transport model. The transport model was history-matched against concentrations of the compounds from the measured groundwater quality data. During history-matching, the transport-only parameters were allowed to vary, while all the groundwater flow parameters were kept fixed.

A posterior parameter ensemble with 159 realisations was obtained through history matching. Concentrations of benzene and naphthalene were adequately reproduced, especially the most important behaviour of decreasing concentrations in most observation bores was successfully simulated. However, bores depicting a decreasing trend followed by increasing concentrations (e.g., NB01S in Springbok and NB02D in Macalister) could not be reproduced. This suggests the existence of a source term near or upgradient of these bores.

**Predictive analysis and impact assessment**

The impact of proposed CSG production at PL253 was assessed in terms of changes to the groundwater flow regime and potential for UCG-related contaminant migration away from the former Linc Energy site at Lot40. The relative impact was assessed by simulating two scenarios: (1) the Base case and (2) PL253 future development plans (FDP). The former simulates the baseline scenario with extraction limited to currently authorised 284 CSG wells. The latter includes the additional 55 CSG wells from the EA. The forecast period was extended up to year 2200.

The particle tracking model was employed to assess potential contaminant flow paths under both FDP scenarios. To address EA comment on the particle density, the allocation of particles was extended to model cells at (1) the gasifiers in Springbok Sandstone and Macalister Coal Seam, (2) the border of Lot40 in the same hydrogeological units and (3) at monitoring bore locations in the layers where they are screened. A sensitivity analysis was performed to assess the number and position of particles released per cells. Outcomes suggested 50 particles per cell provides sufficient resolution.

The impact prediction was analysed with all 159 realisations from the history matched parameter ensemble. Impacts were then assessed by comparing quantities of interest (QoI) between the two FDP scenarios. The defined QoIs are (1) the year when the hydraulic gradient at Lot40 reverts from inward to outward, (2) the maximum particle distance from the boundary of Lot40 over the simulated period and (3) particle locations at the end of 2200.

Results showed that uncertainty in forecasted outcomes is large. However, the difference between the two FDP scenarios is minor, and notably the PL253 FDP scenario does not always result in less favourable outcomes.

The difference between the minimum hydraulic head within Lot40 and head at its boundary was utilised as a proxy to identify when the gradient will be reversed in Lot40. Model results suggested that drawdown recovery at Lot40 may occur anytime between the present and the next 100 years. However, the difference between FDP scenarios is less than 5 years for all parameter realisations. Regardless of the uncertainty in forecasting the absolute value, uncertainty in the relative impact of the PL253 FDP is small. Additionally, the likelihood of a slower recovery is almost the same for the Base case FDP as it is for the PL253 FDP.

Similar observations can be made when comparing simulated particle distances from the boundary of Lot40. Particle tracking results highlighted large uncertainty regarding where UCG-related contaminants may reach within the simulated period. The spatial extent to which simulated particles may reach can be over 2 km from the boundary of Lot40. However, once again, the difference

between the FDP scenarios is minor. Furthermore, in neither case do particles reach existing or proposed CSG wells during the simulated period.

Uncertainty in the spatial extent is dominated by the pathways that particles take as they migrate vertically downwards from the Springbok. Particles released in the Macalister layer travel shorter distances from the site during the simulated period and tend to remain within the boundary of Lot40. Constraining the uncertainty around predictions of contaminant movement would benefit from improved characterisation of (1) current spatial distribution of contaminant, in particular within the Springbok layer and (2) vertical connectivity between the Springbok and Macalister layers at and around the site.

In addition to the particle tracking, predictive modelling was also conducted based on the posterior ensemble from the history-matched transport model comparing the same two FDP scenarios. Two different Quantities of Interest were used for the transport model: (1) forecasted concentrations around Lot40 and (2) the predicted year at which the hydrocarbons would completely deplete were assessed and compared between the scenarios. Moreover, concentrations at the boundary of Lot40 were compared with the Fresh Water Guidelines (ANZECC & ARMCANZ, 2000).

Results from the predictive model showed that the maximum simulated concentrations would mostly be below the guidelines before the end of the simulated period for both scenarios. Moreover, simulated results suggested that concentrations of benzene would reach values below the corresponding limit of reporting (LOR) between 2033 and 2052 in Springbok, and between 2030 and 2051 in Macalister. Similarly for naphthalene, predictions suggest that concentration values will reach values below LOR between 2021 and 2044 in Springbok, and between 2018 and 2037 in Macalister. A few model realisations predicted the migration of the contaminants out of the Lot40 (south and west) mainly due to the future abstraction of the Hopeland Site that is located in that direction.

These predictions suggest a minimal impact from the proposed 55 CSG wells on the migration of the contaminants. This is possibly due to ongoing diminishing of the contaminants extent, controlled mainly by the natural attenuation processes (e.g., sorption and degradation) than advective transport driven by the CSG wells. In addition, most of the 55 CSG wells are not proposed to target WCM Macalister and none of them target Springbok. Finally, most of CSG wells will start their operations from 2027 when the contaminant extent have already dissipated because of sorption and degradation as confirmed by predictive modelling.

**Final remarks**

In summary, despite the significant uncertainty associated with migration and attenuation of the residual UCG selected contaminants, the comparison of the different predictive scenarios suggests that the proposed field development plan at PL253 is unlikely to have a significant impact in comparison to the baseline case.

# Table of Contents

# List of Appendices

# List of Figures

# List of Tables

# Acronyms and Abbreviations

| | |
|---|---|
| CMA | Cumulative Management Area |
| CSG | Coal seam gas |
| CSIRO | Commonwealth Scientific and Industrial Research Organisation |
| DES | Department of Environment and Sciences |
| DRN | drain boundary package |
| EA | Environmental Authority |
| FDP | Future Development Plan |
| GHB | General head boundary package |
| GMP | Groundwater Monitoring Plan |
| IES | Iterative ensemble smoother |
| INTERA | INTERA Geosciences Pty Ltd |
| K | Horizontal hydraulic conductivity |
| Km | Kilometre |
| Kv | Vertical hydraulic conductivity |
| m | Meter |
| MAW | Multi-aquifer well package |
| MF6 | MODFLOW 6 |
| MFUSG | MODFLOW-USG |
| NSE | Nash–Sutcliffe efficiency coefficient |
| OGIA | Office of Groundwater Impact Assessment |
| PDC | Prior-data conflict |
| PL | Production License |
| PL253 | Production License 253 |
| QoI | Quantity of Interest |
| RCH | Recharge package |
| RMSE | Root mean square error |
| RPUVR | Relative parameter uncertainty variance reduction |
| SD | Standard Deviation |
| Sr | Specific retention |
| Ss | Specific storage |
| Sy | Specific yield |
| TVK | Time-varying conductivity package |
| TVS | Time-varying storage package |
| UCG | Underground coal gasification |
| UWIR | Underground water impact report |
| WCM | Walloon Coal Measures |
| WEL | Well boundary package |

# 1.0 Introduction

Arrow Energy Pty Ltd (Arrow) is seeking to undertake coal seam gas production on the production licence 253 (PL253). This licence encompasses the former site of underground coal gasification (UCG) by Linc Energy operation in MDL309 on Lot40 DY85 (henceforth Lot40), where residual hydrocarbon contamination and other UCG by-products are understood to be present within the groundwater. Arrow has been conducting monitoring, modelling, and annual reporting around the former UCG site since 2018 (Arrow, 2021).

Following the review of Arrow's most recent work at the area, the Department of Environment and Sciences and Innovation (DESI) has approved an Environmental Authority (EA) (No. 0001401 in effect on 25 May 2023) for an initial 55 well production field. This EA requires Arrow Energy to address comments from the reviews of the modelling works, and further peer review of work to satisfy the conditions of this EA.

In order to address the impacts of the proposed CSG operations at PL253 on groundwater flow and contaminant migration from the former Linc Energy site at Lot40 DY85, Arrow has commissioned INTERA Geosciences Pty Ltd (INTERA) to 1) update conceptual site model, 2) based on updated conceptual site model, develop the groundwater flow model and conduct history matching, 3) implement uncertainty analysis, 4) conduct particle tracking and contaminant transport modelling, 5) undertake predictive analysis, and (6) conduct impact assessment, aiming at fulfilling the EA requirements, addressing CSIRO comments on the previous work. This report will be to subjected to peer review as is required by the EA Water Condition.

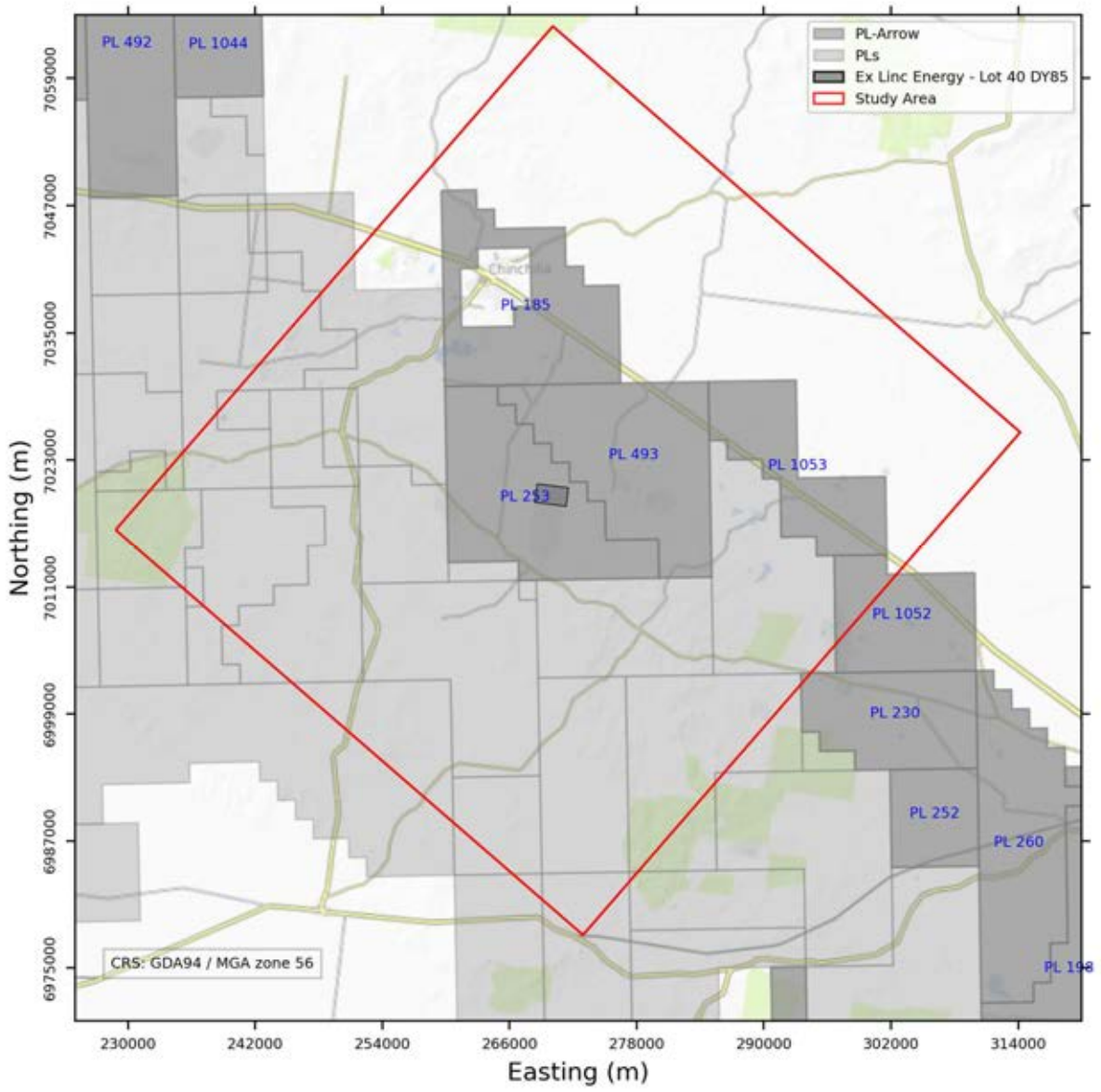


Figure 1-1 – Location map of PL 253 and adjacent production license areas.

## 1.1 Scope of Work

### 1.1.1 Conceptual Site Model

Following the EA requirements (Water Condition 3), the overarching scope of the conceptual site model is to:

- Characterise the residual contaminant source of Lot40 on DY85 using:
  - Information available on Lot40 DY85 including existing wells both on and off Lot40DY85; and
  - Information obtained under condition Water 5 and condition Water 7,
- Identify mobilisation pathways and present the groundwater pressure and flow regime around Lot40 on DY85,

- Provide an analysis of how contaminants may migrate over time with and without Stage 1 Activities,
- Provide uncertainties in conceptualisation resulting from formation heterogeneity, preferential pathways, and structural influences, and
- Assess the potential for long-term release of contaminants in the groundwater.

To accomplish this, the conceptual site model was developed by reviewing the prior conceptualisation and hydrogeological information, incorporating new monitoring data acquired since the last groundwater modelling round undertaken by AGE (2023), and updating the conceptualisation based on the newly available data. The focus of the conceptualisation has been on the potential for contaminant migration and impacts of proposed Arrow operations into the groundwater environment.

### 1.1.2 Numerical Groundwater Flow and Transport Model

The overall objective of the study is to develop a numerical groundwater single phase flow and transport model capable of providing predictive estimates of the groundwater impacts associated with the proposed CSG operations, to quantify the inherent hydrogeological uncertainty, to assess its impact on the predictions of interest, and to evaluate the ability of available data to constrain predictive uncertainty. The groundwater model, developed based on updated conceptual site model, is presented in section 2.0. The groundwater model then was history-matched (annually at a minimum) and updated with the data collected through annual groundwater monitoring program (GMP) conducted by Arrow Energy.

This report describes the conceptual site model, the numerical groundwater flow model, the contaminant transport model (including particle tracking) and the predictive modelling accompanied by the impact assessment. Each modelling stage (i.e., flow and transport) is followed by the respective model construction, data assimilation and uncertainty analysis (Doherty, 2022).

Specific requirements for groundwater modelling are outlined in the EA (Water Conditions 2 and 4) and are summarised as follows:

- A groundwater model must be developed that targets aquifers on and in the vicinity of Lot40 on DY85 including the Springbok Sandstone and the Macalister coal seam (and its relevant aquifers) of the Walloon Coal Measures that will measure and predict changes in:
    - contaminant movement in groundwater,
    - groundwater flow direction and
    - drawdown due to future CSG activities.
- Be history matched with updated data on an annual basis and include an assessment of the effect of data assimilation on parameter uncertainty reduction.
- Extend the predictive period to, at least, the year 2200 and resolve inconsistencies between the amended EA and previous modelling.
- Include a transport model with dual porosity/permeability capability (secondary permeability from fractures and rock matrix), validated against measured data.
- Include particle tracking, with particles placed in specified locations, as well as an assessment of the placement and density of particle placement on predictions of interest.

- Provide predictive uncertainty analysis of the simulated Quantities of Interest.

Detailed modelling objectives are presented in the following section.

## 1.2 Modelling Objectives

Objectives of the work described herein follow the Water Conditions Water 2(3*)* from the Environmental Authority EA0001401 that states the development of "*a groundwater model that targets aquifers on and in the vicinity of Lot 40 on DY85 including the Springbok Sandstone and the Macalister coal seam (and its relevant aquifers) of the Walloon Coal Measures that will measure and predict changes in contaminant movement, groundwater flow direction and drawdown*".

In addition, the relevant groundwater model in condition *Water 2(3)* follows the condition *Water 4* that states the model to:

1) Be calibrated annually (at a minimum) and updated with the data collected as part of the GMP required under condition Water 2(4) and the site conceptualisation model under condition Water 3 to inform the Annual Report under condition Water 9,
2) Include a simulation period to at least the year 2200 that extends to beyond when groundwater levels are expected to have recovered in 2040 and contaminant transport off-site becomes possible,
3) Include a contaminant transport model that: a. uses the most recent water quality data for validation; and b. has dual porosity or permeability capability (fracture and matrix) to better represent transport into and out of dead pore volumes and fractures that might contain residual sources of contaminants,
4) Include a review and assessment of the density of particle tracking,
5) Include particle starting locations of: a. multiple particles per cell, both horizontally and vertically; b. multiple particles located on each edge of Lot40 DY85; c. multiple particles on the northern edge of gasifier 5; d. multiple particles at each groundwater monitoring well location including HSMB1S HSMB4S;
6) Assess the effect of particle tracking starting in wells that have exhibited elevated Underground Coal Gasification contaminants,
7) Assess particle tracks (travel times, distances and trajectories) to inform where to best install new groundwater monitoring wells required by condition Water 5 and condition Water 11,
8) Include a sensitivity analysis and uncertainty analysis,
9) Analyse the prior and posterior parameter distributions to provide insight into which parameters are constrained, and which are not, and to compare the calibrated parameter set with the ensemble,
10) Provide correlation coefficients, standard error of estimate, 95% upper and lower limit for the parameters; a. Initial concentration of component species in water; b. Longitudinal dispersivity; c. Transverse dispersivity; d. Bulk density; e. Adsorption coefficient; f. Freundlich adsorption isotherm; g. First order decay coefficient in water and soil.
11) Describe impacts of the authorised activities relative to the Quantity of Interest,
12) Discuss the value of using non-reactive chemicals as tracers to improve solute transport calibration,
13) Discuss characterisation of the initial contamination source term,
14) Discuss how model parameter values near the gasifiers are influenced by observed potentiometric data and any bias in parameter estimates introduced by calibrating against recovery head observations without accounting for possible dual phase flow,

15) Resolve inconsistencies in the number of coal seam gas wells between the amended EA and groundwater modelling report; and Permit Environmental authority EA0001401.
16) Resolve inconsistencies between modelled development scenarios and document assumptions and rationale to support the selected model simulation period.

### 1.2.1 Summary of Reviewer Comments and EA Conditions

Previous modelling efforts (AGE, 2023) have been subjected to external review for the Environmental Authority (CSIRO, 2023 and OGIA, 2023). Table 1-1 summarises reviewer comments, action taken and the corresponding section of the current report where they are addressed.

**Table 1-1 – Summary of EA reviewer comments and the corresponding section in the current report.**

| EA Condition | Water | Response | Section |
|---|---|---|---|
| Be calibrated annually (at a minimum) and updated with the data collected as part of the GMP required under condition Water 2(4) and the site conceptualisation model under condition Water 3 to inform the Annual Report under condition Water 9. | 4(1) | Groundwater flow model was history matched to most recent data. | 3.2 |
| Include a simulation period to at least the year 2200 that extends to beyond when groundwater levels are expected to have recovered in 2040, and contaminant transport off-site becomes possible. | 4(2) | The simulation period was extended to the year 2200. | 3.2.2 and 4.4 |
| Include a review and assessment of the density of particle tracking. | 4(4) | A sensitivity analysis to particle placement density was undertaken. | Appendix G |
| Include particle starting locations of a. multiple particles per cell, both horizontally and vertically; b. multiple particles located on each edge of Lot40 DY85; c. multiple particles on the northern edge of gasifier 5; d. multiple particles at each groundwater monitoring well location including HSMB1S HSMB4S. | 4(5) | Particles starting locations were updated to include:<br>a) multiple particles per cell, both horizontally and vertically<br>b) multiple particles located on each edge of Lot40 DY85<br>c) multiple particles on the northern edge of gasifier 5<br>multiple particles at each groundwater monitoring well location including HSMB1S HSMB4S. | 4.2 and Appendix G |
| Assess the effect of particle tracking starting in wells that have exhibited elevated Underground Coal Gasification contaminants. | 4(6) | The effect of particle tracking starting in wells that have exhibited elevated Underground Coal Gasification contaminants was assessed by placing particles at model cells at all of the above-mentioned bores. | 4.2 and Appendix G |

| EA Condition | Water | Response | Section |
|---|---|---|---|
| Assess particle tracks (travel times, distances and trajectories) to inform where to best install new groundwater monitoring wells required by condition Water 5 and condition Water 11. | 4(7) | New monitoring bores Hopeland 34 to Hopeland 37 were installed based on a previous particle tracking model developed by AGE (2023). Here we showed the estimated simulated concentration in those bores. | 4.4.4 |
| Include a sensitivity analysis and uncertainty analysis. | 4(8) | Non-linear uncertainty analysis was undertaken for predictive simulations, employing an ensemble of model parameter sets. Previous approaches applied to this site have been limited to linearised approximations to post-calibration uncertainty, which may underestimate uncertainty.<br><br>The parameter ensemble is obtained through history matching using an iterative ensemble smoother method. As part of this approach, models are simulated with prior (i.e. “uncalibrated”) parameters as well as posterior (i.e. “calibrated) parameters.<br><br>Comparison of changes in parameters and model outputs between the prior and posterior, provide insight into which are affected by history matching.<br><br>In terms of a broader sensitivity analysis. While sensitivity analysis can be a valuable tool for exploring the sensitivity of model outputs to individual parameter variation, it can be computationally prohibitive for highly parameterized models like the one presented. Sensitivity analysis alone provides little insight into how the uncertainty around model parameters propagates to model outputs, or how combinations of parameters influence outputs of interest. Instead, this study provides a comprehensive uncertainty quantification, including relative parameter uncertainty variance reduction (RPUVR). This uncertainty quantification combines parameter uncertainty with sensitivity analysis (and a description of model error and measurement uncertainty) to provide a quantification of model output uncertainty that is not achievable by sensitivity analysis alone. | 3.2, 3.3, 4.3.2, and Appendix C |

| EA Condition | Water | Response | Section |
|---|---|---|---|
| Analyse the prior and posterior parameter distributions to provide insight into which parameters are constrained, and which are not, and to compare the calibrated parameter set with the ensemble. | 4(9) | Prior and posterior were analysed to provide the required insights. | 3.2.5.2, 4.3.2.4.6, Appendix C, 3.2.4 and Appendix B |
| Provide statistics for the several model input parameters. | - | Statistics of the model input parameters were provided. | 3.2.4 and Appendix B |
| Include a contaminant transport model that: a. uses the most recent water quality data for validation; and b. has dual porosity or permeability capability (fracture and matrix) to better represent transport into and out of dead pore volumes and fractures that might contain residual sources of contaminants. | 4(3) | A contaminant transport model for benzene and naphthalene was built and history-matched with the latest groundwater quality data provided by Arrow. Dual domain mass transfer was included. | 4.3 |
| Characterise the residual contaminant source of Lot 40 on DY85 using:<br>a. Information available on Lot 40 DY85 including existing wells both on and off Lot40DY85; and<br>b. Information obtained under condition Water 5 and condition Water 7. | 3(1) | The residual contaminant source of Lot 40 on DY85 was characterized using all available data and the spatial distribution of contaminants was determined.<br>In addition, data conditioning was used to include uncertainty around the geometry of the residual contaminant distribution. | 2.6 and 4.3.1.2.2 |
| Identify mobilisation pathways and present the groundwater pressure and flow regime around Lot40 on DY85. | 3(2) | Mobilisation pathways were identified using particle tracking and contaminant transport modelling.<br>The groundwater pressure and flow regime around Lot40 on DY85 were investigated using maps of ensemble mean hydraulic head at several simulated times, along with indicators of vertical and lateral gradient at Lot40 on DY85. | 4.4.2 and 4.3 |
| Provide an analysis of how contaminants may migrate over time with and without Stage 1 Activities. | 3(3) | Predictive particle tracking and contaminant transport modelling were conducted to analyse how contaminants may migrate over time with and without Stage 1 Activities (two scenarios).<br>Maximum particle tracking distance from the Lot40 boundary is presented for both scenarios. Probability maps of particle location by 2200 are also shown.<br>Results show that there is a minor difference with or without Stage 1 activities. | 4.4.2 and 4.3 |

| EA Condition | Water | Response | Section |
|---|---|---|---|
| Provide uncertainties in conceptualisation resulting from formation heterogeneity, preferential pathways and structural influences. | 3(4) | A highly parameterised approach was adopted which considers uncertainties in conceptualisation resulting from formation heterogeneity, preferential pathways, and structural influences. | 3.2.4 |
| Assess the potential for long-term release of contaminants in the groundwater. | 3(5) | A mass rate was included in the gasifiers (layer 6). The mass rate was adjusted to represent the depletion of the source over long-term timescales. This was history-matched against the observation data. However, the location and magnitude of the source remains highly uncertain. Thus, it is recommended to pinpoint their location and concentrations to be able to better assess the release into groundwater. | 4.3.1.2.1 and 6.0 |
| Provide correlation coefficients, standard error of estimate, 95% upper and lower limit for the parameters; a. Initial concentration of component species in water; b. Longitudinal dispersivity; c. Transverse dispersivity; d. Bulk density; e. Adsorption coefficient; f. Freundlich adsorption isotherm; g. First order decay coefficient in water and soil. | 4(10) | Statistical parameters (correlation coefficients, standard error of estimate, 95% upper and lower limit for the parameters) were presented for<br>a. The initial concentration of component<br>species in water.<br>b. Longitudinal dispersivity.<br>c. Transverse dispersivity.<br>d. Bulk density.<br>e. Adsorption coefficient.<br>f. adsorption isotherm.<br>g. First order decay coefficient in water and soil | 4.3.2.3 |
| Discuss the value of using non-reactive chemicals as tracers to improve solute transport calibration. | 4(12) | Here, we discuss particle tracking as a good approach to model the advective behaviour of a non-reactive tracer and as a risk-conservative approach. | 4.3.1.1.1 |
| Describe impacts of the authorised activities relative to the Quantity of Interest. | 4(11) | Where appropriate, QoI's have been defined. These are complemented with other model derived outputs to facilitate analysis and discussion. | 5.0 |
| Discuss characterisation of the initial contamination source term. | 4(13) | A mass rate was included in the gasifiers (layer 6). to represent the source term and serve as a proxy for contamination source characterisation. The mass rate was adjusted to represent the depletion of the source over long-term timescales. | 4.3.1.2.1 and 6.0 |

| EA Condition | Water | Response | Section |
|---|---|---|---|
| Discuss how model parameter values near the gasifiers are influenced by observed potentiometric data and any bias in parameter estimates introduced by calibrating against recovery head observations without accounting for possible dual phase flow. | 4(14) | History matching against recovery may introduce bias if the dual-phase flow is ignored. Several strategies are employed to minimize bias, including localisation and the use of measurement noise.<br>Notwithstanding, history matching induced bias may affect absolute predictions. However, from a contaminant movement perspective, a single-phase model should provide risk-conservative forecasts of how far contaminants may be expected to move. | 3.2.5.4 |
| Resolve inconsistencies in the number of coal seam gas wells between the amended EA and groundwater modelling report; and Permit Environmental authority EA0001401. | 4(15) | 55 additional CSG wells were simulated in the PL253 FDP scenario, in addition to the approved FDP and the six Hopeland pilot wells. | 3.3.1 |
| Resolve inconsistencies between modelled development scenarios and document assumptions and rationale to support the selected model simulation period. | 4(16) | Modelled development scenarios and simulations have been updated according to reviewer recommendations. | 3.3.1 |

# 2.0 Site Conceptual Model

The following section describes the hydrogeological and hydrochemical conceptualisation of the site that follows the EA Condition Water (3), that states the site conceptual model in EA condition Water 2(2) must:

1. Characterise the residual contaminant source of Lot 40 on DY85 using:
    a. Information available on Lot 40 DY85 including existing wells both on and off Lot40DY85; and
    b. Information obtained under condition Water 5 and condition Water 7,
2. Identify mobilisation pathways and present the groundwater pressure and flow regime around Lot 40 on DY85,
3. Provide an analysis of how contaminants may migrate over time with and without Stage 1 Activities,
4. Provide uncertainties in conceptualisation resulting from formation heterogeneity, preferential pathways and structural influences and
5. Assess the potential for long-term release of contaminants in the groundwater.

## 2.1 Site Setting and Available Data

### 2.1.1 Site Location

The site corresponds to the Petroleum License PL253 which extends over an area of 229 $km^2$ and the surrounding PL (PL493 and PL185). It is located approximately 20 km south-east of Chinchilla, Queensland (Figure 2-1) and comprises the former Linc Energy Limited site that operated a pilot underground coal gasification (UCG), resulting in residual UCG by-products like hydrocarbon compounds. The former Linc Energy site is located on Lot40 DY85 (hereby Lot40), at 357 Kummerows Road, Hopeland, approximately 2.6 km West of PL493 at its closest point, and 10 km South of PL185 (Figure 2-1).

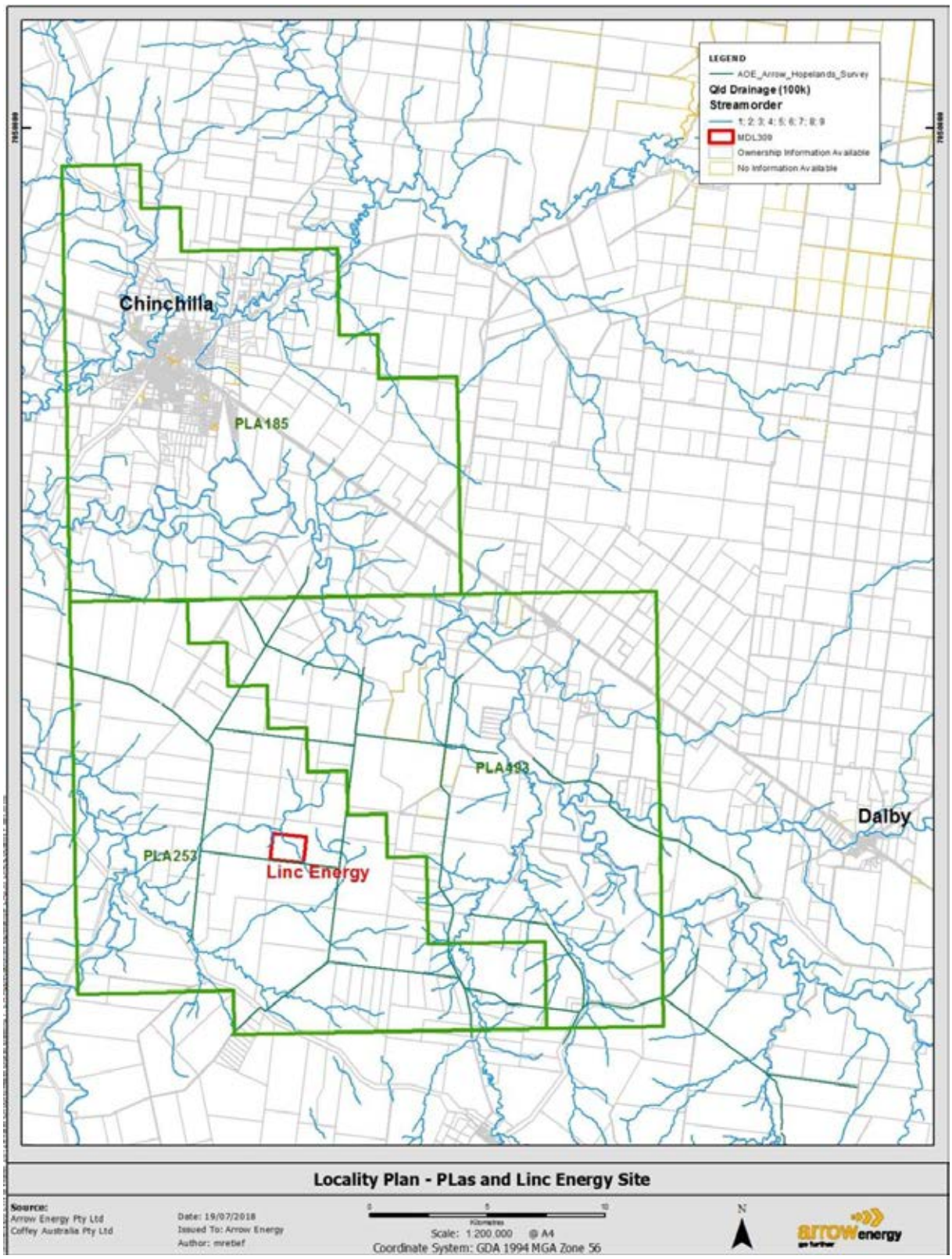


Figure 2-1 – Location plan of PL 253 and adjacent PLs (Arrow, 2020).

## 2.1.2 Underground Coal Gasification and Site History

Underground Coal Gasification (UCG) involves the drilling of injection and production wells into a target coal seam. In this process, air, oxygen, and steam are injected into the coal seam via the

injection well. Then the coal is ignited, and combustion gases are extracted at a production well (SKM, 2006). The pathway between the injection well and the production well is established by either directional drilling, electrolinking, or reverse combustion (SKM, 2006).

The former Linc Energy site (Lot40) underwent UCG trial operations resulting in the movement of contaminants which has been attributed to the potential fracturing of the surrounding materials (AECOM, 2018). This section outlines the key aspects of the UCG trial operations and summarises the history of the site, focusing on Lot40.

#### 2.1.2.1 UCG Trials and Operations

Before the commencement of UCG trials in 1999, the site was known as “Capowie” cattle station with some areas used for cropping (AECOM, 2018). Legacy structures, including cattle yards and farm buildings, remain on site. UCG trials began in 1999 to assess the safety and efficacy of various well configurations (injection and production) (AECOM, 2018).

The initial gasifier, Gasifier 1, operated from 1999 to 2002 (AECOM, 2018). In 2006, Linc Energy Limited submitted an Initial Advice Statement (IAS) to the Queensland Government (AECOM, 2018). Upon receiving approvals, a series of additional gasifiers (G2-G5) were installed and operated between 2007 and 2013 (AECOM, 2018). Perkins et al (2013) and AECOM (2018) summarized the site activities that are described in this chapter.

The Gasifier 2 (2007) was operated for only three months (AECOM, 2018). The gasifier's link between the wells was tried via high-pressure air fracturing. According to estimations, the use of pressures well above the fracture threshold of the surrounding formation caused damage that extended up to 2 km. Given the water inflow and gas outflow, this made the Gasifier 2 unsuitable for UCG and forced the following gasifiers to work under low pressures to avoid reopening fractures (AECOM, 2018).

Gasifier 3 (2008-2009): Initiated in August 2008, this gasifier aimed to test horizontal drilling techniques to connect vertical wells (AECOM, 2018). It encountered issues potentially linked to damage from Gasifier 2, including vertical leakage and pressure depletion, which eventually led to a roof collapse (AECOM, 2018).

Gasifiers 4 and 5 (2010-2013): Both gasifiers operated under low pressures (AECOM, 2018). Problems, such as water ingress into the chambers, were likely exacerbated by the formation damage from Gasifier 2’s overpressure (AECOM, 2018).

In 2016, Linc Energy declared bankruptcy (AECOM, 2018). The Hopeland Site has been disclaimed to the State of Queensland and is now maintained by the Department of Natural Resources, Mines and Energy (DNRME) (AECOM, 2018). The Department of Environment and Science (DESI) investigated the extent of environmental harm that has occurred on and in the surrounds of the Hopeland Site due to the Linc Energy project (AECOM, 2018).

#### 2.1.2.2 Contamination Events

Gasifiers-injected air or oxygen and its respective combustion are understood to have caused fracturing while contributing to increased pressures during operations (AECOM, 2018). After a period of higher pressures than the background levels, voids left by the gasifier operations became sinks for local groundwater, forming depressurized zones into which groundwater flowed from surrounding higher-pressure areas. This phenomenon has resulted in local depressurised zones around the gasifiers (AECOM, 2018).

It is expected that, while the gasifiers were operational, gas phase contaminants could have moved out from the gasifier capture zones through fractures in the Springbok Sandstone as well as laterally in the coal through permeable pathways (AECOM, 2018). These gas phase contaminants would have condensed into dissolved phase contaminants in groundwater as temperatures and pressures decreased away from the gasifiers (AECOM, 2018).

#### 2.1.2.3 AECOM (2018) Conceptualisation

The Hopeland Site is situated within the Surat Basin, which mainly consists of unconsolidated sediments, Springbok Sandstones, and Juandah Coal Measures. The UCG trials at the Hopeland Site were aimed at the Macalister Upper (or A) and Lower (or B) seams of the Juandah Coal Measures within the Surat Basin. The roof of the coal seam dips at an angle ranging from 1° to 5° to the south-southeast.

There are two significant water-bearing horizons at the Hopeland Site as follows:

- Discontinuous lenses of higher permeability sandstone within the Springbok Sandstone. This horizon is characterised by low permeability compared to other aquifer sequences in the Surat Basin and contains groundwater with high total dissolved solids (approximately 5,000 – 30,000 mg/L).
- Confined groundwater within the Macalister A and B coal seams. This horizon is characterised by low to moderate permeability compared to other aquifer sequences in the Surat Basin and contains groundwater with lower total dissolved solids (less than 2,000 mg/L).

Several potential mechanisms of recharge to the coal seams are being considered, including recharge from the Condamine River, diffuse recharge at the sub-crop areas of the Juandah Coal Measures, or recharge through the more porous portions of the overlying alluvium and/or Springbok Sandstone into the coal seams.

Groundwater levels at the Hopeland Site, located approximately 30 meters below the surface and associated with the coal seams, are not considered to discharge into the surface water drainages, such as the Condamine River or Wambo Creek.

### 2.1.3 Study Area

The extent of the study area in the hydrogeological model (conceptual and numerical) is considered to be larger than PL253 (3,674 $km^2$). This is the same area adopted by GHD (2019) and subsequent studies (Figure 2-2), encompassing roughly a 20 km radius from Lot40 DY85 which incorporates PL253, PL493 and PL185, as well as adjacent areas so that the area is large enough to capture key hydrogeological stresses and their area of influence during past and future activities.

The rectangular-shape study area was rotated so that the northeastern boundary approximates the extent of Walloon Coal Measures, while the northwest and southeastern boundaries are roughly parallel to the strata dip and regional groundwater flow direction. From a numerical modelling perspective, the boundaries of the study area were defined so that potential boundary effects are minimised and that potential flow pathways can be fully simulated within the required timeframes.

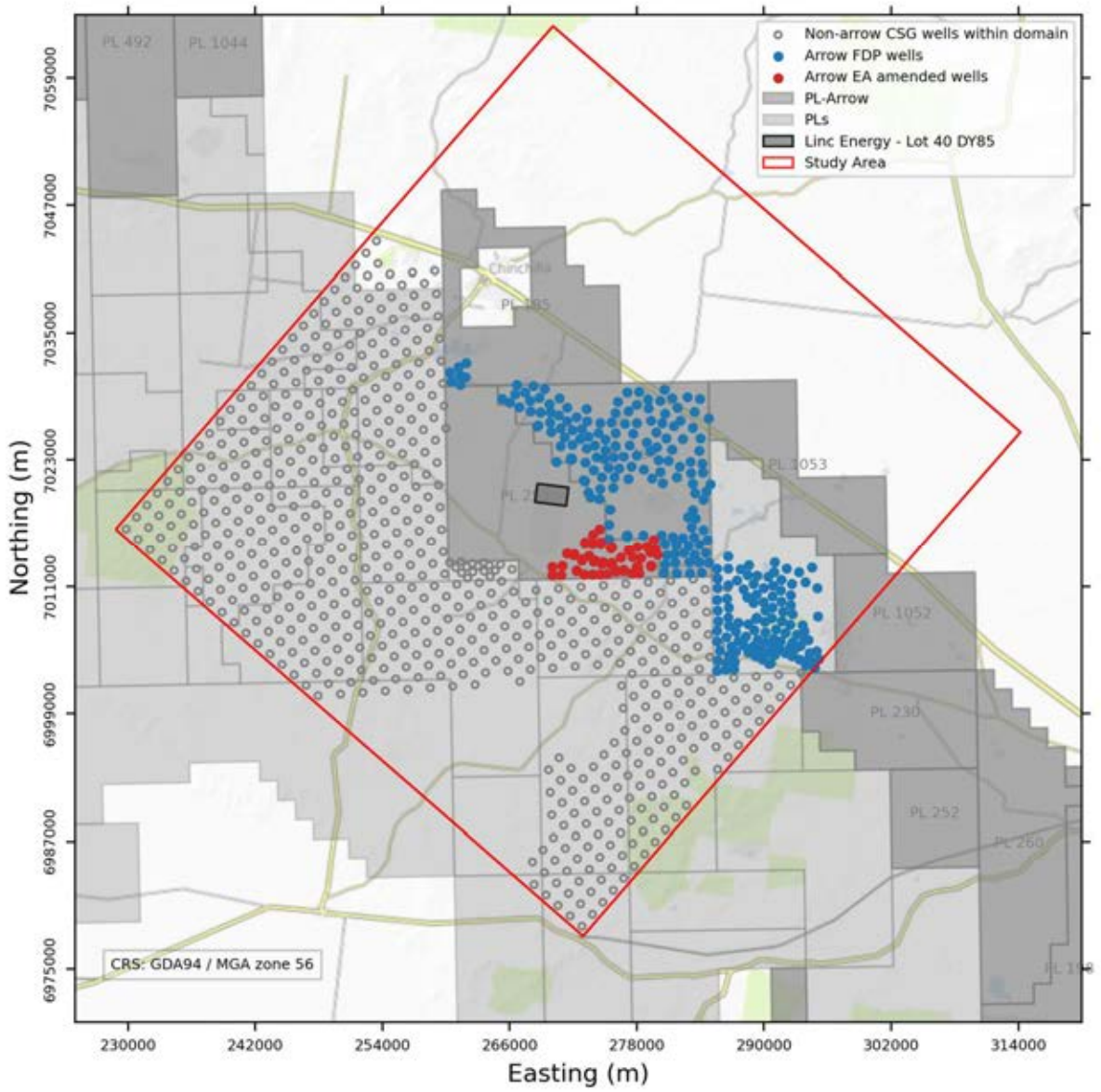


Figure 2-2 – Study area (model domain), PLs , Lot40 boundaries and CSG wells.

### 2.1.4 Available Data

The conceptual model presented in this report was developed based on the analysis and review of several data sources including multiple aspects of PL253 hydrogeology, hydrochemistry and impact assessment, as summarised in Table 2-1. The majority of the data has been provided by Arrow, while public available information was obtained from government websites.

Table 2-1 – Summary of data sources used in the development of the conceptual model.

| Description | Source | Format | Usage |
|---|---|---|---|
| OGIA reports | Public reports | PDF's | Background information, hydrogeological parameters, information on regional structures and conceptualisation |
| Previous reports on PL253 | Arrow | PDF's | Background information, conceptualisation update |
| Groundwater monitoring data | Arrow | Multiple spreadsheets | Historical and current groundwater levels for boreholes in the vicinity of PL253 |
| Groundwater quality | Arrow | Multiple spreadsheets | Source characterisation, mapping of groundwater concentrations |
| Geology data & hydrostratigraphic surfaces | Arrow | XYZ points for tops and bottoms of the different formations. | Definition of geometry of the different hydrogeological units. Identification of potential structures |
| Previous modelling files | Arrow | Raw inputs from MODFLOW-USG files and Groundwater Vistas files | Definition of geometry of the different hydrogeological units. Identification of potential structures |
| Groundwater borehole and monitoring data | QLD Groundwater borehole database<br>Arrow | Multiple tables in text format | Identification of potential receptors<br>Adjust model layers |
| Proposed development plans | Arrow | Shapefiles and spreadsheets with proposed abstraction rates | Qualitative assessment of effects from pumping into groundwater flows for conceptualisation, and quantitative assessment during the development of the numerical model |

## 2.2 Hydrostratigraphy

The study area is located within the Surat Basin, a broad intra-cratonic basin that spans an area of approximately 300,000 km$^2$ in southeastern Queensland and northeastern New South Wales. This basin is part of the broader Great Artesian Basin (GAB) complex and shares boundaries with the Eromanga Basin to the west and the Clarence-Moreton Basin to the east (Rigby and Kantsler, 1987). Figure 2-3 displays the stratigraphic column of the Surat Basin with focus on the Walloon Coal Measures (OGIA, 2021 and Scott et al., 2004).

The Surat Basin is characterised by a combination of non-marine sedimentary rock layers formed during the Jurassic period, along with a mixture of non-marine and marine Early Cretaceous rock layers (OGIA, 2016). The sedimentation process began in the Early Jurassic period, leading to the creation of the Precipice Sandstone. Over the Jurassic and Early Cretaceous periods, the basin experienced multiple sedimentation episodes, involving the accumulation of sediments from rivers, lakes, and coal-swamp environments, as the basin gently subsided (OGIA, 2016).

The deposits in the Surat Basin are similar to those in the Eromanga Basin. It's suggested that a raised land area between the two basins acted as a natural boundary, dividing them. During the Aptian period, there was a sea-level rise, causing the basin to shift to shallow marine conditions. This led to the deposition of the Wallumbilla Formation, a part of the Rolling Downs Group. This was the first marine sediment sequence to be deposited since the Permian period (Exon, 1976).

The Surat Basin's history of sedimentation is closely tied to various geological events and landforms. In the central area of sediment accumulation, known as the Mimosa Syncline, the basin rests on sediments from the Permo-Triassic Bowen Basin. On the edges of the basin, the Surat sequence sits on top of crystalline basement rocks (Exon, 1976).

Stratigraphic surfaces (Figure 2-3), provided by Arrow (2020), allowed to define the geometry for the different hydrogeological units, as illustrated in Figure 2-4. Detailed information on the extent, thickness and tops of each of the major hydrostratigraphic units is presented in the following sections.

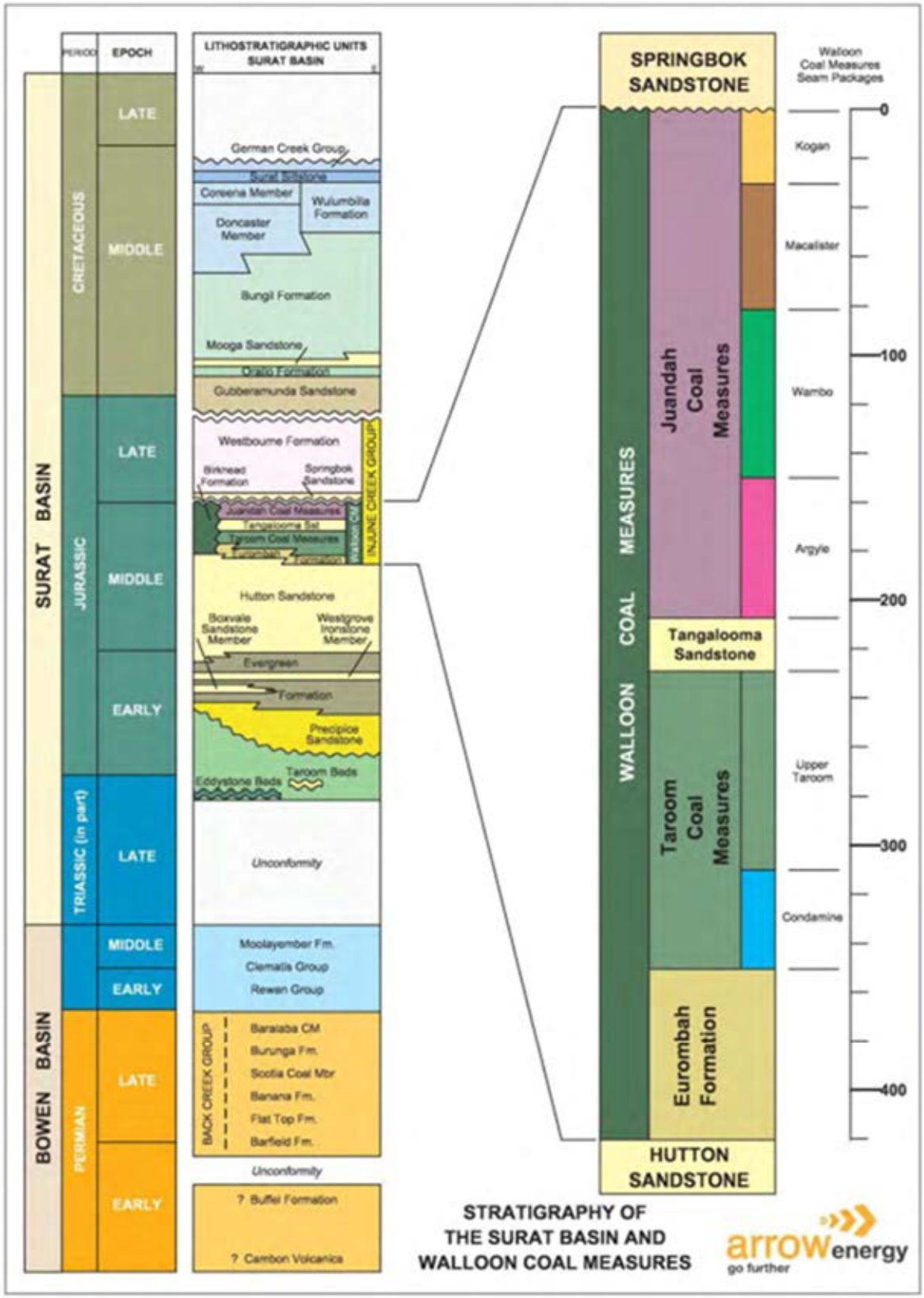


Figure 2-3 – Hydrostratigraphy of the Surat Basin and Walloon Coal Measures (McKellar, 1999).

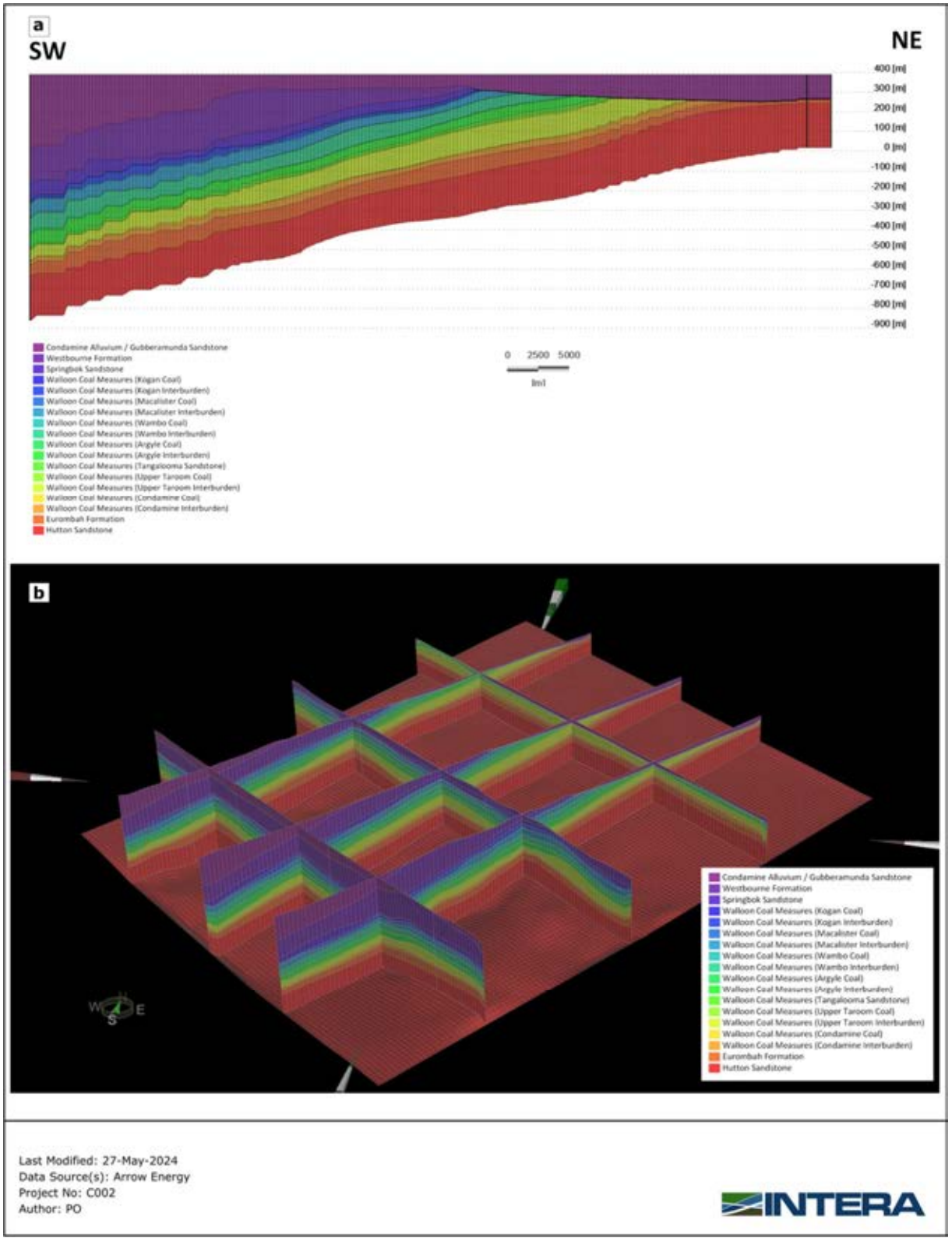


Figure 2-4 – (a) Schematic cross section and (b) schematic fence diagram of the study area.

### 2.2.1 Condamine Alluvium/Gubberamunda Sandstone

The Condamine Alluvium represents a significant accumulation of alluvial sediments within this geographical region incised into Jurassic Surat Basin sequence (OGIA, 2019). The Surat Basin subcrops most of the central alluvium (OGIA, 2021b). The alluvial and sheetwash deposits of the Condamine River and tributaries form a broad plain between Millmerran and Chinchilla (OGIA, 2016). The Gubberamunda Sandstone comprises a sequence of fine to coarse-grained, quartzose to sublabile sandstone, interbedded with minor conglomerate, siltstone and mudstone with thicknesses between 45 to 300 m (OGIA, 2016).

The Gubberamunda Sandstone is present in the study area along the southwestern border forming the upper-most hydrostratigraphic unit there (GHD, 2019). These two units comprise the uppermost aquifers in the study area. However, they are not contiguous and are laterally separated by the outcrop of the older Westbourne Formation and Springbok Sandstone (AGE, 2020). Elevation of the top of these formations and their thicknesses are shown in Figure 2-5. The Condamine Alluvium is present in the northeastern part of the study domain, with thicknesses in the order of 100-150 m. The Gubberamunda Sandstone occurs in the southwestern section of the site, dipping towards the southwest. The formation thickness increases towards the southwest, characterised by a lower thickness in the centre of the domain reflecting outcrops of underlying formations.

The Condamine Alluvium region contains sediment deposits characterised by a mixture of fine to coarse-grained gravels, channel sands, and intermittent layers of clay with a thick clayey sheetwash sequence overlying the floodplain deposits (OGIA, 2016). The sheetwash deposits in this area take on a wedge-like configuration, with their greatest thickness observed in the eastern portion and gradually thinning towards the west. This alluvial material tends to become finer in texture as it moves downstream and along the edges. The thickness of alluvium ranges from less than 10 m, in the headwaters and along the floodplain margins, to 130 m in the central floodplain near Dalby (OGIA, 2016).

The erosion from the Condamine River has shaped its valley in alignment with the strike of the Walloon Coal Measures, which constitutes the main geological basement of the alluvial deposits within the main central plain (Huxley, 1982; OGIA, 2019). On the western margin of the alluvium, the Springbok Sandstone forms basement to the alluvium where it occurs between the Walloon Coal Measures and the alluvium. Isolated thin patches of Tertiary sediments have also been identified below the Condamine alluvium and overlying the Walloon Coal Measures.

Underlying the Condamine Alluvium is a less permeable undifferentiated clay-dominated layer, known as the 'transition zone' (OGIA, 2016). This is a combination of basal alluvial clays of the Condamine Alluvium and weathered Walloon Coal Measures. Where present, the transition zone ranges from less than 1 m to just over 15 m in thickness (OGIA, 2016). OGIA (2016) concluded that there is generally low connectivity between these two units due to low vertical permeability of the transition zone. However, this transition zone is not a continuous layer; where it is absent or thin, connection may occur (OGIA, 2016).

Hydraulic properties are horizontally and vertically variable. Recorded hydraulic conductivities range from 0.2 to 781 m/d. The upper sheetwash layer has lower values (0.2 to 2 m/d). The generally accepted view is that moderate values (3 to 30 m/d) are representative of the alluvium material, with higher values (>30 m/d) occurring locally (OGIA, 2016). Reported storativity values for the alluvium range from 4 $x10^{-6}$ to 6 $x10^{-5}$ and the specific yield is estimated to be around 1% to 10% (OGIA, 2016).

The groundwater from the Condamine Alluvium, located in the western part of the domain, is extensively used for agricultural purposes. It spans a wide alluvial plain stretching between Millmerran and Chinchilla, with a width exceeding 20 km. Recharge is primarily from the Condamine River and its tributaries, as well as from rainfall and irrigation return flow (OGIA, 2016). Diffuse recharge from rainfall is considered negligible due to the significant clay near the surface (Dafny and Silburn, 2014). Likewise, irrigation return flow may contribute to recharge but is likely to be relatively low, and completely absent in the vicinity of PL253 (OGIA, 2016).

The Gubberamunda Sandstone comprises a sequence of fine to coarse-grained, quartzose to sub-labile sandstone, interbedded with minor conglomerate, siltstone and mudstone with thicknesses between 45 to 300 m (OGIA, 2016). It overlies the Westbourne Formation, which acts as an aquitard separating it from underlying units. Vertical hydraulic gradients between the Gubberamunda and Springbok sandstones show upward vertical gradients (>20 m) consistently observed from nested monitoring sites around Miles and Chinchilla (OGIA, 2016).

The Gubberamunda Formation is a highly productive aquifer, providing supply for livestock, industry and urban users within the Surat basin. Reported horizontal hydraulic conductivities range from $1x10^{-4}$ to 3.6 m/d and vertical permeability approximately half an order of magnitude smaller (OGIA, 2016). Recharge occurs where the formation outcrops in the north and eastern margins of the Surat Basin. Mean recharge rates are 4.6 mm/yr (OGIA, 2016).

In some locations, where the Gubberamunda Formation outcrop has been eroded and incised to expose the water table at surface it provides groundwater discharge to some surface water systems and GDEs. In the study area these are mostly highly modified GDE surface drainage (OGIA, 2016).

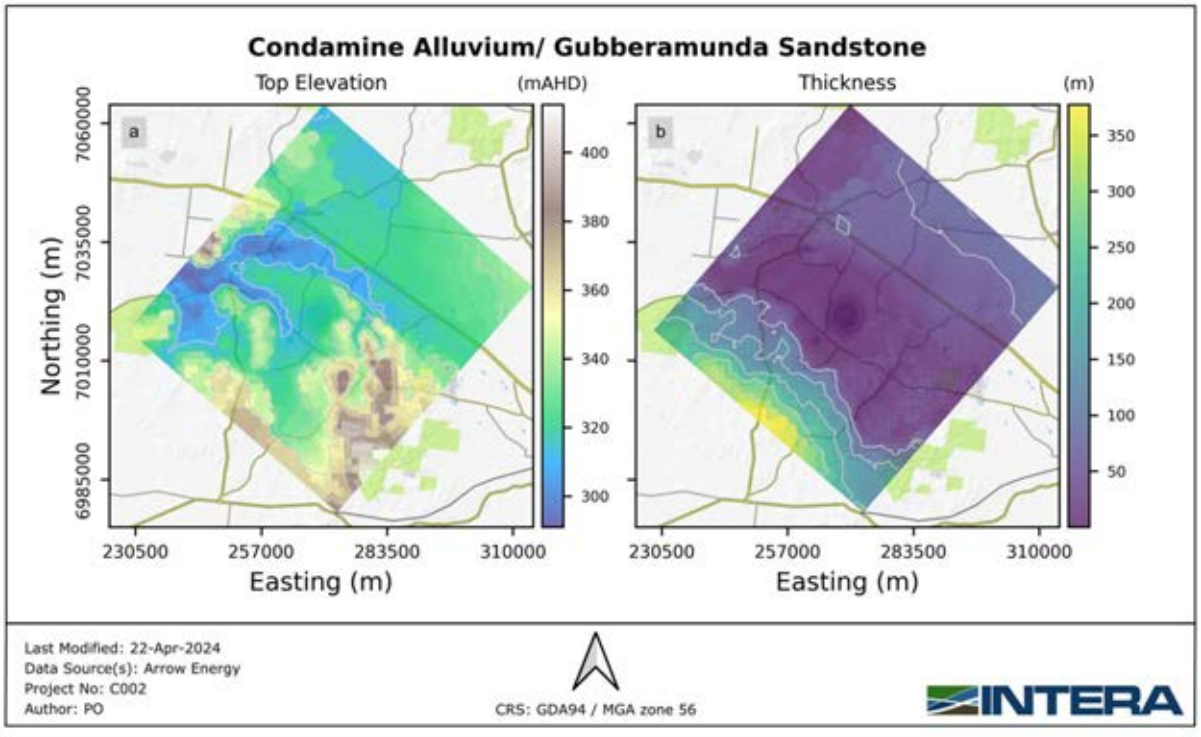


Figure 2-5 – (a) Elevation of top and (b) isopach of the Condamine Alluvium/Gubberamunda Sandstone; red rectangle marks the location of Lot40 DY85. Formation geometry is adapted from AGE (2020).

### 2.2.2 Westbourne Formation

The Westbourne Formation primarily consists of interbedded shale and siltstone, with minor fine to very fine-grained quartzose sandstone. The formation was deposited in lakes and deltas in the Surat Basin and lies conformably on the Springbok Sandstone (OGIA, 2016).

The Westbourne Formation is recognised as both an aquitard and a confining layer for the underlying Springbok Sandstone (OGIA, 2021b), comprising primarily interlayered mudstone and siltstone with only limited occurrences of sandstone (OGIA, 2019). In the study area the formation dips towards the southwest (Figure 2-6). The unit pinches out towards the northeast where it has been eroded, and thickness increases towards the south with mean of 150 m reaching a maximum thickness of 360 m (AGE, 2020).

Recorded median hydraulic conductivity values are around 3 $x10^{-5}$ to 9 $x10^{-1}$ m/d for horizontal conductivity, and 1.8 $x10^{-4}$ to 2.4 $x10^{-2}$ m/d for vertical hydraulic conductivity (OGIA, 2016). Mean annual recharge is estimated between 1.8 and 2.2 mm/yr (OGIA, 2016). There are no mapped areas of groundwater discharge from the Westbourne formation (OGIA, 2016).

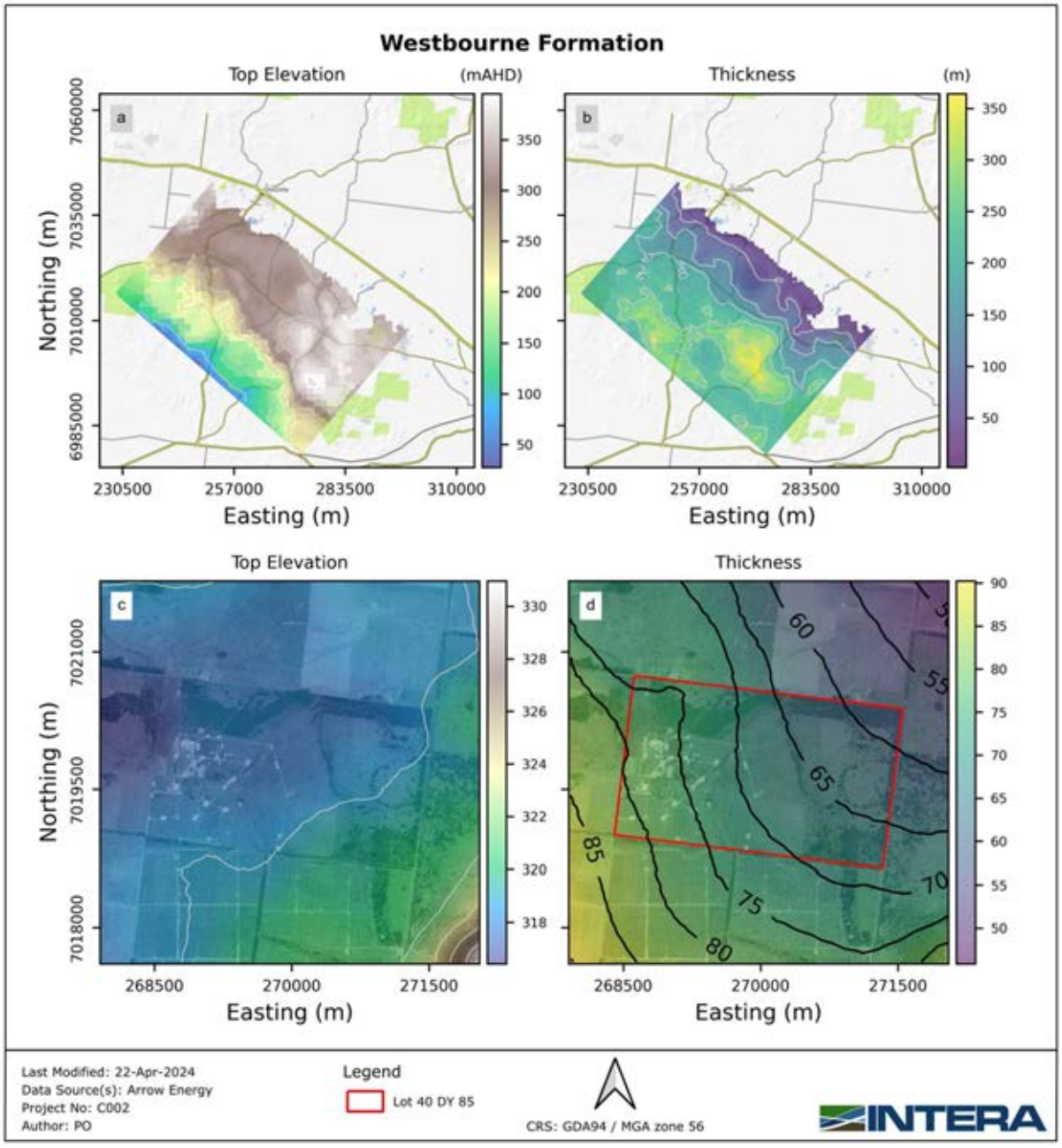


Figure 2-6 – Maps of top elevations and isopachs of the Westbourne Formation. (a) top elevation of the formation (b) isopachs, (c) and (d) display the top elevation and isopach around the area of Lot40 DY85. Formation geometry is adapted from AGE (2020).

### 2.2.3 Springbok Sandstone

The Springbok Sandstone overlies the Walloon Coal Measures (OGIA, 2021b). Within the study are, it is overlain by the Westbourne Formation aquifer to the southwest. It is overlain by the Condamine Alluvium to the northeast, where the Condamine valley has incised.

The Springbok Sandstone is characterised by feldspar and lithic clasts ranging from medium to fine-grained. Occasional pebbly layers, siltstone, mudstone, and sporadic thin bentonite and coal layers have also been observed in this unit. The upper unit of the Springbok Sandstone is usually made up of alternating layers of fine to coarse-grained sandstone containing feldspathic to lithic material, as

well as siltstone and mudstone (OGIA, 2016). On the other hand, the lower unit of the Springbok Sandstone mainly consists of coarse to very coarse grained sandstone and does not contain significant coal seams (OGIA, 2016). Within the lower unit, stacked channel sandstones make up over 71% of the composition, resulting in a higher permeability compared to the upper unit. The lower Springbok Sandstone lies on top of the Walloon Coal Measures with an unconformity (OGIA, 2016).

The Springbok Sandstone has traditionally been categorised as an aquifer (OGIA, 2021b), primarily attributable to its abundant sandstone composition. However, recent data evaluation indicates that it is, in fact, a heterogeneous sequence characterised by the prevalence of aquitard materials, albeit with notable regional disparities (OGIA, 2016). The principal factors contributing to the observed low permeability within this formation are believed to be compaction and cementation processes (QGC, 2013).

In the study area, Springbok Sandstone's thickness is on average around 40 m, reaching a maximum of 117 m towards the south (Figure 2-7). The formation dips towards the southwest. There appear to be two zones of different thickness: in the western quadrant with thicknesses in the order of 20-50 m, and the southeastern quadrant where thickness increases to between 80-117 m. The formation pinches out to the northeast, where it is overlain by Condamine Alluvium.

The Springbok Sandstone outcrops on the northern and eastern corners of the Surat Basin and dips slightly towards the south (OGIA, 2016). Recharge occurs where the formation outcrops. Average recharge rate is 1.8 mm/yr (OGIA, 2016). This unit is not extensively targeted for water supply in comparison to other shallower aquifers. Within the outcrop of the Springbok Sandstone there are areas of groundwater discharge to surface. At these locations the groundwater table is shallow, and deep-rooted terrestrial GDEs may occur (OGIA, 2016).

This unit is situated between the Walloon Coal Measures and the overlying Westbourne Formation. The deposition of the Springbok Sandstone occurred within the eroded surface of the Walloon Coal Measures, resulting in a pronounced variability within the unit (OGIA, 2016). In numerous instances, the Springbok Sandstone exhibits a substantial proportion of mudstone and siltstone components, characterised by extremely low permeability (OGIA, 2016). In areas where these components are prevalent, they tend to act as isolating barriers, impeding the movement of groundwater between these geological formations (OGIA, 2016). However, the effect of CSG activities in the underlying Walloon Coal Measures within the study area is evidenced by the gradual lowering of piezometric heads in a number of bores screened in the Springbok Sandstone and Walloon Coal Measures. This suggests that connection between the formations is prevalent in the area (GHD, 2019).

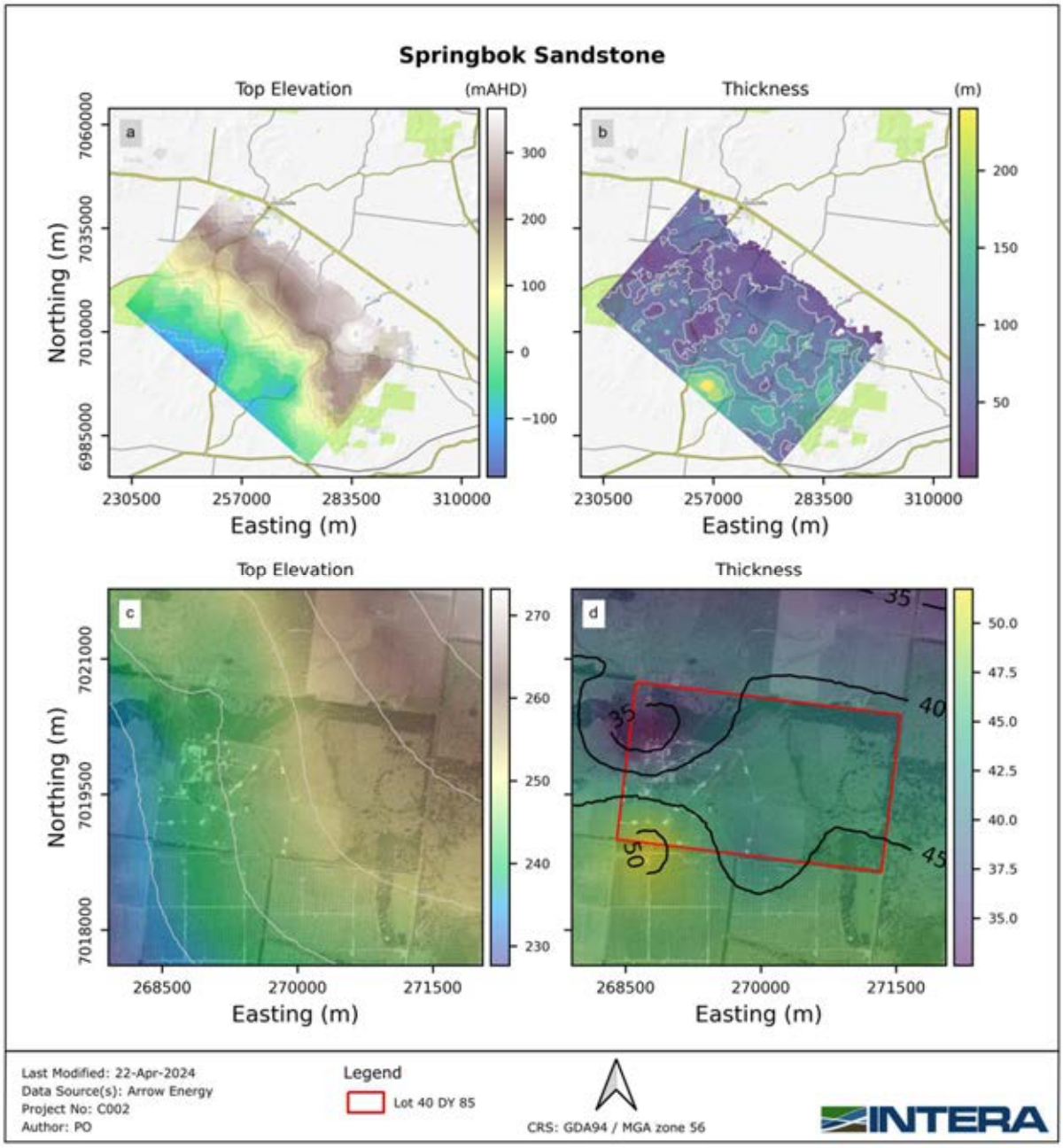


Figure 2-7 – Maps of top elevations and isopachs of the Springbok Formation. (a) top elevation of the formation (b) isopachs, (c) and (d) display the top elevation and isopach around the area of Lot40 DY85. Formation geometry is adapted from AGE (2020).

In the area of Lot40 DY85, the Springbok Sandstone exhibits a thickness that varies from 31 to 50 m. Two potential permeable zones have been identified within this formation, as indicated by double screening intervals in most of the monitoring bores (refer to Table 2-3). Logging analysis conducted by Arrow (personal communication, 2024), however, does not indicate a substantial variation in permeability. These zones range in thickness from 1-2 m in the shallower permeability zone to 6 m in the deeper permeability zone.

### 2.2.4 Walloon Coal Measures

The Walloon Coal Measures (WCM) is mainly comprised by deposits of the following types: fluvial, lacustrine deposits of siltstone, mudstone, fine to medium-grained lithic sandstone and coal (OGIA, 2016). Regionally, the Walloon Coal Measures are typically classified as a leaky aquitard. The Walloon Coal Measures is the main gas extraction reservoir in the Surat Basin. These measures are covered by the Springbok Sandstone in a way that sometimes cuts into the coal measures, even erasing upper coal seams in certain places (Hamilton et al., 2014). The Walloon Coal Measures overlie the low permeability Eurombah Formation.

The Walloon Coal Measures dips slightly towards the Mimosa Syncline. Outcrops of this formation can be observed southwards on the northern and southeastern edges of the Surat Basin (OGIA, 2016). The formation averages 300 m in thickness and reaches its maximum thickness of over 600 m in the north of the Mimosa Syncline. Within the study area, thicknesses are relatively constant around 300 m reaching up to 400 m.

This Walloon Coal Measures exhibit a high degree of heterogeneity and anisotropy. Its composition is predominantly marked by isolated permeable coal seams and sandstone units, which are predominantly enveloped by low-permeability sequences of mudstones, siltstones, or fine-grained sandstones. In the majority of instances, even the coarser sandstone units encountered within this formation demonstrate relatively low permeability when compared to the coal seams. This results in notable permeability contrasts of two to three orders of magnitude between the coal seams and the intervening interburden. Coals in the Walloon Coal Measures are thin, discontinuous seams interbedded in generally low-permeability sediments (OGIA, 2016).

The internal structure of the Walloon Coal Measures can be divided into distinct sections: the Upper Juandah, Lower Juandah, Tangalooma Sandstone, and Taroom coal measures. Notably, the Upper Juandah, Lower Juandah, and Taroom coal measures are where the gas-producing coal seams are primarily located (OGIA, 2016). While there are numerous coal seams, they comprise generally less than 10% of the total thickness of the Walloon Coal Measures (OGIA, 2016). Permeable coal seams tend to occur in discontinuous lenses up to 1 m thick, although typically less than 0.4 m thick. The lateral extent of individual coal plies (lenses) ranges from 500 to 3000 m (OGIA, 2016).

The upper section of the Walloon Coal Measures, located above the highest coal seam, is referred to as the upper non-coal zone. Acting as an 'upper aquitard,' this unit adds resistance to flow between the Walloon Coal Measures and the overlying lower Springbok Sandstone. However, when coal directly meets the unconformity, this zone is absent. Furthermore, the upper non-coal zone displays varying lithological composition and permeability characteristics.

Within the Juandah Formation, the upper coal zone is referred to as the Macalister seam (OGIA, 2016, 2019, 2021). Three distinct seams within the Macalister have been identified (informally named seams A, B, and C), with individual thicknesses varying from 1 m up to 10 m when all the seams are merged together. Up to date, in the area of Lot40 DY85, two seams have been identified from bore intersections (e.g., HSMB6 and HSMB7).

Estimated long-term mean recharge rate in the Walloon Coal Measures is 3.6 mm/yr, with a maximum of 5 mm/yr (OGIA, 2016).

Across the majority of the CMA, groundwater flow in the area south of the Great Dividing Range is towards the south and west, consistent with the southwest regional dip of the formation. There are no known areas of groundwater discharge from the Walloon Coal Measures (OGIA, 2016).

### 2.2.5 Eurombah Formation

As described in QGC (2016), the Eurombah Formation is an aquitard which lies below the Walloon Subgroup. The formation consists of an upward fining sequence of thickly cross-bedded, fine-grained sandstones that range from labile to sub-labile, interspersed with siltstones and mudstones. Occasionally, thin coal seams are also present (OGIA, 2016). This formation is believed to have been deposited in a fluvial environment, marked by periods of rapid sedimentation leading to sequences that become progressively finer upwards. The unit's aquitard properties are evident from core data, showing generally low porosity and ambient air permeability values (OGIA, 2016).

The Eurombah Formation is present across the entire site domain. The formation dips towards the southwest, reaching depths greater than -500 mAHD (Figure 2-9). Thickness is relatively constant in the order of 150 m, which decreases to around 25 m in a relatively small zone at the northeast of the model domain.

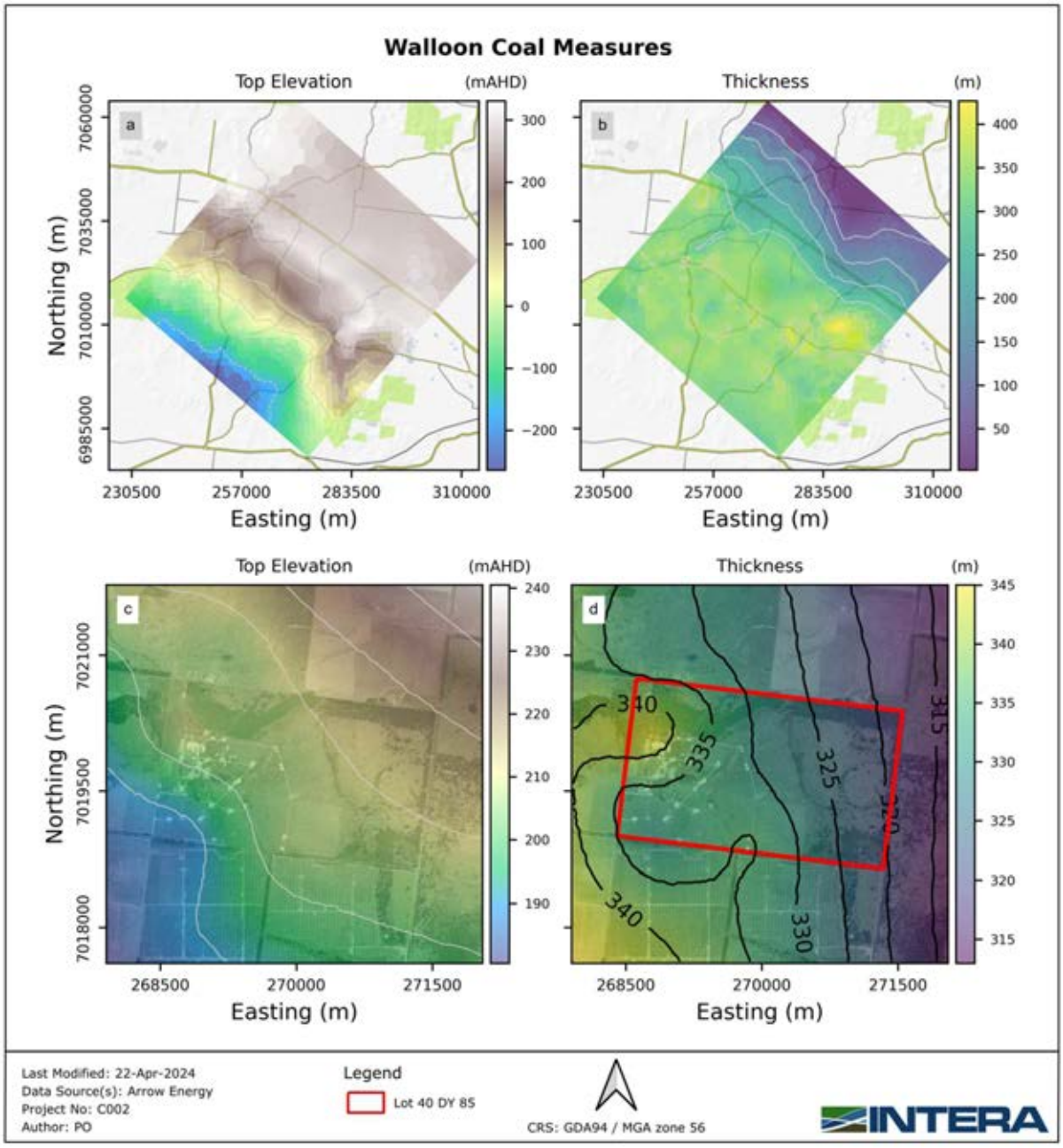


Figure 2-8 – Maps of top elevations and isopachs of the Wallon Coal Measures (including all seams and interburden). (a) top elevation of the formation (b) isopachs, (c) and (d) display the top elevation and isopach around the area of Lot40 DY85. Formation geometry is adapted from AGE (2020).

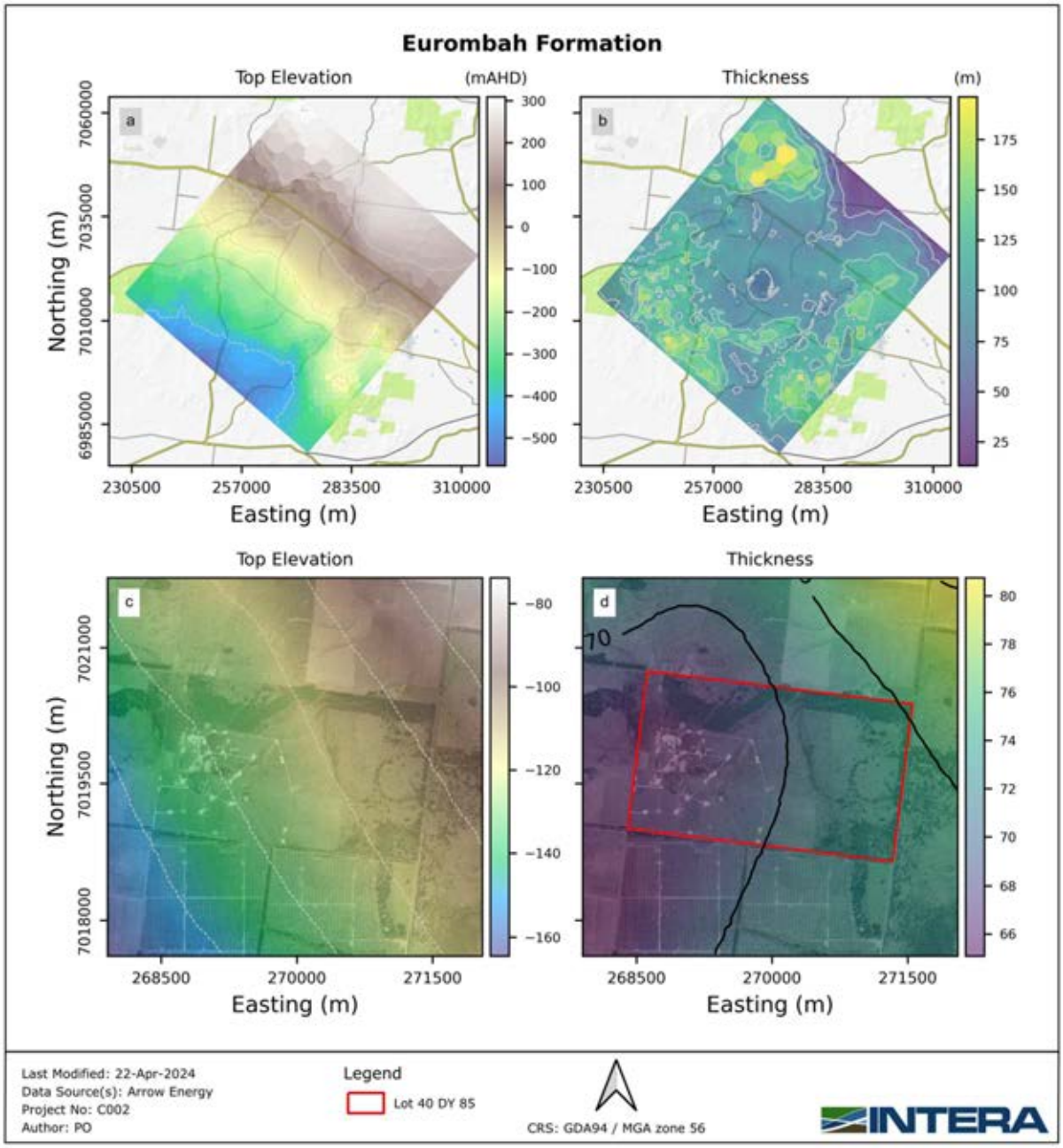


Figure 2-9 – Maps of top elevations and isopachs of Eurombah Formation. (a) top elevation of the formation (b) isopachs, (c) and (d) display the top elevation and isopach around the area of Lot40 DY85. Formation geometry is adapted from AGE (2020).

### 2.2.6 Hutton Sandstone

The Hutton Sandstone overlies the Evergreen Formation and sits below the Eurombah formation (Cook and Draper 2013). It was formed by the deposition of sediments from meandering rivers on a wide floodplain. (Exon, 1976). Due to this origin, the Hutton Sandstone displays significant heterogeneity, showing notable changes in both composition and arrangement both horizontally and vertically, particularly towards the eastern boundary of the Surat Cumulative Management Area (OGIA, 2016). The primary rock type consists of sandstone ranging from easily breakable to rich in quartz, which is found alongside layers of siltstone and shale. Similar to the Springbok Sandstone, the Hutton Sandstone is split into upper and lower units. According to QGC (2014), the upper portion

of the Hutton Sandstone generally includes greater proportions of permeable quartzose sandstones compared to the lower Hutton Sandstone, which contains higher proportions of lithic fragments.

The Hutton formation dips towards the southwest, reaching maximum depths of -600 mAHD within the study area (Figure 2-10). Figure 2-10 suggests that it thins out to 160 m in the vicinity of Lot40 DY85, whilst elsewhere thicknesses are generally in the order of 200-300 m.

Pressures in the Hutton Sandstone are sub-artesian but higher than those in overlying Walloon Coal Measures. The Eurombah Formation aquitard restricts the hydraulic connection between these two units. The outcrop zones of the Hutton Sandstone are further east than the model domain and the aquifer is not expected to interact with the surface within the area.

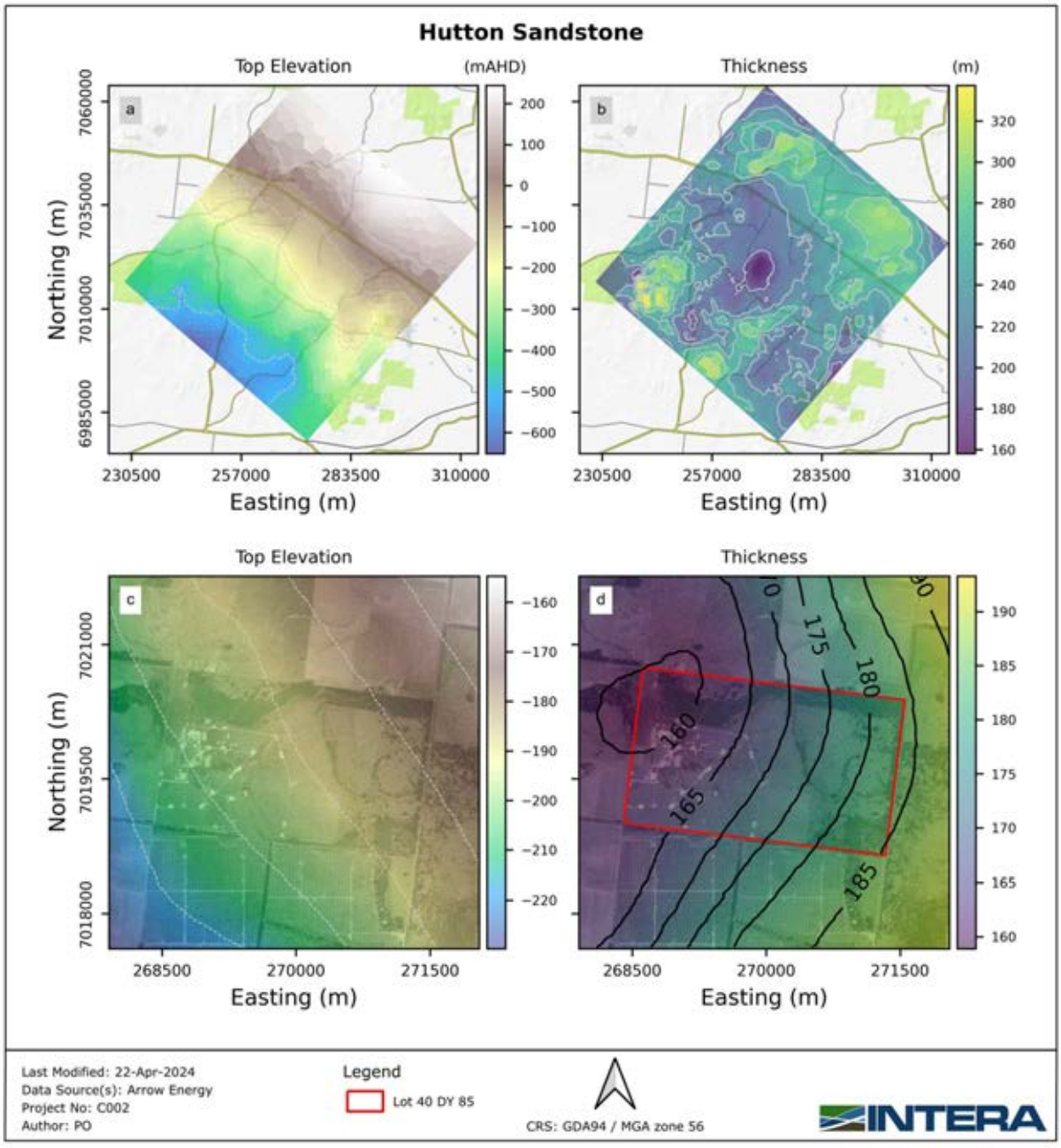


Figure 2-10 – Maps of top elevations and isopachs of the Hutton Sandstone. (a) top elevation of the formation (b) isopachs, (c) and (d) display the top elevation and isopach around the area of Lot40 DY85. Formation geometry is adapted from AGE (2020).

## 2.3 Groundwater Levels and Flow Regime

The characterisation of groundwater levels and potentiometry within the study area has been undertaken through the analysis of an extensive groundwater level dataset provided by Arrow and complemented by publicly available data from the Queensland Groundwater Borehole Database (Regional Development, Manufacturing and Water of Queensland, 2024). The inferred groundwater contours were constructed using groundwater level data from 2023 and complemented with previous years for a more robust interpolation. The OGIA (2021) model's groundwater surfaces were used to guide the interpolation using co-Kriging.

This analysis aimed at investigating historical groundwater trends in the study area, identifying mobilisation pathways and presenting the groundwater pressure and flow regime around Lot40 on DY85 as required by EA Condition Water 3. To accomplish this, the data set was analysed as follows:

- Analysis of horizontal spatial distribution of groundwater levels within the different hydrogeological units using the last measurements from 2023 (when available), or the last measurement of each monitoring bore, in cases where a bore did not have data in 2023.
- Analysis of vertical hydraulic gradients through inspection of groundwater level data in four nested monitoring sites (Hopeland-17, Kogan North-79, Wyalla-18, and Dundee-20).
- Analysis of historical groundwater trends in boreholes using groundwater level time series.

Regionally, groundwater flow in the Surat Basin tends to be south to southwest, following the regional flow direction in the Great Artesian Basin (OGIA, 2016), as illustrated in Figure 2-11. Within the shallower aquifers (especially the Condamine Alluvium), groundwater tends to have a more topographically driven flow patterns, mostly following the flow direction of the Condamine River.

### 2.3.1 Condamine Alluvium

As previously described, groundwater flows within the Condamine Alluvium tend to follow the flow direction of the Condamine River, which is predominantly northwest (Figure 2-12). Locally, in the study area, groundwater levels in the Condamine Alluvium range from 290 to 300 mAHD (Figure 2-13) and generally follow the topography. Groundwater levels outside this range mostly describe Gubberamunda/Westbourne/Springbok in the elevated areas of outcrop. Groundwater flow converges towards the Condamine River and flow towards northwest. Moreover, as mentioned in section 2.2.1, the Condamine Alluvium is present in the northeastern part of the study area, while the southern part being dominated by the Gubberamunda Sandstone, suggesting that there is no potential flow from the study area to the Condamine Alluvium.

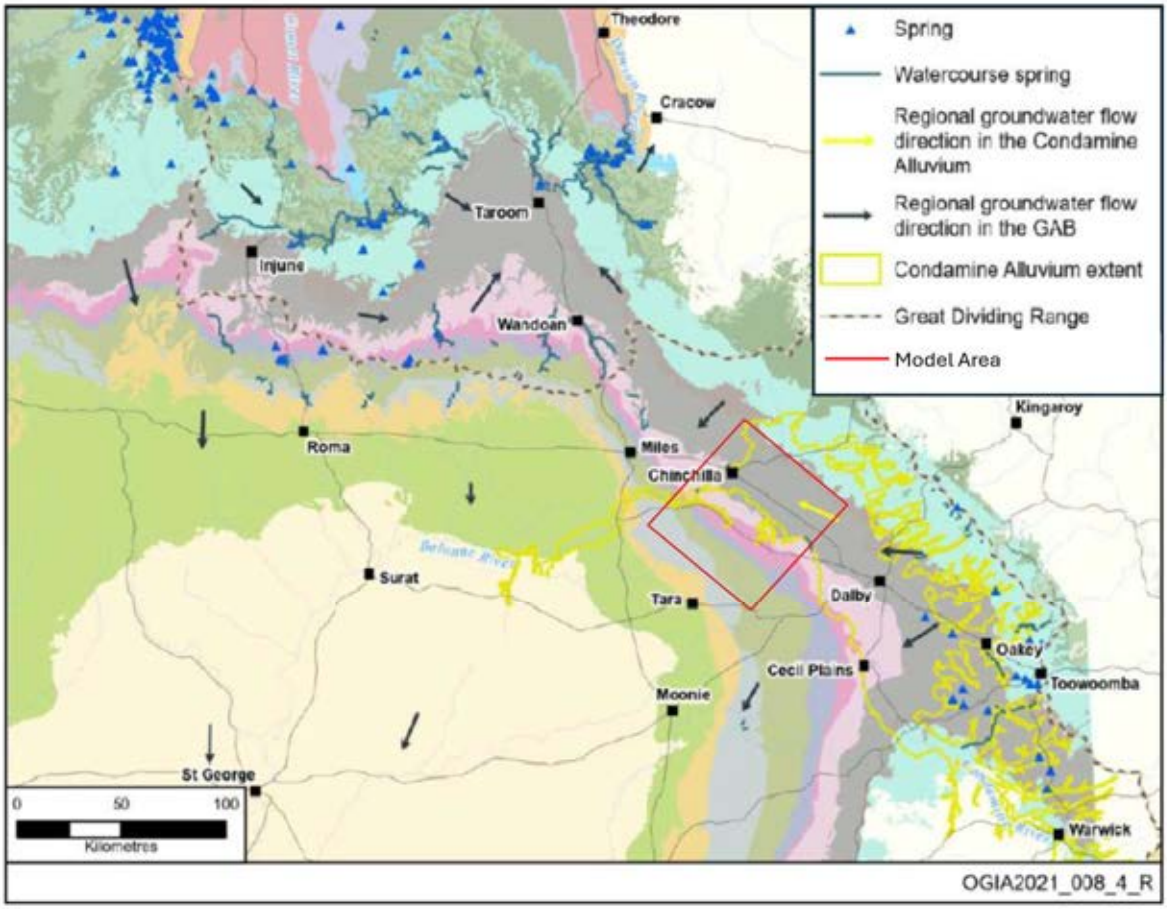


Figure 2-11 – Schematic representation of main groundwater systems in the Surat CMA (OGIA, 2021).

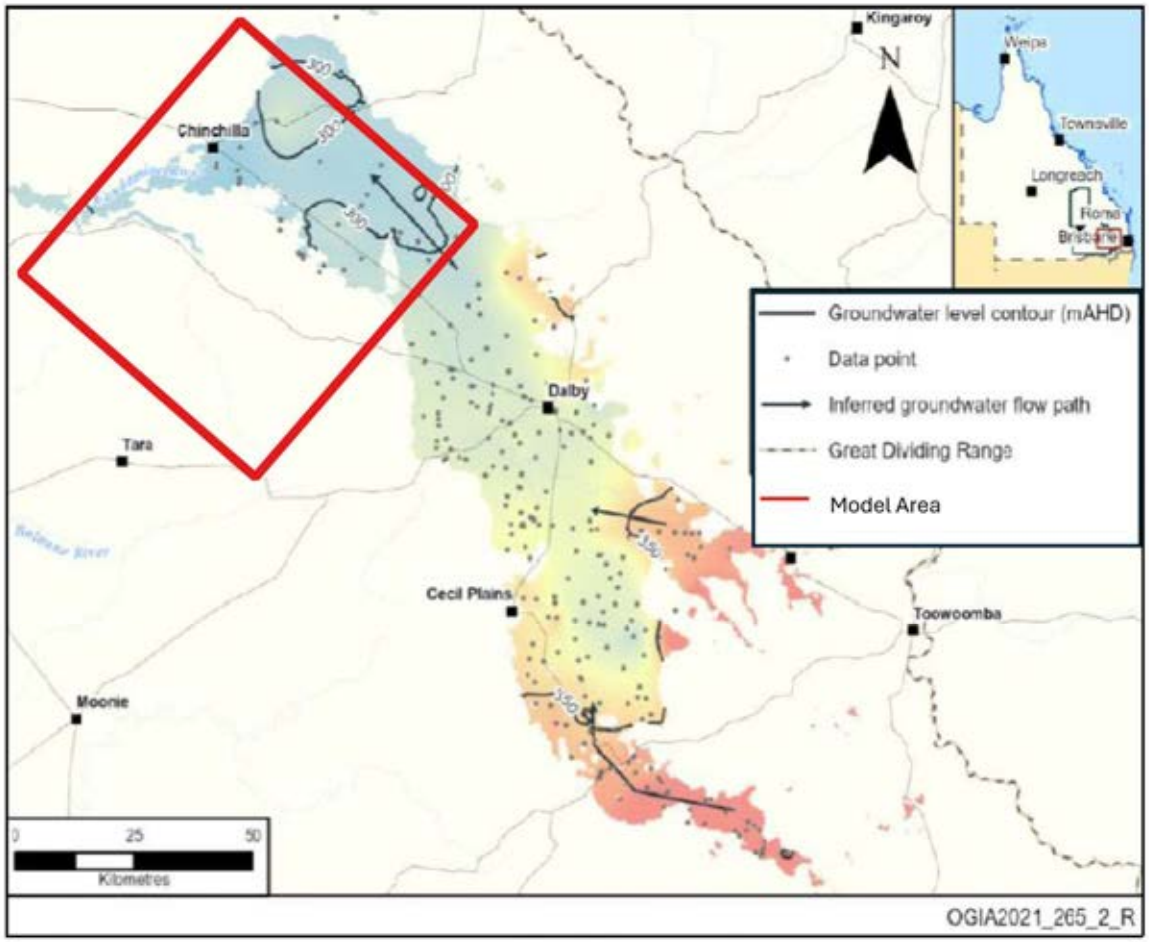


Figure 2-12 – Schematic representation groundwater levels within the Condamine Alluvium (OGIA, 2021).

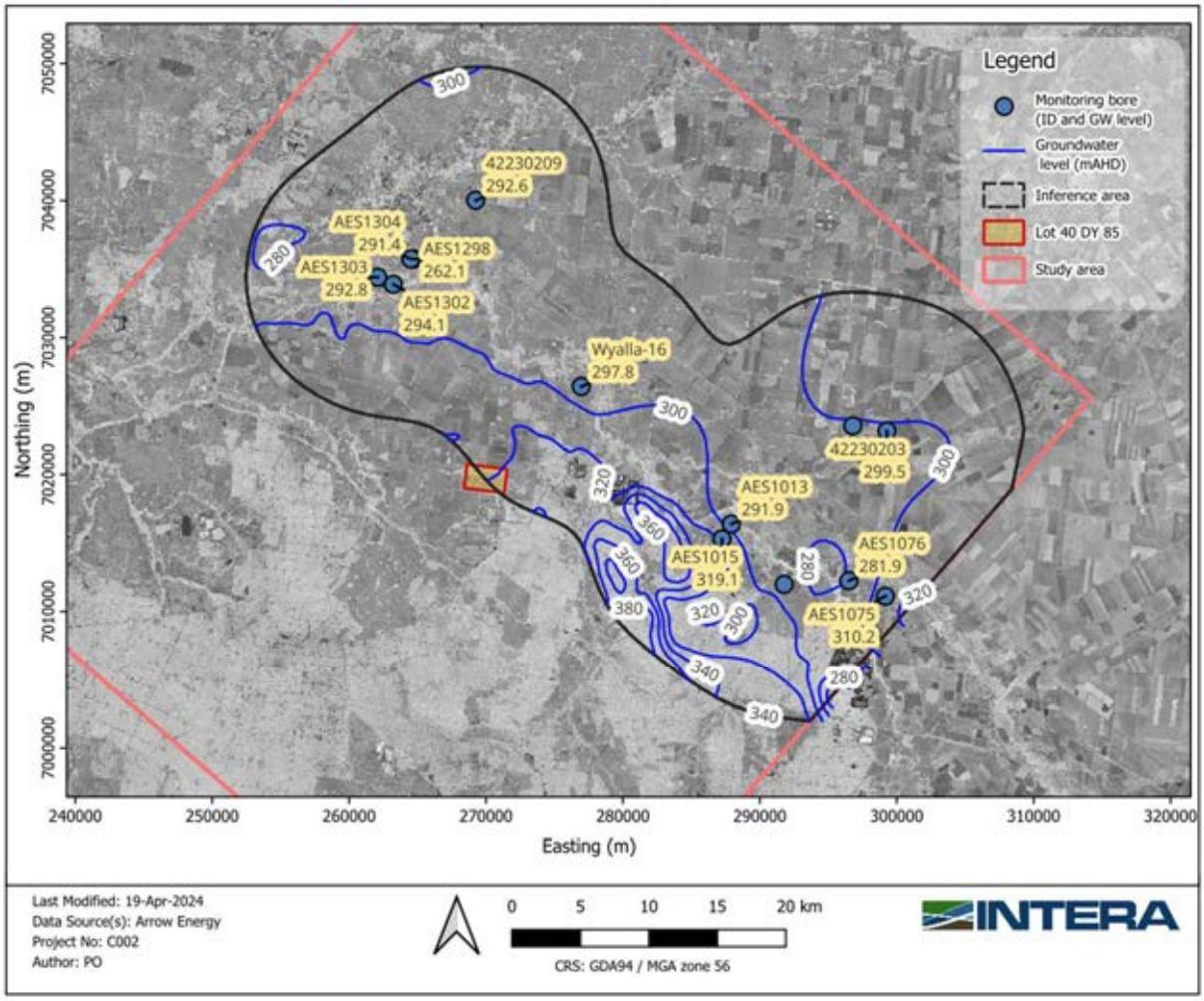


Figure 2-13 – Interpreted groundwater levels in the Condamine Alluvium and Gubberamunda Sandstone.

## 2.3.2 Springbok Sandstone

Regional maps show groundwater levels in this unit are below 300 mAHD in the study area (OGIA, 2021) and the groundwater within the Springbok Sandstone flows towards the south. Locally, groundwater levels in Springbok Sandstone range from 309 to 272 mAHD. Interpreted groundwater contours suggest flow within this unit occurs from south to north (Figure 2-14a).

At a study area or regional scale, and offsite of the former Linc UCG production site, groundwater levels in the Springbok Sandstone vary from approximately 287 to 297 mAHD (Figure 2-14a), and they are higher than those in the WCM Macalister Seam, which range from 220 to 191 mAHD. Monitoring bores offsite of Lot40 DY85 (e.g., 297.1 and 286 mAHD in Hopeland-22 and HSMB7, respectively) indicate groundwater levels higher than onsite bores (e.g., 227 mAHD in HSMB3S2). This shows that the current gradient is inward toward Lot40 DY85 and reflect the effects of the former UCG operations.

Springbok has a northwards local gradient from NB01S where Benzene concentration has increased, indicating either long term equilibration of contaminant concentrations in a low permeable environment or northerly movement of contaminants in this area.

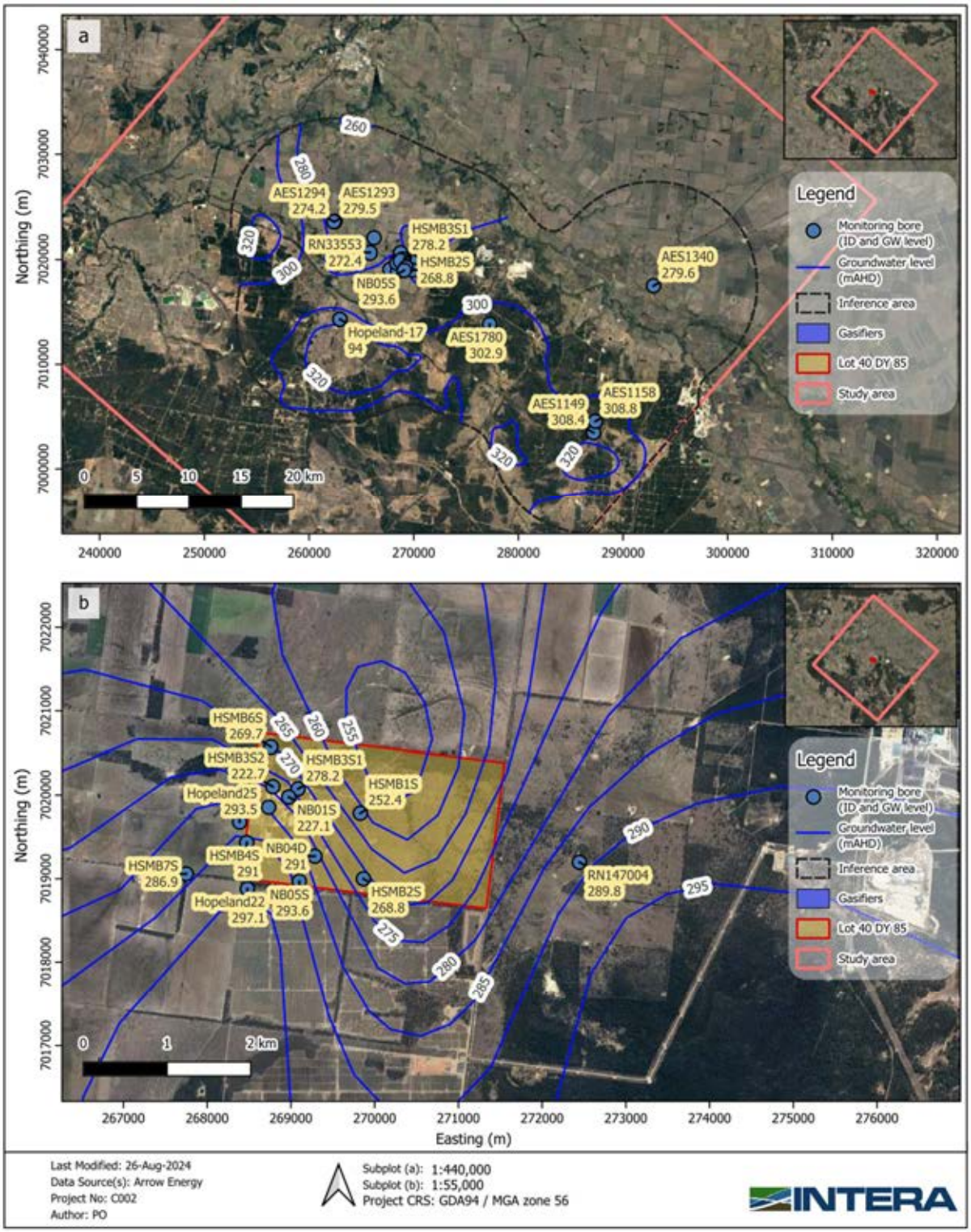


Figure 2-14 – Interpreted groundwater levels in the Springbok Sandstone. a) an overview of the groundwater contours, and b) zoomed-in view around Lot40 DY85.

### 2.3.3 Wallon Coal Measures

Regionally, groundwater levels within the Walloon Coal Measures present significant depressurisation along the southwest edges of this unit, due to the groundwater extraction

associated with the CSG production. This depressurisation results in lower hydraulic heads compared to the over- and under-lying units, thus producing vertical groundwater gradients from those units towards the Wallon Coal Measures.

Figure 2-15 to Figure 2-20 present the local groundwater heads and contours for the following members of the Walloon Coal Measures (WCM): Kogan, Macalister, Wambo, Argyle, Taroom Coal Measures. The following observations can be made about the groundwater levels:

- Groundwater levels in the Kogan member (upper WCM) range broadly from 270 to 320 mAHD (Figure 2-15). Groundwater contours suggest flow within this unit to occur from east of the inference area mainly to south-west.

- Regionally and offsite, groundwater levels, as inferred from the contours, in the Macalister member range broadly from 100 to 300 mAHD (Figure 2-16), with a minimum measured level of 94 mAHD in HL17. Groundwater contours suggest flow within this unit mainly to occur with local variations such as from the Hopeland pilot test. Inside and around Lot40 DY85, groundwater gradients in the Macalister are to the south-east, with a local depression in the area of bores NB02D and M15. In addition, there is a high variability in groundwater levels within a relatively small area in Lot40 DY85, ranging from 190 to 250 mAHD.

- Groundwater levels in the Wambo range broadly from 284 (bore AES1074, not shown in Figure 2-17) to 313 mAHD (Figure 2-17) and are generally higher than in Macalister, indicating an upward gradient. This suggests that the migration of contaminants from the overlying Macalister is unlikely. Groundwater flow interpreted from the contours suggests higher levels at the east of the inference area and flow mainly towards the west to north-west of the domain.

- Groundwater levels in the Argyle range broadly from 152 to 294 mAHD (Figure 2-18). Groundwater contours suggest flow within this unit occurs towards the south-west.

- For the Taroom Coal Measures member of WCM, Figure 2-19 depicts a schematic conceptualisation of the groundwater levels and flow (OGIA, 2021). According to this figure, groundwater in the study area flow from north to south with levels around 250 mAHD. Locally, groundwater levels for the Taroom Coal Measures are presented in Figure 2-20. Groundwater levels range broadly from -24to 299mAHD. Groundwater contours suggest flow within this unit varies from northeastern to the south, southwestern and west, with local variations.

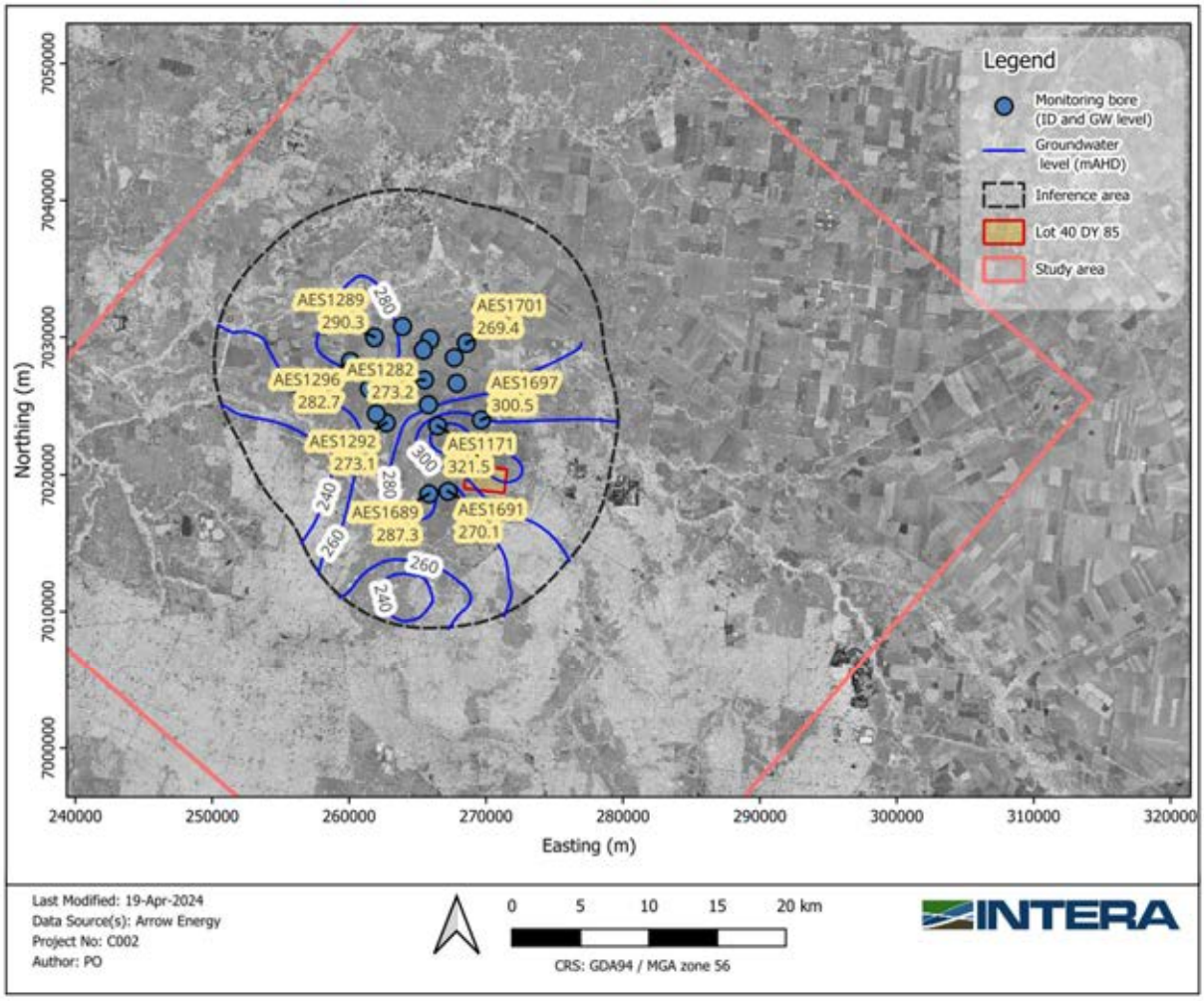


Figure 2-15 - Interpreted groundwater levels in the Kogan member of WCM.

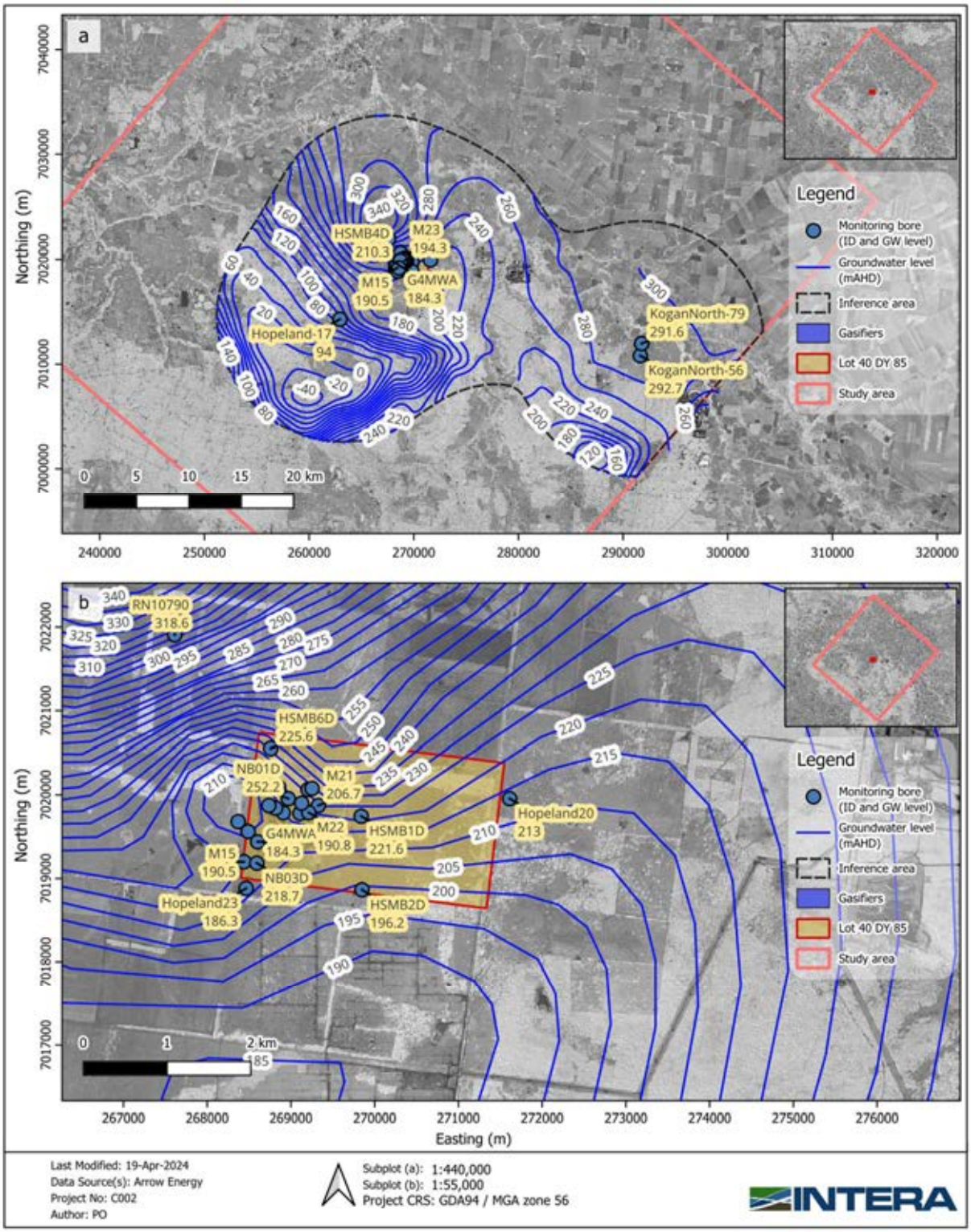


Figure 2-16 - Interpreted groundwater levels in the Macalister member of WCM. a) an overview of the groundwater contours, and b) zoomed-in view around Lot40Lot40 DY85.

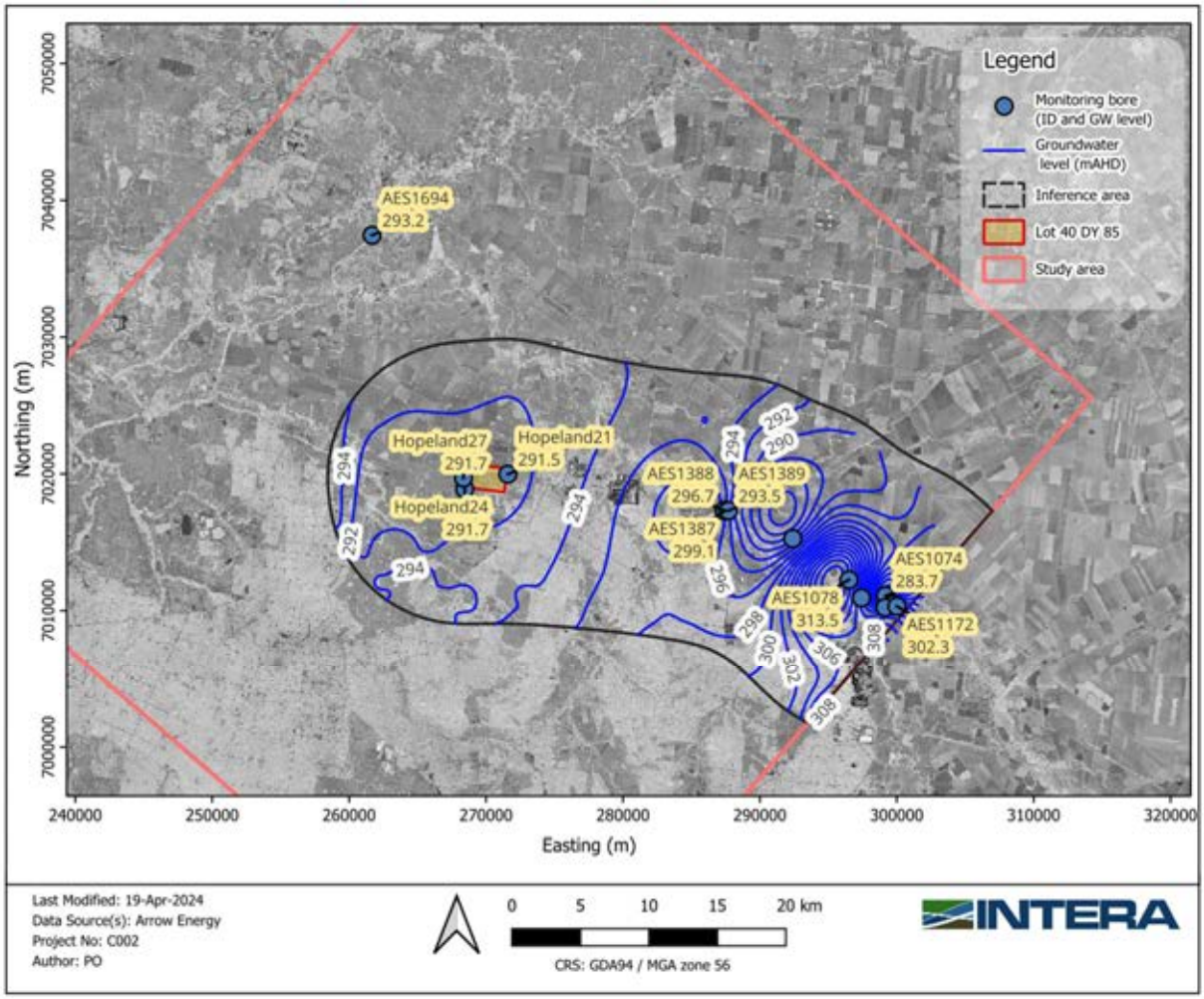


Figure 2-17 - Interpreted groundwater levels in the Wambo (WCM).

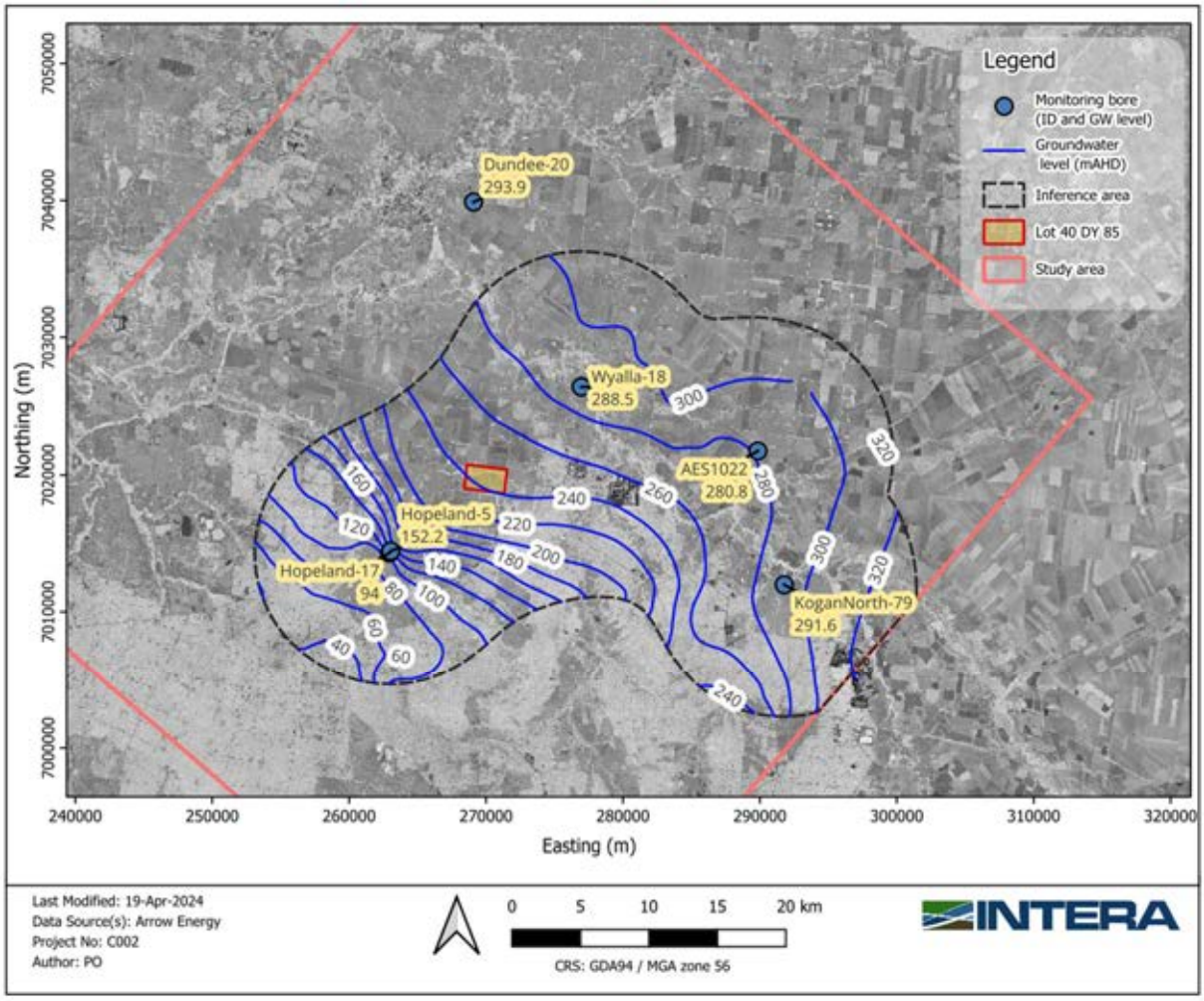


Figure 2-18 - Interpreted groundwater levels in the Argyle (WCM).

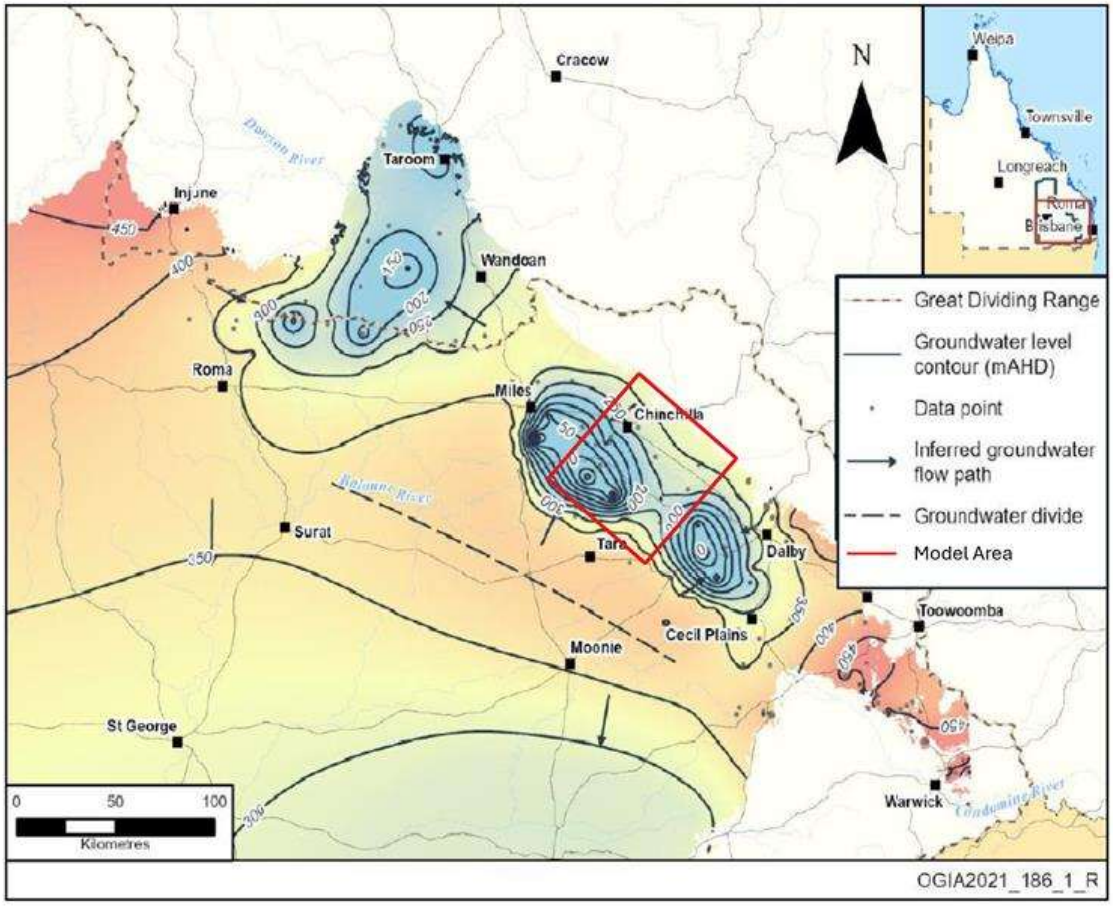


Figure 2-19 - Schematic representation groundwater levels within the Taroom Coal Measures (extracted from OGIA, 2021).

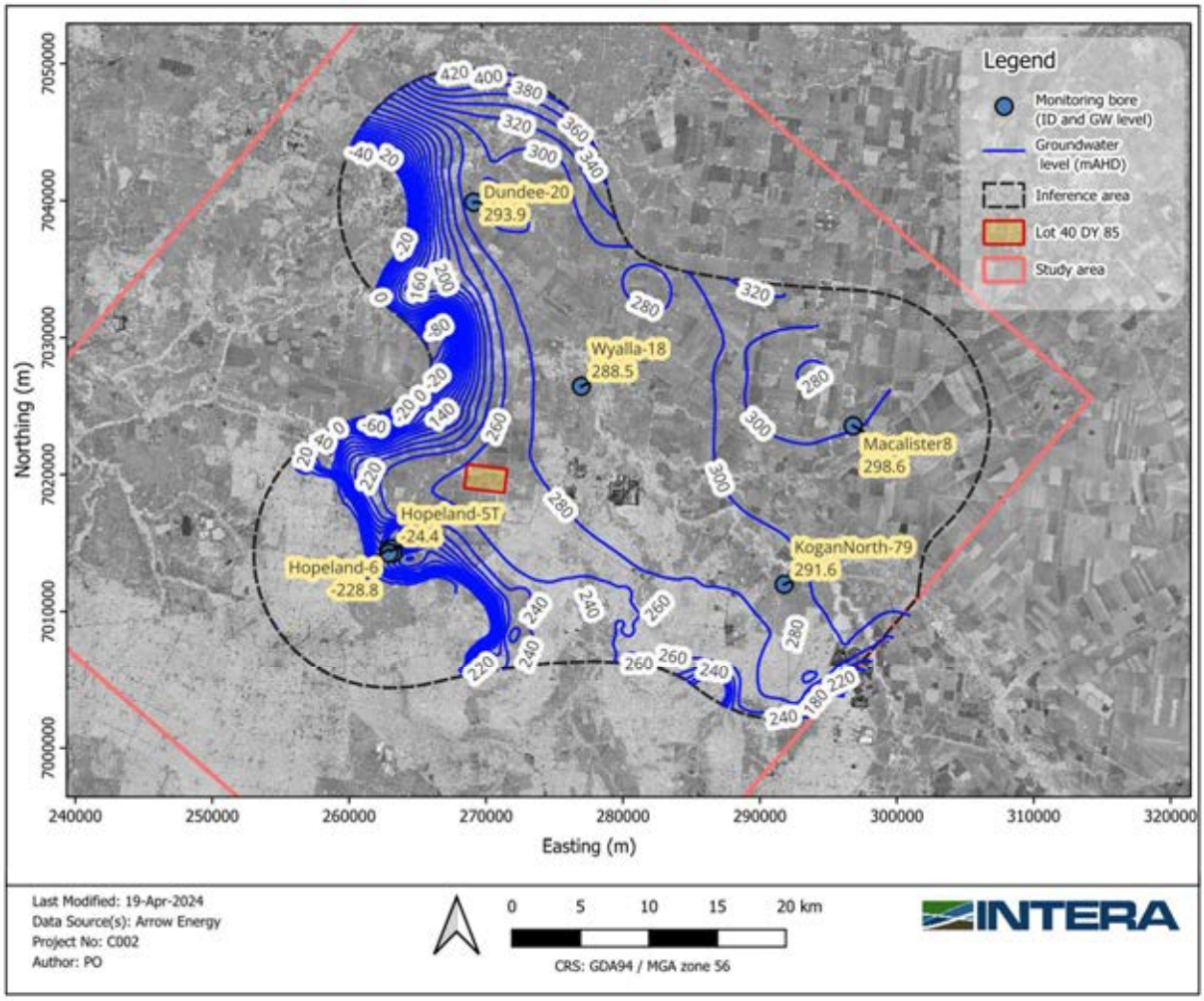


Figure 2-20 - Interpreted groundwater levels in Taroom Coal Measures.

### 2.3.4 Hutton Sandstone

At a regional scale, the groundwater levels vary from 350 to 500 mAHD as can be observed in Figure 2-21 (OGIA, 2021). Site-specific groundwater levels in the Hutton Sandstone range from 244 to 316 mAHD, with interpreted contours resulting in levels around 280 mAHD in Lot40 DY85. Groundwater flow, as indicated by the interpreted contours (Figure 2-22), occurs from west to east at the westernmost part of the inference area, and then to the south in the eastern part of the area. Groundwater levels in this unit are higher than those in the lower members of the WCM, indicating an upward vertical gradient. In addition, the presence of an aquitard (Eurombah formation) between this unit and the WCM suggests that the Hutton Sandstone could be omitted from the numerical model if needed (e.g., better numerical efficiency).

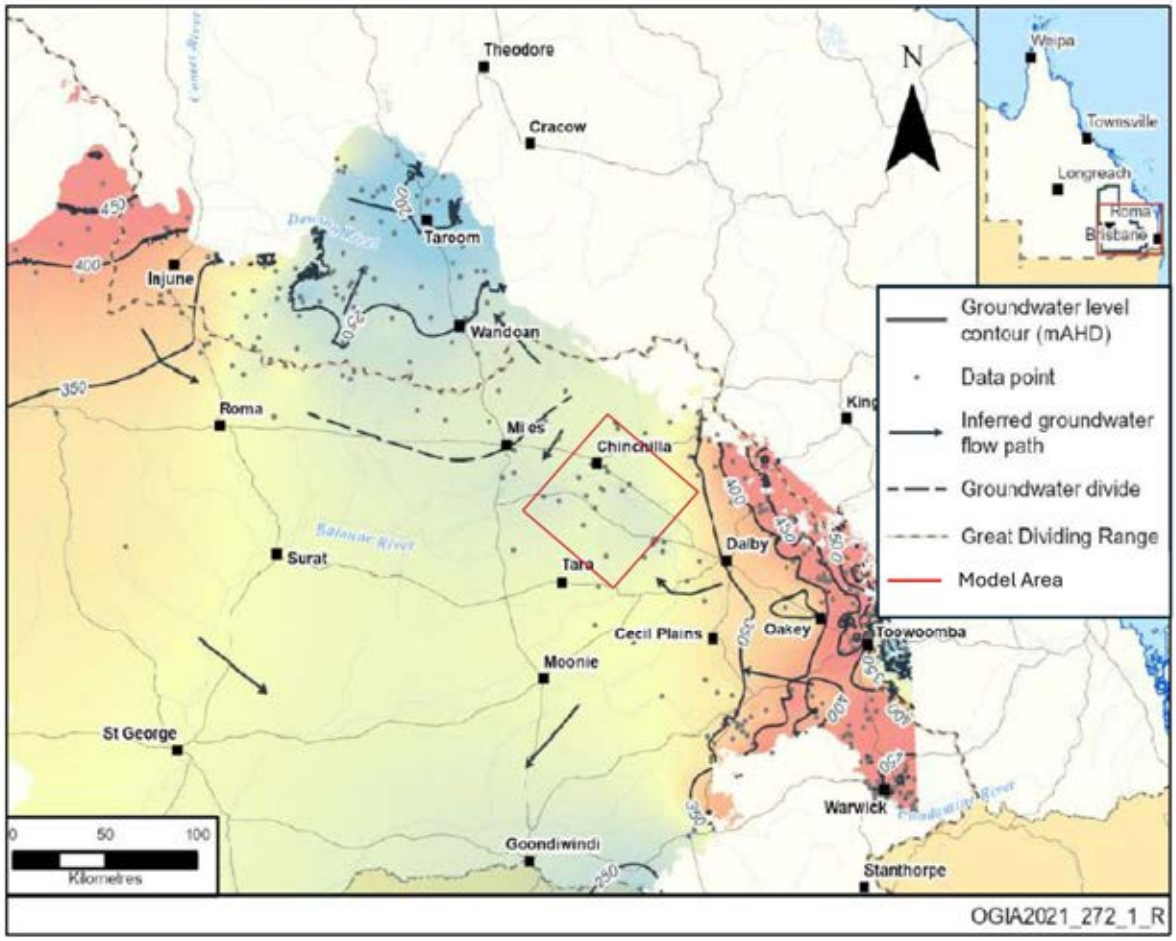


Figure 2-21 – Schematic representation groundwater levels within the Hutton Sandstone (extracted from OGIA, 2021).

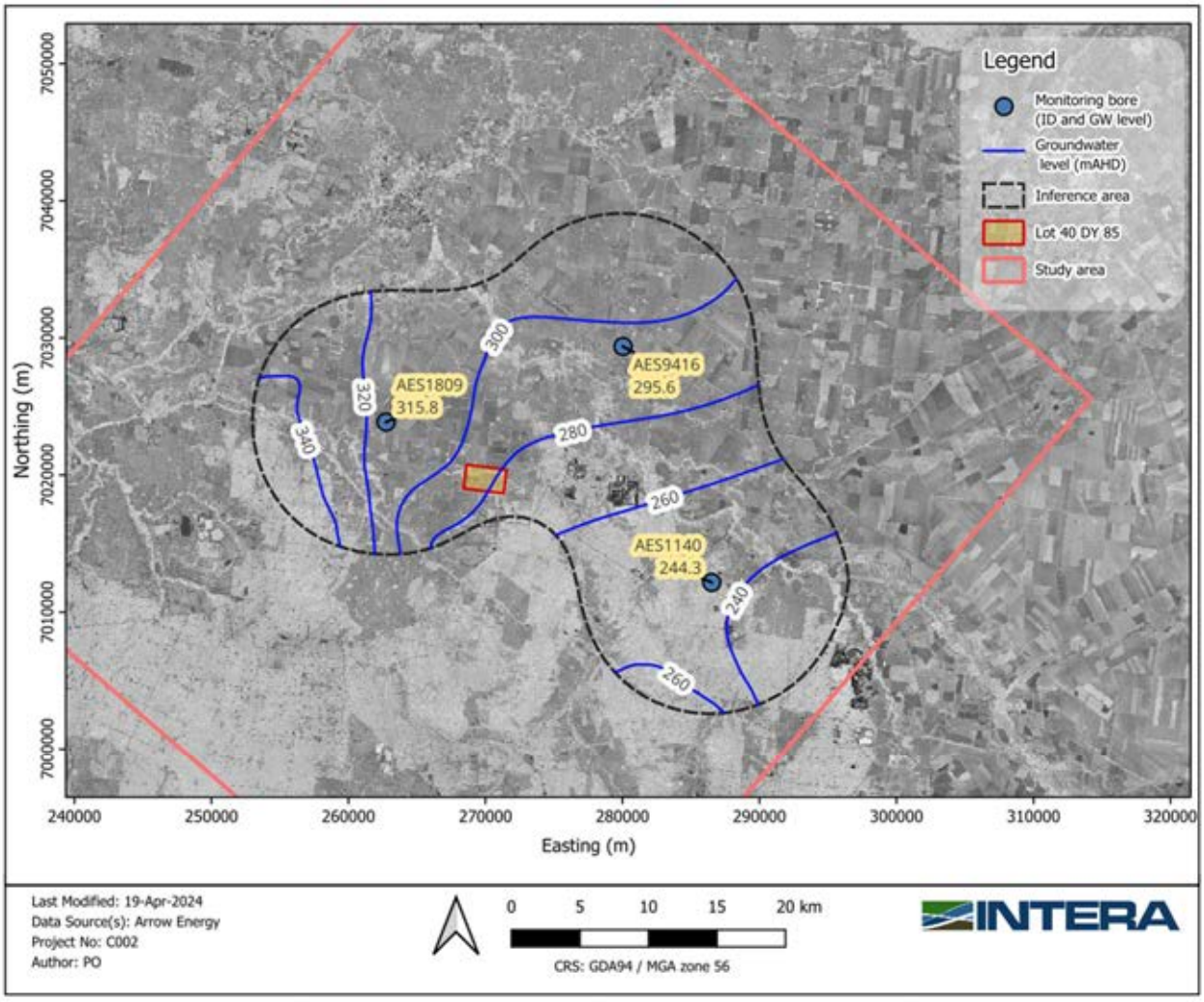


Figure 2-22 - Interpreted groundwater levels in the Hutton Sandstone.

### 2.3.5 Vertical Hydraulic Gradients

The analysis of groundwater level at the nested monitoring sites illustrates the significant vertical gradients within the basin, and the level of depressurisation within the Walloon Coal Seam units resulting from CSG production. Hydrographs for the four nested sites located in the vicinity of PL253 are displayed in Figure 2-23.

The magnitude of the head differences is often related to the proximity of the monitoring sites to ongoing CSG production activities in the basin. The borehole Hopeland-17 (Figure 2-23 (a)) is the one with the largest head gradients, the differences of up to 200 m head. Groundwater heads measured in the lowest seams of the Walloon Coal measures (particularly in Upper Taroom) show the largest degree of depressurisation. Groundwater heads of the overlying seams (and the underlying Condamine Coal in the monitoring Dundee-20) are mostly above the heads in the Upper Taroom, indicating vertical gradients and vertical flows (both downwards and upwards) towards this seam.

Vertical gradients on the remaining nested sites, Kogan North-79, Wyalla-18 and Dundee-20 (Figure 2-23 (b) to (d)), have shown smaller vertical gradients. Nevertheless, it can be observed a progressive increase in the head differences over the years, as the depressurisation footprint from the CSG extraction expands towards those areas.

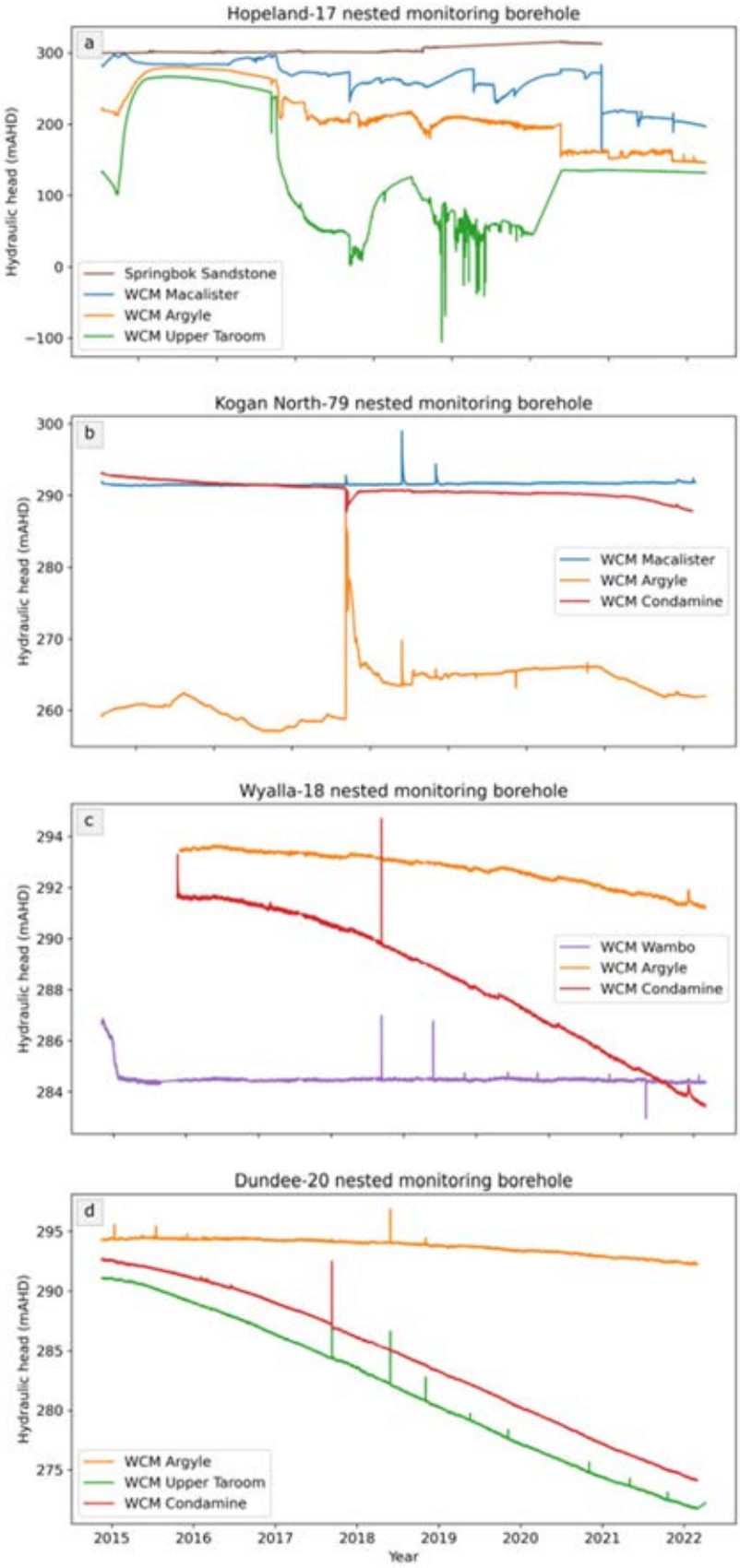


Figure 2-23 - Hydrographs at the (a) Hopeland-17 (b) Kogan-79, (c) Wyalla-18 and (d) Dundee-20 nested monitoring sites.

The analysis of groundwater contour plots for the different units (presented and discussed in the previous sections) indicates that both Springbok Sandstone (overlying) and Hutton Sandstones have higher hydraulic heads than the Walloon Coal Measures, suggesting that vertical flow from the Walloon Coal Measures to other vertically adjacent units is unlikely.

Onsite bores' groundwater levels in the Springbok and WCM Macalister formations are presented in Figure 2-24. Groundwater levels in the area of Lot40 DY85 show consistent higher heads in the Springbok sandstone than in the WCM Macalister.

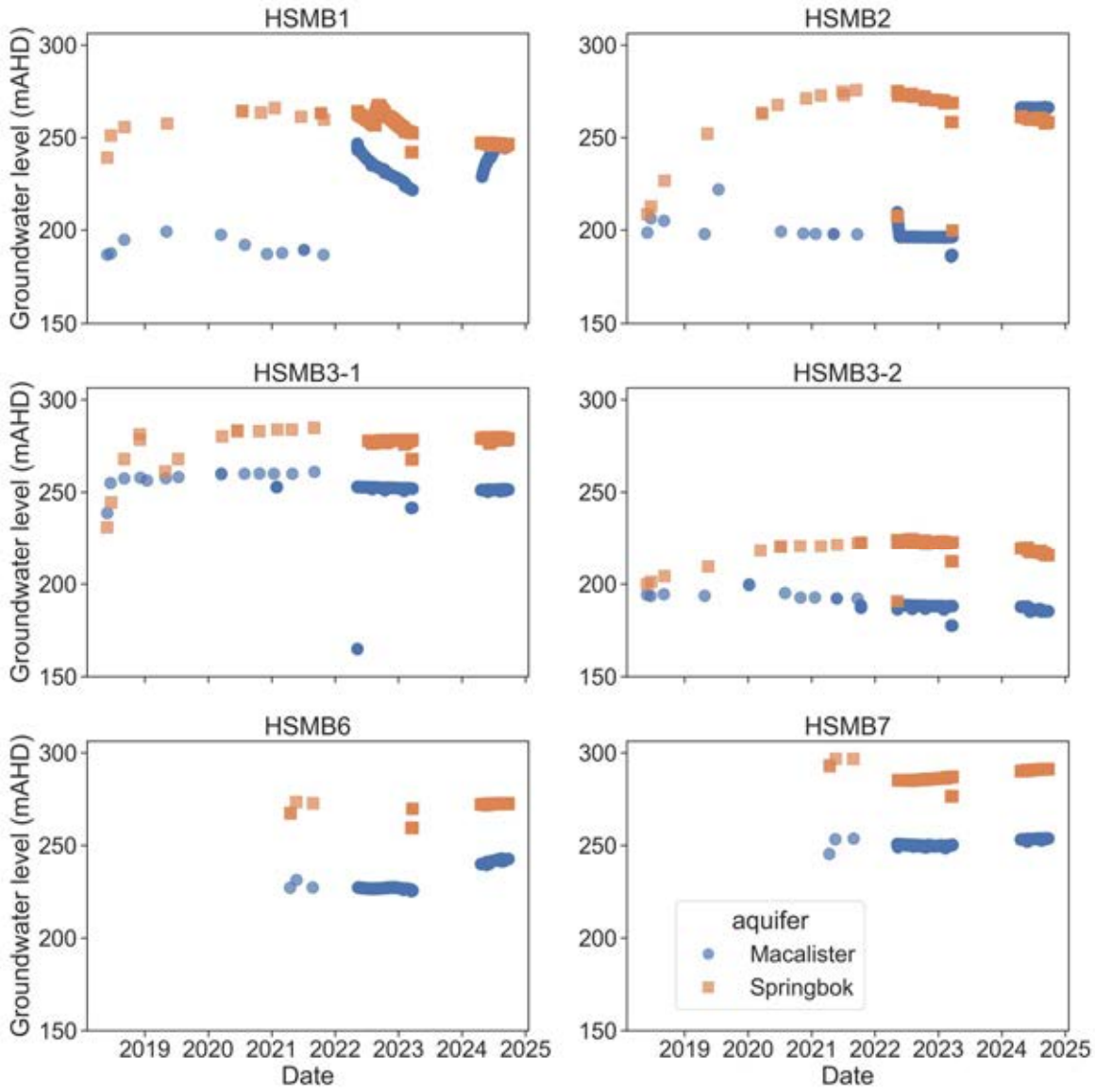


Figure 2-24 - Groundwater level plots of monitoring boreholes located onsite and within the Springbok and Macalister formations.

### 2.3.6 Groundwater Level Trends

Historical groundwater levels of different hydrogeological units have been analysed in order to assess temporal groundwater level trends. The available data encompass several monitoring locations, with historical measurements predominantly obtained between 2013-2023. Hydrographs and the respective location of monitoring boreholes are presented in Figure 2-25 to Figure 2-28, suggesting that groundwater levels have remained generally stable within the study area, with exception of the areas in proximity to ongoing CSG production activities as it can be observed in the monitoring boreholes installed within the Walloon Coal Measures (such as the Hopeland-17 nested monitoring site).

Regionally, the Walloon Coal Measures show lateral variability in permeability and transmissivity. This is illustrated when comparing drawdowns in bores located offsite and at different distances from the former UCG operations. For instance, Wyalla-18 is located 8 km northeast of Lot40 DY85 and Dundee-20 is 20 km north of Lot40 DY85. Bore Hopeland-17 (HL-17), on the other hand, is located 7 km southwest of Lot40 DY85. These are multi-aquifer monitoring bores, which are measuring comparable portions of the Taroom Coal Measures (upper and Condamine) and the WCM Argyle. Bores Wyalla-18 and Hopeland-17 also monitor the WCM Wambo and WCM Macalister, respectively. Figure 2-23 present the groundwater levels time series for these bores, including Dundee-20. Drawdown in the WCM Argyle, Upper Taroom and Condamine Seam is greater around Hopeland-17 than in the northern part, where Wyalla-18 and Dundee-20 are located, probably due to the Hopeland pilot test and other CSG production close by to the south and west.

Locally and onsite (Lot40 DY85), monitoring bores in Springbok have shown variable trends of groundwater levels over time. Notably, bore HSMB1S (Figure 2-25) showed a continuous decrease in groundwater levels until a rebound in mid-2022 followed by a resumption of the decreasing trend. Bore HSMB4S, on the other hand, has displayed a consistent increasing trend since late 2022.

Locally and onsite (Lot40 DY85), monitoring bores in the WCM Macalister have remained constant over time, except for bore HSMB1D (Figure 2-26) that showed a consistent decrease in groundwater since mid-2022.

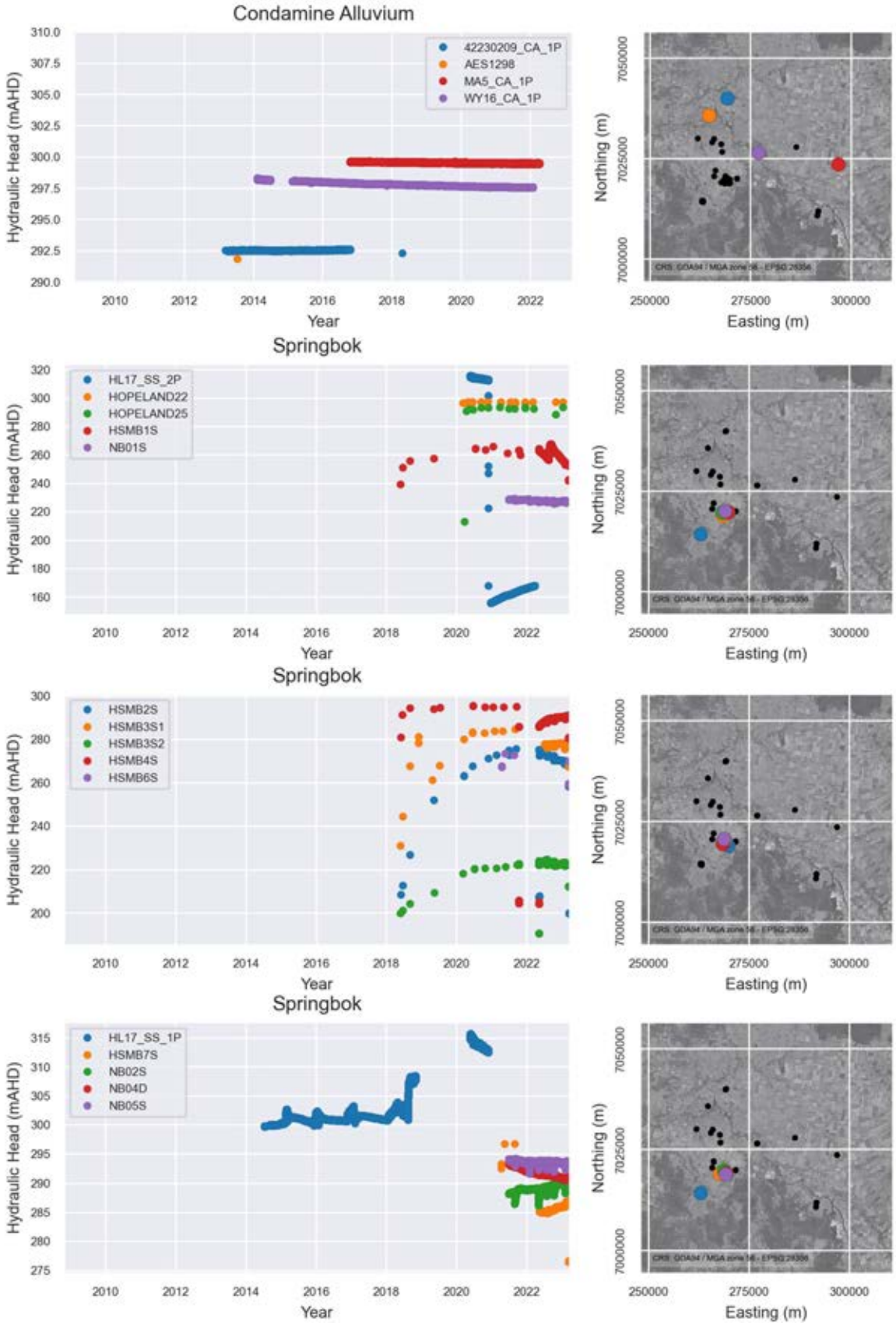


Figure 2-25 - Hydrographs from monitoring boreholes within the Condamine Alluvium and Springbok Formations. Subplot maps to the right of the scatter plot display the approximate locations of the depicted bores in relation to the rest of the bore field.

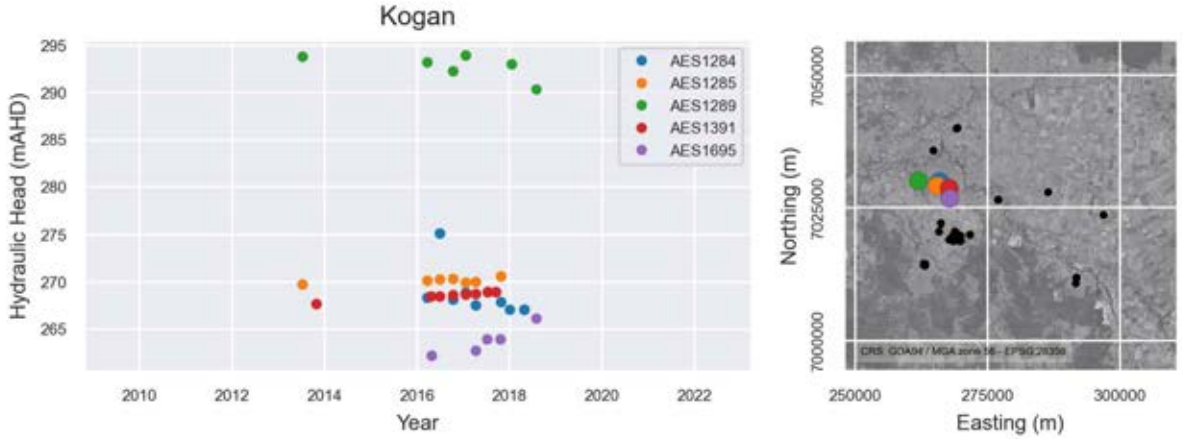
Kogan
Hydraulic Head (mAHD)
Year
AES1284
AES1285
AES1289
AES1391
AES1695
Northing (m)
Easting (m)

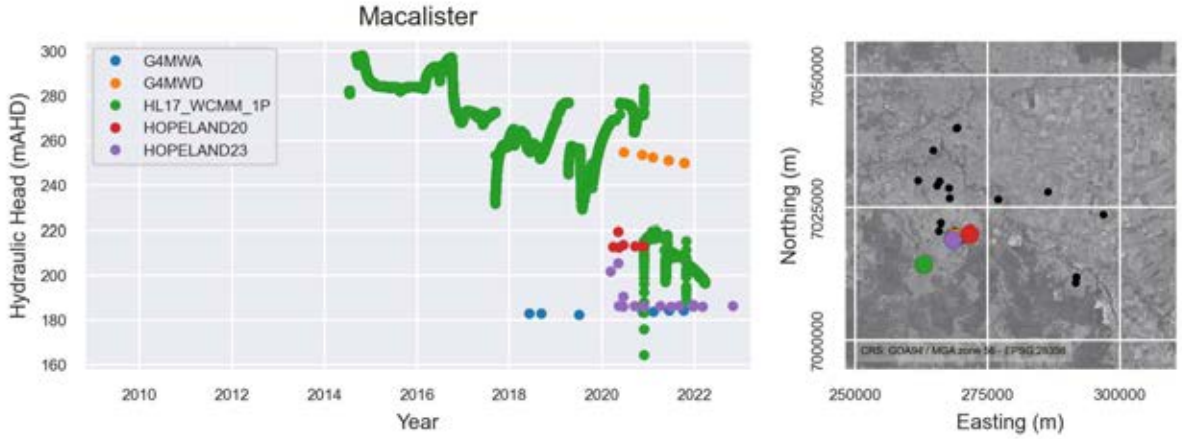
Macalister
Hydraulic Head (mAHD)
Year
G4MWA
G4MWD
HL17_WCMM_1P
HOPELAND20
HOPELAND23
Northing (m)
Easting (m)

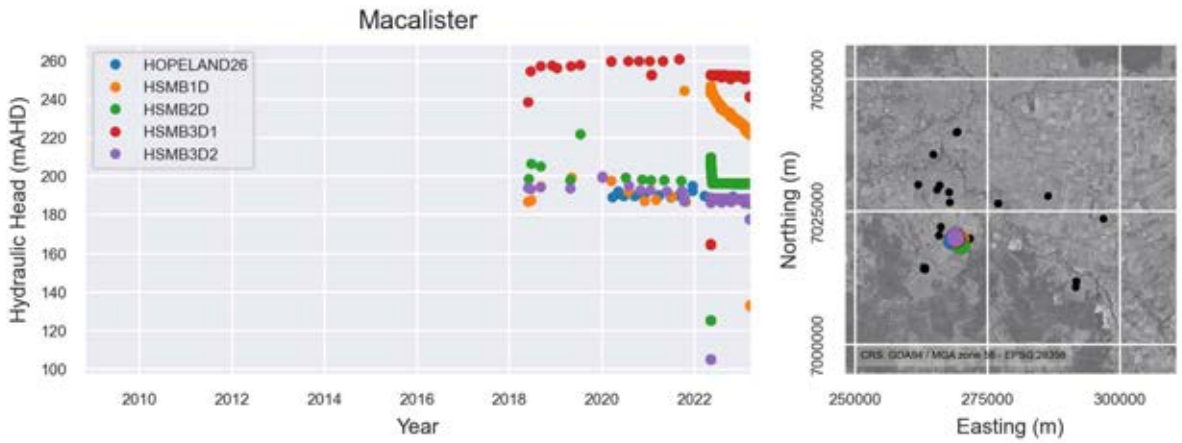
Macalister
Hydraulic Head (mAHD)
Year
HOPELAND26
HSMB1D
HSMB2D
HSMB3D1
HSMB3D2
Northing (m)
Easting (m)

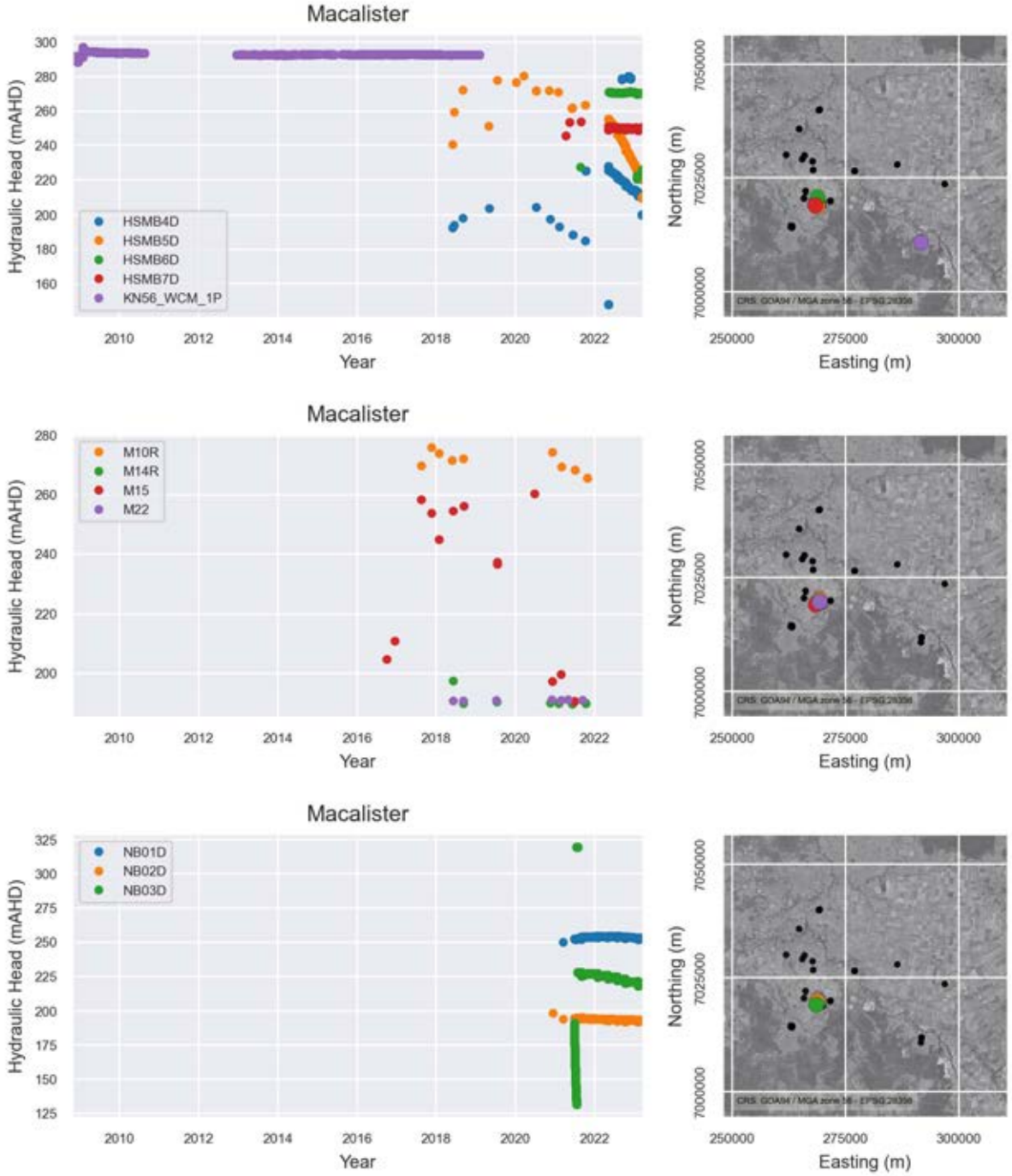


Figure 2-26 - Hydrographs from monitoring boreholes within Kogan and Macalister Formations. Subplot maps to the right of the scatter plot display the approximate locations of the depicted bores in relation to the rest of the bore field.

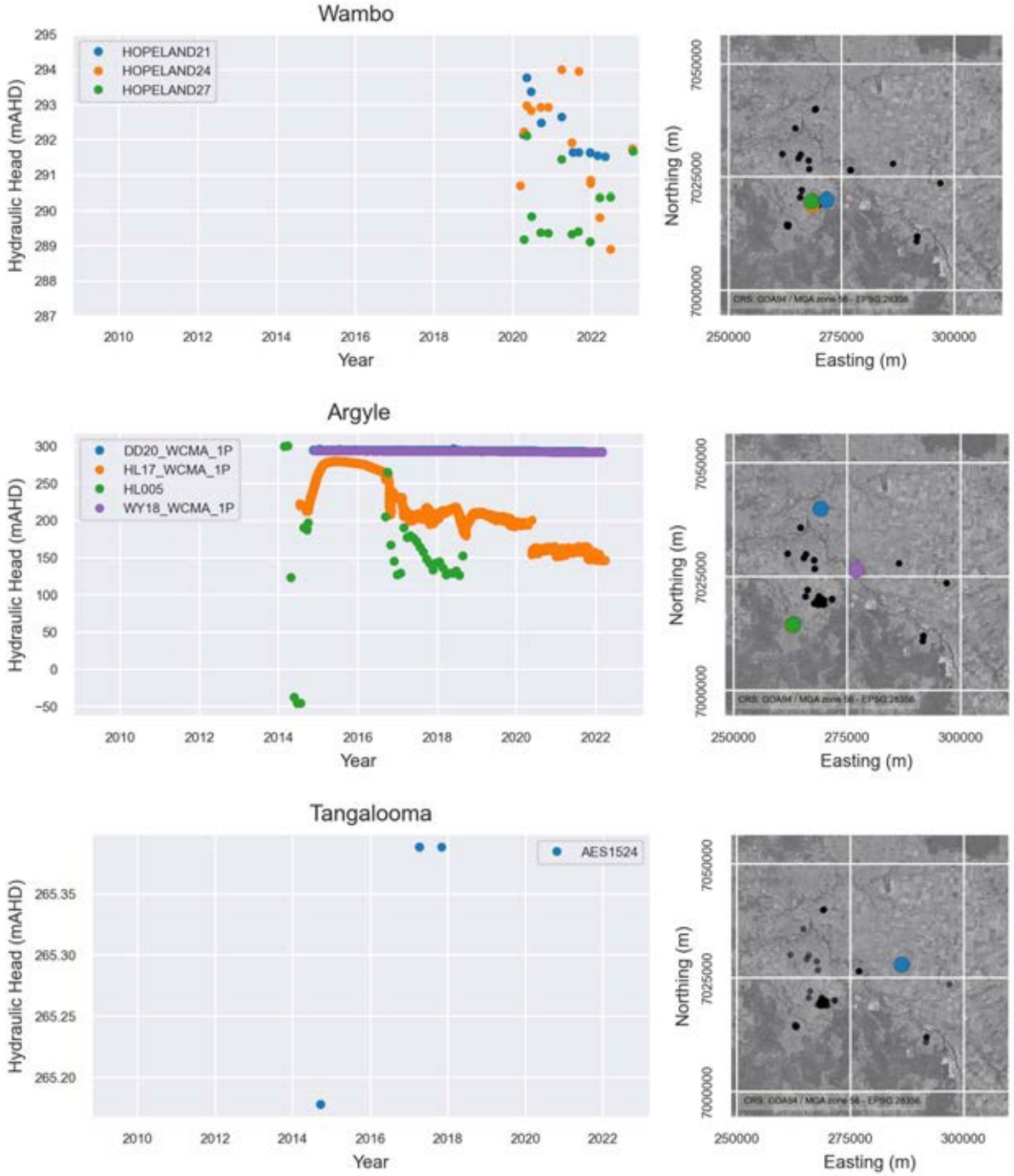


Figure 2-27 - Groundwater level hydrographs from monitoring boreholes within Wambo, Argyle and Tangalooma formations. Subplot maps to the right of the scatter plot display the approximate locations of the depicted bores in relation to the rest of the bore field.

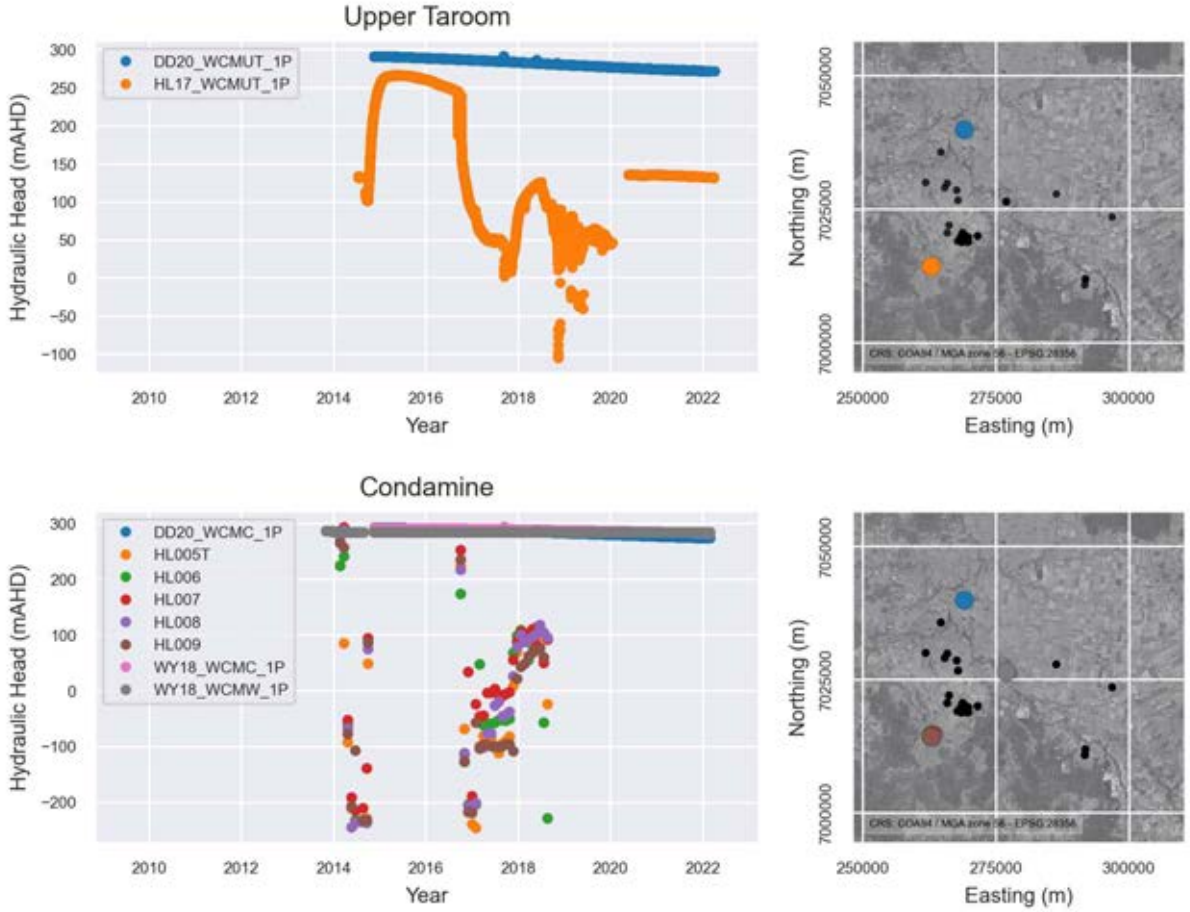


Figure 2-28 - Groundwater level hydrographs from monitoring boreholes within Upper Taroom and Condamine Formations. Subplot maps to the right of the scatter plot display the approximate locations of the depicted bores in relation to the rest of the bore field.

## 2.4 Expected Hydrogeological Parameters

An extensive set of hydrogeological tests has been undertaken in the Surat Basin through hydrogeological and CSG exploration studies, as well as groundwater impact assessments. OGIA (2016) compiled a vast permeability database of the Surat Basin as part of their hydrogeological conceptualisation studies. This database contains thousands of tests obtained from Core, DST, pumping tests and petrophysics summarised in Figure 2-29 and Figure 2-30.

Local parameter ranges for the study area were derived based on the hydraulic parameter estimates compiled by OGIA, and previous conceptualisation and numerical modelling studies undertaken for the PL253 area. These ranges are presented in Table 2-2, and represent aquifer parameters in undisturbed (i.e., no fracturing or porosity changes due to UCG activities) and saturated (i.e., single phase liquid) conditions. Historical UCG activities performed in the site may have produced changes in material properties from compiled values given that:

- Gasification of coal seams may have result in increased porosity and, consequently, effective porosity and hydraulic conductivity. In terms of fluid migration, while increased hydraulic conductivity may increase seepage velocities, the increase in porosity would promote a direct decrease in groundwater level.

- In terms of the numerical modelling under single-phase assumptions, parameter estimates undertaken in areas under multi-phase conditions may result in overestimates of hydraulic conductivity, as viscosity of gases are commonly much smaller than water.

## 2.5 Structures

The hydrogeological characterisation of faults and other structures in the Surat Basin have been subjected to extensive research in OGIA studies (2016 and 2020). These studies classify faults as regional and local faults. Regional faults are characterised by their extensive lateral continuity and significant vertical offsets, while local faults are more restricted both in length and displacement.

Overall, the faults in the Surat Basin are locally extensional mapped faults with displacement usually less than 20 metres, which makes their mapping and delineation challenging. Within the study area, the analysis of the hydrostratigraphic surfaces (displayed in section 2.2) suggests the presence of a few structures aligned southwest-northeast. These faults are relatively small (5-10 km in length) with subtle displacements hardly noticeable in the stratigraphic surfaces. Furthermore, these structures are positioned relatively far from the Lot40 DY85 area (> 10 km) and, consequently, have little effect on the local flow dynamics.

Local fault systems have been identified within and around the Lot40 DY85. Two faults, each measuring no more than 1,400 meters in length, crosscut the lot. These fault lines exhibit orthogonal orientations, with one striking in a NE-SW direction, and the other in a NW-SE direction. The impact of these faults on pressure can be observed by looking at the groundwater levels in bores HSMB3S1 and HSMB3S2 within the Springbok Sandstone. HSMB3S1 exhibits a groundwater level approximately 50 mAHD compared to HSMB3S2. This is further discussed in the groundwater numerical model (section 3.0)

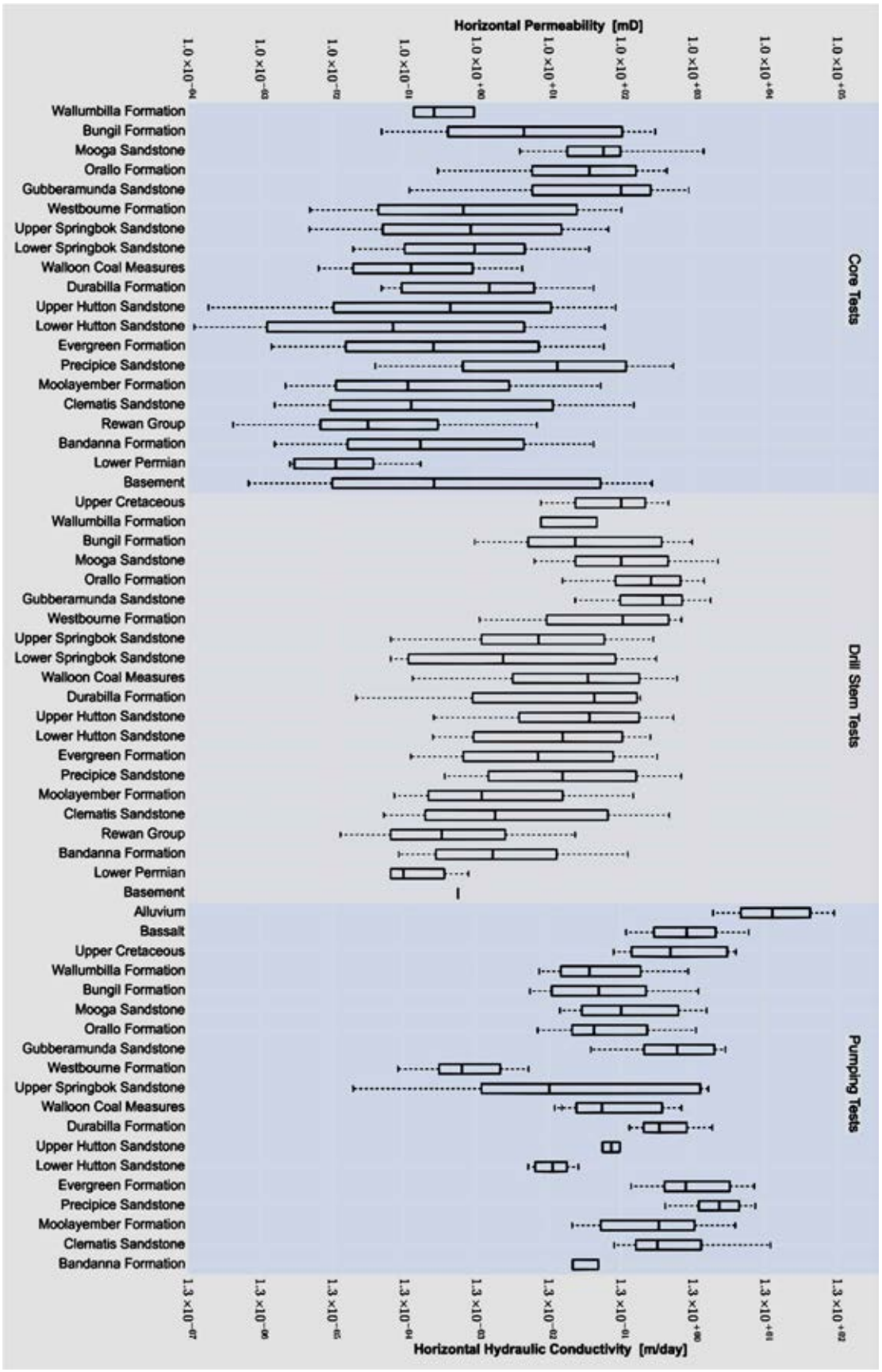


Figure 2-29 - Summary of horizontal hydraulic conductivity and horizontal permeability data for the different formations in the Surat Basin (extracted from OGIA, 2016).

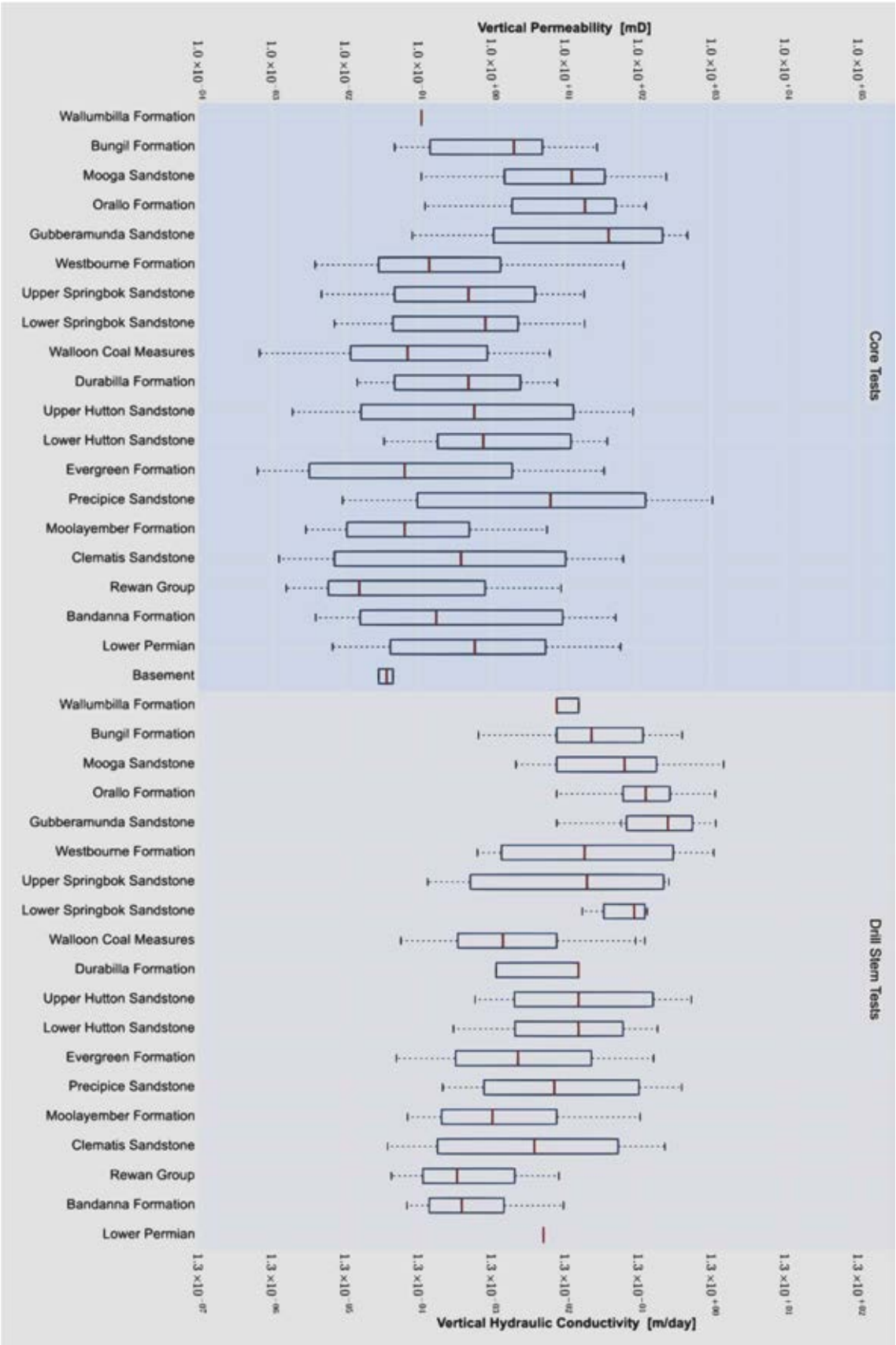


Figure 2-30 - Summary of vertical hydraulic conductivity and vertical permeability data for the different formations in the Surat Basin (extracted from OGIA, 2016).

Table 2-2 – Expected local hydrogeological parameters (extracted from AGE, 2020)

| Hydrostratigraphic Unit | Horizontal Hydraulic conductivity (m/d) | Vertical Hydraulic Conductivity (m/d) | Specific Yield (-) | Specific Storage ($m^{-1}$) |
|---|---|---|---|---|
| Condamine Alluvium/ Gubberamunda Sandstone | 0.3 - 30 | $3x10^{-4}$ - 3 | 0.002-0.15 | $2.3 x10^{-7}$ - $2 x10^{-5}$ |
| Westboume Formation | 0.1-10 | $1x10^{-4}$- 1 | 0.001-0.1 | $2.3 x10^{-7}$ - $2 x10^{-5}$ |
| Springbok Sandstone | $1x10^{-3}$ - $1x10^{-1}$ | $1x10^{-7}$ - $1x10^{-3}$ | 0.001-0.1 | $2.3 x10^{-7}$ - $2 x10^{-5}$ |
| Walloon Coal Measures (Kogan Coal) | $1x10^{-3}$ - $5x10^{-1}$ | $1x10^{-7}$ - $5x10^{-3}$ | 0.001-0.1 | $2.3 x10^{-7}$ - $2 x10^{-5}$ |
| Walloon Coal Measures (Kogan Interburden) | $5x10^{-3}$ - $5x10^{-1}$ | $5x10^{-6}$ - $5x10^{-2}$ | 0.001-0.1 | $2.3 x10^{-7}$ - $2 x10^{-5}$ |
| Walloon Coal Measures (Macalister Coal) | $1x10^{-3}$ - $5x10^{-1}$ | $1x10^{-7}$ - $5x10^{-3}$ | 0.001-0.1 | $2.3 x10^{-7}$ - $2 x10^{-5}$ |
| Walloon Coal Measures (Macalister Interburden) | $1x10^{-4}$ - $5x10^{-1}$ | $1x10^{-7}$ - $5x10^{-2}$ | 0.001-0.1 | $2.3 x10^{-7}$ - $2 x10^{-5}$ |
| Walloon Coal Measures (Wambo Coal) | $1x10^{-3}$ - $5x10^{-1}$ | $1x10^{-7}$ - $5x10^{-3}$ | 0.001-0.1 | $2.3 x10^{-7}$ - $2 x10^{-5}$ |
| Walloon Coal Measures (Wambo Interburden) | $5x10^{-4}$ - $5x10^{-2}$ | $5x10^{-8}$ - $5x10^{-4}$ | 0.001-0.1 | $2.3 x10^{-7}$ - $2 x10^{-5}$ |
| Walloon Coal Measures (Argyle Coal) | $1x10^{-3}$ - $5x10^{-1}$ | $1x10^{-7}$ - $5x10^{-3}$ | 0.001-0.1 | $2.3 x10^{-7}$ - $2 x10^{-5}$ |
| Walloon Coal Measures (Argyle Interburden) | $1x10^{-5}$ - $5x10^{-3}$ | $1x10^{-8}$ - $5x10^{-4}$ | 0.001-0.1 | $2.3 x10^{-7}$ - $2 x10^{-5}$ |
| Walloon Coal Measures (Tangalooma Sandstone) | $1x10^{-7}$ - $1x10^{-1}$ | $1x10^{-10}$ - $1x10^{-2}$ | 0.001-0.1 | $2.3 x10^{-7}$ - $2 x10^{-5}$ |
| Walloon Coal Measures (Upper Taroom Coal) | $1x10^{-3}$ - $5x10^{-1}$ | $1x10^{-7}$ - $5x10^{-3}$ | 0.001-0.1 | $2.3 x10^{-7}$ - $2 x10^{-5}$ |
| Walloon Coal Measures (Upper Taroom Interburden) | $1x10^{-3}$ - 1 | $1x10^{-6}$ - 0.1 | 0.001-0.1 | $2.3 x10^{-7}$ - $2 x10^{-5}$ |
| Walloon Coal Measures (Condamine Coal) | $1x10^{-3}$ - $5x10^{-1}$ | $1x10^{-7}$ - $5x10^{-3}$ | 0.001-0.1 | $2.3 x10^{-7}$ - $2 x10^{-5}$ |
| Walloon Coal Measures (Condamine Interburden) | $1x10^{-3}$ - $1x10^{-1}$ | $1x10^{-7}$ - $5x10^{-3}$ | 0.001-0.1 | $2.3 x10^{-7}$ - $2 x10^{-5}$ |
| Eurombah Formation | $1x10^{-7}$ - $1x10^{-1}$ | $1x10^{-10}$ - $1x10^{-2}$ | 0.001-0.1 | $2.3 x10^{-7}$ - $2 x10^{-5}$ |
| Hutton Sandstone | $1x10^{-3}$ - $1x10^{-1}$ | $1x10^{-7}$ - $5x10^{-3}$ | 0.001-0.1 | $2.3 x10^{-7}$ - $2 x10^{-5}$ |

## 2.6 Groundwater Quality

The following section presents the groundwater quality for the Site. Macalister Seam (Walloon Coal Measures) and Springbok are the main hydrogeological units depicting measurable concentrations of organic contaminants such as benzene and naphthalene, and thus are the focus of the hydrochemistry described in this section. Arrow Energy collects samples from four bores outside of Lot40 DY85 (bores Hopeland 22, Hopeland 25, HSMB6S and HSMB7S) and one landholder bore (RN147004) in the Springbok Sandstone. DES/DoR have collected samples from 11 other monitoring bores installed in the Springbok Sandstone on and around the site. For the Walloon Coal Measures, Arrow Energy monitors four off-site monitoring (Hopeland 23, Hopeland 26, HSMBD6D, and HSMB7D) and 4 landholder bores (RN10790, RN15811, RN15868, and RN160158).

The majority of the observation bores were installed inside and around Lot40 DY85 as displayed in Figure 2-31. GHD (2020) identified benzene, toluene and naphthalene as the main UCG contaminants. Thus, concentration data for BTEX (benzene, ethylbenzene, toluene, total xylenes) and naphthalene is presented to illustrate the extent of the contaminants over the site. It is noteworthy to mention that the source of the contaminant can result from the UCG activities but also from coal and drilling products used during the bores construction. In addition to the aforementioned compounds, this section also includes a discussion about major ion chemistry to identify bores that have representative groundwater of the medium and have not been affected by external factors such as drilling fluids.

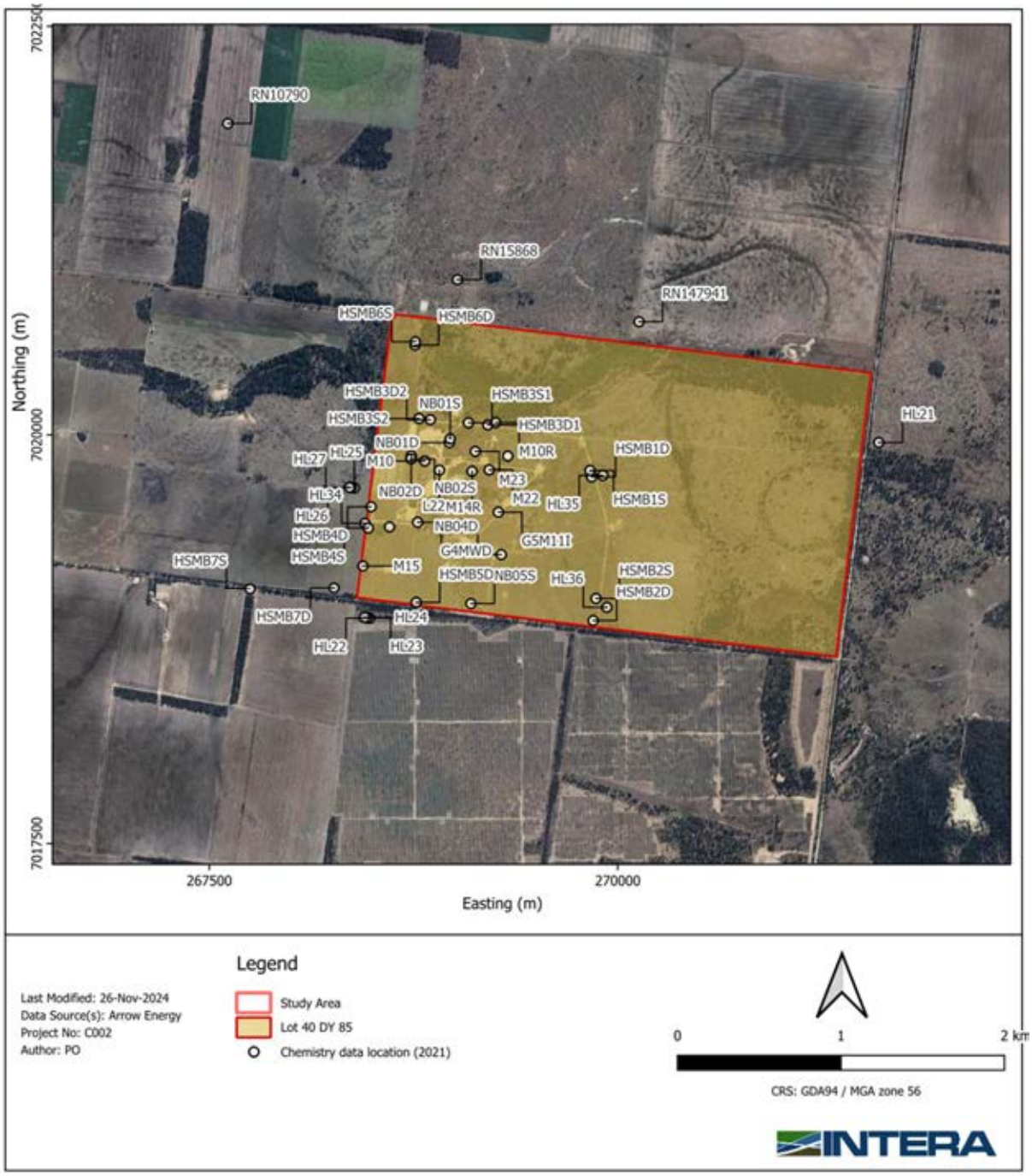


Figure 2-31 – Location of bores with relevant groundwater quality data.

## 2.6.1 Springbok Sandstone

Aqueous major ion chemistry is displayed as a Piper plot in Figure 2-32. This figure presents all the samples collected from 2018 to 2023 for the bores located in and around the Lot40 DY85. All groundwater samples presented neutral to slightly basic pH and are classified as sodium-potassium-chloride-sulphate type.

HSMB4S contains elevated potassium (Figure 2-33) and could potentially indicates the bore's water is not a representative sample from the formation. Groundwater chemistry from this bore may represent remnant drill fluids chemicals (e.g., potassium chloride) and, thus, samples from this bore

are not considered to be representative of the Springbok Sandstone groundwater. Moreover, on-site bores with two perforation intervals between 100 and 110 meters below the ground level (mbgl) contain higher concentrations of benzene compared to boreholes with only one perforation interval (Table 2-3) and Figure 2-33. It remains unclear whether this indicates that the 100-110 mbgl interval is less contaminated or if bores with two perforation intervals have connected two water-bearing units with varying contaminant concentrations. These nuances will be addressed in the history-matching and uncertainty analysis of the contaminant transport model.

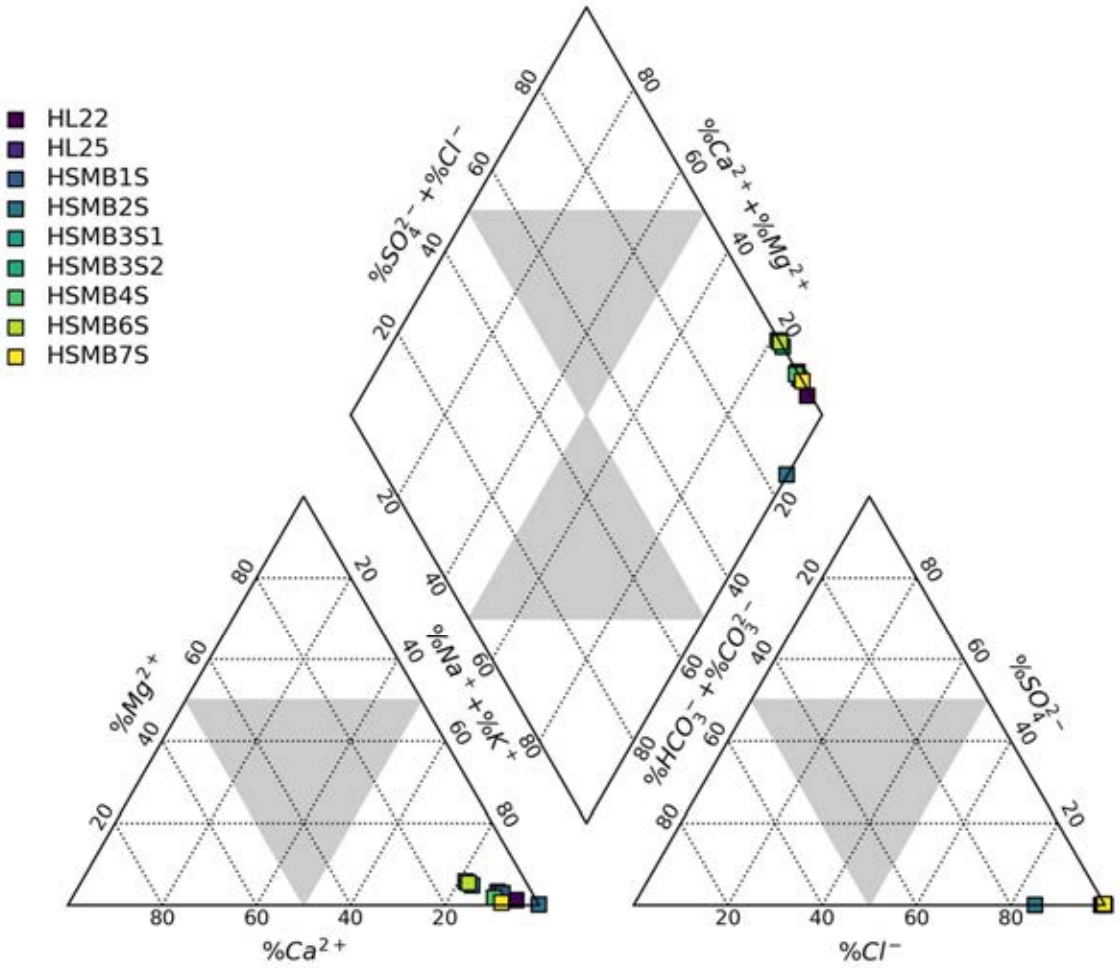


Figure 2-32 - Piper diagram for Springbok Sandstone groundwater samples (2021-2024) collected within and around Lot40 DY85. Concentration data provided by Arrow Energy.

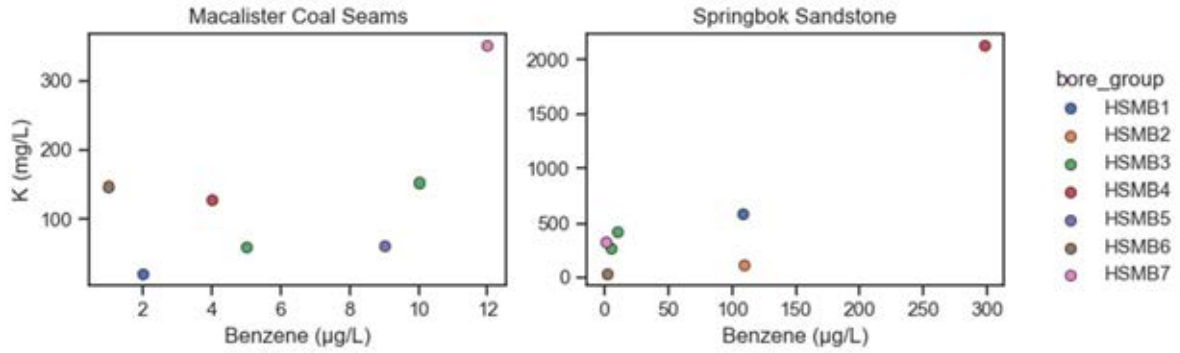


Figure 2-33 – Benzene vs potassium plot for samples collected up to October 2023. Concentration data provided by Arrow Energy.

Table 2-3 – Springbok sandstone monitoring bore perforation intervals.

| Bore ID | Perforation 1 | Perforation 2 |
|---|---|---|
| HSMB1S | 88.5-90.28 | 105-111 |
| HSMB2S | 91-92.78 | 104-110 |
| HSMB3S1 | 90.5-92.28 | 104-110 |
| HSMB3S2 | 94-95.78 | 103.5-106.5 |
| HSMB4S | 94.5-97.5 | 106.5-108.28 |
| HSMB6S | 86.75-92.75 | Nil |
| HSMB7S | 103.75-106.75 | Nil |
| NB01S | 85.40-91.40 | Nil |
| NB02S | 85.41-91.4 | Nil |
| NB04(D)S | 102.5-108.5 | Nil |
| NB05S | 102.5-108.5 | Nil |

*Data provided by Arrow Energy.

Spatial distribution of benzene (selected as proxy for BTEX compounds) and naphthalene concentrations corresponding to 2021 and 2023 are shown in Figure 2-34. Latest available sample data of BTEX and Naphthalene for each bore is presented in Table 2-4.This is further addressed during the numerical transport model in section 3.3.1.

Springbok Sandstone's groundwater quality data (Table 2-4) shows substantial concentration of BTEX and naphthalene mainly located inside the boundaries of Lot40 DY85 and near the gasifiers. Notably, NB01S shows the highest concentration of BTEX (e.g., benzene of 2,000 µg/L). However, monitoring bores outside Lot40 DY85 show no evidence of measurable concentrations of BTEX or Naphthalene, suggesting the contamination is contained inside the area of Lot40 DY85.

Time series concentration graphs of benzene, toluene and naphthalene for selected bores (Figure 2-35) depict a likely breakthrough of contaminants in mid-2018 followed by a sharp decrease in concentration until 2021. From 2020 to 2021, the decreasing trend in the concentrations of benzene and naphthalene appeared to be less pronounced, suggesting that the interplay between the contaminant source and the degradation process has reached a pseudo steady state. This is further

analysed in the contaminant transport model in section 4.3. After 2022, data depicts a similar trend to that of 2020-2021 with concentrations subjected to a slight decrease in time and even reaching levels below limit of reporting for naphthalene. This is further addressed during the numerical transport model in section 3.3.1.

Table 2-4 – Springbok Sandstone groundwater quality data. Latest sample data available for each bore.

| Bore | Date | Benzene (ug/L) | Ethylbenzene (ug/L) | Naphthalene (ug/L) | Toluene (ug/L) | Total xylenes (ug/L) |
|---|---|---|---|---|---|---|
| HL22 | 2024-06-09 | <1.0 | <2.0 | <1.0 | <2.0 | <2.0 |
| HL25 | 2024-06-08 | <1.0 | <2.0 | <1.0 | <2.0 | <2.0 |
| HL34 | 2024-07-24 | <1.0 | <2.0 | <1.0 | <2.0 | <2.0 |
| HL35 | 2024-07-24 | <1.0 | <2.0 | <1.0 | <2.0 | <2.0 |
| HL36 | 2024-07-24 | <1.0 | <2.0 | <1.0 | <2.0 | <2.0 |
| HSMB1S | 2024-06-26 | 129.0 | <2.0 | 1.7 | 10.0 | 4.0 |
| HSMB2S | 2024-03-26 | - | - | - | - | <2.0 |
| HSMB2S | 2024-06-13 | 105.0 | <2.0 | 1.6 | 13.0 | - |
| HSMB3S1 | 2024-06-07 | 4.0 | <2.0 | <1.0 | <2.0 | <2.0 |
| HSMB3S2 | 2024-06-11 | 11.0 | <2.0 | 2.4 | 3.0 | <2.0 |
| HSMB4S | 2024-06-26 | 274.0 | <2.0 | 2.5 | 20.0 | <2.0 |
| HSMB6S | 2024-06-06 | 2.0 | <2.0 | <1.0 | 4.0 | <2.0 |
| HSMB7S | 2024-06-07 | <1.0 | <2.0 | <1.0 | <2.0 | <2.0 |
| NB01S | 2024-06-14 | 3460.0 | 33.0 | <1.0 | 692.0 | 107.0 |
| NB02S | 2024-06-11 | 9.0 | <2.0 | <1.0 | <2.0 | <2.0 |
| NB04D | 2024-03-25 | - | - | - | - | <2.0 |
| NB04D | 2024-06-25 | <1.0 | <2.0 | 1.2 | <2.0 | - |
| NB05S | 2024-06-11 | 1.0 | <2.0 | <1.0 | 4.0 | <2.0 |
| RN107857 | 2018-06-21 | <1.0 | <2.0 | <5.0 | <2.0 | <2.0 |
| RN147004 | 2024-06-12 | <1.0 | <2.0 | <1.0 | <2.0 | <2.0 |
| RN33553 | 2018-07-12 | <1.0 | <2.0 | <5.0 | <2.0 | <2.0 |

*Concentration data provided by Arrow Energy.

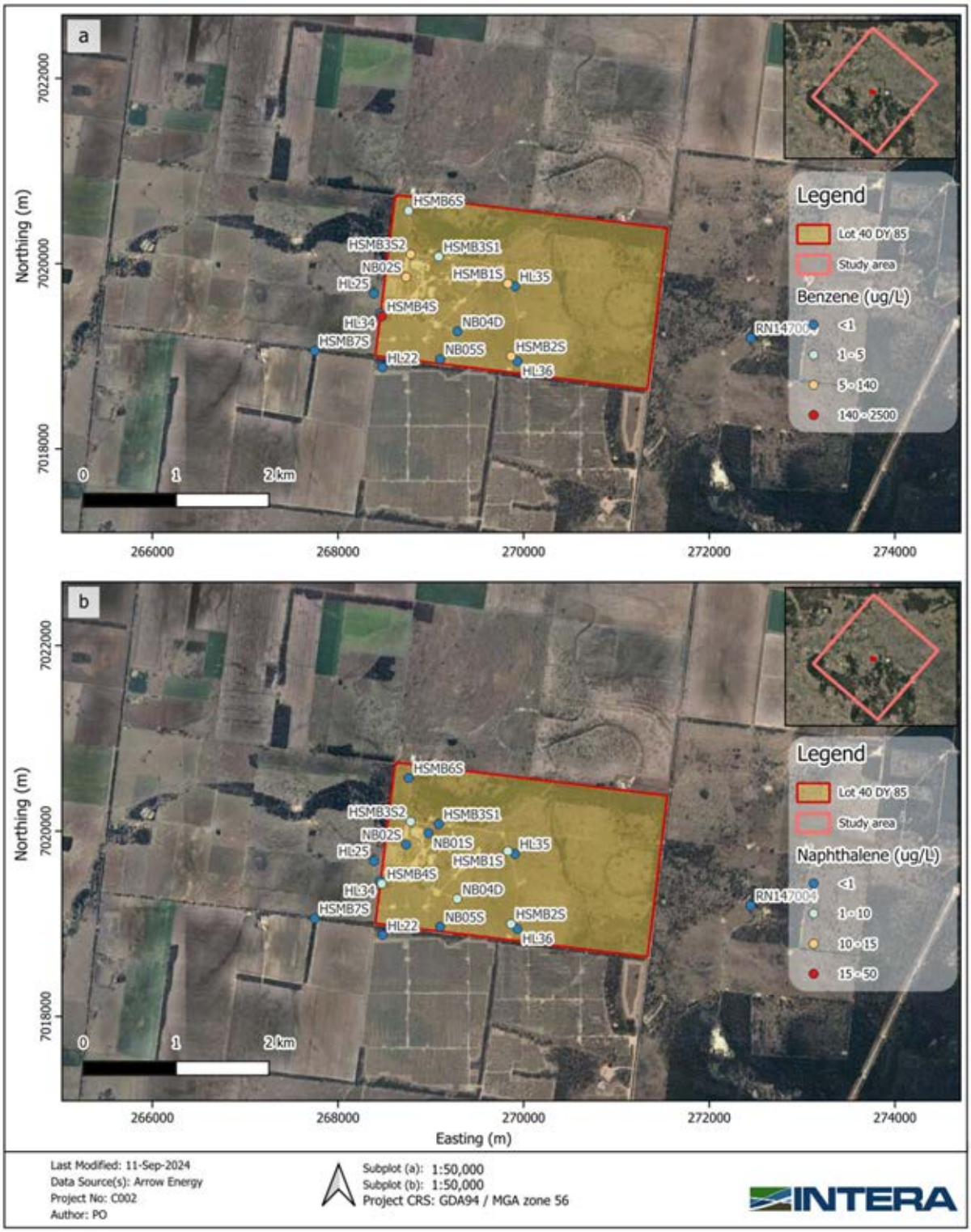


Figure 2-34 – Springbok Sandstone concentrations of (a) benzene and (b) naphthalene measured during 2021-2024. Concentration data provided by Arrow Energy.

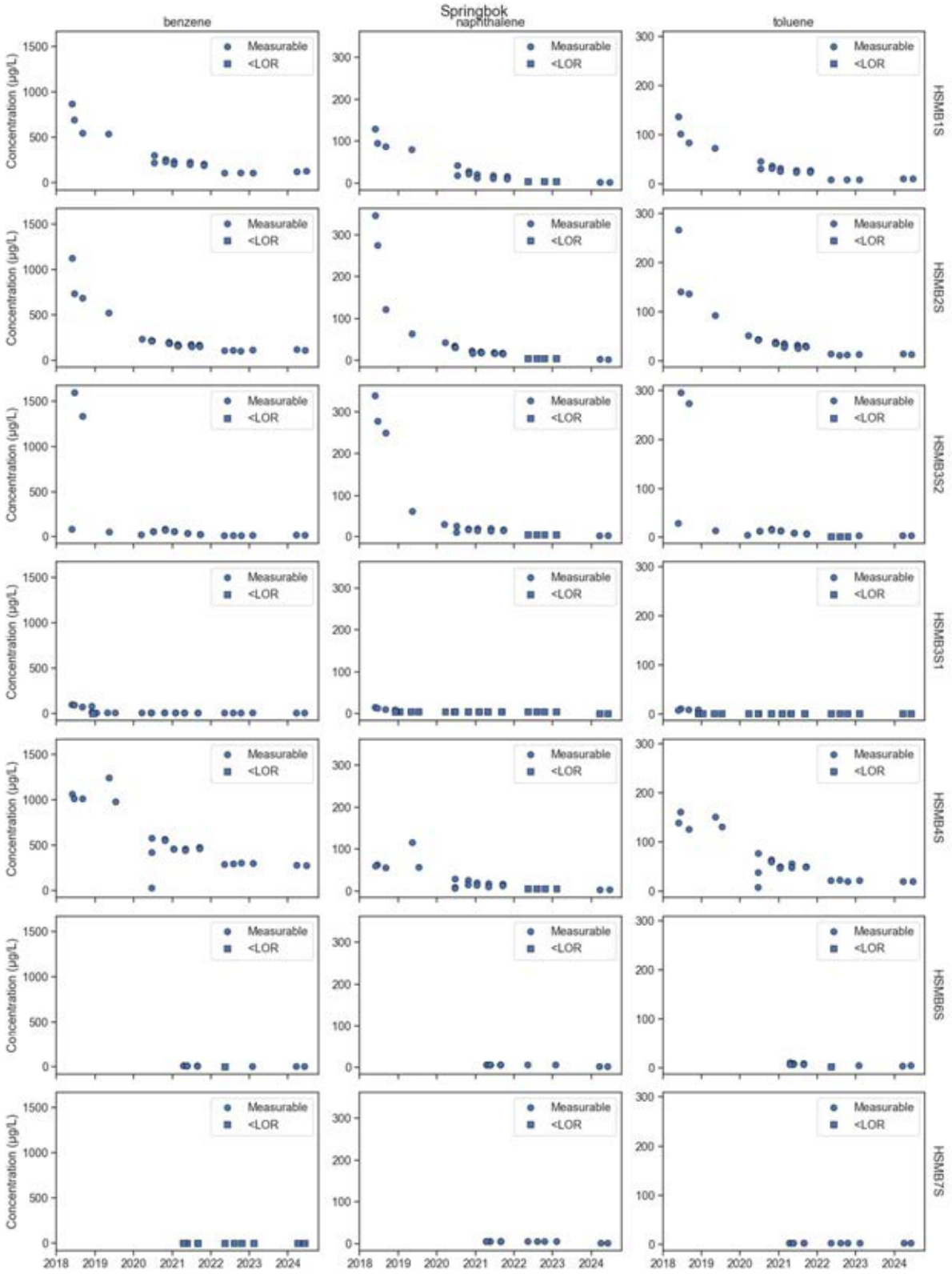


Figure 2-35 – Time series of selected bores for benzene, toluene and naphthalene in Springbok Sandstone. Concentration data provided by Arrow Energy.

## 2.6.2 Walloon Coal Measures (Macalister)

Groundwater chemistry within the Walloon Coal Measures is highly variable with up to 8 major groups identified (Raiber, 2013). Major ion chemistry is displayed as a piper plot in Figure 2-36 presenting all the samples collected from 2018 to 2023 for the bores monitoring the Walloon Coal Measures located in and around the Lot40 DY85. All groundwater samples were slightly basic pH and classified as sodium-potassium-chloride-bicarbonate type.

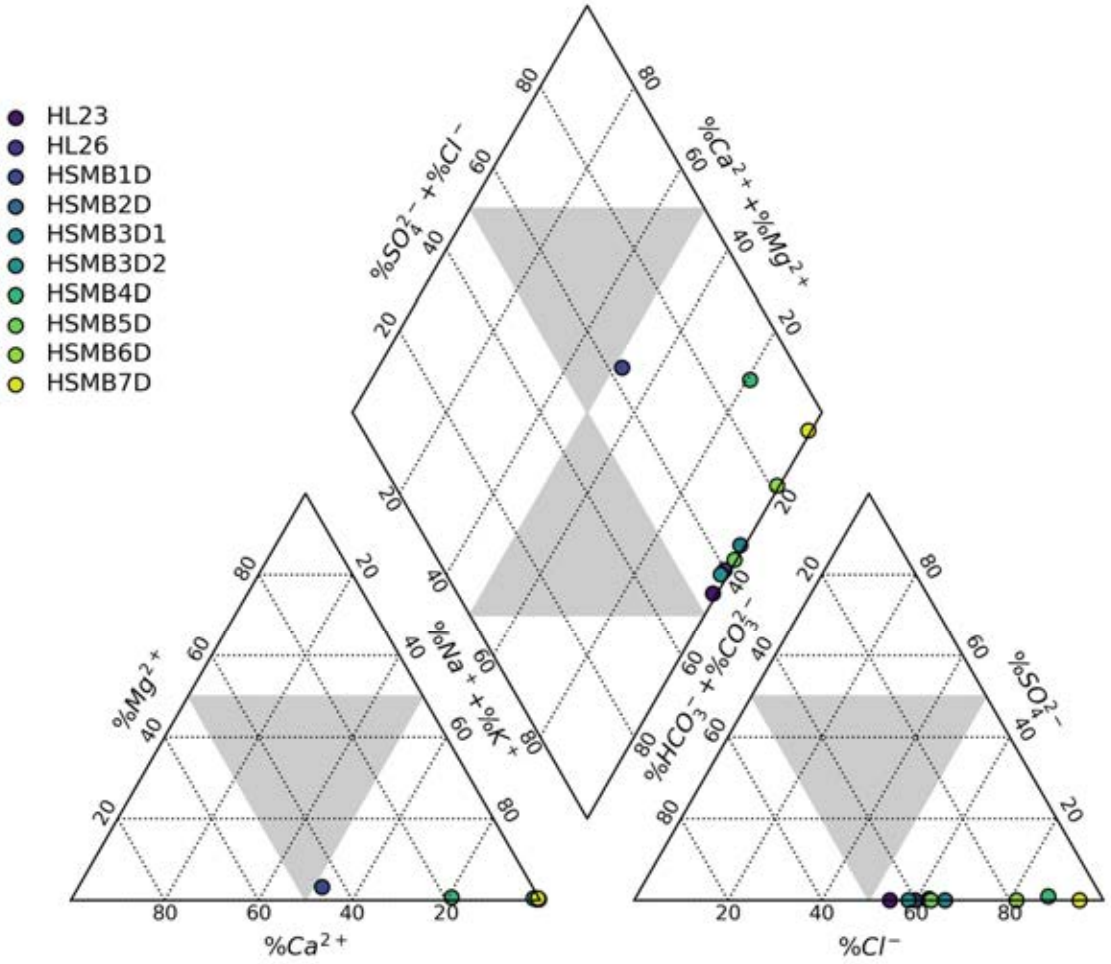


**Figure 2-36 – Piper diagram for Walloon Coal Measures groundwater samples (2021-2024) collected from within and around Lot40 DY85. Concentration data provided by Arrow Energy.**

Spatial distribution of benzene (selected as proxy for BTEX components) and naphthalene concentration in 2023 are shown in Figure 2-37. Latest available sampling data of BTEX and Naphthalene for each bore is presented in Table 2-5. Similar to the observed distribution for Springbok Sandstone, Walloon Coal Measures (Macalister) shows substantial concentration of BTEX and naphthalene mainly located inside the boundaries of Lot40 DY85 and near the gasifiers. M22 shows the highest concentration of BTEX and naphthalene. Compared to Springbok Sandstone, Walloon Coal Measures show lower concentrations of BTEX and naphthalene. Monitoring bores outside Lot40 DY85 show no evidence of measurable concentrations of BTEX or Naphthalene, suggesting the contamination is contained inside the area of Lot40 DY85.

Similar to the behaviour in Springbok Sandstone, time series graphs of selected bores for benzene and naphthalene (Figure 2-38) depict a breakthrough of contaminants in mid-2018 followed by a sharp decrease in concentration until 2020. From 2021, a slight increasing trend in the concentration of benzene is observed except for HSMB5D. From 2022 up to 2023, naphthalene and toluene show mostly values below the corresponding limit of reporting, while benzene being the only specie with measurable concentrations. This is further addressed during the numerical transport model in section 3.3.1.

Table 2-5 – Walloon Coal Measures (Macalister) groundwater quality data. Latest sample data available for each bore.

| Bore | Date | Benzene (ug/L) | Ethylbenzene (ug/L) | Naphthalene (ug/L) | Toluene (ug/L) | Total xylenes (ug/L) |
|---|---|---|---|---|---|---|
| G4MWA | 2021-10-11 | <1.0 | <2.0 | <5.0 | <2.0 | <2.0 |
| G4MWD | 2021-10-14 | <1.0 | <2.0 | <5.0 | <2.0 | <2.0 |
| G5M11I | 2017-02-08 | <1.0 | <2.0 | <5.0 | <2.0 | <2.0 |
| HL23 | 2024-06-10 | <1.0 | <2.0 | <1.0 | <2.0 | <2.0 |
| HL26 | 2024-06-09 | <1.0 | <2.0 | <1.0 | <2.0 | <2.0 |
| HSMB1D | 2024-06-14 | 1.0 | <2.0 | <1.0 | <2.0 | <2.0 |
| HSMB2D | 2024-06-26 | <1.0 | <2.0 | <1.0 | <2.0 | <2.0 |
| HSMB3D1 | 2024-06-07 | 5.0 | <2.0 | <1.0 | <2.0 | <2.0 |
| HSMB3D2 | 2024-06-11 | 2.0 | <2.0 | <1.0 | <2.0 | <2.0 |
| HSMB4D | 2024-06-26 | <1.0 | <2.0 | <1.0 | <2.0 | <2.0 |
| HSMB5D | 2024-04-03 | 9.0 | <2.0 | <1.0 | <2.0 | <2.0 |
| HSMB6D | 2024-06-06 | <1.0 | <2.0 | <1.0 | <2.0 | <2.0 |
| HSMB7D | 2024-06-07 | 8.0 | <2.0 | <1.0 | <2.0 | <2.0 |
| L22 | 2019-07-05 | <1.0 | <2.0 | <5.0 | <2.0 | <2.0 |
| M10 | 2018-09-13 | <1.0 | <2.0 | <5.0 | <2.0 | <2.0 |
| M10R | 2021-10-28 | <1.0 | <2.0 | <5.0 | <2.0 | <2.0 |
| M14R | 2021-10-16 | 65.0 | <2.0 | <5.0 | <2.0 | <2.0 |
| M15 | 2021-07-02 | <1.0 | <2.0 | <5.0 | <2.0 | <2.0 |
| M21 | 2018-09-11 | <1.0 | <2.0 | <5.0 | <2.0 | <2.0 |
| M22 | 2021-09-17 | 230.0 | 13.0 | 47.0 | <2.0 | 10.0 |
| M23 | 2018-09-11 | 26.0 | <2.0 | <5.0 | <2.0 | <2.0 |
| NB01D | 2024-03-27 | <1.0 | - | - | - | <2.0 |
| NB01D | 2024-06-25 | - | <2.0 | <1.0 | <2.0 | - |
| NB02D | 2024-06-13 | 18.0 | <2.0 | <1.0 | <2.0 | <2.0 |
| RN10790 | 2021-09-02 | <1.0 | <2.0 | <5.0 | <2.0 | <2.0 |
| RN147941 | 2018-09-05 | <1.0 | <2.0 | <5.0 | <2.0 | <2.0 |
| RN15868 | 2020-11-26 | <1.0 | <2.0 | <5.0 | <2.0 | <2.0 |
| RN160158 | 2024-06-12 | <1.0 | <2.0 | <1.0 | <2.0 | <2.0 |
| RN24466 | 2018-06-20 | <1.0 | <2.0 | <5.0 | <2.0 | <2.0 |
| RN87897 | 2016-10-07 | <1.0 | <2.0 | <5.0 | <2.0 | <2.0 |

*Concentration data provided by Arrow Energy.

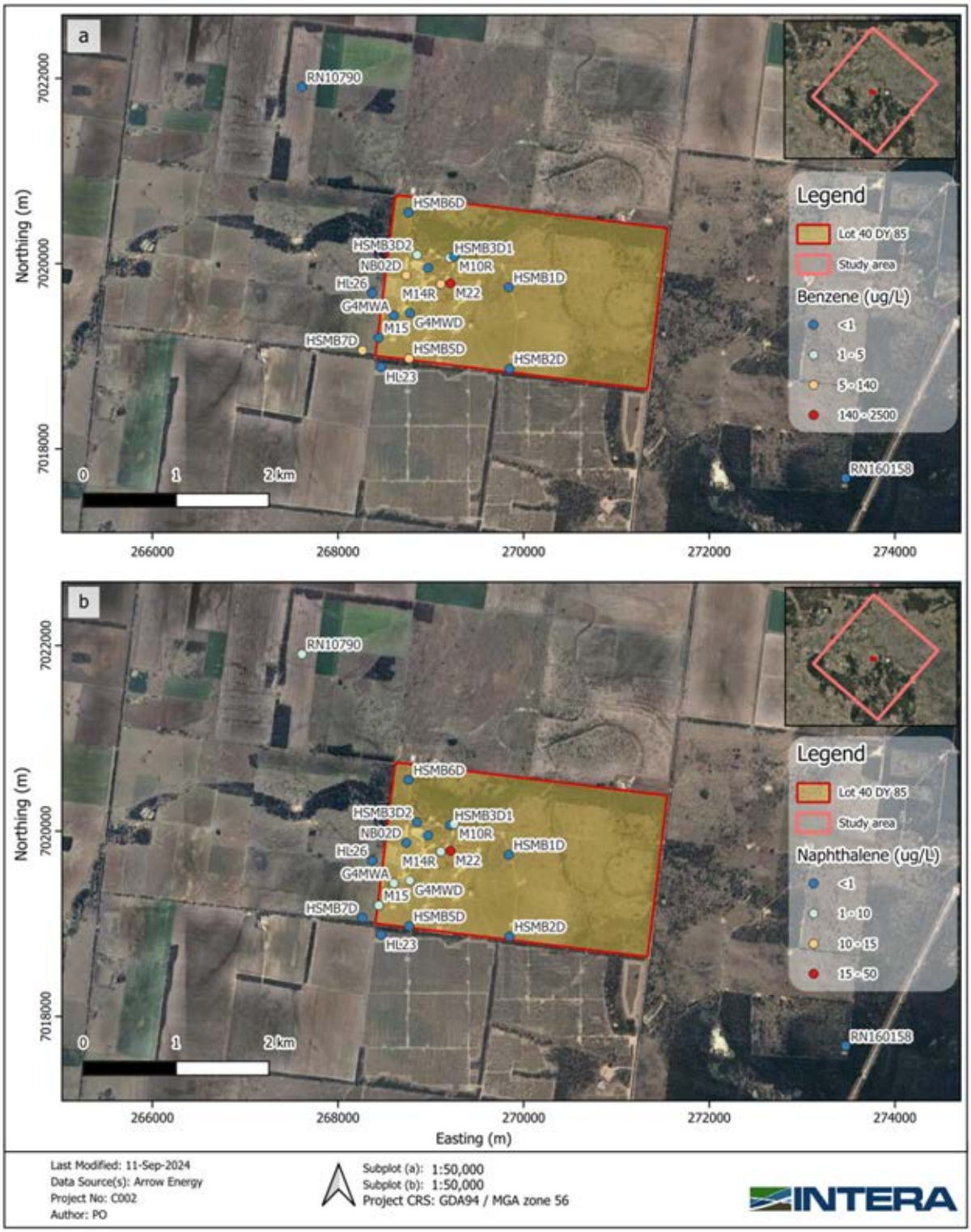


Figure 2-37 – Walloon Coal Measures (Macalister) concentrations of benzene and naphthalene measured during 2021 and 2024. Concentration data provided by Arrow Energy.

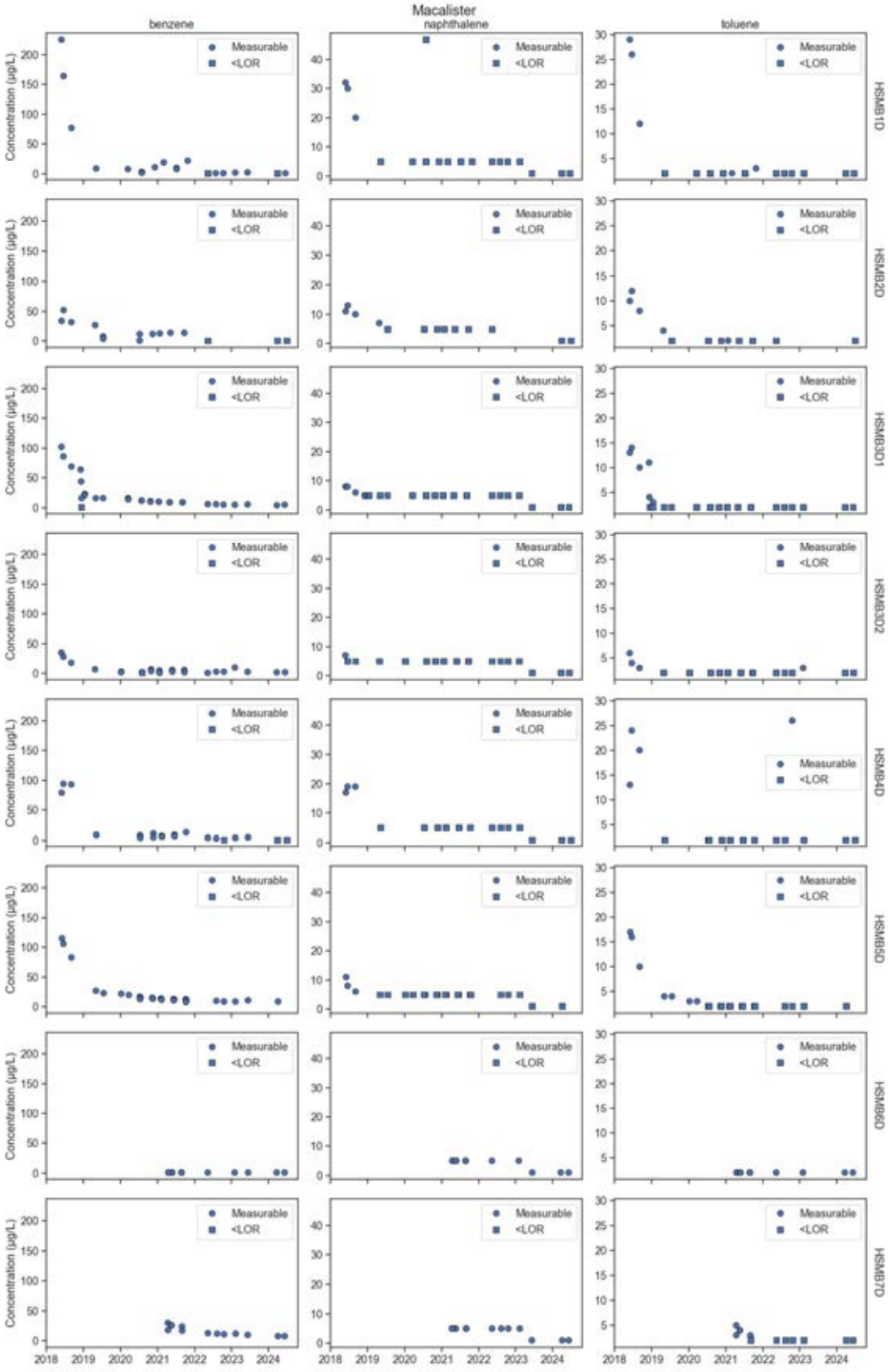


Figure 2-38 – Time series of selected bores for benzene, toluene and naphthalene in Walloon Coal Measures (Macalister). Concentration data provided by Arrow Energy.

### 2.6.2.1 Onsite and Offsite impacts

Elevated concentrations of potassium (mean of 2000 mg/L, with maximum above 7500 mg/L for HSMB4D) and benzene (mean of 68 µg/L) have been reported in groundwater samples from bores HSMB1D, HSMB2D, HSMB3D1 HSMB3D2 and HSMB4D in 2018 which are located within the Lot40. These two contaminants have exhibited a consistently decreasing trends from 2018 to 2023, as shown in Figure 2-39, with concentrations less than 150 mg/L and 15 µg/L for potassium and benzene in 2023, respectively. There is substantial uncertainty around the source of this contamination and whether it is related to UCG activities or residual drilling fluids. This is further addressed during the numerical transport model in section 3.3.1.

Offsite impacts are monitored at locations Hopeland-23, Hopeland-26 and HSMB7D. HSMB7D has reported no detectable naphthalene and decreasing concentrations of benzene with the latest result being 8 µg/L. In addition, Hopeland-23 and 26 have shown no indication of UCG contamination. Moreover, None of the Arrow Hopeland pilot test bores (Hopeland 17) showed an indication of UCG contamination (Arrow, 2020).

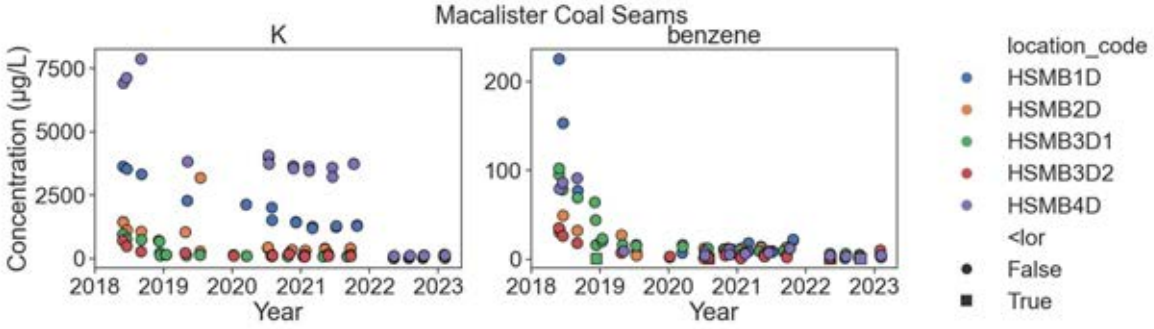


**Figure 2-39 – Comparison of time series for potassium and benzene in boreholes that exhibited elevated levels of both K and Benzene in 2018, followed by subsequent decrease in concentrations. Concentration data provided by Arrow Energy.**

## 2.7 CSG Development Plan

The proposed development plan by Arrow has changed from the plan documented in the 2020 Conceptual model technical note (Arrow, 2020). The updated development plan has been designed to minimise potential impacts to the groundwater environment in the Macalister coal seam and Springbok Sandstone at the former UCG site. The Field Development Plan (FDP) includes a total of 339, from which 55 wells are still to be approved and are expected to be in production between 2027 and 2037. These wells have a summarised peak abstraction rate of about 11 ML/d, as stated in the Field Development Plan provided by Arrow Energy. In addition to the 339 CSG wells, Arrow will abstract water from six wells in the Hopeland Pilot Test site.

The proposed development plan is expected to have a low impact in these units given that:

- The proposed development plan does not consider the production from the Macalister seam over most of the PL253, with the nearest production well in the Macalister seam units located at 2.5-3 km to the south and east from Lot 40. The production will be mainly in Wambo, Argyle and Kogan (Figure 2-40). From the 339 wells, 55 are still subjected to approval by the EA. Those 55 wells will target mainly Wambo (42), and only 11 wells will target Macalister.

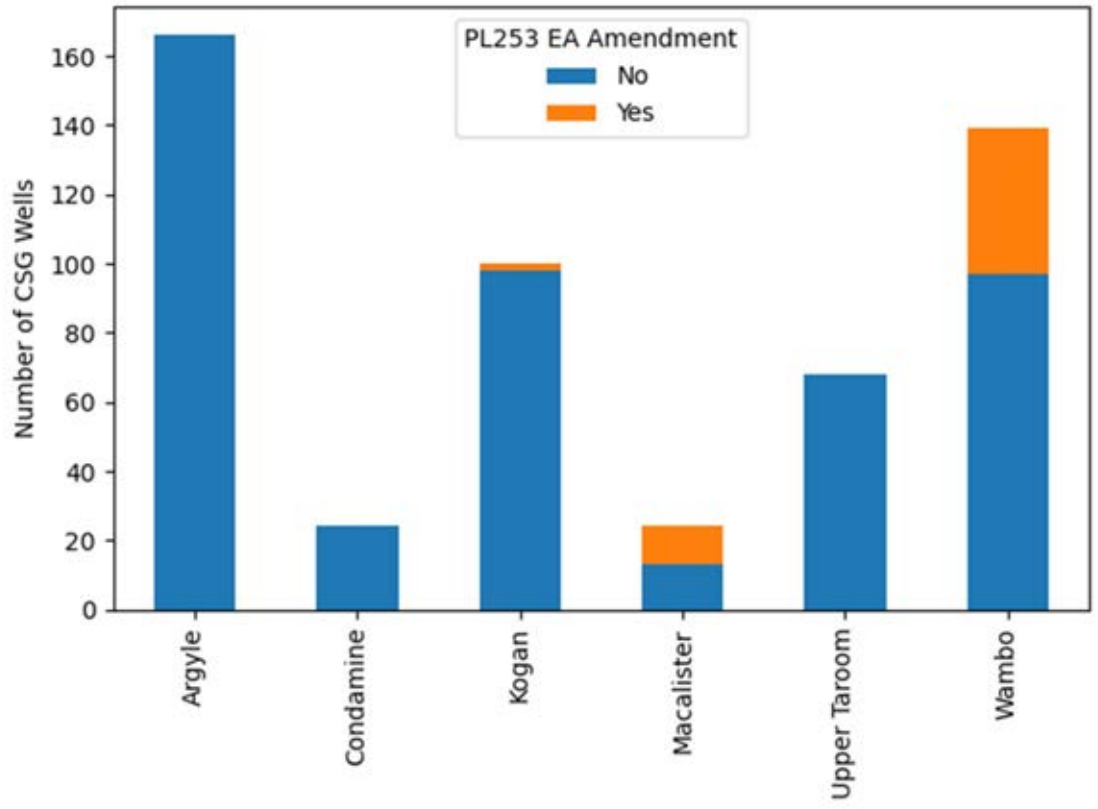


Figure 2-40 – Bar plot of CSG wells' targets. Orange colours display the 55 wells pending approval from the current work.

- The proposed production areas will be phased. Initial production has been estimated to start in 2025 and includes wells on the far south-eastern corner of PL253 and wells along the south-west boundary adjacent to QCC tenure already in production. The wells in the SE corner are about 10 km from the site, whilst wells on the western boundary are in areas significantly depressurised by adjacent production and hence cause less incremental pressure drawdown then other areas of the tenure. In 2026, wells in the SE corner of the tenure will be in production, the closest well is approximately 3 km from the site.
- In terms of flow rates, wells online by 2025 will promote a total abstraction rate of 1.5 ML/d (Figure 2-42). In 2029, 62 wells along the southeast border will be in place with a planned total abstraction rate of 12 ML/d (Figure 2-43). In the following years (2030-2035), active wells will be spread over the tenure and closer to the site. Maximum abstraction rates will vary between 0-4 ML/d (Figure 2-43 and Figure 2-44). During the last active years (2043-2047), between 7 to 24 wells will be active along the north-eastern boundary, with a maximum abstraction rate of 5 ML/d (Figure 2-45 and Figure 2-46).
- On top of the wells in the FDP plan, six Hopeland site wells are expected to start abstracting water from 15-10-2027 at a rate that would keep the groundwater level in the wells 30 m above the position of bottom of the screens.
- It is important to note that information of non-Arrow CSG wells is limited and will have to be extracted from the OGIA groundwater model (2021).

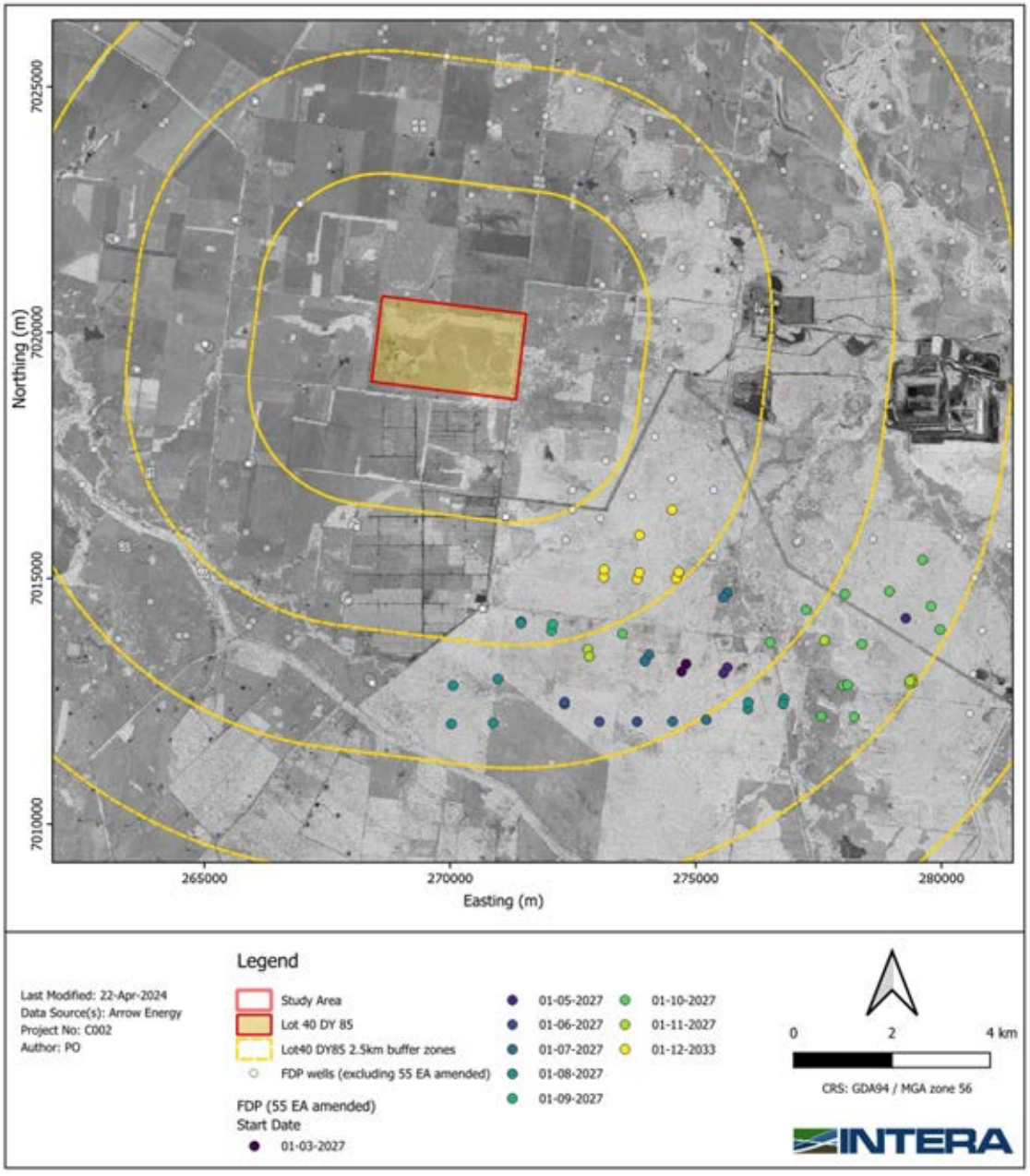


Figure 2-41 – Proposed production wells (Data Source: Arrow Energy's FDP).

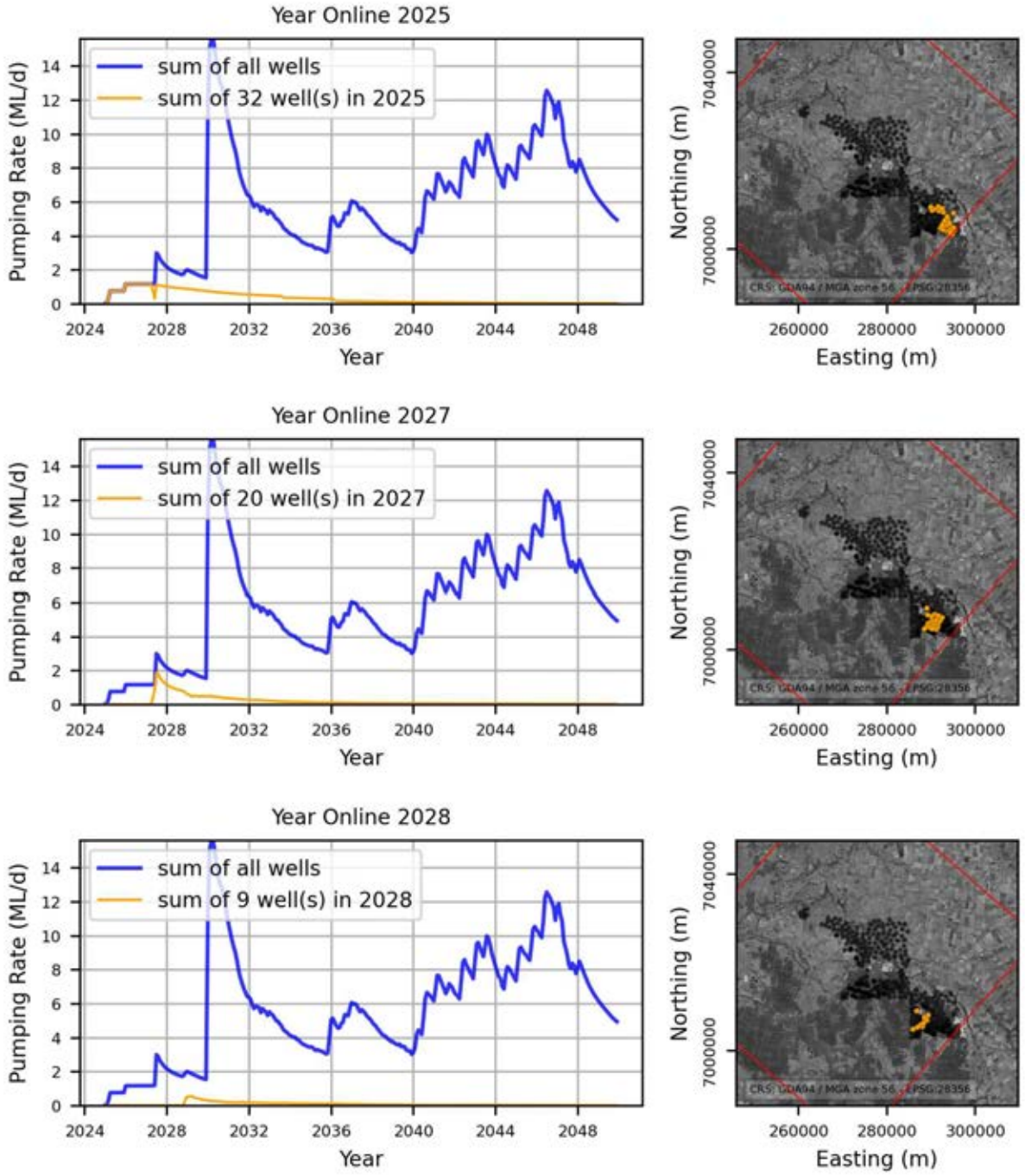


Figure 2-42 – Pumping rates (in ML/d) summarised for all wells started in years 2025, 2027, and 2028 (orange), sum of all pumping rates (blue) and map showing well(s) location. Data Source: Arrow Energy.

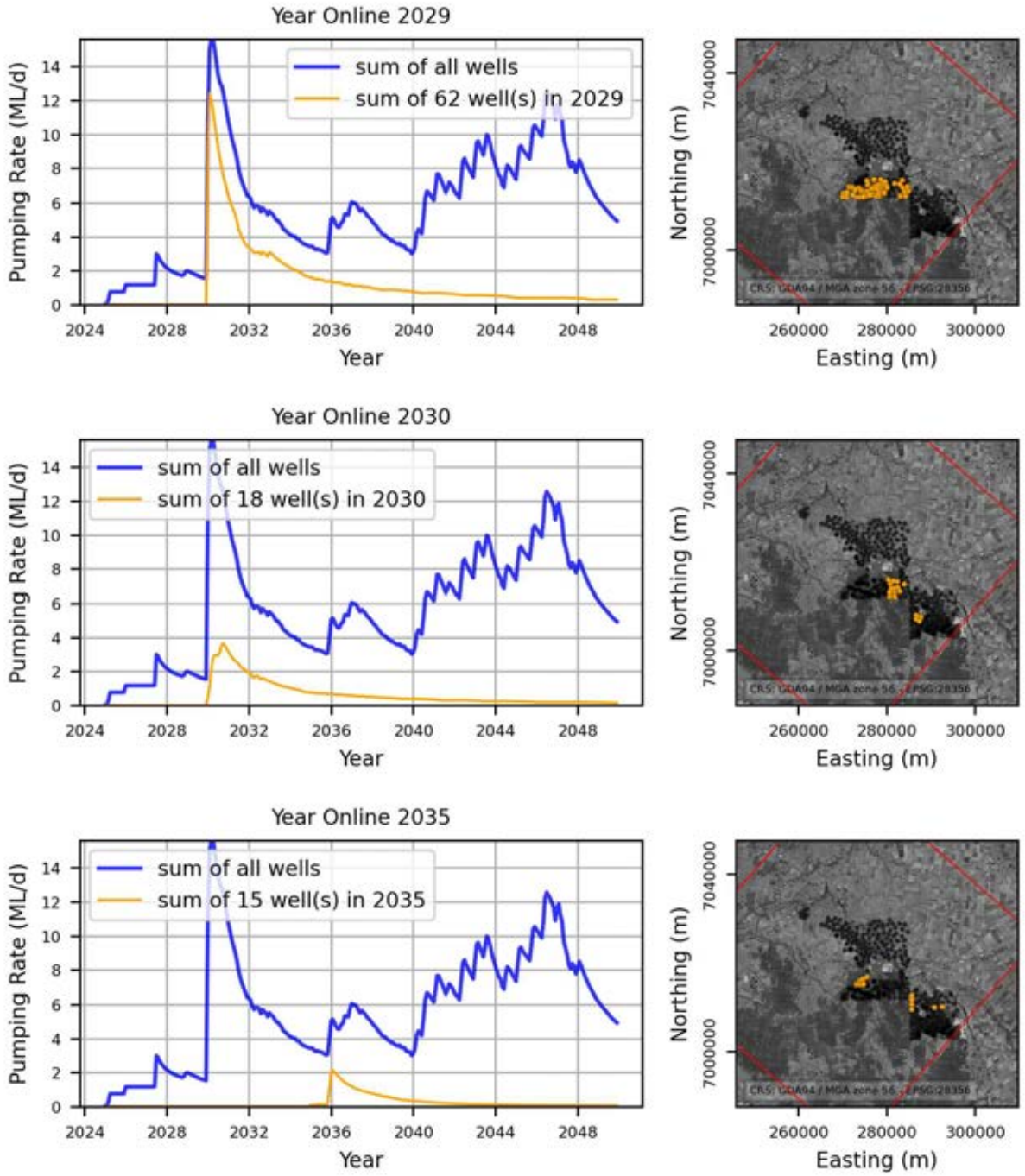


Figure 2-43 – Pumping rates (in ML/d) summarised for all wells starting in years 2029, 2030, and 2035 (orange), sum of all pumping rates (blue) and map showing well(s) location. Data Source: Arrow Energy.

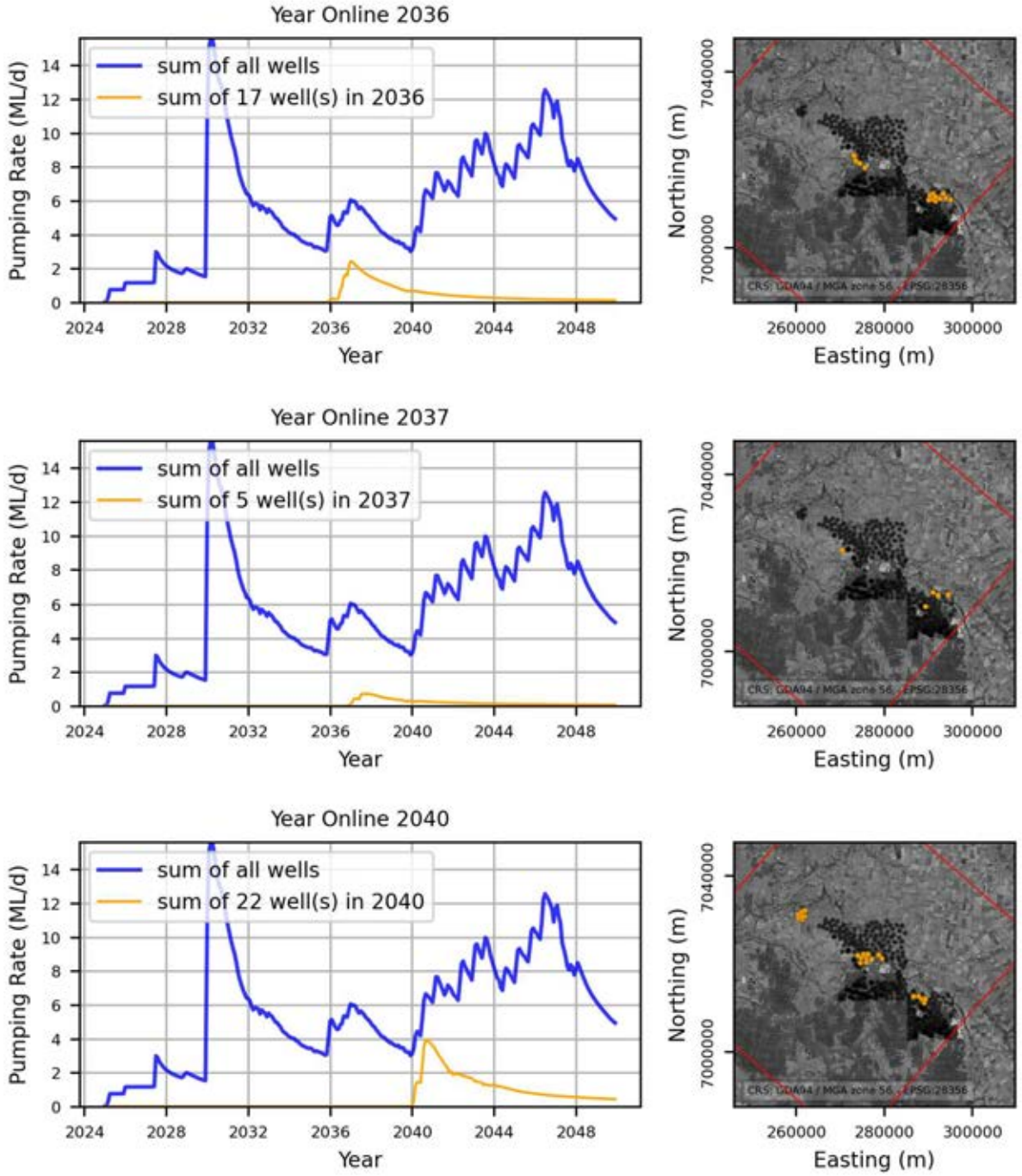


Figure 2-44 – Pumping rates (in ML/d) summarised for all wells starting in year 2036, 2037 and 2040 (orange), sum of all pumping rates (blue) and map showing well(s) location. Data Source: Arrow Energy.

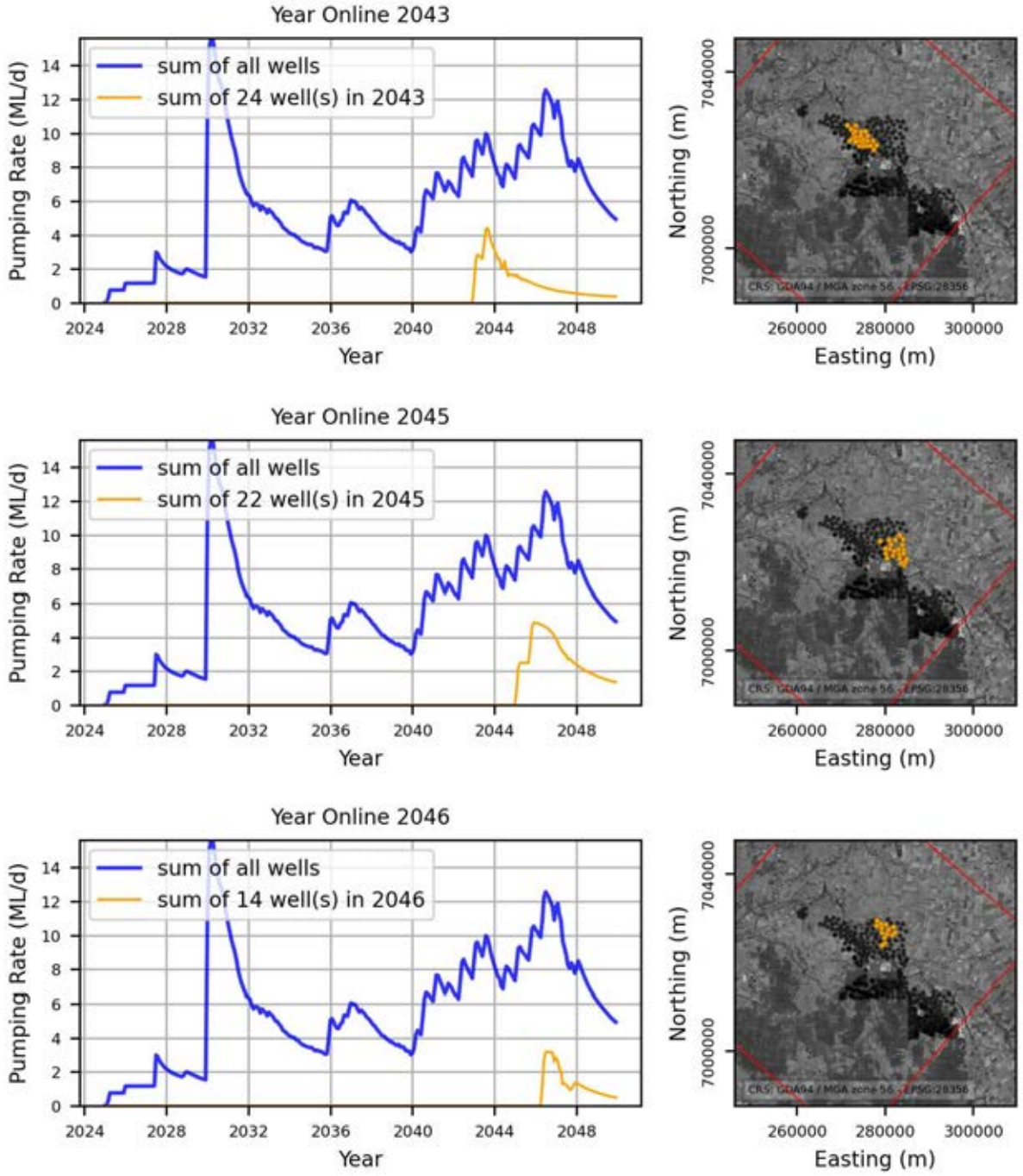


Figure 2-45 – Pumping rates (in ML/d) summarised for all wells starting in year 2043, 2045, and 2047 (orange), sum of all pumping rates (blue) and map showing well(s) location. Data source: Arrow Energy.

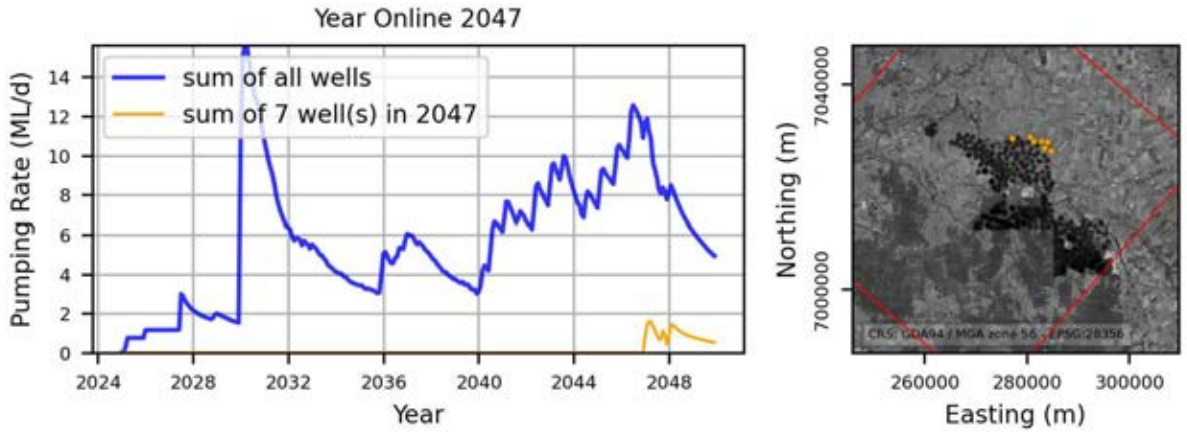


Figure 2-46 – Pumping rates (in ML/d) summarised for all wells starting in year 2037 (orange), sum of all pumping rates (blue) and map showing well(s) location. Data source: Arrow Energy.

## 2.8 Source-Receptor Pathway Assessment

The analysis and review of current hydrogeological information and conceptual site model allowed the assessment of potential source-receptor pathways with focus in the numerical model, summarised in Table 2-6. Potential contamination sources in Lot40 DY85 may have been derived from UCG activities within the Macalister coal seam. Contaminants may be located within the seam, or in adjacent strata. Groundwater contamination may migrate off site through (1) primary mobilisation with groundwater flow through porous media, (2) flow through secondary permeability created as a result of activities in Lot40 DY85. Preferential pathways (fractures) may exist, however bore records at the site do not show evidence of fractures (Arrow, 2021; GHD, 2019). It is possible that vertical fracturing occurred at the gasifiers, however there is no evidence of widespread lateral fracturing (Arrow, 2021; GHD, 2019).

Previous modelling works (AGE, 2023) suggest that depressurisation promoted by CSG extraction will retain groundwater movement within the site (Arrow, 2020). The nearest potential receptors are located to the west of the site, where four bores are positioned along the pathway to monitor and capture any groundwater impacts, should groundwater begin migrating toward the CSG production wells. Nevertheless, estimated groundwater travel times to these bores are expected to be sufficiently slow considering management measures proposed by Arrow to be implemented. Figure 2-47 displays groundwater bores registered in the Queensland Groundwater Bore database, queried on 09/09/2023. Figure 2-48 displays a closer look at identified water supply bores in the vicinity of the site. Bores are classified by type. The majority of registered bores are classified as monitoring (of various types). Given the lack of additional information, bores labelled as 'water supply' are a priori assumed to be intended for consumptive use. Therefore, without further information about this bore, it is also assumed that all bores have the potential to be affected in a conservative approach.

A single potential supply bore was identified within the area of Lot40 DY85. A second bore was identified to the East, within 2.5 km of the lot boundary. Despite the proximity, post-development gradients are expected to be in the opposite direction. The majority of identified supply bores are beyond 2.5 km from the site border (2.5km was the maximum travel distance by 2060 identified for an ensemble of model simulations reported in AGE,2023). Bores located to the southwest are expected to have a higher probability to be affected under long-term (>200 yr) post-development conditions.

Table 2-6 – Summary of Source-Pathway-Receptor analysis.

| | Description | Comments |
|---|---|---|
| Source | Dissolved hydrocarbons within the Springbok Sandstone | Measurable concentrations of BTEX and Naphthalene have been found. The extent of contamination plume is likely restricted given that various adjacent monitoring wells show very little or non-detectable values. Analysis of the historical concentrations show some reduction in BTEX, suggesting either migration of the contaminants and/or natural attenuation. |
| | Dissolved hydrocarbons in the Macalister Seam | BTEX concentrations within the Macalister Seam have been detected at the boundary of Lot40. Off-site monitoring bores (HSMB7D) have reported no detectable naphthalene and decreasing concentrations of benzene that correlates with potassium trends. |
| | Dissolved hydrocarbons in the gasifiers installed in the Macalister Seam | BTEX concentrations within the Macalister Seam in monitoring bores next to gasifiers have been detected. |
| Pathways | Horizontal migration towards downstream groundwater boreholes | Groundwater flow and dissolved hydrocarbons will possibly migrate towards downgradient areas. The migration is likely limited in the Walloon Coal Measures given the high degree of depressurisation occurring in the site. Previous studies (AGE, 2023) indicate a maximum groundwater travel distance of 2.5 km from Lot40 by 2060, although degradation of BTEX and Naphthalene compounds are likely to reduce this travel distance substantially. |
| | Vertical migration through units over and underlying the Macalister Seam and Springbok Sandstone | Based on the current vertical gradients, dissolved hydrocarbons within Macalister Seam and Springbok Sandstone are unlikely to migrate vertically, as both over- and underlying units present higher hydraulic head values. Vertical migration will be unlikely beyond the base of Walloon Coal Measures as the heads in the Condamine Coal are considerably higher. |
| Receptors | Downgradient groundwater users | The majority of water supply boreholes are positioned beyond 2.5 km from the Lot40 area. These boreholes are unlikely to be affected by contamination as most BTEX plumes tend to be shorter than 61 m length (Newell and Connor, 1998). |
| | CSG field site workers and treatment | Potential movement of contaminants and following extraction of water from CSG activities could result in direct contact of contaminated water with site workers. |
| | Workers operating monitoring bores on or adjacent to Lot 40 DY85 | Hierarchy of controls are implemented in design of monitoring bores, workers on site are educated on risks, trained in standard operating procedures to minimise exposure to contaminants. |

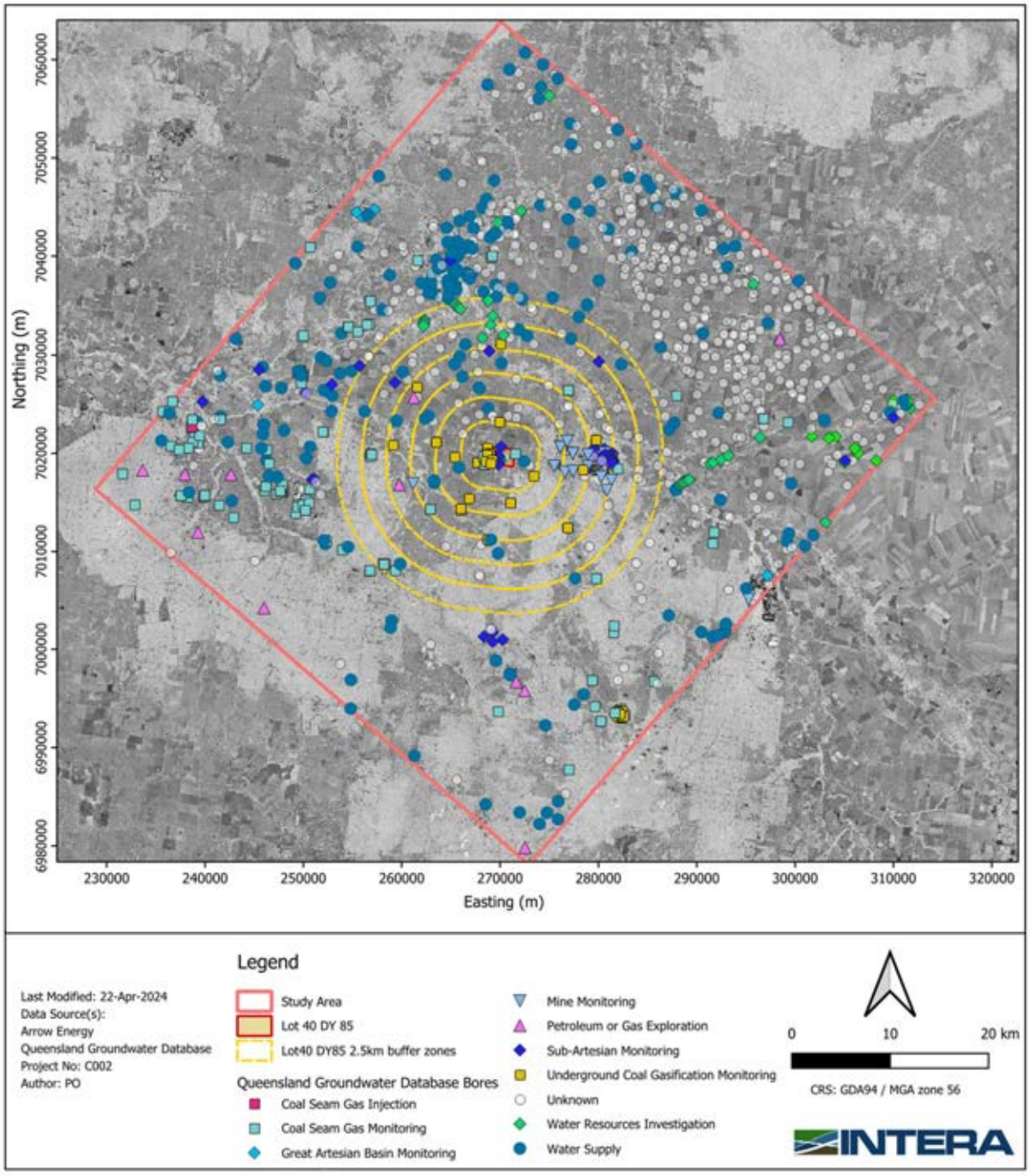


Figure 2-47 – Groundwater boreholes identified in the Queensland Groundwater Bore database.

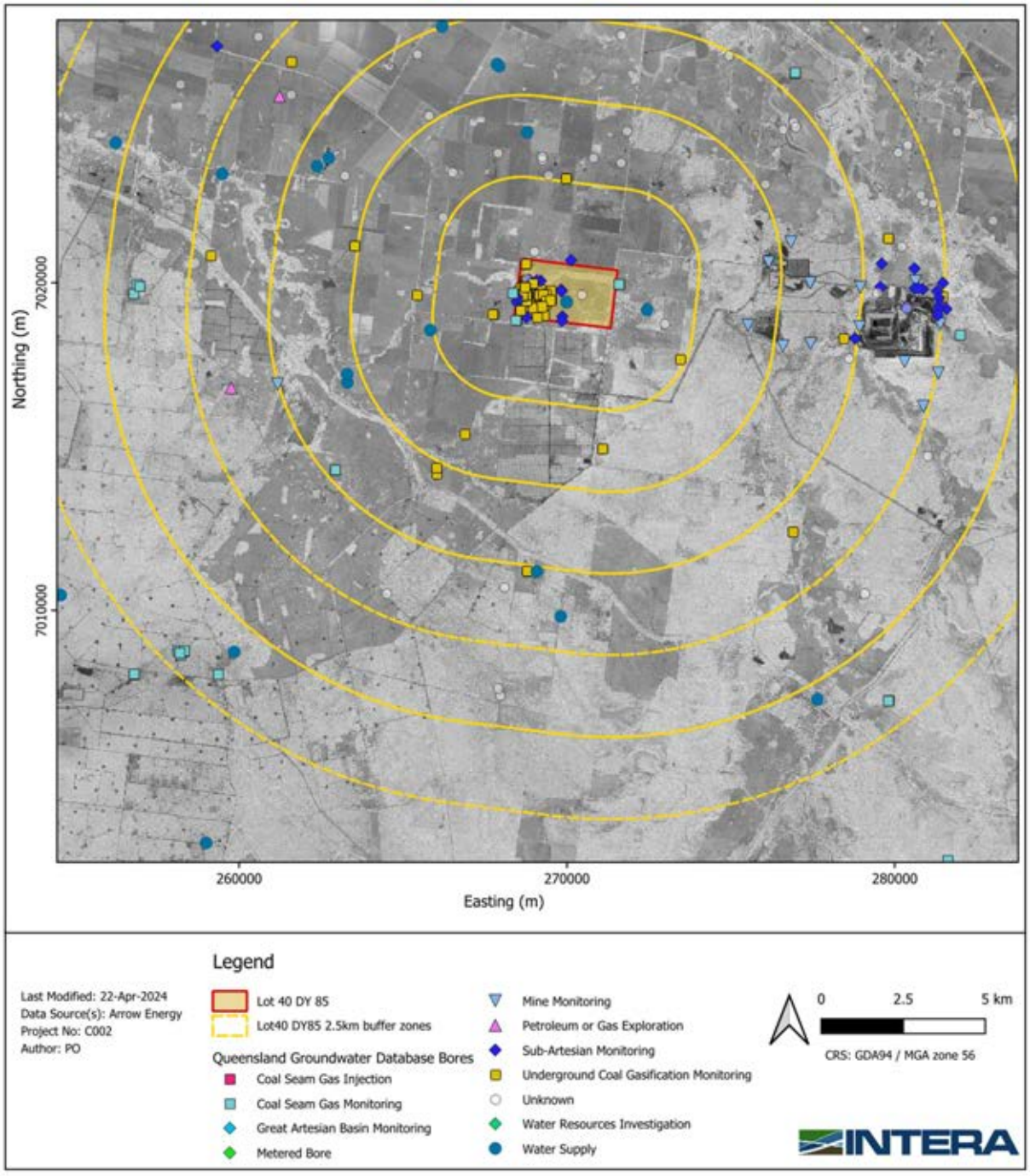


Figure 2-48 – Zoom-in of groundwater boreholes identified in the Queensland Groundwater Bore database.

## 2.9 Fracturing

Research undertaken by CSIRO (2004) indicated the potential for UCG-related fracturing at the site associated with two distinct mechanisms. The first mechanism consists of the creation of underground voids due to combustion of coal, leading to collapse, while the second mechanisms is associated with injection pressures with potential to promote fracturing and connect the injection well to production well.

Satellite interferometry data shown in Figure 2-49 was compiled by Arrow (2020) to assess ground movement across the site between 2012 and 2017. These data suggest minimal downward ground

movement and, in most areas, upwards movement. Furthermore, no substantial movement suggesting subsidence related to the collapse of gasifiers' roof is apparent.

Nevertheless, as previously mentioned, there is the potential for fracturing to have been induced during the start-up and operation of the gasifiers. Although, in general, hydraulic gradients have not substantially changed over time, it's important to consider the possibility of increased lateral or vertical changes in permeability. A conclusive statement cannot be made relying solely on hydraulic gradients and the available information.

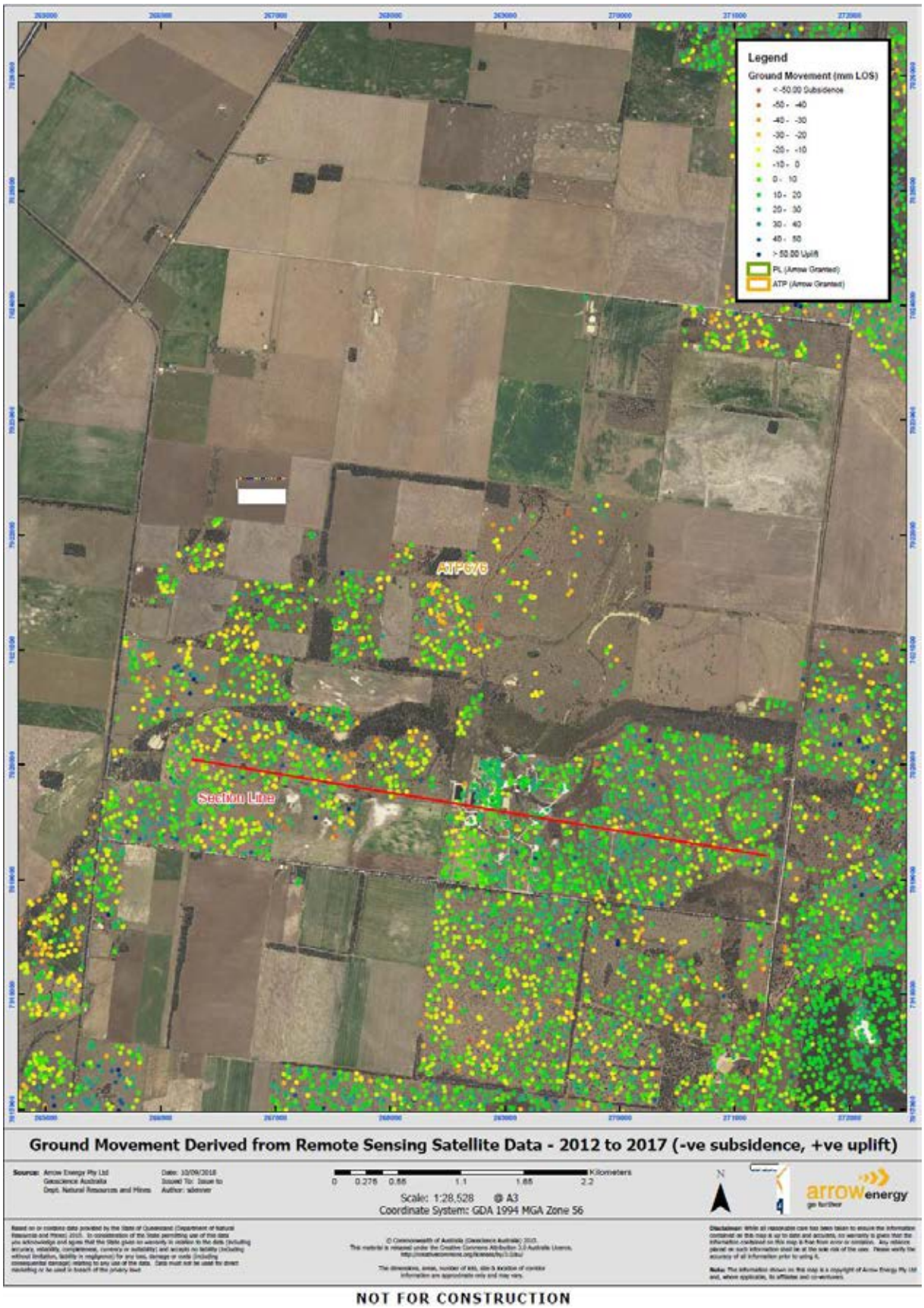


Figure 2-49 – Ground movement between 2012 and 2017 derived from remote sensing data (Arrow, 2020).

## 2.10 Summary of the site conceptual model

The following schematic Figure 2-50 summarises the key aspects of the SCM that are relevant to the numerical single-phase flow and transport model. These key elements are:

- Groundwater levels
  - A local depression of groundwater levels has been proposed to have occurred because of the UCG trials (AECOM, 2018).
  - Groundwater level trends show a recovery from these events.
- Source of contaminants
  - A source was assumed to be present in the gasifiers (Macalister). This source is uncertain respect to the actual concentration and the rate of depletion.
  - No source was assumed in Springbok. However, a source has been proposed to exist in this layer from gases that escaped from the UCG trials and condensed in Springbok (AECOM, 2018). We have opted to not simulated this in the numerical model due to the high uncertainty and potential bias that this could add to the predictions.
- Recharge: Spatially variable recharge in the upward layers would vary between 0.2 to 1 mm/year.
- Hydraulic parameters: Conceptualisation and parameter ranges is coming from the OGIA (2021) model (regional parameters) and AGE (2023).
- Transport parameters: Physical transport parameters will present high uncertainty.
- CSG extraction
  - Arrow CSG extraction is expected to occur approximately at least 2.5 km from the Lot40 and mainly in Wambo, Argyle and Kogan.
  - Non-Arrow CSG extraction has to be extracted from OGIA model (2021). Uncertainty around the rates has to be included in the model.

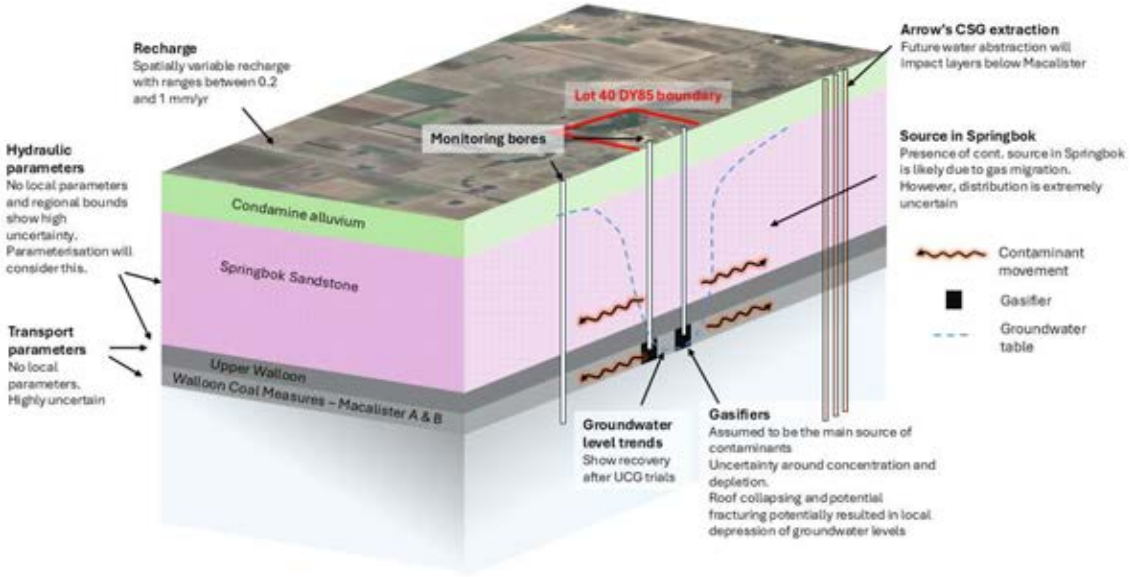


Figure 2-50 – Summary of the conceptual model and the key elements relevant to the numerical model (adapted from EPIC, 2020).

# 3.0 Groundwater Flow Model

The following section presents the groundwater model. This model follows the EA Condition Water (4) that states that the model should target aquifers on and in the vicinity of Lot 40 on DY85 including the Springbok Sandstone and the Macalister coal seam (and its relevant aquifers) of the Walloon Coal Measures. This model will measure and predict changes in contaminant movement, groundwater flow direction and drawdown. The model will:

1) Be calibrated annually (at a minimum) and updated with the data collected as part of the GMP required under condition Water 2(4) and the site conceptualisation model under condition Water 3 to inform the Annual Report under condition Water 9.
2) Include a simulation period to at least the year 2200 that extends to beyond when groundwater levels are expected to have recovered in 2040, and contaminant transport off-site becomes possible.

## 3.1 Model Description

The most recent generation of modelling of the site was undertaken by AGE (2023) (henceforth referred to as the AGE model). The groundwater flow model reported herein represents continued development of the AGE model, with additional updates to model structure and boundary conditions.

The model structure was developed based on AGE (2023) and updated to align model layer elevations with corresponding geological layers identified in borehole logs. Boundary condition values were updated to reflect the most current version of regional scale cumulative impact modelling undertaken by OGIA.

The simulated period was divided into history matching and predictions. Therefore, the history matching and predictive modelling is presented in two consecutive sections after the model description is presented.

### 3.1.1 Conversion from MFUSG to MF6

The AGE model was converted from MODFLOW-USG (MFUSG) to MODFLOW 6 (MF6) (Hughes et al., 2017). MF6 provides options for unstructured grids as well as greater flexibility in terms of model input/output file structure. These facilitate pre- and post-processing during history matching and uncertainty analysis.

MF6 is also the current flagship software for groundwater modelling at the United States Geological Survey, undergoing continuous development as well as being strongly supported by the FloPy (Bakker et al, 2022) Python library, enabling a fully scripted workflow for model construction and deployment, thereby enhancing the reproducibility of the modelling workflow. Lastly, the modular characteristic of MF6 facilitate the addition of groundwater solute transport and particle tracking models as plugins that can be "turned on and off" as required.

### 3.1.2 Model Layers

Following the AGE model discretisation, each hydrogeological unit of interest was assigned to a unique model layer. The spatial extent of each hydrogeological unit was assigned by intercepting

active cells in the AGE model with cells in the MF6 model, accounting for the relative intersected area. Remaining cells in each layer of the MF6 model were assigned as inactive flow-through cells.

Table 3-1 presents model layers and the corresponding hydrogeological unit, and the equivalent OGIA model layers and hydrostratigraphic units which coincide with the PL253 model domain. Figure 3-1 displays a three-dimensional view of the grid.

Layer bottom and top elevations were interpolated from AGE model cells to the corresponding MF6 model cells to maintain the same geometry. However, the elevations of layer contacts (i.e., layers bottom elevation) extracted from the AGE model, did not align with the contact elevations obtained from bore logs in the vicinity of Lot40. To resolve this, the bottom elevation of layers 2 to 6 were re-interpolated from bore log data provided by Arrow.

For the interpolation, layer bottom elevations in the AGE model were sampled over the entire domain, excluding Lot40 and its surrounding area within a 4 km radius. These were merged with elevations recorded in bore log data within Lot40. Interpolated values with this merged dataset were assigned to bottom elevations in the MF6 model. Bottom elevations of the layers not recorded in the bore logs (i.e., 7 to 18) were shifted downwards to retain the same thicknesses employed in the AGE model.

Table 3-1 – Model layers and corresponding hydrogeological unit from OGIA (2021).

| Hydrostratigraphic units | Model layer | OGIA (2021) model layer | OGIA (2021) hydrostratigraphic units |
|---|---|---|---|
| Condamine Alluvium/ Gubberamunda Sandstone | 1 | 7 | Gubberamunda Sandstone |
| Westbourne | 2 | 8 | Westbourne Formation |
| Springbok | 3 | 9, 10 | Upper and Lower Springbok |
| WCM Kogan | 4 | 12 | Upper Juandah Coal |
| WCM Kogan Interburden | 5 | - | - |
| WCM Macalister | 6 | 13 | Upper Juandah Coal |
| WCM Macalister Interburden | 7 | - | - |
| WCM Wambo | 8 | 14 | Lower Juandah Coal |
| WCM Wambo Interburden | 9 | - | - |
| WCM Argyle | 10 | 15 | Lower Juandah Coal |
| WCM Argyle Interburden | 11 | - | - |
| WCM Tangalooma | 12 | 16 | Lower Juandah Coal |
| WCM Upper Taroom | 13 | 17 | Taroom Coal |
| WCM Upper Taroom Interburden | 14 | - | - |
| WCM Condamine | 15 | - | - |
| WCM Condamine Interburden | 16 | - | - |
| Eurombah Fm | 17 | - | - |
| Hutton | 18 | 19, 20 | Upper and Lower Hutton Sandstone |

*WCM: Walloon Coal Measures

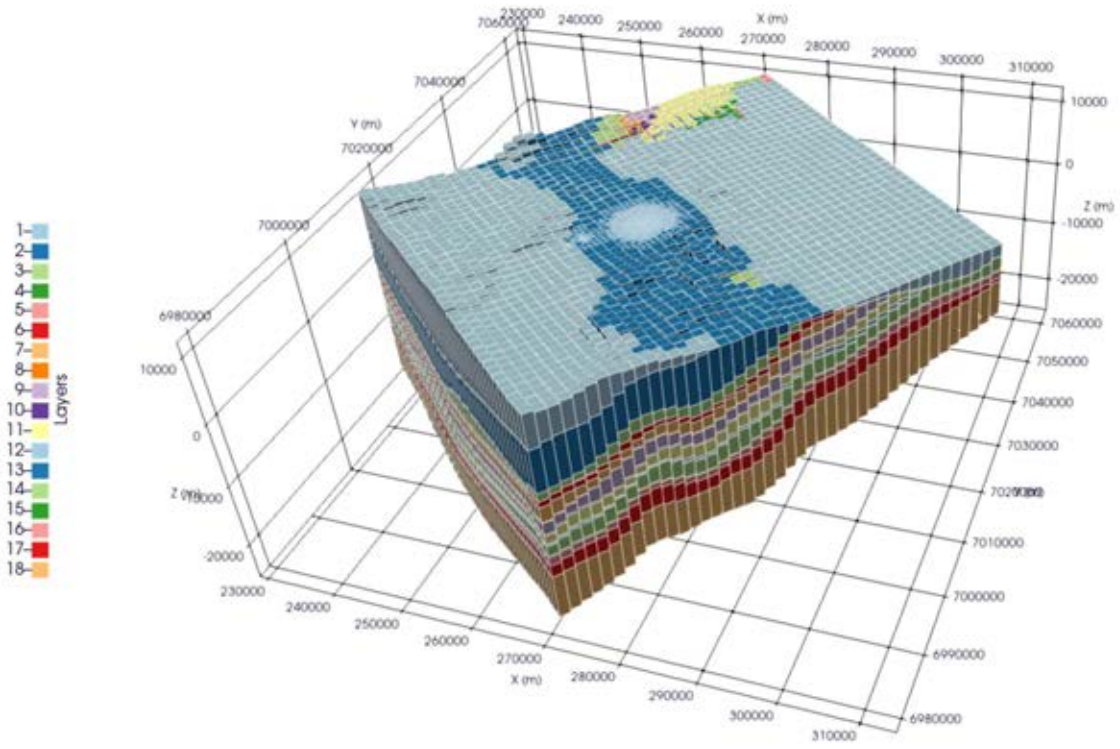


Figure 3-1 – Three-dimensional view of the model grid; colours denote active cells in respective layers and hydrogeological units. Vertical exaggeration x 30.

### 3.1.3 Model Grid

The model setup employed a quadtree unstructured grid enabling local refinement in areas of interest, such as the Lot40 DY 85 (referred as Lot40) and the Hopeland pilot-test site. It was opted to switch from a Voronoi mesh to a quadtree grid, as this facilitates a fully scripted workflow and removes the reliance on proprietary software. The quadtree grid was generated using the open-source software GRIDGEN (Lien et al, 2017).

A base coarse cell size of 1500 by 1500 m was assigned following the Underground Water Impact Report (UWIR) model (henceforth referred to as the OGIA model) discretisation (OGIA, 2021). Localised refinement was added in the area surrounding Lot40, using buffers of 1, 2.5 and 4 km radius, resulting in cell lengths of 23, 95 and 185 m respectively. Further refinement was added around the gasifiers and Hopeland site. Cells in gasifier-affected areas were refined to 12 by 12 m. Cells within a 1 km radius of the Hopeland site were refined to 23 by 23 m, resulting in a total of 12,225 cells per layer.

A plan view of the model grid and refinement near the gasifiers is presented in Figure 3-2. Layer discretisation was maintained according to the AGE model, resulting in a total of 18 layers and an overall count of 220,050 cells of which 197,236 are active.

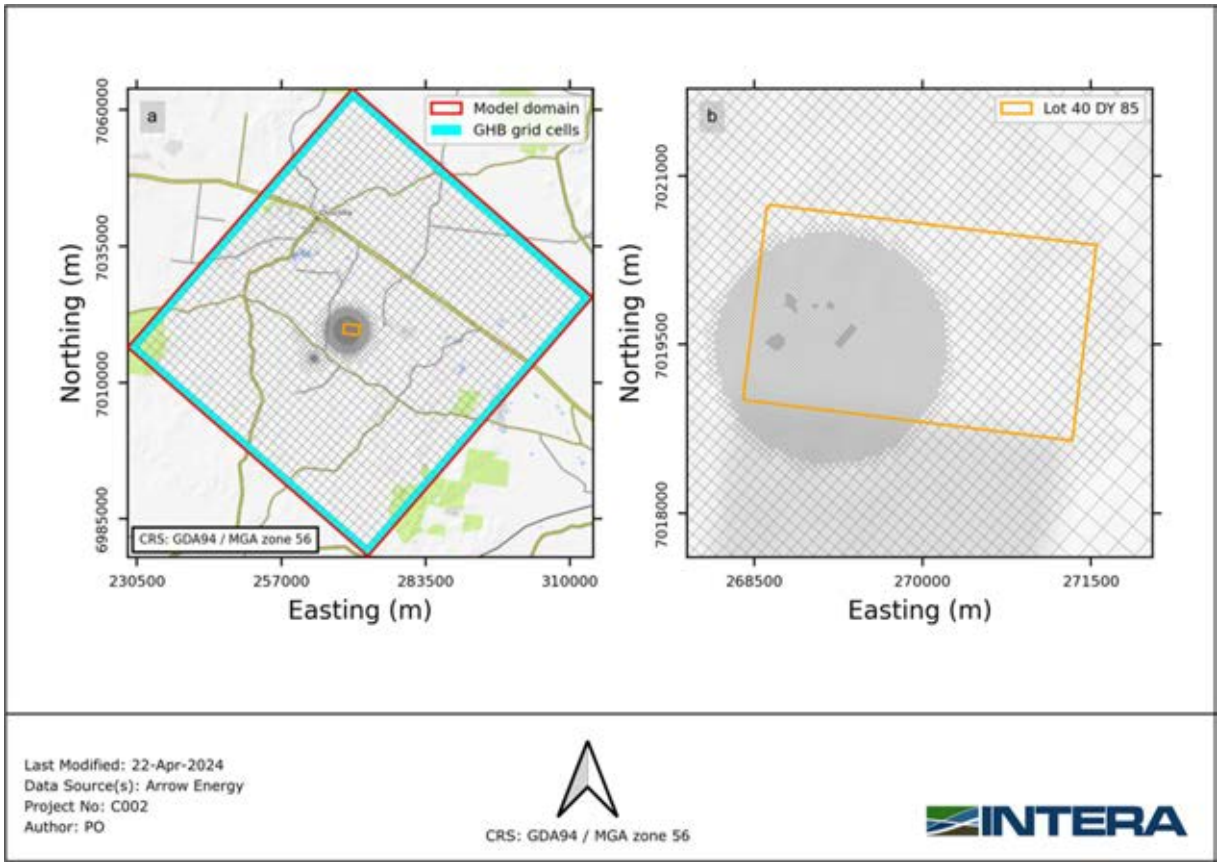


Figure 3-2 – Map of model grid: (a) plan view of model grid over the whole domain (including GHB cells), and (b) local refinement in Lot40 and gasifiers.

## 3.1.4 Boundary Conditions

### 3.1.4.1 Gasifiers

Operation of the UCG gasifiers at the former Linc Energy site (Lot40) is expected to have caused (1) depressurisation as water and gas were removed, and (2) alteration of the hydraulic properties due to the formation of a void where coal was consumed by the combustion process, as well as the potential for wider scale fracturing extending up into overlying formations and 1 to 2 km laterally (AECOM, 2018), caused by the combustion or subsequent collapse of the void.

Linc Energy's gasifiers and the depressurisation associated with their past UCG operation were simulated using the drain (DRN) package, following the approach employed by AGE (2023). In addition, UCG-driven changes in the hydraulic properties were simulated using the time-varying conductivity (TVK) and storage (TVS) packages available in MF6, as is described in 3.1.5.

Gasifier-affected areas were extracted from the AGE model and allocated to corresponding cells. DRN boundary conditions were assigned to these cells in layer 6 (WCM Macalister). DRN elevations were set equal to the elevation of the bottom of the layer, with a conductance of 100 $m^2/d$ based on the previous work by AGE (2023). Herein we acknowledge this value as uncertain and DRN conductance was parameterised and included as an adjustable parameter during history matching and predictive uncertainty analysis. DRNs are active during the period in which UCG was in operation and are deactivated upon closure.

### 3.1.4.2 CSG Wells

#### 3.1.4.2.1 Arrow CSG Wells

A total of 339 Arrow CSG wells (approved) are simulated. These include 284 CSG wells in the Future Development Plan (FDP) and the 55 CSG wells approved in the EA. Wells are assigned to model cells according to targeted formation and whether the well is vertical or inclined. For inclined wells, a linear trajectory between the top and the bottom grid cell was calculated and then assigned to the intersecting grid cells. Time series of production rates, provided by Arrow, were assigned to respective WEL boundary conditions.

Extraction from existing and proposed Arrow CSG wells were apportioned across screened layers using a transmissivity weighted approach. This ensures that the volume extracted per layer was proportional to the relative hydraulic conductivity and thickness.

A model pre-processor was included as part of the forward run, so that weights are re-calculated in accordance with updated hydraulic parameters during data assimilation and uncertainty analysis. Flow rate per layer for a well ($Q_i$) was calculated using the following equation (1):

$$Q_i = \frac{K_i b_i Q}{\sum_{i=1}^{N} K_i b_i} \quad (1)$$

where $Q$ is the total pumping rate, $K$ is hydraulic conductivity, $b$ is thickness, $i$ is the layer index number and $N$ is the number of screened layers. It is worth noting that this approach does not account for changes in saturated thickness as it was not considered the objective of the present study. Additionally, doing so would require the use of the multi-aquifer well (MAW) package or updating of the weights during the model simulation, at the cost of model run-time and numerical stability.

#### 3.1.4.2.2 Non-Arrow CSG Wells

Non-Arrow CSG wells were simulated using the MF6 WEL package. Imposed extraction rates for existing and proposed non-Arrow CSG wells within the model domain were extracted from the Office of Groundwater Impact Assessment (OGIA) 2021 model, following the standard approach described in AGE (2020). CSG wells in the OGIA model are simulated using a custom implementation of the drain package, which was not available in other public domain versions of MODFLOW. OGIA simulated drain discharge rates were extracted and mapped to the corresponding cells and layers in the MF6 model, accounting for the relative area of cells in each model. Imposed non-Arrow CSG WEL rates were parameterised and included as adjustable parameters.

#### 3.1.4.2.3 Hopeland Pilot Wells

The Hopeland test site located on PL253 around 8 km southwest of the former Linc Energy site (Lot40), includes six authorised pilot CSG bores. Several years of measured groundwater level response to CSG pilot tests were available from this site, including data from multi-level piezometers. However, some of the available data were from bores which are being subjected to pumping.

Bores in the Hopeland pilot-test site were simulated using the Multi-Aquifer Well (MAW) Package, which uses the continuity equation to simulate the effect of groundwater pumping on water levels in pumping wells open to multiple aquifers. MAW were not used to simulate other CSG wells, because

they incur a large computational cost. However, as the Hopeland site consists of a small number of wells screened across multiple layers with history matching pertinent data, the cost was warranted.

MAW calculates a composite average head at the cells linked to the well. Neville and Tonkin (2004) showed that this approach provides an excellent comparison to analytical approaches for representing heads in a pumped well, irrespective of cell size. Thus, MAW package enables simulation of heads within a pumped well to be included in the history matching process at the cost of an additional two parameters per bore: bore diameter and conductance.

In a similar fashion, AGE (2020) relied on correcting measured data using the Thiem equation. As described in their report, this approach implies an *a priori* correction to measured data, assuming a known value of *T* and well radius. However, as hydraulic parameters are adjusted during the history matching process, the Thiem equation should be re-applied to account for the new hydraulic properties of the model cells in which the well is simulated. To our knowledge, this was not done. To avoid this issue, here we use the MAW package, and include MAW conductance and well radius as adjustable parameters. In this manner, corrections are applied during the simulation.

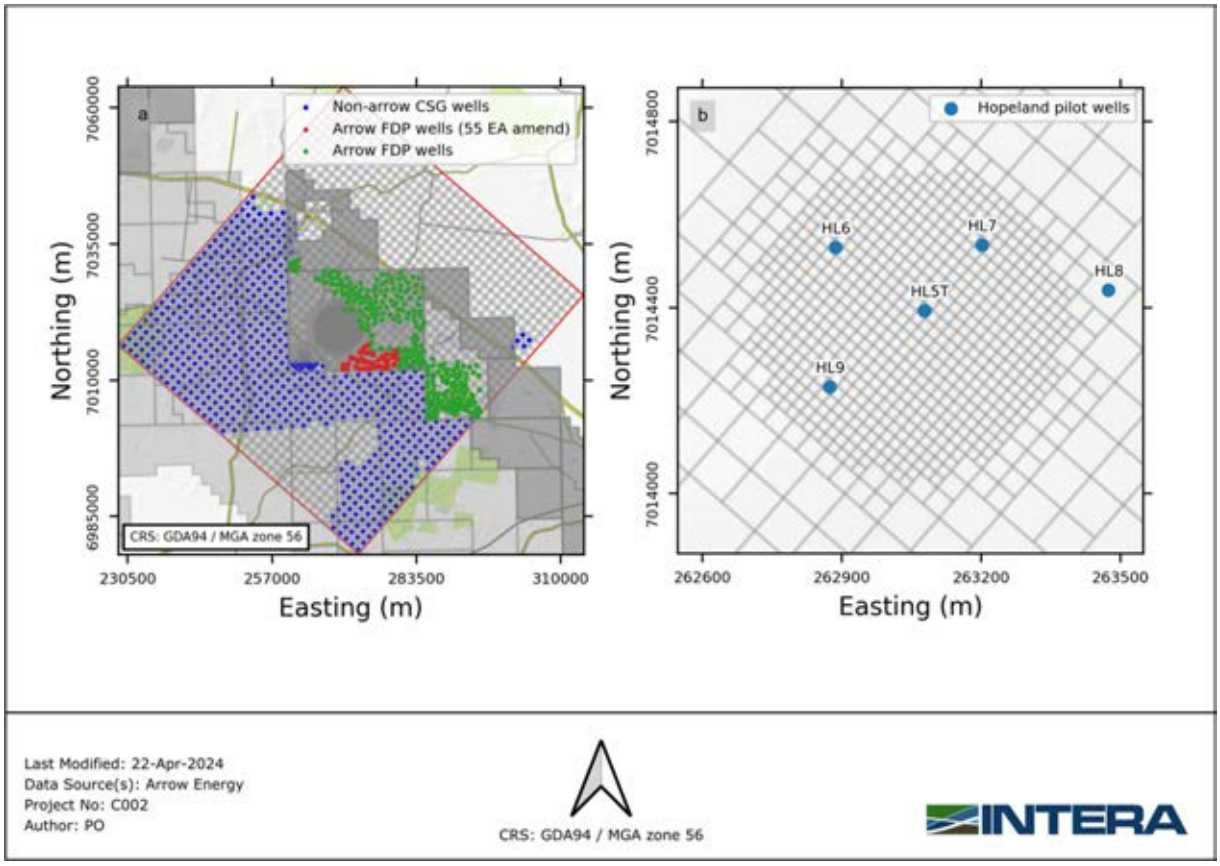


Figure 3-3 – CSG well locations withing the model domain for (a) non-Arrow CSG and Arrow CSG wells (divided by EA amended and FDP) and (b) Hopeland pilot-test well locations.

### 3.1.4.3 External Boundary Conditions

General Head Boundaries (GHB) were implemented along the model external boundaries. GHBs are assigned using time-varying heads from the extracted OGIA (2021) groundwater model to account for regional CSG activities.

The GHB nodes are mapped to model boundaries cells using the heads from the closest OGIA model cell in the corresponding model layer. The conductance of each GHB node was determined by the thickness, cell edge length, and horizontal hydraulic conductivity. Both GHB's head and conductance were parameterised using spatially varying pilot points and adjusted during history matching.

#### 3.1.4.4 Topographic Surface Drains

MF6 drain (DRN) boundary conditions were assigned to the uppermost active cells. Drain elevations are set equal to the top elevation of each model cell. This ensures that simulated hydraulic heads do not exceed topographic surface elevation. Observations constraining that discharge through these drains should be zero provide an additional source of information for parameter estimation.

#### 3.1.4.5 Recharge

A spatially varying time-constant recharge rate was assigned to all uppermost active cells (i.e., reflecting formations present at outcrop) using the MF6 RCH package. Recharge rates were sourced from the AGE model. Initial recharge rates are 3.5, 1.0 and 0.2 mm/year for the Condamine Alluvium, Gubberamunda Sandstone and Westbourne Formation, respectively. Spatial distribution of recharge rates was parameterised using pilot points and adjusted during history matching.

### 3.1.5 Hydraulic Properties

Hydraulic properties were defined as spatially continuous and varying within each hydrogeological unit. Initial hydraulic parameter values for horizontal hydraulic conductivity (K), specific storage (Ss) and specific yield (Sy) were assigned according to initial (i.e., prior mean) values used by the AGE model, described in AGE (2023). Ranges of these properties are also presented in the conceptual model (section 2.4). Calibrated parameters from the AGE model were not employed to reduce the potential of introducing calibration induced bias. Vertical hydraulic conductivity (Kv) was assigned as the ratio of horizontal and vertical hydraulic conductivity. K in an individual cell was defined as isotropic. A summary of these values is presented in Table 3-2. Further details on the parameterisation of these properties can be found in section 3.2.4.

Table 3-2 – Summary of initial hydraulic properties in the groundwater model.

| Layer | K (m/d) | Kv (K/Kv ratio) | Specific storage ($m^{-1}$) | Specific yield (-) |
|---|---|---|---|---|
| 1 | 3 | 0.01 | $1 \times 10^{-5}$ | 0.02 |
| 2 | 1 | 0.01 | $1 \times 10^{-6}$ | 0.01 |
| 3 | 0.01 | 0.001 | $1 \times 10^{-6}$ | 0.01 |
| 4 | 0.022 | 0.001 | $1 \times 10^{-6}$ | 0.01 |
| 5 | 0.05 | 0.01 | $1 \times 10^{-6}$ | 0.01 |
| 6 | 0.022 | 0.001 | $1 \times 10^{-6}$ | 0.01 |
| 7 | 0.007 | 0.01 | $1 \times 10^{-6}$ | 0.01 |
| 8 | 0.022 | 0.001 | $1 \times 10^{-6}$ | 0.01 |
| 9 | 0.005 | 0.001 | $1 \times 10^{-6}$ | 0.01 |
| 10 | 0.016 | 0.001 | $1 \times 10^{-6}$ | 0.01 |
| 11 | 0.00022 | 0.01 | $1 \times 10^{-6}$ | 0.01 |
| 12 | 0.00002 | 0.01 | $1 \times 10^{-6}$ | 0.01 |
| 13 | 0.022 | 0.001 | $1 \times 10^{-6}$ | 0.01 |
| 14 | 0.032 | 0.01 | $1 \times 10^{-6}$ | 0.01 |

| Layer | K (m/d) | Kv (K/Kv ratio) | Specific storage ($m^{-1}$) | Specific yield (-) |
|---|---|---|---|---|
| 15 | 0.022 | 0.001 | $1 \times 10^{-6}$ | 0.01 |
| 16 | 0.01 | 0.001 | $1 \times 10^{-6}$ | 0.01 |
| 17 | 0.0001 | 0.01 | $1 \times 10^{-6}$ | 0.01 |
| 18 | 0.01 | 0.001 | $1 \times 10^{-6}$ | 0.01 |

#### 3.1.5.1 Time-Varying Material Properties

UCG-driven changes in the hydraulic properties were simulated using the time-varying conductivity (TVK) and storage (TVS) packages. To avoid large increases in head, time-varying properties were introduced during the operation of the gasifiers. Thus, the overall magnitude of the change in hydraulic properties was distributed across the stress periods corresponding to when each gasifier commenced its operation.

The area of influence of TVS and TVK was extended up to 1 km radius from the centre point of the Lot40 and up through all overlying layers (except for layer 1). Time-varying properties for the void cells in layer 6 were set to 100 m/d for K and Kv, 1 for Sy and $5 \times 10^{-6}$ $m^{-1}$, whilst for cells overlying voids only post-closure Kv was increased to 0.02 m/d. All other cells affected by time-varying properties were assumed to stay equal to pre-UCG values, however this value was allowed to vary during history matching and uncertainty quantification as described in chapter 3.2.

The area of influence of TVK and TVS was extended in comparison to that of AGE (2023), as, when evaluating the model with an ensemble of parameters sampled from the prior probability distribution, it was found that the model was unable to capture observed behaviour at many of the monitoring bores in overlying formations (e.g., Springbok). To address this, the area of influence was extended up to 1 km radius from the centre point of the Lot40, according to observed extent of impacts described in AECOM (2018).

## 3.2 History Matching

History matching refers to the process of adjusting model parameters until the model is able to adequately reproduce observed historical data or past events. Calibration, by definition, seeks to history match a unique solution to a problem that is non-unique in nature. Hence, a history-matching process was applied using Bayesian methods, which is described in the following section.

### 3.2.1 Approach

History-matching and uncertainty analysis was undertaken using an Iterative Ensemble Smoother (IES) method, as implemented in PESTPP-IES (White et al. 2020), using a highly parameterised approach. Due to long model run-times, and to facilitate the plug-and-play of transport and particle tracking models, the workflow was split into two phases: (1) history matching and (2) predictive analysis.

A posterior parameter ensemble was obtained through history matching a simulation of the historical period against observation data. The IES algorithm, detailed in Chen and Oliver (2013; 2017) and White et al., (2018), starts with an ensemble of random parameter fields each representing a sample from the prior parameter probability distribution. As the algorithm iterates, these samples are adjusted to become representations of the posterior parameter probability. This posterior parameter ensemble was subsequently employed to sample the posterior probability distribution of predictions of interest with a model that simulates the predictive period.

### 3.2.2 History Matching Period

The history matching period covers from 01-01-2000 to 01-01-2025. This period was simulated with a total of 146 stress periods. The first stress period was steady state, whilst the remainder are transient. The first 15 transient stress periods have a length of 1 year. Subsequent stress periods are refined to 1-month periods comprising a single time-step. As previously mentioned, stress period 16 (01-01-2014) marks the closure of the UCG gasifiers. Therefore, stress periods involving the implementation of time-varying material packages were divided into 10 time-steps, each with linearly increasing lengths, to facilitate the convergence.

### 3.2.3 Targets

#### 3.2.3.1 Heads and Vertical Head Differences

Time-series of groundwater heads collected at monitoring bores throughout the model domain were compared to simulated values at the corresponding cell in the model. The location of the bores within the model domain is presented in Figure 3-4, with a zoom-in highlighting the main bores in Lot40. Most of the observations pertain to model layers 3 and 6 (i.e., Springbok and WCM Macalister), in particular at Lot40.

The most comprehensive dataset dates back from 2014 in Hopeland pilot-test site and from 2018 in Lot40. As described above, this time frame was discretised to monthly intervals in the model. Thus, to match model outputs to measured times, MF6 simulated outputs were time-interpolated to the datetime at which measured data was recorded. This was accomplished with a custom Python script which post-processes MF6 outputs as part of the forward run. Time-interpolated model outputs are employed as observations in the PEST dataset.

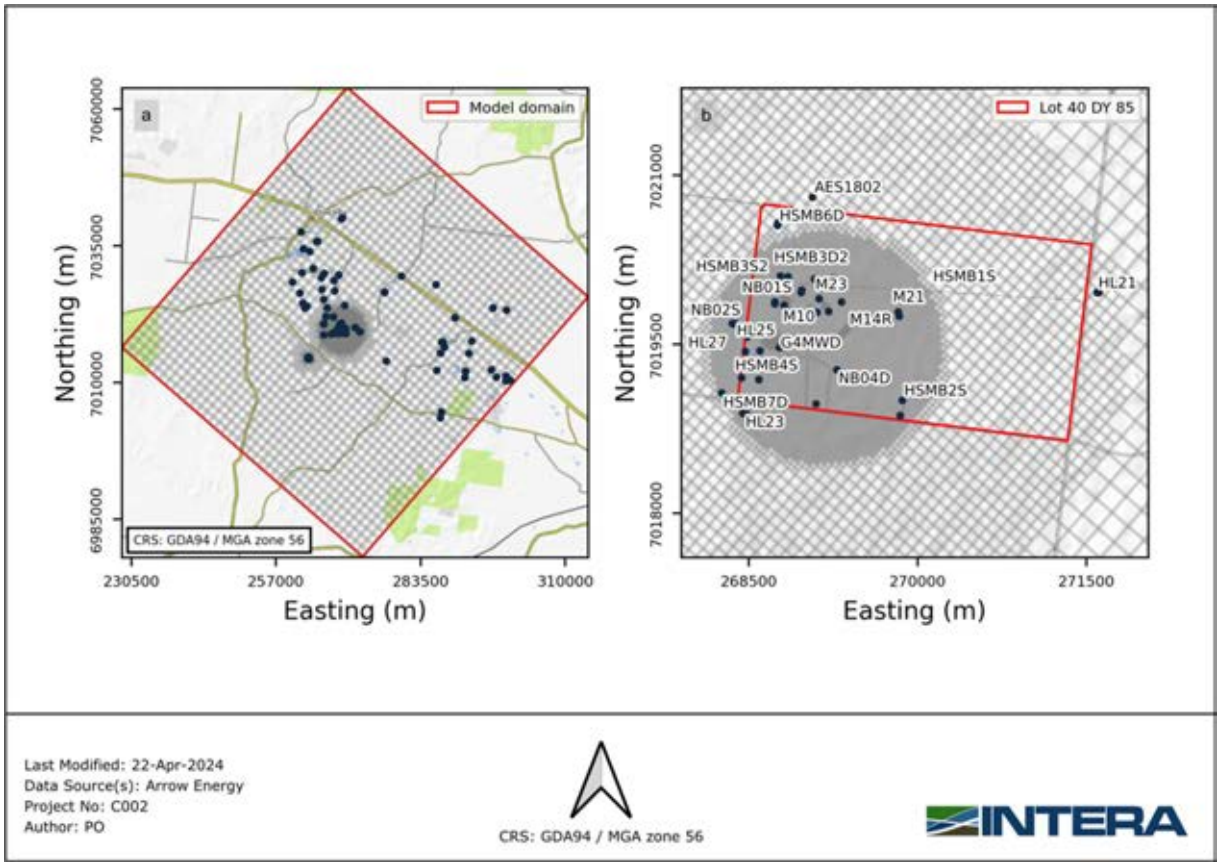


Figure 3-4 – Location of bores with hydraulic head data employed as history matching targets.

In addition, and where available, time series of the difference in groundwater levels between hydrostratigraphic units were employed as targets for history matching. Nested bores and HSBM bores series were used for this purpose. Figure 3-5 shows the locations of bores within the model domain employed for vertical head difference targets.

As previously discussed, the implemented history matching approach relies on the assumption of measurement noise (which conceptually includes both measurement error and model error). To reduce the potential for overfitting, a unique realisation of observation noise was added to each observation value.

During history matching each parameter realisation was adjusted to minimise the misfit with a unique realisation of observations plus noise. This ensures that the final ensemble of parameters account for uncertainty inherent in observed data, whilst avoiding overfitting.

For both absolute values and vertical head differences, measurement noise was sampled from a gaussian distribution with an assumed standard deviation of 1 m.

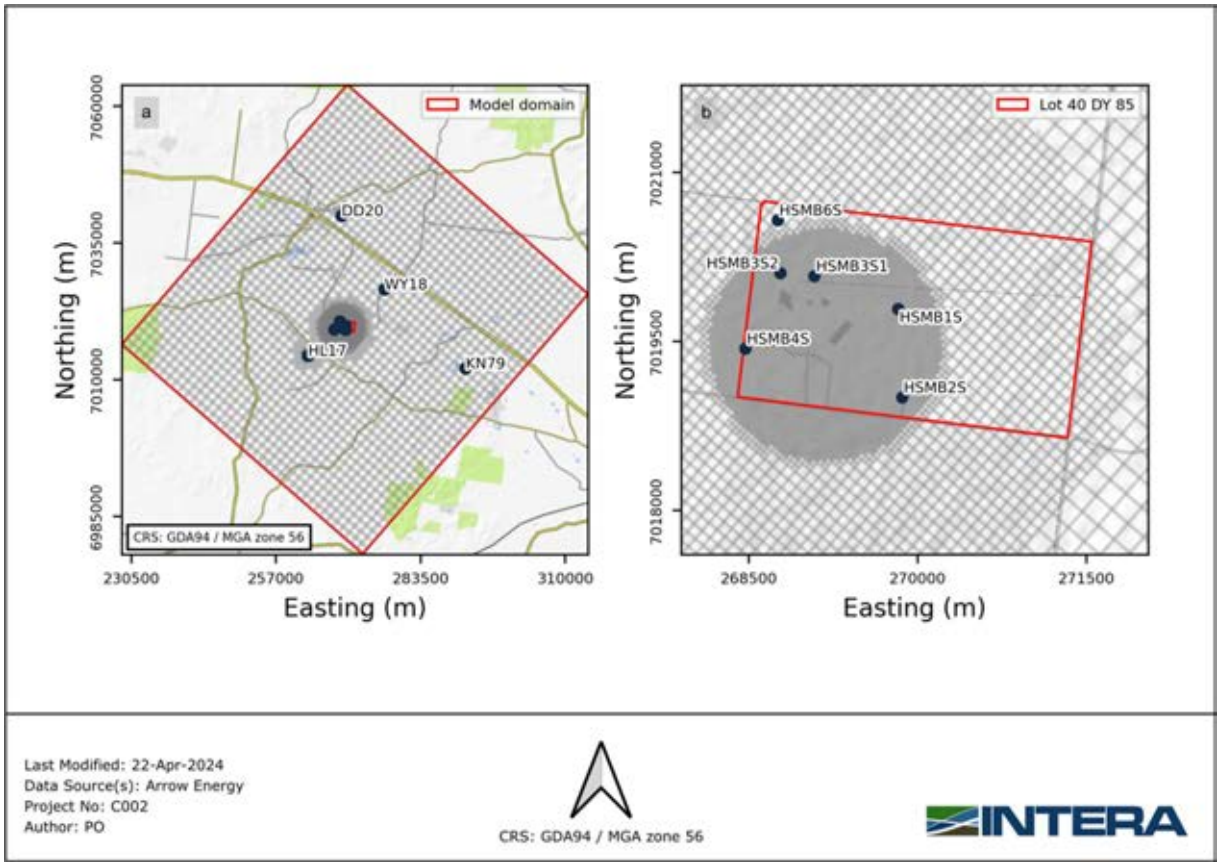


Figure 3-5 – Location of history matching targets for vertical head differences.

### 3.2.3.2 One-Sided Constraints

#### 3.2.3.2.1 Well Flow Rate Reduction

The automatic flow rate reduction option was activated for the MAW package simulating the Hopeland pilot-test. This option throttles simulated pumping rates in the MAW package if simulated hydraulic heads approach a user-defined minimum depth. Doing so improves numerical stability; however, it can result in different imposed and simulated water budgets (Hughes et al, 2017). Using this option facilitates model converge during history matching but allows for the generation of parameters in which the simulated pumping rates are different from those which were observed. To avoid this possibility, one-sided observations were included to promote that flow rate reduction should not occur. This informs the history matching process to avoid parameter values that would not have been able to support actual measured pumping rates. No noise was considered for this observation type.

#### 3.2.3.2.2 Topographic Surface Drains

As previously described, DRN boundary conditions were imposed on all cells in the upper-most active layer. DRN elevation was set equal to surface topographic elevation. This promotes that hydraulic heads do not exceed topographic elevation. One-sided observations that discharge through these DRN boundaries are zero were included as history matching targets. This informs the history matching process to avoid parameter values that would result in groundwater discharge to surface where this is known to not occur. No noise was considered for this observation type.

#### 3.2.3.3 Prior Data Conflict

Prior data conflict (PDC) occurs when simulated outputs from the prior parameter ensemble fail to encompass measured values (i.e., measured values do not fall within the range of values generated by running the model with the prior parameter ensemble). This implies that extreme parameter values would be required in order to fit these observations (combinations of values that are physically unlikely) (White et al, 2020). It is often a sign of error in the conceptual or numerical model and/or in the data and undertaking history matching in the presence of prior-data conflict is not recommended as it can generate bias (Hemmings et al, 2020).

In instances where adjustments to parameter ranges and assessments of measured data quality could not reasonably resolve PDC, conflicting observations were excluded from the calibration dataset using the PESTPP-IES automated PDC conflict resolution option (White et al, 2020). As previously discussed, to mitigate the loss of information content from dropping observations, secondary observation types (i.e., vertical differences of heads) were included in the calibration dataset. This ensures that, even if absolute measured values were not replicated by the model, at least the temporal dynamics were still available to inform parameter values.

### 3.2.4 Parameterisation

The following section provides a description of the parameterisation employed for history matching and uncertainty analysis.

#### 3.2.4.1 Pilot Points

Pilot points were employed for spatially varying parameters such as horizontal and vertical hydraulic conductivity, specific storage, specific yield and recharge. Pilot points were also used to parameterise the extent and magnitude of the time-varying hydraulic conductivity and storage parameters, as well as GHB heads and conductance.

It is generally assumed that correlation between a pair of spatial parameters decreases with increasing distance. Thus, parameters which were close together were denoted as having higher (positive) correlation with each other than with those which were far apart. Covariance matrices for pilot point parameters were constructed using functionality available in pyEMU (White et al., 2016). Spatial correlation was described with an exponential variogram with range depending on the average distance between pilot points and anisotropy of 1 (e.g., isotropic), unless otherwise stated.

#### 3.2.4.2 Hydraulic Properties

The following hydraulic properties were parameterised with a combination of pilot points and zonally constant multipliers:

- horizontal hydraulic conductivity (K),
- vertical hydraulic conductivity (Kv),
- specific storage (Ss),
- specific yield (Sy), and
- recharge (rch).

A combination of pilot points (fine-scale) and zonally constant (coarse-scale) multiplier parameters was applied. Coarse scale parameters enable the history matching process to introduce large shifts in parameters values. Further fine-tuning of spatial heterogeneity was introduced with the fine-scale

pilot points. Final parameter values imposed on the model were constrained by “ultra” lower and upper bounds to prevent unreasonable values being assigned to model input files (see Appendix A)

The same set of pilot points were used for all the above parameters, in all model layers. For each layer, where a pilot point coincides with inactive cells, it was ignored. Pilot point distribution was coarser outside of Lot40 and denser within the Lot40 and around the Hopeland pilot-test site. Figure 3-6 shows the distribution of the pilot points over the entire model domain (Figure 3-6 (a)) and at Lot40 (Figure 3-6 (b)). Appendix A provides a summary of model parameters adjusted during history matching and uncertainty analysis.

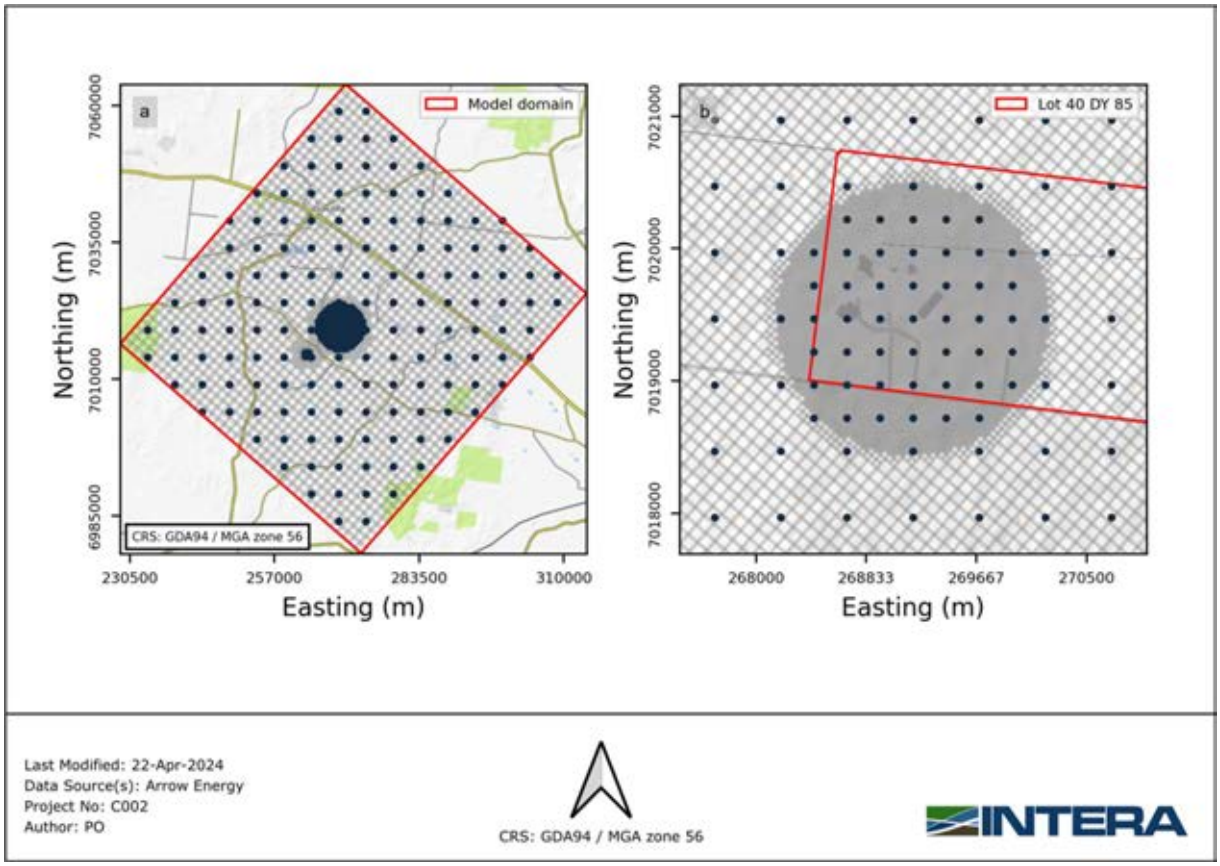


Figure 3-6 – Pilot point distribution for hydraulic parameters and recharge in (a) entire domain and (b) zoom-in on Lot40.

### 3.2.4.3 Boundary Conditions

Relevant boundary conditions were also parameterised, including GHB heads and conductance, abstraction rates of non-Arrow wells simulated using the WEL package and Hopeland pilot-test wells.

#### 3.2.4.3.1 External General-Head Boundary

Pilot points along the four boundaries of the domain were used to parameterise the GHB conductance and heads, with multipliers and direct values, respectively. Spatial correlation was setup with a range of 3000 m and isotropic. An additional model-wide multiplier parameter was employed for each simulation stress-period to account for time-varying uncertainty (or noise) of GHB inputs from the OGIA model. Figure 3-7 (a) displays the pilot points for the GHB boundary conditions.

#### 3.2.4.3.2 Non-Arrow CSG and Pilot Test Wells

Multiplier parameters were assigned to each individual non-Arrow CSG well rate in the WEL input files. These multipliers were allocated to fluctuate within a range of 0.5 and 2. The same multiplier per rate was used for all stress periods, without accounting for uncertainty in changes over time.

Conductance of Hopeland pilot-test wells was directly parameterised with bounds set between 1 x $10^{-3}$ and 10 $m^2$/d. Well radius was parameterised with a multiplier that varies between 0.1 and 10. Each WEL and MAW element was assumed to be independent, and no correlation between parameters was considered.

#### 3.2.4.3.3 Gasifier Cell Drain Conductance

Gasifiers conductance was parameterised with parameter multipliers with bounds between 1x$10^{-3}$ and 100 $m^2$/d. Parameter correlation was specified with a range of 200 m and an anisotropy of 1. The same conductance multiplier was used for all stress periods, without accounting for uncertainty in changes over time.

### 3.2.4.4 Time-Varying Hydraulic Properties

Time-varying hydraulic properties were applied to simulate the potential changes in permeability arising from the former UCG operation. The change was applied at stress period (15) corresponding to the cease of operation of the UCG gasifiers. Time-varying properties were parameterised using multiplier pilot points.

Two distinct sets of pilot points were employed: (1) a dense set of points within the gasifier cells and (2) a coarser set within a 1 km radius around Lot40. These two sets differ in the initial parameter values and their bounds.

The first set reflects the gasifier voids, taking extreme permeability and storage values. The second set reflects potential alteration to material induced by UCG operations. For the latter, initial values and lower bounds were set equal to pre-UCG hydraulic properties, however upper bounds were allowed to increase to allow for the possibility of increased permeability and/or storage.

In addition to these two sets of pilot points, the interpolation of the time-varying property parameter fields was constrained by a set of points placed in a circumference with 1 km radius around the gasifiers. Pilot points at the boundary were fixed and imposed hydraulic properties equal to background values. This approach generates a smooth transition between the area outside the buffer and the area extending from the gasifier grid cells. Thus, sharp contrasts in hydraulic properties were avoided promoting numerical stability.

Figure 3-7 (b) shows pilot points employed for time-varying properties, classified by gasifier or extended area, and depicting the boundary constrains applied. Appendix A provides a summary of time-varying parameters adjusted during history matching and uncertainty analysis.

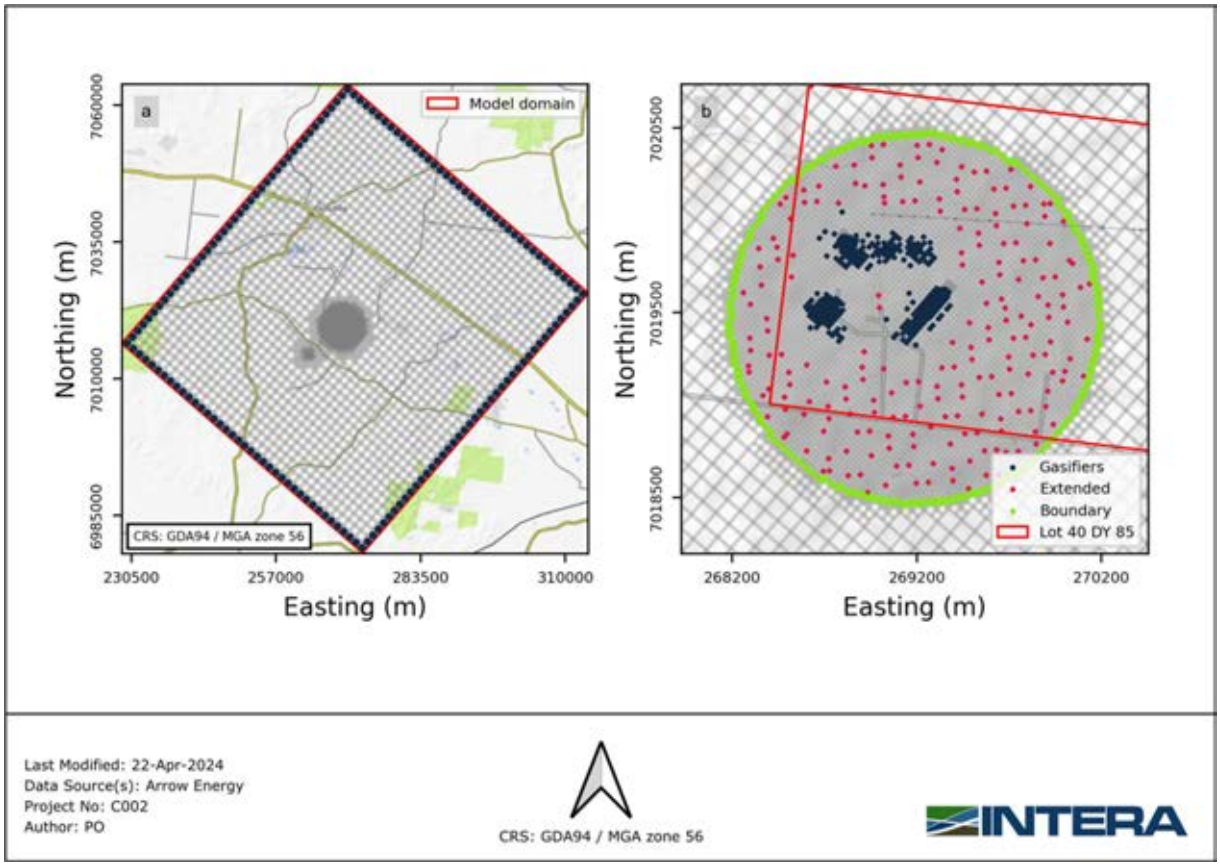


Figure 3-7 – Pilot point distribution for (a) GHB boundary conditions and (b) time-varying hydraulic parameters.

### 3.2.4.5 Localisation

Estimating the empirical cross-covariance between a large set of parameters and observations from a limited number of instances can lead to false cross-correlations (Chen and Olivier, 2017). This can cause unnecessary adjustments to some parameters. Moreover, when a calibration dataset consists of many independent observations, a small ensemble size may not offer sufficient degrees of freedom to replicate these data (Chen and Olivier, 2017; White et al., 2020).

To address these issues, localisation can be used. Originating from the ensemble Kalman filter terminology, "localisation" is a method that uses only "local" covariances to inform unobserved states in a spatially distributed filtering problem (Chen and Olivier, 2017). Through localisation, a large-scale parameter estimation problem can be turned into a series of smaller-scale independent parameter estimation problems. Localisation reduces the propensity for false cross-correlation at the expense of a diminished ability to match measured data and reduce uncertainty (Luo et al., 2018).

PESTPP-IES supports localisation through use of a localisation matrix. Constructing such a matrix relies on user to specify groups of parameters which each observation may or may not influence. Alternatively (or in tandem), PESTPP-IES also supports correlation-based, automatic adaptive localisation which uses the parameter ensemble and resulting model-output observation ensemble to calculate a Pearson correlation coefficient between each adjustable parameter and each non-zero-weighted observation (White et al., 2020). If this coefficient is significantly different from the background correlation coefficient, the observation is deemed to influence that parameter.

A user-specified localisation matrix was constructed and used in tandem with PESTPP-IES's automatic adaptive localisation option. Distance-based localisation was specified, mapping pilot point parameters to observations from bores within a 3 km radius and no further than three model layers (i.e., an observation only influences parameter changes if the pilot point is within a distance of 3 km and 3 model layers). MAW parameters were mapped solely to observations from the Hopeland set of bores. Layer-scale multiplier parameters and non-arrow CSG multipliers were mapped to all non-zero weighted observations. Gasifier DRN parameters were mapped to bores in Lot40.

## 3.2.5 Results

History matching was undertaken with a prior ensemble composed of 160 parameter realisations. Of these, 159 realisations remained in the posterior ensemble. As previously discussed, propensity for cross correlation with such a relatively small ensemble size was avoided using purposefully designed localisation. Three iterations were sufficient for PESTPP-IES to achieve reasonable fit between measured observations and the simulated ensemble without underestimating uncertainty. Proceeding for more iterations may have resulted in a better fit with measured data, but at the expense of inducing bias and/or variance collapse. Experience has shown that in high-dimensional non-linear problems such as parameter estimation of groundwater models, the value of continuing past three iterations is rapidly outweighed by the abovementioned costs.

### 3.2.5.1 Targets

Comparisons of modelled and measured groundwater levels are shown in Figure 3-8 and Figure 3-9. Figure 3-10 and Figure 3-11 display the statistical distribution of Root Mean Square Error (RMSE) and the Nash–Sutcliffe efficiency coefficient (NSE), for all posterior parameter realisations.

Figure 3-8 presents a one-to-one plot for heads and vertical head differences, where each observed measurement is compared to the value simulated by each ensemble realisation. The "base" posterior parameter realisation, which deviates the least from prior information and is thus the closest to a "calibrated" parameter set in the deterministic sense, is highlighted for clarity.

Overall, the model was able to replicate observed groundwater levels, except for the smaller vertical head difference observations and absolute heads below 200 mAHD. These are mostly related to the Hopeland pilot wells. As discussed in section 3.1.4.2.3, heads in these bores were subjected to pumping. Their simulation may therefore be subject to significant structural error. Excluding this data from the statistics and scatter plot (see Figure 3-9) shows that the model was able to achieve an acceptable (and unbiased) fit with the remainder of the observation data. Moreover, as is shown in Figure 3-10, all realisations achieve scaled RMSE values for absolute head targets that fall below the 10% target typically adopted for transient calibration (Barnett et al, 2012).

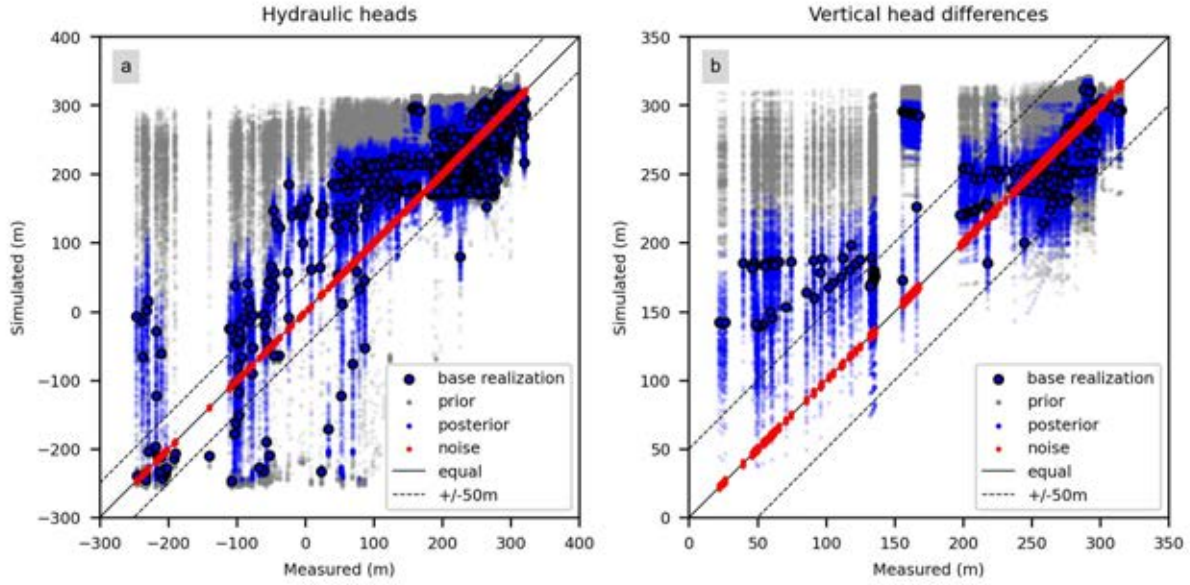


Figure 3-8 – Comparison between measured and simulated values for all (a) head and (b) vertical head difference observations for the prior (grey dots) and posterior (blue dots) ensembles. The solid black line corresponds to the identity line.

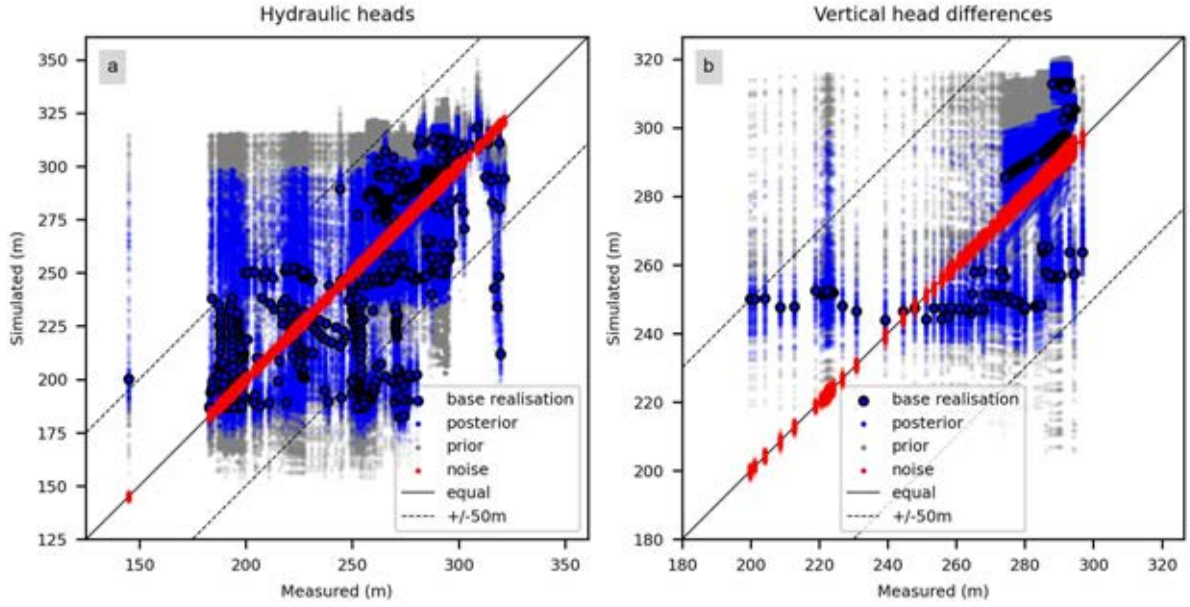


Figure 3-9 – Comparison between measured and simulated values for (a) head and (b) vertical head difference observations omitting observations at the Hopeland pilot site.

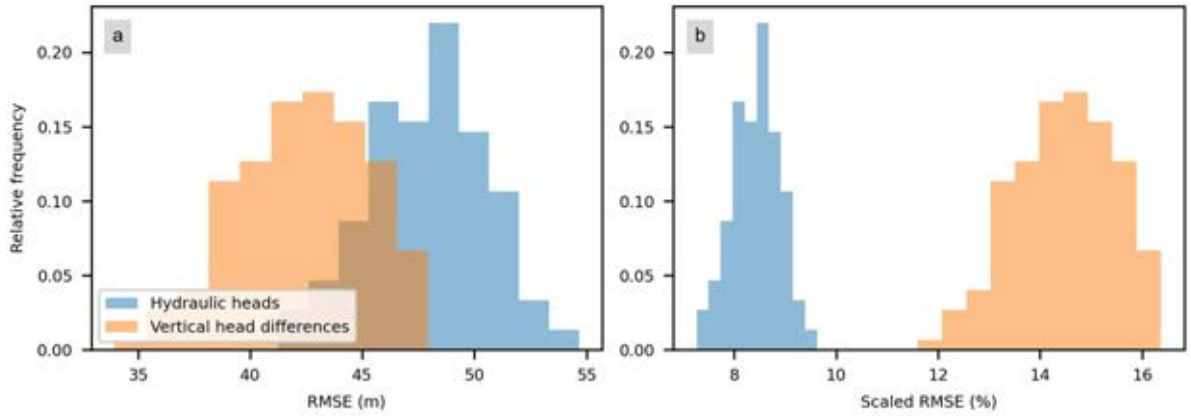


Figure 3-10 – Ensemble of posterior (a) RMSE and (b) Scaled RMSE calculated for absolute head and vertical head difference observations.

At Arrow's instruction, the statistical distribution of the Nash–Sutcliffe efficiency coefficient (NSE) and its normalised value (NNSE) for all posterior realisations of simulated observations were calculated. Results are shown in Figure 3-11. The NSE value can vary from negative infinity to 1. When the NSE value is close to 1, it suggests a strong correlation. If the NSE value is 0, it implies that the average of the data is just as predictive as the transient series of simulated values. If the NSE value falls below 0, the average of the data becomes a more reliable predictor. Some authors consider values of NSE between 0.5 and 0.6 "*satisfactory*", between 0.6 and 0.7 "*good*" and values above 0.75 "*very good*" (i.e., Moriasi, 2015). However, the primary concern was the enhancement in NSE outcomes following a new round of history matching, rather than the NSE value itself (Anderson et al, 2015).

Posterior realisations of hydraulic heads presented a mean NSE of 0.76, while vertical head differences shown a mean NSE of 0.7. Overall, according to the criteria employed in Moriasi (2015), the ensemble achieved "*satisfactory*" to "*very good*".

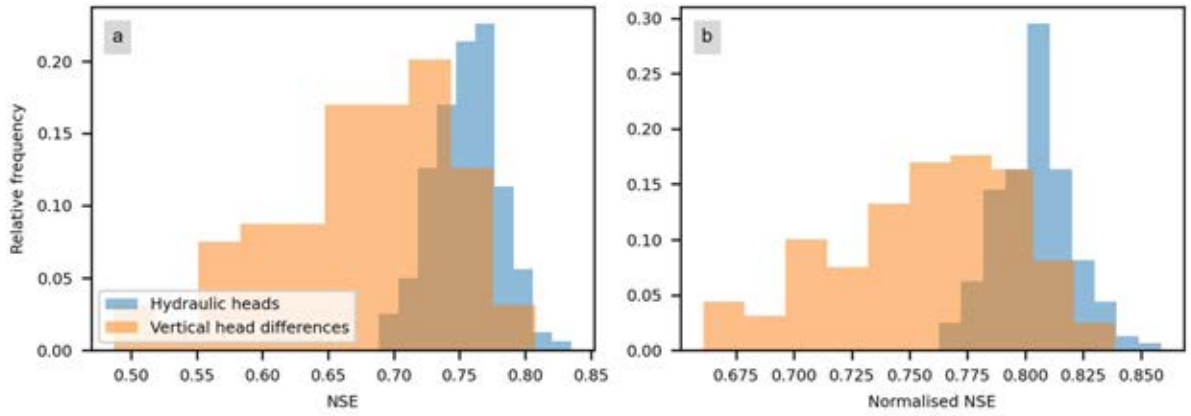


Figure 3-11 – Ensemble of posterior (a) NSE and (b) Normalised NSE calculated for absolute head and vertical head difference observations.

Lastly, Figure 3-12 displays the statistical distribution of one-sided observations. For surface drainage (left panel), values below zero denote groundwater discharge through topographic DRN boundary conditions. Target discharge was zero. For well flow reduction observations (right panel), values below zero are the amount that an imposed well rate has been reduced do the MAW well flow

reduction option. Target well flow reduction was zero. Over 95% of posterior realisations respected the one-sided constraints of no surface drainage and no well flow reduction.

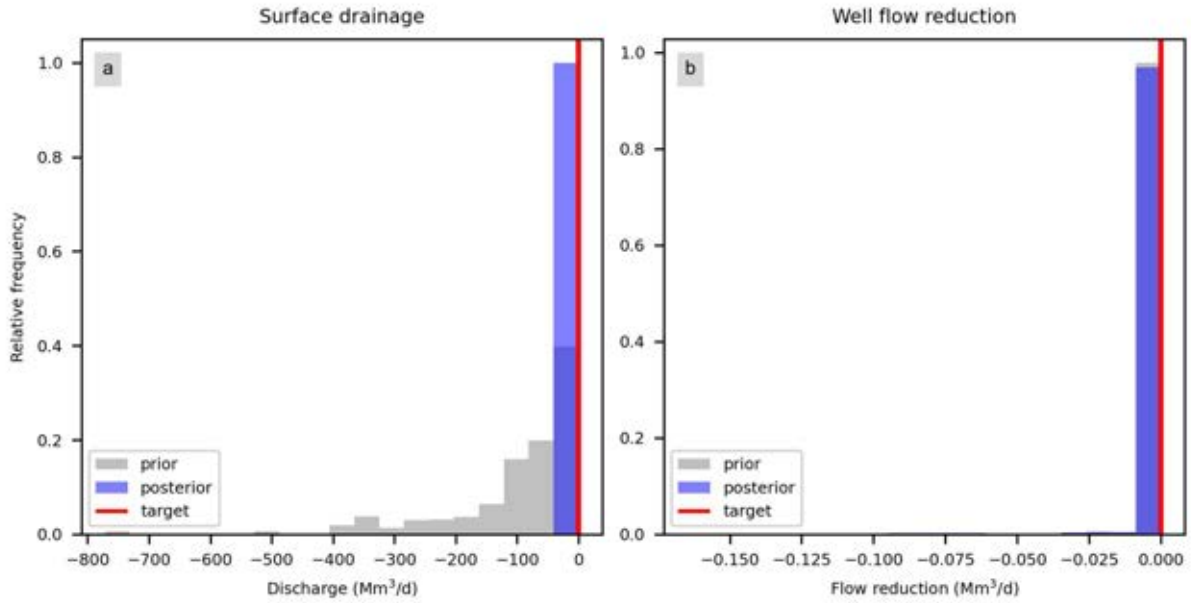


**Figure 3-12 – Prior and posterior distributions of one-sided constraint observation groups (a) discharge through topographic drains and (b) well flow reduction at the Hopeland pilot test bores.**

#### 3.2.5.1.1 Hydraulic Heads

Comparisons between measured and simulated time-series are shown for selected Lot40's monitoring bores in Figure 3-13 and Figure 3-14, and Hopeland pilot-test wells in Figure 3-15. Overall, the ensemble of simulated results included the measured values. The changes in groundwater level over time are generally well reproduced, with a few exceptions. Several sites in the Springbok Sandstone showed an apparent recovery from 2018 to 2021 (HSMB2S and HSMB3S1). Although some realisations replicated this behaviour, they did not reflect the mean of the ensemble. This suggests that there was conflicting information from different observations.

Most observations of HSMB bores were within the range of simulated values of the prior (grey lines in Figure 3-14), except for some measured values in bores HSMB2S and the entirety of HSMB3S2 measured heads (Springbok Sandstone). The case of bore HSMB3S2 was particularly noteworthy, as it is in close proximity to HSBM3S1 (within the simulated ensemble) but displayed measured heads that were 50 m lower. This indicates that there may be a feature between these two bores which was not accounted for in the model and/or parameterisation scheme.

Figure 3-15 compares time-series of head measured at bores in the Hopeland test site, and corresponding values simulated with the prior and posterior parameter ensembles. Simulation of bores with the MAW package, and inclusion of MAW parameters during history matching facilitated fitting measured values in bores subject to extraction (i.e., HL005 to HL009 in Figure 3-15).

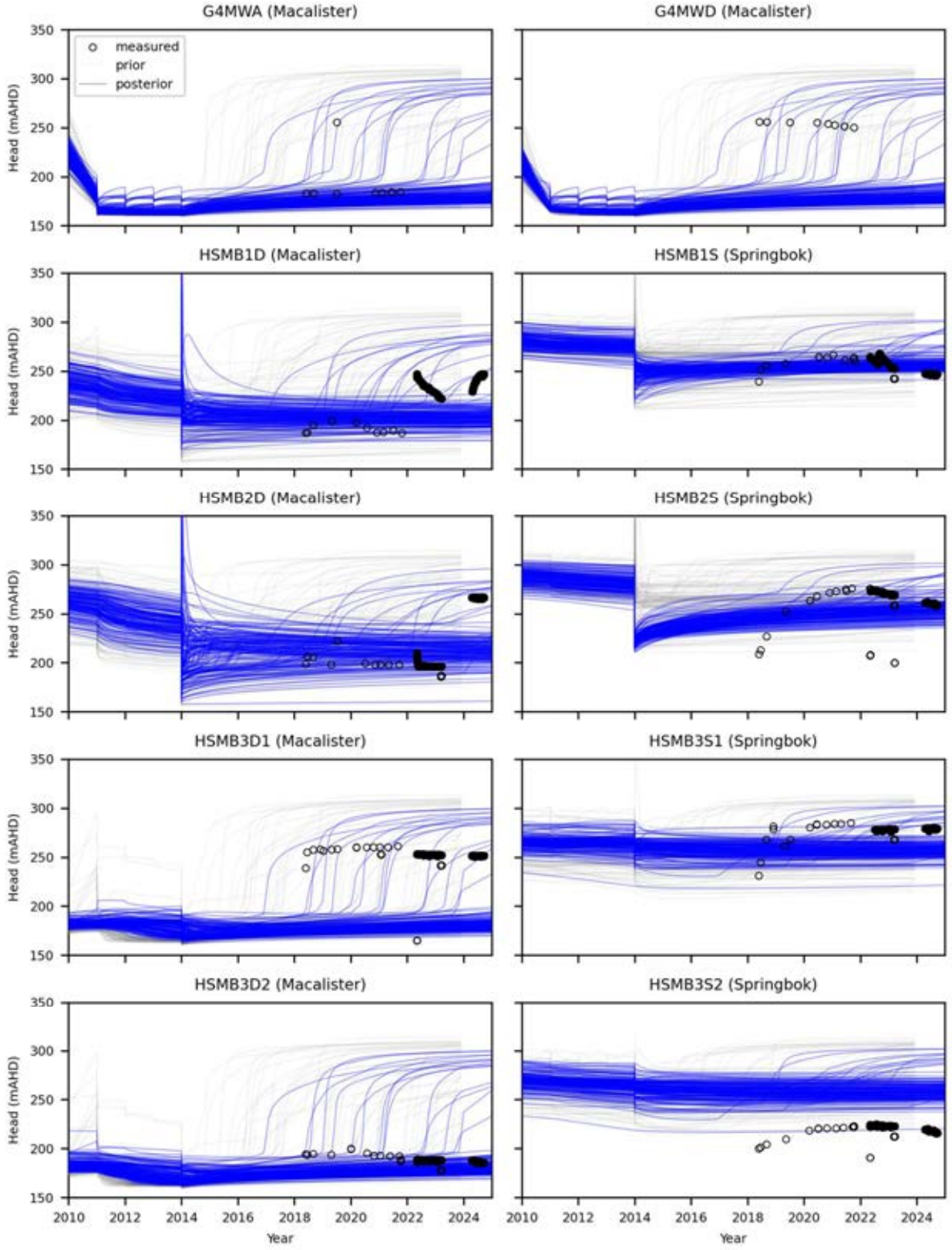


Figure 3-13 – Comparison between measured time-series of hydraulic heads (HSMB1 to HSMB3 and G4MW bores) and simulated values. Line colours denote prior (grey lines) and posterior (blue lines) simulated ensemble.

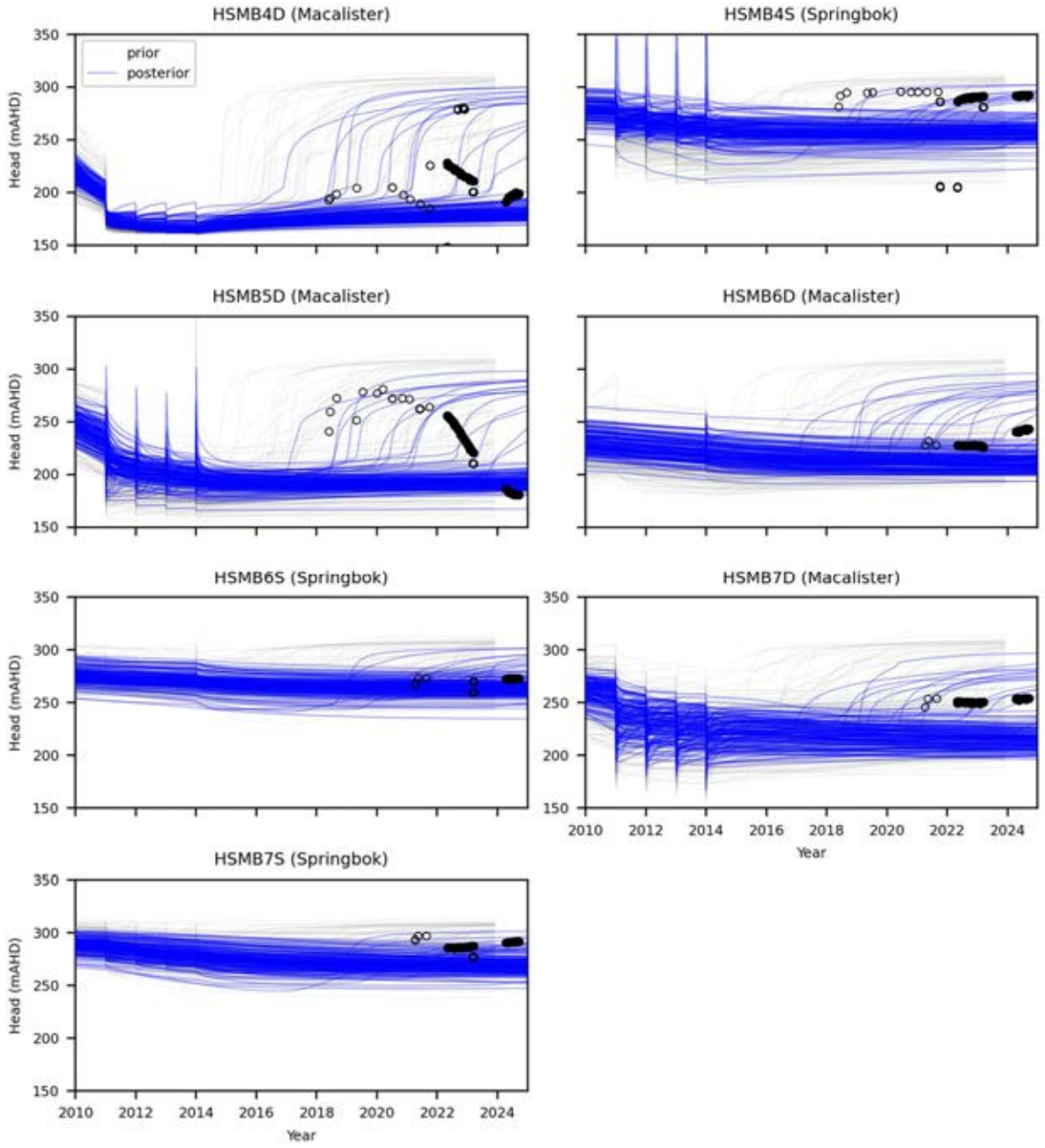


Figure 3-14 – Comparison between measured time-series of hydraulic heads (HSMB4 to HSMB7) and simulated values. Line colours denote prior (grey lines) and posterior (blue lines) simulated ensemble.

In general, the model realisations showed consistent recovery after 2017 which coincides with the period when most of the wells stopped operating. However, while observation data also shows recovery after this period, the simulated ensemble tended to overestimate recovery. This can be particularly observed in bores HL005 to HL009 and HL17_WCMUT_1P. The fact that measured values during the recovery often resulted in prior-data conflict (i.e., not even the prior was able to replicate them), ensured that PESTPP-IES did not attempt to fit them. This may have effectively protected against introducing bias. Regardless, trends at each of these bores were generally respected and the Hopeland pilot site is far enough removed from the area of concern that it is unlikely to have a significant impact on predictions of interest.

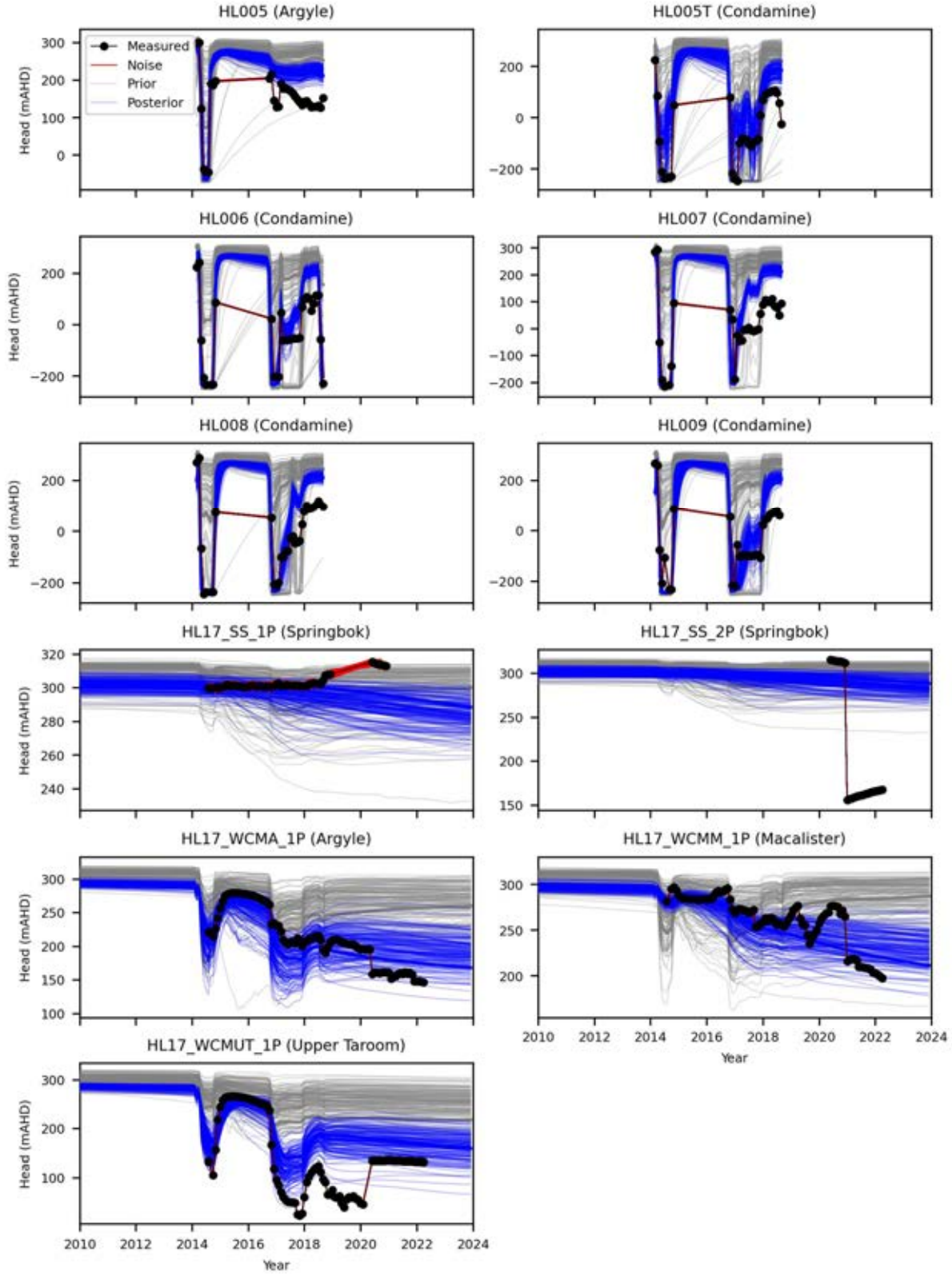


Figure 3-15 – Comparison between measured time-series of hydraulic heads, noise (Hopeland pilot site bores) and simulated values. Line colours denote prior (grey lines) and posterior (blue lines) simulated ensemble.

#### 3.2.5.2 Posterior Parameter Distributions

The following section discusses the spatial distribution of parameter uncertainty reduction, to provide insight into where (which) parameters were constrained through history matching as requested in the EA. This was accomplished by comparing the prior and posterior variance of model parameters.

The "relative parameter uncertainty variance reduction" (RPUVR) of each parameter shows the information content of the observation dataset as it pertains to different parameters, and to different groups of parameters. RPUVR is calculated as:

$$\text{RPUVR} = 1 - \left(\frac{posterior\ parameter\ uncertainty\ variance}{prior\ parameter\ uncertainty\ variance}\right)$$

This ratio varies between 0 and 1. Larger values indicate greater reduction in parameter uncertainty in comparison to prior parameter uncertainty. Thus, a high ratio may still be accompanied by a high level of parameter uncertainty; however, this uncertainty will be much lower than it was prior to data assimilation. Thus, RPUVR provides a qualitative representation of where history-matching has been most effective in reducing parameter uncertainty.

Figure 3-16 shows RPUVR for pilot points parameters employed for K in each layer, zoomed in on the area around the Hopeland site and Lot40 (plots for other pilot point parameters are presented in Appendix C). The remaining of the model domain is not presented, as RPUVR is near-zero. Brighter colours denote larger variance reduction in contrast to darker colours. As it can be seen, parameter uncertainty was generally only reduced in the vicinity of the Lot40 and at the Hopeland pilot site, where the majority of observation data is located. Figure 3-17 displays a closer view of RPUVR for K and the ratio of vertical to horizontal hydraulic conductivity (Kv) in model layer 6 (i.e., WCM Macalister).

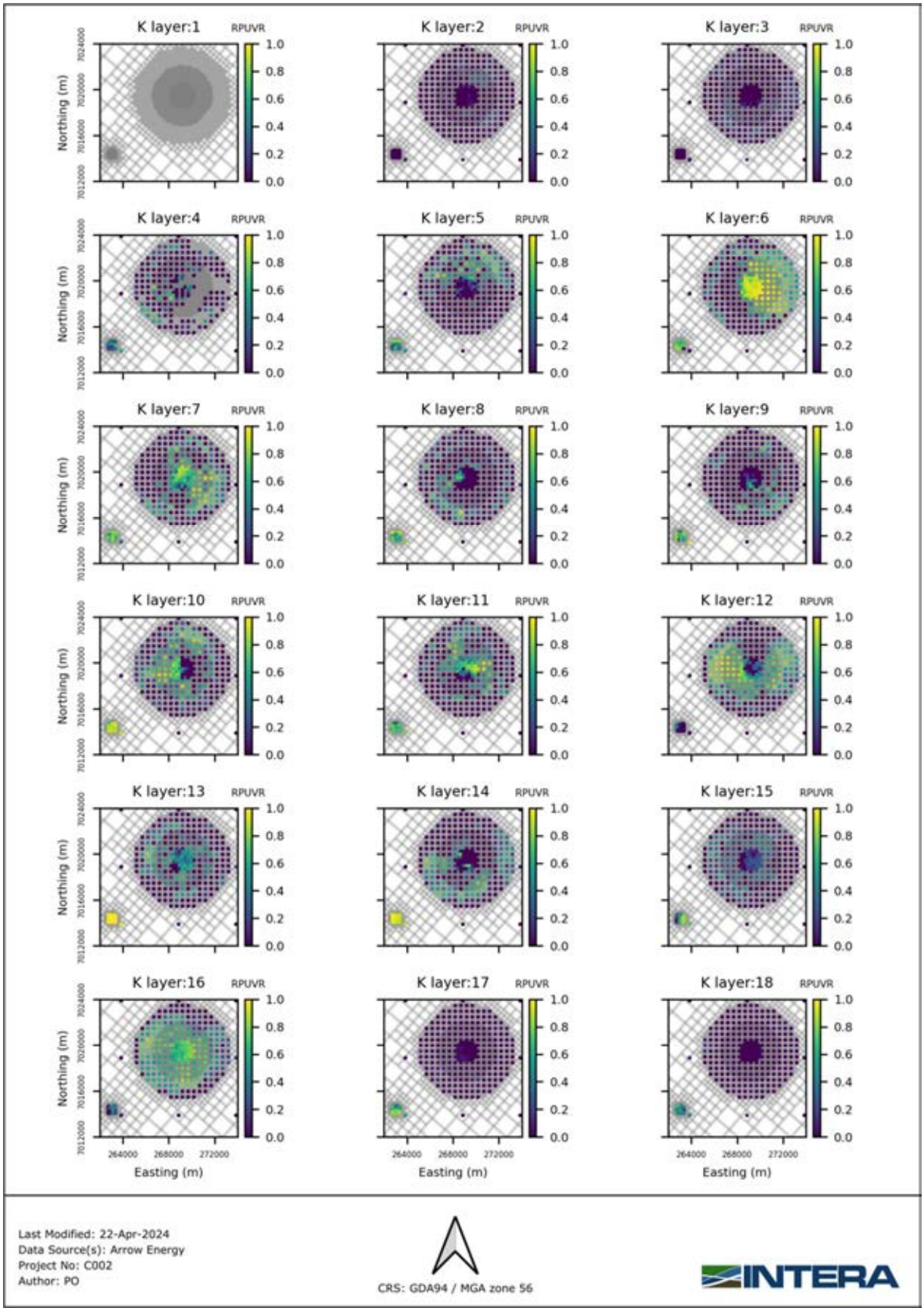


Figure 3-16 – Relative parameter variance reduction for hydraulic conductivity (K) pilot point parameters in each model layer.

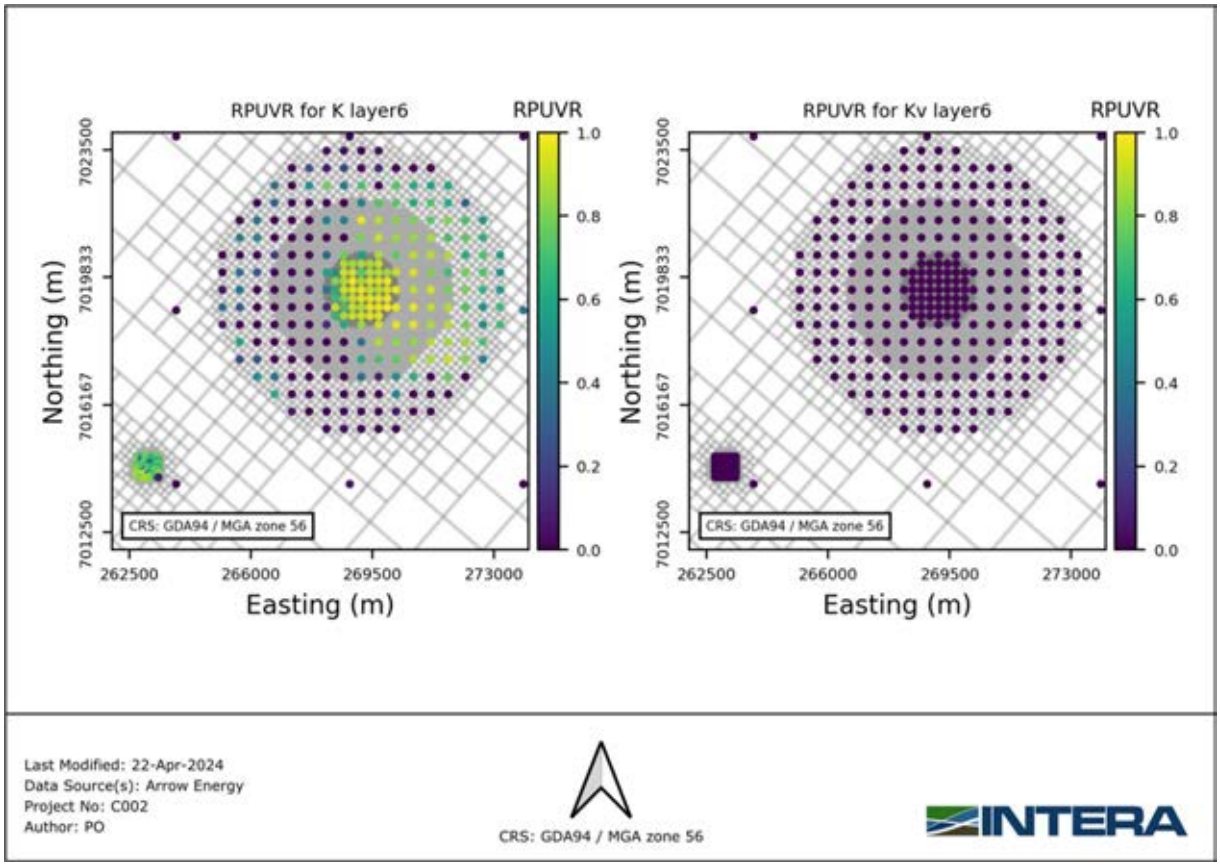


Figure 3-17 – Relative parameter uncertainty variance reduction for hydraulic conductivity (K) and ratio of vertical hydraulic conductivity (Kv) pilot point parameters near Lot40 and the Hopeland pilot site in model layer 6 (i.e., WCM Macalister).

From the figures shown above and in Appendix B, it would appear that history matching had a relatively minor effect on parameter uncertainty. However, when inspecting changes in distribution for other non-spatially distributed parameters (see Appendix C) the value of history matching is more apparent.

Figure 3-18 presents an example for the layer-wide multiplier for K and Kv in layer six. As described in chapter 3.2.4, most hydraulic properties and boundary conditions were parameterised with a combination of (fine-scale) pilot point and (coarse-scale) layer-wide multiplier parameters. Posterior parameter distributions for the coarse-scale parameter groups tend to be reduced. This implies that available observation data contains information that allowed the broad scale range of hydraulic properties to be reduced, but contains relatively little (or at least, spatially constrained) information on the spatial distribution of hydraulic property values. In Appendix C, histograms of prior and posterior parameter probability distributions for all parameter groups are shown.

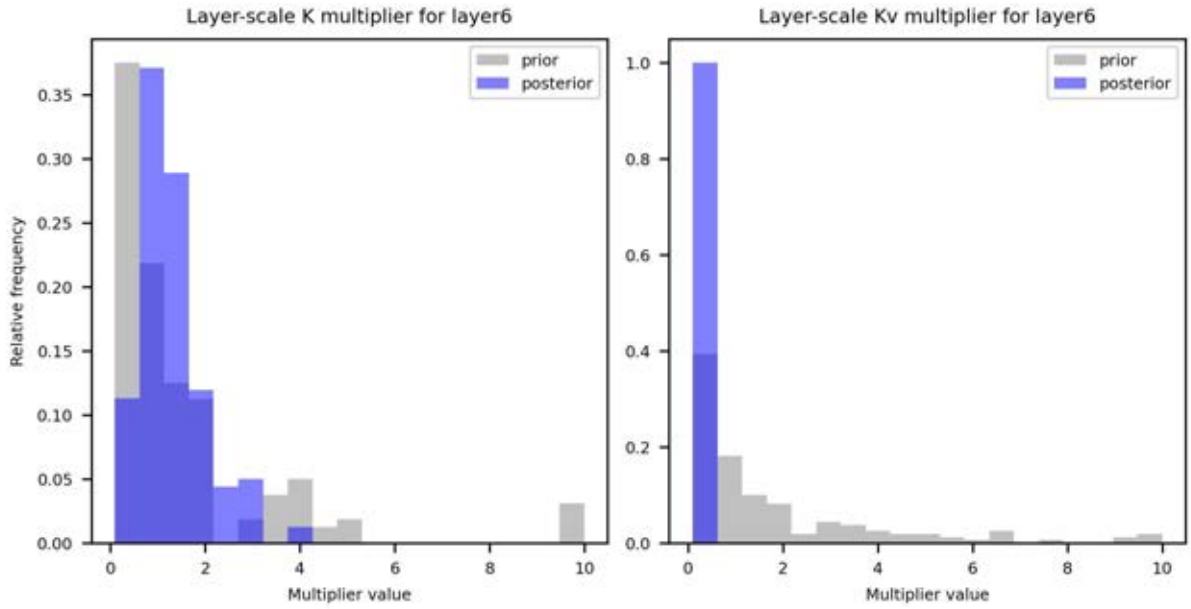


Figure 3-18 – Prior and posterior distributions of the coarse-scale multiplier parameter for (left) K and (right) Kv in model layer 6.

### 3.2.5.3 Water Budgets

Figure 3-19 displays time-series of simulated water budget components for the ensemble of prior and posterior parameters. History matching resulted in decreased discharge via surface topographic drains, as well as less total inflow through GHBs. Posterior range of recharge was slightly diminished. Despite allowing non-Arrow CSG wells to be adjustable, there was little discernible change after history matching.

As per suggested criteria in Barnett et al (2012), all parameter realisations resulted in a near-zero percent mass balance error and no convergence issues.

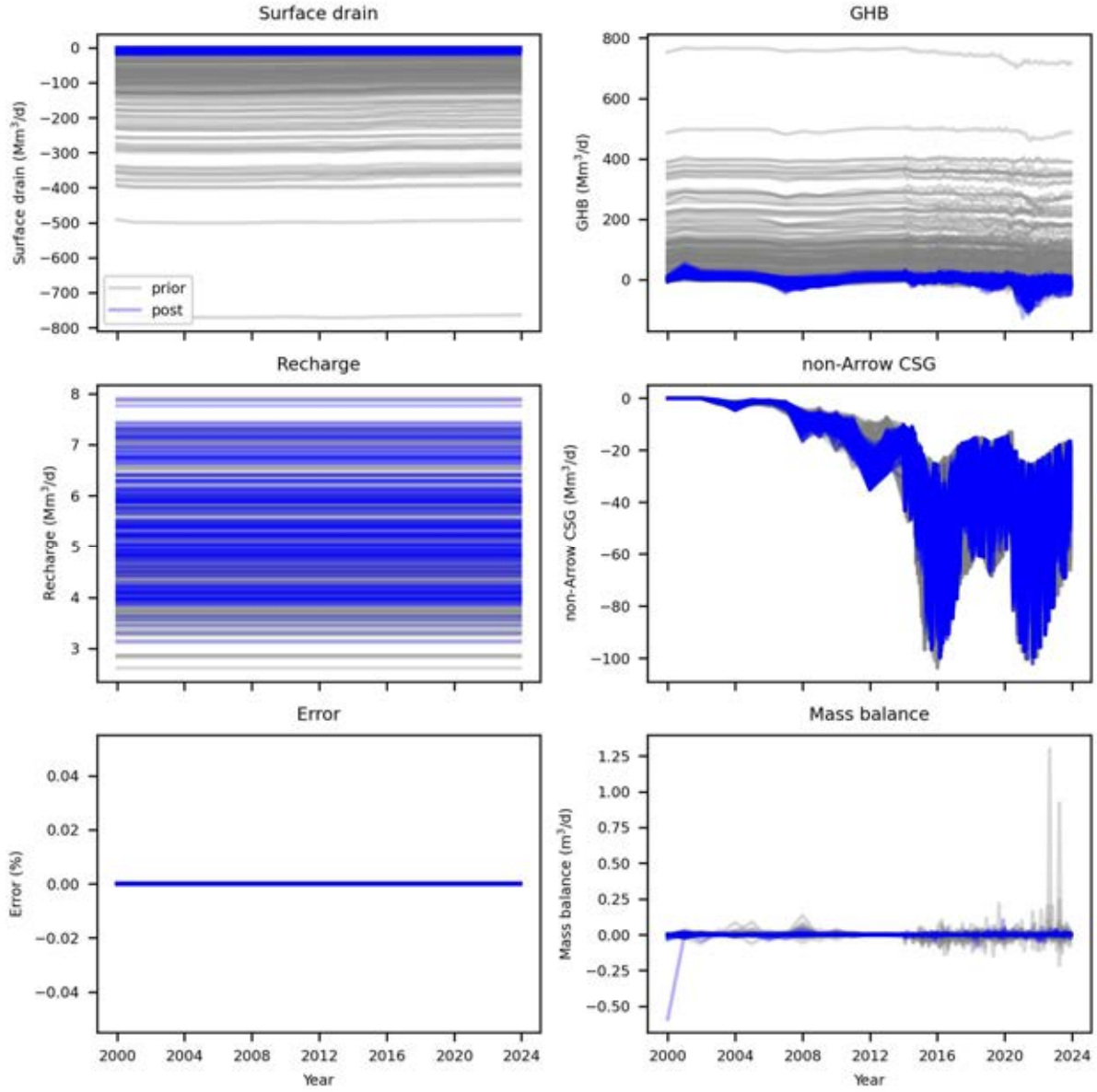


Figure 3-19 – Time-series of simulated water budget components simulated with the prior (grey) and posterior (blue) parameter ensembles.

### 3.2.5.4 Comments on Omitting Dual-Phase Flow

Studies have suggested that neglecting dual-phase flow can result in an overestimation of the impact of CSG depressurisation (Herckenrath et al., 2015; Moore et al., 2013; Moore et al., 2015). Moore et al., 2013 and 2015 conducted an extensive study on the flow conditions near a semi-synthetic coal bed methane extraction well-field. They compared the pressures computed by a conventional single-phase groundwater flow model with those computed by a multiphase reservoir simulator. The study revealed that the drawdowns computed by a single-phase groundwater flow model can significantly surpass those computed by a multiphase reservoir model, both near extraction well-fields and at considerable distances from them.

Moore et al., 2013 and 2015 identified two main reasons for the overestimation of pressure drawdown by a standard groundwater model. Firstly, as gas desorbs from the coal matrix due to coal

seam depressurisation, it reduces the relative permeability of the water phase in the cleat system, where fluid flow occurs. This reduction in water phase permeability impedes the outward propagation of the extraction-induced cone of depressurisation. Secondly, gas displaces water from the coal. Even in areas of low coal porosity, the volume of water released by gas generation in cleats significantly exceeds that released from elastic storage, further mitigating the transient outward propagation of extraction-induced drawdown. To account for these effects in regional impact modelling, OGIA implements a hybrid approach where the above effects are approximated in a modified single-phase groundwater flow model designed for regional scale impact assessment (Herckenrath et al., 2015).

Modelling described in the current report employs a single-phase flow approach. From a predictive standpoint this is not of significant concern, with some caveats. Predictions of interest for this study were related to the migration of contaminants from the Lot40. Should it occur, movement away from the site will be induced by drawdown resulting from neighbouring CSG operations. As discussed above, drawdown simulated by a single-phase model will be overestimated. Thus, from a contaminant movement perspective, a single-phase model should provide risk-conservative forecasts of how far contaminants may be expected to move. This of course assumes that (1) parameters employed in the single-phase model were representative of the real-world system and (2) simulated extraction rates from CSG wells reflect actual rates.

## 3.3 Predictive Modelling

### 3.3.1 Simulated Scenarios - CSG Wells

Two scenarios for the Future Development Plan (FDP) were simulated:

a) Base case FDP and
b) PL253 FDP.

The base case FDP scenario corresponds to the currently authorised CSG wells (290) including the six Hopeland pilot wells. The PL253 FDP scenario includes the additional 55 CSG wells from the EA, resulting in a total of 345 wells.

The location of active wells in both scenarios are depicted in Figure 3-20. The location of the CSG (Arrow and non-Arrow) wells are presented for the base case FDP (Figure 3-20 (a) and (b)) and PL253 FDP scenarios (Figure 3-20 (c) and (d)). A summary of the number of Arrow's CSG wells included in the scenarios is presented in Figure 3-20, which includes a breakdown of wells expected to be completed into the Macalister Coal Seam and those expected to target the underlying coal seams.

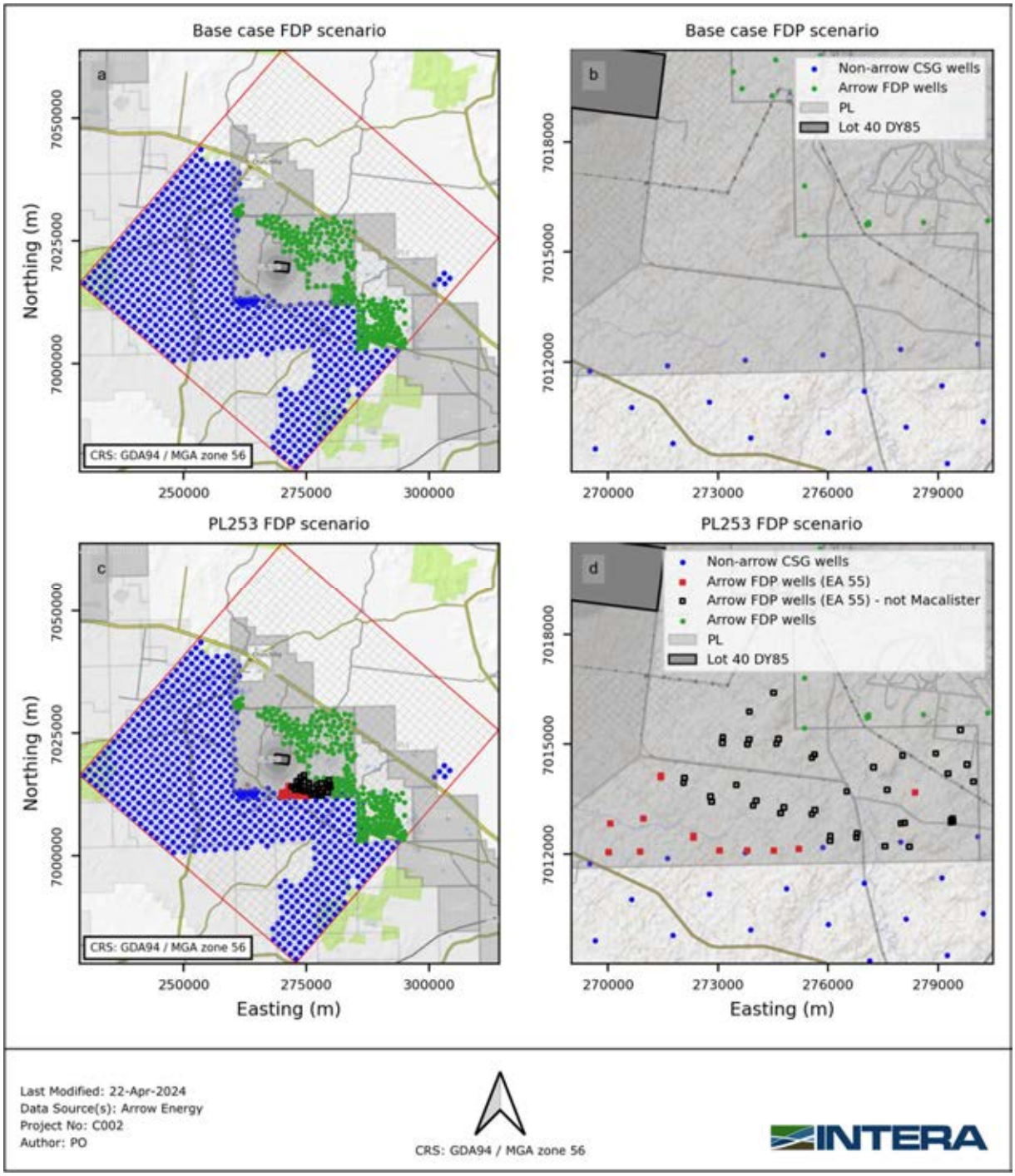


Figure 3-20 – Simulated predictive scenarios. (a) base case scenario (Non-arrow CSG wells and Arrow CSG wells not in PL253) and (b) zoom-in of area south-east from Lot40. (c) base case scenario including the 55 EA amended CSG wells and (d) zoom-in of area south-east from Lot40 showing the 55 wells.

Table 3-3 – Arrow CSG wells simulated in the two FDP scenarios.

| Scenario | Approval | CSG wells targeting Macalister | CSG wells targeting below Macalister | Total CSG wells |
|---|---|---|---|---|
| Base case FDP | Currently approved | 7 | 277 | 284 |
| | Hopeland Wells | 5 | 1 | 6 |
| PL253 FDP | Currently approved | 7 | 277 | 284 |
| | Hopeland Wells | 5 | 1 | 6 |
| | EA amendment | 12 | 43 | 55 |

### 3.3.2 Predictive Flow Model Setup

The setup of the predictive model remained unchanged from the history matching except for the extent of the simulated period, and Arrow's CSG wells which were simulated according to the two scenarios described in detail in section 3.3.1. Therefore, boundary conditions such as non-Arrow CSG wells, recharge, general head boundary, topographic surface drains, and gasifiers were identical to the history matching model setup.

The simulated predictive period covered a timeframe from 01-01-2025 to 01-01-2225, thus including the history matching period and 200 years after the end of that period. Up until 01-01-2025, the time discretisation remained the same as in the history matching period. From that date until 2200, each stress period corresponds to one year, resulting in a total of 311 simulated stress periods.

Both the Base case and Arrow FDP were simulated with all realisations of the history matched parameter ensemble. The impacts of the proposed Arrow FDP were estimated by comparing results between the Base case and FDP scenarios for each realisation.

### 3.3.3 Quantities of Interest

As water levels recover within the former UCG site recovers, contaminant movement away from site was expected to become more likely. Predictions of interest are the extent to which contaminants may disperse, the paths they can be expected to take and at the time at which they may be expected to migrate away from the site.

The following quantities of interest (QoI) derived from simulated outputs were considered:

- Year in which the hydraulic gradient at Lot40 inverts
- Vertical gradient between Springbok Sandstone and WCM Macalister

These were complemented with other derived model outputs and discussed in the following sections.

While the uncertainty in predicted outcomes remains substantial, the findings indicate that the impact of the PL253 FDP scenario on both the flow regime and particle transport near the former UCG site was relatively insignificant when compared to that of the Base Case FDP scenario.

### 3.3.4 Impact Prediction

Predicted groundwater pressure and the flow regime around Lot40 on DY85 is presented in the following section. Subsequently, gradient direction within the site and timeframe until recovery has occurred are also discussed.

#### 3.3.4.1 Hydraulic Heads

Spatial distributions of hydraulic heads were compared between scenarios to illustrate the evolution of gradients around the site at key moments in the forecast period for both FDP scenarios. To highlight the impact of proposed wells in the PL253 FDP scenario, the differences between heads are also shown, along with the associated spatial distribution of uncertainty.

Hydraulic heads are presented for the years 2021, 2024, 2030, 2050, 2080 and 2200. These years effectively represent the stages before, during, and after the FDP operations. Furthermore, the years 2050 and 2080 were chosen to emphasise the most likely period for the transition of the groundwater gradient at Lot40 from inward to outward.

Figure 3-21 displays maps of mean hydraulic heads in WCM Macalister simulated with the posterior ensemble under the PL253 FDP. Figure 3-22 shows the corresponding standard deviations. For the sake of brevity, similar maps for the Springbok Sandstone and Wambo Coal seams are included in Appendix D. Maps of the standard deviation of simulated hydraulic heads are also included in Appendix D. For comparison, maps of mean and standard deviation in hydraulic heads for the Base Case Scenario are presented in Appendix E.

Average simulated hydraulic heads in Figure 3-21 show the regional gradient from north-east to south-west during 2021 and 2024, as well as the cone of depression associated to the former UCG operation in the Macalister. In 2030, heads to the south-west rise on average 10 to 20 m, associated to changes in non-Arrow CSG production rates. Drawdown associated to the proposed 55 wells in PL253 is evident at this time, causing a shift in regional hydraulic gradients. However, as the cone of depression at Lot40 was still present, local gradients remained towards the site. By 2050, drawdown from CSG wells have begun to dissipate and mostly recovered by 2080. Recovery at Lot40 was still not complete by 2080. By 2200 hydraulic heads in Macalister would have mostly recovered. By this time, regional gradients in the Macalister were small and return to a north-east to south-west direction.

Standard deviation of simulated hydraulic heads in the Macalister are shown in Figure 3-22. Larger standard deviation implies greater uncertainty in simulated head at the respective model cell. Values displayed in Figure 3-22 show that uncertainty was larger at areas affected by both Arrow and non-Arrow CSG production wells, as well as at Lot40. The former illustrates uncertainty regarding the impact of CSG production on heads. The latter reflects uncertainty in time until recovery at Lot40, as will be discussed in a subsequent section.

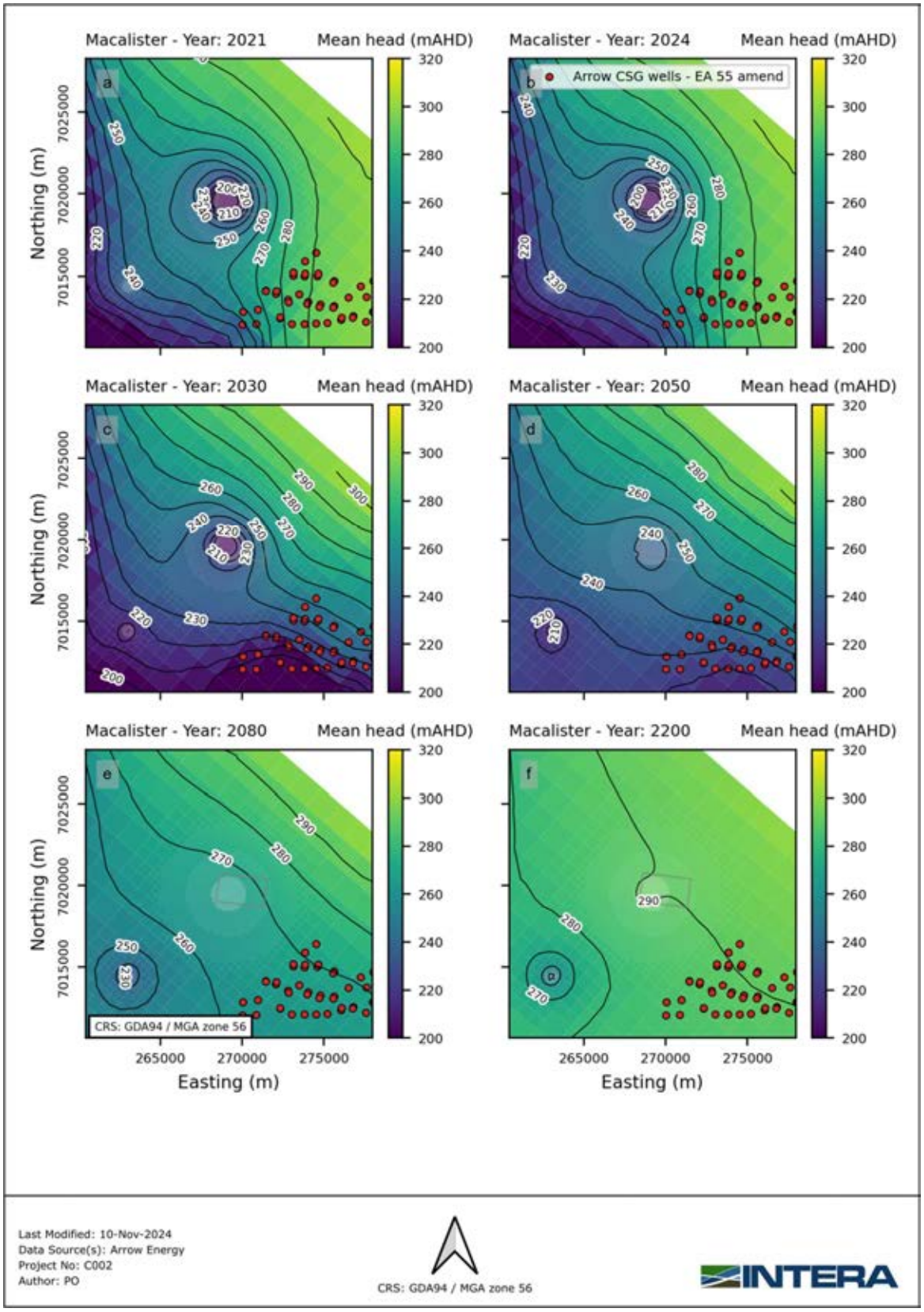


Figure 3-21 – Maps showing the mean in hydraulic heads for all posterior ensemble realisations (PL253 FDP scenario) in layer 6 (Macalister Coal Seam). Each subplot (a) to (f) displays the mean hydraulic heads for 2021, 2024, 2030, 2050, 2080 and 2200.

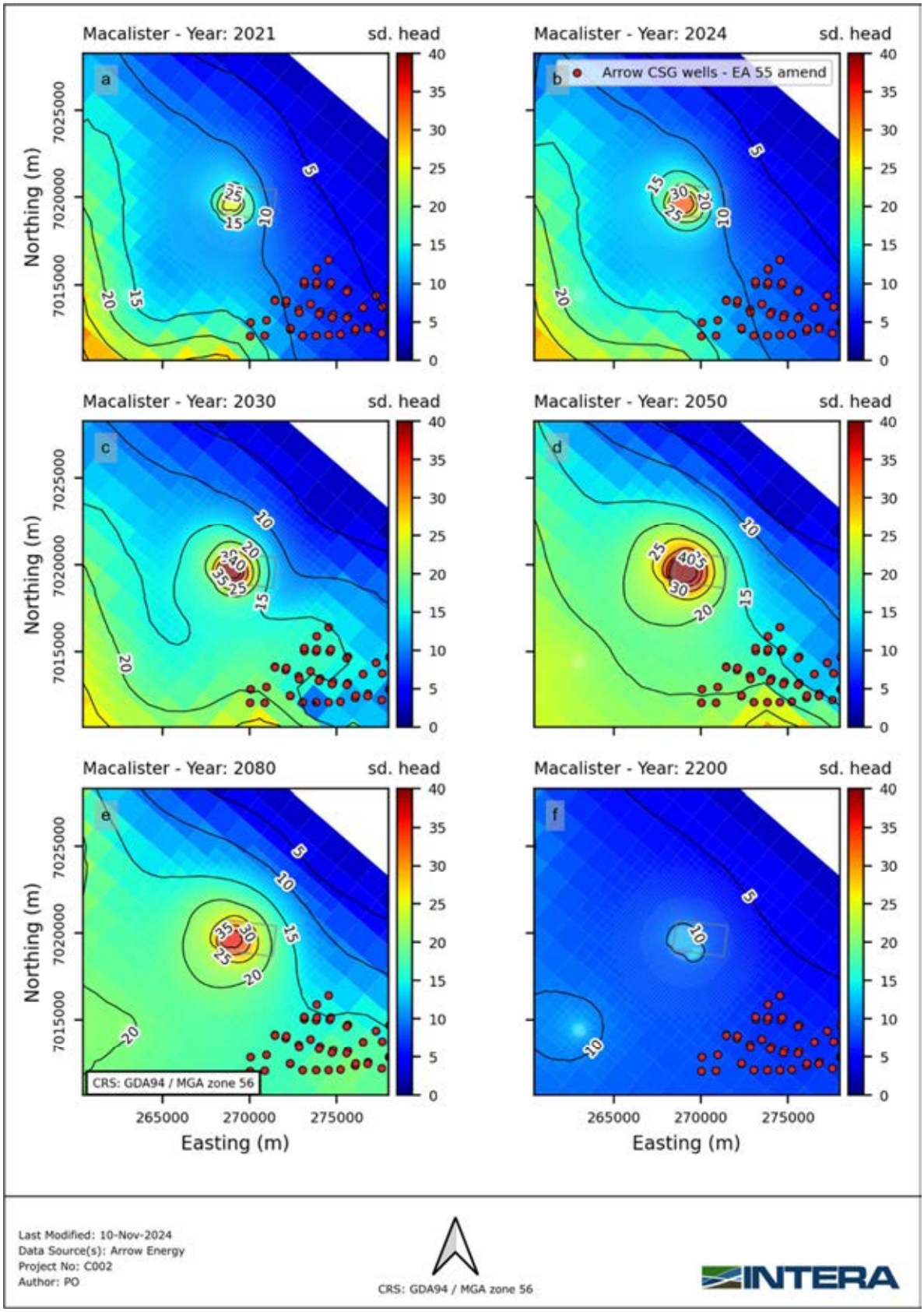


Figure 3-22 – Maps showing the standard deviation in hydraulic heads for all posterior ensemble realisations (PL253 FDP scenario) in layer 6 (Macalister Coal Seam). Each subplot (a) to (f) displays the mean hydraulic heads for 2021, 2024, 2030, 2050, 2080 and 2200.

#### 3.3.4.2 Difference in Hydraulic Heads

Figure 3-23 presents maps depicting the mean differences between the Base case and the PL253 FDP scenario for the Macalister. Similar figures for the Springbok and Wambo are included in Appendix F. Additionally, maps of the standard deviation of the differences between scenarios is also included in Appendix F. These figures were generated by calculating the difference in hydraulic head between each corresponding realisation in both scenarios, and then presenting the mean of those values.

As expected, the most significant differences between simulated scenarios occur during the period in which the 55 proposed wells in PL253 were active.

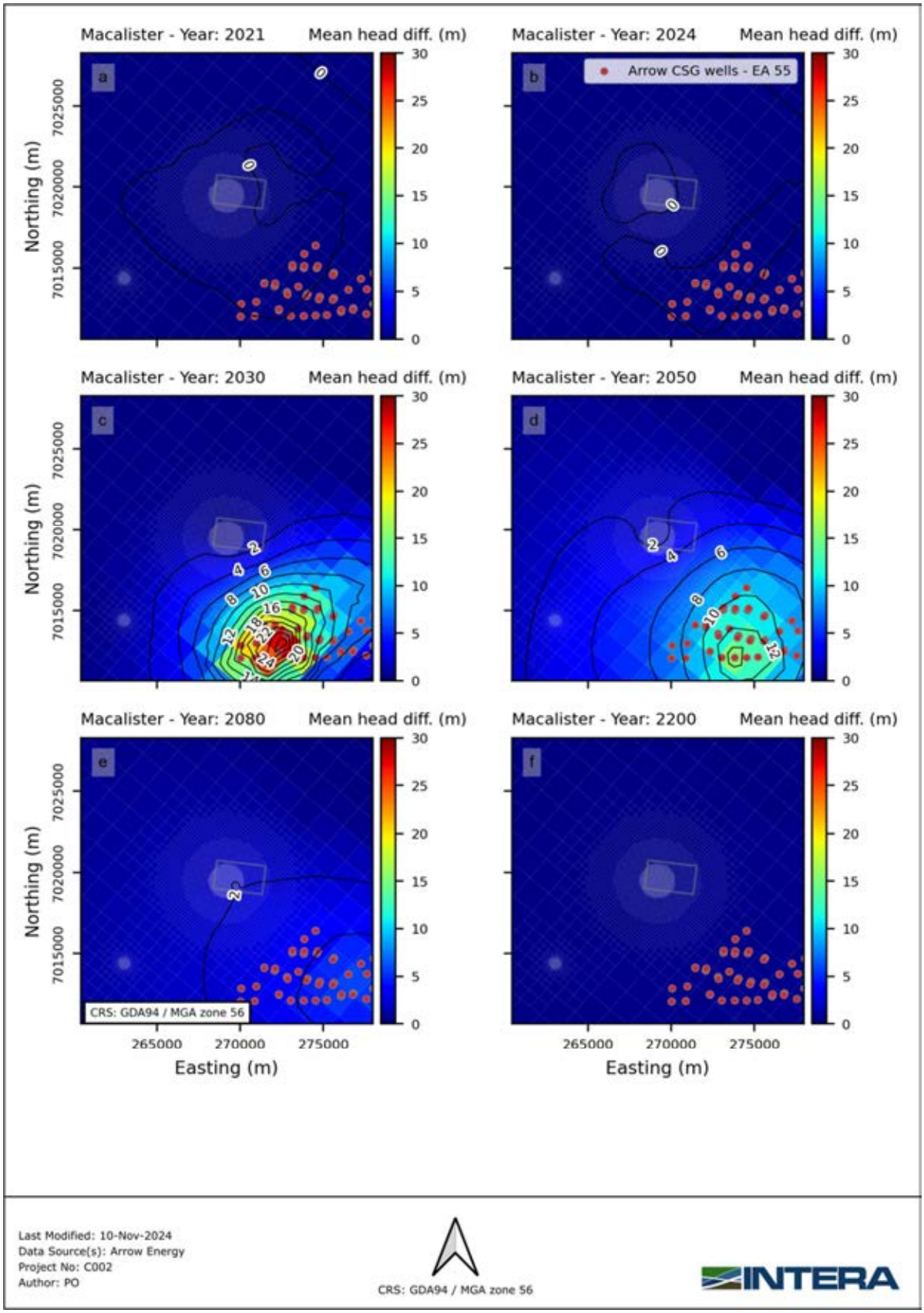


Figure 3-23 – Maps showing the mean difference in hydraulic heads between scenarios for all posterior ensemble realisations in layer 6 (Macalister Coal Seam). Each subplot (a) to (f) displays the mean difference in hydraulic heads for 2021, 2024, 2030, 2050, 2080 and 2200.

### 3.3.4.3 Hydraulic Gradient Reversal in Lot40

The following section presents results on the timeframe in which drawdown recovery at Lot40 enables groundwater flow away from the site.

Figure 3-24 (a and b) displays time-series of minimum simulated hydraulic heads within Lot40. Figure 3-24 (c and d) presents the difference between minimum head within Lot40 and at the boundary of the lot. The latter was employed as a proxy of the gradient across the lot boundary. When the difference was less than zero, some point within Lot40 has head lower than the lowest point along the boundary. This is an indication that, at some position on the boundary, the hydraulic gradient may be inwards. Once the difference becomes greater than zero, the gradient must be reversed. Figure 3-25 summarises the years in which inversion occurs. Given the relatively small area, and the lack of other stresses within the boundary, this metric provides an approximate indicator of horizontal gradient direction in- or outwards from the site.

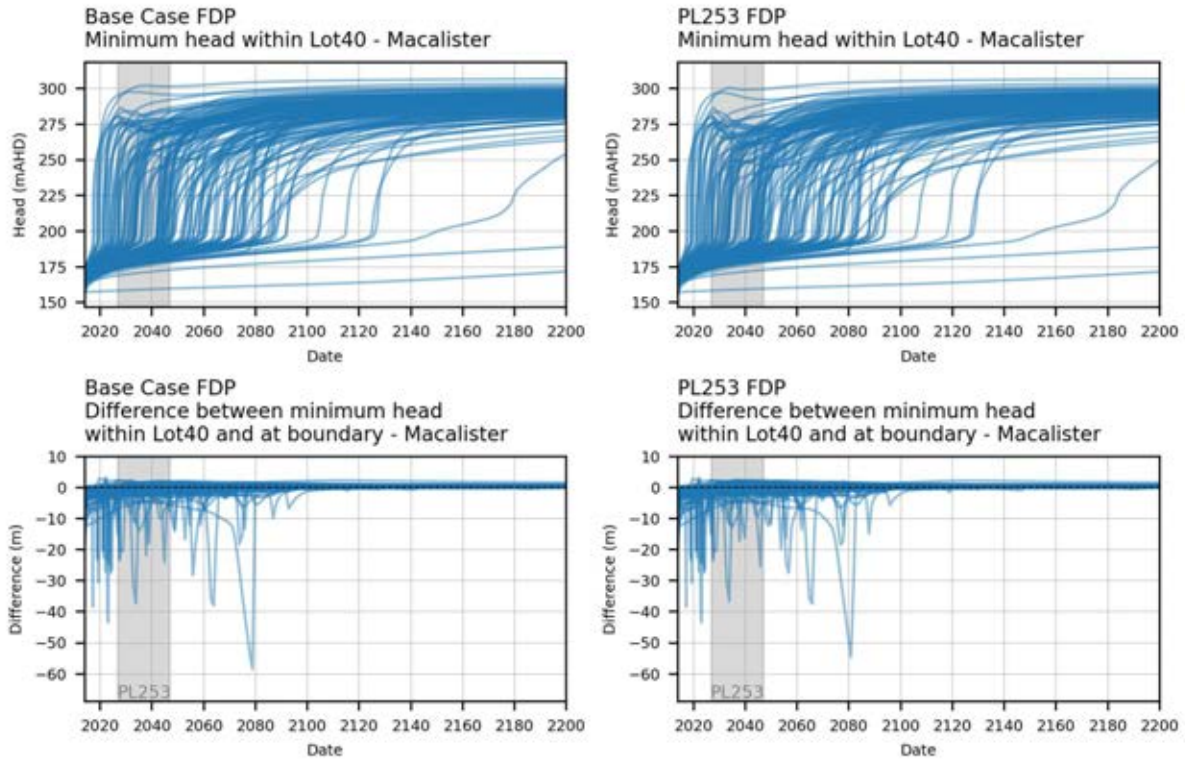


**Figure 3-24 – Ensemble of time-series of (top) minimum simulated head in the Macalister within Lot40 and (bottom) the difference between minimum head within the lot and at the boundary, employed as an indicator of horizontal gradient direction.**

Figure 3-25 displays histograms of the year in which gradient reversal occurs, based on the minimum head difference within and at the boundary of Lot40. As can be seen, simulated results suggest that gradient reversal may occur anytime between the present and the year 2100.

Results shown in Figure 3-24 and Figure 3-25 show that uncertainty was large regarding when recovery within Lot40 will occur. However, the differences between the Base case and PL253 FDP scenarios show that the influence of proposed production in PL253 is expected to have a minor impact on the rate of recovery and inversion of gradient from the lot.

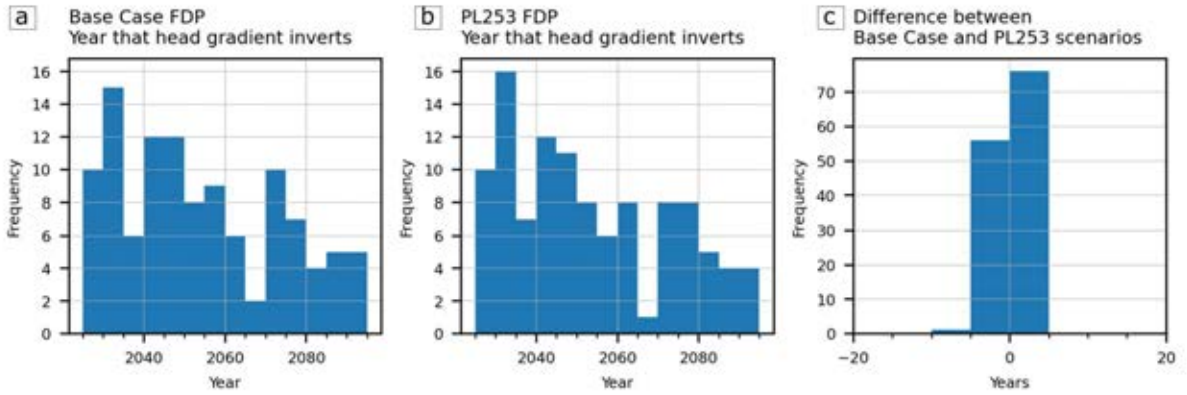


**Figure 3-25 – Histograms of year in which hydraulic head gradient in the Macalister is entirely outwards from Lot40 for the (a) Base case FDP, (b) PL253 FDP scenario and (c) the difference in years between FDP scenarios.**

Figure 3-26 (a and b) shows time-series of the maximum vertical head difference between the Macalister and Springbok layers within Lot40 for both scenarios. Again, uncertainty in the vertical gradient was large. However, simulated vertical head differences were always greater than zero, thus vertical flow direction was always downwards (from Springbok to Macalister). Vertical flow direction does not reverse during the simulated period.

Differences between the Base and PL253 FDP scenarios (Figure 3-26 c) were mostly between -10 and 10 m. Values less than zero indicate that the vertical differences for the PL253 FDP were larger (i.e., there was a stronger downward gradient in the PL253 FDP than in the Base case FDP). Time series shown in Figure 3-26 show characteristic peaks. These occur due to delays in the system returning to equilibrium for the PL253 FDP in comparison to the Base case.

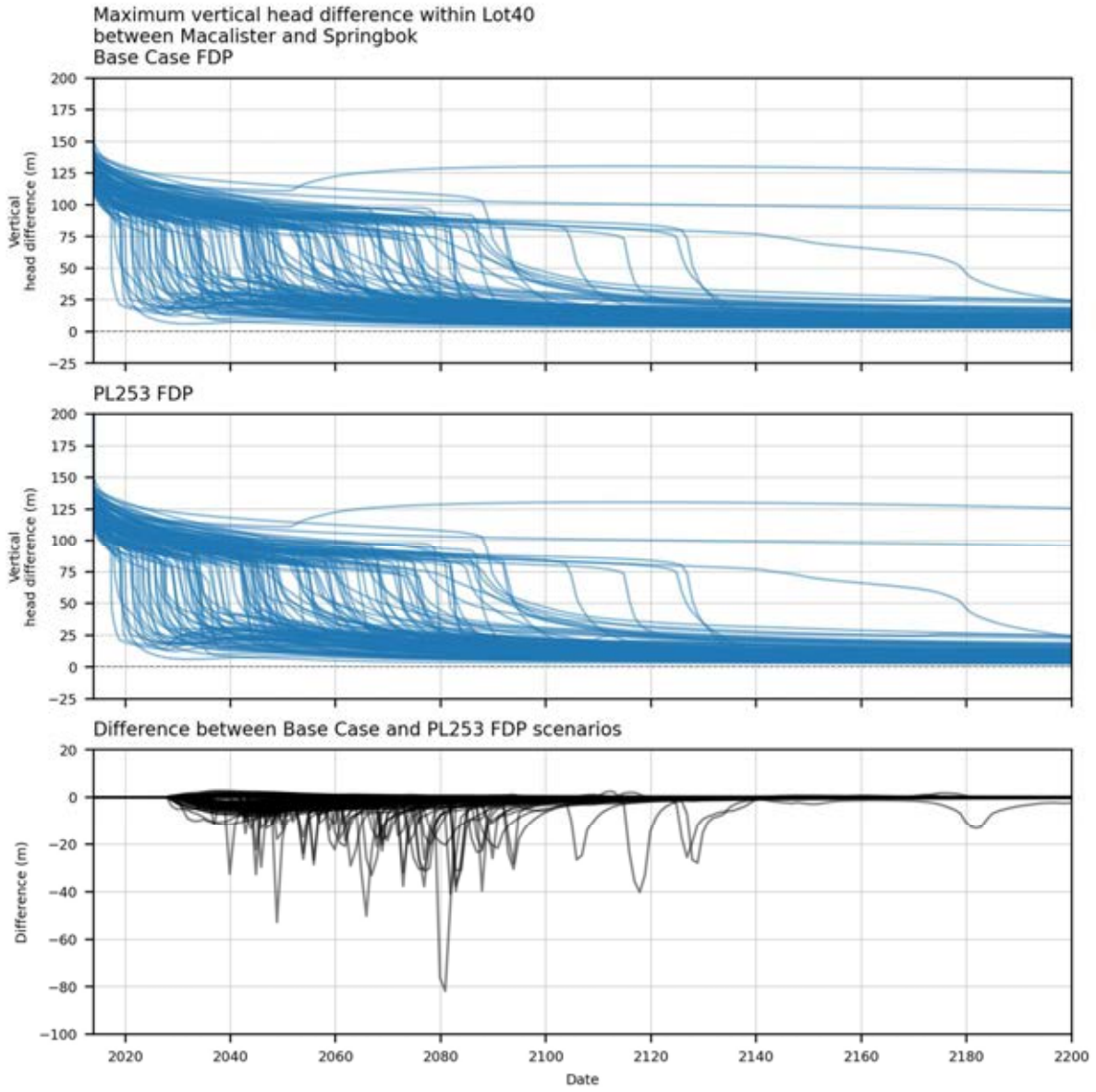


Figure 3-26 – Ensemble of time-series of simulated vertical head difference between the Springbok and Macalister layers within Lot40 for the (top) Base case FDP, (middle) PL253 FDP and (bottom) the difference between both scenarios.

# 4.0 Particle Tracking and Contaminant Transport Models

## 4.1 Approaches

Two approaches were considered to assess the impact of the proposed field development plan on migration of contaminants within PL253, in particular around and within Lot40 DY85. These include particle tracking and contaminant transport modelling.

First, the particle tracking model was used to assess potential contaminant flow paths without including natural attenuation processes, effectively simulating the centre of a plume of a conservative tracer. A contaminant transport model was then developed based on the groundwater flow numerical model. Unlike particle tracking model, the contaminant transport model includes mechanical dispersion, molecular diffusion, as well as natural attenuation (sorption and biodegradation/decay) and dual domain mass transfer processes continuously occurring within subsurface and have a profound impact on migration and attenuation of the existing contaminants.

## 4.2 Particle Tracking

### 4.2.1 Particle Tracking Model Description

Particle tracking was employed to assess potential contaminant flow paths under the Future Development Plan scenarios. The particle tracking was developed based on the history-matched groundwater flow model and did not undergo further history matching. Particle tracking will fulfill the following EA conditions Water 4(4) and Water 4(5):

4) Include a review and assessment of the density of particle tracking.

5) Include particle starting locations of:

a) multiple particles per cell, both horizontally and vertically,
b) multiple particles located on each edge of Lot40 DY85,
c) multiple particles on the northern edge of gasifier 5,
d) multiple particles at each groundwater monitoring well location including HSMB1S and HSMB4S,

6) Assess the effect of particle tracking starting in wells that have exhibited elevated Underground Coal Gasification contaminants.

7) Assess particle tracks (travel times, distances and trajectories) to inform where to best install new groundwater monitoring wells required by condition Water 5 and condition Water 11.

#### 4.2.1.1 Particle Sources

In their review of previous groundwater modelling at PL253, CSIRO (2023) recommended that a higher particle density be employed to allow a more comprehensive simulation of potential flow paths. Further recommendations included placing particles along the border of Lot40 and at monitoring bores where UCG related contaminants have been detected.

EA conditions specify that particles should be included in the following locations:

a) Multiple particles per cell, both horizontally and vertically,
b) Multiple particles on each edge of Lot40 DY85,

c) Multiple particles on the northern edge of gasifier 5,
d) Multiple particles at each groundwater monitoring well location, including HSMB1S-HSMB4S.

To address these recommendations, particles were placed in:

- Model cells along the border of gasifier cells in the Macalister and Springbok layers,
- Model cells along the border of Lot40 in the Macalister and Springbok layers,
- Model cells at monitoring bore locations, in the layers in which they were screened.

Additionally, multiple particles per cell both horizontally and vertically were considered and the sensitivity of selected model forecasts to the density of particle placement was assessed (see Appendix G). Outcomes suggest that 50 particles per cell provide sufficient resolution to capture simulated flow paths, both horizontally and vertically. 50 particles were placed within each model cell listed above. Particles were released in the year 2019, following the approach taken by AGE (2023).

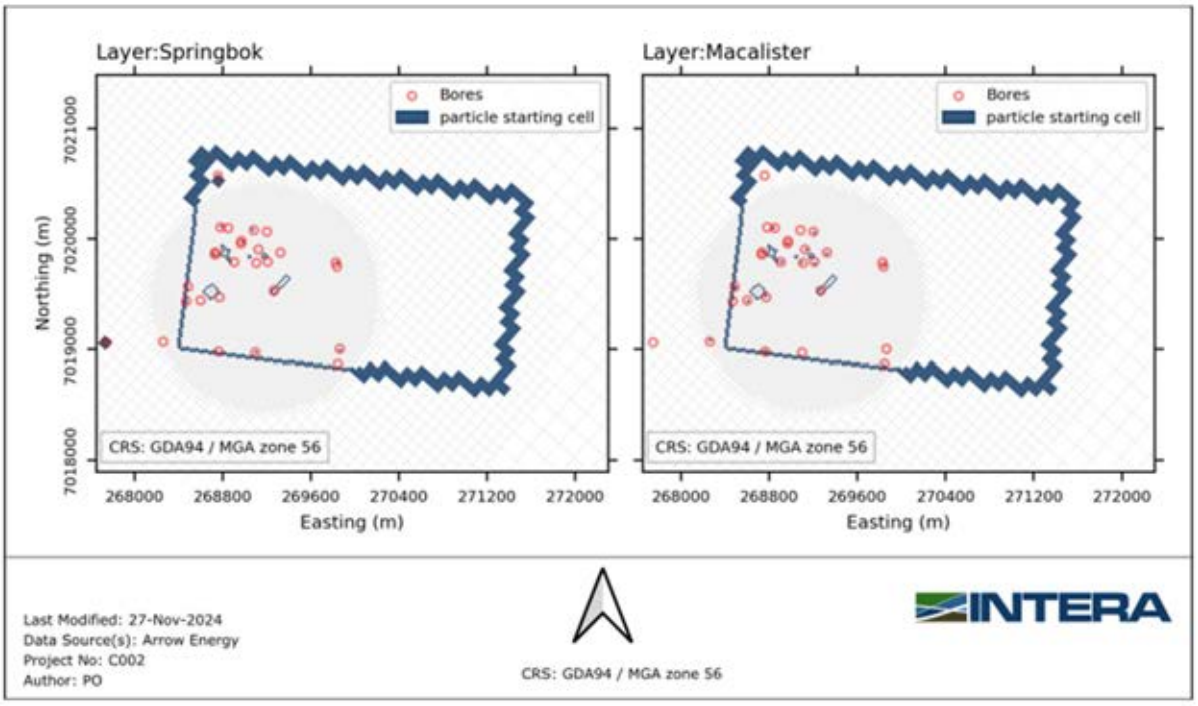


Figure 4-1 – Map of model cells in which particles were released.

#### 4.2.1.2 Effective Porosity

Effective porosity employed by the particle tracking model was parameterised as a function of specific yield (Sy) and specific retention (Sr). Spatial distribution of Sy was obtained during history matching of the groundwater flow model. Sr values were randomly sampled for each model layer, considering a log-normal distribution with a mean of 1%. Lower and upper bounds were 0.1% and 10%, respectively. Bounds reflect a range of 4 standard deviations.

Porosity values employed by the particle tracking model were computed from the sum of Sy and Sr (Table 4-1). Note that, where time-varying properties were imposed, values of Sy reflect post-UCG operation conditions.

Table 4-1 – Summary of porosity's mean, minimum and maximum values employed in the particle tracking model. Corresponding values of Sr and Sy are also presented.

| Layer | Sy | | | Sr | | | Porosity | | |
|---|---|---|---|---|---|---|---|---|---|
| | Min | Mean | Max | Min | Mean | Max | Min | Mean | Max |
| 1 | 0.002 | 0.036 | 0.20 | 0.001 | 0.016 | 0.1 | 0.003 | 0.052 | 0.30 |
| 2 | 0.001 | 0.017 | 0.10 | 0.001 | 0.020 | 0.1 | 0.002 | 0.037 | 0.20 |
| 3 | 0.001 | 0.015 | 0.27 | 0.001 | 0.023 | 0.1 | 0.002 | 0.038 | 0.37 |
| 4 | 0.001 | 0.023 | 0.34 | 0.001 | 0.020 | 0.1 | 0.002 | 0.043 | 0.44 |
| 5 | 0.001 | 0.019 | 1.00 | 0.001 | 0.021 | 0.1 | 0.002 | 0.040 | 1.00 |
| 6 | 0.001 | 0.304 | 1.00 | 0.001 | 0.023 | 0.1 | 0.002 | 0.327 | 1.00 |
| 7 | 0.001 | 0.019 | 0.10 | 0.001 | 0.020 | 0.1 | 0.002 | 0.038 | 0.20 |
| 8 | 0.001 | 0.017 | 0.10 | 0.001 | 0.016 | 0.1 | 0.002 | 0.033 | 0.20 |
| 9 | 0.001 | 0.018 | 0.10 | 0.001 | 0.021 | 0.1 | 0.002 | 0.039 | 0.20 |
| 10 | 0.001 | 0.016 | 0.10 | 0.001 | 0.021 | 0.1 | 0.002 | 0.038 | 0.20 |
| 11 | 0.001 | 0.017 | 0.10 | 0.001 | 0.020 | 0.1 | 0.002 | 0.038 | 0.20 |
| 12 | 0.001 | 0.018 | 0.10 | 0.001 | 0.018 | 0.1 | 0.002 | 0.036 | 0.20 |
| 13 | 0.001 | 0.021 | 0.10 | 0.001 | 0.019 | 0.1 | 0.002 | 0.040 | 0.20 |
| 14 | 0.001 | 0.025 | 0.10 | 0.001 | 0.022 | 0.1 | 0.002 | 0.047 | 0.20 |
| 15 | 0.001 | 0.016 | 0.10 | 0.001 | 0.021 | 0.1 | 0.002 | 0.038 | 0.20 |
| 16 | 0.001 | 0.019 | 0.10 | 0.001 | 0.020 | 0.1 | 0.002 | 0.040 | 0.20 |
| 17 | 0.001 | 0.018 | 0.10 | 0.001 | 0.019 | 0.1 | 0.002 | 0.036 | 0.20 |
| 18 | 0.001 | 0.016 | 0.10 | 0.001 | 0.024 | 0.1 | 0.002 | 0.040 | 0.20 |

## 4.3 Contaminant Transport Modelling

The contaminant transport model (it is also referred to solute transport model interchangeably) was developed based on the history-matched groundwater flow model (refer to Chapter 2.0), fulfilling the EA condition Water 4 (3):

a) uses the most recent water quality data for validation; and
b) has dual porosity or permeability capability (fracture and matrix) to better represent transport into and out of dead pore volumes and fractures that might contain residual sources of contaminants.

### 4.3.1 Model Description

Structural features of the solute transport model were inherited from the groundwater flow model, such as grid discretisation, flow boundary conditions, hydraulic properties, and defined stresses as the Arrow and non-Arrow CSG wells.

The model employed the solute transport solver of MODFLOW-6 (MF6), which supports the use of an unstructured grid while providing the option to use the advanced packages from MF6. It is noteworthy that the solute transport model was set up as an independent simulation from the groundwater flow model, providing the flexibility to use a different time-stepping scheme, if needed. History matching on the transport model was conducted from 01-01-2018 until 01-01-2025, similar to the initial model setup time from AGE (2023).

#### 4.3.1.1 Simulated Contaminants

Benzene and naphthalene were selected to be simulated due to their higher concentrations in the chemical data compared to the rest of the BTEXN (Benzene, toluene, ethylbenzene, xylene and naphthalene) compounds. These compounds were also adopted in previous modelling of the site (AGE, 2023). Furthermore, benzene has been shown to degrade more slowly than the rest of the BTEXN compounds (Prommer et al., 2003), making it a good indicator for the extent of contaminated groundwater. It is noteworthy that different hydrocarbon compounds exhibit varying degradation rates in groundwater, resulting in distinct time scales for contaminant depletion, thus highlighting the need to simulate more than one compound. At this stage, the decision was made to exclude the explicit simulation of a conservative compound, as explained in the following sub-section.

##### 4.3.1.1.1 Simulation of a Conservative Tracer

The use of a conservative (non-reactive) compound is highly informative when history matching solute transport models. Conservative tracers inform the extent to which dilution might be a controlling factor for the depletion of a plume, in addition to conditioning physical transport parameters (Prommer et al., 2003). This section aims to fulfill the EA condition Water 4 (12) as following: "*Discuss the value of using non-reactive chemicals as tracers to improve solute transport calibration*".

Typically, good non-reactive tracer are anions with low background concentrations, such as iodide, bromide, or even chloride, when the background-contaminated contrast is noticeable. The dataset provided by Arrow only includes information on chloride. Unfortunately, background concentrations of chloride could not be resolved with the available data. Sodium was discussed by Arrow as a possible non-reactive tracer due to its higher concentration in the hydrocarbon-bearing fluids, however it is subjected to sorption and cation exchange processes with calcium and magnesium in groundwater (Appelo and Postma, 2005).

Nevertheless, an approximation of the advective behaviour of a plume centre (i.e., how fast the front of a plume would move) of a non-reactive tracer was simulated using particle tracking, which is described in Section 4.2. Although particle tracking was not history-matched, it does provide a risk-conservative prediction of the extent of the contaminants.

#### 4.3.1.2 Boundary Conditions

##### 4.3.1.2.1 Contaminant Source

Following CSIRO (2023) advice, a continuous contaminant source was assumed to be present in the model in gasifiers locations. Previous studies (e.g., Eberhardt and Grathwohl, 2002) has shown that non-aqueous phase liquids (NAPL) compounds, such as benzene and naphthalene, tend to linger in the source zone and dissolve into the groundwater at a rate depending on the composition of the NAPL mixture, the solubility of the NAPL compounds, and the groundwater flow velocity. Eberhardt and Grathwohl (2002) have estimated timescales for NAPL source depletion in groundwater between weeks and thousands of years.

In the present work, the contaminant source was incorporated into the model in all cells representing the gasifiers (only in layer 6). The source was added using the Mass Source Loading package (SRC) from MF6, which allows the inclusion of a mass rate (mass per unit of time) into the system. The mass rate was updated during each stress period to account for the depletion of the NAPL source. The rate was subsequently updated employing a linear function and depending on the

initial mass rate in the gasifiers. These two parameters were included in the model parameterisation and uncertainty analysis. The linear decrease of the mass loading rate was an approximation aimed at reproducing the rate at which contaminants would be delivered into the groundwater from the source. This approach was consistent with observations from experimental and modelling studies of hydrocarbon source depletion (Eberhardt and Grathwohl, 2002), although it does not explicitly simulate the source.

#### 4.3.1.2.2 Initial Contaminant Distribution

Scarce to non-existent information of contaminant concentration was available during the operation of the gasifiers. The most comprehensive data dates back from 2018 with some bores (G5M11I, L22, M10, M10R, M14R, M15, RN24466, RN33553 and RN87897) presenting concentration data in 2016 and 2017 (see data points in Figure 4-2 and Table H.1 in Appendix H). Hence, it was deemed appropriate to include the initial conditions (contaminant distribution) from the year 2018 onward following the approach applied by AGE (2023).

The initial contaminant distribution was generated using Universal Kriging (see to Figure 4-2). The first data point from each bore was utilised and the Limit of reporting (LOR) was assumed to be representative of measurement below the LOR. This differs from the approach taken by AGE (2023), which used half of the LOR. The initial conditions were parameterised and included in the uncertainty analysis. This is further explained in Section 4.3.2.3.1. Initial conditions were then included in the model from the stress period corresponding to 01-01-2018, using the Constant Concentration (CNC) package from MF6.

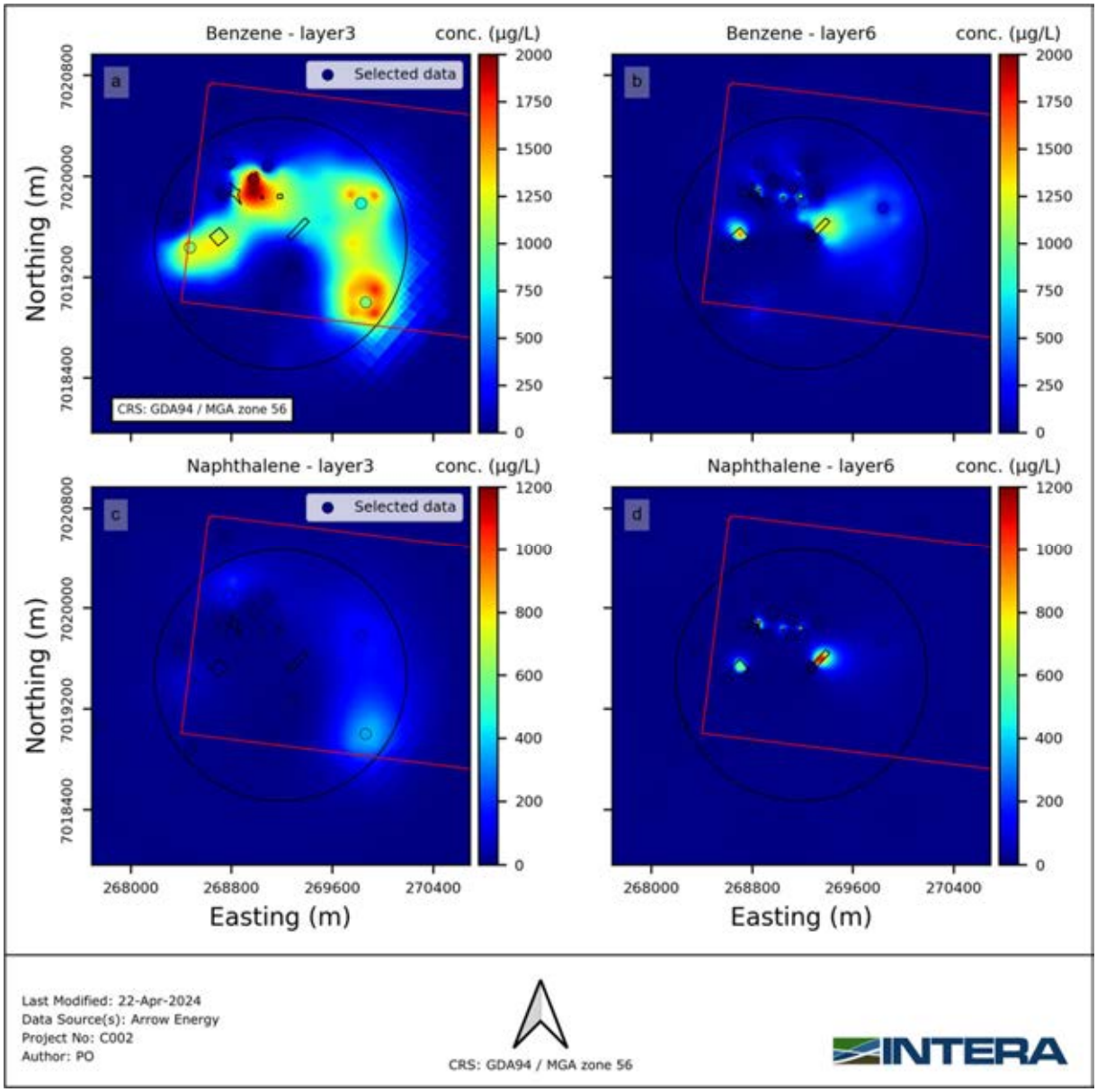


Figure 4-2 – Base realisation of the interpolated concentration field for benzene (subplots (a) and (b)) and naphthalene (subplots (c) and (d)) in layers 3 and 6. The selected monitoring bores and concentrations used for the interpolation are also presented.

#### 4.3.1.3 Transport Physical Properties

Upon dissolution in groundwater, hydrocarbon compounds undergo both advective and dispersive transport phenomena. Then, the advective-dispersive behaviour is mainly controlled by:

(1) Groundwater flow velocities and
(2) Mechanical dispersion from small scale variations in flow paths (at sub-cell scale).

Following the advice from CSIRO (2023) a dual-domain mass transfer approach was included to consider the diffusive transport to and from dead pores and microfractures.

The advective transport of the model was inherited from the groundwater model flow velocities using the ADV package from MF6 and was simulated using the total variation diminishing (TVD)

scheme solver. The following sections define the parameters relevant to mechanical dispersion and dual-domain mass transfer.

#### 4.3.1.3.1 Dispersivity

Dispersivity is an important property in solute transport. It accounts for the spreading of solutes as they travel through the aquifer. This process combines two processes: mechanical dispersion caused by variations in water velocity within the porous media, and molecular diffusion driven by concentration gradients. Dispersivity was set up with the DSP package of MF6. Values of longitudinal ($\alpha_l$), transverse horizontal ($\alpha_{th}$) and transverse vertical ($\alpha_{tv}$) dispersivity were defined for mechanical dispersion on a layer-by-layer basis. Molecular diffusion, on the other hand, was specified for each compound based on experimental data (Gustafson and Dickhut, 1994). The parameterisation of dispersivity, initial values and limits are presented in Section 4.3.2.3.

#### 4.3.1.3.2 Dual-domain Mass Transfer

In order to fulfill the EA Condition Water 4 (3) and following the advice from CSIRO (2023), the dual-domain mass transfer was included in the model to simulate the influence of cell-scale fractures and micropores (referred to as the immobile domain) that are not subjected to groundwater flow but interact with the aquifer through diffusion. This can cause transport deviations when compared to an ideal homogenous field, mainly controlled by preferential flow and rate-limited mass transfer between the immobile domain and the rest of the aquifer (hence the mobile domain) (Feehley and Zheng, 2000).

Dual-domain mass transfer was defined in the model by assigning a different porosity for each domain and a mass-rate transfer coefficient that governs the interaction between both domains. Essentially, solute concentrations in the mobile domain can “diffuse” in and out of the immobile domain depending on the concentration gradients.

The IST package from MF6 was utilised for this purpose. It is noteworthy that attenuation parameters such as sorption coefficients and degradation rates had to be assigned independently to both domains. These were included in history matching and predictive uncertainty analysis.

### 4.3.1.4 Natural Attenuation Properties

Biogeochemical processes, often referred to as natural attenuation, play a crucial role in determining the fate and transport of hydrocarbons. Simplified attenuation processes were included to simulate the interaction of dissolved hydrocarbons with the surrounding aquifer material.

#### 4.3.1.4.1 Sorption

The influence of sorption on the dissolved concentration of hydrocarbons varies with the type of aquifer material. However, this effect is only important when the flow field is transient or on the early stages of the contamination event (Prommer et al., 2002). Practically, an appropriate sorption model selection between linear and nonlinear (Freundlich or Langmuir) is adopted based on laboratory batch or columns experiments and can be extremely difficult to estimate based only on measured field aqueous data (Prommer et al, 2003). Initially, a non-linear sorption using Freundlich isotherm was incorporated into the model, following the advice from CSIRO (2023). However, the option to run a model with dual-domain mass transfer and non-linear sorption simultaneously is still under development by the U.S.G.S for MODFLOW-6 and currently undergoing testing. By incorporating non-linear sorption into the transport models, especially for benzene, we encountered

substantial non-convergence issues and non-tractable issues like extreme long runs. Therefore, a linear approach was adopted with a partition coefficient ($K_d$) defined as:

$$K_d = K_{oc}\, F_{oc} \tag{2}$$

Where $K_{oc}$ corresponds to the organic carbon-water partition coefficient and $F_{oc}$ denotes the fraction of organic carbon in the aquifer material. Initial values and upper and lower bounds of $K_{oc}$ were obtained from the published literature (references presented in Table 4-5) and values of $F_{oc}$ were estimated to have a mean of 35% for coal seam layers and 10% for non-coal seam layers, as per CSIRO (2023) advice. The parameterisation of sorption, initial values and limits are presented in Section 4.3.2.3.

To provide a comparison between linear and non-linear sorption using the model parameterisation, Figure 4-3 presents the ensemble of sorption rates (logarithmic axis scales) arising from the prior parameter ensembles. As it can be observed in that figure, the ensembles from linear and non-linear sorption overlap in a vast area of the plot and behave similarly at higher aqueous concentrations.

The main difference is that at lower aqueous concentrations the non-linear sorption model has a lower solid concentration. This suggests that the nonlinear sorption would be more risk conservative at low aqueous concentrations compared to the linear model. Therefore, the adoption of a linear sorption was sensible due to the tractability of the models and to achieve better convergence for the model ensembles.

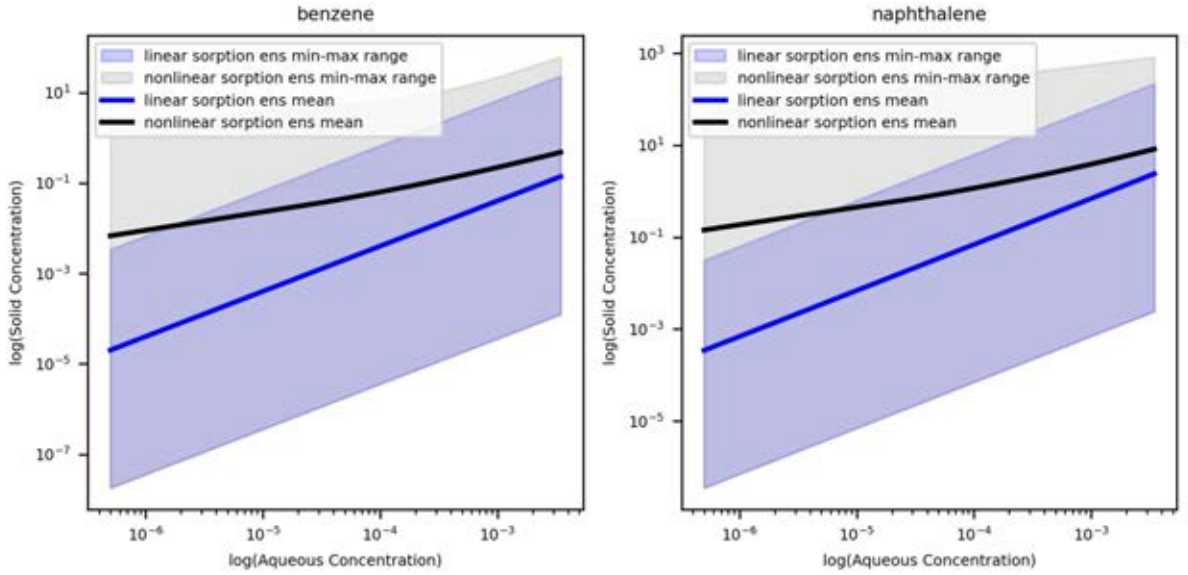


Figure 4-3 – Comparison between linear and non-linear sorption rates using the prior parameter ensembles for benzene and naphthalene.

#### 4.3.1.4.2 Degradation

Biologically mediated degradation (biodegradation) is one of the dominant processes that decreases the aqueous concentration of hydrocarbons, especially in the absence of groundwater stresses (Prommer et al., 2003). For the purpose of this model, biodegradation was included as a first-order decay function. The decay constant values were mainly obtained from Suarez and Rifai (1999), where a comprehensive compilation of several experimental (in situ, field and laboratory) data is

available. The parameterisation of degradation, initial values and limits are presented in Section 4.3.2.3.

## 4.3.2 History Matching

### 4.3.2.1 Approach and Period

The approach for history matching the contaminant transport model was the same as that of the groundwater flow model. Thus, PESTPP-IES (White et al. 2020) was used for history matching and uncertainty analysis. The same period as the history-matched groundwater flow model was set up covering from 01-01-2000 to 01-01-2025. The history matching of the transport model started from the history-matched posterior parameter ensemble from the groundwater model. Subsequently, only the transport-unique parameters were allowed to vary, and the hydraulic parameters were kept constant. Observations of measured concentrations of benzene and naphthalene were used as history matching targets.

### 4.3.2.2 Targets

#### 4.3.2.2.1 Contaminant Concentrations in Monitoring Bores

Time-series of aqueous concentrations of benzene and naphthalene collected at monitoring bores throughout the model domain were compared to simulated values at the corresponding cell in the model. The location of the bores within the model domain is presented in Figure 4-4 for bores in Springbok (Figure 4-4 (a)) and WCM Macalister (Figure 4-4 (b)), with a zoom-in highlighting the main bores within Lot40.

The vast majority of the observations were in layers 3 or 6 (i.e., Springbok and WCM Macalister), in particular around Lot40. The most comprehensive dataset dates back from 2018 in Lot40. As described for the groundwater flow model, this timeframe was discretised to monthly intervals. Thus, to match model outputs to measured times, MF6 simulated outputs were time-interpolated to the datetime at which measured data was recorded.

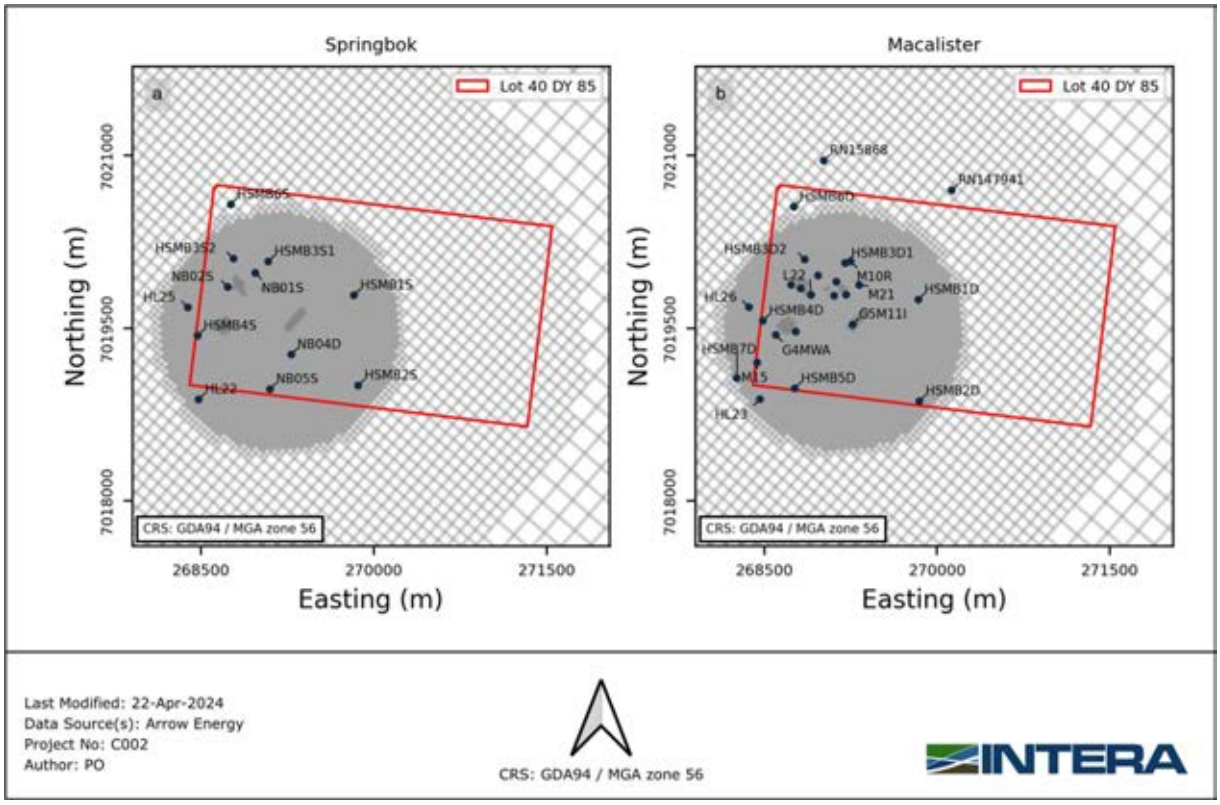


Figure 4-4 – Location of bores with concentration data employed as history matching targets in (a) Springbok and (b) Macalister.

### 4.3.2.3 Parameterisation

#### 4.3.2.3.1 Initial Concentration Fields

Ordinary kriging was used for generating realisations of the spatial distribution of benzene and naphthalene initial concentration. These realisations were then conditioned using the concentration data presented in Appendix H and described in Section 4.3.1.2.2. PESTPP-IES was used to conduct the conditioning, and 200 realisations were run for two non-variance reduction iterations. Subsequently, 159 of the 200 realisations were carried onto the prior parameter ensemble of the solute transport model for the history-matching process.

Evenly distributed pilot points were employed to interpolate the field of each realisation. These pilot points also carry spatially varying geostatistical parameters, which were adjusted directly. The geostatistical parameters were bearing, anisotropy, correlation length, and initial value (e.g., concentrations), which were allowed to vary according to the ranges described in Table 4-2. Covariance matrices for the pilot point geostatistical parameters were constructed using spatial correlations from an exponential variogram with the range depending on the average distance between pilot points and anisotropy of 1 (e.g., isotropic).

In addition to this set of evenly distributed pilot points, the following pilot points were also employed to incorporate 'soft' knowledge into the realisations of the concentrations field (Figure 4-5):

- Pilot points corresponding to the location of the observations (monitoring bores).
- Pilot points along a 1.5 km buffer with fixed value corresponding to the LOR.
- Pilot points at the centre of the gasifiers.

The pilot points coinciding with the location of monitoring bores were included to constrain the concentration values at these locations. Parameter bounds for pilot points coinciding with monitoring bores and concentration values above LOR were allowed to vary between 0.9 and 1.5 times the initial value, thus assuming a higher concentration at the start of 2018, adopting a risk-conservative approach.

On the other hand, parameter bounds for pilot points coinciding with monitoring bores and concentration values below the LOR were allowed to vary between 0.1 and 1.01 times the initial value (i.e., LOR). This assumes that these bores were likely to represent the absence of dissolved hydrocarbons.

The boundary constraint, applied using a 1.5 km buffer with pilot points around the perimeter, prevented the interpolation from overestimating the extent of the contaminant distribution. These parameter values were fixed and not adjustable.

Pilot points at the centre of the gasifiers were also included depending on the size of the gasifier area. Initial concentrations were assumed to be 1,000 µg/L (AGE, 2023). The parameter bounds were defined as the same as those for the evenly distributed pilot points (Table 4-2).

Table 4-2 – Hyper-parameterisation of evenly distributed and gasifier pilot points for prior conditioning.

| Geostatistical parameter | Lower bound | Upper bound | Initial Value |
|---|---|---|---|
| Concentration | 0.1 x LOR | 1.2 x maximum concentration | * |
| Bearing (°) | 0.0018 | 180 | 90 |
| Anisotropy | 1 | 10 | 1 |
| Correlation length (m) | 315 | 629 | * |

* Depends on initial interpolated values as described in section 4.3.1.2.2.

Measured concentration data, as detailed in Appendix H, were utilised as observations to inform the conditioning. Inequality observations were employed for concentrations above and below the LOR. Values below the LOR were configured as “less than” inequalities, while values above the LOR were configured as “greater than” inequalities. Localisation (e.g., Chen and Oliver, 2016) was used to ensure that observations of a specific component only inform the initial conditions of that component.

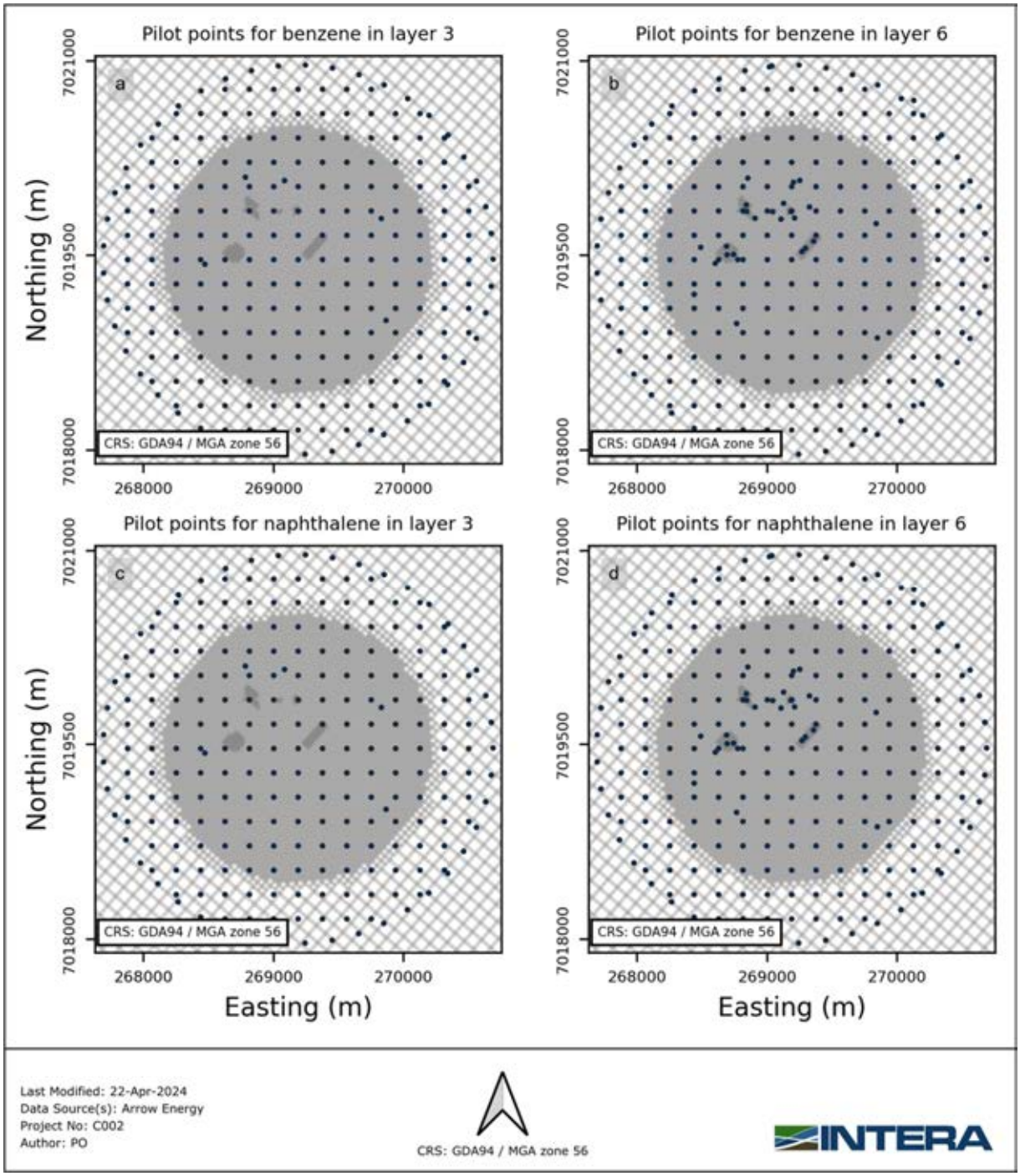


Figure 4-5 – Pilot points used for the initial concentration field of benzene and naphthalene in layers 3 and 6.

#### 4.3.2.3.2 Effective porosity

Effective or mobile porosity (i.e., of the mobile domain), used in the contaminant transport model, was parameterised as a function of specific yield (Sy) and specific retention (Sr). Spatial distribution of Sy was obtained during history matching of the groundwater flow model. Sr values were randomly sampled for each model layer.

Sr values were sampled from a log-normal distribution with a mean of 1%. Lower and upper bounds were 0.1% and 10%, respectively. Bounds reflect a range of four standard deviations. Porosity

employed in the transport model was computed from the sum of Sy and Sr (Table 4-3). Sr values were parameterised and subjected to history matching and thus resulting in variations of porosity and Sr compared to the particle tracking model.

**Table 4-3 – Summary of porosity's mean, minimum and maximum values employed in the contaminant transport model. Corresponding values of Sr and Sy are also presented.**

| Layer | Sy | | | Sr | | | Porosity | | |
|---|---|---|---|---|---|---|---|---|---|
| | Min | Mean | Max | Min | Mean | Max | Min | Mean | Max |
| 1 | 0.002 | 0.036 | 0.20 | 0.001 | 0.018 | 0.1 | 0.003 | 0.054 | 0.30 |
| 2 | 0.001 | 0.017 | 0.10 | 0.001 | 0.017 | 0.1 | 0.002 | 0.034 | 0.20 |
| 3 | 0.001 | 0.015 | 0.27 | 0.001 | 0.020 | 0.1 | 0.002 | 0.035 | 0.37 |
| 4 | 0.001 | 0.023 | 0.34 | 0.001 | 0.017 | 0.1 | 0.002 | 0.040 | 0.44 |
| 5 | 0.001 | 0.019 | 1.00 | 0.001 | 0.018 | 0.1 | 0.002 | 0.037 | 1.00 |
| 6 | 0.001 | 0.304 | 1.00 | 0.001 | 0.017 | 0.1 | 0.002 | 0.322 | 1.00 |
| 7 | 0.001 | 0.019 | 0.10 | 0.001 | 0.019 | 0.1 | 0.002 | 0.038 | 0.20 |
| 8 | 0.001 | 0.017 | 0.10 | 0.001 | 0.022 | 0.1 | 0.002 | 0.039 | 0.20 |
| 9 | 0.001 | 0.018 | 0.10 | 0.001 | 0.020 | 0.1 | 0.002 | 0.038 | 0.20 |
| 10 | 0.001 | 0.016 | 0.10 | 0.001 | 0.016 | 0.1 | 0.002 | 0.033 | 0.20 |
| 11 | 0.001 | 0.017 | 0.10 | 0.001 | 0.015 | 0.1 | 0.002 | 0.033 | 0.20 |
| 12 | 0.001 | 0.018 | 0.10 | 0.001 | 0.016 | 0.1 | 0.002 | 0.035 | 0.20 |
| 13 | 0.001 | 0.021 | 0.10 | 0.001 | 0.017 | 0.1 | 0.002 | 0.038 | 0.20 |
| 14 | 0.001 | 0.025 | 0.10 | 0.001 | 0.017 | 0.1 | 0.002 | 0.042 | 0.20 |
| 15 | 0.001 | 0.016 | 0.10 | 0.001 | 0.017 | 0.1 | 0.002 | 0.033 | 0.20 |
| 16 | 0.001 | 0.019 | 0.10 | 0.001 | 0.017 | 0.1 | 0.002 | 0.036 | 0.20 |
| 17 | 0.001 | 0.018 | 0.10 | 0.001 | 0.014 | 0.1 | 0.002 | 0.032 | 0.20 |
| 18 | 0.001 | 0.016 | 0.10 | 0.001 | 0.017 | 0.1 | 0.002 | 0.034 | 0.20 |

#### 4.3.2.3.3 Pilot Points

Pilot points were employed for spatially varying parameters such as longitudinal, transverse horizontal, and transverse vertical dispersivity, as well as immobile porosity and molecular diffusion. The spatial distribution of the pilot points matches the one used for the groundwater model, employing a combination of (fine-scale) pilot point and (coarse-scale) layer-wide multiplier parameters., as described in Section 3.2.4 and Figure 3-6. Initial values and bounds of dispersion parameters and molecular diffusion are presented in Table 4-4.

**Table 4-4 – Pilot points parameters initial values and bounds.**

| Dispersivity parameter | Compound | Initial value | Lower bound | Upper bound |
|---|---|---|---|---|
| $\alpha_l$ (m) | Benzene and Naphthalene | 20 | 1 | 30 |
| $\alpha_{th}$ (m) | Benzene and Naphthalene | 0.2 | 0.05 | 1 |
| $\alpha_{tv}$ (m) | Benzene and Naphthalene | 0.05 | 0.01 | 0.1 |
| Immobile porosity (%) | Benzene and Naphthalene | 0.1 | $5 \times 10^{-4}$ | 50 |
| Diffusion ($m^2/d$) | Benzene | $9.4 \times 10^{-5}$ | $8.9 \times 10^{-5}$ | $9.9 \times 10^{-5}$ |
| | Naphthalene | $6.5 \times 10^{-5}$ | $6.2 \times 10^{-5}$ | $6.8 \times 10^{-5}$ |

#### 4.3.2.3.4 Layer Constant Parameters

The following properties were parameterised as a constant value for both compounds and within each layer:

- Bulk density in the mobile and immobile domain,
- Mass exchange rate coefficient between mobile and immobile domain.

Bulk density parameter bounds were set up to vary between 1,400 to 1,900 Kg/$m^3$ for coal layers and 1,900 to 2,600 Kg/$m^3$ for non-coal layers, following the previous work by AGE (2023). Exchange coefficient was parameterised with bounds between $1x10^{-4}$ and $1x10^{-2}$ (1/d) with an initial value of $1x10^{-3}$ (1/d) and allowed to vary between layers.

In addition, compound-specific parameters that were also parameterised per layer but allowed to vary between compounds were:

- Sorption coefficients ($K_d$) in the aqueous and solid phases and in mobile and immobile domains,
- Degradation rate in both aqueous and solid phases and in mobile and immobile domains.

Sorption partition coefficients ($K_d$) were parameterised from the $K_{oc}$ coefficients values listed in Table 4-5. Mean, maximum and minimum values were used as initial values and upper-lower bounds, respectively. Moreover, $F_{oc}$ values were parameterised between 15 to 40% for coal layers, and $1x10^{-4}$ to 25% for non-coal layers (refer to Table 4-5for references). Same initial values and parameter bounds were applied for mobile and immobile domains.

**Table 4-5 – Compiled $K_{oc}$ Values from published literature**

| Components | $K_{oc}$ (L/kg) | $K_{oc}$ ($m^3$/kg) | Source |
|---|---|---|---|
| Naphthalene | 830 | 0.83 | Kishi et al., (1990) |
| | 843 | 0.84 | Vowles and Mantoura (1987) |
| | 871 | 0.87 | Karickhoff (1981) |
| | 907 | 0.91 | Stauffer and MacIntyre (1986) |
| | 912 | 0.91 | Hodson and Williams (1988) |
| | 960 | 0.96 | Southworth and Keller (1986) |
| | 1000 | 1 | Southworth and Keller (1986) |
| | 1000 | 1 | Kan and Tomson (1990) |
| | 1096 | 1.1 | McCarthy and Jiminez (1985) |
| | 1161 | 1.16 | Lokke (1984) |
| | 1290 | 1.29 | Rippen et al., (1982) |
| | 1300 | 1.3 | Karickhoff et al., (1979) |
| | 1333 | 1.33 | Karickhoff (1982) |
| | 1400 | 1.4 | Podoll et al., (1989) |
| | 1413 | 1.41 | Szabo et al., (1990a) |
| | 1440 | 1.44 | Rippen et al., (1982) |
| | 1445 | 1.45 | Szabo et al., (1990a) |
| | 1610 | 1.61 | Rippen et al., (1982) |
| | 1861 | 1.86 | Barrett et al., (1994) |
| | 1950 | 1.95 | Wood et al., (1990) |
| Benzene | 31 | 0.03 | Chiou et al., (1983) |
| | 38 | 0.04 | Seip et al., (1986) |
| | 44 | 0.04 | Seip et al., (1986) |
| | 49 | 0.05 | Abdul et al., (1987) |
| | 54 | 0.05 | Seip et al., (1986) |
| | 60 | 0.06 | Karickhoff (1981) |
| | 63 | 0.06 | Piwoni and Banerjee (1989) |
| | 66 | 0.07 | Szabo et al., (1990a) |
| | 74 | 0.07 | Szabo et al., (1990a) |

| Components | $K_{oc}$ (L/kg) | $K_{oc}$ ($m^3$/kg) | Source |
|---|---|---|---|
| | 83 | 0.08 | Karickhoff et al., (1979) |
| | 92 | 0.09 | Rogers et al., (1980) |
| | 100 | 0.1 | Rogers et al., (1980) |

Similarly, decay coefficients were parameterised from the mean and standard deviation of the combined data set from Suarez and Rifai (1999), as is described in Table 4-6. The mean of the data was considered as initial value and four times the standard deviation as the upper parameter bound for coal layers. For non-coal layers, the mean was set as the upper bound and $1x10^{-5}$ (1/d) as the initial value. This is due to an expected slower biodegradation rate in these layers. Molecular diffusion was allowed to vary +-50% of the initial value. Same initial values and parameter bounds were applied for mobile and immobile domains.

Table 4-6 – Decay data for benzene and naphthalene used in model setup and parameterisation.

| Compounds | Statistics | Decay (1/d) | | | |
|---|---|---|---|---|---|
| | | Field and Laboratory | In situ | Laboratory | All data combined |
| Benzene | Mean | 0.008 | 0.03 | 0.012 | 0.0167 |
| | SD | 0.016 | 0.006 | 0.02 | 0.014 |
| Naphthalene | Mean | 0.232 | 0.237 | 0.228 | 0.232 |
| | SD | 0.64 | 0.733 | 0.573 | 0.649 |

*Source: Suarez and Rifai (1999).

Finally, the source depletion linear rate and the Initial concentration in the source were parameterised as cell-scale parameters for all the cells corresponding to gasifiers (layer 6). A summary of the layered-constant parameterisation is presented in Table 4-7.

Table 4-7 – Summary of layered constant parameters. Initial values, upper and lower bounds.

| Parameter | Compounds | Layer | Initial value | Lower bound | Upper bound |
|---|---|---|---|---|---|
| Bulk density (Kg/ $m^3$) | Benzene and Naphthalene | Coal | 1,600 | 1,400 | 1,900 |
| | | Non-coal | 2,200 | 1,900 | 2,600 |
| Mass exchange rate (1/d) | Benzene and Naphthalene | All | $1x10^{-3}$ | $1x10^{-4}$ | $1x10^{-2}$ |
| Sorption - $K_{oc}$ ($m^3$/kg) | Benzene | All | 0.065 | 0.03 | 0.1 |
| | Naphthalene | All | 1.2 | 1.95 | 0.83 |
| Sorption mobile and immobile- $F_{oc}$ (%) | Benzene and Naphthalene | Coal | 35 | 15 | 40 |
| | Benzene and Naphthalene | Non-coal | 10 | $5x10^{-4}$ | 25 |
| Decay mobile and immobile (1/d) | Benzene | Coal | 0.0167 | $1x10^{-6}$ | 0.073 |
| | Naphthalene | Coal | 0.232 | $1x10^{-6}$ | 2.83 |
| | Benzene | Non-coal | $1x10^{-5}$ | $1x10^{-6}$ | 0.0167 |
| | Naphthalene | Non-coal | $1x10^{-5}$ | $1x10^{-6}$ | 0.232 |
| Source - initial rate (µg/d) | Benzene | All | 1 | 0.1 | 100 |
| | Naphthalene | All | 1 | 0.1 | 100 |
| Source - depletion rate slope (µg/$d^2$) | Benzene | All | $1x10^{-3}$ | $1x10^{-4}$ | $1x10^{-2}$ |
| | Naphthalene | All | $1x10^{-3}$ | $1x10^{-4}$ | $1x10^{-2}$ |

#### 4.3.2.3.5 Localisation

Following the approach used in the groundwater modelling, a localisation matrix was built in tandem with PESTPP-IES's automatic adaptive localisation option. Benzene and naphthalene concentrations (field observations) were used to update the contaminant transport model parameters that are common to both compounds such as bulk density and dispersivity. In addition, compound-specific parameters such as sorption coefficients and degradation rates were only informed by the corresponding compound observations.

### 4.3.2.4 Results

All 159 realisations remained in the contaminant transport posterior ensemble. Two iterations of PESTPP-IES were sufficient to achieve reasonable fit between measured observations and the simulated ensemble.

#### 4.3.2.4.1 Simulated Versus Measured Observations

Overall, the model was able to replicate observed concentrations of benzene and naphthalene. Therefore, Figure 4-6 presents a one-to-one plot where each observed measurement is compared to the value simulated by each ensemble realisation. The dotted black line represents the identity line, while the red dots represent observation noise. The grey and blue dots are simulated concentrations with the prior and posterior parameter ensembles, respectively. It is important to note that for each observed value, there are 159 simulated values (one for each parameter realisation).

The simulated posterior ensemble was able to reproduce lower values of concentrations but struggled with the higher concentrations. Higher concentrations were typically observed at the beginning of the time series for each bore, while lower concentrations observed towards the end of the time series. Thus, matching this behaviour suggests that the model is reproducing the main effects from the processes affecting the attenuation of the contaminants, which is important for making reasonable predictions.

Concentrations of benzene above 2,000 ug/L were not matched. These observations correspond to the bores NB01S and HSMB3S2. The first bore showed an uptrend from 2,000 to >4,000 since 2018. HSMB3S2 depicted an initial concentration in 2018 followed by two high concentrations data events in 2019 that do not agree with the long-term trend. Similarly, HSMB3S2 shows high concentrations of naphthalene in 2019 which were also not matched in the posterior simulated ensemble.

In addition, statistical distribution of Root Mean Square Error (RMSE) and Scaled Mean Square Error (scaled RMSE) are shown in Figure 4-7. All realisations of benzene and naphthalene achieved scaled RMSE values (Figure 4-7 (b) and (c)) below the 10% target typically adopted for transient calibration (Barnett et al, 2012).

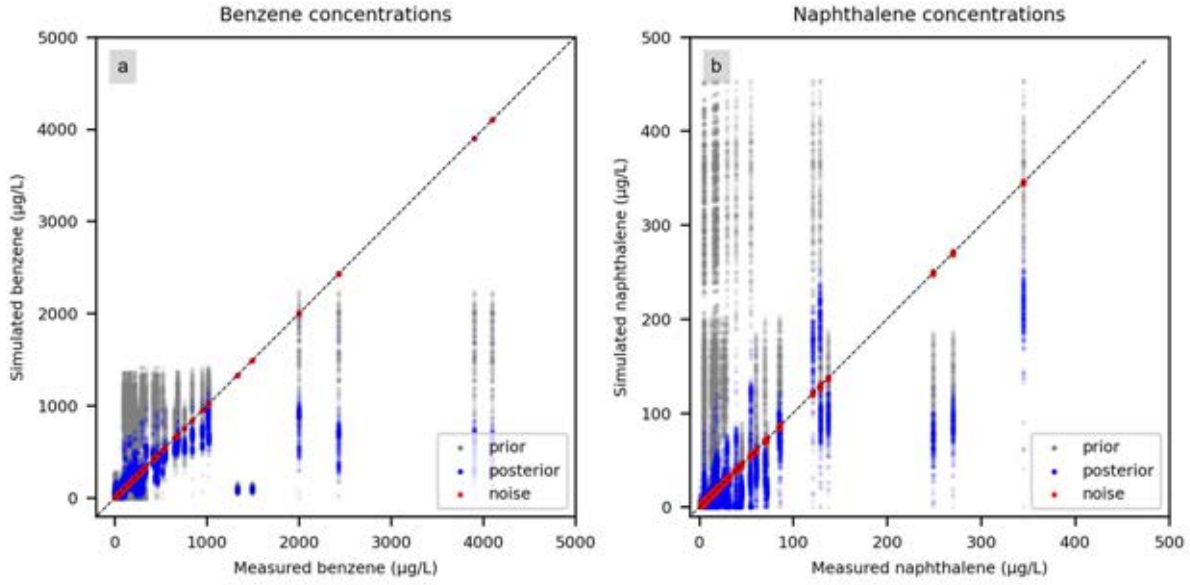


Figure 4-6 – One-to-one plot. Comparison between measured and simulated values for concentrations of (a) benzene and (b) naphthalene for the prior (grey dots) and posterior (blue dots) ensembles. The solid black line corresponds to the identity line.

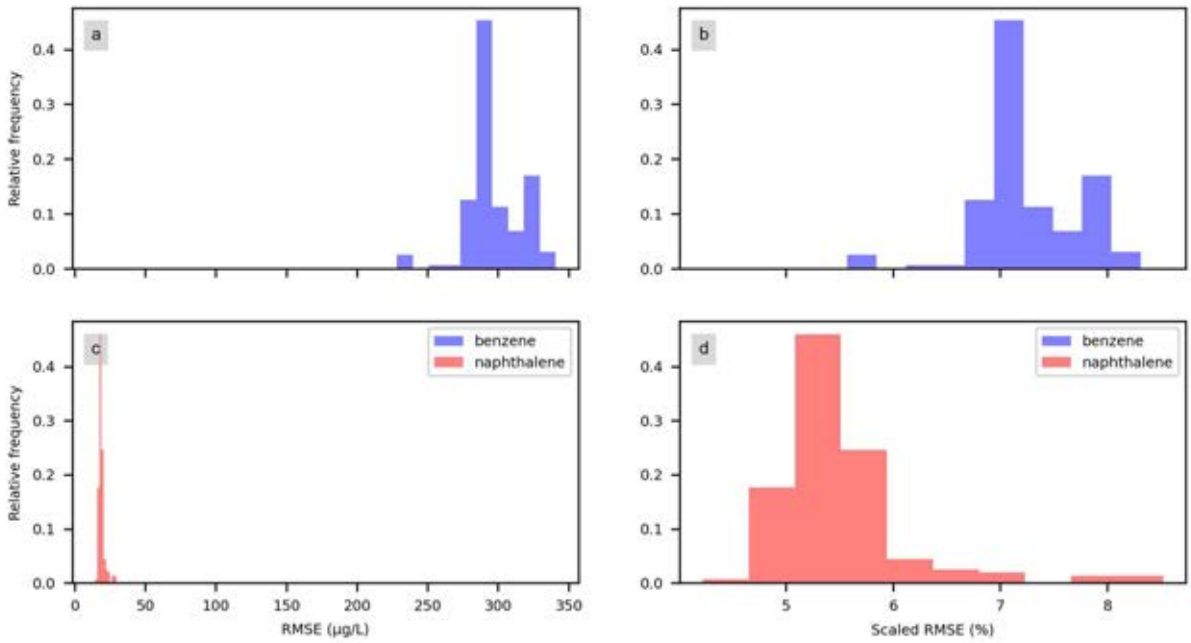


Figure 4-7 – Posterior ensemble metrics of (a) benzene RMSE, (b) benzene scaled RMSE, (c) naphthalene RMSE and (c) naphthalene scaled RMSE, calculated from the simulated concentrations.

#### 4.3.2.4.2 Simulated Benzene – Time-Series

Plots of the simulated benzene concentrations from the posterior ensemble at bores of interest, compared against measured data, are presented for Macalister (Figure 4-8 and Figure 4-9) and Springbok (Figure 4-10). The realisations from the posterior ensemble captured the behaviour of benzene in bores that either depict a decline in concentration or remain stable (e.g., HSMB3D1, HSMB5D, HSMB6D, M10R, and M15), while struggled to reproduce increasing concentrations. It is

noteworthy that the posterior ensemble was able, more often than not, to reproduce the declining measurements of each bore. Additionally, when the posterior ensemble did not match the observed concentrations, as in G4MWD, HSMB1D and HSMB3S1, it simulated higher concentrations than observed.

Simulated benzene in Macalister usually matched or underestimated the observations when these were below LOR (e.g., M15 and M10R). It is noteworthy that bores showing an increase in concentration preceded by a decrease in concentration (M14R, M22, and NB02D) were not able to be reproduced, even with the inclusion of a contaminant source rate in the gasifiers.

Simulated benzene in Springbok (Figure 4-10) was able to capture the measured observations as it is shown in bores HSMB1S, HSMB2S, HSMB4S and HSMB6S. Similar to bores in Macalister, the posterior ensemble overestimated the concentration in bores that did not match, as in HSMB3S2. In addition, simulated benzene in Springbok matched or underestimated the observations when these were below LOR (e.g., HSMB7S). It is noteworthy that, the only bore not captured by the posterior ensemble was NB01S, which is the only bore increasing in concentration in Springbok. This could suggest the existence of remnant contaminant source close to NB01S that are not yet characterised.

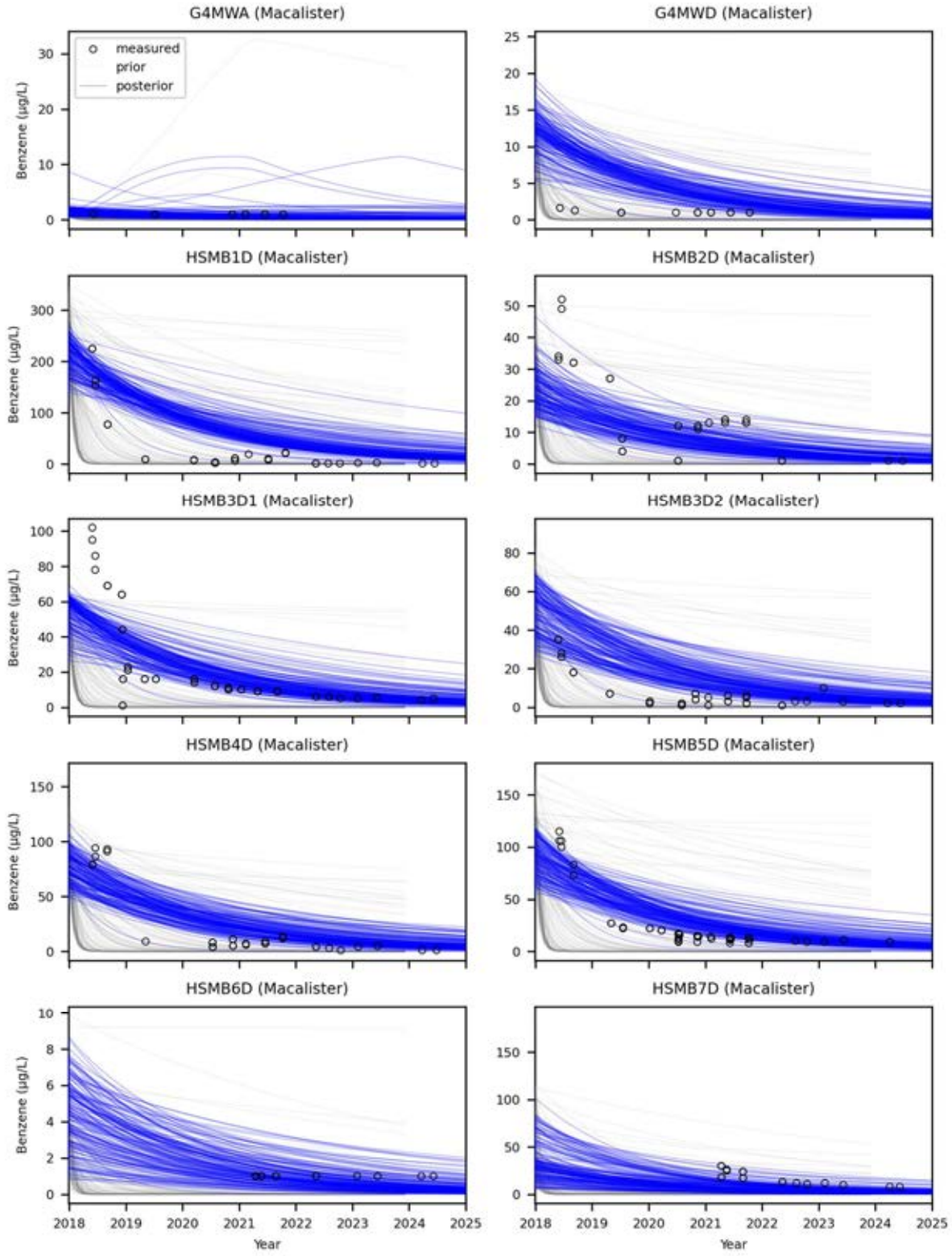


Figure 4-8 – Comparison between measured time-series of concentrations of benzene in WCM (G4MW and HSMB bores), noise and simulated values. Line colours denote prior (grey lines) and posterior (blue lines) simulated ensemble.

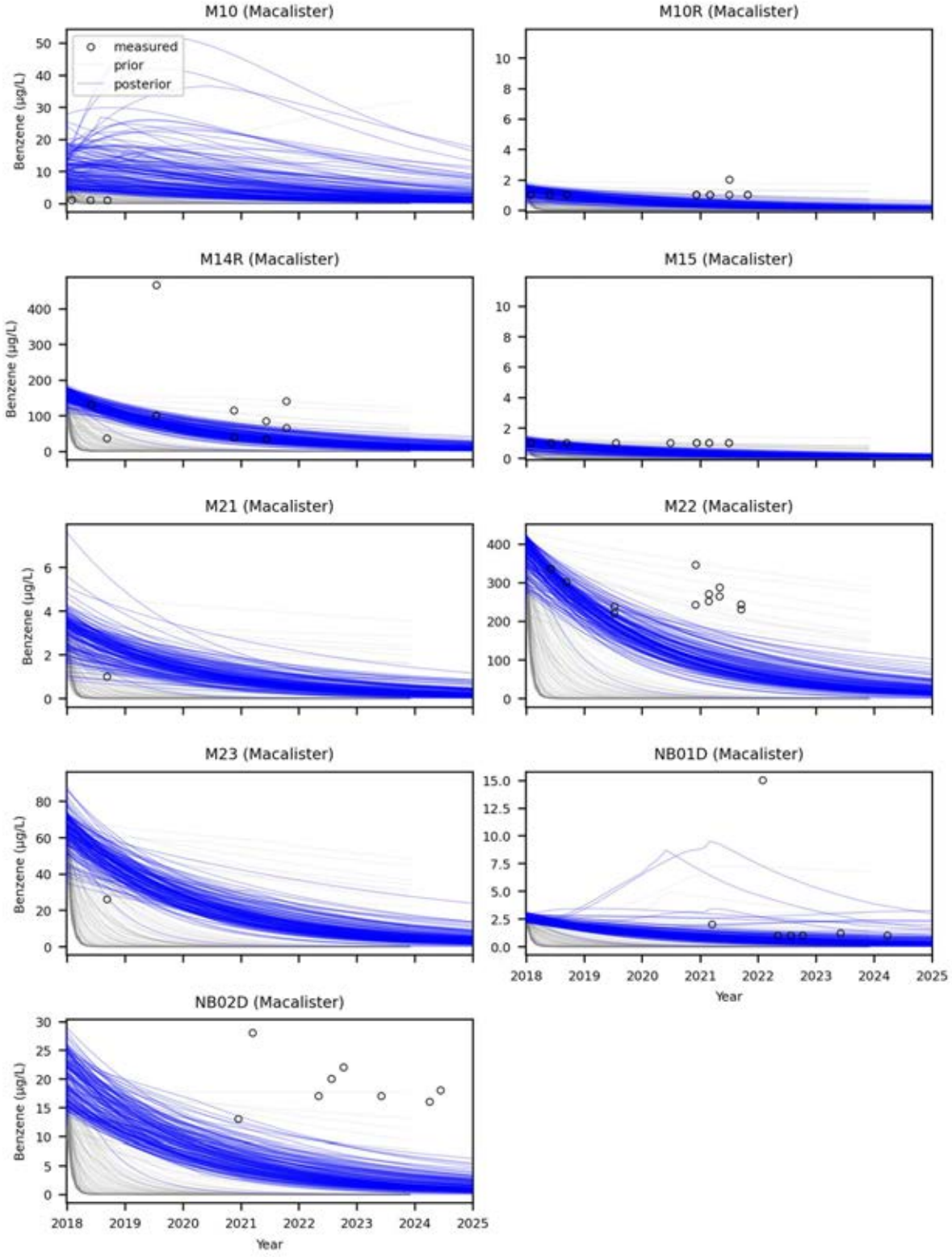


Figure 4-9 – Comparison between measured time-series of concentrations of benzene in WCM (M and NB bores), noise and simulated values. Line colours denote prior (grey lines) and posterior (blue lines) simulated ensemble.

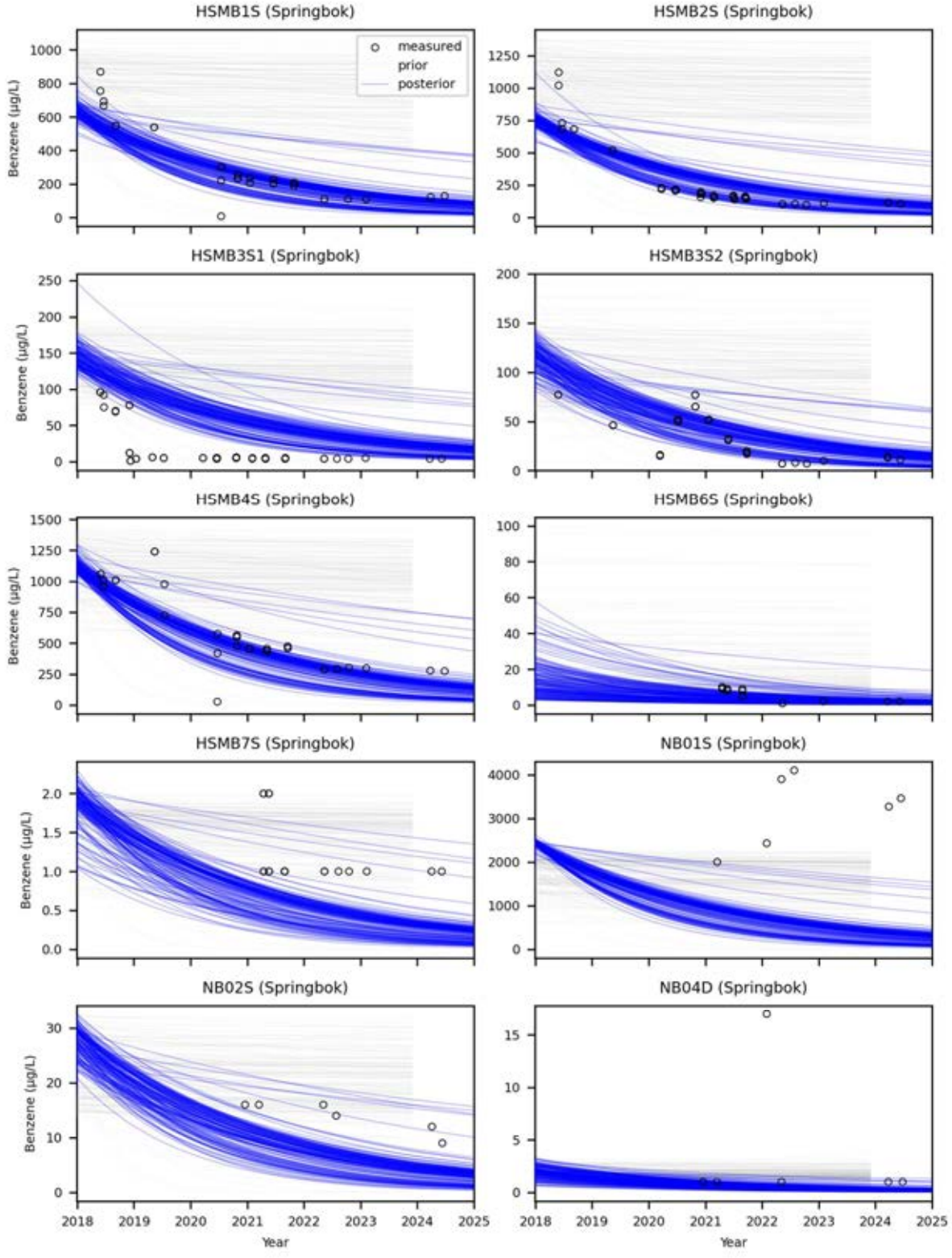


Figure 4-10 – Comparison between measured time-series of concentrations of benzene in Springbok, noise and simulated values. Line colours denote prior (grey lines) and posterior (blue lines) simulated ensemble.

#### 4.3.2.4.3 Simulated Benzene – Spatial Distribution Over Time

The posterior ensemble of simulated benzene exhibits attenuation over time between 2018 and 2024 for both Springbok Sandstone and WCM Macalister. However, this trend accompanies significant variability across posterior realisations. To visualize this, Figure 4-11 and Figure 4-12 depict the spatial distribution of benzene for the years 2018, 2020, 2022, and 2024. In these figures, ensemble mean maps are displayed in the left column, accompanied by standard deviation maps in the right column, illustrating the variability in contaminant distribution.

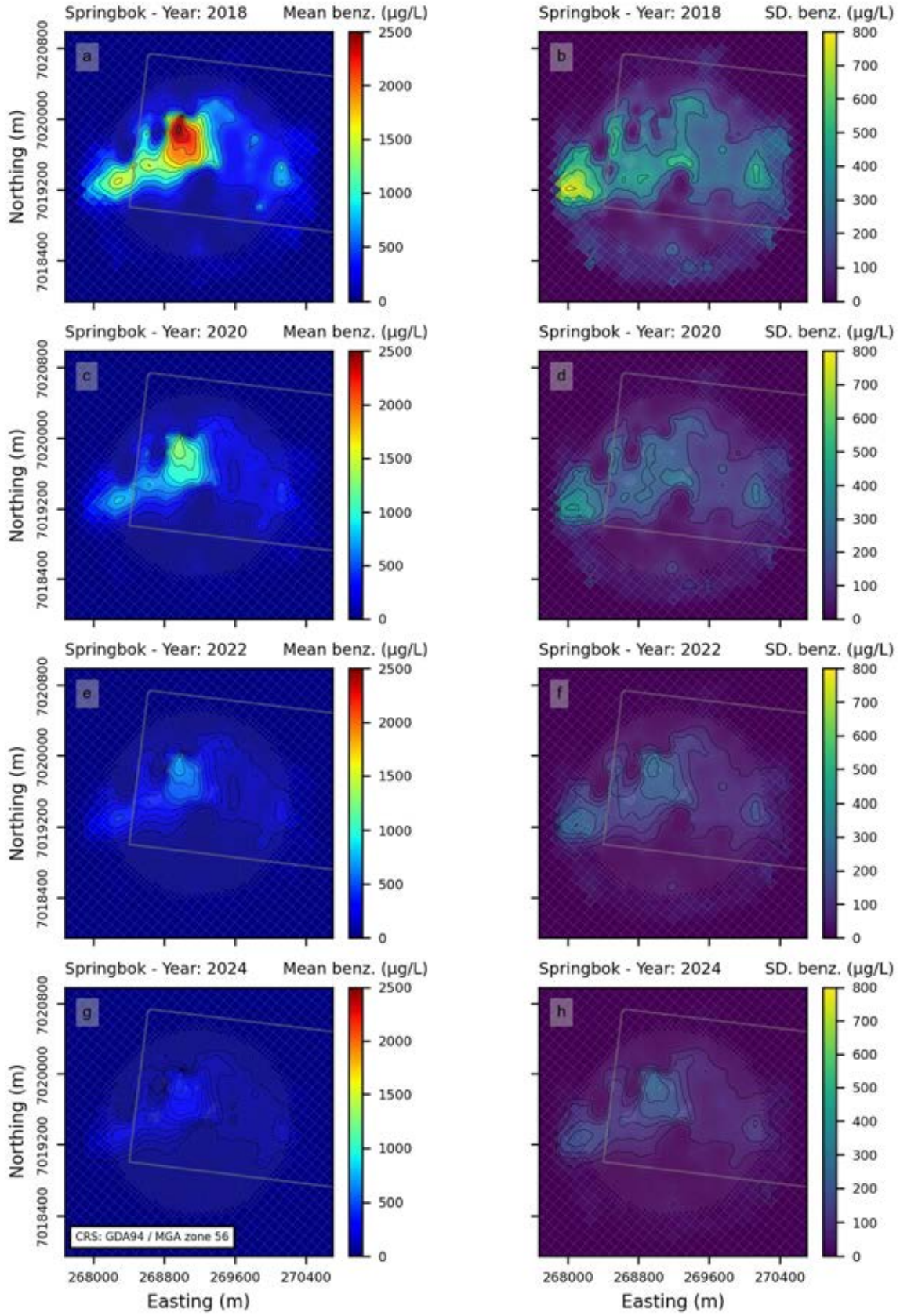


Figure 4-11 – Simulated benzene concentration maps for Springbok Sandstone. The left column displays ensemble mean concentration maps spanning from 2018 to 2024, while the corresponding standard deviations of the posterior ensemble are depicted in the right column.

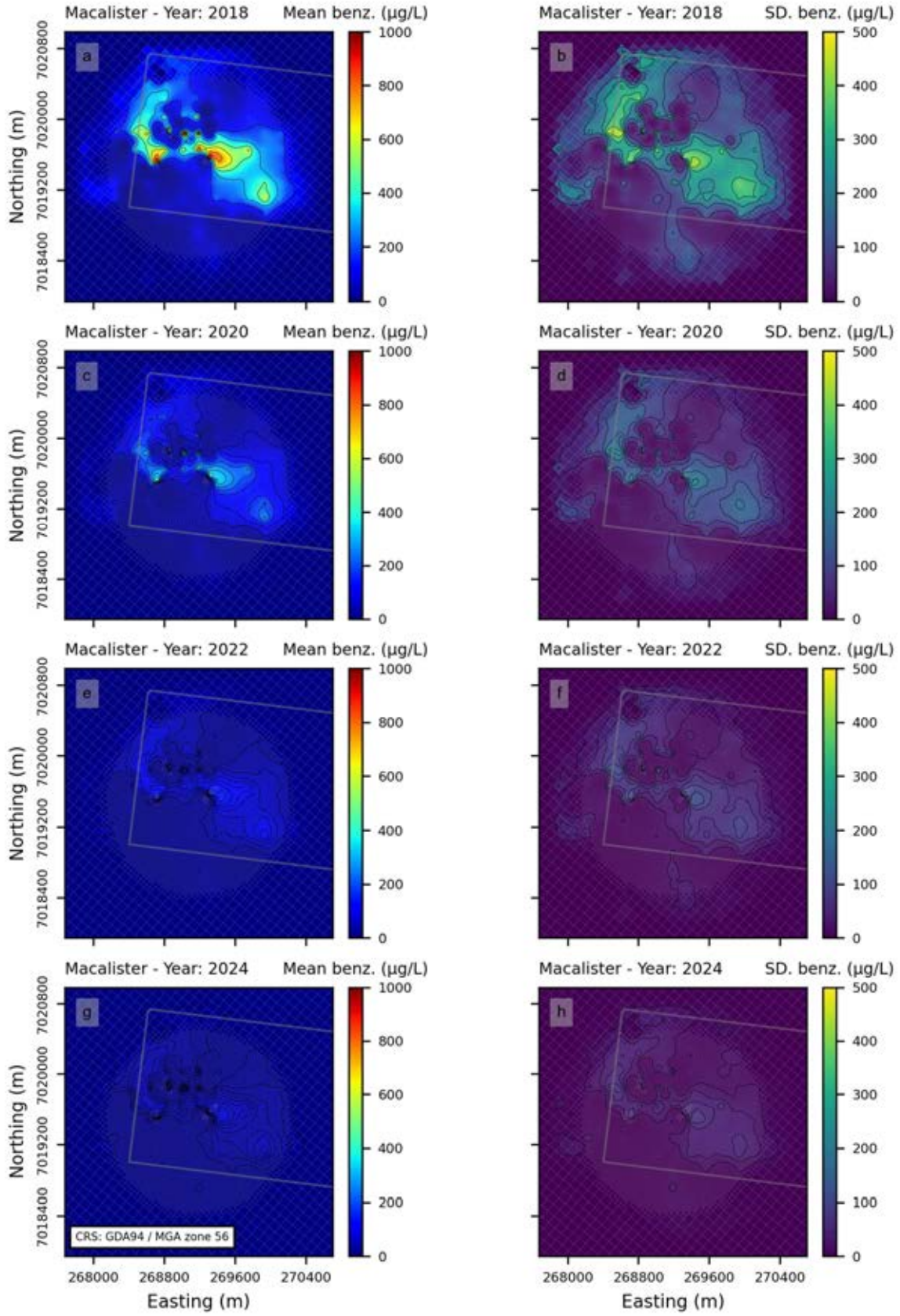


Figure 4-12 – Simulated benzene concentration maps for WCM Macalister. The left column displays ensemble mean concentration maps spanning from 2018 to 2024, while the corresponding standard deviations of the posterior ensemble are depicted in the right column.

#### 4.3.2.4.4 Simulated Naphthalene – Time-Series

Plots of the simulated naphthalene concentrations against measured data from the posterior ensemble at bores of interest are presented for Macalister (Figure 4-13 and Figure 4-14) and Springbok (Figure 4-15). In general, the realisations from the posterior ensemble captured the behaviour of naphthalene. In line with this, simulated naphthalene showed fewer points with prior data conflict than the simulated benzene.

Simulated naphthalene in Springbok (Figure 4-15) was able to capture the measured observations as it is shown in bores HSMB1S, HSMB2S, HSMB3S1, HSMB3S2, HSMB4S and HSMB6S. Simulated naphthalene in Springbok matched or underestimated the observations when these were below LOR (e.g., HSMB7S, NB01S, NB02S and NB04D).

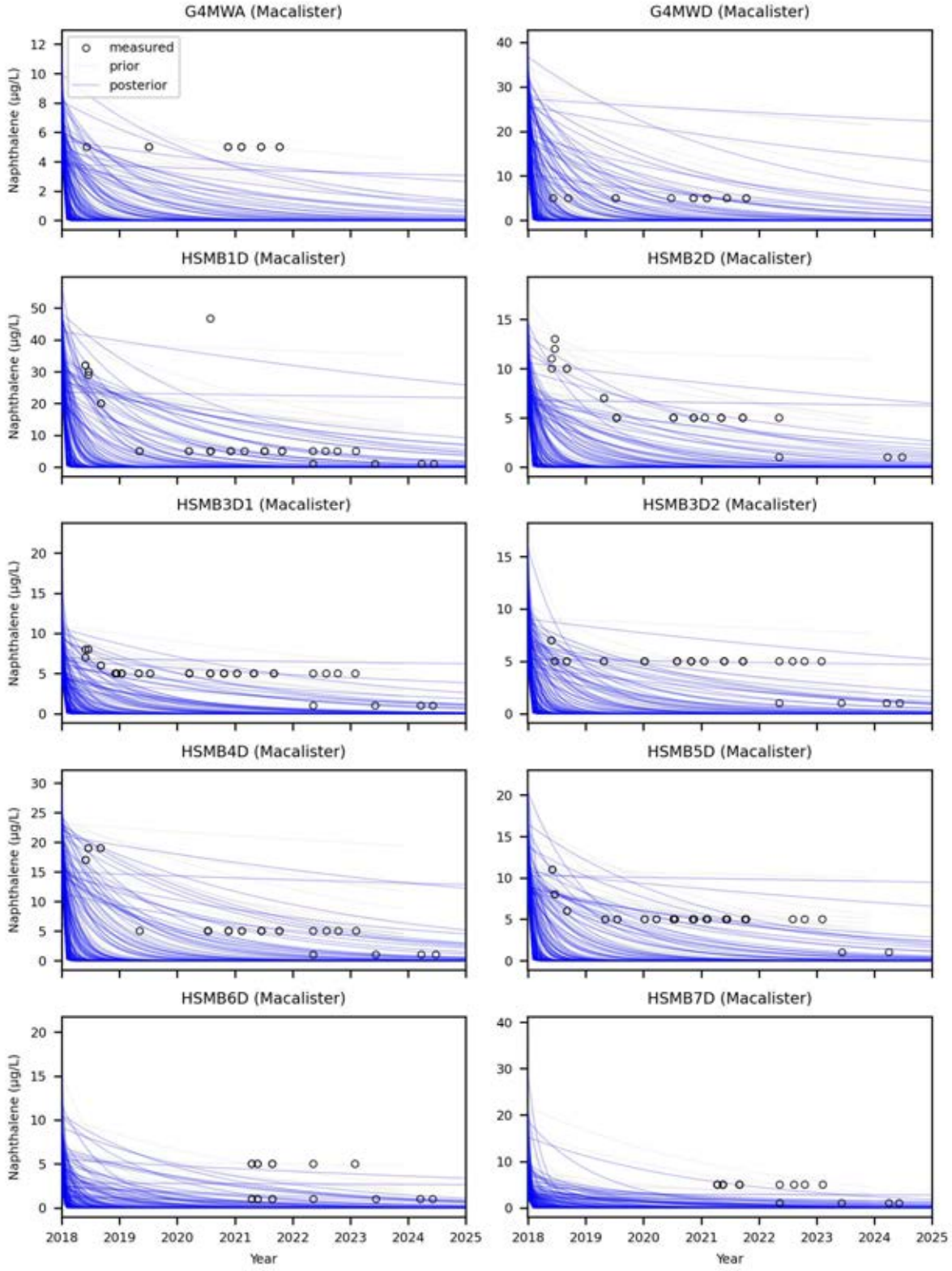


Figure 4-13 – Comparison between measured time-series of concentrations of naphthalene in WCM (G4MW and HSMB bores), noise and simulated values. Line colours denote prior (grey lines) and posterior (blue lines) simulated ensemble.

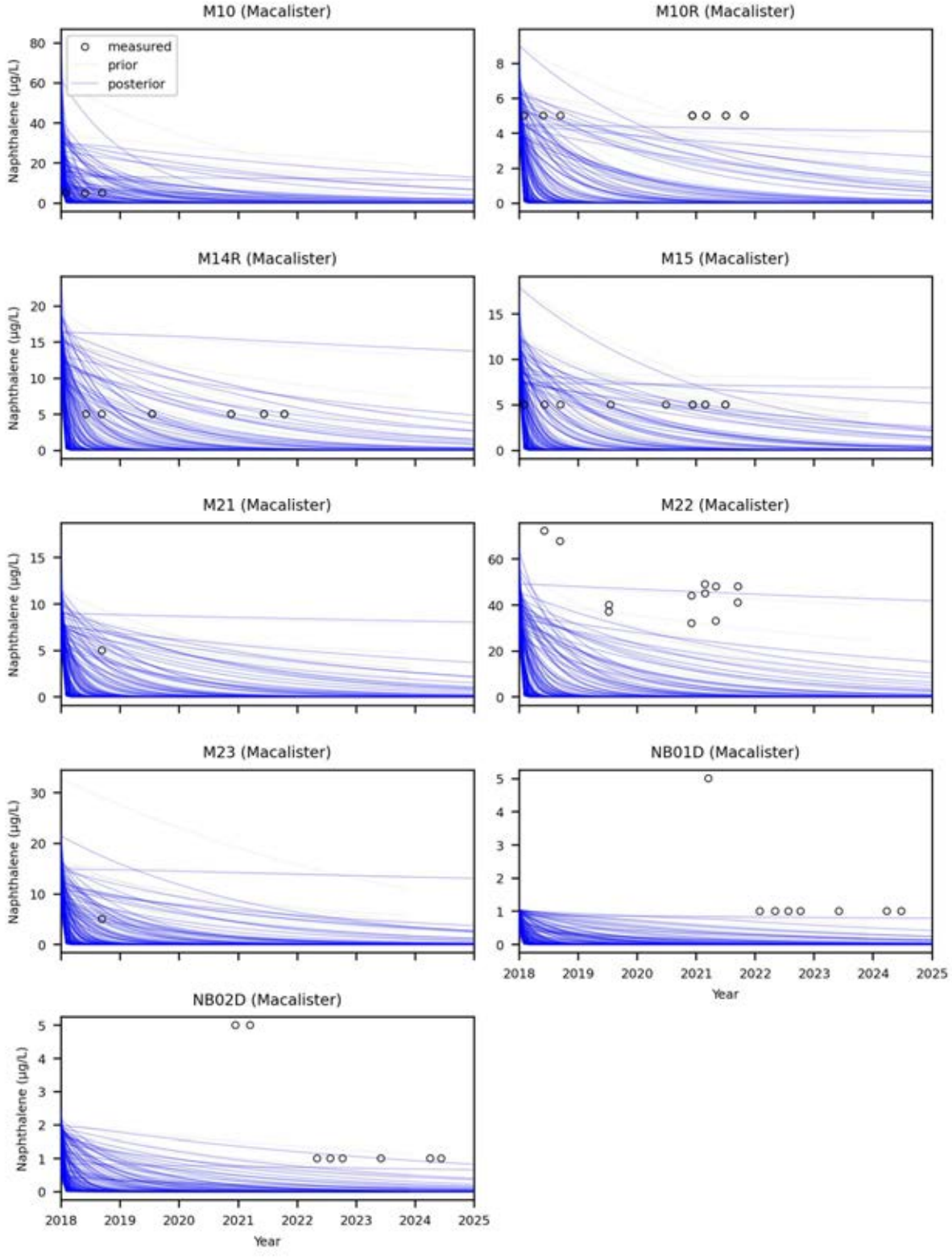


Figure 4-14 – Comparison between measured time-series of concentrations of naphthalene in WCM (M and NB bores), noise and simulated values. Line colours denote prior (grey lines) and posterior (blue lines) simulated ensemble.

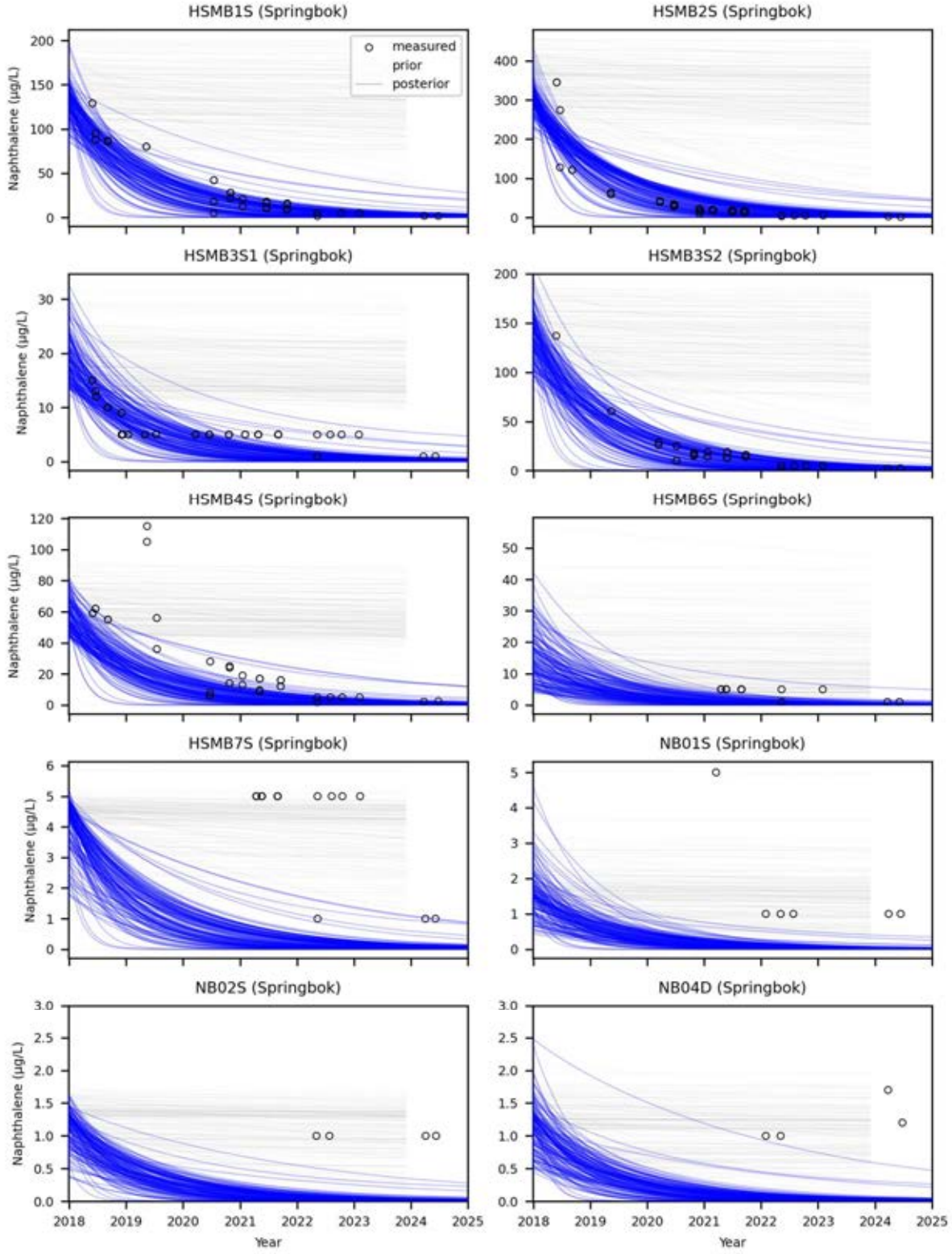


Figure 4-15 – Comparison between measured time-series of concentrations of naphthalene in Springbok, noise and simulated values. Line colours denote prior (grey lines) and posterior (blue lines) simulated ensemble.

#### 4.3.2.4.5 Simulated Naphthalene – Spatial Distribution Over Time

The posterior ensemble of simulated naphthalene exhibits attenuation over time between 2018 and 2024 for both Springbok Sandstone and WCM Macalister. However, this trend accompanies significant variability across posterior realisations. To visualise this, Figure 4-16 and Figure 4-17 depict the spatial distribution of naphthalene for the years 2018, 2020, 2022, and 2024. In these figures, ensemble mean maps are displayed in the left column, accompanied by standard deviation maps in the right column, illustrating the variability in contaminant distribution.

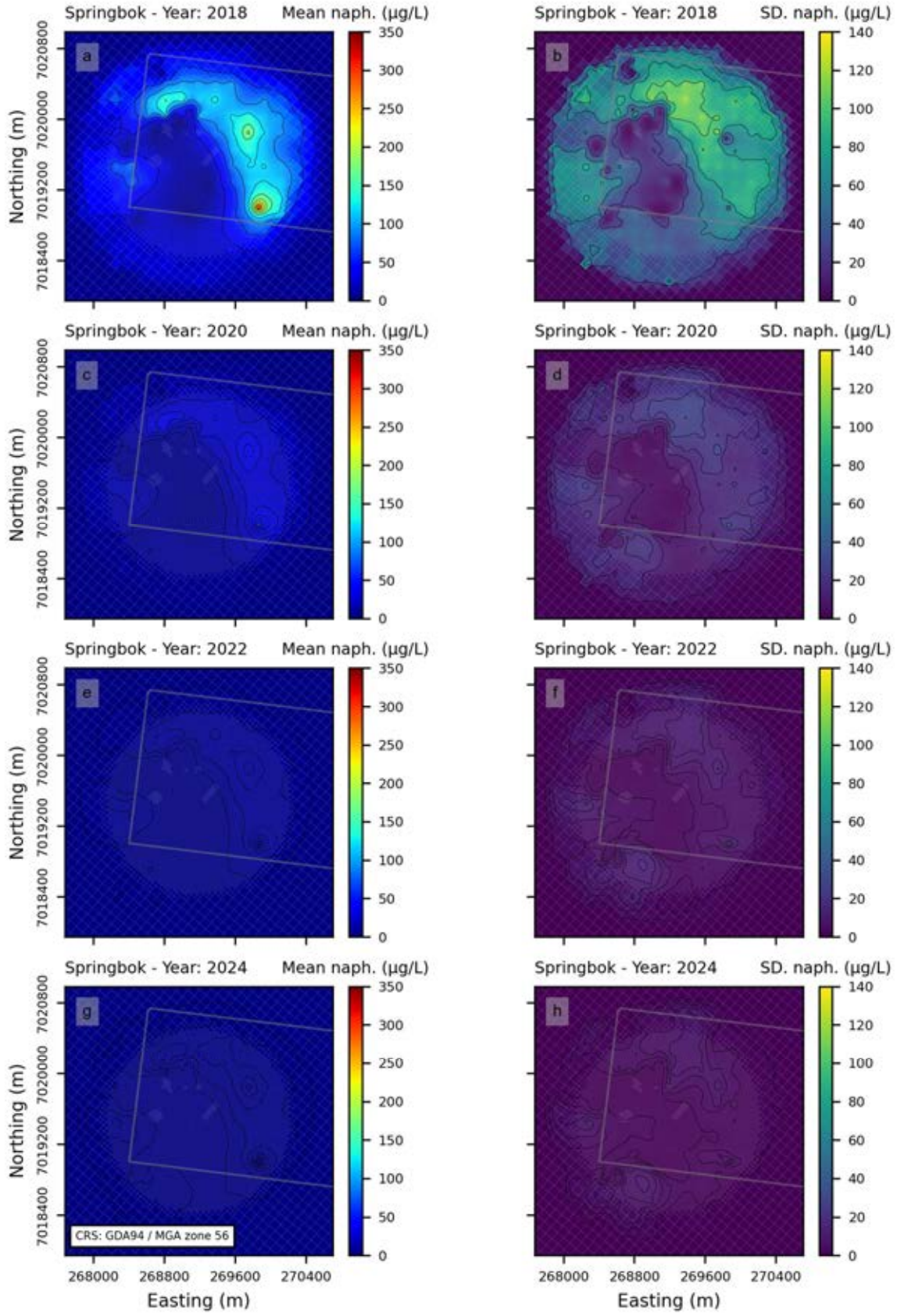


Figure 4-16 – Simulated naphthalene concentration maps for Springbok Sandstone. The left column displays ensemble mean concentration maps spanning from 2018 to 2024, while the corresponding standard deviations of the posterior ensemble are depicted in the right column.

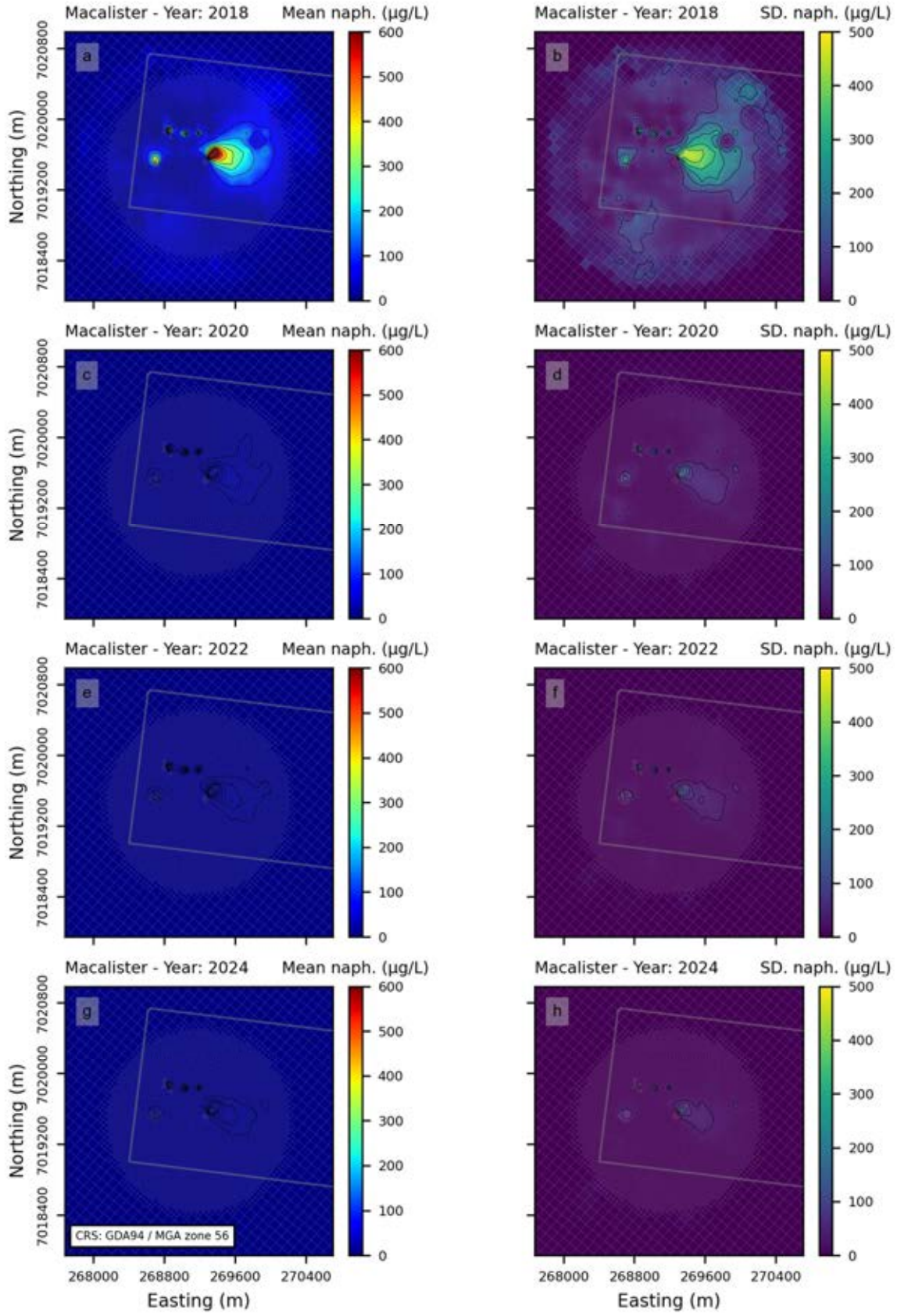


Figure 4-17 – Simulated naphthalene concentration maps for WCM Macalister. The left column displays ensemble mean concentration maps spanning from 2018 to 2024, while the corresponding standard deviations of the posterior ensemble are depicted in the right column.

#### 4.3.2.4.6 Posterior Parameter Distribution

Similar to the explanation for the groundwater flow model, history matching has the potential to reduce uncertainties associated with model parameters. It is informative to display this reduction spatially, especially when the parameterisation employed pilot points. The relative parameter uncertainty variance reduction (RPUVR) as defined in Chapter 3.2.5.2, helps to understand the extent to which the observation data was useful in making the parameter more certain. Figure 4-18 displays maps of Relative parameter variance reduction for longitudinal and transverse horizontal dispersivity in layers 3 (Springbok) and 6 (WCM Macalister). Brighter colours denote larger variance reduction in contrast to darker colours. As it can be seen, parameter uncertainty was greatly reduced in the area of the Lot40. The rest of the parameters and corresponding RPUVR maps are presented in Appendix J.

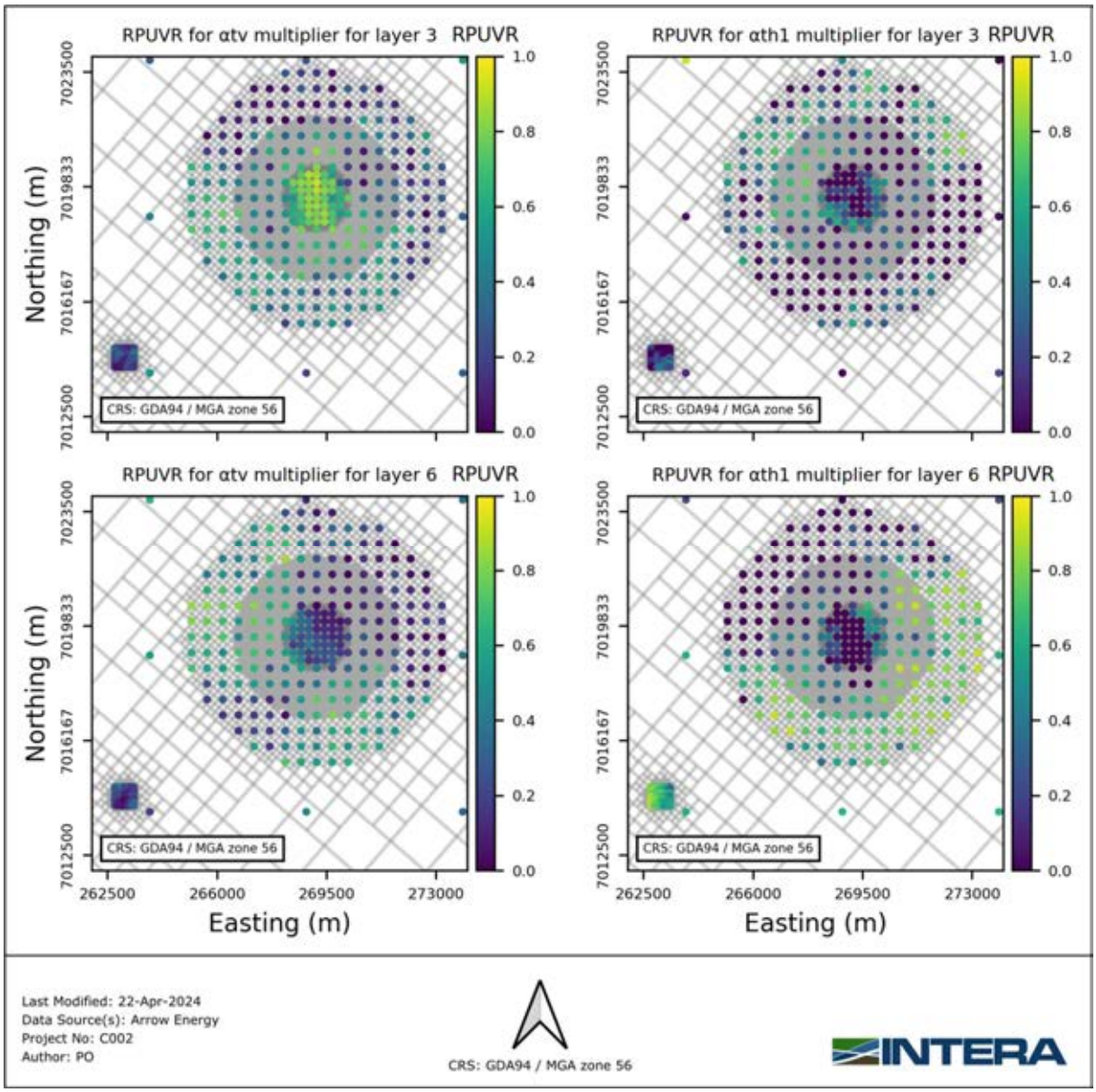


Figure 4-18 – Relative parameter variance reduction for longitudinal and transverse horizontal dispersivity pilot point parameters near Lot40 and the Hopeland pilot site in model layers 3 and 6 (i.e., Springbok and WCM Macalister).

Figure 4-19 presents the histograms of prior and posterior ensembles for the layer-wide multiplier for longitudinal and transverse horizontal dispersivity in layers 3 and 6. Similar to what was described in Chapter 4.4 for hydraulic properties and boundary conditions, posterior parameter distributions for the coarse-scale transport parameter groups tend to be reduced. Particularly in Figure 4-19, the reduction was more noticeable for layer 3 than layer 6. In general, this implies the existing measured data contains some information to reduce the coarse scale parameters, while little to none to reduce the uncertainty at a smaller scale. The remaining parameters and corresponding histograms are presented in Appendix I.

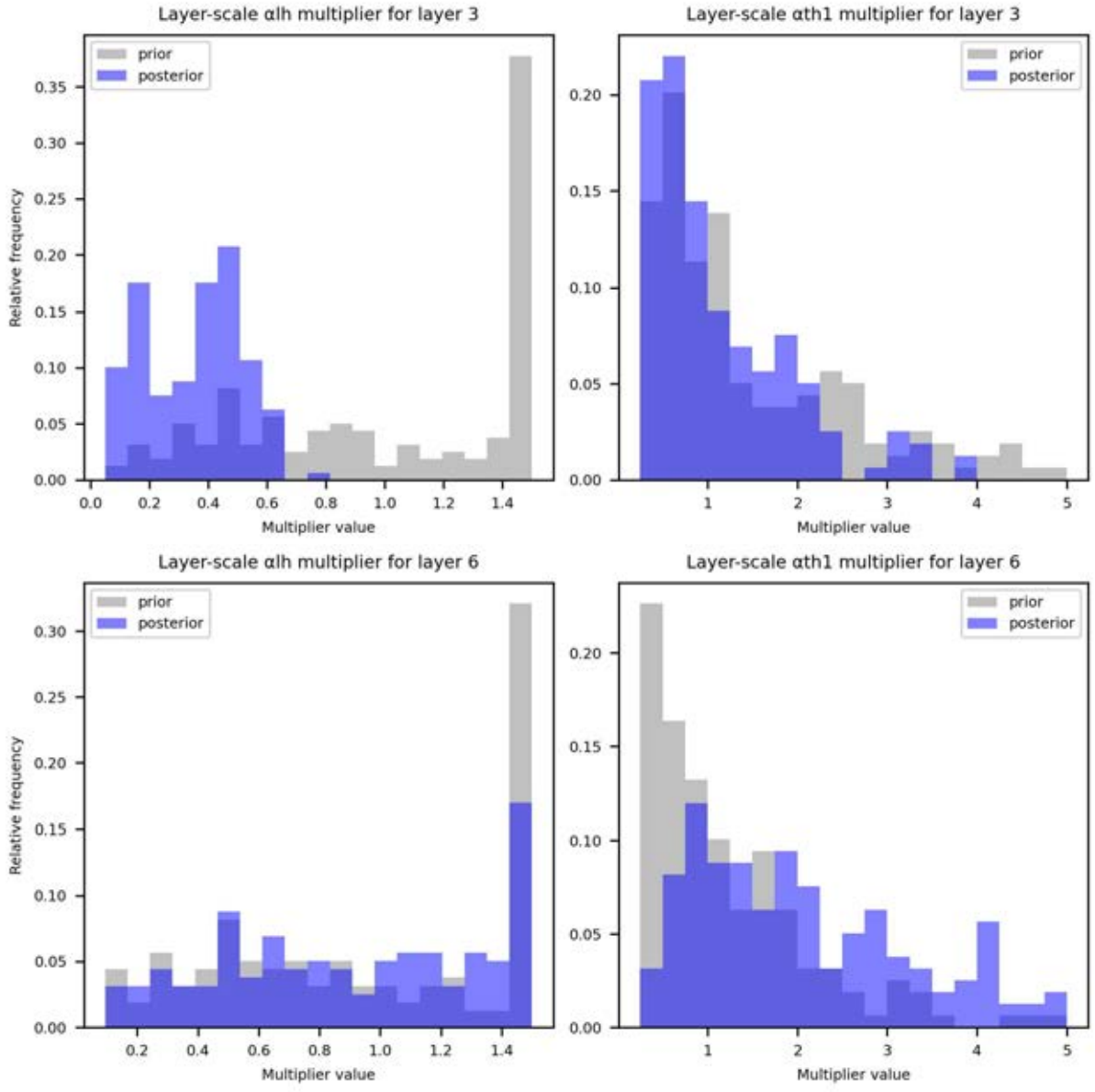


Figure 4-19 – Prior and posterior distributions of the coarse-scale multiplier parameter for longitudinal and transverse horizontal dispersivity in model layers 3 and 6.

Prior and posterior distributions and the relative variance reduction was also explored for the hyper-parameters used in the parameterisation of the initial concentrations of benzene and naphthalene. Figure 4-20 and Figure 4-21 present maps of RPUVR for benzene and naphthalene, respectively, and in layers 3 and 6. For benzene (Figure 4-20), it can be observed that a substantial variance reduction

was achieved in the initial concentration, but also in the anisotropy and bearing assigned to the pilot points (Figure 4-20 (a)-(d) and (g)-(h)). These were all hyper-parameters that influence the shape of the benzene spatial distribution, thus, implying that the distribution of the initial conditions was highly informed by the history matching process.

With respect to naphthalene (Figure 4-21), appreciable variance reduction can also be observed for anisotropy and bearing, but it was lower compared to the hyper-parameters of benzene. However, initial concentrations of naphthalene assigned to the pilot points were also highly informed by the history matching process (Figure 4-21 (g) and (h)).

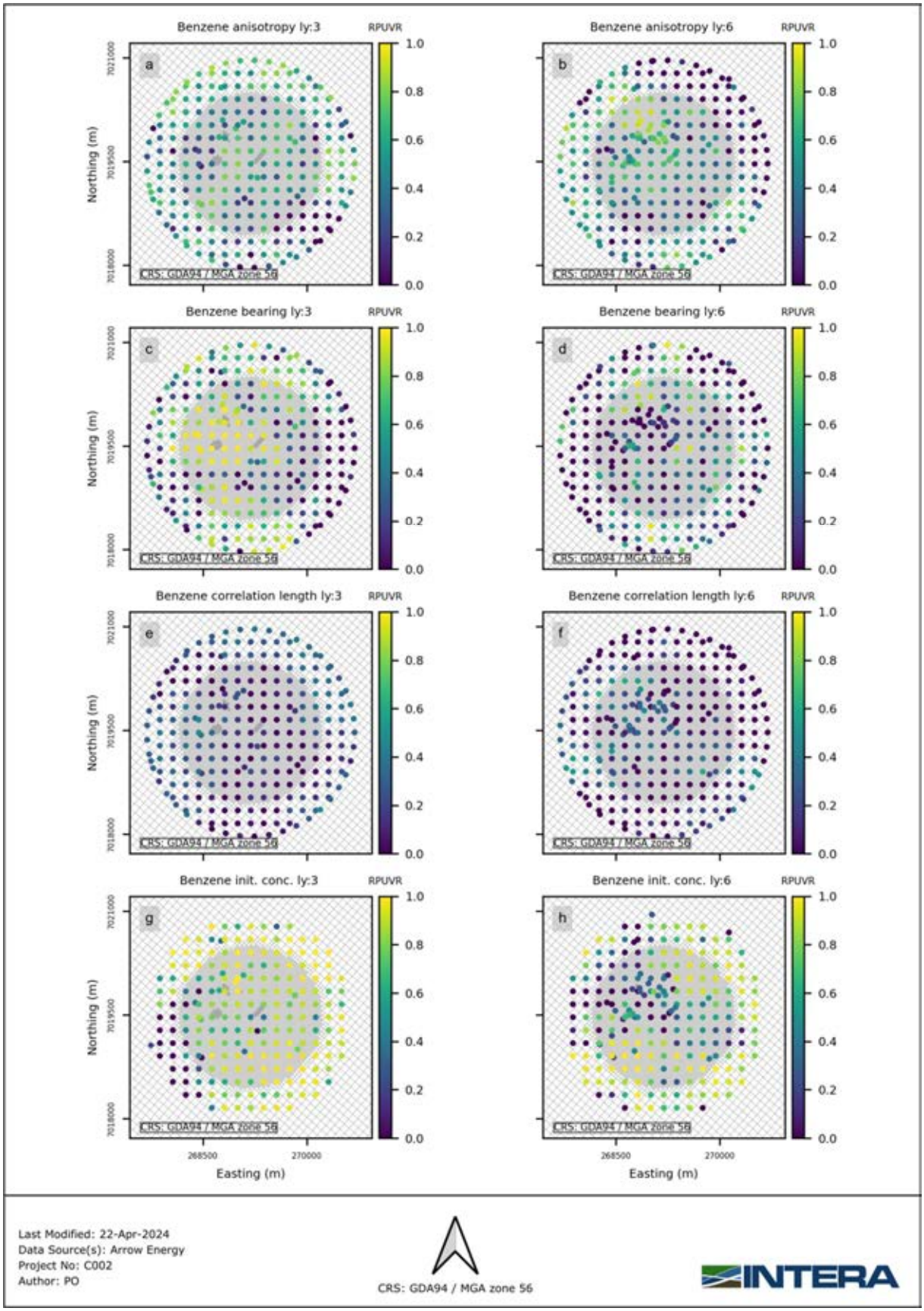


Figure 4-20 – Relative parameter variance reduction for hyper-parameters used in the interpolated initial concentration field of benzene. Hyper-parameter RPUVR for model layers 3 and 6 are presented (i.e., Springbok and WCM Macalister).

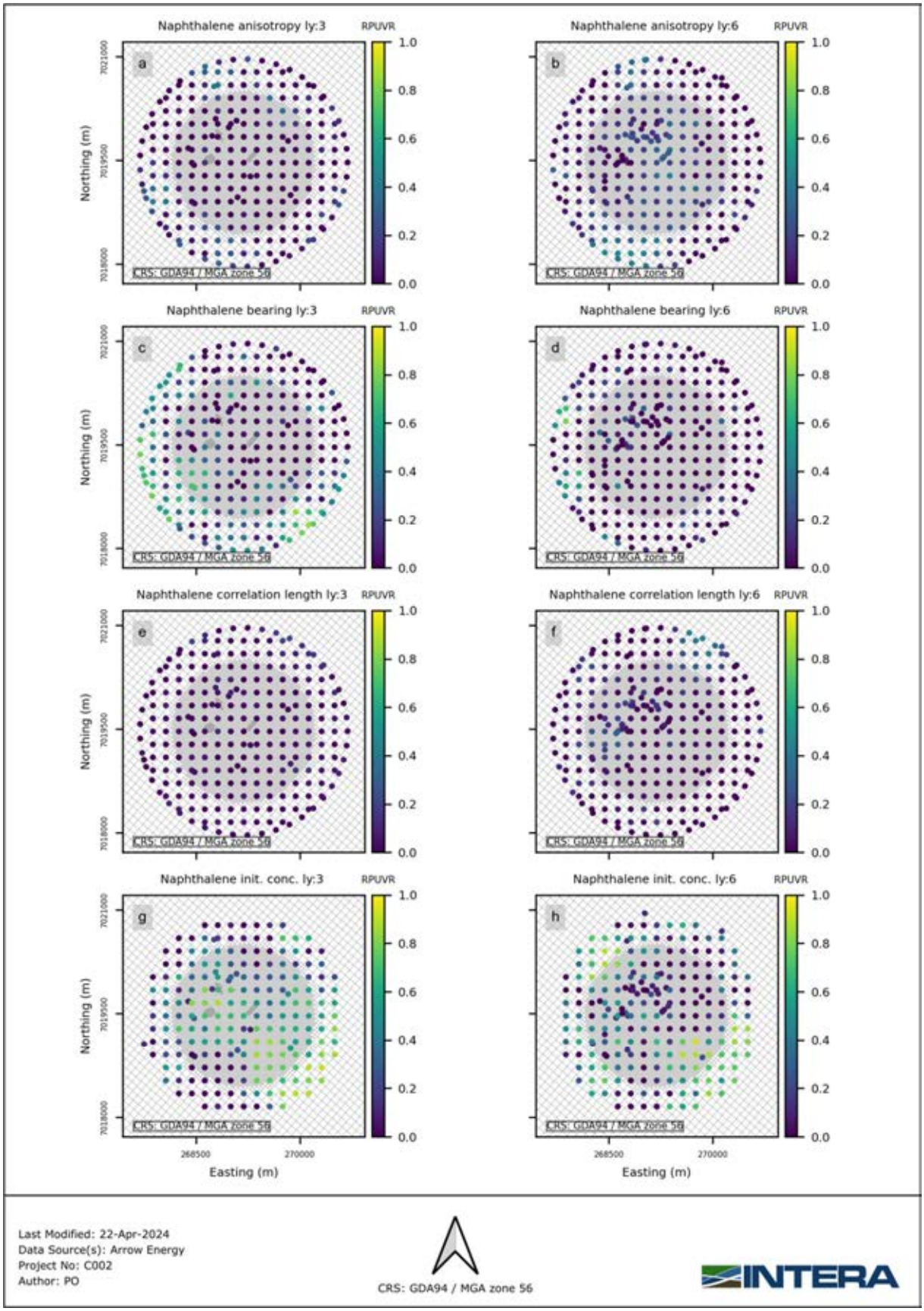


Figure 4-21 – Relative parameter variance reduction for hyper-parameters used in the interpolated initial concentration field of naphthalene. Hyper-parameter RPUVR for model layers 3 and 6 are presented (i.e., Springbok and WCM Macalister).

#### 4.3.2.4.7 Mass Budget

Figure 4-22 displays time-series of simulated mass budget components for the ensemble of prior and posterior parameters. As per criteria suggested in Barnett et al (2012), all parameter realisations result in a near-zero percent mass balance error and no convergence issues.

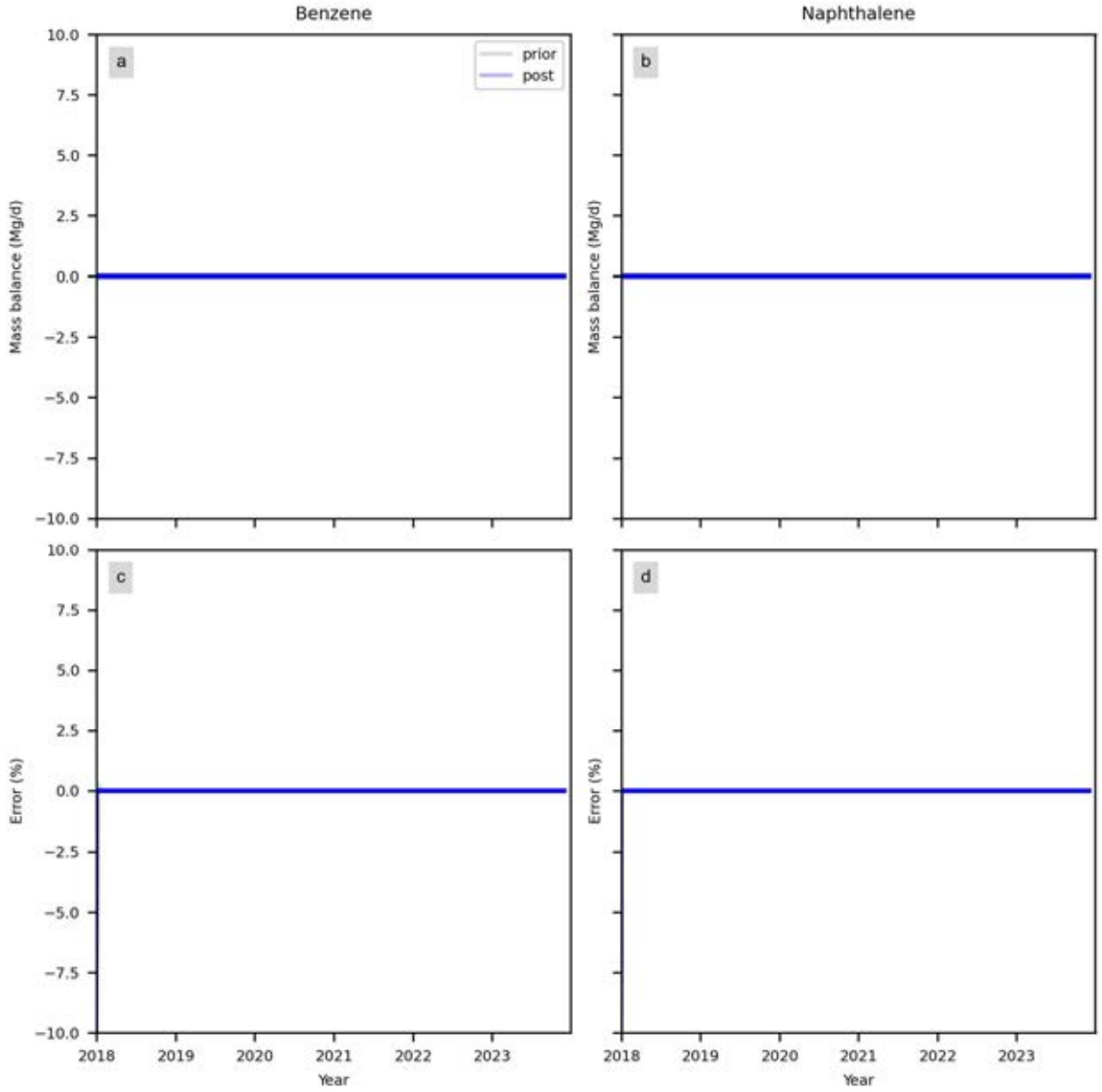


Figure 4-22 – Time-series of simulated mass balance and error percentage simulated with the prior (grey) and posterior (blue) parameter ensembles.

## 4.4 Predictive Modelling

### 4.4.1 Simulated Scenarios - CSG Wells

As described in section 3.3.1, two scenarios for the Future Development Plan (FDP) were simulated:

c) Base case FDP and
d) PL253 FDP.

The base case FDP scenario corresponds to the currently authorised CSG wells (290) including the six Hopeland pilot wells. The PL253 FDP scenario includes the additional 55 CSG wells from the EA, resulting in a total of 345 wells. The location of active wells in both scenarios are depicted in Figure 3-20.

## 4.4.2 Particle Tracking

### 4.4.2.1 Predictive Particle Tracking Model Setup

The particle tracking model setup is described in section 4.2.1. In addition, the flow field used for the particle tracking model was the same as the posterior predictive ensemble presented in the groundwater flow predictive modelling (see section 3.3.2).

### 4.4.2.2 Quantities of Interest

The following quantities of interest (QoI) derived from simulated outputs were considered:

- Maximum particle distance from the boundary of Lot40 over the simulated period
- Particle locations at the end of the simulated period (year 2200)

These were complemented with other derived model outputs and discussed in the following sections.

### 4.4.2.3 Particle Distance from Lot40

Figure 4-23 presents time series of the maximum distance particles travel from the Lot40 boundary under the two different FDP scenarios. The figure also illustrates the difference between these scenarios. The particles under consideration were those released at specific locations: monitoring bores, the Lot40 boundary, and gasifiers.

Distances that were less than zero indicate that the particles were within the Lot40 boundary, while distances greater than zero signify that the particles have moved outside the boundary. The left panels of Figure 4-23 use orange and blue lines to represent the maximum distance travelled by particles for each parameter realisation under the Base case FDP and PL253 FDP, respectively.

The right panels of Figure 4-23 depict the difference in the maximum distance travelled by particles between the Base case and PL253 FDP for each parameter realisation. This difference was calculated by subtracting the maximum distance in the Base case FDP from that in the PL253 FDP. Where differences were greater than zero, maximum particle distances were greater for the Base case FDP.

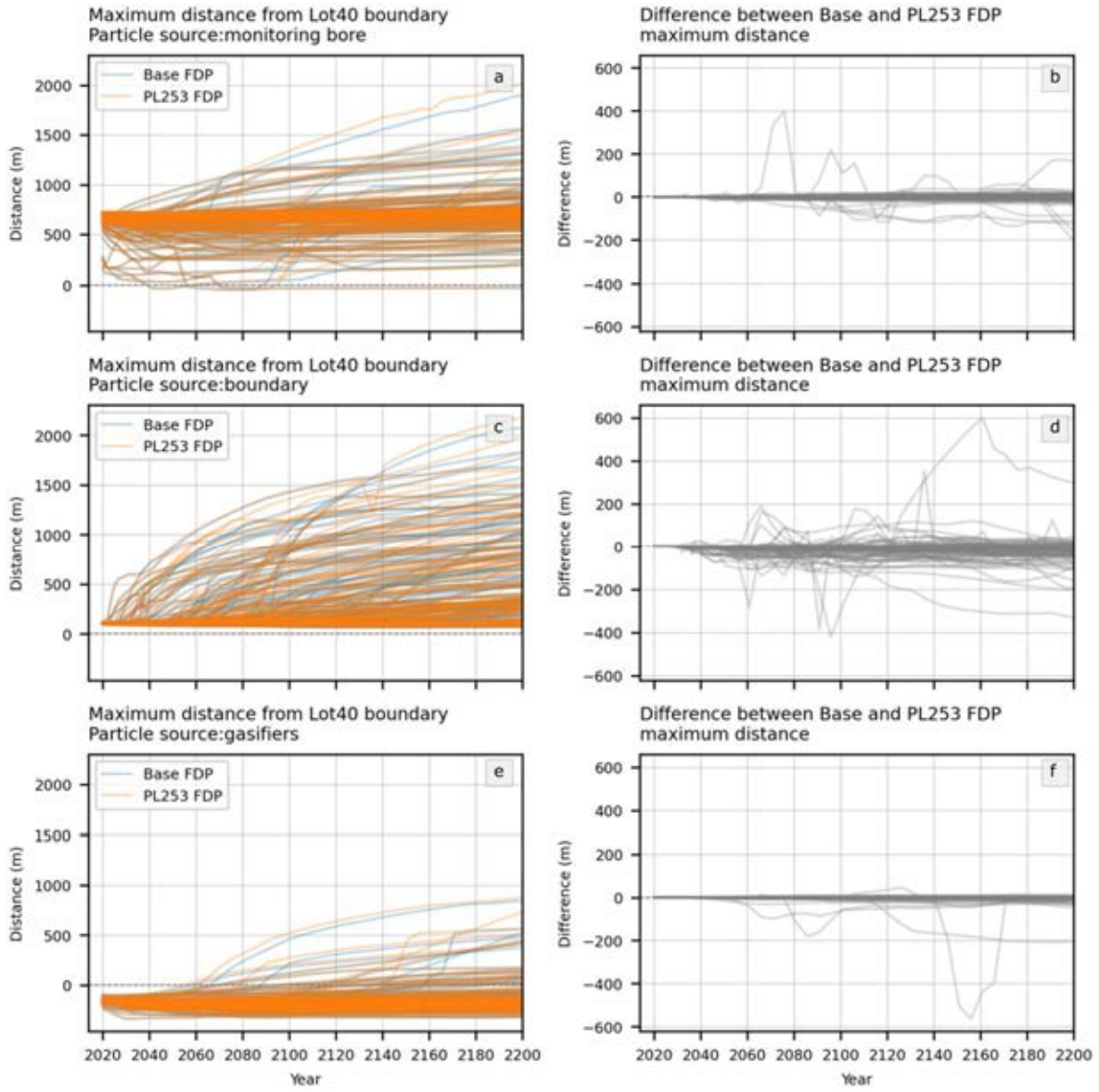


Figure 4-23 – Time series of (a-c-e) maximum distance from the Lot40 boundary and (b-d-f) difference between maximum distance for the Base and PL253 FDP scenarios, simulated with the posterior parameter ensemble. Distances less or greater than zero are within and outside the boundary, respectively.

Results show that proposed production within PL253 has a minor impact on the simulated maximum travel distance. In some cases, the PL253 FDP scenario resulted in smaller distances than those simulated with the Base Case FDP scenario. As shown in the histograms in Figure 4-24, for particles released at monitoring bores and at the gasifiers, differences between FDP scenarios were between -120 and 120 m. Uncertainty for particles released at the boundary was slightly larger, between -330 and 300 m. The distribution of differences was centred near zero.

Maximum distances of particles released at monitoring bores were dominated by particles released at HMBS7S, which is located furthest from the boundary of Lot40. Particles released there started outside the lot. For the majority of realisations, maximum distance increased gradually over the simulated period. A maximum distance less than 1300 m was achieved for 95% of model runs (see Figure 4-24). A few realisations achieve up to 2235 m distance from the lot boundary.

Maximum distance for particles released at the boundary were always greater than zero. This is because particles were placed in model cells intersected by the boundary line. Some of these particles were placed outside the boundary. For all model realisations, at least one boundary particle remained outside the limits of the lot during the simulated period. For 95% of simulated realisations boundary particles did not move more than 1600 m from the boundary. Some achieve up to 2230 m distance.

For most realisations, particles released at the gasifiers did not exit the lot during the simulation period. For realisations in which they did, the time at which a particle leaves the lot varied significantly. The earliest that occurs is for a single extreme case, around the year 2050. For the majority of realisations, particles released from the gasifiers left the lot after the year 2100. In 95% of the simulated scenarios, the maximum distance achieved by gasifier particles from the lot boundary was 500 meters. A few realisations achieved up to 1000 m.

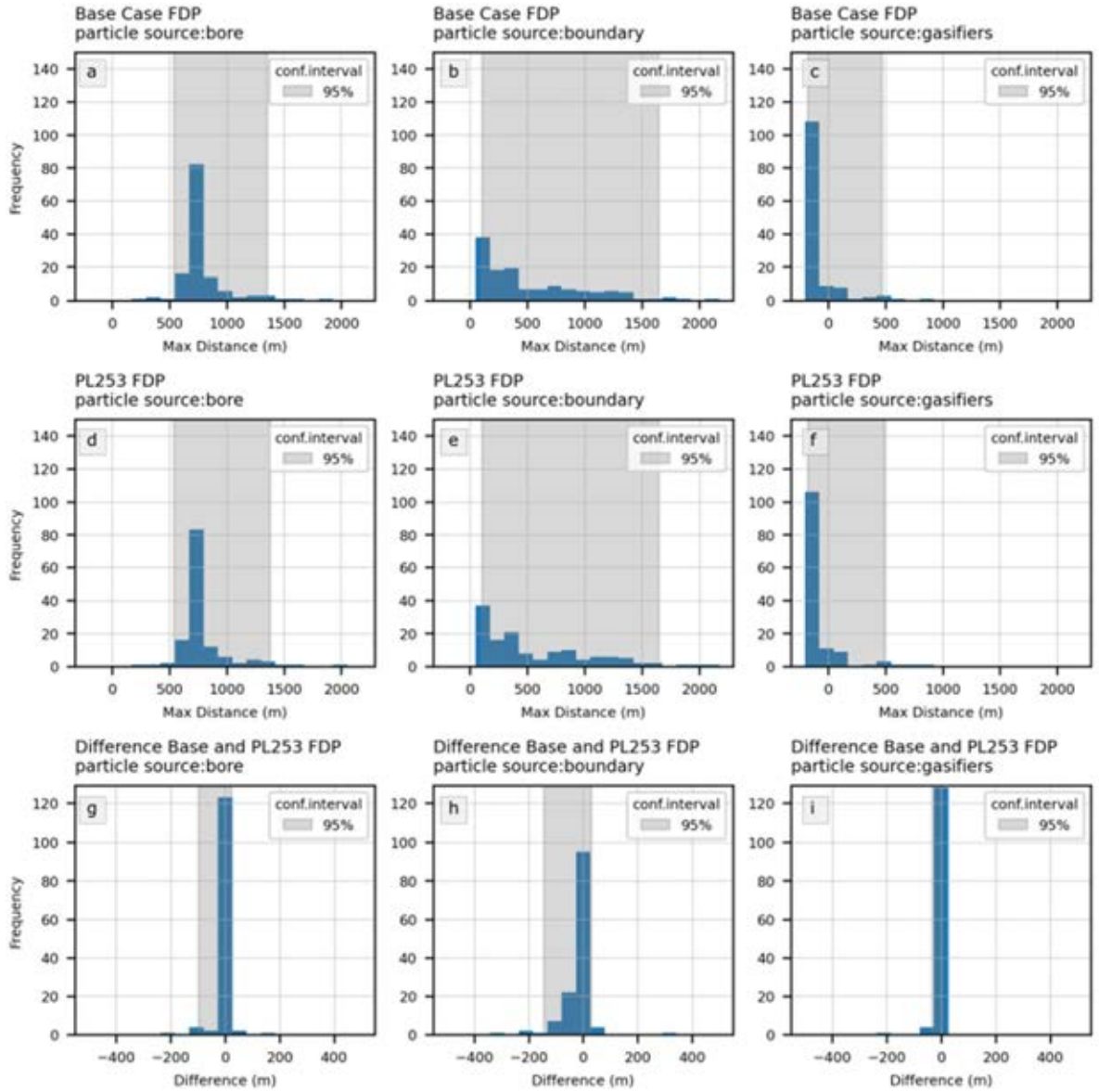


**Figure 4-24 – Histograms of maximum particle distance from the Lot40 boundary during the forecast period, simulated with posterior parameter ensemble for (a-b-c) the Base case FDP, (d-e-f) the PL253 FDP and (g-h-i) the difference between both scenarios. Distances less or greater than zero are within and outside the boundary, respectively. Note that the x-axis on the bottom-middle panel is truncated for legibility.**

Figure 4-25 displays particle tracks for the parameter realisation which results in gasifier particles leaving Lot40 in the year 2050. Particle tracks for this case show that gasifier particles that achieved the maximum distance originated in the Springbok layer and travelled laterally though the Macalister Interburden and Macalister meaning that they migrated horizontally and downward. Particle tracks displayed are for the PL253 FDP case, however results for the Base case FDP are visually indistinguishable.

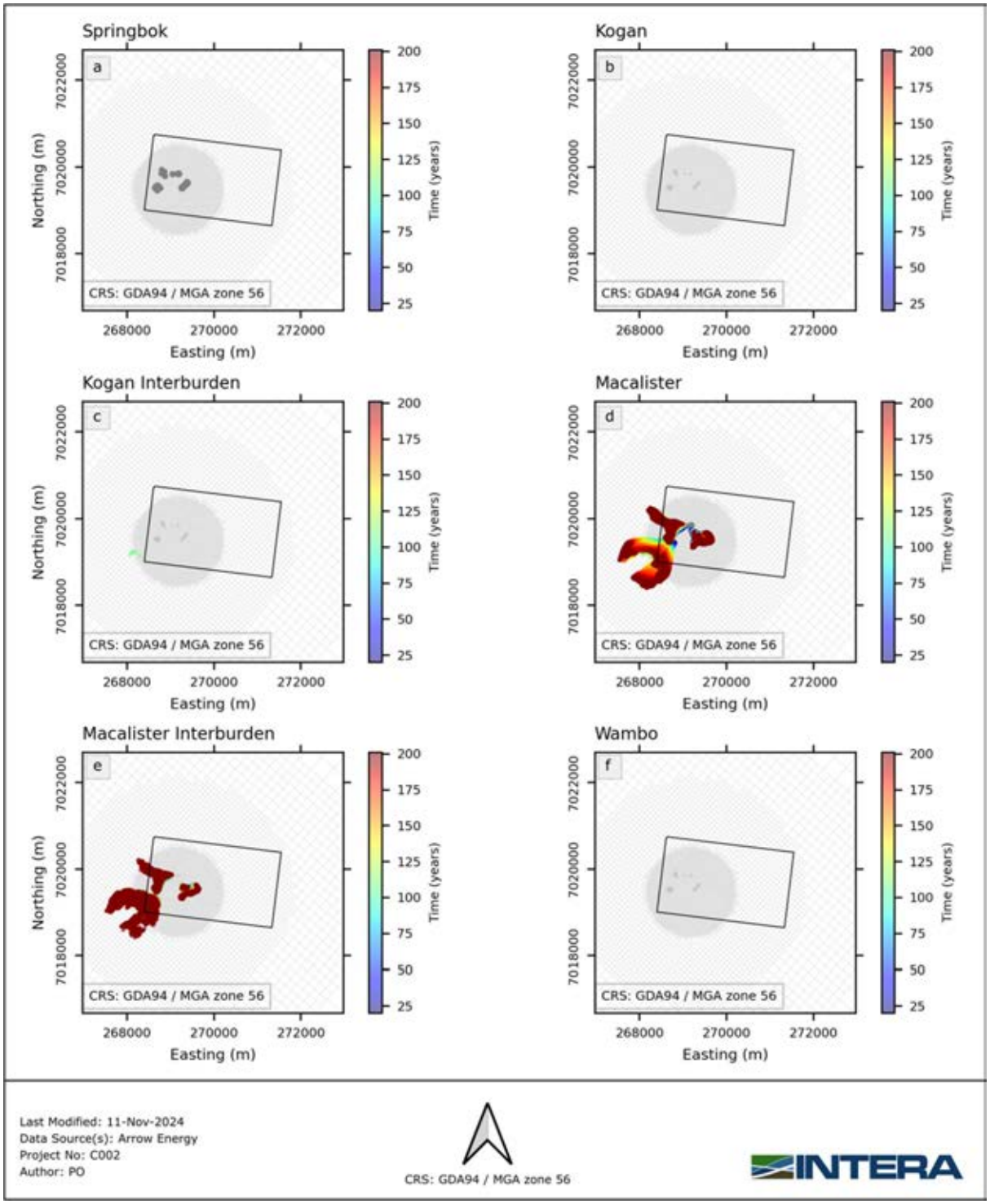


Figure 4-25 – Particle tracks for particles released at gasifier cells. Simulated with the single parameter realisation which results in maximum distance for particles released at gasifiers (PL253 FDP scenario).

Table 4-8 provides summary statistics of particle distances over the entire simulated period. Particles released at the boundary and at monitoring bores achieved greatest distances from the boundary. This was largely due to their starting locations.

Table 4-8 – Summary statistics of simulated particle distances from Lot40 boundary for both FDP scenarios over the entire simulated period for all parameter realisations in the posterior ensemble.

| Particle Source | Scenario | Distance from Lot40 boundary (m) | | |
|---|---|---|---|---|
| | | min | average | max |
| Monitoring bores | Base FDP | -875.9 | -361.7 | 1907.9 |
| | PL253 FDP | -875.9 | -361.2 | 2020.9 |
| Lot40 boundary | Base FDP | -876. | -70.4 | 2075.7 |
| | PL253 FDP | -876.0 | -68.6 | 2175.4 |
| Gasifiers | Base FDP | -875.9 | -478.0 | 840.9 |
| | PL253 FDP | -875.9 | -478.0 | 875.7 |

The largest difference in the maximum distance a particle achieved occurs for particles released at monitoring bores. These achieved a greater distance from the boundary in the Base Case FDP scenario, than those in the PL253 FDP scenario (~300 m difference).

Particles released at gasifiers and at the lot boundary achieved a greater distance in the PL253 scenario. Differences between the maximum distance were less than 60 m.

#### 4.4.2.4 Particle Existence Probability Map

Figure 4-26 and Figure 4-27 display probability maps of a particle existing in model cells in the year 2200 for the PL253 and Base case FDP, respectively. Figure 4-28 shows the difference between them. These maps were produced by counting the number of realisations for which each cell contains a particle. The obtained value was then divided by the total number of realisations. Red colours indicate that there was a high probability that a particle may be located in the cell. Blue colours indicate a low, but non-zero, probability.

Uncertainty regarding where particles may be located outside the limits of Lot40 in 2200 was large. However, no realisation resulted in particles reaching existing or proposed CSG wells during the simulated timeframe.

There was no clear preferential pathway for particles that left Lot40. Particles may be located in a large area outside the lot (coloured areas in Figure 4-26 and Figure 4-27). However, the probabilities of particles being in an individual cell did not vary significantly and was consistently low (between 10% and 20%).

Furthermore, as was previously discussed regarding Figure 4-25, particles that exceeded the boundary of Lot40 tended to originate in the Springbok layer. The lateral spreading mostly occurred as particles migrated vertically down towards the Macalister and Wambo. This was reinforced by the high probability of particles being located at cells near the gasifiers in the Macalister layer. Particles that started within the lot in the Macalister layer, did not tend to leave the lot within the simulated time frame.

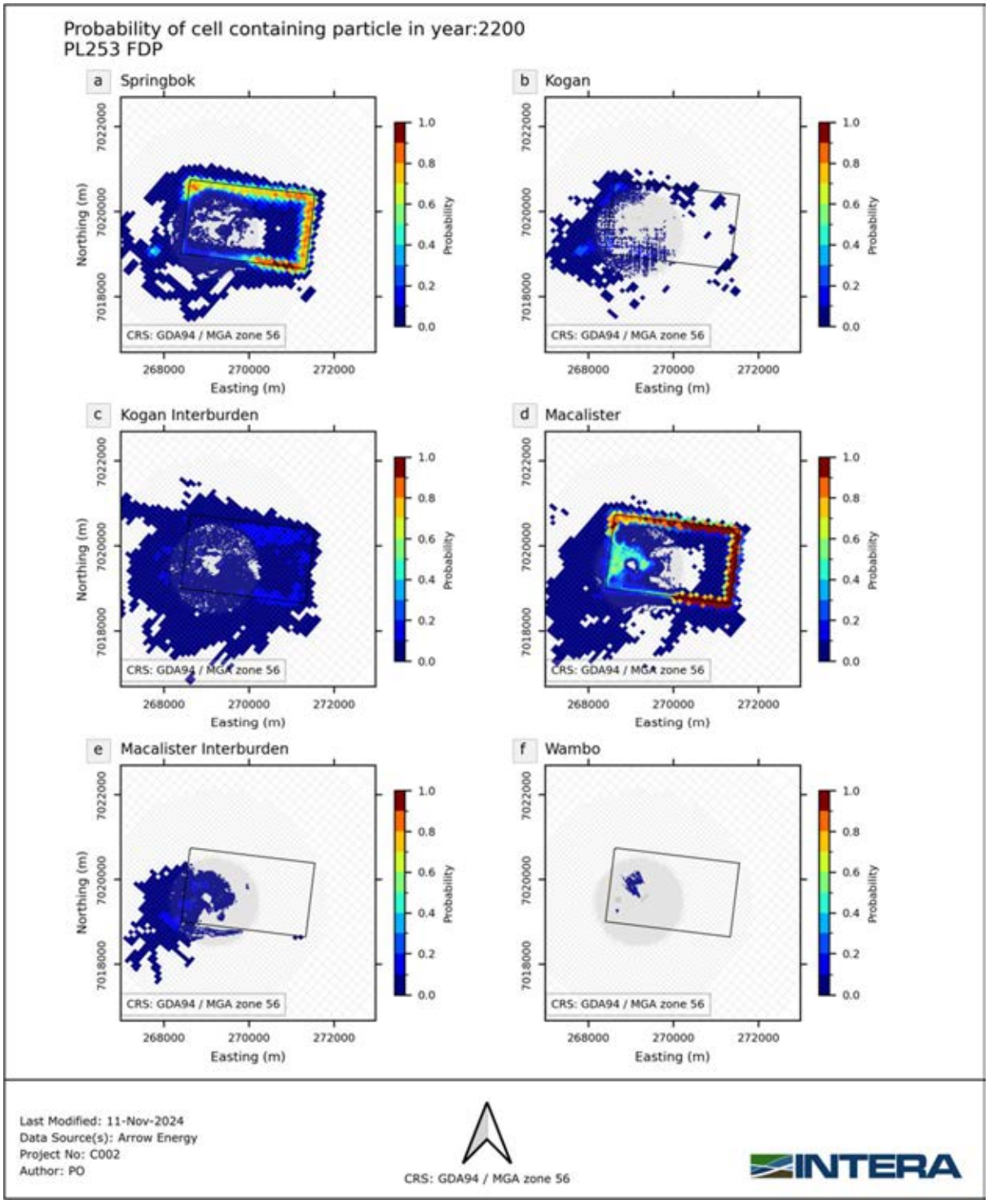


Figure 4-26 – Probability that a cell contains a particle in the year 2200 for the PL253 FDP scenario.

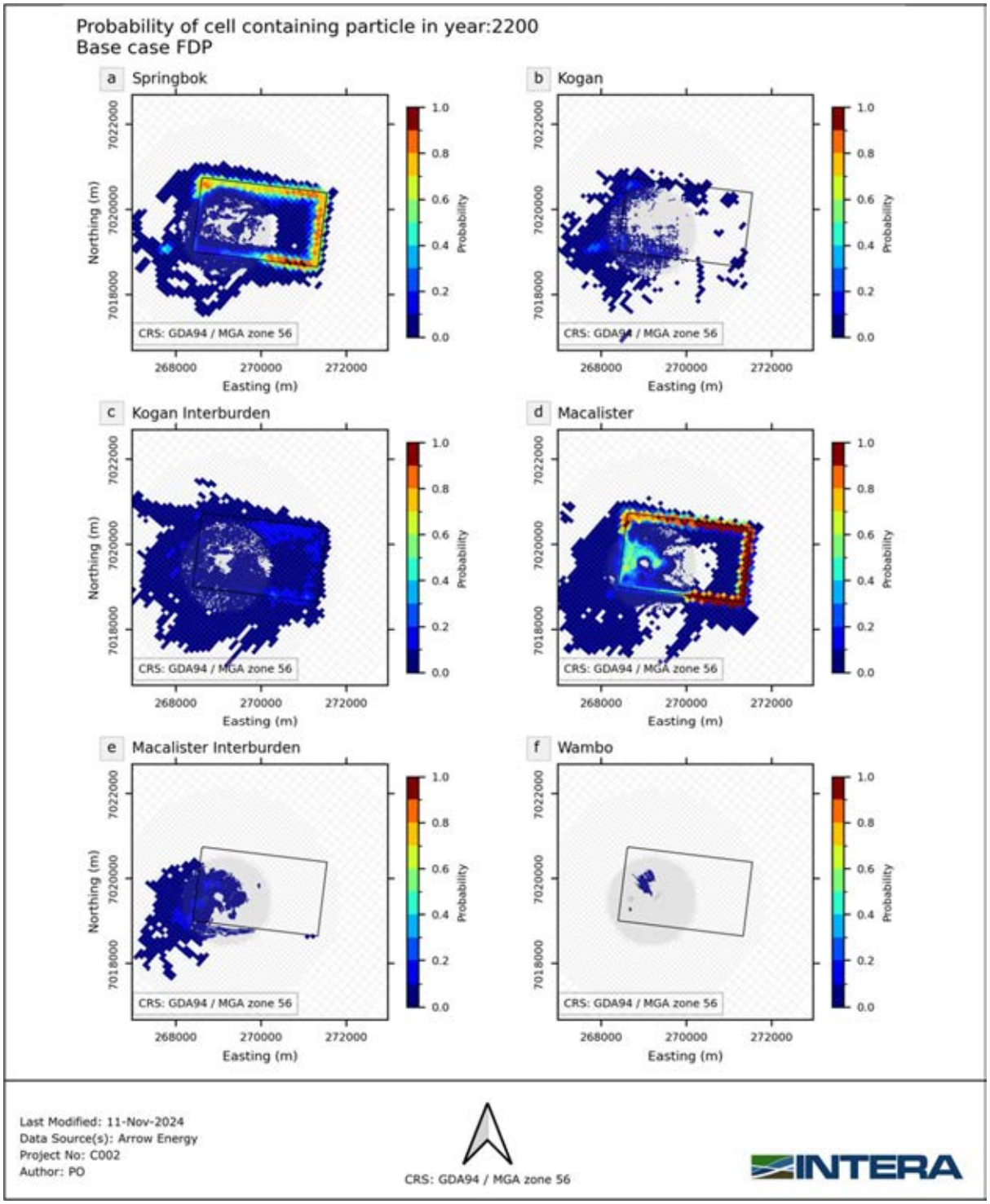


Figure 4-27 – Probability that a model cell contains a particle in the year 2200 for the Base case FDP scenario.

Figure 4-28 shows the spatial distribution in difference between probability of a cell containing a particle for the Base and PL253 FDP scenarios. Red coloured cells are more likely to contain a particle in the Base case FDP. Blue coloured cells are more likely to contain particles in the PL253 FDP scenario. Differences between the scenarios are minimal (less than 5% difference for any given cell).

However, results indicated that extraction from the proposed wells in PL253 may marginally reduce the likelihood of contaminant movement, which is likely due to production at PL253 smoothing out the hydraulic gradient around the site.

Notably, for the PL253 FDP there was a higher likelihood of particles being in the Kogan Interburden layer in 2200. Whilst the Base case FDP has a higher likelihood of particles being located in the deeper Macalister layer. This implies that the Base case FDP may result in faster vertical downward movement of particles from the Springbok layer.

In the Springbok, Kogan and Macalister layers red coloured cells tend to be to the West of blue coloured cells. Indicating that the Base case FDP was more likely to result in movement of particles towards the West (i.e., towards non-Arrow CSG wells).

Lastly, the PL253 FDP scenario has a higher probability of particles migrating down into the Macalister Interburden layer. This can be attributed to the increased extraction in the Wambo for this scenario. However, once again, the difference in probability between FDP scenarios was minimal.

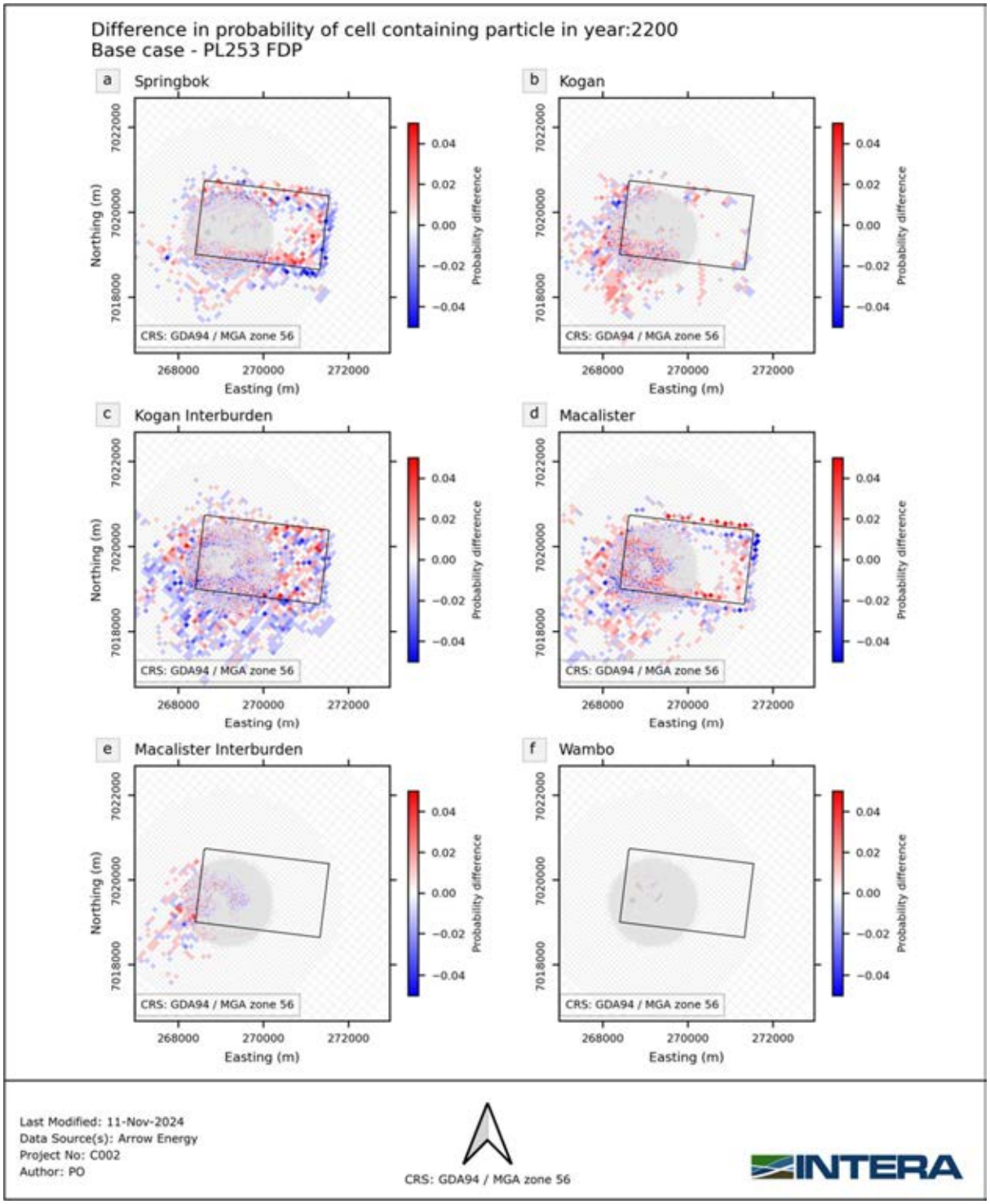


Figure 4-28 – Difference in probability that a model cell contains a particle in the year 2200 for the Base case FDP and PL253 scenarios. Values that are greater or less than zero indicate higher probability for the Base case and PL253 case, respectively.

## 4.4.3 Contaminant Transport

### 4.4.3.1 Predictive Contaminant Transport Setup

The setup of the predictive model remained unchanged from the transport history matching except for the extent of the simulated period, and the Arrow's CSG wells which were simulated according to the two scenarios described in detail in section 3.3.1. Therefore, boundary conditions such as non-Arrow CSG wells, Arrow CSG wells outside PL25, recharge, general head boundary, topographic surface drains, and gasifiers were identical to the history matching model setup.

The simulated predictive period covered a timeframe from 01-01-2025 to 01-01-2200, thus including the history matching period. Up to 01-01-2024, the time discretisation remained the same as in the history matching period. From that date until 2200, each stress period corresponds to one year, resulting in a total of 311 simulated stress periods.

### 4.4.3.2 Quantities of Interest

Both the Base case and Arrow FDP were simulated with all realisations of the history matched parameter ensemble from the groundwater solute transport model. The impacts of the proposed Arrow FDP were estimated by comparing results between the Base case and FDP scenarios for each realisation.

As pressure within the former UCG site recovers, contaminant movement away from site is expected to become more likely. Predictions of interest were the extent to which contaminants may disperse, time of arrival at points of interest and the timescale to achieve degradation.

The following quantities of interest (QoI) derived from simulated outputs were considered:

- Year at which the contaminants reach full or near full attenuation.
- Depletion of concentrations at the boundary of Lot40.
- Evolution of the contaminant distribution throughout predictive years and at the end of the simulated period.

These were complemented with other derived model outputs and discussed in the following sections.

### 4.4.3.3 Concentration at Boundary of Lot40

The concentrations of benzene and naphthalene at the boundary of Lot40 were used as a proxy to evaluate the timescale required to achieve the depletion of the contaminants, as well as to assess the migration of contaminants outward from Lot40 for the next 40 years. Figure 4-29, Figure 4-30, Figure 4-31 and Figure 4-32 present the concentration over time of benzene and naphthalene for the grid cells intersecting the boundary of Lot40 in layers 3 and 6 (Springbok and WCM Macalister, respectively). Both FDP (Base case and PL253) scenarios were included, and grid cells were grouped according to their position at the East, West, South or North boundary of Lot40. In these figures, the realisation with highest concentration was used to calculate mean and P90 intervals. Thus, the ensembles mean for each boundary cell and for each scenario was plotted (thin dotted black and solid blue lines representing the scenarios). In addition, the P90 confidence interval was also plotted in shades of blue and grey for the PL253 and Base case scenarios, respectively. Values corresponding to the 95% level of protection from the Fresh Water Guidelines (ANZECC & ARMCANZ, 2000) were

also included as a horizontal red line for comparison. These values correspond to 950 and 16 µg/L for benzene and naphthalene, respectively.

Figure 4-29 shows the maximum simulated concentrations of benzene around Lot40 in layer 3 (Springbok Sandstone). The predictive model forecasted that eastern, southern and northern boundaries already present values below the Fresh Water Guideline. The western boundary has realisation near the P90 showing values close to the Fresh Water Guideline and not decreasing over time, likely due to the future abstraction from the Hopeland Site. When comparing the two scenarios, it can be observed that in the PL253 FDP scenario had a minimal influence in the simulated benzene time-series around Lot40.

Figure 4-30 shows the maximum simulated concentrations of benzene around Lot40 in layer 6 (WCM Macalister). Depletion of benzene around Lot40 was forecasted to reach values below the Fresh Water Guideline by, at least by 2021 in all boundaries. When comparing the two scenarios, it can be observed that in the PL253 FDP scenario, there was a minimal influence of the 55 CSG Arrow in the simulated benzene time-series around Lot40.

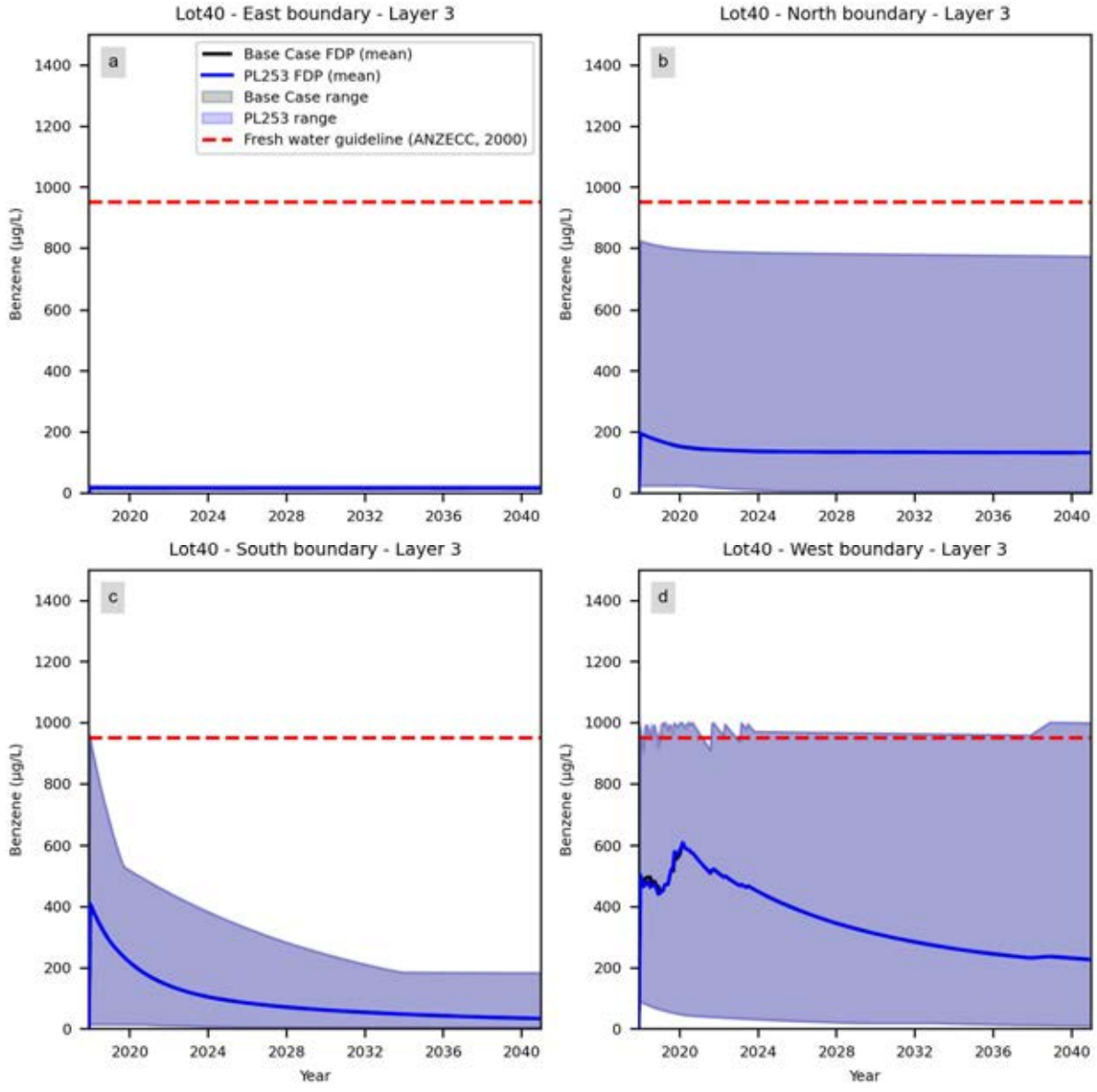

Figure 4-29 – Time-series of maximum simulated concentrations of benzene in layer 3 at the boundaries of Lot40 for the Base Case and PL253 FDP scenario. (a) eastern, (b) northern, (c) southern and (d) western boundary.

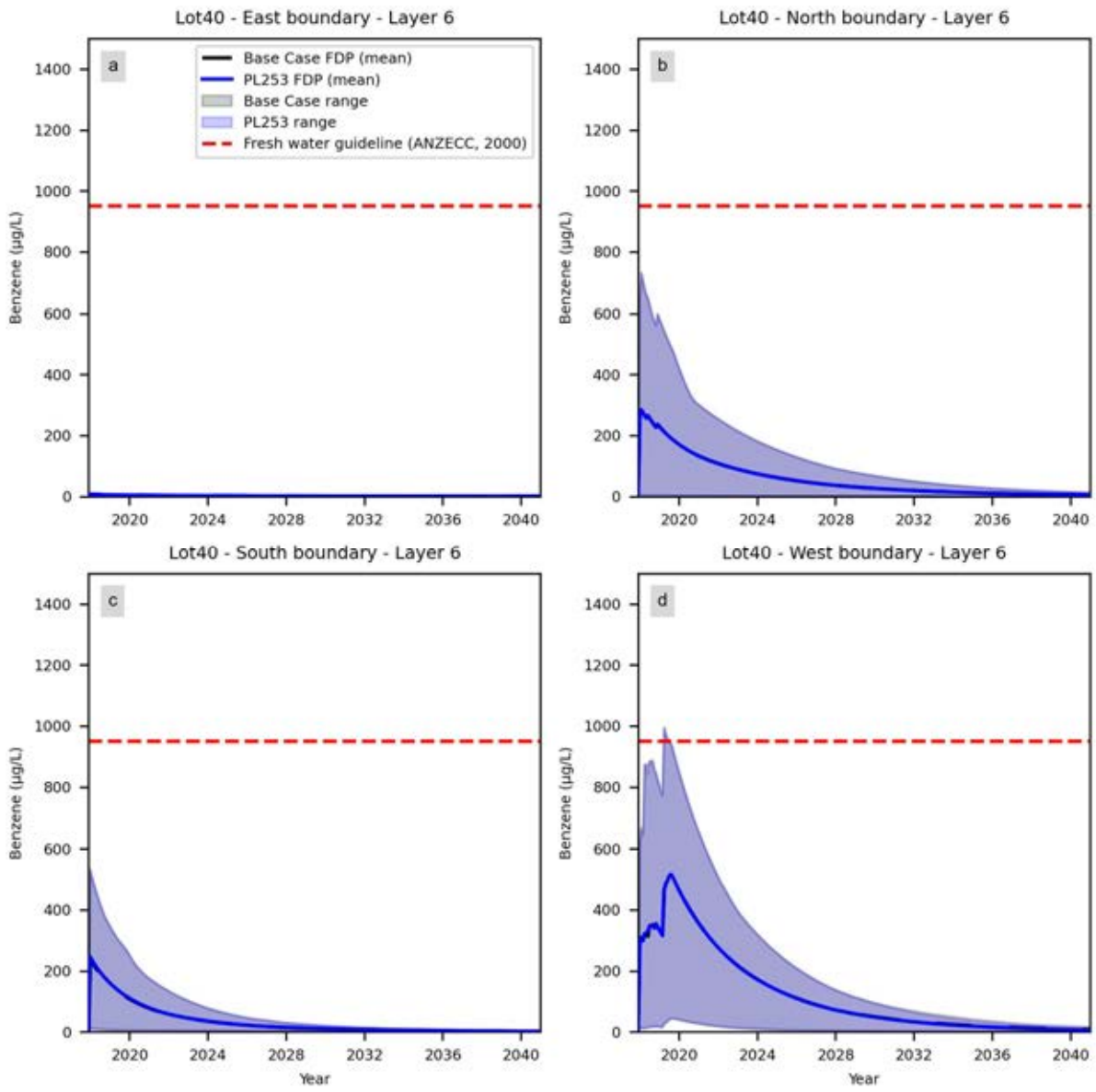


Figure 4-30 – Time-series of maximum simulated concentrations of benzene in layer 6 at the boundaries of Lot40 for the Base Case and PL253 FDP scenario. (a) eastern, (b) northern, (c) southern and (d) western boundary.

Figure 4-31 shows the maximum simulated concentrations of naphthalene around Lot40 in Springbok Sandstone (layer 3). Depletion of naphthalene around Lot40 was forecasted to reach values below the Fresh Water Guideline by 2021 (eastern boundary in Figure 4-31 (a)) the earliest and after 2040 for the rest of boundaries. For naphthalene, some realisations show no depletion and even migration of contaminants outwards of the Lot40 through the southern and western boundaries. This is likely due to the continuous forecasted pumping from the Hopeland Site. Comparison between the two scenarios for layer 3 shows little to no effect of the PL253 FDP scenario in the depletion of naphthalene around Lot40. However, for the Base case scenario, it is noticeable a greater effect from the Hopeland Site abstraction in the migration of contaminant, as it can be seen in the western boundary.

Figure 4-32 shows the maximum simulated concentrations of naphthalene around Lot40 in layer 6. Depletion of naphthalene around Lot40 was forecasted to reach values below the Fresh Water Guideline only in the eastern boundary. At that boundary, lower initial conditions influenced the depletion of naphthalene. At the western, northern and southern boundary, depletion was forecasted to be achieved after 2040 (Figure 4-32 (a)). Comparison between the two scenarios for layer 6 shows little to no effect of the PL253 FDP scenario in the depletion of naphthalene around Lot40. It is noteworthy that similar to layer 6, some realisations show no depletion of naphthalene and even migration from the Lot40 and outward mainly due to the abstraction from the Hopeland Site.

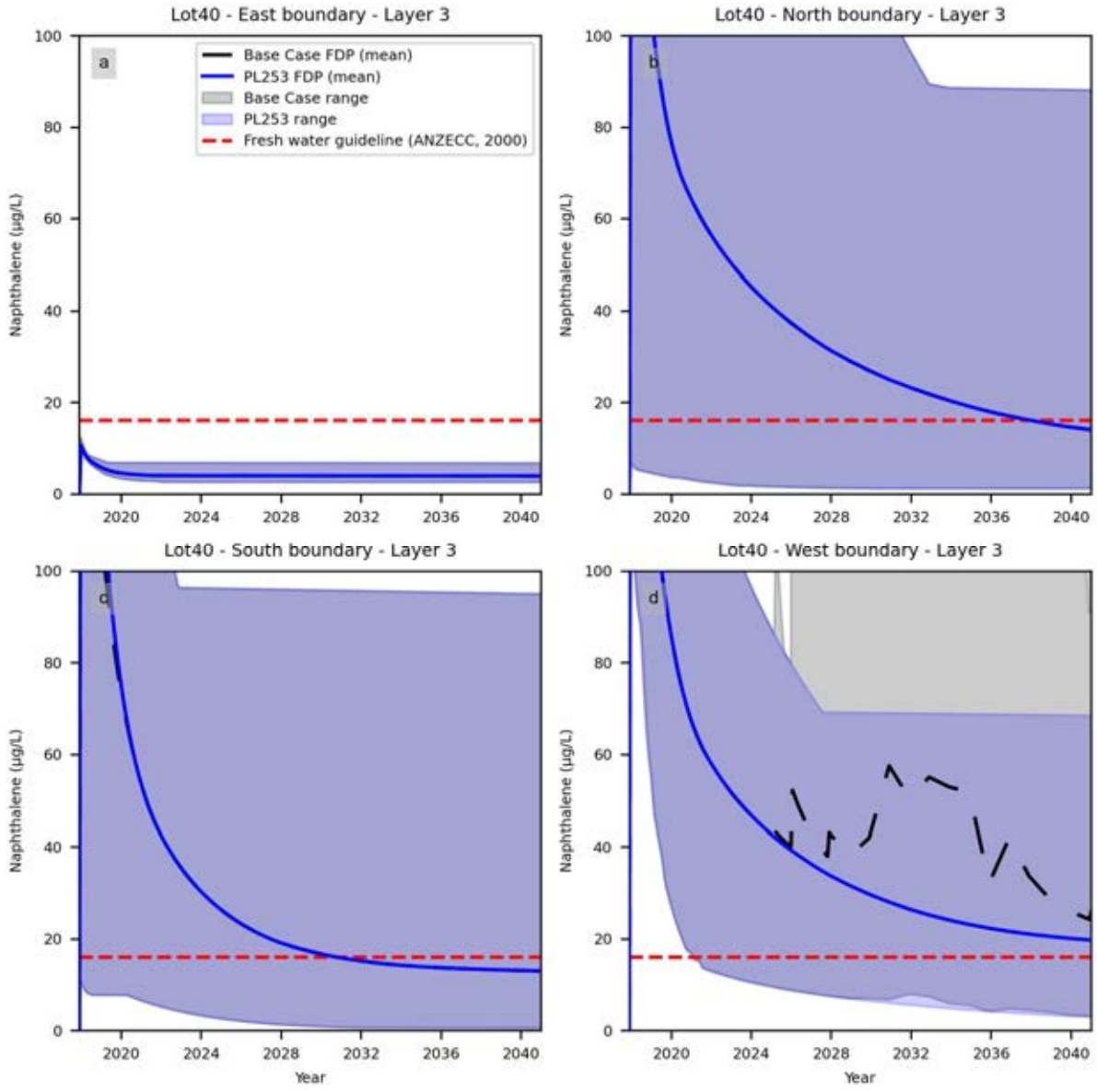


Figure 4-31 – Time-series of maximum simulated concentrations of naphthalene in layer 3 at the boundaries of Lot40 for the Base Case and PL253 FDP scenario. (a) eastern, (b) northern, (c) southern and (d) western boundary.

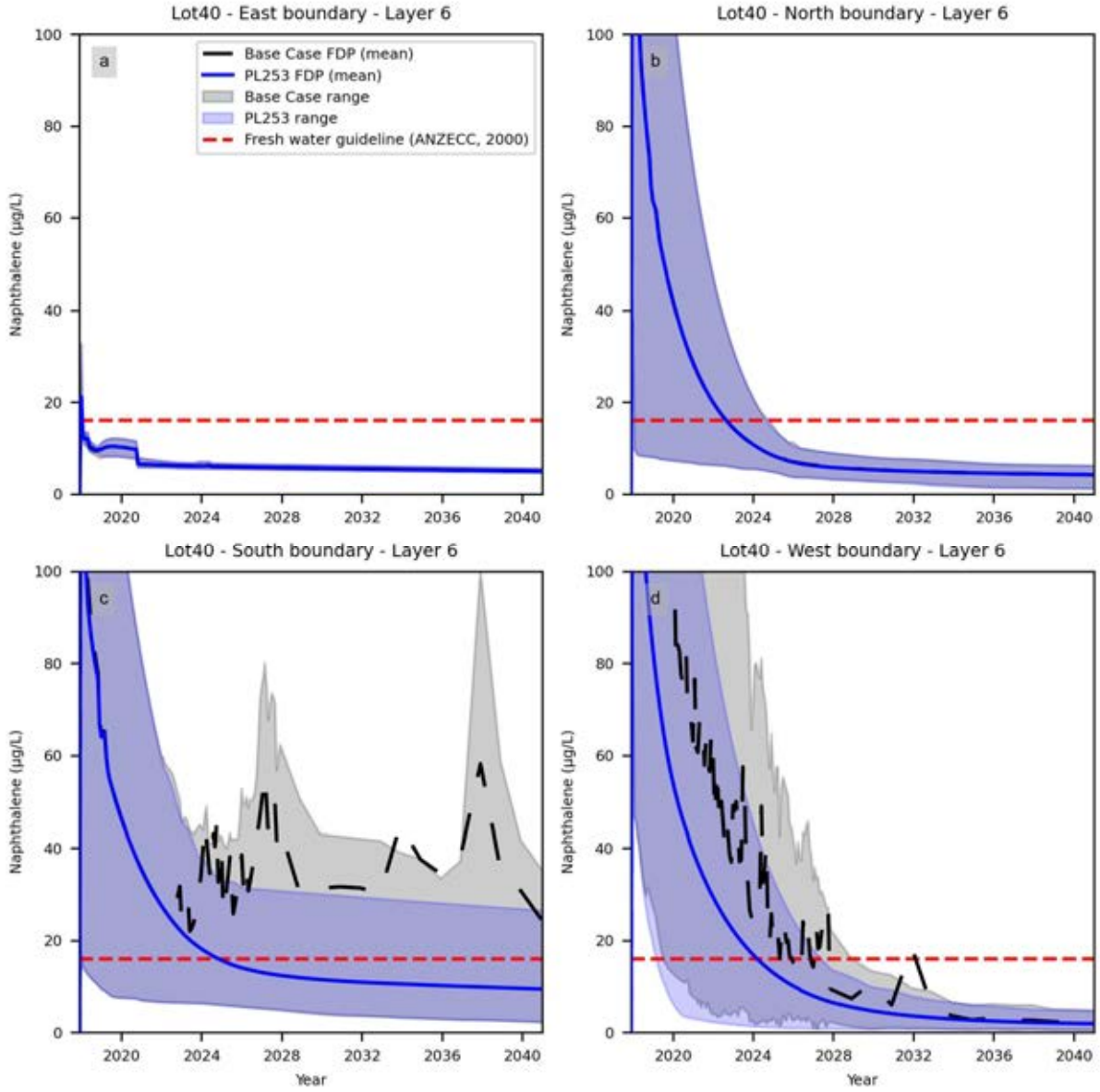


Figure 4-32 – Time-series of maximum simulated concentrations of naphthalene in layer 6 at the boundaries of Lot40 for the Base Case and PL253 FDP scenario. (a) eastern, (b) northern, (c) southern and (d) western boundary.

#### 4.4.3.4 Contaminant Attenuation Timescale

The following section describes the predictions regarding when the contaminants will completely attenuate. The quantity of interest selected to analyse this prediction was the year at which 99% of the model cells reached simulated concentrations below the LOR. This metric was then compared between the scenarios to evaluate the influence of the proposed 55 CSG wells (PL253 FDP) against the Base Case FDP. Values of 1 µg/L were considered as the limits of reporting (LOR) for benzene and naphthalene, respectively, based on the investigation limits presented in the EA Water Conditions.

The predicted year at which the simulated contaminants achieved values below the LOR for each FDP scenario is presented in the histograms of Figure 4-33 and Figure 4-34 for benzene and naphthalene, respectively. These figures display all realisations for the Base Case FDP scenario in the

top row (subplots (a) and (b)) and for the PL253 FDP in the mid row (subplots (c) and (d)). The bottom row of the figures (subplot (e) and (f)) presents the difference between the scenarios.

From the simulated ensemble, benzene (Figure 4-33) in Springbok was forecasted to attenuate completely between 2033 and 2052, as observed in the 95% confidence interval. The forecasted mean year of the ensemble was 2045 (Base Case FDP) and 2046 (PL253 FDP). In Macalister, the benzene concentrations was forecasted to attenuate completely between 2030 and 2051, as per the 95% confidence interval and the forecasted mean year for the completely degradation of benzene was 2036 (Base Case FDP) and 2038 (PL253 FDP). The previous contaminant transport model (AGE, 2023) predicted that the benzene would attenuate completely in Springbok between 2035 and 2040 with 95% confidence. Similarly, AGE (2023) predicted with 95% confidence that benzene in Macalister would degrade between 2020 and 2025.

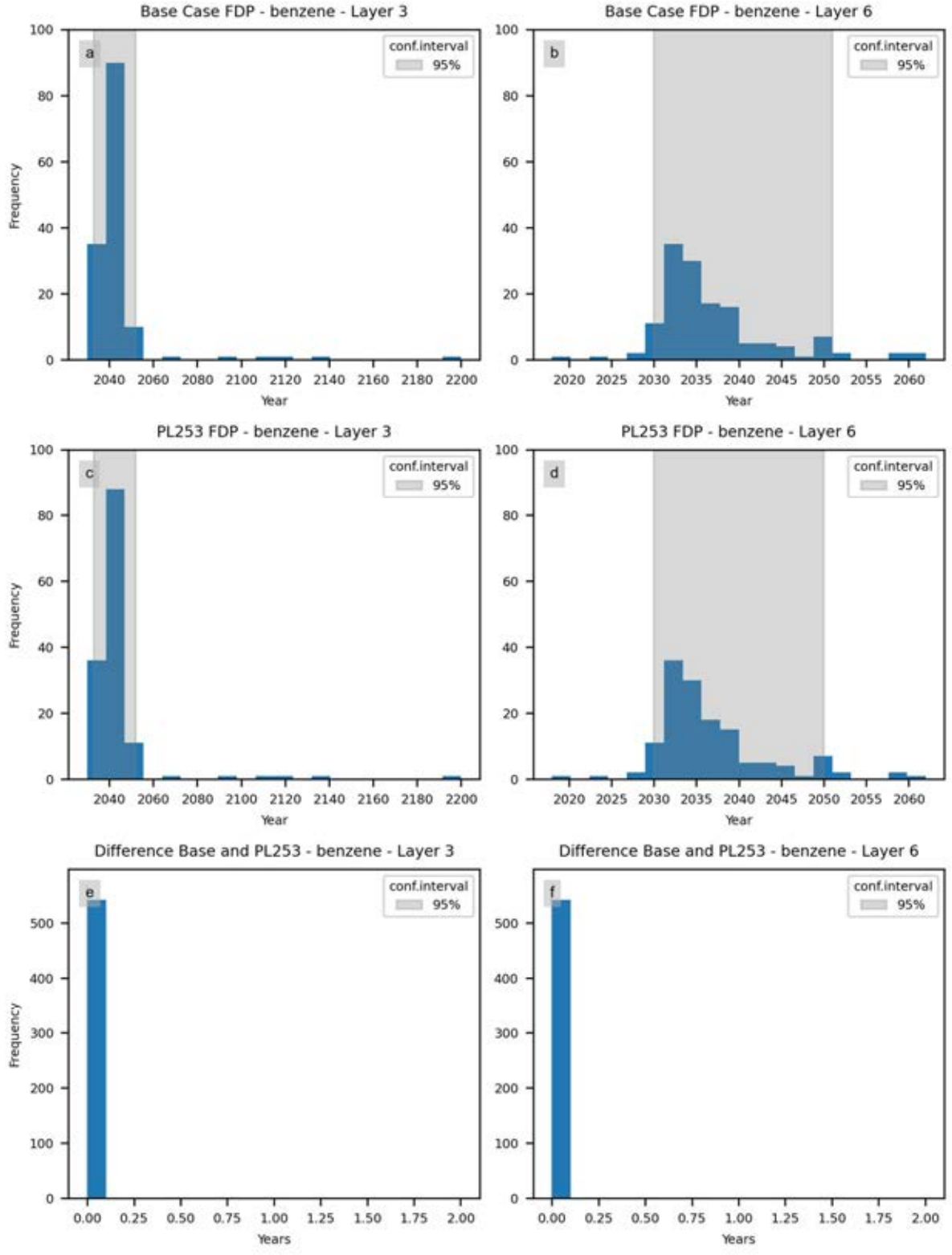


Figure 4-33 – Histograms of the year at which 99% of model cells achieved values of benzene below LOR (1 µg/L) in layers 3 and 6 (i.e., Springbok and WCM Macalister) for the Base Case and PL253 FDP scenarios. Subplots (c) and (d) show the difference between the Base Case and PL253 FDP.

The naphthalene concentration (Figure 4-34) in Springbok was forecasted to attenuate completely between 2021 and 2044, as per the 95% confidence interval. The forecasted mean year was 2031 (Base Case FDP) and 2029 (PL253 FDP). Moreover, the naphthalene concentration in Macalister was forecasted to attenuate completely between 2018 and 2037, as per the 95% confidence interval, and the forecasted mean year was 2023 and 2022 for both the Base Case and PL253 FDP scenarios. The previous contaminant transport model (AGE, 2023) predicted that the naphthalene would attenuate completely in Springbok (values below LOR) between 2020 and 2025 with 95% confidence. Similarly, AGE (2023) predicted with 95% confidence that naphthalene in Macalister would degrade between 2018 and 2020.

Small differences in the predicted years between FDP scenarios resulted from the simulated posterior ensembles. It was forecasted that the PL253 FDP scenario would delay the attenuation of the contaminants by between less than 1 to 4 years (95% confidence), with most realisations falling in the less than 1 year timescale and worst cases forecasting an attenuation delay of 6-9 years. Therefore, the influence of the 55 proposed CSG wells would be minimal in the predicted timescales for the contaminants attenuation. This is possibly due to the behaviour of benzene and naphthalene being dominated by the natural attenuation parameters, i.e., sorption and more importantly biodegradation, than the advective-driven transport from the Arrow proposed CSG wells. It is noteworthy that, AGE (2023) model resulted in small differences between scenarios for both compounds even though the PL253 FDP scenarios had more proposed CSG wells than the current (amended) scenario.

To complement these predictions, maps of benzene and naphthalene concentrations in Springbok and Macalister, for both scenarios (Base Case and PL253 FDP) are presented in Appendices K and L. These maps present the mean and standard deviation of the respective compound concentration for selected years, including the initial conditions (year 2018). A summary of the predicted years to achieve contaminant depletion under the Base Case and PL253 FDP scenarios is presented in Table 4-9.

Table 4-9 – Summary of predicted years to achieve contaminant depletion.

| Compound | Statistics | Base Case FDP | PL253 FDP | Base Case FDP | PL253 FDP |
|---|---|---|---|---|---|
| | | Springbok | Springbok | Macalister | Macalister |
| Naphthalene | P5 | 2021 | 2021 | 2018 | 2018 |
| | Mean | 2031 | 2029 | 2023 | 2022 |
| | P95 | 2044 | 2043 | 2037 | 2036 |
| Benzene | P5 | 2033 | 2033 | 2030 | 2030 |
| | Mean | 2045 | 2045 | 2036 | 2038 |
| | P95 | 2052 | 2052 | 2051 | 2050 |

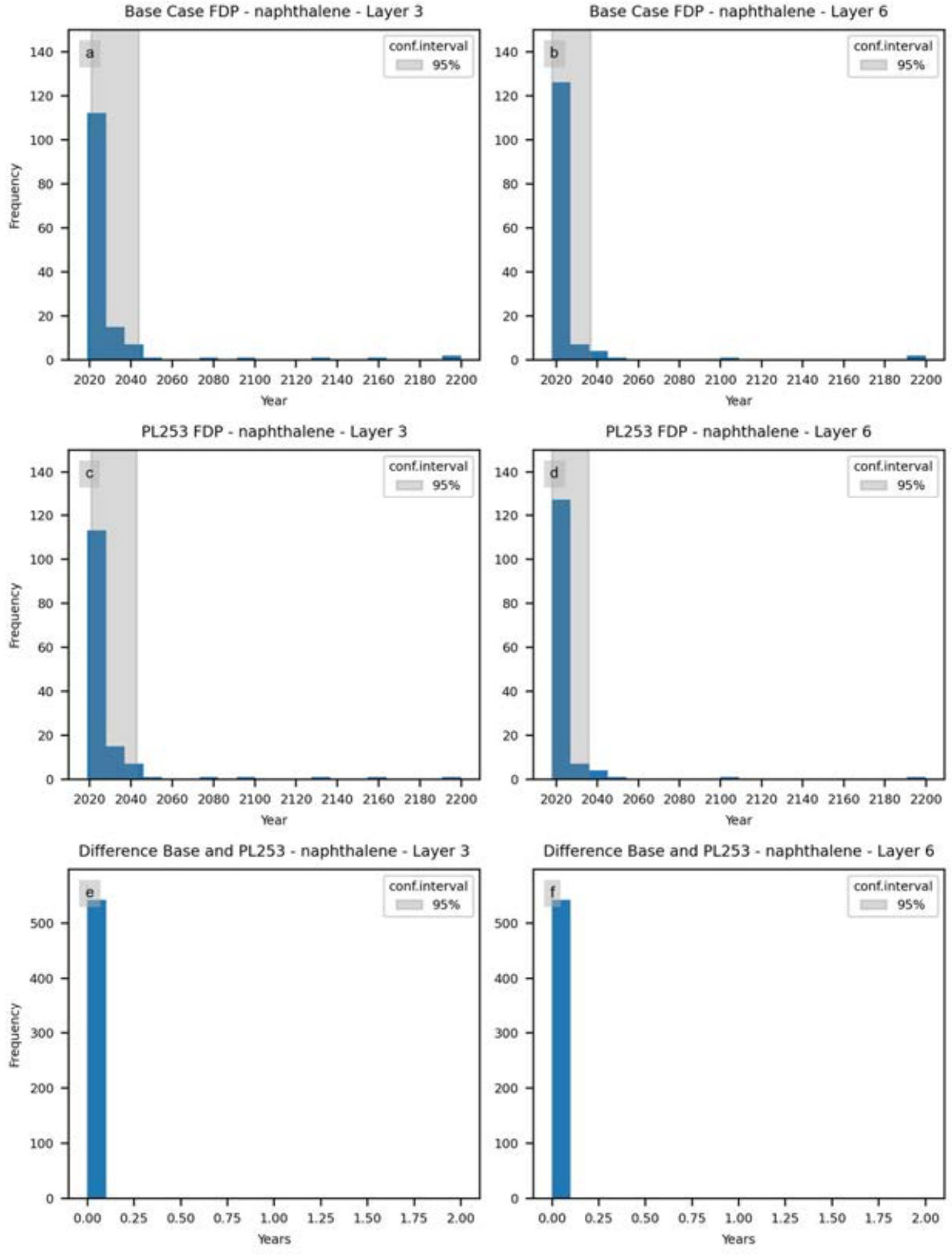


Figure 4-34 – Histograms of the years at which 99% of model cells achieved values of naphthalene below LOR (1 µg/L) in layers 3 and 6 (i.e., Springbok and WCM Macalister) for the Base Case and PL253 FDP scenarios. Subplots (c) and (d) show the difference between the Base Case and PL253 FDP.

### 4.4.4 Concentration at New Monitoring Bores

During 2024, Arrow Energy installed four new monitoring bores in the Lot40: HL34, HL35, HL36 and HL37. The figures below display the posterior ensemble mean and the uncertainty bands of the simulated benzene and naphthalene concentrations (Figure 4-36). A map with the bore locations is also included in Figure 4-35. The concentration trends over time indicate that these monitoring bores would effectively help capturing any contaminant migration, enhancing the monitoring network.

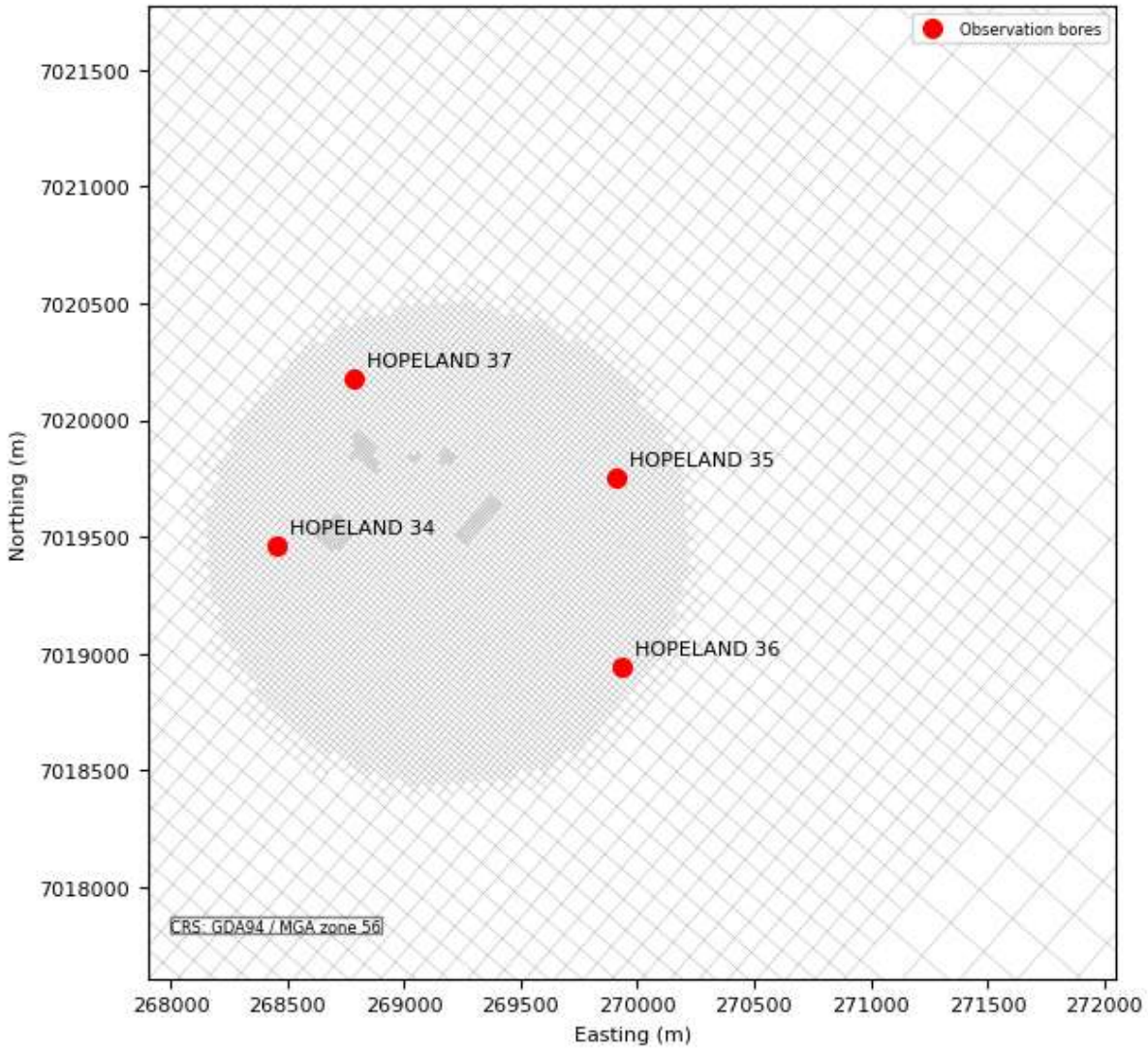


Figure 4-35 – Map of the newly installed monitoring bores.

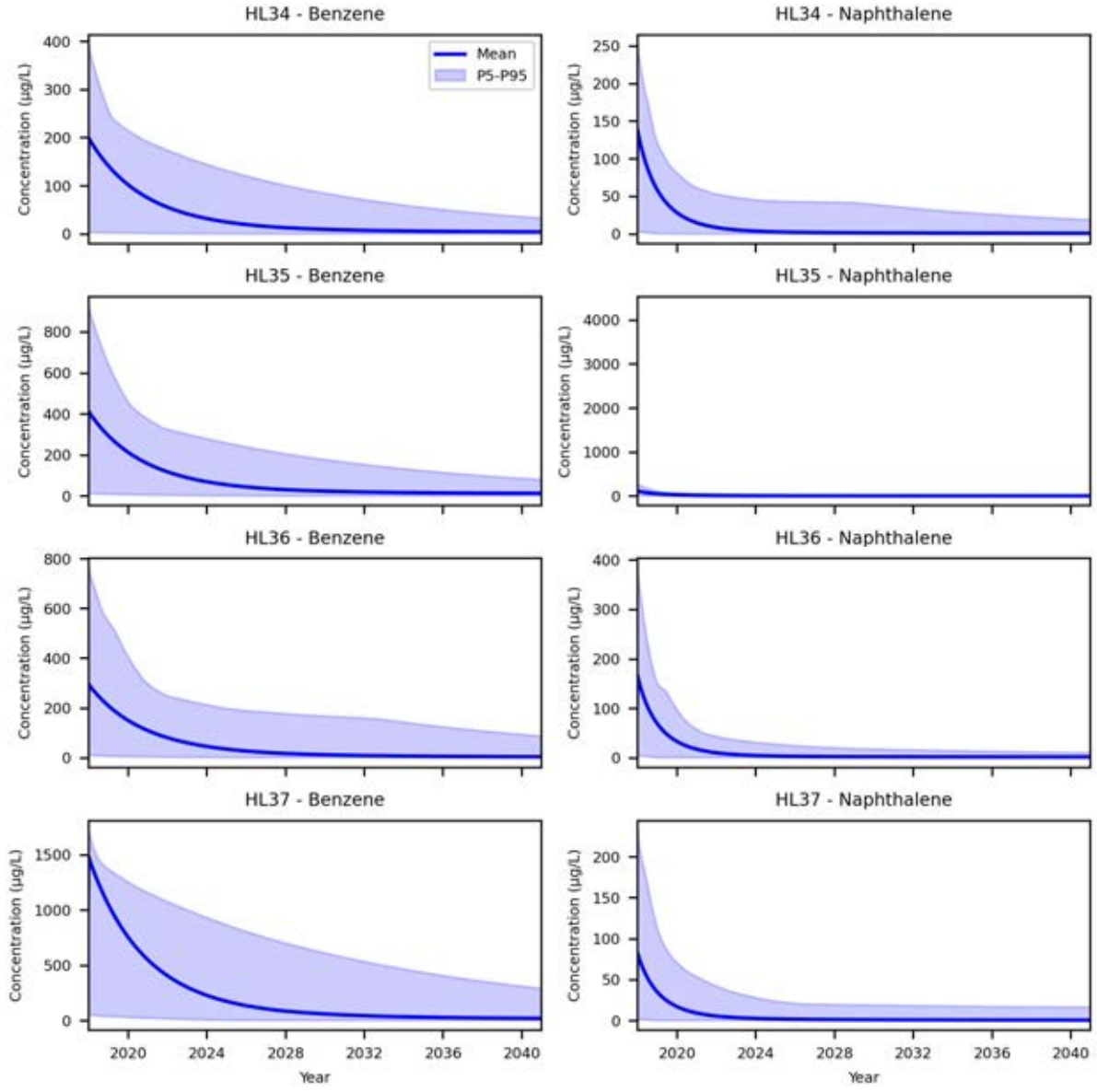


Figure 4-36 – Simulated ensemble mean concentrations for the newly installed monitoring bores.

# 5.0 Impact Assessment

This section assesses the impact of the 55 proposed CSG wells (Stage 1 activities and PL253 FDP scenario as described in the modelling chapters) on the potential groundwater receptors identified in the site conceptual model. To support this assessment, predictive modelling under uncertainty was conducted for the groundwater flow, particle tracking, and contaminant transport models. The resulting predictions on the quantities of interest helped to evaluate the impact of Stage 1 activities. As a general disclaimer, model uncertainties around the quantities of interest remained large with the available data.

The main results from the predictive groundwater modelling efforts regarding the proposed activities for Stage 1 were:

- PL253 FDP will have a minimal impact on the gradient reversal in Lot40. This reversal is expected to happen anywhere between 2024 and 2090.
- Vertical gradients will always remain downwards from Springbok to WCM Macalister, effectively avoiding migration of contaminants upwards.

The main results from the predictive particle tracking model regarding the proposed activities for Stage 1 were:

- Particle tracking showed that PL253 FDP will have minimal impact regarding how far contaminants would travel without attenuation and spreading.
- Effectively, particle tracking showed a worst-case outcome where contaminants will not travel more than 2,075 to 2,175meters from the Lot40.

The main results from the predictive contaminant transport model regarding the proposed activities for Stage 1 were:

- As suggested by the flow and particle tracking predictions, the contaminants have likely already reached a steady-state condition and the 55 CSG wells will not substantially increase the size of the contaminant spatial distribution.
- Theres is minimal influence of the PL253 FDP in the contaminant depletion in and around the Lot40.
- Under the PL253 FDP (55 CSG Wells or Stage 1), contaminants in Springbok Sandstone would reach complete attenuation (LOR < 1 ug/L and 95% confidence) around 2052 for benzene and 2043 for naphthalene.
- Under the PL253 FDP, contaminants in WCM Macalister would reach complete attenuation (LOR < 1 ug/L and 95% confidence) around 2050 for benzene and 2036 for naphthalene.
- The 55 CSG wells operation will most likely delay the depletion of the contaminants by up to 1 year, with some predictions extending to 4-9 years.

Groundwater receptors in and around PL253 correspond mainly to water supply bores. These bores are all located more than 2.5 km away from the Lot40 (see section 2.8 and Figure 2-48). According to the modelling predictions, contaminants would not travel beyond 2,100 m from Lot40, as projected around the year 2200. Moreover, complete attenuation of the contaminants is expected to occur before 2052 and 2043 for benzene and naphthalene, respectively, thus lowering the risk of contaminants moving further downstream to receptors beyond 2.5 km.

In summary, there is minimal impact of the 55 proposed CSG wells regarding the extent of the contaminants. However, the 55 CSG wells will most likely delay the depletion of the contaminants by up to 1 year to a maximum of 4 to 9 years as shown in extreme realisations. Uncertainty around these predictions remain large.

# 6.0 Summary and Conclusions

## 6.1 Conceptualisation

A conceptual model was developed for the PL253 area and its vicinity as part of groundwater modelling and uncertainty analyses. The scope of the conceptual modelling was addressed the Condition Water (3), that states the site conceptual model in EA condition Water 2(2) should characterise the residual contaminant source of Lot 40 on DY85, identify mobilisation pathways and present the groundwater pressure and flow regime around Lot 40 on DY85, provide an analysis of how contaminants may migrate over time, provide uncertainties in conceptualisation resulting from formation heterogeneity, preferential pathways and structural influences; and assess the potential for long-term release of contaminants in the groundwater.

The conceptual modelling works performed a mapping of the different hydrostratigraphic units using the previous groundwater modelling work as a base, as well as analyses of groundwater levels and concentrations of selected hydrocarbons in the available monitoring boreholes. Current snapshots of head and concentration distributions were analysed.

In relation to prior monitoring data, current groundwater level and concentration levels remain mostly stable, with exception of groundwater levels in boreholes closer to ongoing CSG extraction activities, located within Lot40 DY85. BTEX and Naphthalene concentrations in monitoring boreholes within Lot40 have decreased from 2020 to date, associated either with migration of the contaminants and/or natural attenuation.

The analysis of potential-receptor pathways suggested that risk of contamination to downgradient groundwater users is low in the short to mid-term, given the current level of depressurisation within the Walloon Coal Measures. Vertical migration of contaminants to other hydrogeological units is also unlikely given the hydraulic heads in this formation are lower than those of the overlying Springbok Sandstone and lower than those of the underlying Wambo interburden. In addition, there is no evidence of vertical fracturing at the gasifiers, although regional fractures have been identified in the Lot40 DY85.

## 6.2 Groundwater Flow

Groundwater modelling of the PL253 area has been developed, continuing from previous efforts by AGE (2023) and GHD (2019) to address requirements of the EA. Work described in this section reflects the first stage, addressing groundwater flow history matching and predictive uncertainty analysis employing particle tracking methods. Subsequent phases will include predictive uncertainty analysis employing fully advective-dispersive solute transport models.

A single-phase groundwater model has been developed in MODFLOW-6, updating model discretisation, geometry and stresses based on borehole logs and hydraulic heads provided by Arrow and input from the most recent generation of regional cumulative impact assessment modelling (OGIA, 2021). History matching was undertaken using ensemble-based methods to facilitate subsequent non-linear predictive uncertainty analysis. The ensemble of history matched models was able to adequately represent measured time-series of hydraulic heads, vertical head differences and other soft-data. All realisations achieved RMSE lower than 10% and near zero mass balance error.

The impact of proposed CSG production at PL253 was assessed in terms of changes to the groundwater flow regime and potential for UCG-related contaminant migration away from the

former Linc Energy site at Lot40. Relative impact was assessed by simulating two scenarios: (1) the Base case and (2) PL253 FDPs. The latter includes the additional 55 wells proposed for PL253. Predictive scenarios were extended to the year 2200.

Results show that uncertainty in forecasted outcomes is large. However, the difference between the two FDP scenarios is minor. And, notably, the PL253 FDP scenario does not always result in the less favourable outcomes.

The anticipated timeframes for drawdown recovery at Lot40 extend from the present to the year 2090. However, the difference between FDP scenarios is less than 5 years. It's worth noting that the Base case FDP has almost the same probability of leading to a slower recovery at Lot40 as the PL253 FDP.

The outcomes from particle tracking underscore a significant degree of uncertainty concerning the potential reach of UCG-related contaminants during the simulation period. The spatial range that the simulated particles could cover is substantial, extending over 2 Km from the lot's boundary. However, it's important to note that the disparity between the FDP scenarios is relatively small.

Uncertainty in the spatial extent is dominated by the pathways that particles take as they migrate vertically downwards from the Springbok. Particles released in the Macalister layer travel shorter distances from the site during the simulated period and tend to remain within the boundary of Lot40. Constraining uncertainty may benefit from data collection that informs characterisation of the current disposition of contaminants, as well as the vertical connectivity between layers at, and near, the site.

In summary, available data was assimilated to constrain forecast uncertainty. However, there remains a significant level of uncertainty regarding the timing and manner of UCG-related contaminant migration from the site. Despite this, when comparing simulated scenarios, it appears that the proposed field development plan at PL253 is not likely to have a substantial impact compared to the baseline scenario.

## 6.3 Contaminant Transport

A groundwater contaminant transport model was developed based on the groundwater model described in Chapter 3.0. Benzene and naphthalene were selected as the simulated compounds. The transport model was history-matched against concentrations of the compounds from the measured groundwater quality data. During history-matching, the transport-only parameters were allowed to vary and all the ‘groundwater flow’ parameters were kept fixed. Concentration trends of benzene and naphthalene were adequately reproduced, especially regarding the most observed behaviour of decreasing concentrations in most observation bores. However, bores depicting a decreasing trend followed by increasing concentrations (e.g., NB01S in Springbok and NB02D in Macalister) could not be reproduced. This could imply the existence of a source term near or upgradient of these bores and possibly in other layers such as Springbok.

Predictive modelling was conducted based on the posterior ensemble from the history-matched transport model. Two FDP scenarios were simulated to assess the effect of the proposed 55 CSG wells. The forecasted concentrations around Lot40 and the predicted year at which the hydrocarbon concentrations would completely deplete were assessed and compared between the scenarios.

Concentrations at the boundary of Lot40 were compared with the Fresh Water Guidelines (ANZECC & ARMCANZ, 2000) for reference. The results showed that the maximum simulated concentrations

always reached values below the guidelines before the end of the simulated period in both scenarios, being naphthalene at the southern boundary of Lot40 the latest to achieve these simulated concentrations at around 2140.

Moreover, simulated results suggest that concentrations of benzene would reach values below LOR between 2033 and 2052 in Springbok and between 2030 and 2050 in Macalister. Similarly for naphthalene, predictions suggest that values would reach below LOR any when between 2021 and 2043 in Springbok, and between 2018 and 2037 in Macalister. These predictions carried more uncertainty as extended further into the future than those simulated in the previous model (AGE, 2023).

The predictions suggest a minor to no influence of the PL253 FDP scenario compared to the Base Case, and thus a minimal effect from the proposed 55 CSG wells in the migration of the simulated contaminants. We suggest this is possibly because the shrinking of the extent of contaminants is mainly controlled by the natural attenuation parameters than the advective transport driven by the CSG wells. In addition, most of the 55 CSG wells are not proposed to extract from Macalister and none of them target Springbok. Thus, their migration effect would be minimal. Finally, most CSG wells start their operations from 2027 when the contaminant extent have already predicted to have shrunk (see maps in Appendices K and L).

## 6.4 Impact Assessment

Finally, there is minimal impact of the 55 proposed CSG wells regarding the extent of the contaminant distribution. However, the 55 proposed CSG wells will most likely delay the attenuation of the contaminants by up to 1 year to a maximum of 4 to 9 years. It is important to note that uncertainty around these predictions remains large. Finally, the current model predictions suggest that considerable exceedances of benzene and naphthalene reaching groundwater supply bores beyond a 2.5 km radius from Lot40 are unlikely.

# 7.0 References

Abdul, A.S., Gibson, T.L., Rai, D.N., 1987. Statistical correlations for predicting the partition coefficient for nonpolar organic contaminants between aquifer organic carbon and water. Hazardous Waste & Hazardous Materials 4(3):211-222.

AECOM, 2018. Conceptual Site Model – Hopeland Site. Prepared for Department of Environment and Science by AECOM Australia Pty Ltd. 12th September 2018.

AGE, 2020. Production Licensing Modelling Support prepared for Arrow Energy by Australasian Groundwater and Environmental Consultants Pty Ltd. June 2020.

AGE, 2023. PL 253 Environmental Approval Amendment Support – Contaminant transport validation – Addendum to AGE (2022) by Australasian Groundwater and Environmental Consultants Pty Ltd. 19th January 2023.

Anderson, M.P., Woessner, W.W. and Hunt, R.J., 2015. *Applied groundwater modeling: simulation of flow and advective transport*. Academic press.

ANZECC & ARMCANZ, 2000. Australian and New Zealand Guidelines for Fresh and Marine Water Quality, Australian and New Zealand Environment and Conservation Council and Agriculture and Resource Management Council of Australia and New Zealand, Canberra.

Appelo, C.A.J., Postma, D., 2005. Geochemistry, groundwater and pollution. CRC Press, Taylor& Francis Group.

Arrow, 2020. PL253 Conceptual model –2020 Update. Technical Note, Surat Gas Project.

Arrow, 2021. Groundwater Characteristics Monitoring Plan.

Bakker, M, Post, V, Hughes, J. D., Langevin, C. D., White, J. T., Leaf, A. T., Paulinski, S. R., Bellino, J. C., Morway, E. D., Toews, M. W., Larsen, J. D., Fienen, M. N., Starn, J. J., and Brakenhoff, D., 2022. FloPy v3.3.7 — release candidate: U.S. Geological Survey Software Release, 15 December 2022.

Barnett, B., Townley, L.R., Post, V., Evans, R.E., Hunt, R.J., Peeters, L., Richardson, S., Werner, A.D., Knapton, A., and Boronkay, A., 2012. Australian groundwater modelling guidelines National Water Commission, Waterlines Report Series No. 82 June 2012 ISBN: 978-1-921853-91-3 (online).

Barrett, M.H., Williamson, D.J., Lerner, D.N., 1994. A continuous flow method for calculating adsorption isotherms of organic pollutants onto aquifer materials. J. Cont. Hydrol. 15:15-25.

Chen, Y., Oliver, D.S., 2013. Levenberg-Marquardt forms of the iterative ensemble smoother for efficient history matching and uncertainty quantification, Computational Geosciences, vol. 17, no. 4, pp. 689–703.

Chen, Y., Oliver, D.S., 2017. Localization and regularization for iterative ensemble smoothers, Computational Geosciences, vol. 21, no. 1, pp. 13–30.

Chiou, C.T., Porter, P.E., Schmedding, D.W., 1983. Partition equilibria of nonionic organic compounds between soil organic matter and water. Environ. Sci. Technol. 17(4):227-231

Cook, A.G., Draper, J.J., 2013. Surat Basin, in Geology of Queensland, ed. Jell PA, Geological Survey of Queensland, Brisbane, pp. 533-539.

CSIRO, 2023. Arrow (Hopeland) - Advice on groundwater modelling and management to the Queensland Department of Environment and Science.

Dafny, E., Silburn, D.M., 2014. The hydrogeology of the Condamine River Alluvial Aquifer, Australia: a critical assessment, Hydrogeology Journal, vol. 22, no. 3, pp. 705-727.

Doherty, J., 2022. Scientifically-Based, Decision-Support Groundwater Modelling: A Conceptual Framework. A Groundwater Decision Support Initiative (GMDSI) monograph.

Eberhardt C., Grathwohl, P., 2002. Time scales of organic contaminant dissolution from complex source zones: coal tar pools vs. blobs. J Contam. Hydrol. 59, 45-66

Exon, N.F., 1976. Geology of the Surat Basin in Queensland, Australia Bureau of Mineral Resources, Canberra.

Feehley, C.E., Zheng, C., Molz, F.J., 2000. A dual-domain mass transfer approach for modeling solute transport in heterogeneous aquifers: Application to the Macrodispersion Experiment (MADE) site. Water Resources Research 36, 2501–2515. doi:10.1029/2000WR900148.

GHD, 2019. Arrow Hopeland Groundwater Study Groundwater Modelling Report – PL253.

Golder, 2010. Assessment of subsidence due to coal seam gas extraction. Report 097626104-011-Rev0. Submitted to Queensland Gas Company.

Gustafson, K.E., Dickhut, R.M., 1994. Molecular diffusivity of polycyclic aromatic hydrocarbons in aqueous solution. Journal of Chemical & Engineering Data. doi: 10.1021/je00014a019

Hamilton, S. K., Esterle, J. S., & Sliwa, R., 2014. Stratigraphic and depositional framework of the Walloon Subgroup, eastern Surat Basin, Queensland. Australian Journal of Earth Sciences, 61(8), 1061–1080.

Herckenrath, D., Doherty, J. and Panday, S., 2015. Incorporating the effect of gas in modelling the impact of CBM extraction on regional groundwater systems, Journal of Hydrology, vol. 523, pp. 587–601.

Hodson, J., Williams., N.A., 1988. The estimation of the adsorption coefficient (Koc) for soils by high performance liquid chromatography. Chemosphere. 17(1):67-77.

Huxley, W.J., 1982. Condamine River Valley Groundwater Investigation: The hydrogeology, hydrology and hydrochemistry of the Condamine River Valley Alluvium, Queensland Water Resources Commission, Brisbane.

Kan, A.T., Tomson, M.B., 1990. Ground water transport of hydrophobic organic compounds in the presence of dissolved organic matter. Environ. Toxicol. Chem. 9:253-263.

Karickhoff, S.W., Brown, D.S., Scott., T.A., 1979. Sorption of hydrophobic pollutants on natural sediments. Water Res. 13:241-248.

Karickhoff, S.W., 1981. Semi-empirical estimation of sorption of hydrophobic pollutants on natural sediments and soils. Chemosphere. 10(8):833-846.

Karickhoff, S.W., 1982. Sorption kinetics of hydrophobic pollutants in natural sediments. Contaminants and Sediments. 2:193-205.

Kishi, H., Kogure, N., Hashimoto, Y., 1990. Contribution of soil constituents in adsorption coefficient of aromatic compounds, halogenated alicyclic and aromatic compounds to soil. Chemosphere. 21(7):867-876.

Lien, J.M., Liu, G., and Langevin, C.D., 2017. GRIDGEN version 1.0.02 -- A computer program for generating unstructured finite-volume grids: U.S. Geological Survey Software Release, 06 January 2017, http://dx.doi.org/10.5066/F79G5JXV.

Lokke, H., 1984. Sorption of selected organic pollutants in Danish soils. Ecotoxicol. Environ. Safety 8:395-409.

Mackay, D., Shiu, W. Y., Ma, K. C., 1992. Illustrated Handbook of Physical-Chemical Properties and Environmental Fate for Organic Chemicals. Volume I – Monoaromatic Hydrocarbons, Chlorobenzenes, and PCB's. Lewis Publishers, Boca Raton, FL.

McCarthy, J.F., Jimenez, B.D., 1985. Interactions between polycyclic aromatic hydrocarbons and dissolved humic material: binding and dissociation. Environ. Sci. Technol. 19(11):1072-1076

Moore, C.R., Doherty, J.E., Howell, S., Erriah, L., de Verteuil, D., Cui, T., 2013. Challenges for upscaling hydraulic properties and processes in the coal seam gas context, CSIRO.

Moore, C.R., Doherty, J., Howell, S., Erriah, L., 2015. Some Challenges Posed by Coal Bed Methane Regional Assessment Modeling. Groundwater 53, 737–747. https://doi.org/10.1111/gwat.12276

Moriasi, D., Gitau, M. Pai, N. and Daggupati, P., 2015. Hydrologic and Water Quality Models: Performance Measures and Evaluation Criteria Transactions of the ASABE (American Society of Agricultural and Biological Engineers) 58(6):1763-1785.

Neville, C.J., Tonkin, M.J., 2004. Modeling multiaquifer wells with MODFLOW. Groundwater 42 (6), 910e919. http://doi.org/10.1111/j.1745-6584.2004.t01-9-.x

Newell, C.J., Connor, J.A., 1998. Characteristics of dissolved petroleum hydrocarbon plumes. American Petroleum Institute. Version 1.1.

OGIA, 2016. Hydrogeological Conceptualisation Report for the Surat Cumulative Management Area. OGIA, Department of Natural Resources and Mines.

OGIA, 2020. Hydrogeological characterization of faults in the Surat Basin. OGIA, Department of Natural Resources and Mines.

OGIA, 2019. Analysis of groundwater level trends in the Hutton Sandstone, Springbok Sandstone and Condamine Alluvium, Surat Cumulative Management Area.

OGIA, 2021a. Modelling of cumulative groundwater impacts in the Surat CMA: approach and methods. Version 1.0.

OGIA, 2021b. Regional flow systems and potentiometry in Queensland's Surat and southern Bowen basins. Version 1.0.

OGIA, 2023. Request for advice on groundwater matters relating to Arrow (Hopeland) Environmental Authority amendment application.

Perkins, G., Du Toit, E., Koning, B., and Ulbrich, A. 2013. Unconventional Oil Production from Underground Coal Gasification and Gas to Liquids Technologies, Society of Petroleum Engineers, presented at the SPE Unconventional Resources Conference and Exhibition-Asia Pacific, Brisbane 11-13 November 2013.

Piwoni, M.D., Banerjee, P., 1989. Sorption of volatile organic solvents from aqueous solution onto subsurface solids. J. Contam. Hydrol. 4(2):163-179.

Podoll, R.T., Irwin, K.C., Parish, H.J., 1989. Dynamic studies of naphthalene sorption on soil from aqueous solution. Chemosphere. 18(11/12):2399-2412.

Prommer, H., Barry D.A., Davis G.B., (2002). Influence of transient groundwater flow on physical and reactive processes during biodegradation of a hydrocarbon plume. J. Contam. Hydrol. 59, 113-131.

Prommer, H., Davis G.B., Barry D.A., Miller C.T., 2003. Modelling the Fate of Petroleum Hydrocarbons in Groundwater. Proceedings of the Fifth National Workshop on the Assessment of Site Contamination.

QGC 2013, Stage 3 Water Monitoring and Management Plan. Chapter 5 - The conceptual model of groundwater flow in the Surat Basin., QGC.

QGC, 2014. Surat Basin Geology. QGC.

QGC, 2016. The conceptual model of groundwater flow in the Surat Basin. Stage 3 Water Monitoring and Management Plan. Chapter 5.

Raiber, M., Cox, M., Cendon, D., Feitz, A. 2013. Groundwater chemistry baseline of the Walloon Coal Measures in the Clarence-Moreton and Surat basins, Queensland, Australia. In: IAH 40th International Congress; 15-20 September 2013; Perth. International Association of Hydrogeologists; 2013. page 190.

Regional Development, Manufacturing and Water of Queensland, 2024. Groundwater Database – Queensland,

Rigby, S.M., Kantsler, A.J., 1987. Marilla Creek – An untested stratigraphy play in the Surat Basin. APPEA Journal, 27 (1), 230-244.

Rippen, G., Ilgenstein, M., Klopffer, W., Poremski, H.J., 1982. Screening of the adsorption behavior of new chemicals: natural soils and model adsorbents. Ecotoxicol. Environ. Safety 6:236-245

Rogers, R.D., McFarlane, J.C., Cross, A.J., 1980. Adsorption and desorption of benzene in two soils and montmorillonite clay. J. Am. Chem. Soc. 14(4):457-460.

Scheibe, T., Chien, Y., 2003. An Evaluation of Conditioning Data for Solute Transport Prediction. Groundwater, 41.

Scott, S., Anderson, B., Crosdale, P., Dingwall, J., Leblang, G., 2004. Revised geology and coal seam gas characteristics of the Walloon Subgroup - Surat Basin, Queensland, in PESA Eastern Australasian Basins Symposium II, pp. 19–22.

Seip, H.M., Alstad, J., Carlberg, G.E., Martinsen, K., Skanne, R., 1986. Measurement of mobility of organic compounds in soils. Sci. Total Environ. 50:87-101.

Sinclair Knight Merz (SKM), 2006. Linc Energy Ltd – Underground Coal Gasification, Gas to Liquids and Power Project. Referral of Proposed Action by Damien Taylor, Project Manager, SKM, Spring Hill, Queensland.

Southworth, G.R., Keller, J.L., 1986. Hydrophobic sorption of polar organics by low organic carbon soils. Water, Air, and Soil Pollution. 28:239-248.

Stauffer, T.B., MacIntyre, W.G., 1986. Sorption of low-polarity organic compounds on oxide minerals and aquifer material. Environ. Toxicol. Chem. 5:949-955.

Suarez, M., and Rifai H.S., (1999). Biodegradation Rates for Fuel Hydrocarbons and Chlorinated Solvents in Groundwater, Bioremediation Journal, 3:4, 337-362, doi: 10.1080/10889869991219433

Szabo, G., Prosser, S.L., Bulman, R.A., 1990a. Determination of the adsorption coefficient (Koc) of some aromatics for soil by RP-HPLC on two immobilized humic acid phases. Chemosphere. 21(6):777-788.

Vowles, P.D., Mantoura., R.F.C., 1987. Sediment-water partition coefficients and HPLC retention factors of aromatic hydrocarbons. Chemosphere. 16(1):109-116.

White, J. T., Fienen, M. N., and Doherty, J. E., 2016. A python framework for environmental model uncertainty analysis. Environ. Model. Softw. 85, 217–228. doi: 10.1016/j.envsoft.2016.08.017

White, J.T., 2018. A model-independent iterative ensemble smoother for efficient history-matching and uncertainty quantification in very high dimensions, Environmental Modelling & Software, vol. 109

White, J.T., Hunt, R.J., Fienen, M.N., and Doherty, J.E., 2020. Approaches to Highly Parameterized Inversion: PEST++ Version 5, a Software Suite for Parameter Estimation, Uncertainty Analysis, Management Optimization and Sensitivity Analysis: U.S. Geological Survey Techniques and Methods 7C26, 52 p., https://doi.org/10.3133/tm7C26.

Wood, A.L., Bouchard, D.C., Brusseau, M.L., Rao, P.S.C., 1990. Cosolvent effects on sorption and mobility of organic contaminants in soils. Chemosphere. 21(4-5):575-587.

# 8.0 Disclaimer

This Technical Report contains the professional opinions of INTERA using its professional judgment and customary practices within the profession. In addition, it relies on information developed and/or provided by others, potentially including the Client. Such information is assumed to be correct. However, INTERA accepts no responsibility for any inaccuracy or error in the information developed and/or provided by others and the impact any such inaccuracies or errors may have on the Technical Report.

Additionally, this Technical Report was prepared for the sole use of the Client and shall not be disseminated to, used by, or relied upon by any other person or entity without the advanced, written consent of both the Client and INTERA. INTERA assumes no liability or responsibility for the unauthorized use of this Technical Memorandum.

# Appendices

# Appendix A Prior Parameter Summary

Table A.1 – Pre-calibration parameter values and upper and lower bounds; prior parameter distributions are sampled from a Gaussian distribution in which initial values are the mean and the range between bounds reflects 4 standard deviations.

| Type | Layer | Lower bound | Upper bound | Initial value |
|---|---|---|---|---|
| K (m/d) | 1 | 3.00E-01 | 3.00E+01 | 3.00E+00 |
| | 2 | 1.00E-01 | 1.00E+01 | 1.00E+00 |
| | 3 | 1.00E-03 | 1.00E-01 | 1.00E-02 |
| | 4 | 1.00E-03 | 5.00E-01 | 2.24E-02 |
| | 5 | 5.00E-03 | 5.00E-01 | 5.00E-02 |
| | 6 | 1.00E-03 | 5.00E-01 | 2.24E-02 |
| | 7 | 1.00E-04 | 5.00E-01 | 7.07E-03 |
| | 8 | 1.00E-03 | 5.00E-01 | 2.24E-02 |
| | 9 | 5.00E-04 | 5.00E-02 | 5.00E-03 |
| | 10 | 5.00E-04 | 5.00E-01 | 1.58E-02 |
| | 11 | 1.00E-05 | 5.00E-03 | 2.24E-04 |
| | 12 | 1.00E-07 | 5.00E-03 | 2.24E-05 |
| | 13 | 1.00E-03 | 5.00E-01 | 2.24E-02 |
| | 14 | 1.00E-03 | 1.00E+00 | 3.16E-02 |
| | 15 | 1.00E-03 | 5.00E-01 | 2.24E-02 |
| | 16 | 1.00E-03 | 1.00E-01 | 1.00E-02 |
| | 17 | 1.00E-07 | 1.00E-01 | 1.00E-04 |
| | 18 | 1.00E-03 | 1.00E-01 | 1.00E-02 |
| Kv (ratio) | 1 | 1.00E-03 | 5.00E-01 | 1.00E-02 |
| | 2 | 1.00E-03 | 1.00E-01 | 1.00E-02 |
| | 3 | 1.00E-04 | 1.00E-02 | 1.00E-03 |
| | 4 | 1.00E-04 | 1.00E-02 | 1.00E-03 |
| | 5 | 1.00E-03 | 5.00E-01 | 1.00E-02 |
| | 6 | 1.00E-04 | 1.00E-02 | 1.00E-03 |
| | 7 | 1.00E-03 | 5.00E-01 | 1.00E-02 |
| | 8 | 1.00E-04 | 1.00E-02 | 1.00E-03 |
| | 9 | 1.00E-04 | 1.00E-02 | 1.00E-03 |
| | 10 | 1.00E-04 | 1.00E-02 | 1.00E-03 |
| | 11 | 1.00E-03 | 5.00E-01 | 1.00E-02 |
| | 12 | 1.00E-03 | 5.00E-01 | 1.00E-02 |
| | 13 | 1.00E-04 | 1.00E-02 | 1.00E-03 |
| | 14 | 1.00E-03 | 5.00E-01 | 1.00E-02 |
| | 15 | 1.00E-04 | 1.00E-02 | 1.00E-03 |
| | 16 | 1.00E-04 | 1.00E-02 | 1.00E-03 |
| | 17 | 1.00E-03 | 5.00E-01 | 1.00E-02 |
| | 18 | 1.00E-04 | 1.00E-02 | 1.00E-03 |

Table A.1 (cont.) – Pre-calibration parameter values and upper and lower bounds; prior parameter distributions are sampled from a Gaussian distribution in which initial values are the mean and the range between bounds reflects 4 standard deviations.

| | | | | |
|---|---|---|---|---|
| Sy (-) | 1 | 2.00E-03 | 1.50E-01 | 2.00E-02 |
| | 2 | 1.00E-03 | 1.00E-01 | 1.00E-02 |
| | 3 | 1.00E-03 | 1.00E-01 | 1.00E-02 |
| | 4 | 1.00E-03 | 1.00E-01 | 1.00E-02 |
| | 5 | 1.00E-03 | 1.00E-01 | 1.00E-02 |
| | 6 | 1.00E-03 | 1.00E-01 | 1.00E-02 |
| | 7 | 1.00E-03 | 1.00E-01 | 1.00E-02 |
| | 8 | 1.00E-03 | 1.00E-01 | 1.00E-02 |
| | 9 | 1.00E-03 | 1.00E-01 | 1.00E-02 |
| | 10 | 1.00E-03 | 1.00E-01 | 1.00E-02 |
| | 11 | 1.00E-03 | 1.00E-01 | 1.00E-02 |
| | 12 | 1.00E-03 | 1.00E-01 | 1.00E-02 |
| | 13 | 1.00E-03 | 1.00E-01 | 1.00E-02 |
| | 14 | 1.00E-03 | 1.00E-01 | 1.00E-02 |
| | 15 | 1.00E-03 | 1.00E-01 | 1.00E-02 |
| | 16 | 1.00E-03 | 1.00E-01 | 1.00E-02 |
| | 17 | 1.00E-03 | 1.00E-01 | 1.00E-02 |
| | 18 | 1.00E-03 | 1.00E-01 | 1.00E-02 |
| Ss ($m^{-1}$) | 1 | 2.00E-07 | 2.00E-05 | 1.00E-05 |
| | 2 | 2.00E-07 | 2.00E-05 | 1.00E-06 |
| | 3 | 2.00E-07 | 2.00E-05 | 1.00E-06 |
| | 4 | 2.00E-07 | 2.00E-05 | 1.00E-06 |
| | 5 | 2.00E-07 | 2.00E-05 | 1.00E-06 |
| | 6 | 2.00E-07 | 2.00E-05 | 1.00E-06 |
| | 7 | 2.00E-07 | 2.00E-05 | 1.00E-06 |
| | 8 | 2.00E-07 | 2.00E-05 | 1.00E-06 |
| | 9 | 2.00E-07 | 2.00E-05 | 1.00E-06 |
| | 10 | 2.00E-07 | 2.00E-05 | 1.00E-06 |
| | 11 | 2.00E-07 | 2.00E-05 | 1.00E-06 |
| | 12 | 2.00E-07 | 2.00E-05 | 1.00E-06 |
| | 13 | 2.00E-07 | 2.00E-05 | 1.00E-06 |
| | 14 | 2.00E-07 | 2.00E-05 | 1.00E-06 |
| | 15 | 2.00E-07 | 2.00E-05 | 1.00E-06 |
| | 16 | 2.00E-07 | 2.00E-05 | 1.00E-06 |
| | 17 | 2.00E-07 | 2.00E-05 | 1.00E-06 |
| | 18 | 2.00E-07 | 2.00E-05 | 1.00E-06 |
| Rch | 1 | 0 | 1.44E-05 | 5.47E-07 |

Table A.2 – Pre-calibration initial multiplier values, initial actual values, standard deviation, and variance for the pilot points employed for the time-varying materials.

| Type | Layer | Hydraulic property | Parameter group | Initial Value | Initial mult. value | Standard deviation | Variance |
|---|---|---|---|---|---|---|---|
| Extended area | 3 | K | tvm.k.pp.layer2.moar | * | 1 | 24.8 | 612.6 |
| | 3 | Kv | tvm.k33.pp.layer2.moar | * | 1 | 24.8 | 612.6 |
| | 3 | Ss | tvm.ss.pp.layer2.moar | * | 1 | 24.8 | 612.6 |
| | 3 | Sy | tvm.sy.pp.layer2.moar | * | 1 | 24.8 | 612.6 |
| | 4 | K | tvm.k.pp.layer3.moar | * | 1 | 24.8 | 612.6 |
| | 4 | Kv | tvm.k33.pp.layer3.moar | * | 1 | 24.8 | 612.6 |
| | 4 | Ss | tvm.ss.pp.layer3.moar | * | 1 | 24.8 | 612.6 |
| | 4 | Sy | tvm.sy.pp.layer3.moar | * | 1 | 24.8 | 612.6 |
| | 5 | K | tvm.k.pp.layer4.moar | * | 1 | 24.8 | 612.6 |
| | 5 | Kv | tvm.k33.pp.layer4.moar | * | 1 | 24.8 | 612.6 |
| | 5 | Ss | tvm.ss.pp.layer4.moar | * | 1 | 24.8 | 612.6 |
| | 5 | Sy | tvm.sy.pp.layer4.moar | * | 1 | 24.8 | 612.6 |
| | 6 | K | tvm.k.pp.layer5.moar | * | 1 | 24.8 | 612.6 |
| | 6 | Kv | tvm.k33.pp.layer5.moar | * | 1 | 24.8 | 612.6 |
| | 6 | Ss | tvm.ss.pp.layer5.moar | * | 1 | 24.8 | 612.6 |
| | 6 | Sy | tvm.sy.pp.layer5.moar | * | 1 | 24.8 | 612.6 |
| Gasifiers | 3 | K | tvm.k.pp.layer2.gas | * | 1 | 24.8 | 612.6 |
| | 3 | Kv | tvm.k33.pp.layer2.gas | * | 1 | 24.8 | 612.6 |
| | 3 | Ss | tvm.ss.pp.layer2.gas | * | 1 | 24.8 | 612.6 |
| | 3 | Sy | tvm.sy.pp.layer2.gas | * | 1 | 24.8 | 612.6 |
| | 4 | K | tvm.k.pp.layer3.gas | * | 1 | 24.8 | 612.6 |
| | 4 | Kv | tvm.k33.pp.layer3.gas | * | 1 | 24.8 | 612.6 |
| | 4 | Ss | tvm.ss.pp.layer3.gas | * | 1 | 24.8 | 612.6 |
| | 4 | Sy | tvm.sy.pp.layer3.gas | * | 1 | 24.8 | 612.6 |
| | 5 | K | tvm.k.pp.layer4.gas | * | 1 | 24.8 | 612.6 |
| | 5 | Kv | tvm.k33.pp.layer4.gas | * | 1 | 24.8 | 612.6 |
| | 5 | Ss | tvm.ss.pp.layer4.gas | * | 1 | 24.8 | 612.6 |
| | 5 | Sy | tvm.sy.pp.layer4.gas | * | 1 | 24.8 | 612.6 |
| | 6 | K | tvm.k.pp.layer5.gas | 100 | 1 | 0.2 | 0.1 |
| | 6 | Kv | tvm.k33.pp.layer5.gas | 1 | 1 | 0.2 | 0.1 |
| | 6 | Ss | tvm.ss.pp.layer5.gas | 1 | 1 | 2.5 | 6.1 |
| | 6 | Sy | tvm.sy.pp.layer5.gas | 1E-6 | 1 | 0.2 | 0.1 |

*Initial values depending on each realisation parameter field.

# Appendix B Relative Parameter Variance Reduction

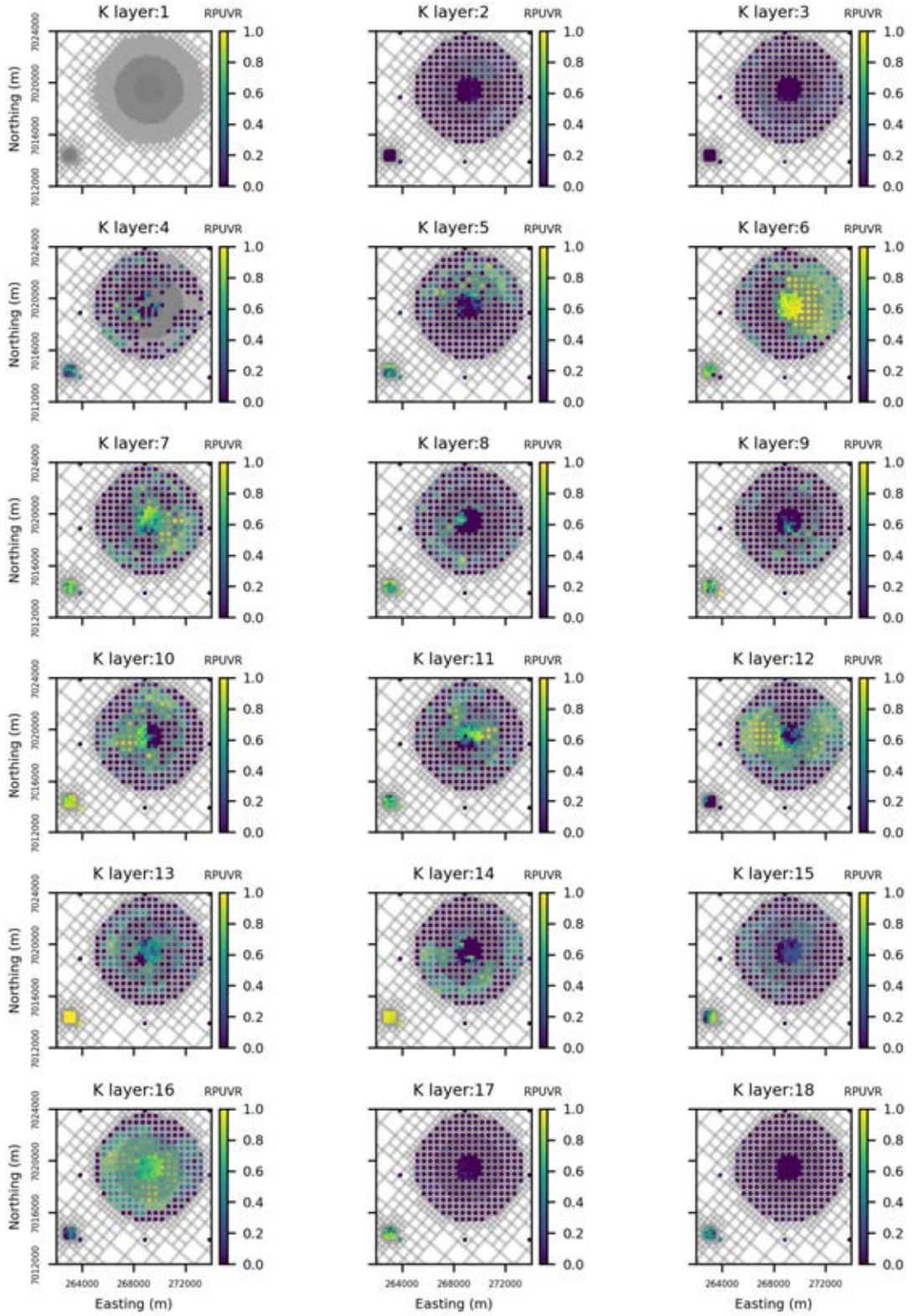
K layer:1
K layer:2
K layer:3
K layer:4
K layer:5
K layer:6
K layer:7
K layer:8
K layer:9
K layer:10
K layer:11
K layer:12
K layer:13
K layer:14
K layer:15
K layer:16
K layer:17
K layer:18
RPUVR
1.0
0.8
0.6
0.4
0.2
0.0
Northing (m)
7012000
7016000
7020000
7024000
264000
268000
272000
Easting (m)

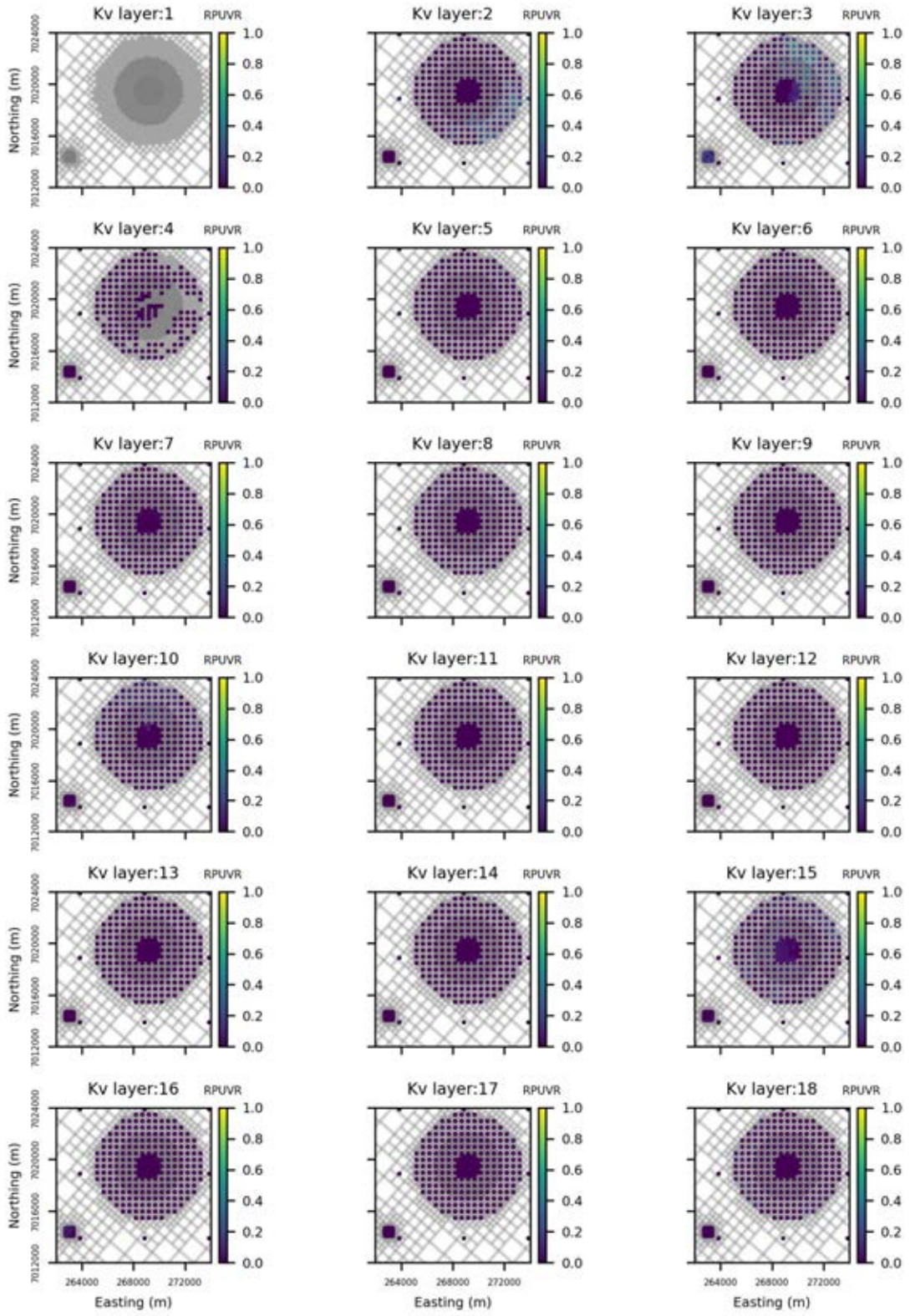
Kv layer:1
Kv layer:2
Kv layer:3
Kv layer:4
Kv layer:5
Kv layer:6
Kv layer:7
Kv layer:8
Kv layer:9
Kv layer:10
Kv layer:11
Kv layer:12
Kv layer:13
Kv layer:14
Kv layer:15
Kv layer:16
Kv layer:17
Kv layer:18
RPUVR
1.0
0.8
0.6
0.4
0.2
0.0
Northing (m)
7012000
7016000
7020000
7024000
264000
268000
272000
Easting (m)

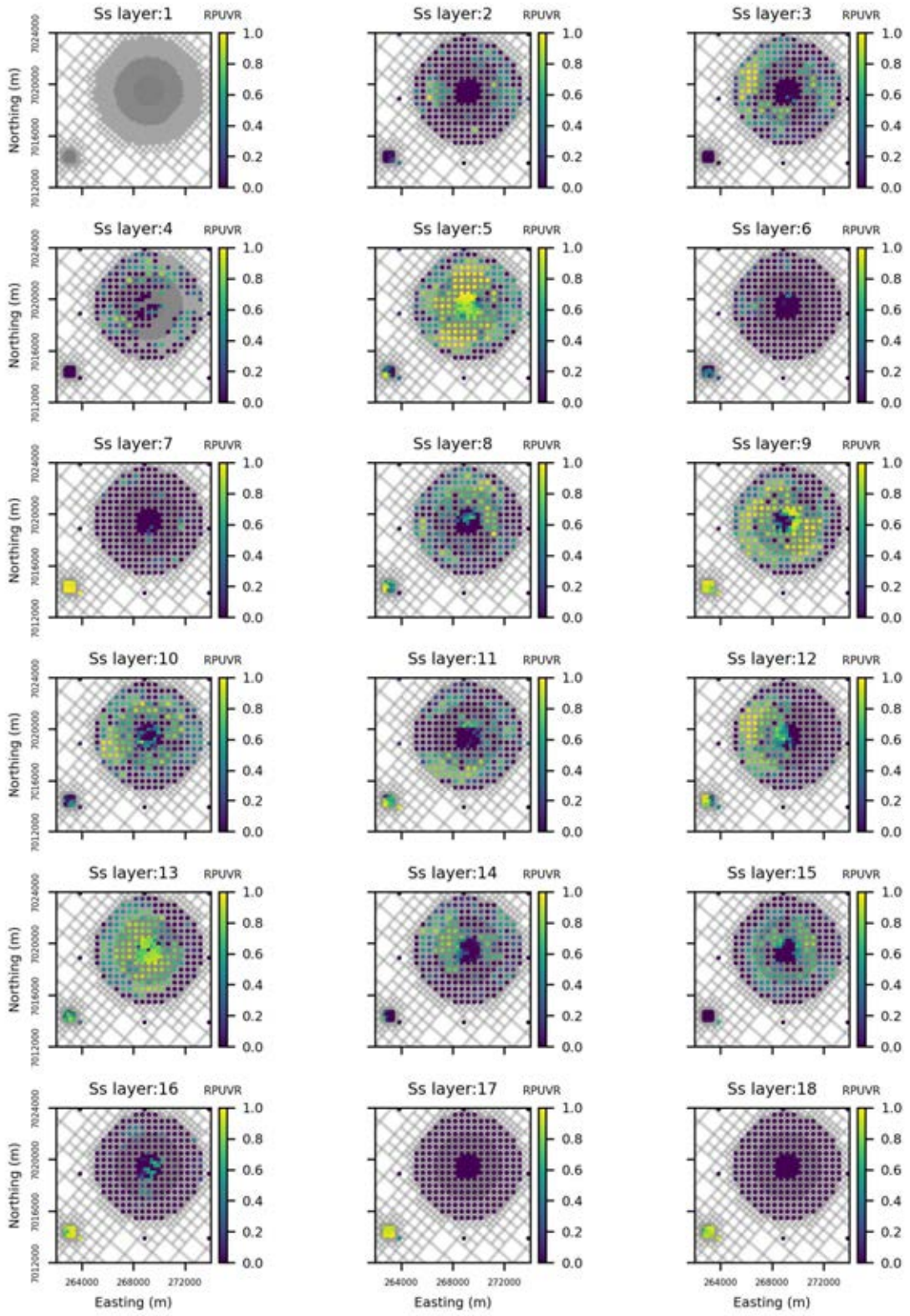
Ss layer:1
Ss layer:2
Ss layer:3
Ss layer:4
Ss layer:5
Ss layer:6
Ss layer:7
Ss layer:8
Ss layer:9
Ss layer:10
Ss layer:11
Ss layer:12
Ss layer:13
Ss layer:14
Ss layer:15
Ss layer:16
Ss layer:17
Ss layer:18
RPUVR
1.0
0.8
0.6
0.4
0.2
0.0
Northing (m)
7024000
7020000
7016000
7012000
264000
268000
272000
Easting (m)

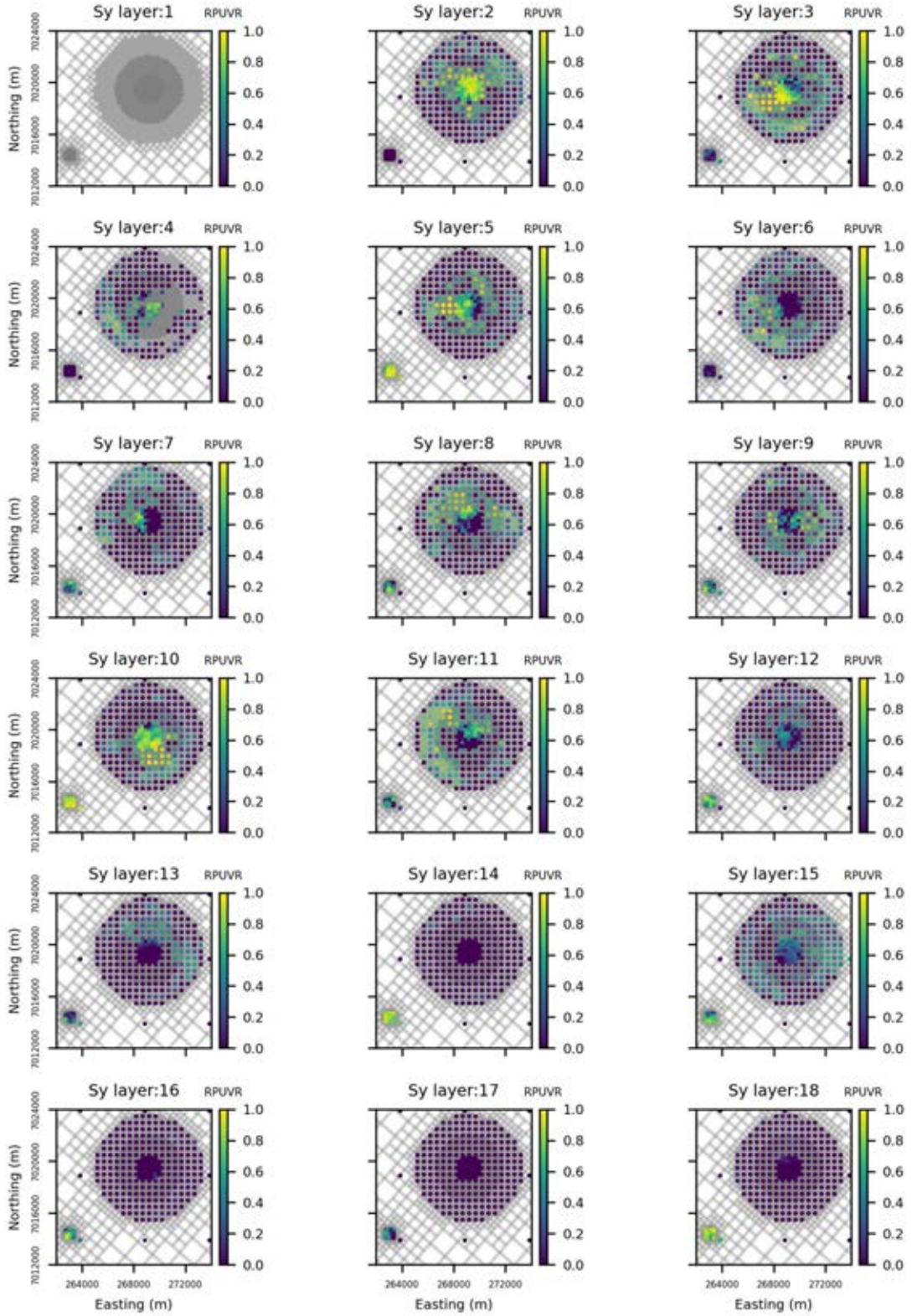
Sy layer:1
Sy layer:2
Sy layer:3
Sy layer:4
Sy layer:5
Sy layer:6
Sy layer:7
Sy layer:8
Sy layer:9
Sy layer:10
Sy layer:11
Sy layer:12
Sy layer:13
Sy layer:14
Sy layer:15
Sy layer:16
Sy layer:17
Sy layer:18
RPUVR
1.0
0.8
0.6
0.4
0.2
0.0
Northing (m)
7012000
7016000
7020000
7024000
264000
268000
272000
Easting (m)

# Appendix C Parameter Group Prior and Posterior Histograms

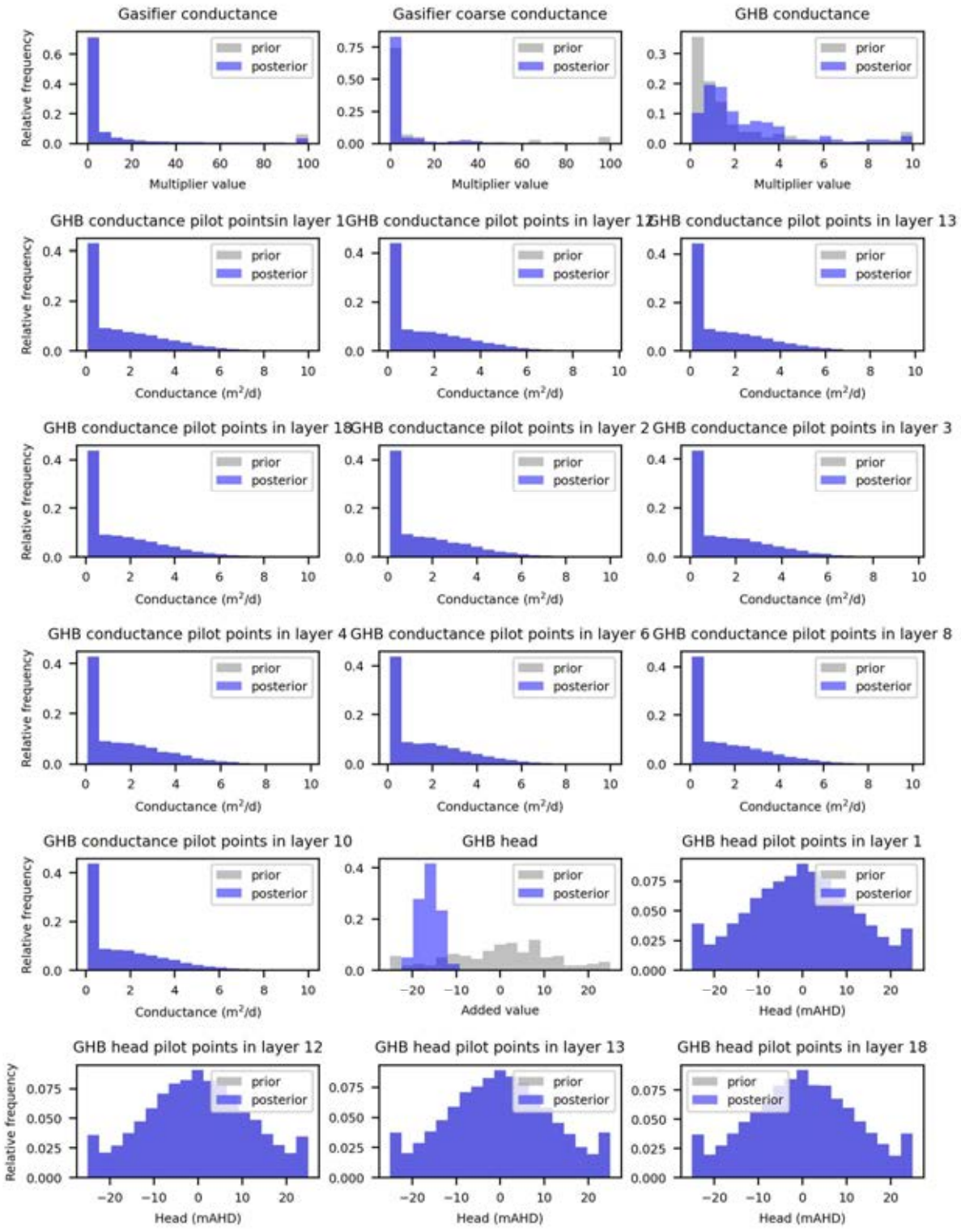
Gasifier conductance
Gasifier coarse conductance
GHB conductance
GHB conductance pilot pointsin layer 1
GHB conductance pilot points in layer 12
GHB conductance pilot points in layer 13
GHB conductance pilot points in layer 18
GHB conductance pilot points in layer 2
GHB conductance pilot points in layer 3
GHB conductance pilot points in layer 4
GHB conductance pilot points in layer 6
GHB conductance pilot points in layer 8
GHB conductance pilot points in layer 10
GHB head
GHB head pilot points in layer 1
GHB head pilot points in layer 12
GHB head pilot points in layer 13
GHB head pilot points in layer 18
prior
posterior
Relative frequency
Multiplier value
Conductance (m²/d)
Added value
Head (mAHD)

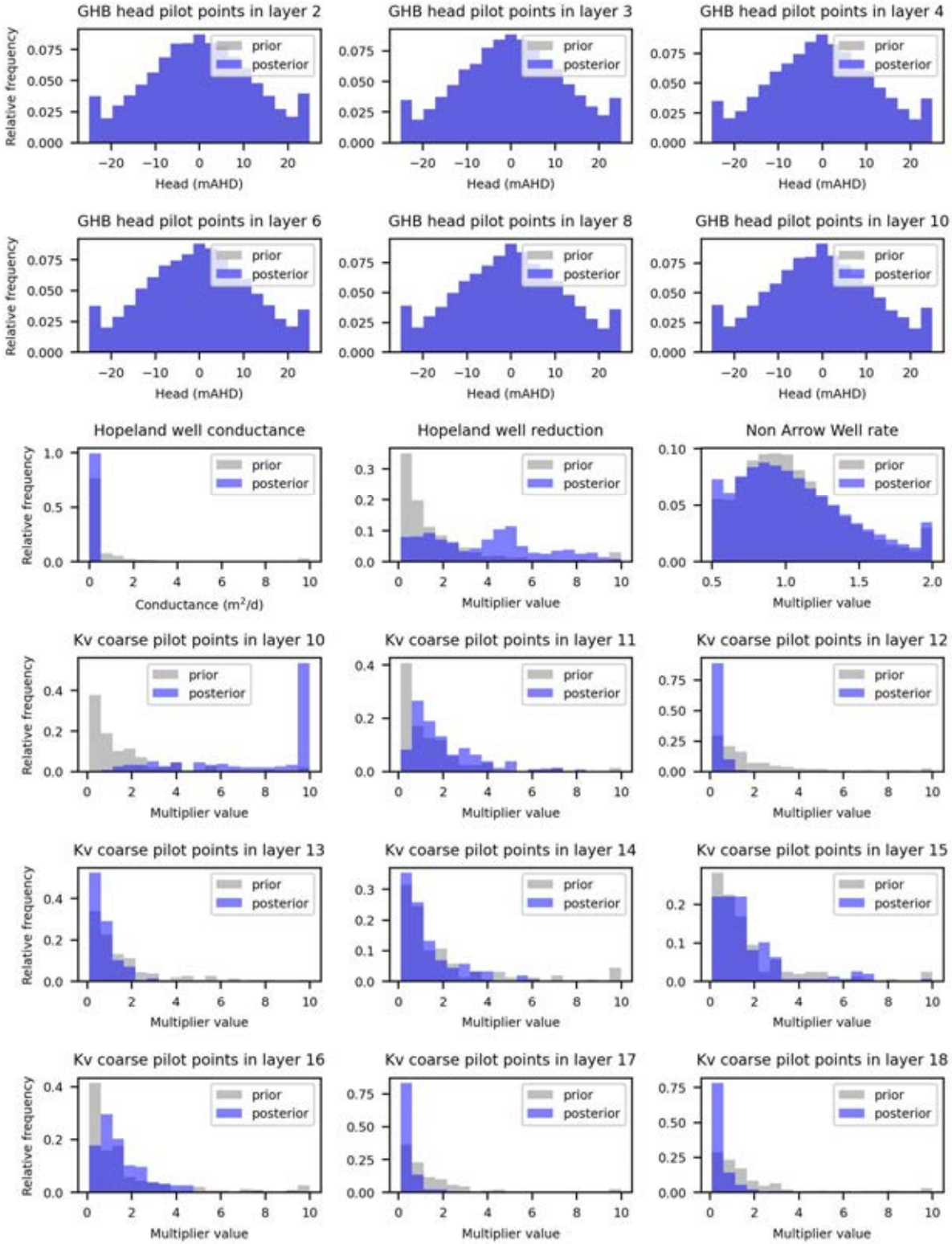
GHB head pilot points in layer 2
GHB head pilot points in layer 3
GHB head pilot points in layer 4
GHB head pilot points in layer 6
GHB head pilot points in layer 8
GHB head pilot points in layer 10
Hopeland well conductance
Hopeland well reduction
Non Arrow Well rate
Kv coarse pilot points in layer 10
Kv coarse pilot points in layer 11
Kv coarse pilot points in layer 12
Kv coarse pilot points in layer 13
Kv coarse pilot points in layer 14
Kv coarse pilot points in layer 15
Kv coarse pilot points in layer 16
Kv coarse pilot points in layer 17
Kv coarse pilot points in layer 18
prior
posterior
Relative frequency
Head (mAHD)
Conductance (m²/d)
Multiplier value

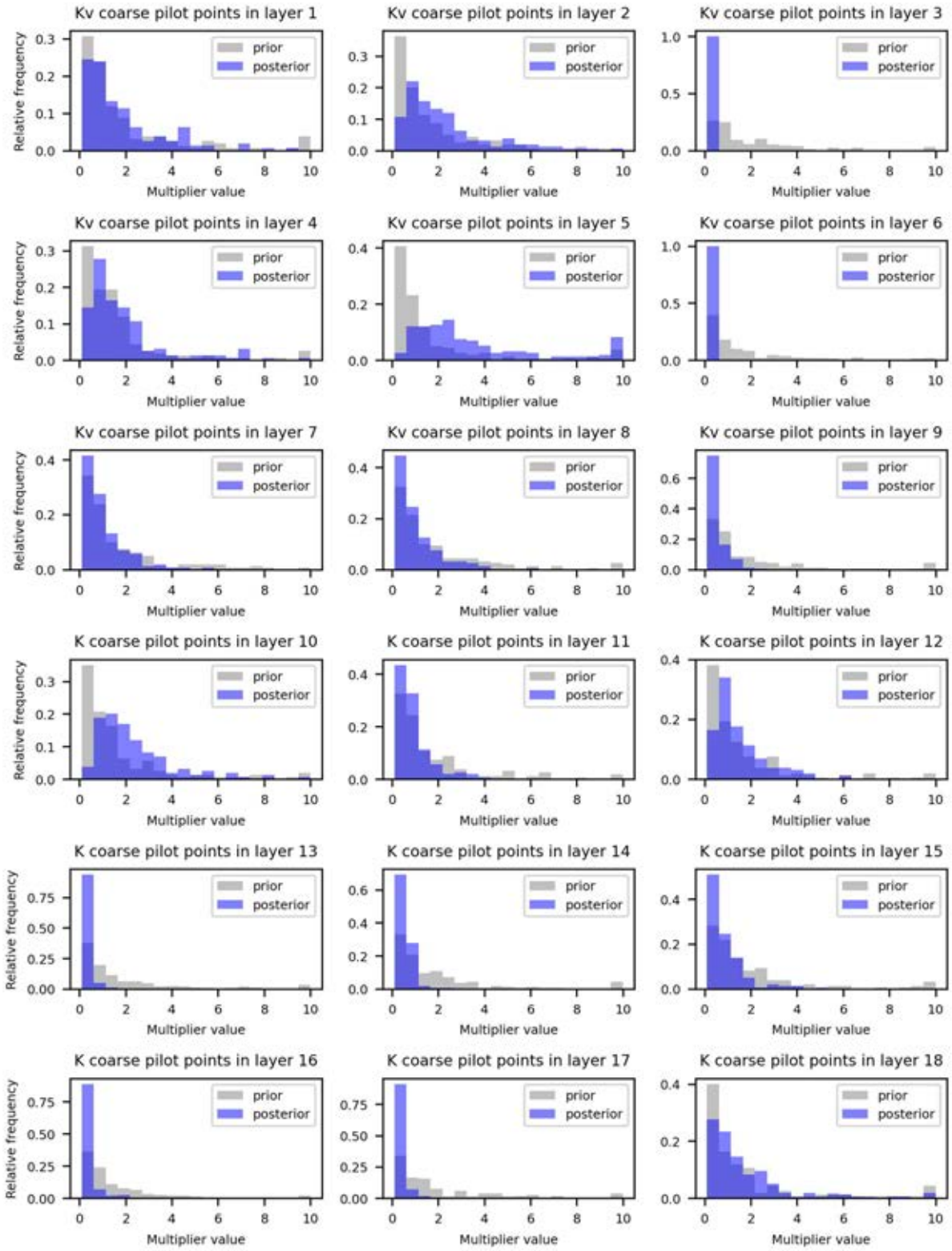
Kv coarse pilot points in layer 1
Kv coarse pilot points in layer 2
Kv coarse pilot points in layer 3
Kv coarse pilot points in layer 4
Kv coarse pilot points in layer 5
Kv coarse pilot points in layer 6
Kv coarse pilot points in layer 7
Kv coarse pilot points in layer 8
Kv coarse pilot points in layer 9
K coarse pilot points in layer 10
K coarse pilot points in layer 11
K coarse pilot points in layer 12
K coarse pilot points in layer 13
K coarse pilot points in layer 14
K coarse pilot points in layer 15
K coarse pilot points in layer 16
K coarse pilot points in layer 17
K coarse pilot points in layer 18
prior
posterior
Relative frequency
Multiplier value

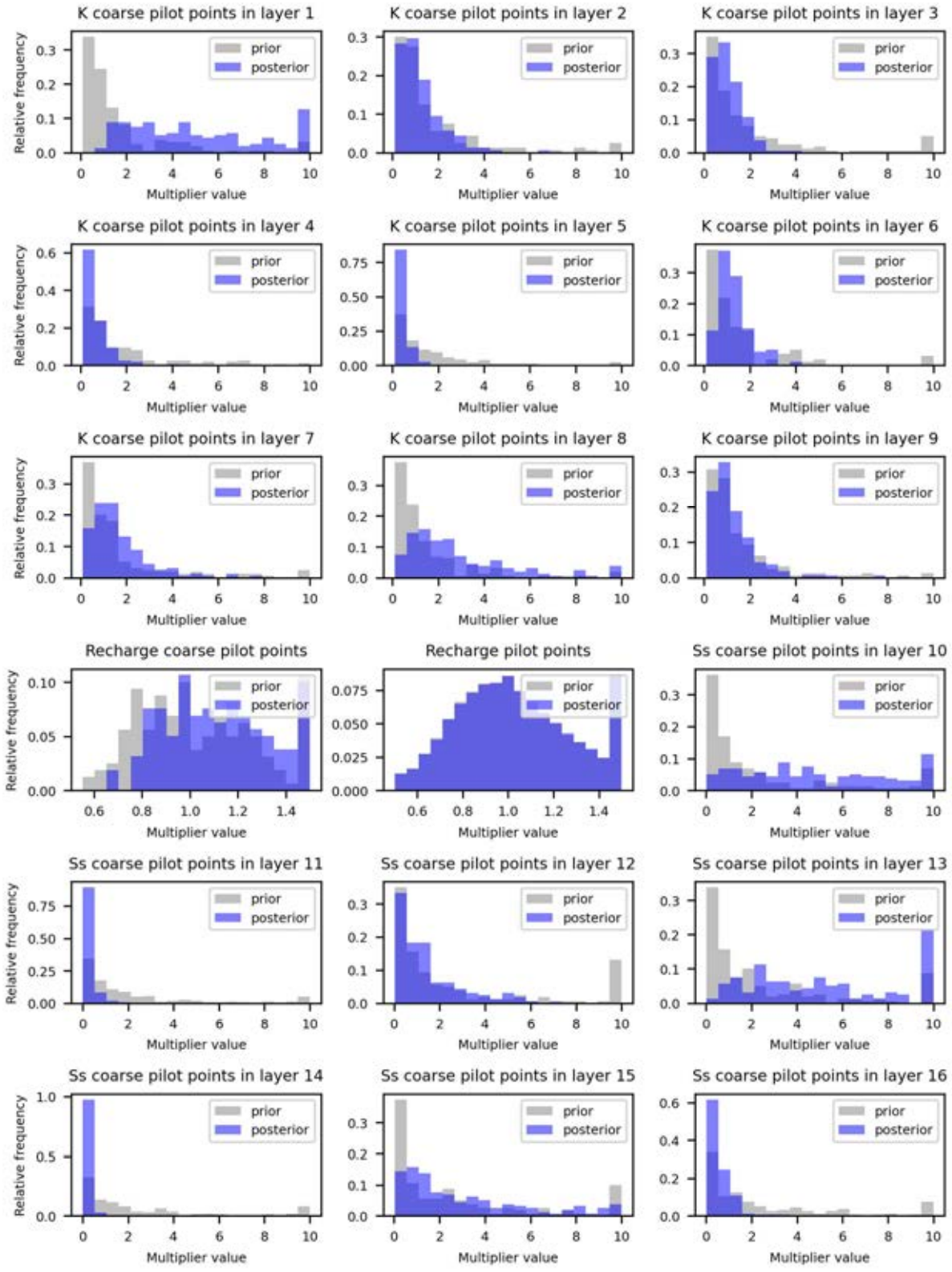
K coarse pilot points in layer 1
K coarse pilot points in layer 2
K coarse pilot points in layer 3
K coarse pilot points in layer 4
K coarse pilot points in layer 5
K coarse pilot points in layer 6
K coarse pilot points in layer 7
K coarse pilot points in layer 8
K coarse pilot points in layer 9
Recharge coarse pilot points
Recharge pilot points
Ss coarse pilot points in layer 10
Ss coarse pilot points in layer 11
Ss coarse pilot points in layer 12
Ss coarse pilot points in layer 13
Ss coarse pilot points in layer 14
Ss coarse pilot points in layer 15
Ss coarse pilot points in layer 16
prior
posterior
Relative frequency
Multiplier value

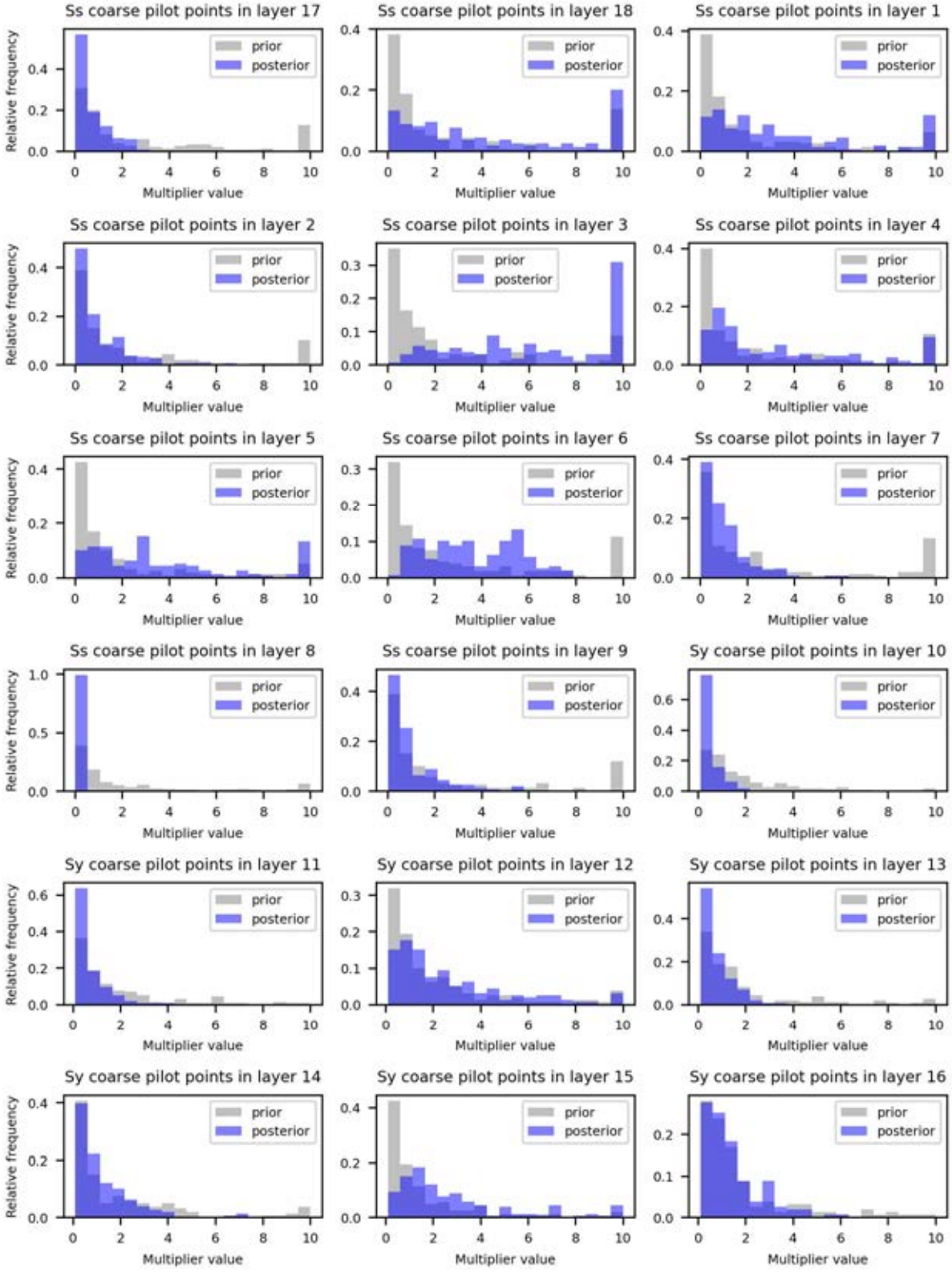
Ss coarse pilot points in layer 17
Ss coarse pilot points in layer 18
Ss coarse pilot points in layer 1
Ss coarse pilot points in layer 2
Ss coarse pilot points in layer 3
Ss coarse pilot points in layer 4
Ss coarse pilot points in layer 5
Ss coarse pilot points in layer 6
Ss coarse pilot points in layer 7
Ss coarse pilot points in layer 8
Ss coarse pilot points in layer 9
Sy coarse pilot points in layer 10
Sy coarse pilot points in layer 11
Sy coarse pilot points in layer 12
Sy coarse pilot points in layer 13
Sy coarse pilot points in layer 14
Sy coarse pilot points in layer 15
Sy coarse pilot points in layer 16
prior
posterior
Relative frequency
Multiplier value

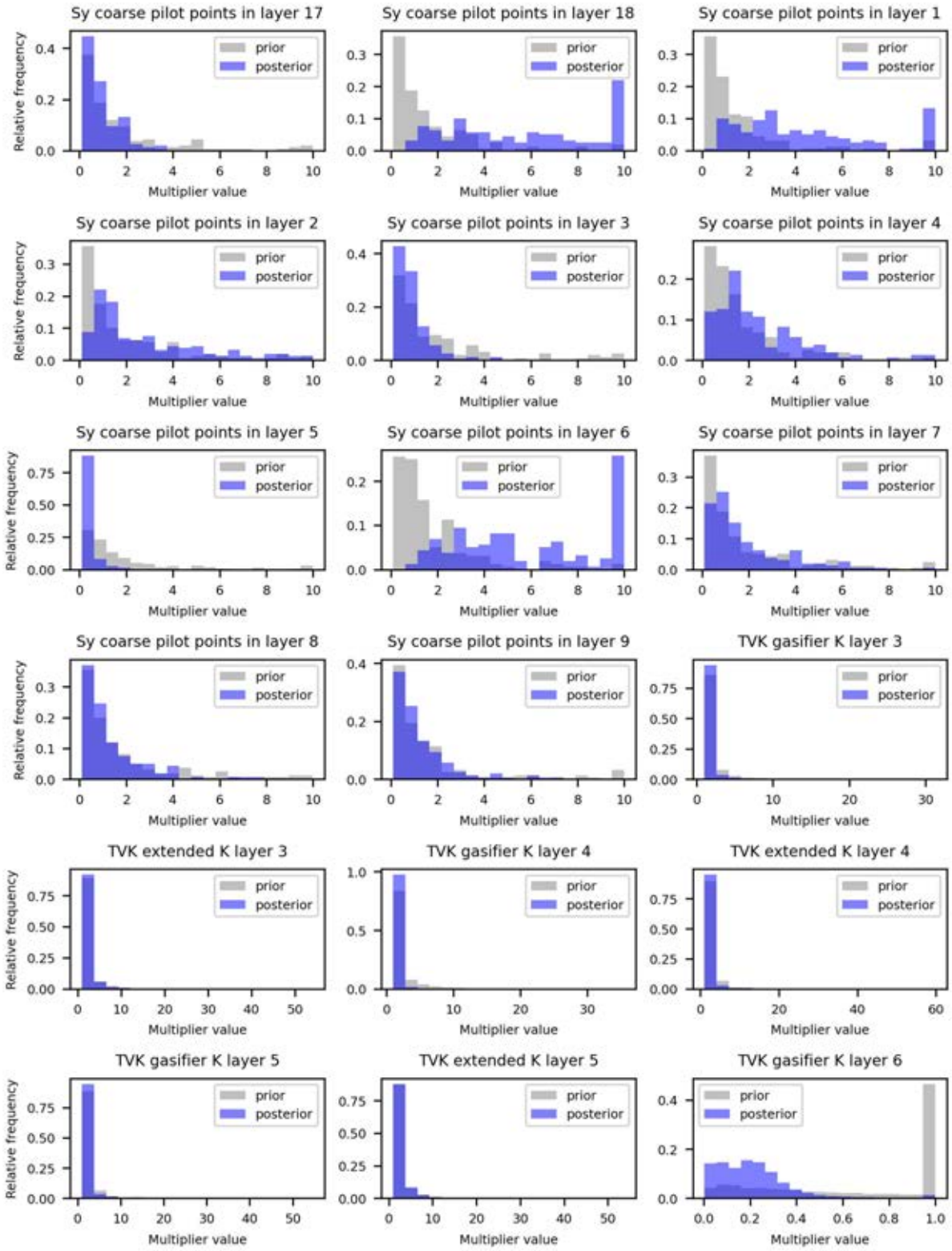
Sy coarse pilot points in layer 17
Sy coarse pilot points in layer 18
Sy coarse pilot points in layer 1
Sy coarse pilot points in layer 2
Sy coarse pilot points in layer 3
Sy coarse pilot points in layer 4
Sy coarse pilot points in layer 5
Sy coarse pilot points in layer 6
Sy coarse pilot points in layer 7
Sy coarse pilot points in layer 8
Sy coarse pilot points in layer 9
TVK gasifier K layer 3
TVK extended K layer 3
TVK gasifier K layer 4
TVK extended K layer 4
TVK gasifier K layer 5
TVK extended K layer 5
TVK gasifier K layer 6
prior
posterior
Relative frequency
Multiplier value

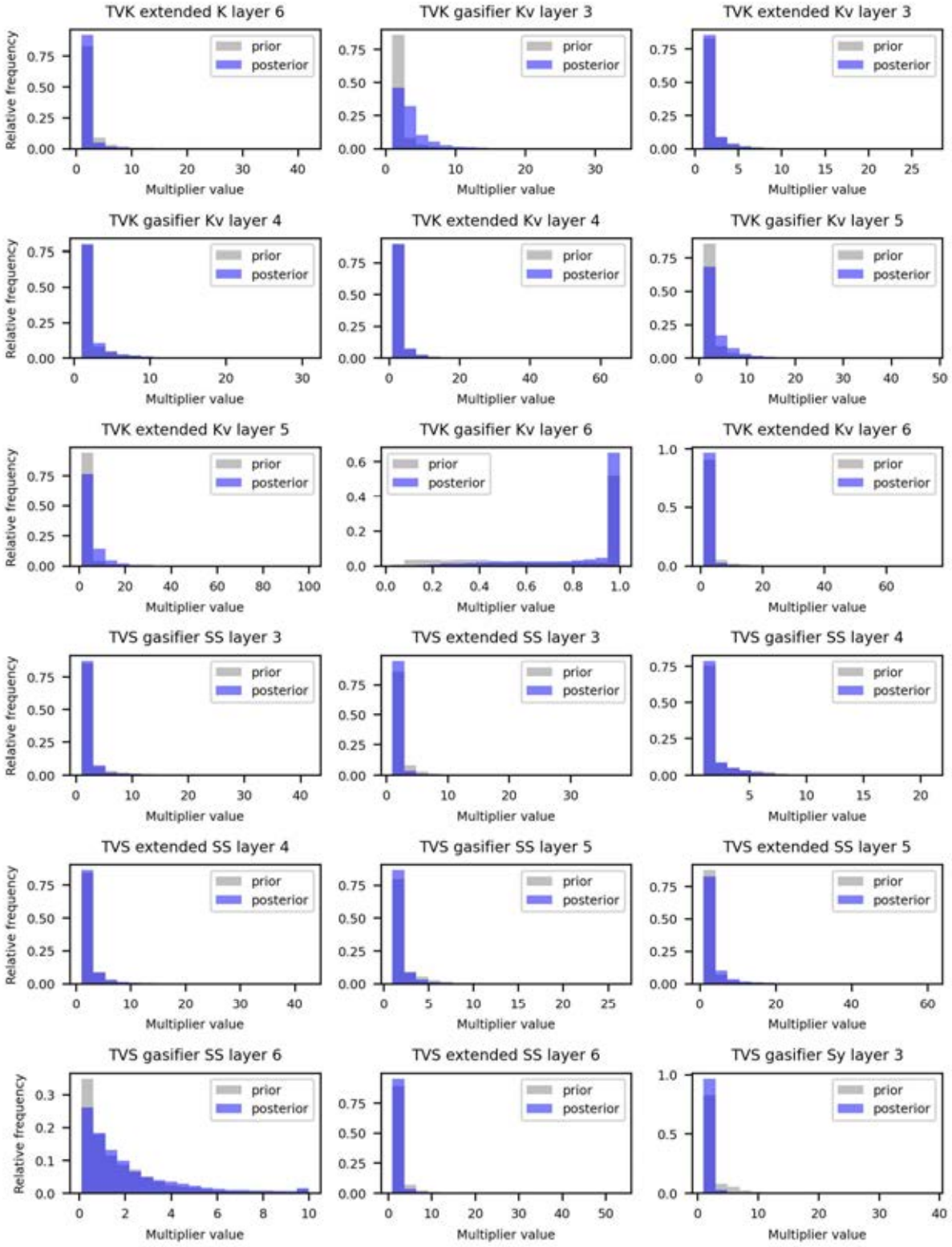
TVK extended K layer 6
TVK gasifier Kv layer 3
TVK extended Kv layer 3
TVK gasifier Kv layer 4
TVK extended Kv layer 4
TVK gasifier Kv layer 5
TVK extended Kv layer 5
TVK gasifier Kv layer 6
TVK extended Kv layer 6
TVS gasifier SS layer 3
TVS extended SS layer 3
TVS gasifier SS layer 4
TVS extended SS layer 4
TVS gasifier SS layer 5
TVS extended SS layer 5
TVS gasifier SS layer 6
TVS extended SS layer 6
TVS gasifier Sy layer 3
prior
posterior
Relative frequency
Multiplier value

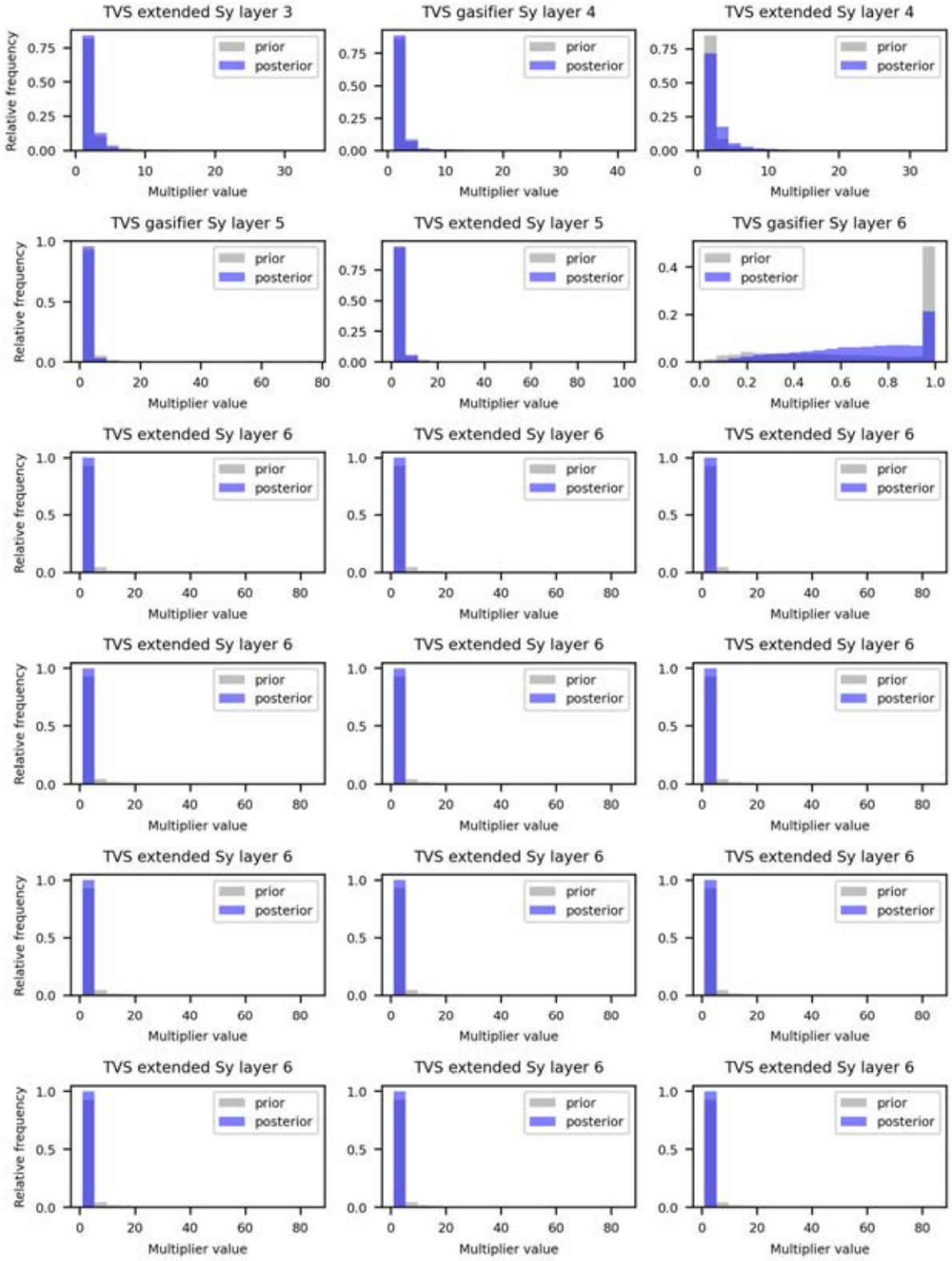
TVS extended Sy layer 3
TVS gasifier Sy layer 4
TVS extended Sy layer 4
TVS gasifier Sy layer 5
TVS extended Sy layer 5
TVS gasifier Sy layer 6
TVS extended Sy layer 6
TVS extended Sy layer 6
TVS extended Sy layer 6
TVS extended Sy layer 6
TVS extended Sy layer 6
TVS extended Sy layer 6
TVS extended Sy layer 6
TVS extended Sy layer 6
TVS extended Sy layer 6
prior
posterior
Relative frequency
Multiplier value

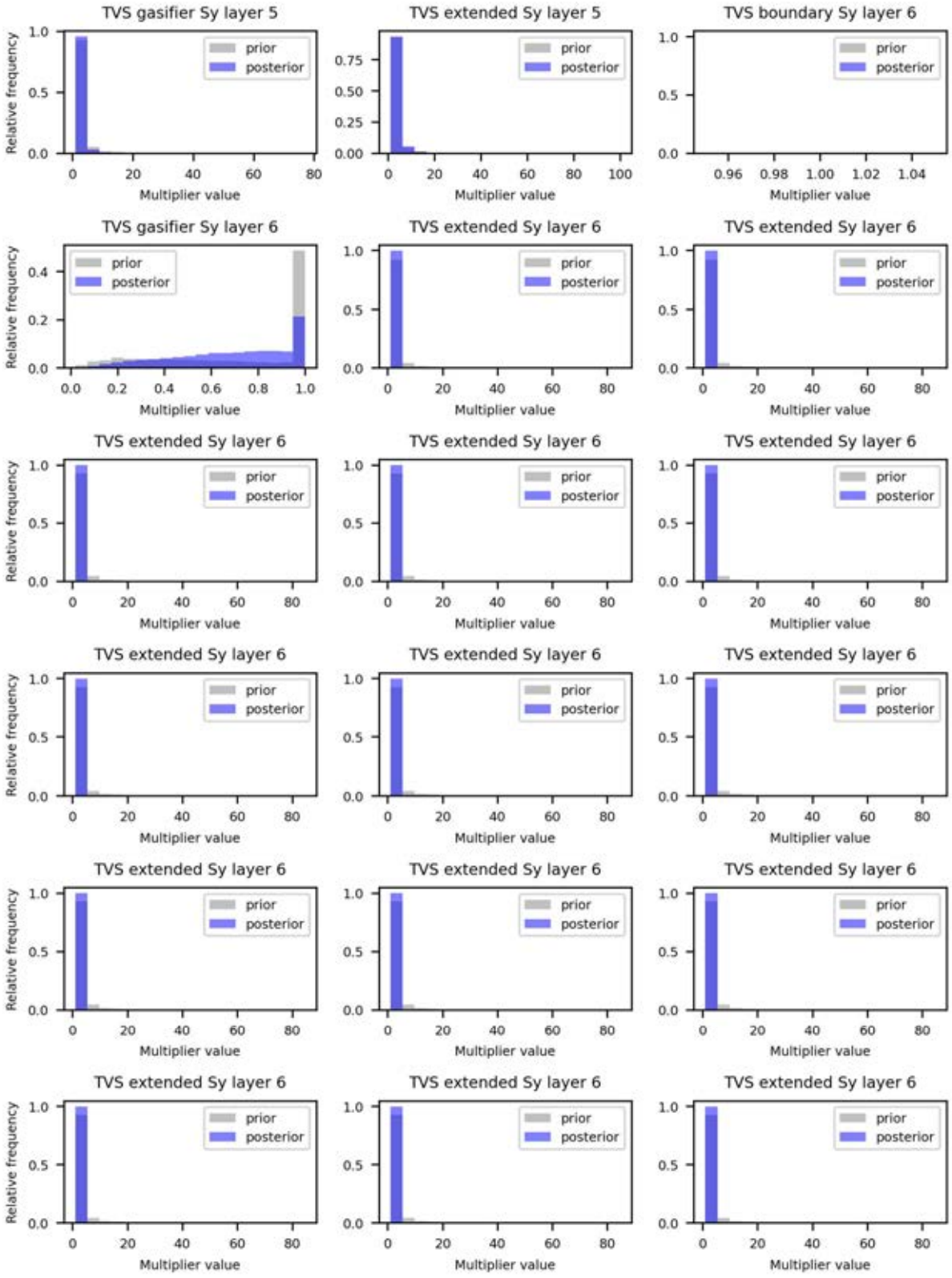
TVS gasifier Sy layer 5
TVS extended Sy layer 5
TVS boundary Sy layer 6
TVS gasifier Sy layer 6
TVS extended Sy layer 6
TVS extended Sy layer 6
TVS extended Sy layer 6
TVS extended Sy layer 6
TVS extended Sy layer 6
TVS extended Sy layer 6
TVS extended Sy layer 6
TVS extended Sy layer 6
TVS extended Sy layer 6
TVS extended Sy layer 6
TVS extended Sy layer 6
prior
posterior
Relative frequency
Multiplier value

# Appendix D Mean and Standard Deviation Maps of Hydraulic Heads for PL253 FDP Scenario

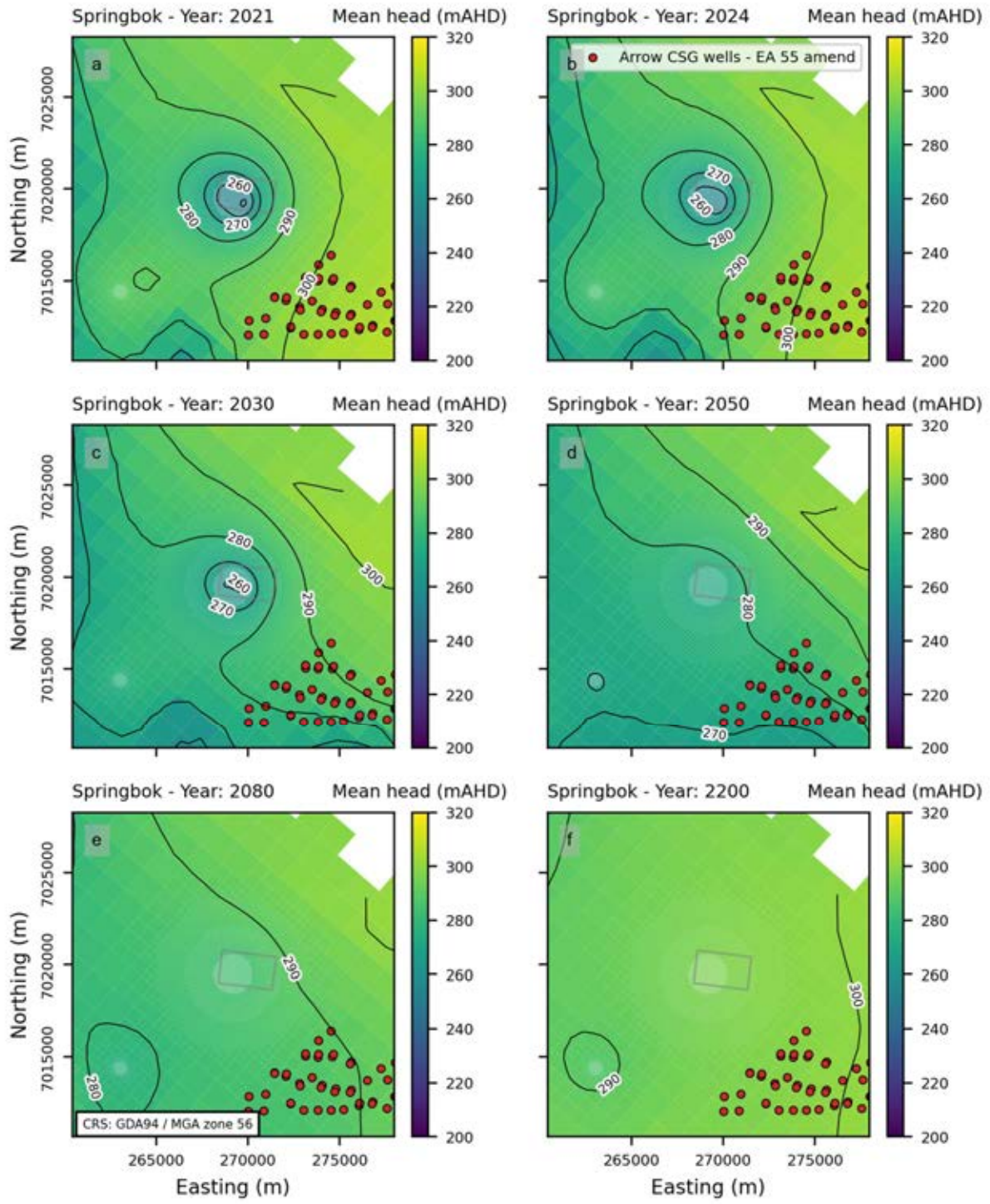


Figure D.1 – Maps showing the mean in hydraulic heads for all posterior ensemble realisations (PL253 scenario) in layer 3 (Springbok Sandstone). Each subplot (a) to (f) displays the mean hydraulic heads for 2021, 2024, 2030, 2050, 2080 and 2200.

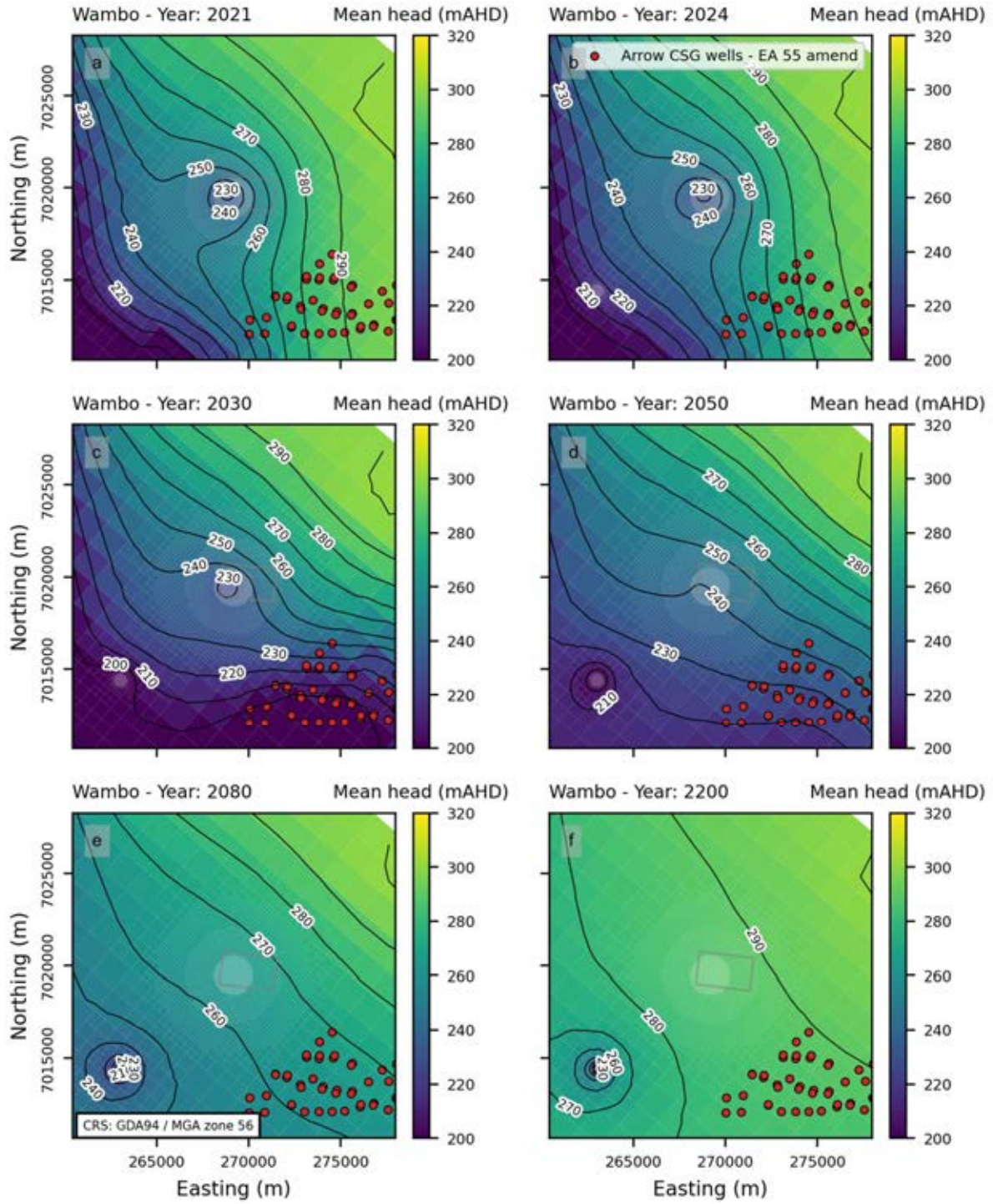


Figure D.2 - Maps showing the mean in hydraulic heads for all posterior ensemble realisations (PL253 scenario) in layer 8 (Wambo Coal Seam). Each subplot (a) to (f) displays the mean hydraulic heads for 2021, 2024, 2030, 2050, 2080 and 2200.

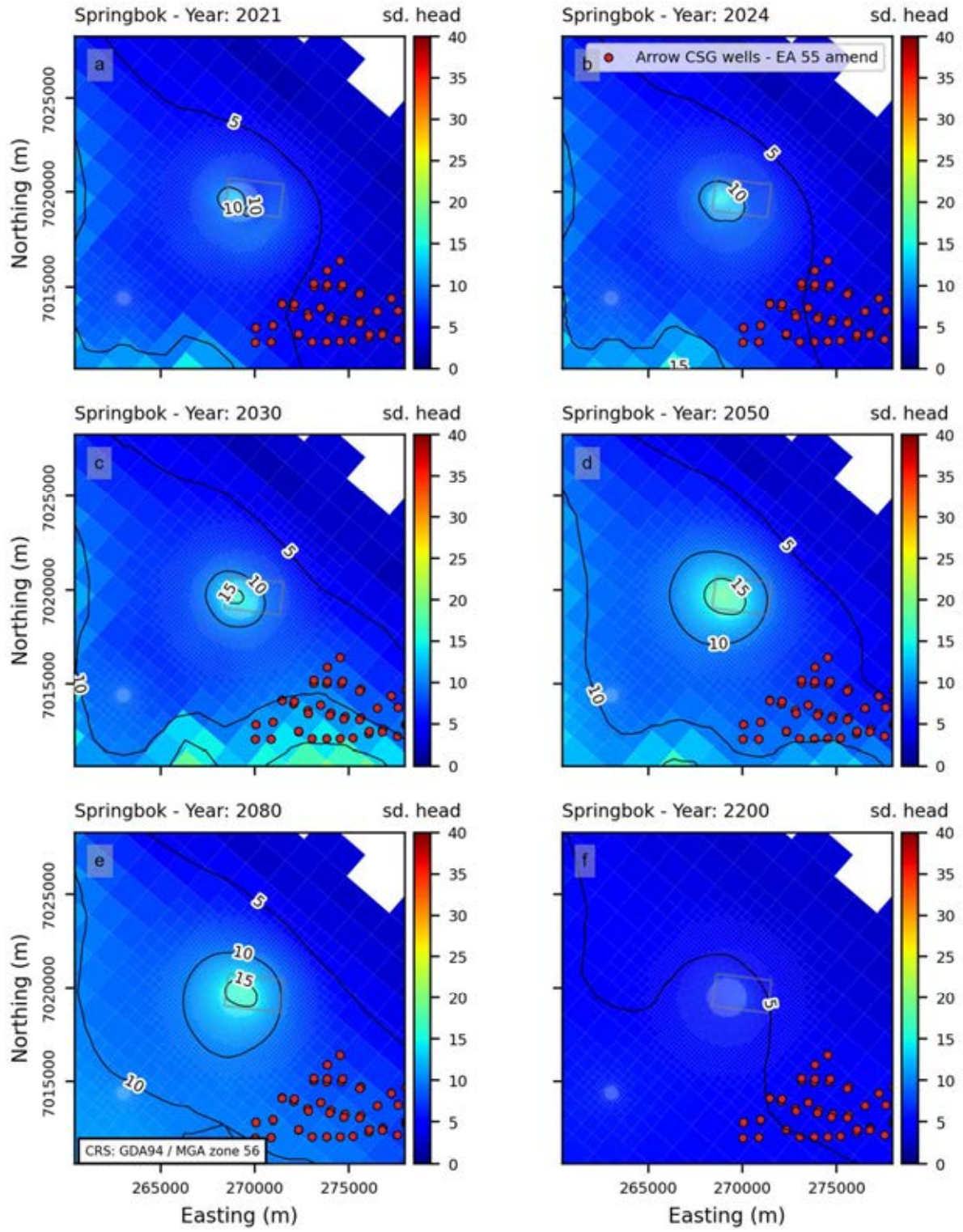


Figure D.3 – Maps showing the standard deviation in hydraulic heads for all posterior ensemble realisations (PL253 FDP scenario) in layer 3 (Springbok Sandstone). Each subplot (a) to (f) displays the mean hydraulic heads for 2021, 2024, 2030, 2050, 2080 and 2200.

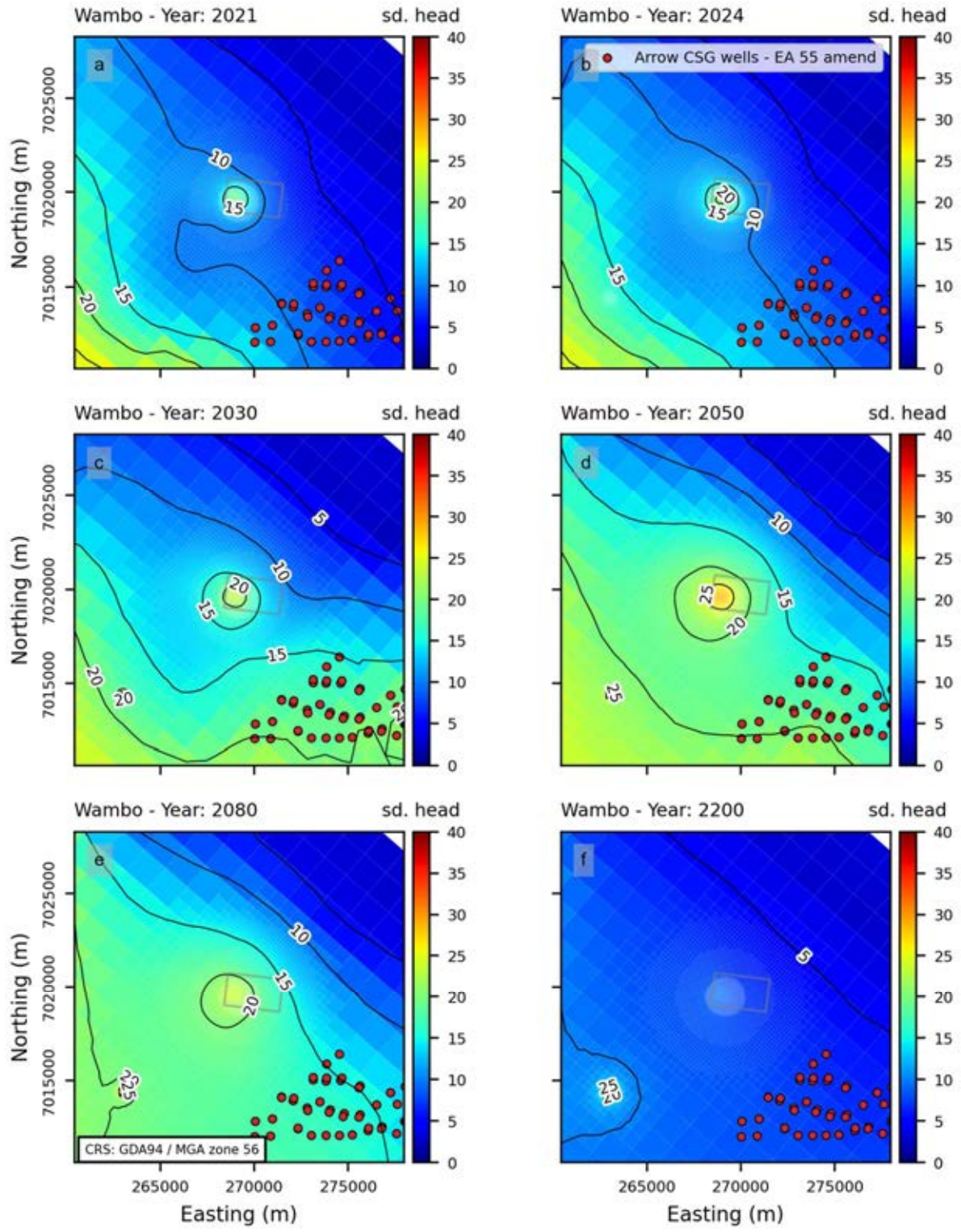


Figure D.4 – Maps showing the standard deviation in hydraulic heads for all posterior ensemble realisations (PL253 FDP scenario) in layer 8 (Wambo Coal Seam). Each subplot (a) to (f) displays the mean hydraulic heads for 2021, 2024, 2030, 2050, 2080 and 2200.

# Appendix E Mean and Standard Deviation Maps of Hydraulic Heads for Base Case FDP Scenario

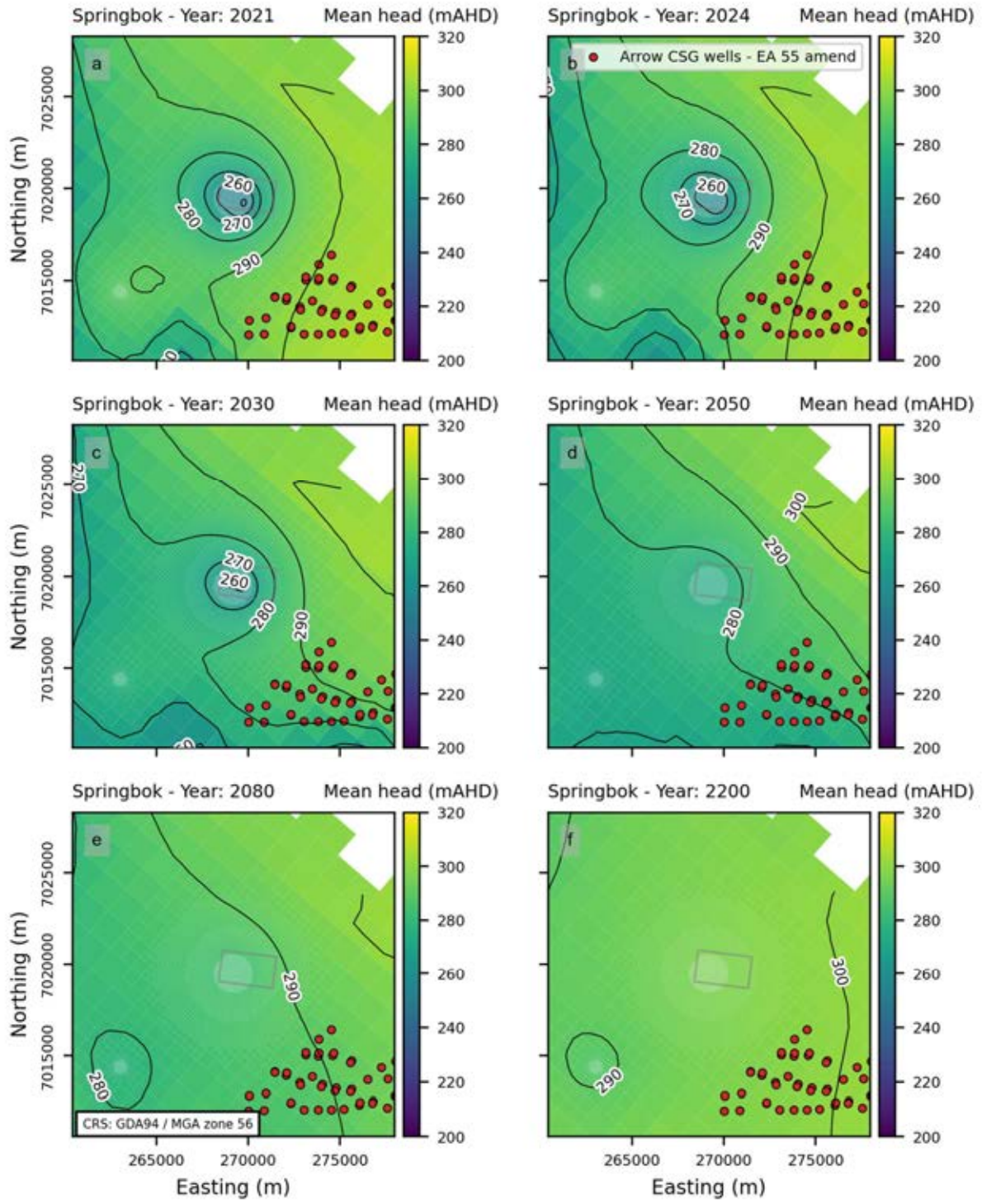


Figure E.1 – Maps showing the mean in hydraulic heads for all posterior ensemble realisations (Base Case scenario) in layer 3 (Springbok Sandstone). Each subplot (a) to (f) displays the mean hydraulic heads for 2021, 2024, 2030, 2050, 2080 and 2200.

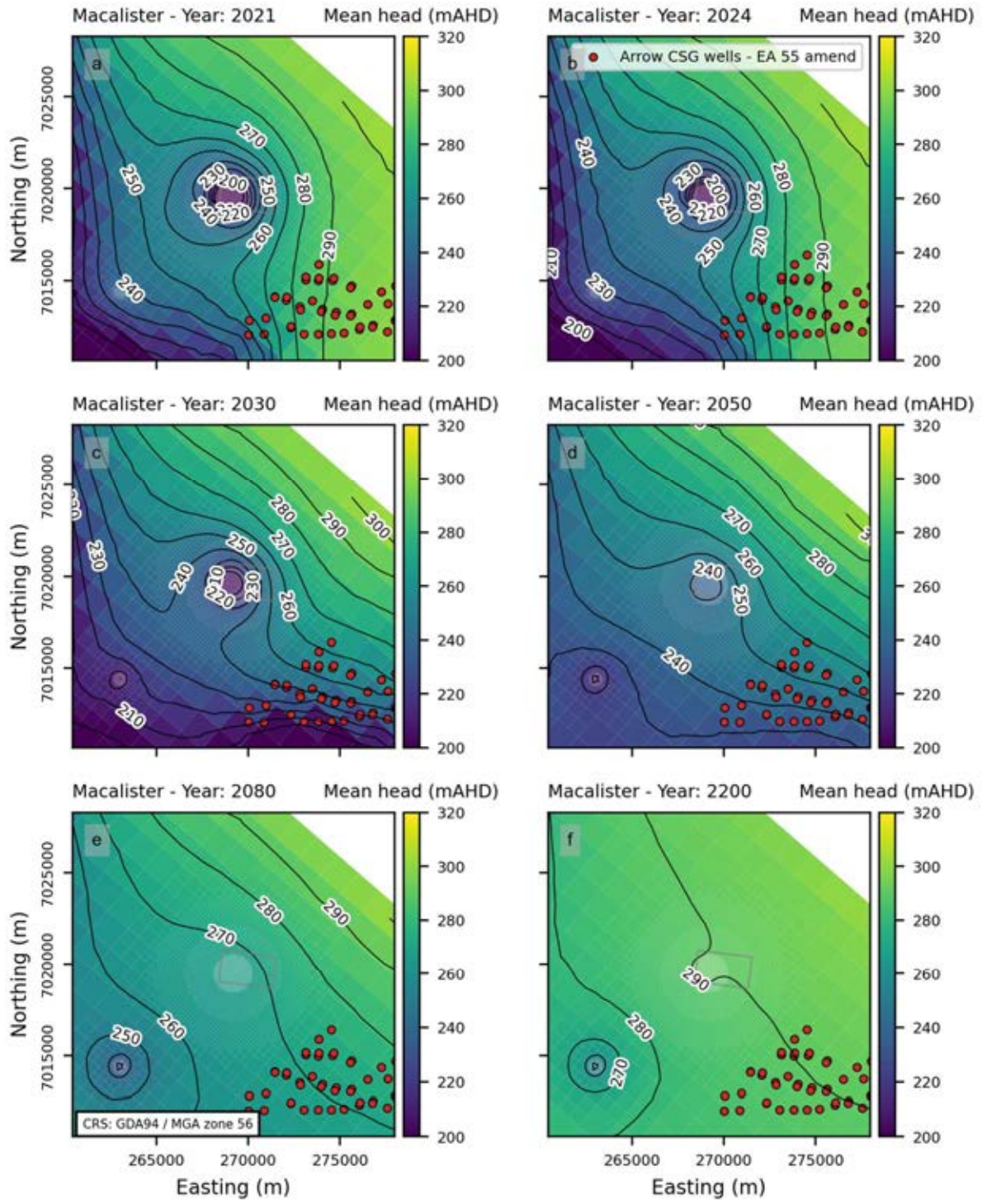


Figure E.2 - Maps showing the mean in hydraulic heads for all posterior ensemble realisations (Base Case scenario) in layer 6 (Macalister Coal Seam). Each subplot (a) to (f) displays the mean hydraulic heads for 2021, 2024, 2030, 2050, 2080 and 2200.

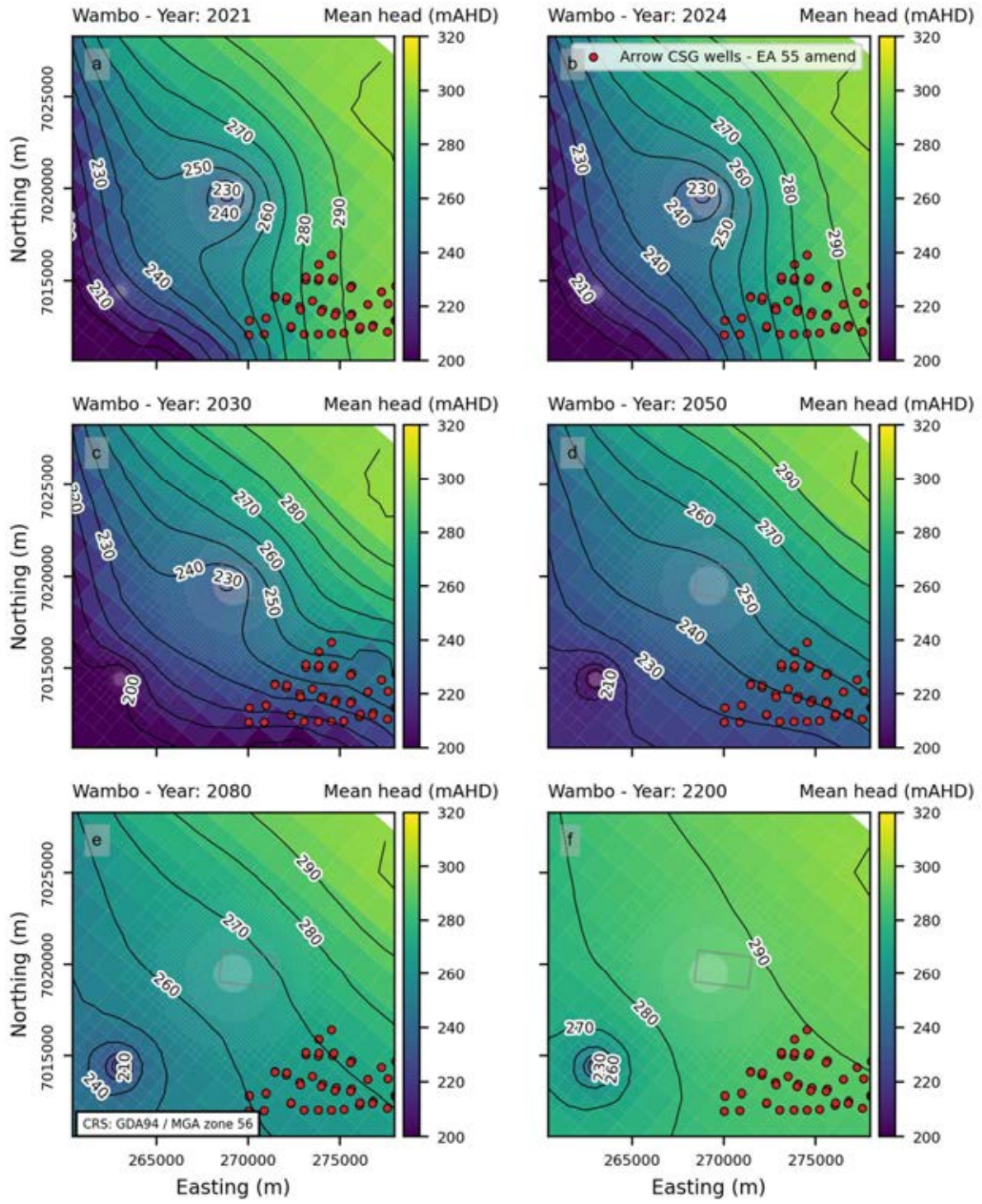


Figure E.3 - Maps showing the mean in hydraulic heads for all posterior ensemble realisations (Base Case scenario) in layer 8 (Wambo). Each subplot (a) to (f) displays the mean hydraulic heads for 2021, 2024, 2030, 2050, 2080 and 2200.

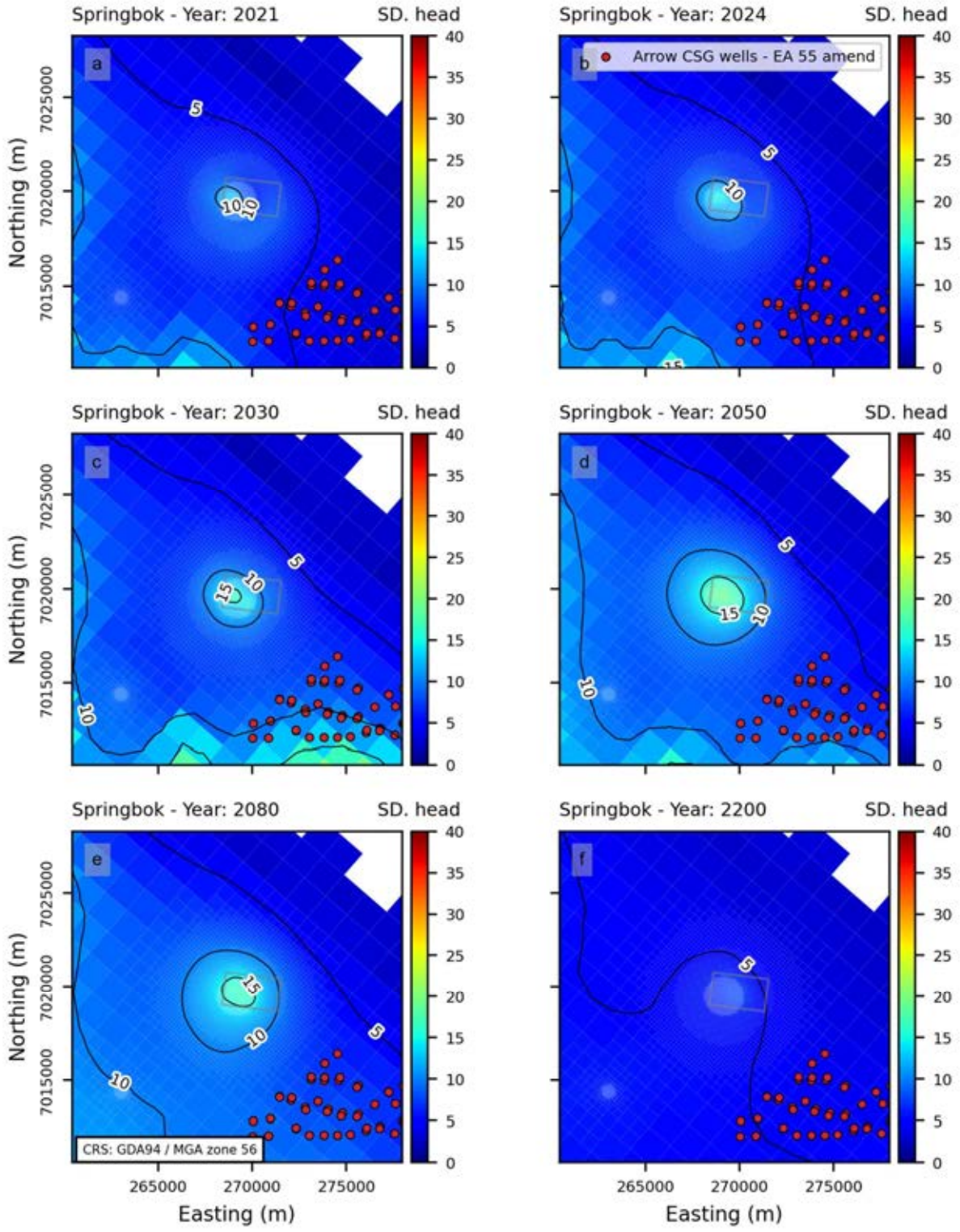


Figure E.4 – Maps showing the standard deviation in hydraulic heads for all posterior ensemble realisations (Base Case scenario) in layer 3 (Springbok Sandstone). Each subplot (a) to (f) displays the mean hydraulic heads for 2021, 2024, 2030, 2050, 2080 and 2200.

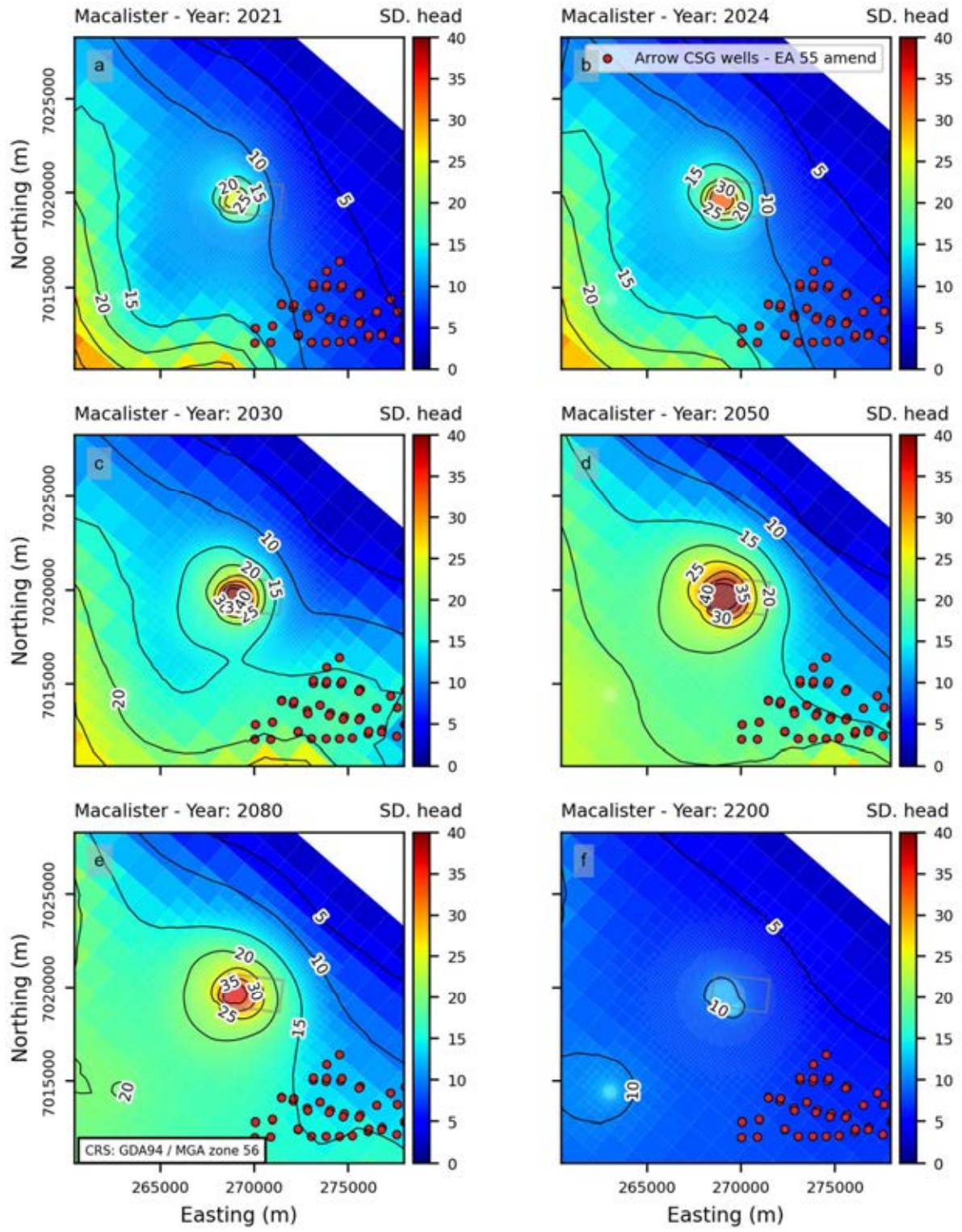


Figure E.5 – Maps showing the standard deviation in hydraulic heads for all posterior ensemble realisations (Base Case scenario) in layer 6 (Macalister Coal Seam). Each subplot (a) to (f) displays the mean hydraulic heads for 2021, 2024, 2030, 2050, 2080 and 2200.

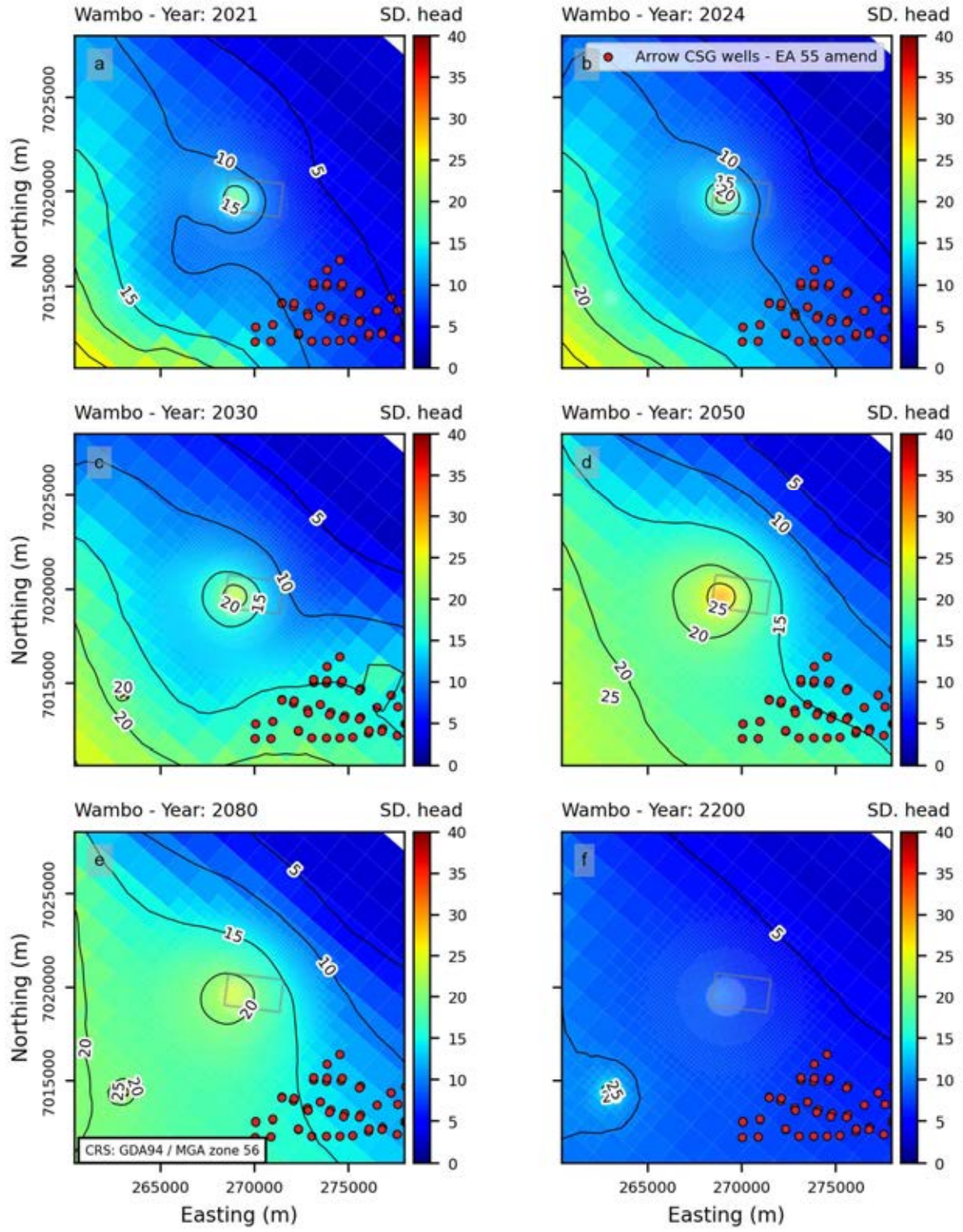


Figure E.6 – Maps showing the standard deviation in hydraulic heads for all posterior ensemble realisations (Base Case scenario) in layer 8 (Wambo Coal Seam). Each subplot (a) to (f) displays the mean hydraulic heads for 2021, 2024, 2030, 2050, 2080 and 2200.

# Appendix F Mean and Standard Deviation of the Differences in Heads Between FDP Scenarios

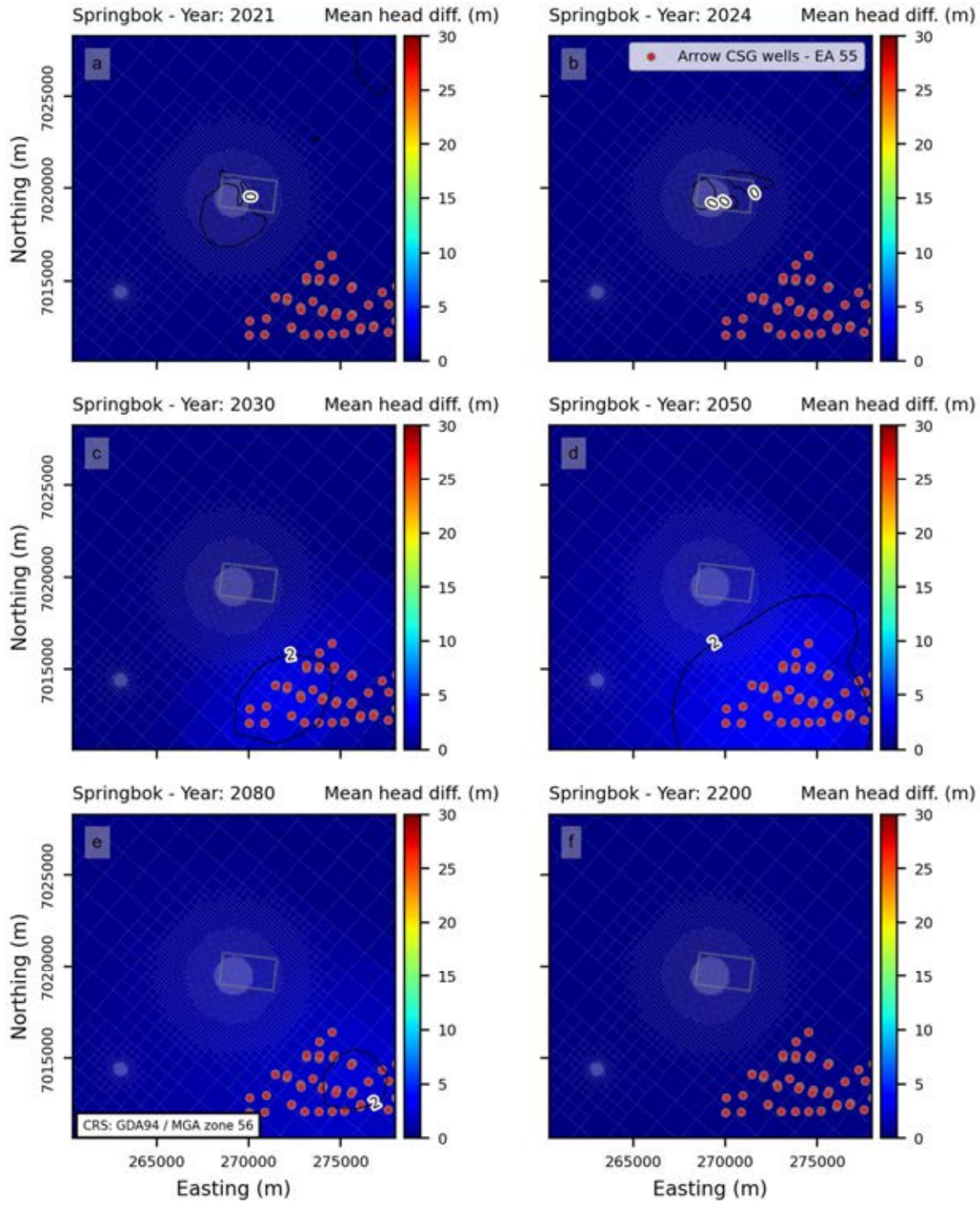


Figure F.1 – Maps showing the mean difference in hydraulic heads between scenarios for all posterior ensemble realisations in layer 3 (Springbok Sandstone). Each subplot (a) to (f) displays the mean difference in hydraulic heads for 2021, 2024, 2030, 2050, 2080 and 2200.

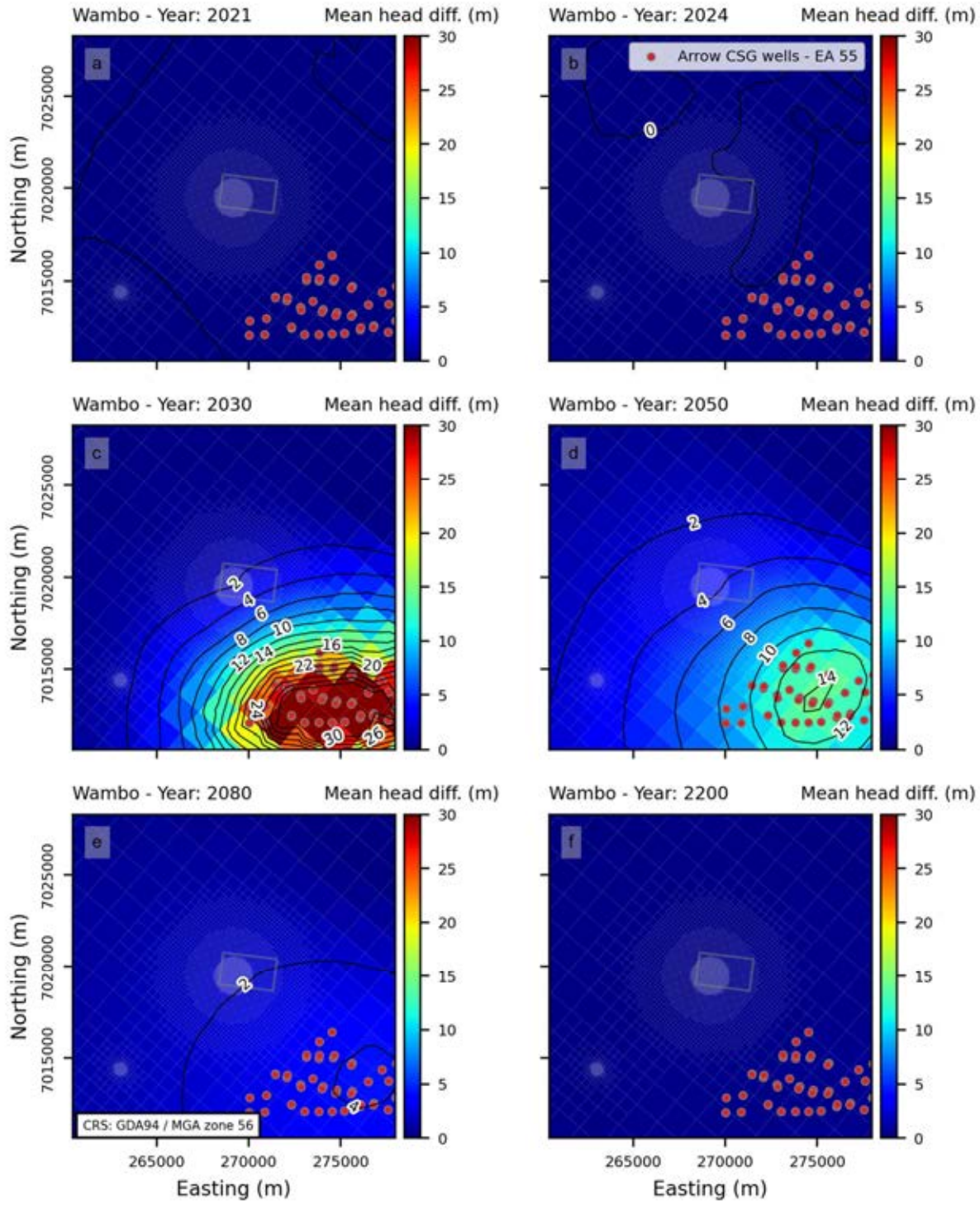


Figure F.2 – Maps showing the mean difference in hydraulic heads between scenarios for all posterior ensemble realisations in layer 8 (Wambo Coal Seam). Each subplot (a) to (f) displays the mean difference in hydraulic heads for 2021, 2024, 2030, 2050, 2080 and 2200.

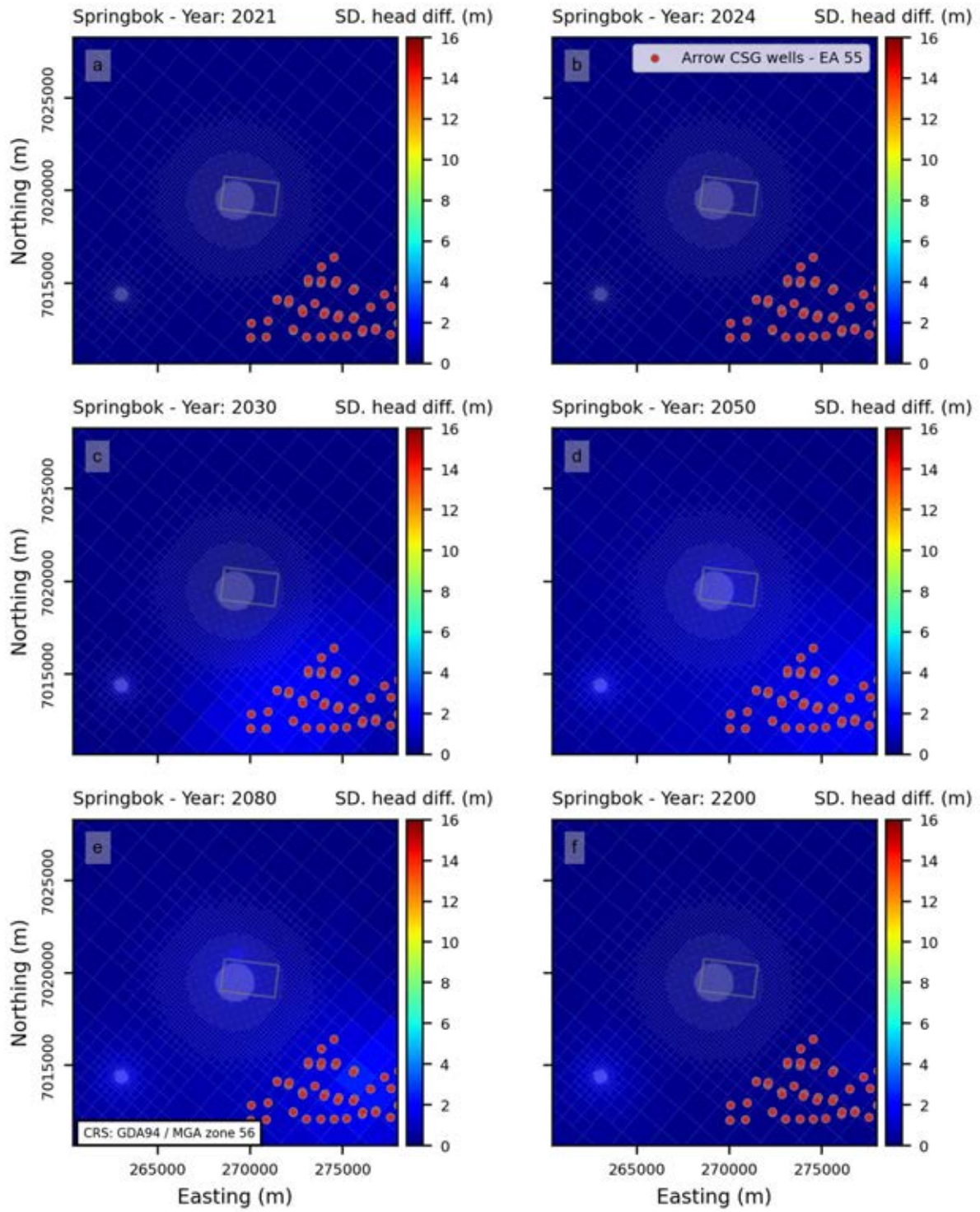


Figure F.3 – Maps showing the standard deviation of the difference in hydraulic heads between scenarios for all posterior ensemble realisations in layer 3 (Springbok Sandstone). Each subplot (a) to (f) displays the mean difference in hydraulic heads for 2021, 2024, 2030, 2050, 2080 and 2200.

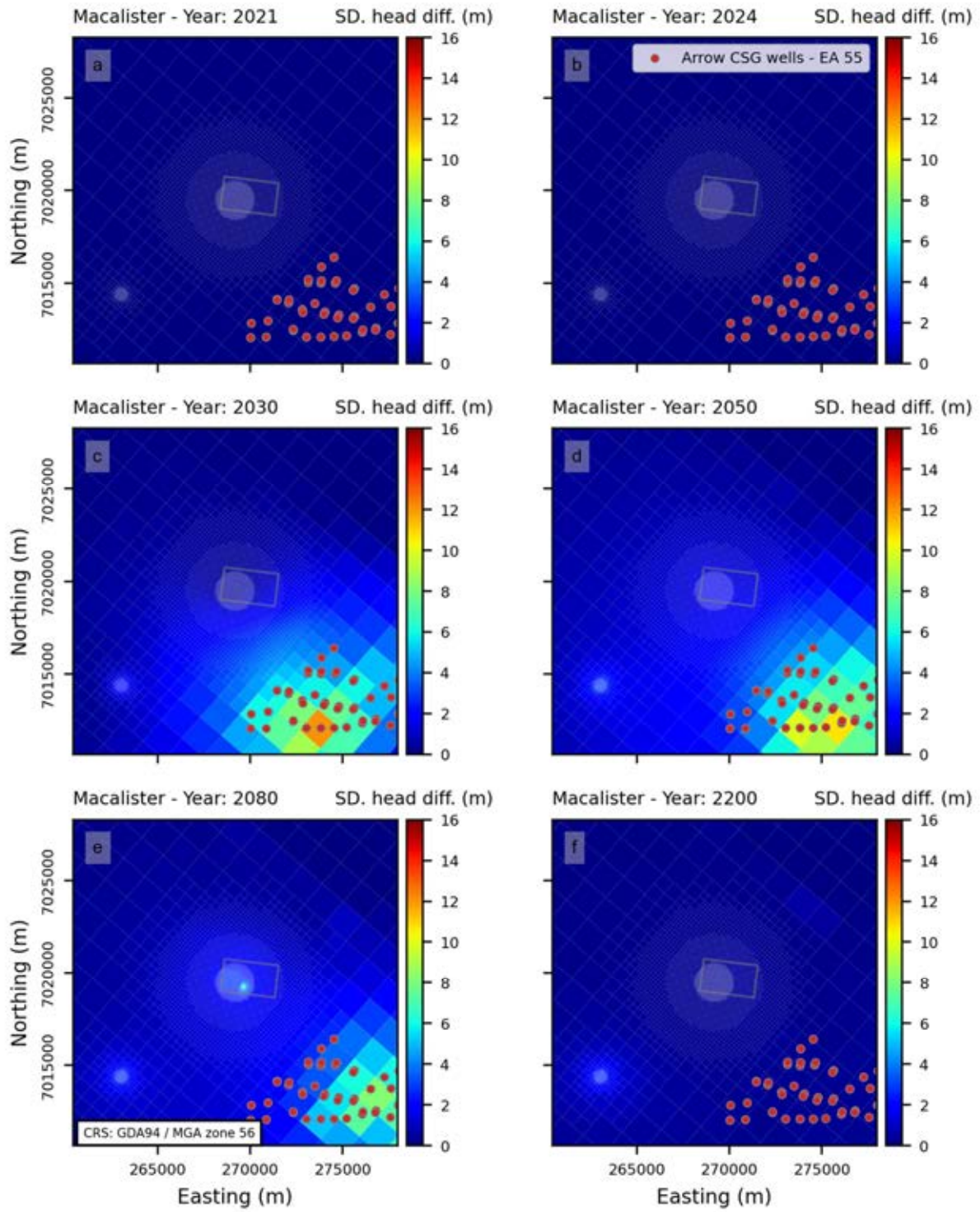


Figure F.4 – Maps showing the standard deviation of the difference in hydraulic heads between scenarios for all posterior ensemble realisations in layer 6 (Macalister Coal Seam). Each subplot (a) to (f) displays the mean difference in hydraulic heads for 2021, 2024, 2030, 2050, 2080 and 2200.

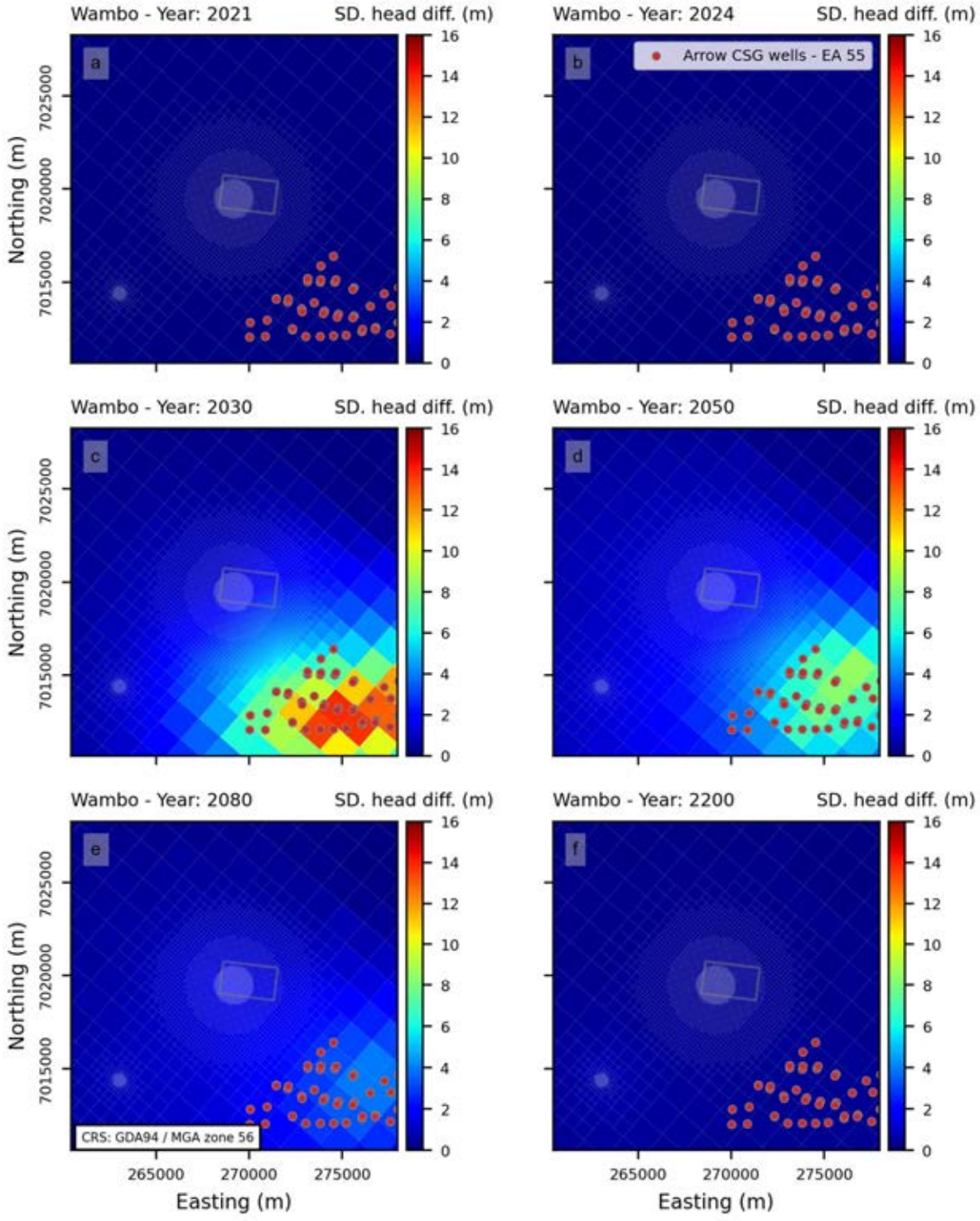


Figure F.5 – Maps showing the standard deviation of the difference in hydraulic heads between scenarios for all posterior ensemble realisations in layer 8 (Wambo Coal Seam). Each subplot (a) to (f) displays the mean difference in hydraulic heads for 2021, 2024, 2030, 2050, 2080 and 2200.

# Appendix G Particle Density Sensitivity Analysis

# 1. Particle Placement Density

In the review of previous groundwater modelling efforts at PL253, CSIRO (2023) recommended that a higher particle density be employed to allow a more comprehensive simulation of potential flow paths. Further recommendations included placing particles along the border of Lot40 and at monitoring bores where UCG contaminants have been detected.

To address these recommendations, particles were placed in:

- Model cells along the border of gasifier cells in the Macalister and Springbok layers
- Model cells along the border of Lot40 in the Macalister and Springbok layers
- Model cells at monitoring bore locations, in the layers where they are screened.

Model cells in which particles are placed are displayed in Figure G.1.

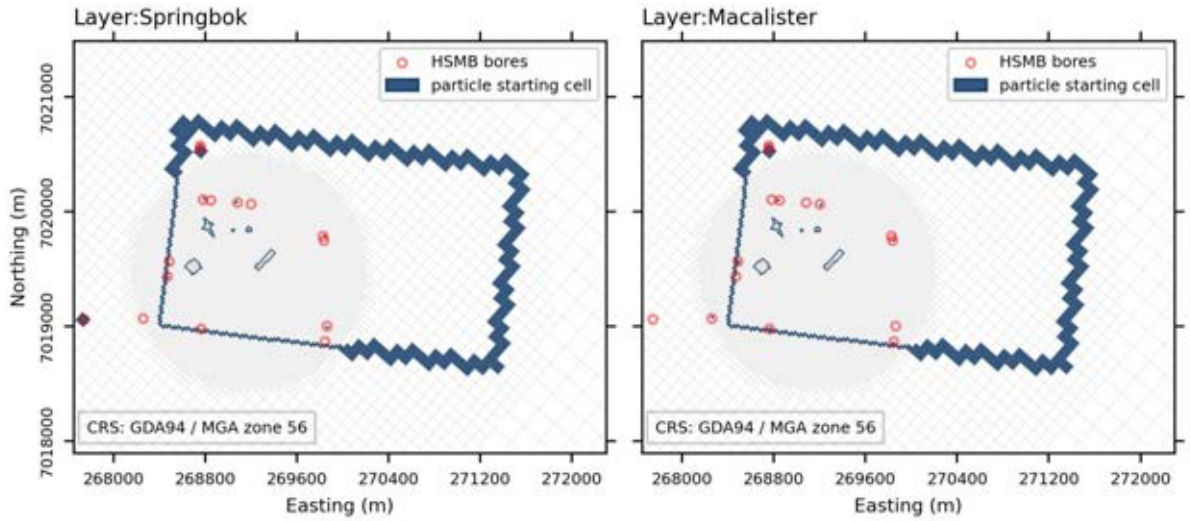


Figure G.1 – Plan view of model cells where particles were placed in the Springbok and Macalister layers.

The effect of particle placement density was assessed regarding to the:

1. Maximum particle distance from the boundary of Lot40 in the year 2200
2. Number of unique model cells containing particles in the year 2200
3. The number of particles that move between layers over the simulated period.

The first criterion reflects the quantity of interest (QoI). However, results may be dominated by travel distance from a single location. Namely, distance of particles released at the monitoring bore which is furthest from the border of Lot40. The second criterion was included to provide a more robust assessment of how placement density affects particle end locations. The last criterion addresses whether particle density is sufficient to reflect vertical flow paths between layers.

The particle density sensitivity analysis is carried out by placing an increasing number of particles within each starting cell. The first particle in a cell is placed at the centre of the corresponding cell. The next six particles are placed in the centre of each cell face. The next eight particles are placed at the cell vertices. Subsequent particles are placed at a random three-dimensional position within the cell.

The analysis is undertaken for a single parameter realisation, for the future development plan (FDP) scenario that includes the proposed 55 CSG wells in PL253. The “base” parameter realisation was

chosen because it deviates the least from the mean of the prior. Conceptually, it is similar to a "calibrated" parameter set obtained through regularised inversion in a deterministic single-model context.

# 2. Results

Figure G.2 shows the effect of the density in particle placements on (left) predicted maximum distance from the boundary of Lot40 and (right) the number of unique cells which contain particles in the year 2200.

There was no significant change for predicted maximum distance when particle density exceeds 6 particles per cell. Once released particles per cell exceeded 50, an increase of approximately 5 m (less than 1% change) was observed.

The number of final unique cells changed by less than 10% between 6 and 100 particles per cell. 50 particles per cell captured 99% of the same cells as using 100 particles per cell.

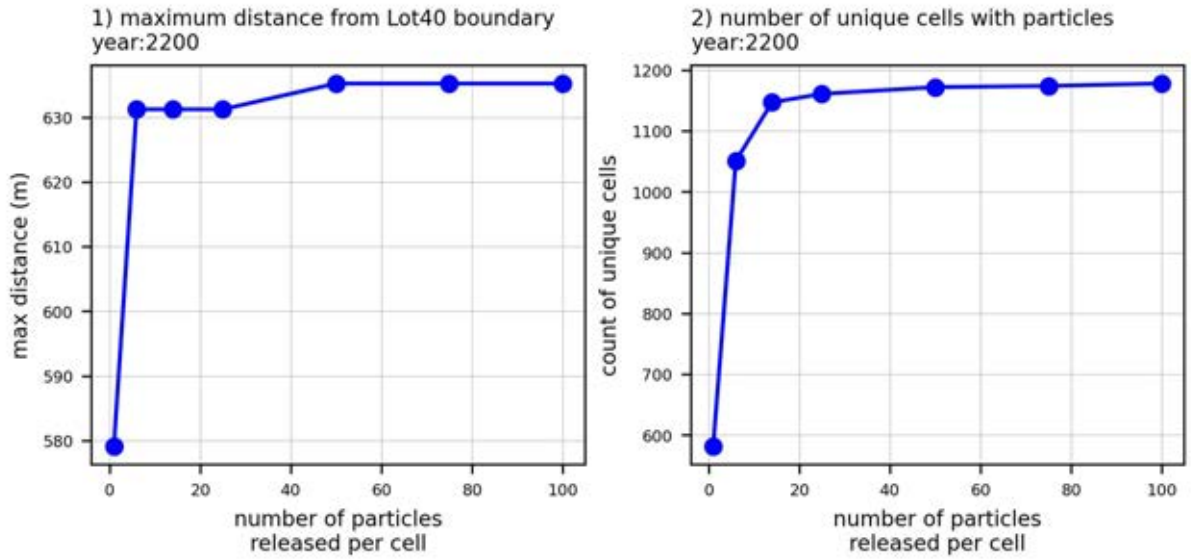


**Figure G.2 – Comparison between number of particles per cell and (1) maximum predicted particle distance from Lot40 boundary and (2) the predicted number of unique cells containing particles in the year 2200.**

Figure G.3 shows the model layers in which particles were located in the year 2200. Although changes are minor after 25 particles released per cell, the relative frequency does not completely converge during this sensitivity analysis. No more particles per cell were tested, as this results in impractical amount of virtual memory requirements to run the model. However, it is of note that as more particles are added, the frequency of particles ending up in layer five (Macalister) increases.

Furthermore, particles that terminate in layer three (Springbok), also originate there. This implies that, at least for this parameter realisation, all vertical movement during the simulated period is downwards. This is highlighted in Figure G.4, which shows the change in layer between when a particle was released and where it terminated in 2200. As can be seen, for all cases vertical movement is always downward from the Springbok (layer three) towards Macalister (layer six). Note that, although it is not visible in the figure, less than 0.001% of released particles terminate the simulation within layers 4, 5 and 7.

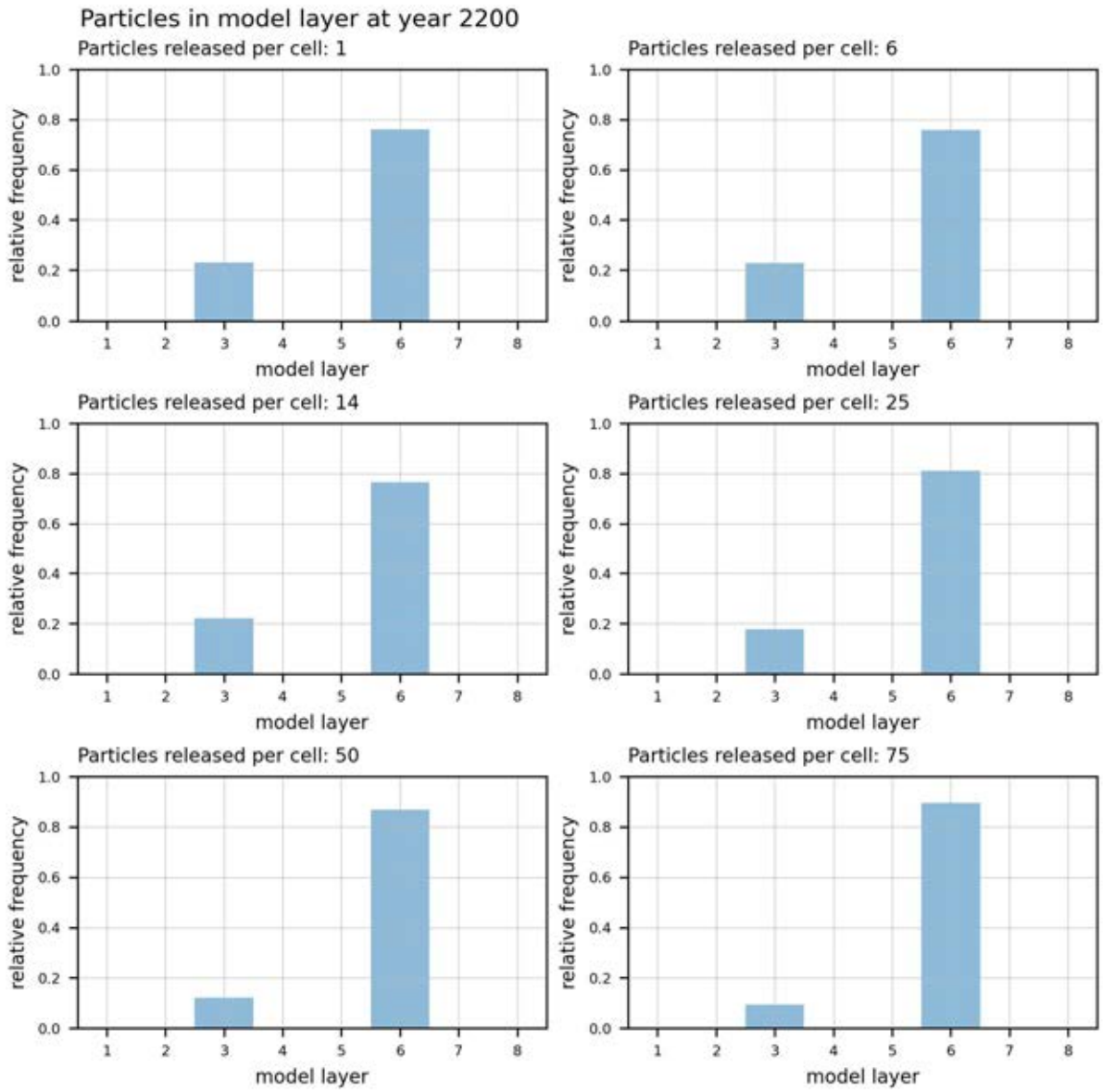


Figure G.3 – Histograms of relative frequency of model layer where particles were in the year 2200.

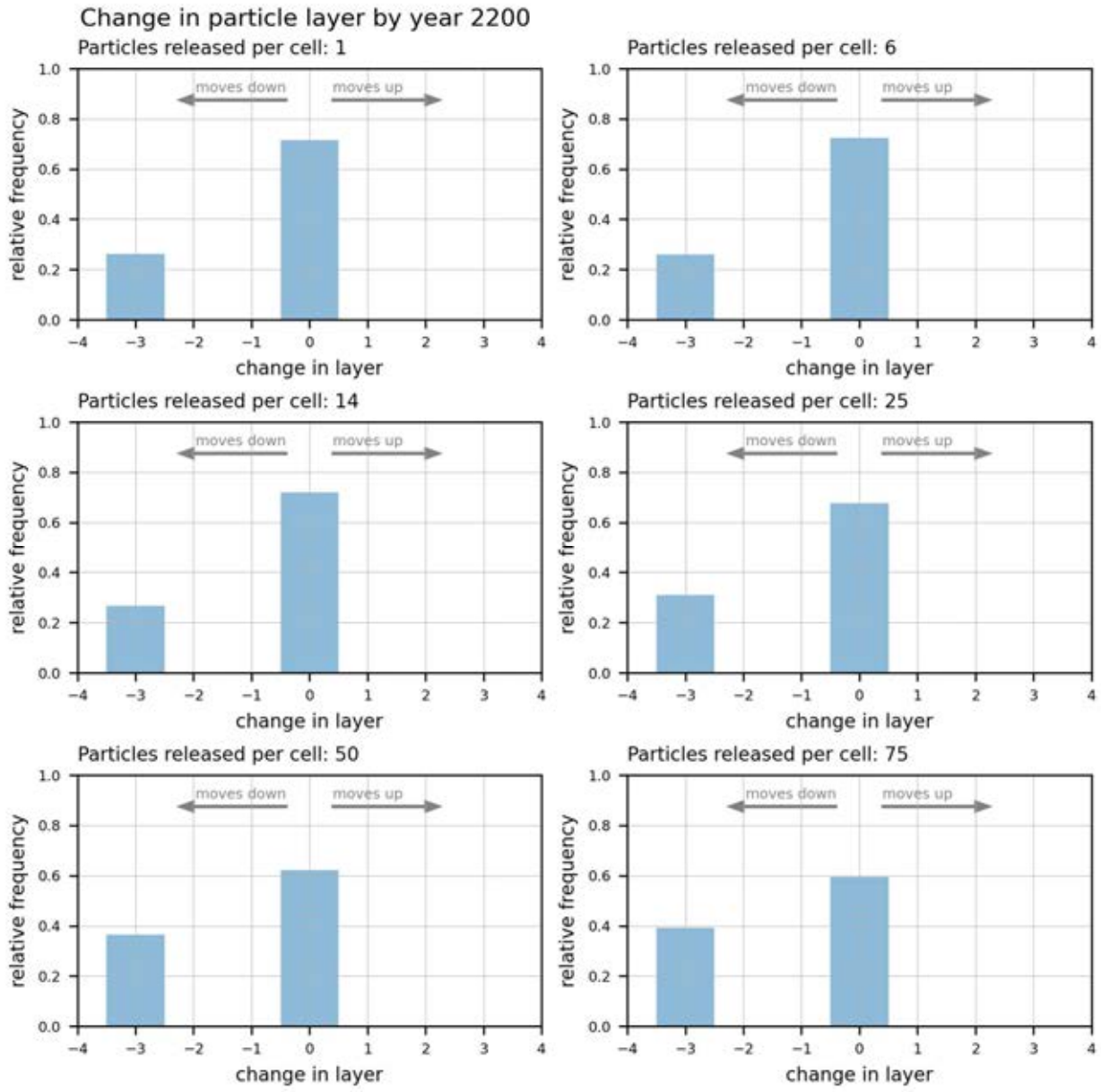


Figure G.4 – Histograms depicting the change in particle layer between the initial position (released) and the final position where it is in the year 2200. Positive and negative values denote vertical movement upwards and downwards, respectively.

# 3. Conclusion

The analysis indicates that a particle placement density of 50 particles per cell is adequate for identifying potential flow paths. The presented results suggest that a reduced density of 16 particles per cell could also be sufficient. However, this assessment only considers a single parameter realisation from the complete forecast ensemble. To incorporate a safety margin while maintaining computational feasibility for the model, the particle density was increased.

# Appendix H Concentration Data Used for Initial Concentration Field

Table H.1 –Concentration data used for initial concentration field.

| Bore | Date | Naphthalene (µg/L) | Benzene (µg/L) |
|---|---|---|---|
| G4MWA | 8/06/2018 | 5 | 1 |
| G4MWD | 8/06/2018 | 5 | 1 |
| G5M11I | 8/02/2017 | 5 | 1 |
| HL21 | 13/03/2020 | 5 | 1 |
| HL22 | 16/03/2020 | 5 | 1 |
| HL23 | 20/03/2020 | 5 | 1 |
| HL24 | 23/03/2020 | 5 | 1 |
| HL25 | 29/03/2020 | 5 | 1 |
| HL26 | 1/04/2020 | 5 | 1 |
| HL27 | 3/04/2020 | 5 | 1 |
| HSMB1D | 30/05/2018 | 32 | 225 |
| HSMB1S | 30/05/2018 | 129 | 755 |
| HSMB2D | 31/05/2018 | 10 | 30 |
| HSMB2S | 31/05/2018 | 345 | 1020 |
| HSMB3D1 | 30/05/2018 | 7 | 95 |
| HSMB3D2 | 29/05/2018 | 7 | 35 |
| HSMB3S1 | 29/05/2018 | 15 | 96 |
| HSMB3S2 | 28/05/2018 | 137 | 77 |
| HSMB4D | 1/06/2018 | 17 | 79 |
| HSMB4S | 1/06/2018 | 59 | 1060 |
| HSMB5D | 4/06/2018 | 11 | 106 |
| HSMB6D | 17/04/2021 | 5 | 1 |
| HSMB6S | 19/04/2021 | 5 | 10 |
| HSMB7D | 13/04/2021 | 5 | 30 |
| HSMB7S | 15/04/2021 | 5 | 2 |
| L22 | 6/02/2017 | 5 | 2 |
| M10 | 20/12/2016 | 10 | 1 |
| M10R | 17/08/2017 | 5 | 1 |
| M14R | 7/02/2017 | 5 | 72 |
| M15 | 20/12/2016 | 10 | 1 |
| M21 | 11/09/2018 | 5 | 1 |
| M22 | 6/06/2018 | 44 | 335 |
| M23 | 11/09/2018 | 5 | 26 |
| NB01D | 18/03/2021 | 1 | 2 |
| NB01S | 18/03/2021 | 1 | 2000 |

| Bore | Date | Naphthalene (µg/L) | Benzene (µg/L) |
|---|---|---|---|
| NB02D | 16/12/2020 | 1 | 13 |
| NB02S | 17/12/2020 | 1 | 16 |
| NB04D | 17/12/2020 | 1 | 1 |
| NB05S | 15/12/2020 | 1 | 2 |
| PZ08CP001d | 17/09/2019 | 5 | 1 |
| PZ08CP001s | 16/10/2019 | 5 | 1 |
| PZ08CP002 | 13/12/2018 | 5 | 1 |
| PZ08CP008d | 12/12/2018 | 5 | 1 |
| PZ08CP009d | 23/01/2019 | 5 | 1 |
| PZ08CP009i | 23/01/2019 | 5 | 1 |
| PZ08CP013 | 24/01/2019 | 5 | 1 |
| RN107857 | 3/01/2018 | 5 | 1 |
| RN10790 | 28/02/2020 | 5 | 1 |
| RN147004 | 26/02/2020 | 5 | 1 |
| RN147941 | 5/09/2018 | 5 | 1 |
| RN15868 | 6/04/2018 | 5 | 1 |
| RN160158 | 22/01/2020 | 5 | 1 |
| RN24466 | 5/10/2016 | 5 | 1 |
| RN33553 | 6/10/2016 | 5 | 1 |
| RN87897 | 7/10/2016 | 5 | 1 |

# Appendix I Transport Parameter Group Prior and Posterior Histograms – Pilot point parameters

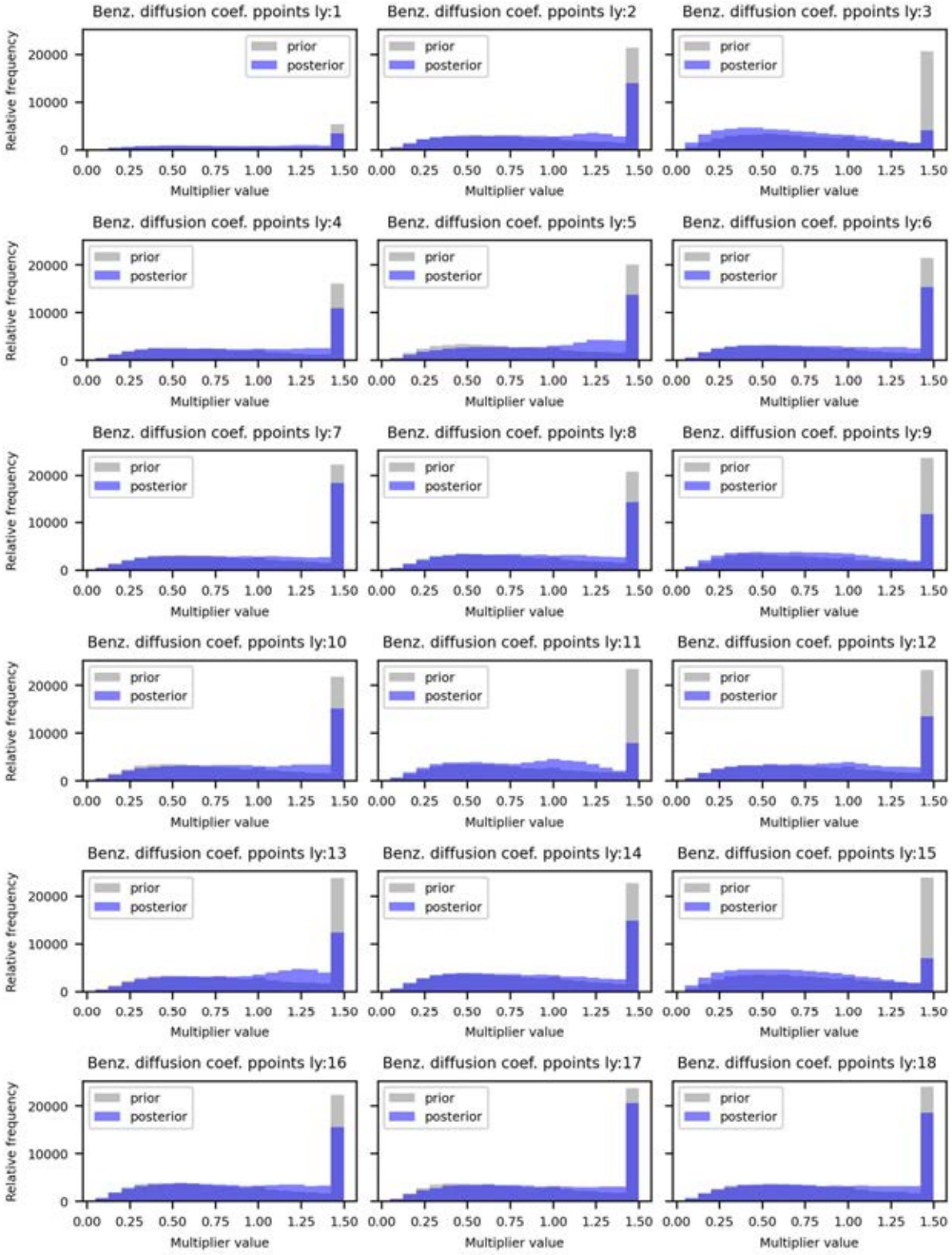
Benz. diffusion coef. ppoints ly:1
Benz. diffusion coef. ppoints ly:2
Benz. diffusion coef. ppoints ly:3
Benz. diffusion coef. ppoints ly:4
Benz. diffusion coef. ppoints ly:5
Benz. diffusion coef. ppoints ly:6
Benz. diffusion coef. ppoints ly:7
Benz. diffusion coef. ppoints ly:8
Benz. diffusion coef. ppoints ly:9
Benz. diffusion coef. ppoints ly:10
Benz. diffusion coef. ppoints ly:11
Benz. diffusion coef. ppoints ly:12
Benz. diffusion coef. ppoints ly:13
Benz. diffusion coef. ppoints ly:14
Benz. diffusion coef. ppoints ly:15
Benz. diffusion coef. ppoints ly:16
Benz. diffusion coef. ppoints ly:17
Benz. diffusion coef. ppoints ly:18
prior
posterior
Relative frequency
0
10000
20000
0.00 0.25 0.50 0.75 1.00 1.25 1.50
Multiplier value

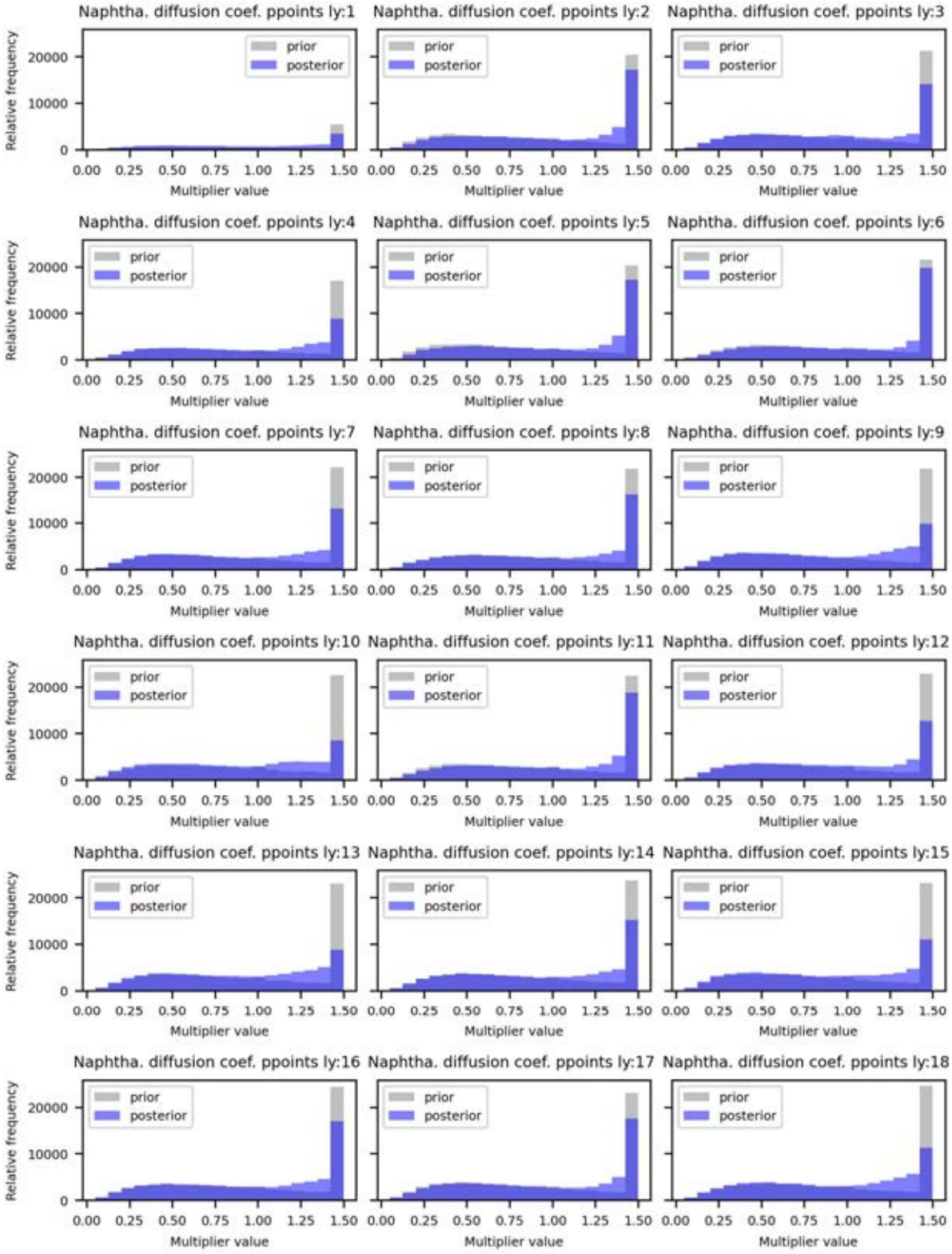
Naphtha. diffusion coef. ppoints ly:1
Naphtha. diffusion coef. ppoints ly:2
Naphtha. diffusion coef. ppoints ly:3
Naphtha. diffusion coef. ppoints ly:4
Naphtha. diffusion coef. ppoints ly:5
Naphtha. diffusion coef. ppoints ly:6
Naphtha. diffusion coef. ppoints ly:7
Naphtha. diffusion coef. ppoints ly:8
Naphtha. diffusion coef. ppoints ly:9
Naphtha. diffusion coef. ppoints ly:10
Naphtha. diffusion coef. ppoints ly:11
Naphtha. diffusion coef. ppoints ly:12
Naphtha. diffusion coef. ppoints ly:13
Naphtha. diffusion coef. ppoints ly:14
Naphtha. diffusion coef. ppoints ly:15
Naphtha. diffusion coef. ppoints ly:16
Naphtha. diffusion coef. ppoints ly:17
Naphtha. diffusion coef. ppoints ly:18
prior
posterior
Relative frequency
0
10000
20000
0.00 0.25 0.50 0.75 1.00 1.25 1.50
Multiplier value

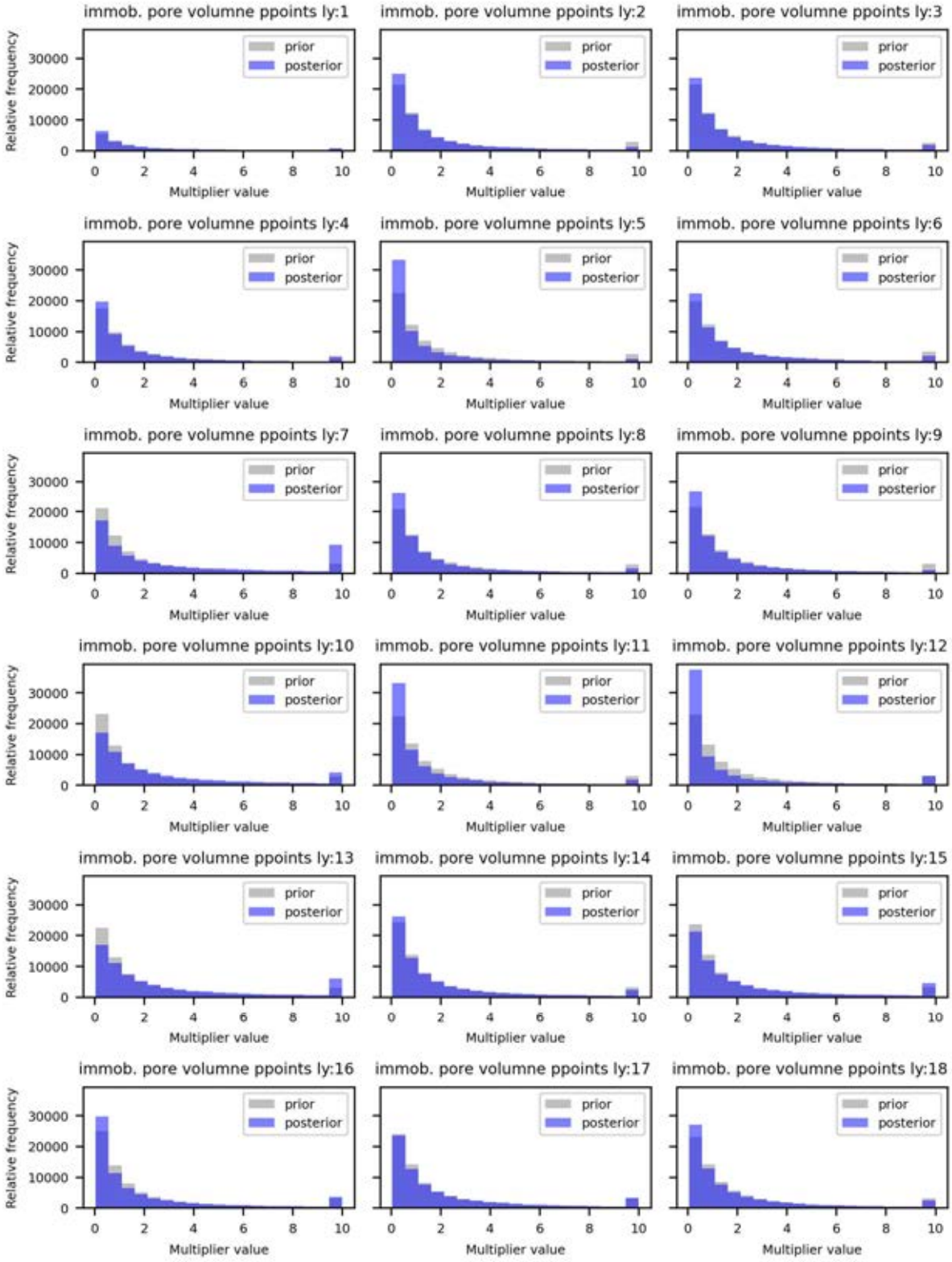
immob. pore volumne ppoints ly:1
immob. pore volumne ppoints ly:2
immob. pore volumne ppoints ly:3
immob. pore volumne ppoints ly:4
immob. pore volumne ppoints ly:5
immob. pore volumne ppoints ly:6
immob. pore volumne ppoints ly:7
immob. pore volumne ppoints ly:8
immob. pore volumne ppoints ly:9
immob. pore volumne ppoints ly:10
immob. pore volumne ppoints ly:11
immob. pore volumne ppoints ly:12
immob. pore volumne ppoints ly:13
immob. pore volumne ppoints ly:14
immob. pore volumne ppoints ly:15
immob. pore volumne ppoints ly:16
immob. pore volumne ppoints ly:17
immob. pore volumne ppoints ly:18
prior
posterior
Relative frequency
Multiplier value
0
10000
20000
30000
0
2
4
6
8
10

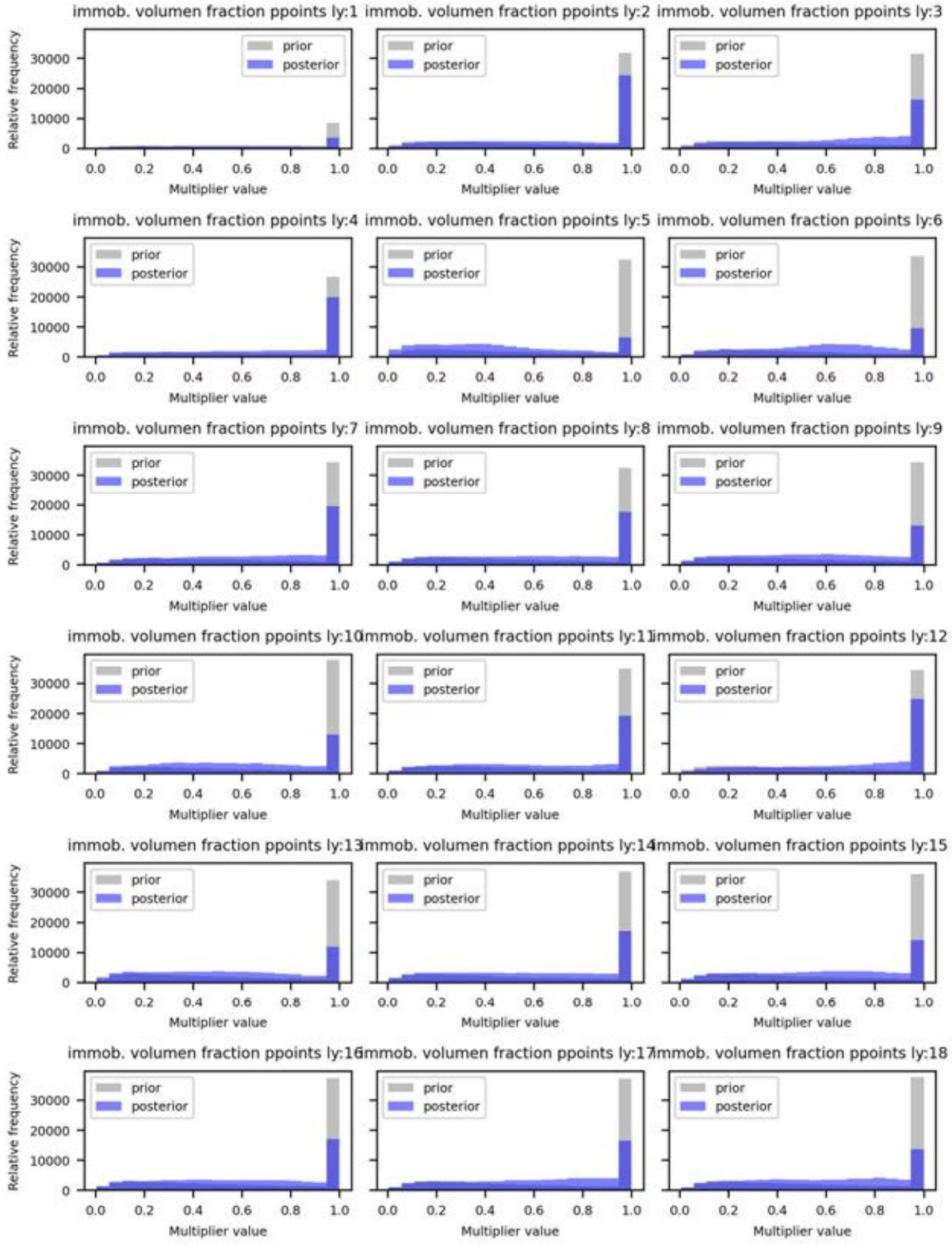
immob. volumen fraction ppoints ly:1
immob. volumen fraction ppoints ly:2
immob. volumen fraction ppoints ly:3
immob. volumen fraction ppoints ly:4
immob. volumen fraction ppoints ly:5
immob. volumen fraction ppoints ly:6
immob. volumen fraction ppoints ly:7
immob. volumen fraction ppoints ly:8
immob. volumen fraction ppoints ly:9
immob. volumen fraction ppoints ly:10
immob. volumen fraction ppoints ly:11
immob. volumen fraction ppoints ly:12
immob. volumen fraction ppoints ly:13
immob. volumen fraction ppoints ly:14
immob. volumen fraction ppoints ly:15
immob. volumen fraction ppoints ly:16
immob. volumen fraction ppoints ly:17
immob. volumen fraction ppoints ly:18
prior
posterior
Relative frequency
Multiplier value
0
10000
20000
30000
0.0
0.2
0.4
0.6
0.8
1.0

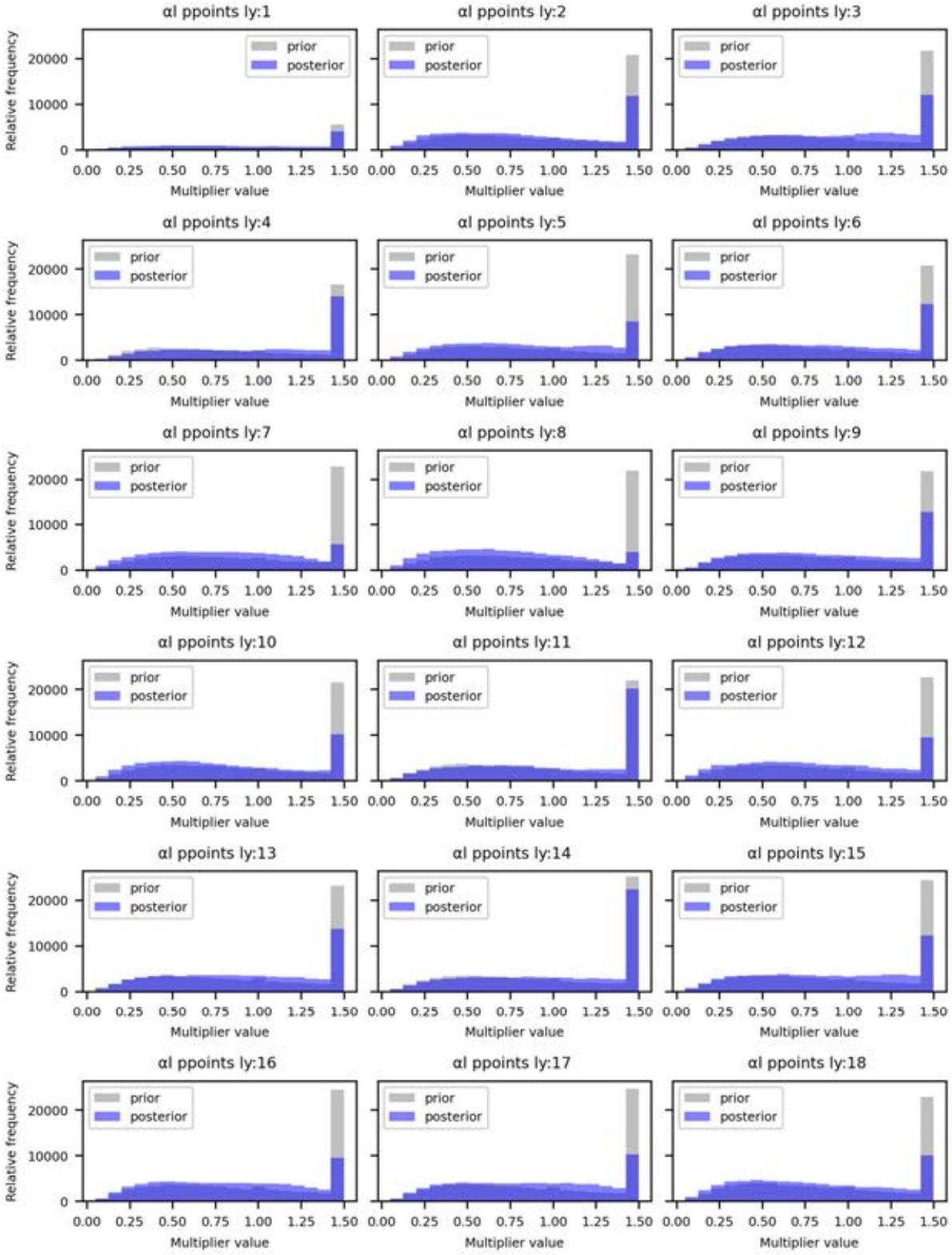
αl ppoints ly:1
αl ppoints ly:2
αl ppoints ly:3
αl ppoints ly:4
αl ppoints ly:5
αl ppoints ly:6
αl ppoints ly:7
αl ppoints ly:8
αl ppoints ly:9
αl ppoints ly:10
αl ppoints ly:11
αl ppoints ly:12
αl ppoints ly:13
αl ppoints ly:14
αl ppoints ly:15
αl ppoints ly:16
αl ppoints ly:17
αl ppoints ly:18
prior
posterior
Relative frequency
Multiplier value
0
10000
20000
0.00 0.25 0.50 0.75 1.00 1.25 1.50

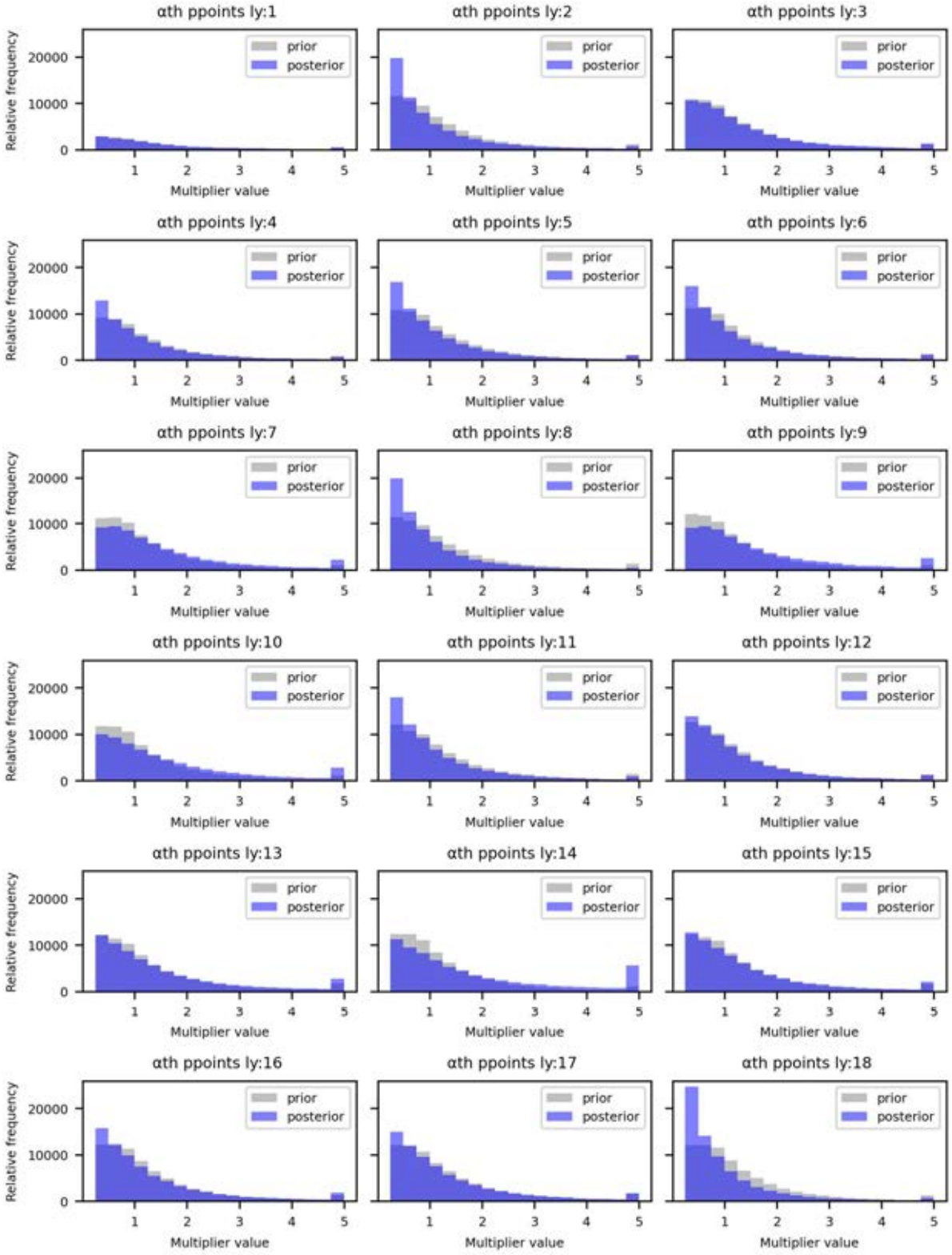
αth ppoints ly:1
αth ppoints ly:2
αth ppoints ly:3
αth ppoints ly:4
αth ppoints ly:5
αth ppoints ly:6
αth ppoints ly:7
αth ppoints ly:8
αth ppoints ly:9
αth ppoints ly:10
αth ppoints ly:11
αth ppoints ly:12
αth ppoints ly:13
αth ppoints ly:14
αth ppoints ly:15
αth ppoints ly:16
αth ppoints ly:17
αth ppoints ly:18
prior
posterior
Relative frequency
Multiplier value
0
10000
20000
1
2
3
4
5

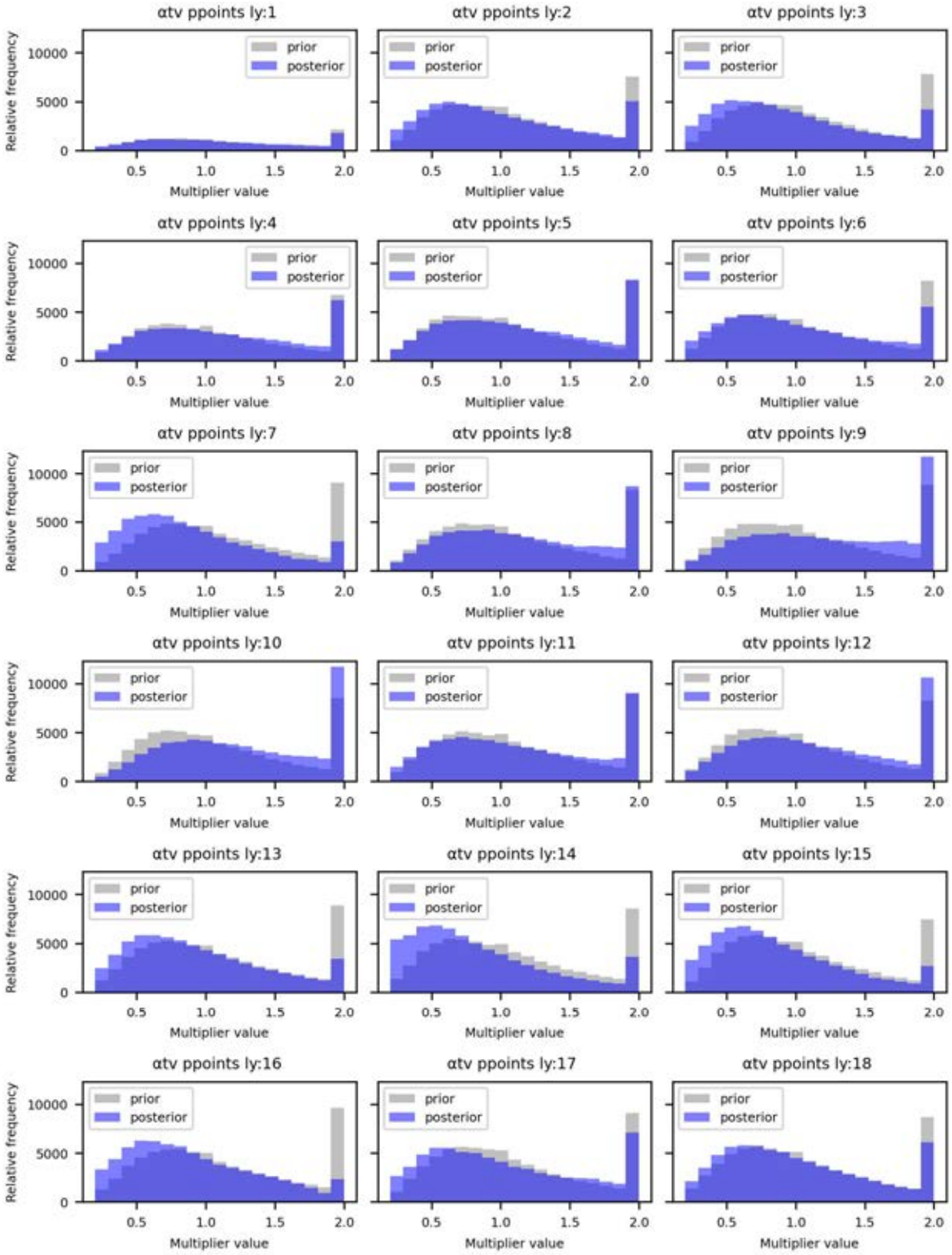
αtv ppoints ly:1
αtv ppoints ly:2
αtv ppoints ly:3
αtv ppoints ly:4
αtv ppoints ly:5
αtv ppoints ly:6
αtv ppoints ly:7
αtv ppoints ly:8
αtv ppoints ly:9
αtv ppoints ly:10
αtv ppoints ly:11
αtv ppoints ly:12
αtv ppoints ly:13
αtv ppoints ly:14
αtv ppoints ly:15
αtv ppoints ly:16
αtv ppoints ly:17
αtv ppoints ly:18
prior
posterior
Relative frequency
Multiplier value
0
5000
10000
0.5
1.0
1.5
2.0

# Appendix J Transport Parameter Group Prior and Posterior Histograms Coarse pilot point parameters

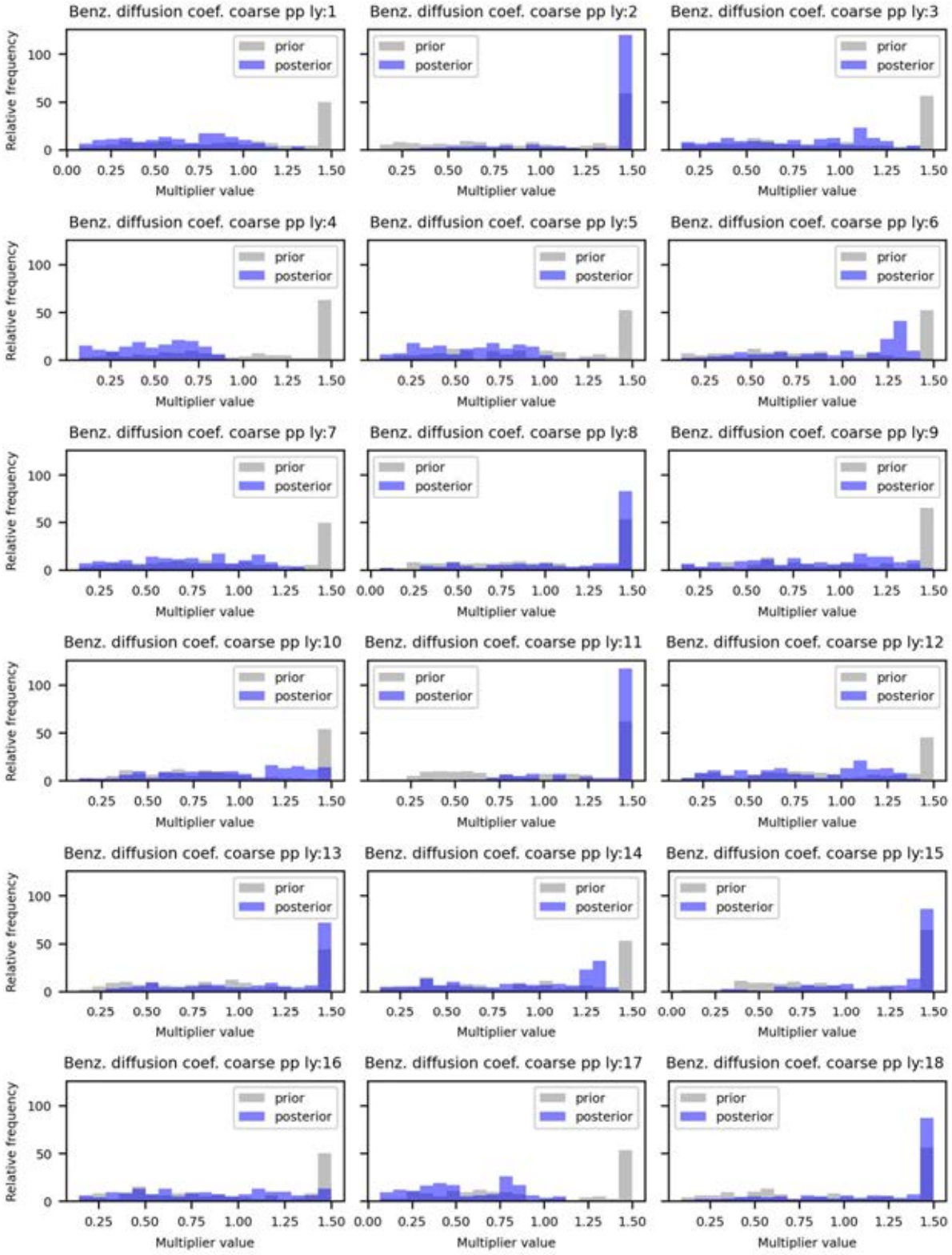
Benz. diffusion coef. coarse pp ly:1
Benz. diffusion coef. coarse pp ly:2
Benz. diffusion coef. coarse pp ly:3
Benz. diffusion coef. coarse pp ly:4
Benz. diffusion coef. coarse pp ly:5
Benz. diffusion coef. coarse pp ly:6
Benz. diffusion coef. coarse pp ly:7
Benz. diffusion coef. coarse pp ly:8
Benz. diffusion coef. coarse pp ly:9
Benz. diffusion coef. coarse pp ly:10
Benz. diffusion coef. coarse pp ly:11
Benz. diffusion coef. coarse pp ly:12
Benz. diffusion coef. coarse pp ly:13
Benz. diffusion coef. coarse pp ly:14
Benz. diffusion coef. coarse pp ly:15
Benz. diffusion coef. coarse pp ly:16
Benz. diffusion coef. coarse pp ly:17
Benz. diffusion coef. coarse pp ly:18
prior
posterior
Relative frequency
Multiplier value

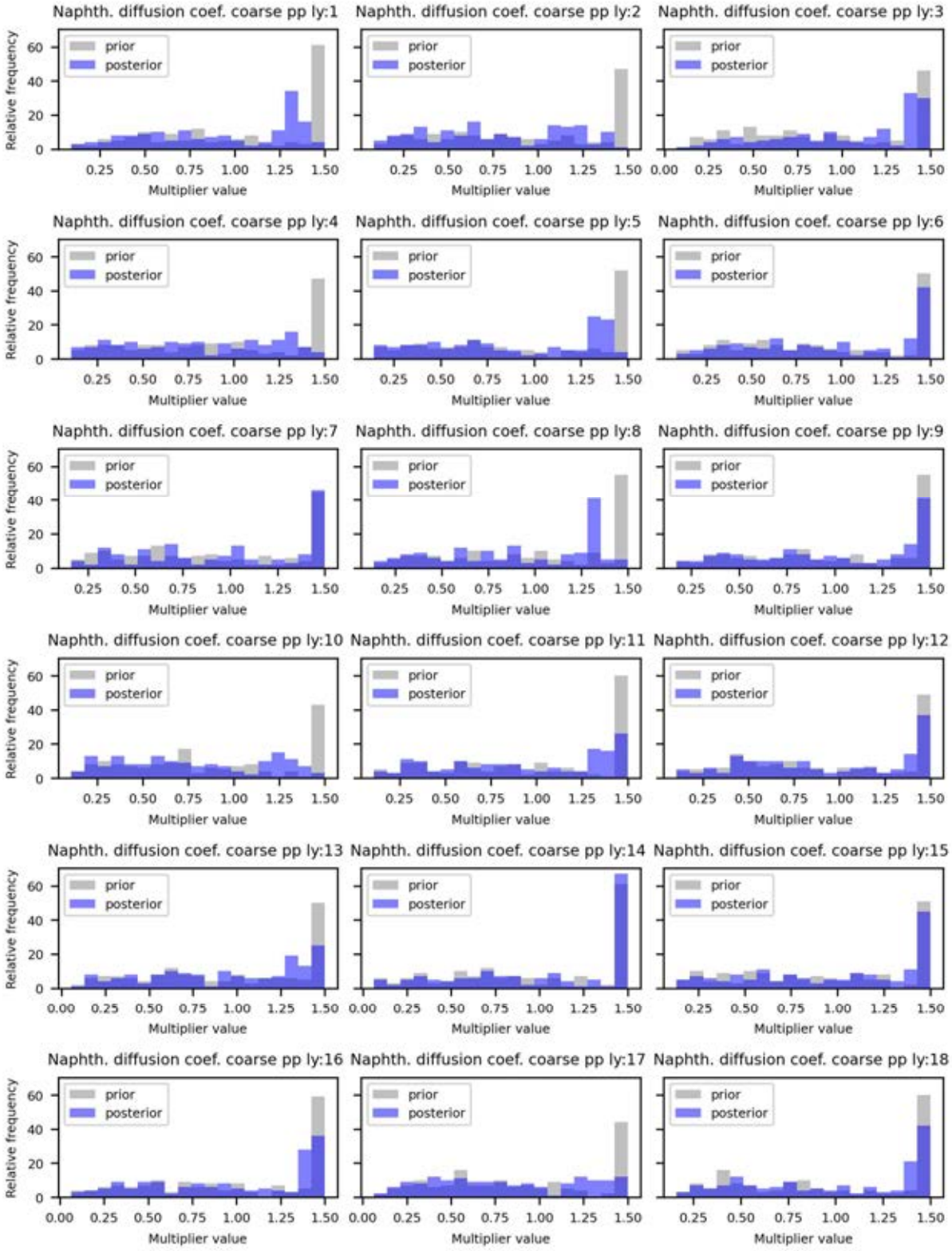
Naphth. diffusion coef. coarse pp ly:1
Naphth. diffusion coef. coarse pp ly:2
Naphth. diffusion coef. coarse pp ly:3
Naphth. diffusion coef. coarse pp ly:4
Naphth. diffusion coef. coarse pp ly:5
Naphth. diffusion coef. coarse pp ly:6
Naphth. diffusion coef. coarse pp ly:7
Naphth. diffusion coef. coarse pp ly:8
Naphth. diffusion coef. coarse pp ly:9
Naphth. diffusion coef. coarse pp ly:10
Naphth. diffusion coef. coarse pp ly:11
Naphth. diffusion coef. coarse pp ly:12
Naphth. diffusion coef. coarse pp ly:13
Naphth. diffusion coef. coarse pp ly:14
Naphth. diffusion coef. coarse pp ly:15
Naphth. diffusion coef. coarse pp ly:16
Naphth. diffusion coef. coarse pp ly:17
Naphth. diffusion coef. coarse pp ly:18
prior
posterior
Relative frequency
Multiplier value

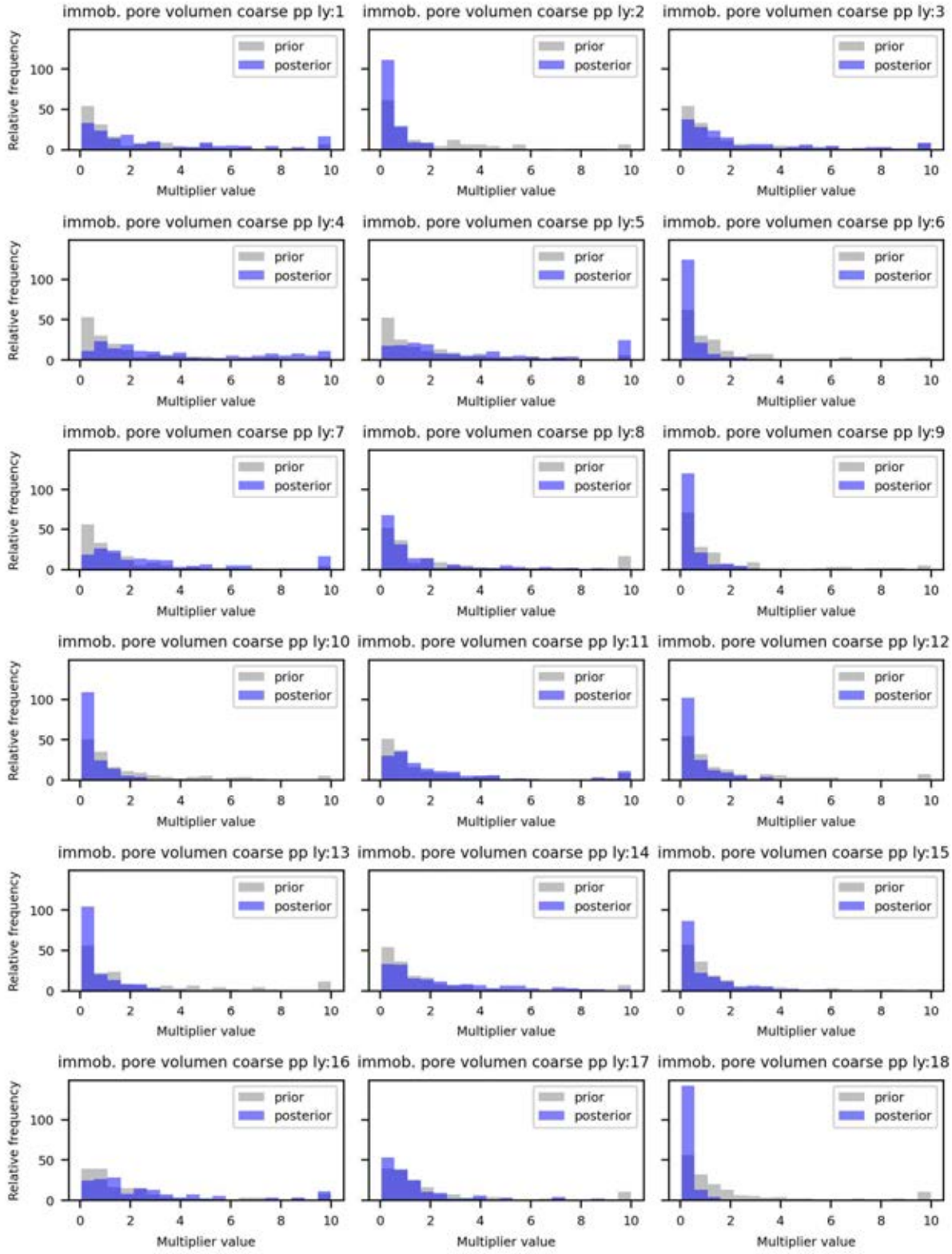
immob. pore volumen coarse pp ly:1
immob. pore volumen coarse pp ly:2
immob. pore volumen coarse pp ly:3
immob. pore volumen coarse pp ly:4
immob. pore volumen coarse pp ly:5
immob. pore volumen coarse pp ly:6
immob. pore volumen coarse pp ly:7
immob. pore volumen coarse pp ly:8
immob. pore volumen coarse pp ly:9
immob. pore volumen coarse pp ly:10
immob. pore volumen coarse pp ly:11
immob. pore volumen coarse pp ly:12
immob. pore volumen coarse pp ly:13
immob. pore volumen coarse pp ly:14
immob. pore volumen coarse pp ly:15
immob. pore volumen coarse pp ly:16
immob. pore volumen coarse pp ly:17
immob. pore volumen coarse pp ly:18
prior
posterior
Relative frequency
Multiplier value

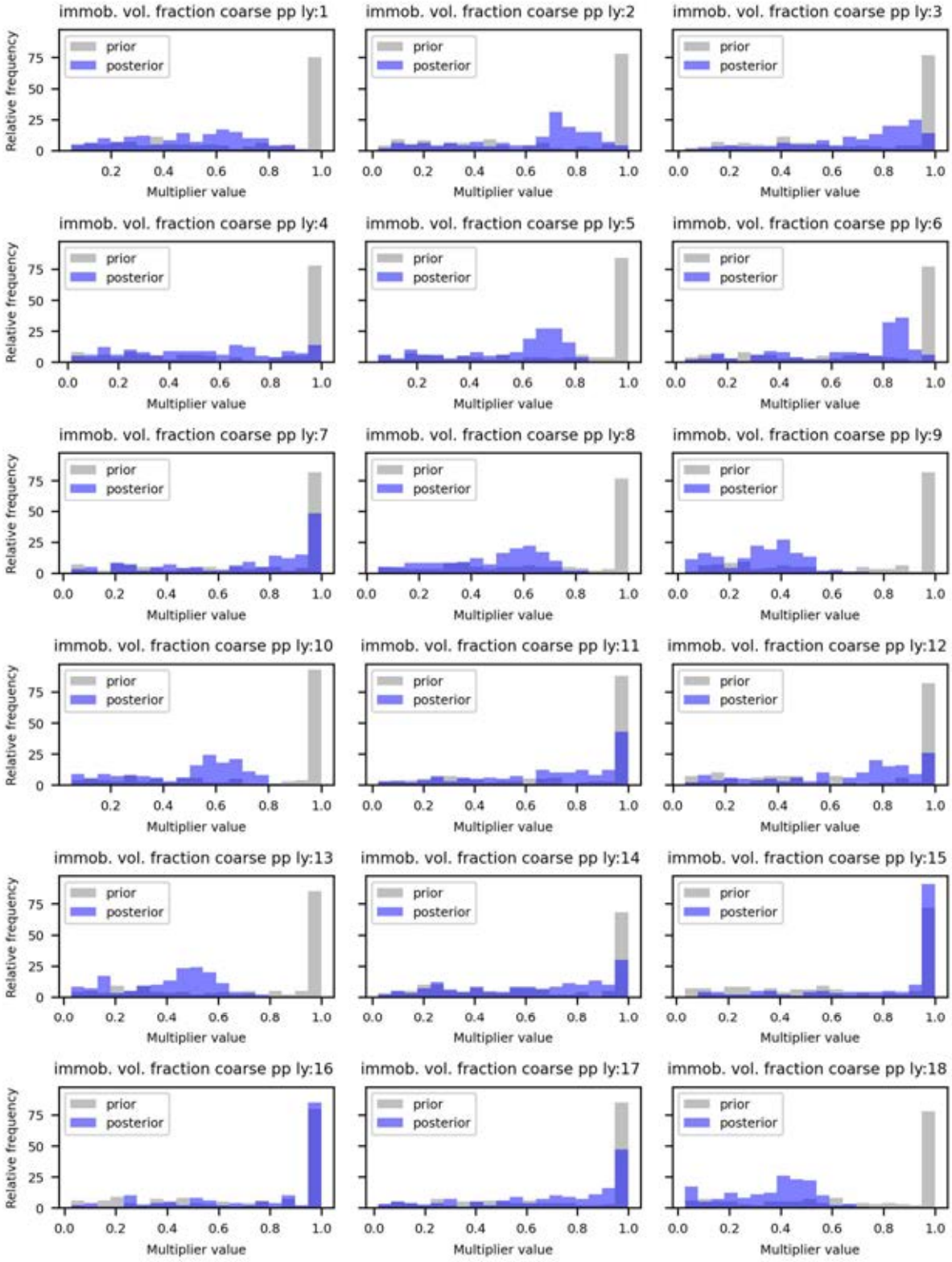
immob. vol. fraction coarse pp ly:1
immob. vol. fraction coarse pp ly:2
immob. vol. fraction coarse pp ly:3
immob. vol. fraction coarse pp ly:4
immob. vol. fraction coarse pp ly:5
immob. vol. fraction coarse pp ly:6
immob. vol. fraction coarse pp ly:7
immob. vol. fraction coarse pp ly:8
immob. vol. fraction coarse pp ly:9
immob. vol. fraction coarse pp ly:10
immob. vol. fraction coarse pp ly:11
immob. vol. fraction coarse pp ly:12
immob. vol. fraction coarse pp ly:13
immob. vol. fraction coarse pp ly:14
immob. vol. fraction coarse pp ly:15
immob. vol. fraction coarse pp ly:16
immob. vol. fraction coarse pp ly:17
immob. vol. fraction coarse pp ly:18
prior
posterior
Relative frequency
Multiplier value

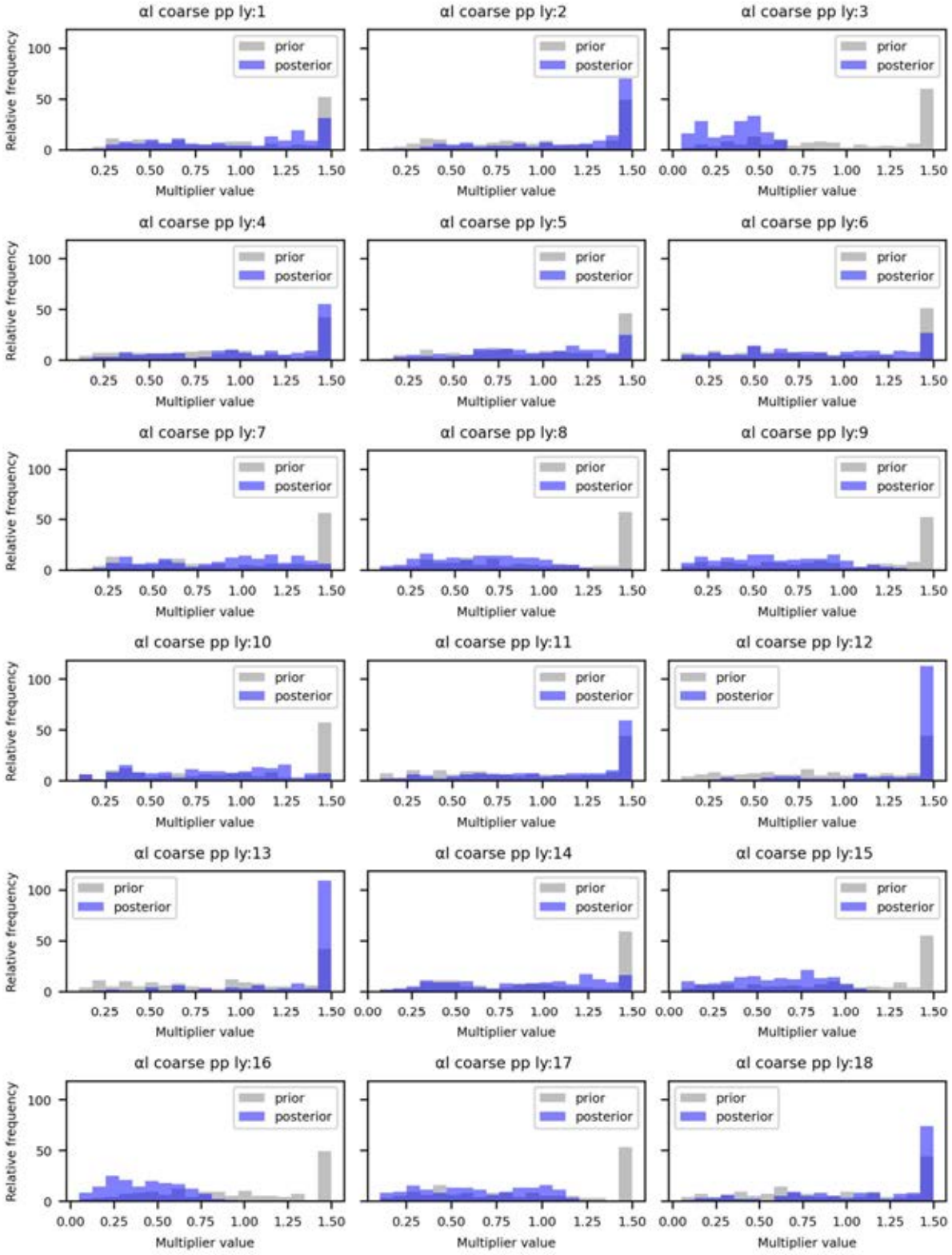
αl coarse pp ly:1
αl coarse pp ly:2
αl coarse pp ly:3
αl coarse pp ly:4
αl coarse pp ly:5
αl coarse pp ly:6
αl coarse pp ly:7
αl coarse pp ly:8
αl coarse pp ly:9
αl coarse pp ly:10
αl coarse pp ly:11
αl coarse pp ly:12
αl coarse pp ly:13
αl coarse pp ly:14
αl coarse pp ly:15
αl coarse pp ly:16
αl coarse pp ly:17
αl coarse pp ly:18
prior
posterior
Relative frequency
Multiplier value

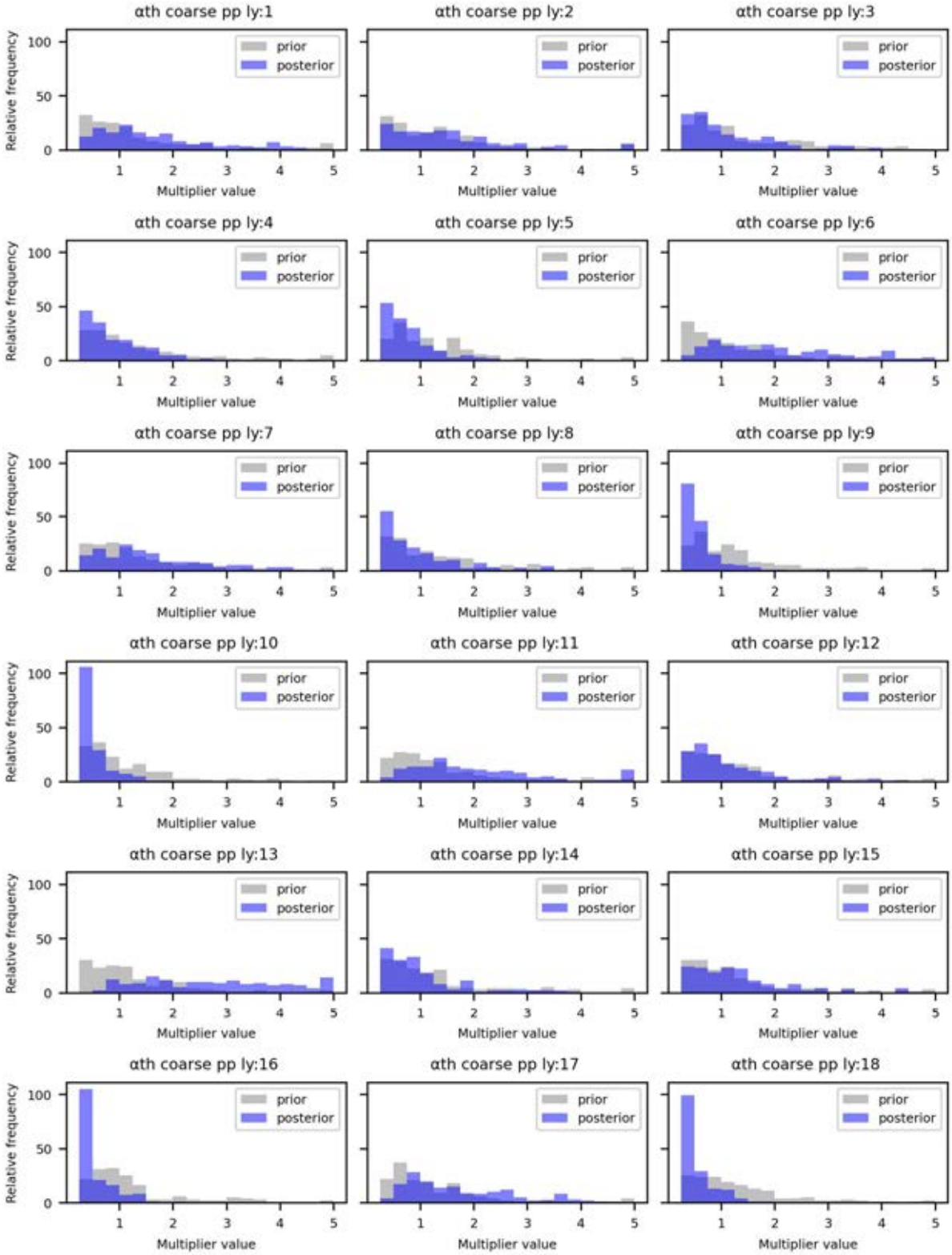
αth coarse pp ly:1
αth coarse pp ly:2
αth coarse pp ly:3
αth coarse pp ly:4
αth coarse pp ly:5
αth coarse pp ly:6
αth coarse pp ly:7
αth coarse pp ly:8
αth coarse pp ly:9
αth coarse pp ly:10
αth coarse pp ly:11
αth coarse pp ly:12
αth coarse pp ly:13
αth coarse pp ly:14
αth coarse pp ly:15
αth coarse pp ly:16
αth coarse pp ly:17
αth coarse pp ly:18
prior
posterior
Relative frequency
Multiplier value
0
50
100
1
2
3
4
5

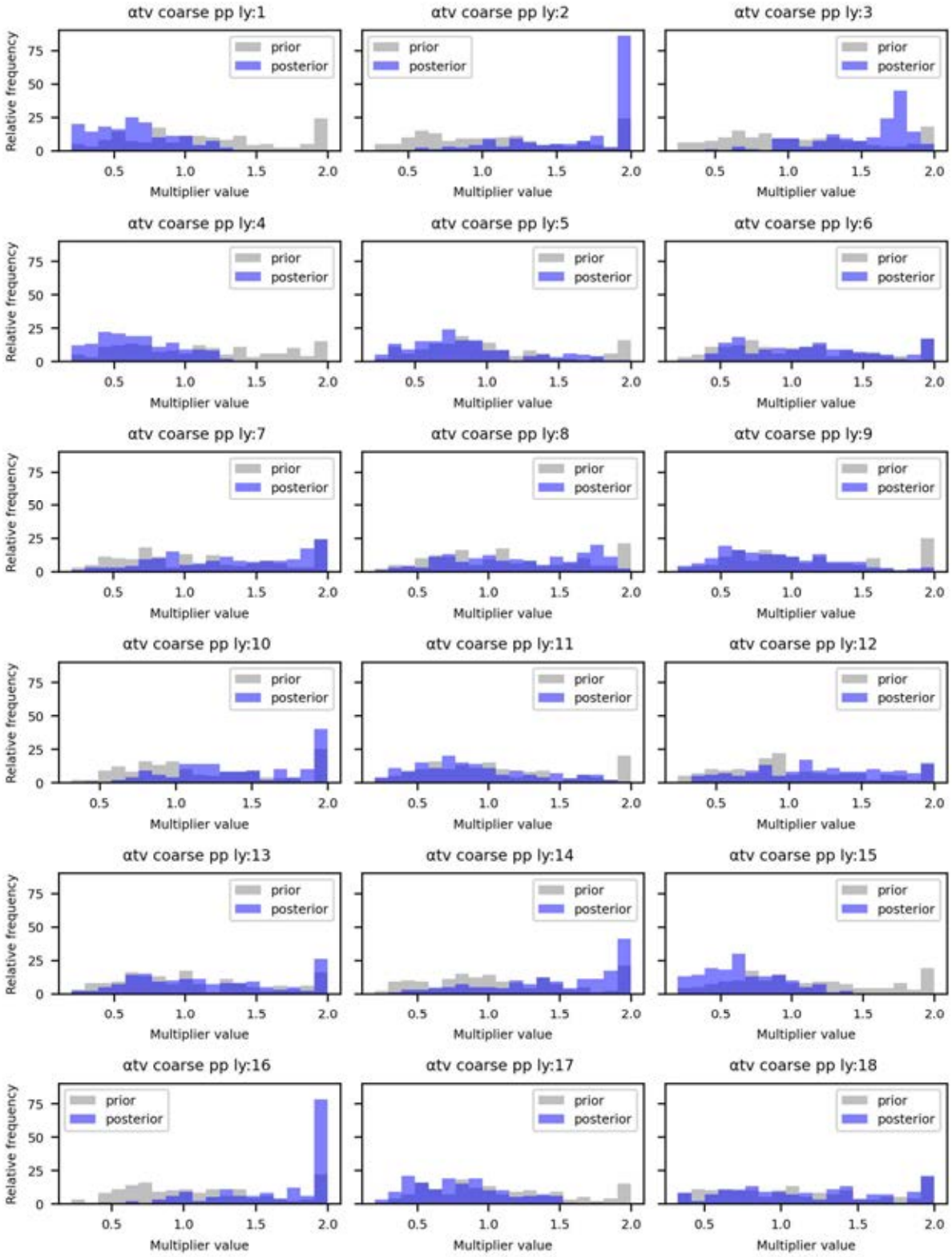
αtv coarse pp ly:1
αtv coarse pp ly:2
αtv coarse pp ly:3
αtv coarse pp ly:4
αtv coarse pp ly:5
αtv coarse pp ly:6
αtv coarse pp ly:7
αtv coarse pp ly:8
αtv coarse pp ly:9
αtv coarse pp ly:10
αtv coarse pp ly:11
αtv coarse pp ly:12
αtv coarse pp ly:13
αtv coarse pp ly:14
αtv coarse pp ly:15
αtv coarse pp ly:16
αtv coarse pp ly:17
αtv coarse pp ly:18
prior
posterior
Relative frequency
Multiplier value
0
25
50
75
0.5
1.0
1.5
2.0

# Appendix K Transport Parameter Group Prior and Posterior Histograms – Layered-constant parameters

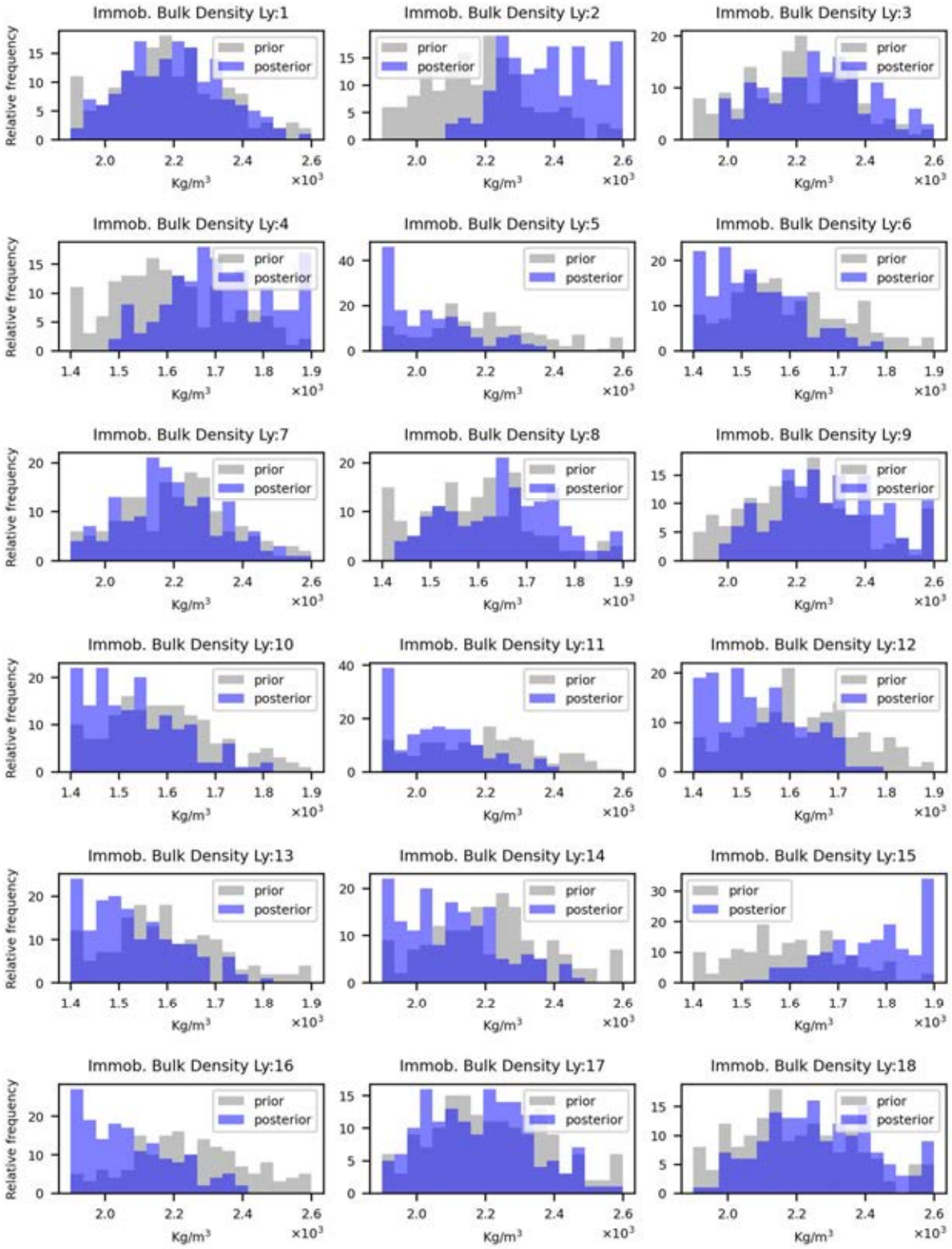
Immob. Bulk Density Ly:1
Immob. Bulk Density Ly:2
Immob. Bulk Density Ly:3
Immob. Bulk Density Ly:4
Immob. Bulk Density Ly:5
Immob. Bulk Density Ly:6
Immob. Bulk Density Ly:7
Immob. Bulk Density Ly:8
Immob. Bulk Density Ly:9
Immob. Bulk Density Ly:10
Immob. Bulk Density Ly:11
Immob. Bulk Density Ly:12
Immob. Bulk Density Ly:13
Immob. Bulk Density Ly:14
Immob. Bulk Density Ly:15
Immob. Bulk Density Ly:16
Immob. Bulk Density Ly:17
Immob. Bulk Density Ly:18
prior
posterior
Relative frequency
Kg/m³
×10³

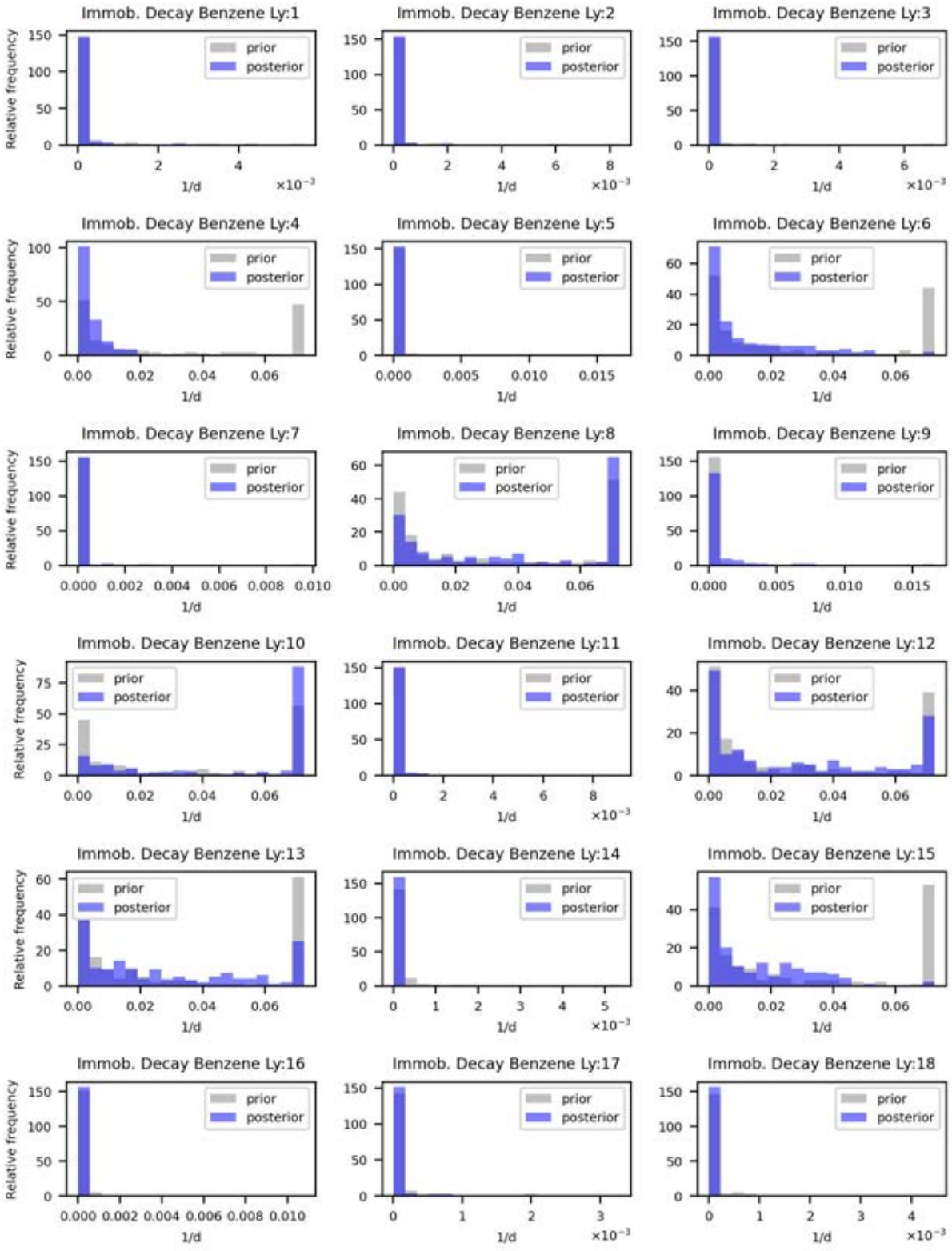
Immob. Decay Benzene Ly:1
Immob. Decay Benzene Ly:2
Immob. Decay Benzene Ly:3
Immob. Decay Benzene Ly:4
Immob. Decay Benzene Ly:5
Immob. Decay Benzene Ly:6
Immob. Decay Benzene Ly:7
Immob. Decay Benzene Ly:8
Immob. Decay Benzene Ly:9
Immob. Decay Benzene Ly:10
Immob. Decay Benzene Ly:11
Immob. Decay Benzene Ly:12
Immob. Decay Benzene Ly:13
Immob. Decay Benzene Ly:14
Immob. Decay Benzene Ly:15
Immob. Decay Benzene Ly:16
Immob. Decay Benzene Ly:17
Immob. Decay Benzene Ly:18
Relative frequency
prior
posterior
1/d
×10⁻³

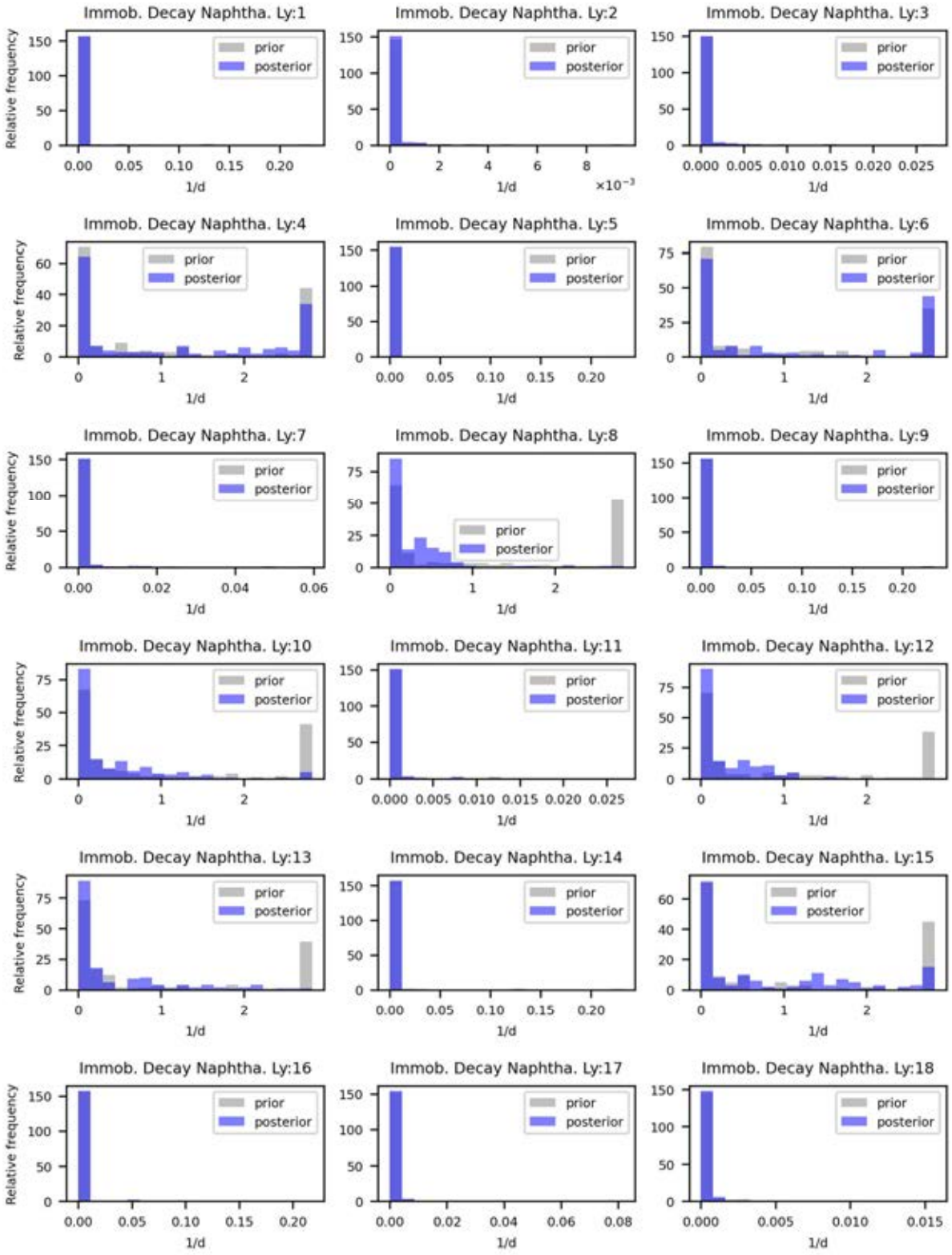
Immob. Decay Naphtha. Ly:1
Immob. Decay Naphtha. Ly:2
Immob. Decay Naphtha. Ly:3
Immob. Decay Naphtha. Ly:4
Immob. Decay Naphtha. Ly:5
Immob. Decay Naphtha. Ly:6
Immob. Decay Naphtha. Ly:7
Immob. Decay Naphtha. Ly:8
Immob. Decay Naphtha. Ly:9
Immob. Decay Naphtha. Ly:10
Immob. Decay Naphtha. Ly:11
Immob. Decay Naphtha. Ly:12
Immob. Decay Naphtha. Ly:13
Immob. Decay Naphtha. Ly:14
Immob. Decay Naphtha. Ly:15
Immob. Decay Naphtha. Ly:16
Immob. Decay Naphtha. Ly:17
Immob. Decay Naphtha. Ly:18
Relative frequency
1/d
prior
posterior

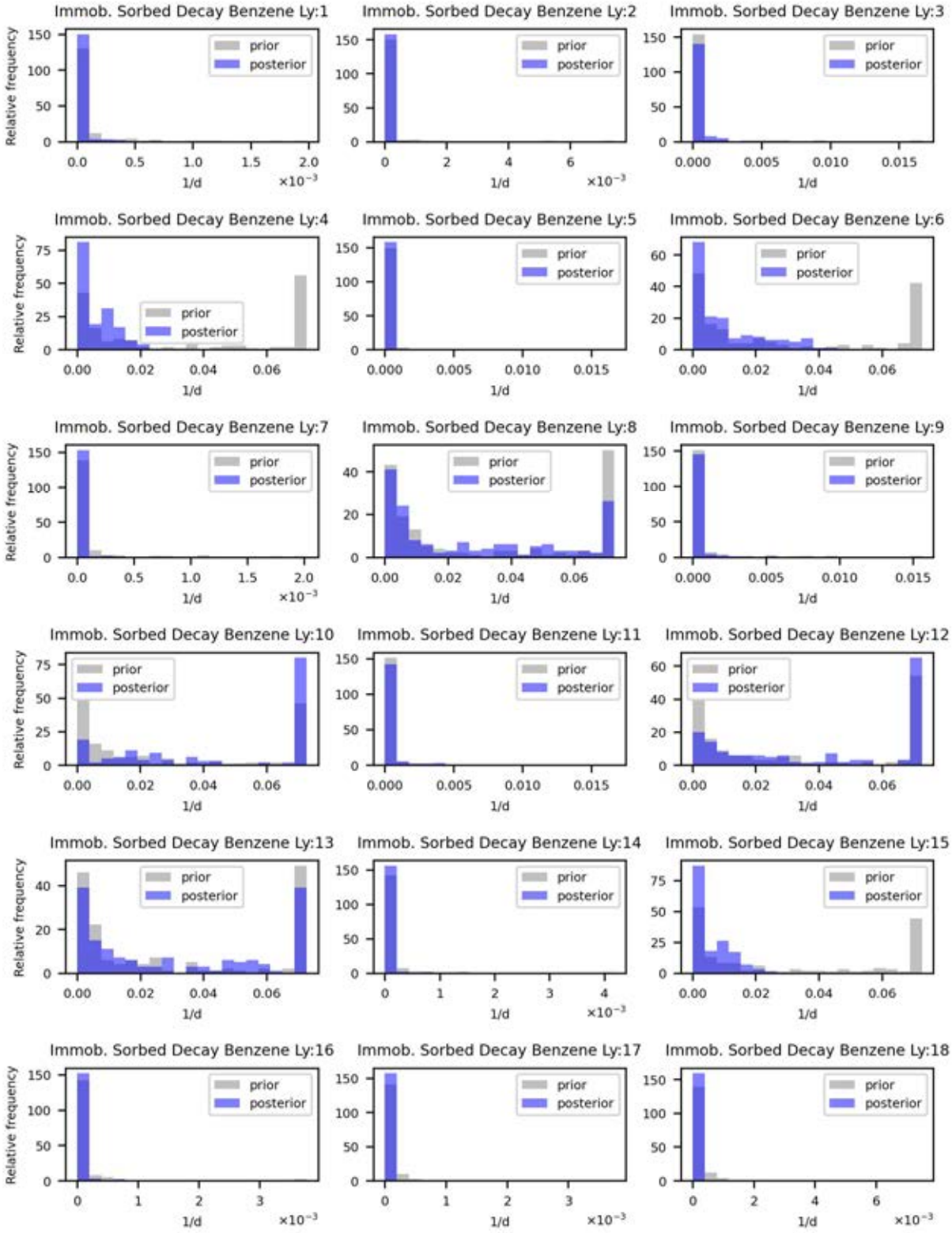
Immob. Sorbed Decay Benzene Ly:1
Immob. Sorbed Decay Benzene Ly:2
Immob. Sorbed Decay Benzene Ly:3
Immob. Sorbed Decay Benzene Ly:4
Immob. Sorbed Decay Benzene Ly:5
Immob. Sorbed Decay Benzene Ly:6
Immob. Sorbed Decay Benzene Ly:7
Immob. Sorbed Decay Benzene Ly:8
Immob. Sorbed Decay Benzene Ly:9
Immob. Sorbed Decay Benzene Ly:10
Immob. Sorbed Decay Benzene Ly:11
Immob. Sorbed Decay Benzene Ly:12
Immob. Sorbed Decay Benzene Ly:13
Immob. Sorbed Decay Benzene Ly:14
Immob. Sorbed Decay Benzene Ly:15
Immob. Sorbed Decay Benzene Ly:16
Immob. Sorbed Decay Benzene Ly:17
Immob. Sorbed Decay Benzene Ly:18
Relative frequency
prior
posterior
1/d
×10⁻³

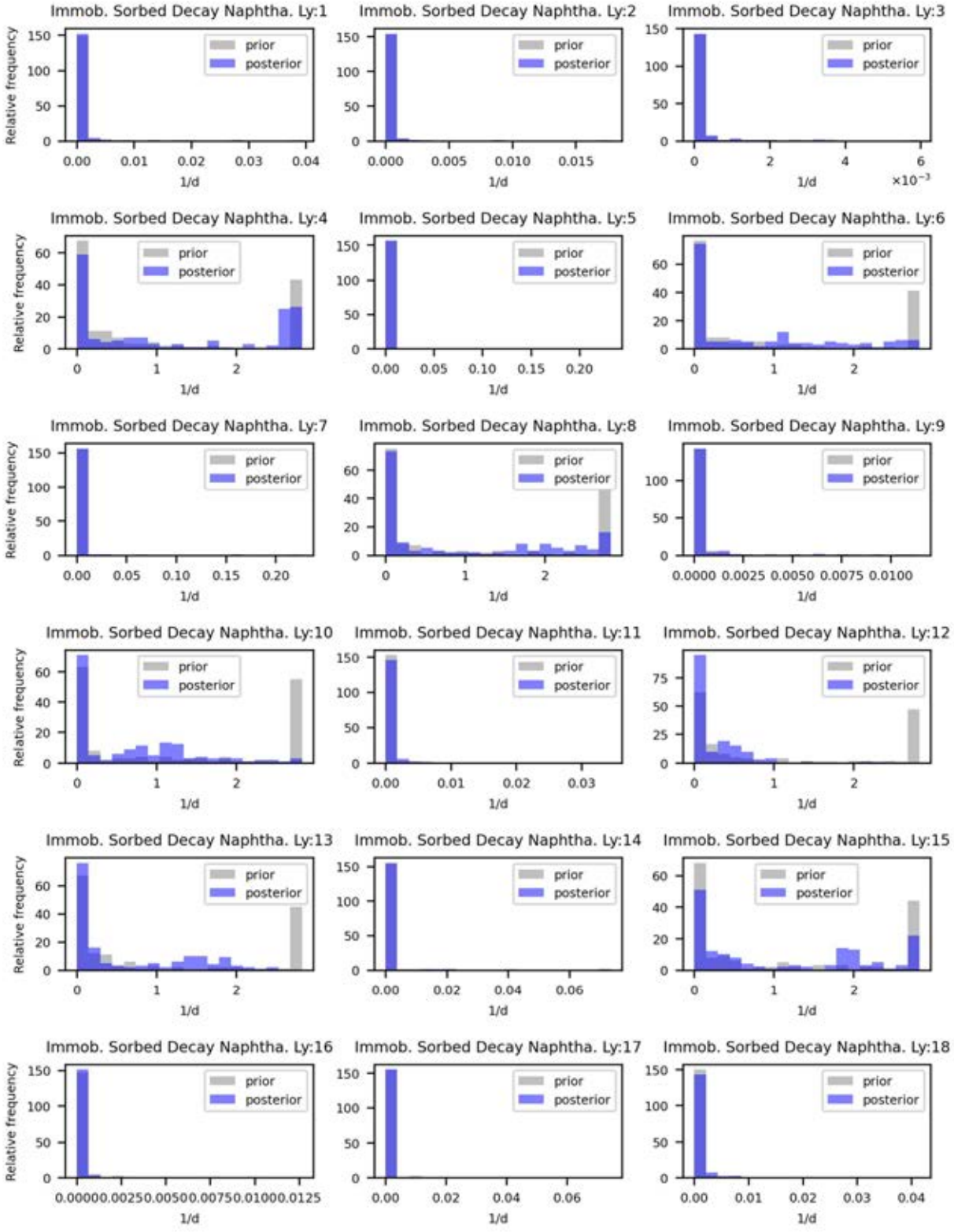
Immob. Sorbed Decay Naphtha. Ly:1
Immob. Sorbed Decay Naphtha. Ly:2
Immob. Sorbed Decay Naphtha. Ly:3
Immob. Sorbed Decay Naphtha. Ly:4
Immob. Sorbed Decay Naphtha. Ly:5
Immob. Sorbed Decay Naphtha. Ly:6
Immob. Sorbed Decay Naphtha. Ly:7
Immob. Sorbed Decay Naphtha. Ly:8
Immob. Sorbed Decay Naphtha. Ly:9
Immob. Sorbed Decay Naphtha. Ly:10
Immob. Sorbed Decay Naphtha. Ly:11
Immob. Sorbed Decay Naphtha. Ly:12
Immob. Sorbed Decay Naphtha. Ly:13
Immob. Sorbed Decay Naphtha. Ly:14
Immob. Sorbed Decay Naphtha. Ly:15
Immob. Sorbed Decay Naphtha. Ly:16
Immob. Sorbed Decay Naphtha. Ly:17
Immob. Sorbed Decay Naphtha. Ly:18
Relative frequency
1/d
prior
posterior

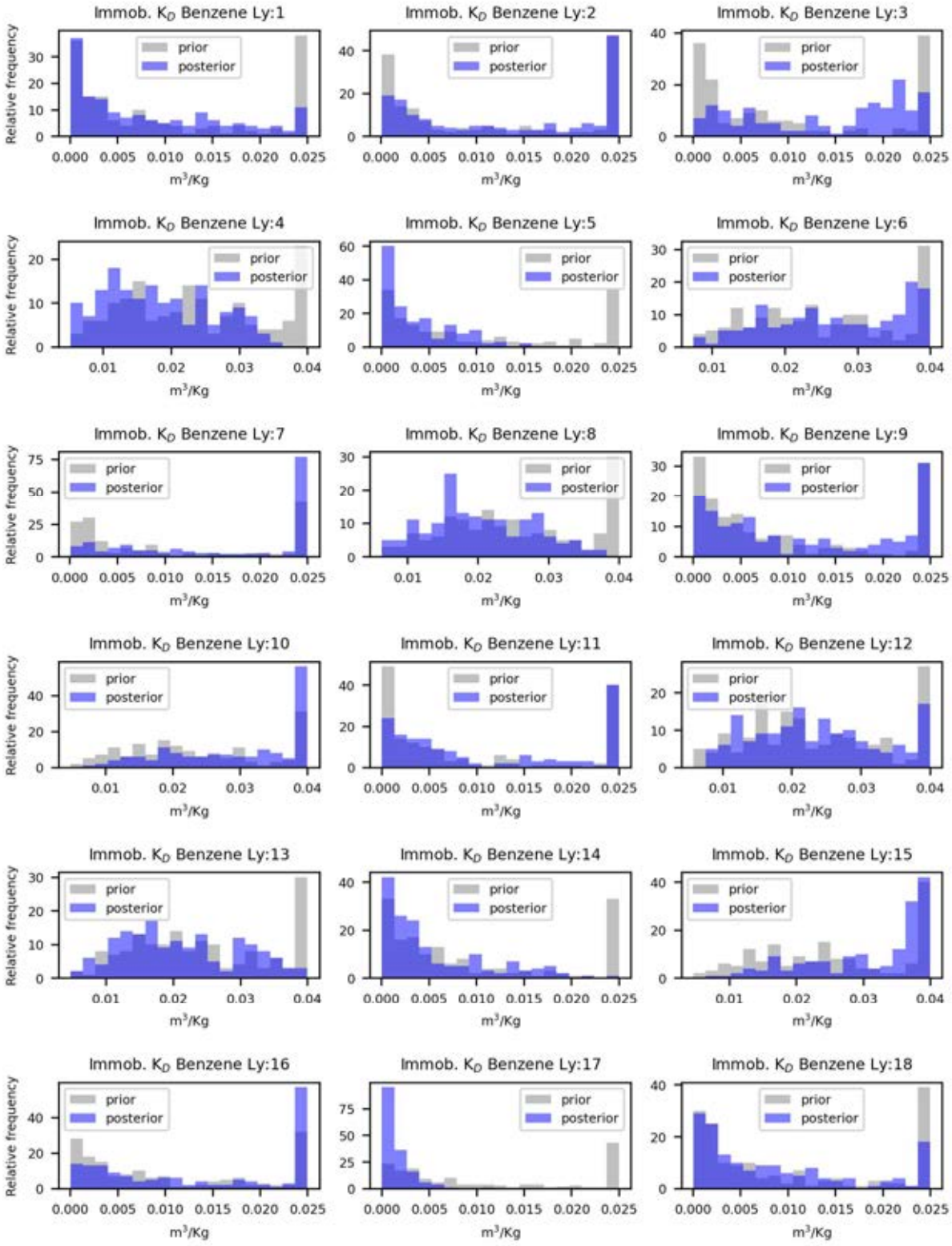
Immob. $K_D$ Benzene Ly:1
Immob. $K_D$ Benzene Ly:2
Immob. $K_D$ Benzene Ly:3
Immob. $K_D$ Benzene Ly:4
Immob. $K_D$ Benzene Ly:5
Immob. $K_D$ Benzene Ly:6
Immob. $K_D$ Benzene Ly:7
Immob. $K_D$ Benzene Ly:8
Immob. $K_D$ Benzene Ly:9
Immob. $K_D$ Benzene Ly:10
Immob. $K_D$ Benzene Ly:11
Immob. $K_D$ Benzene Ly:12
Immob. $K_D$ Benzene Ly:13
Immob. $K_D$ Benzene Ly:14
Immob. $K_D$ Benzene Ly:15
Immob. $K_D$ Benzene Ly:16
Immob. $K_D$ Benzene Ly:17
Immob. $K_D$ Benzene Ly:18
prior
posterior
Relative frequency
$m^3/Kg$

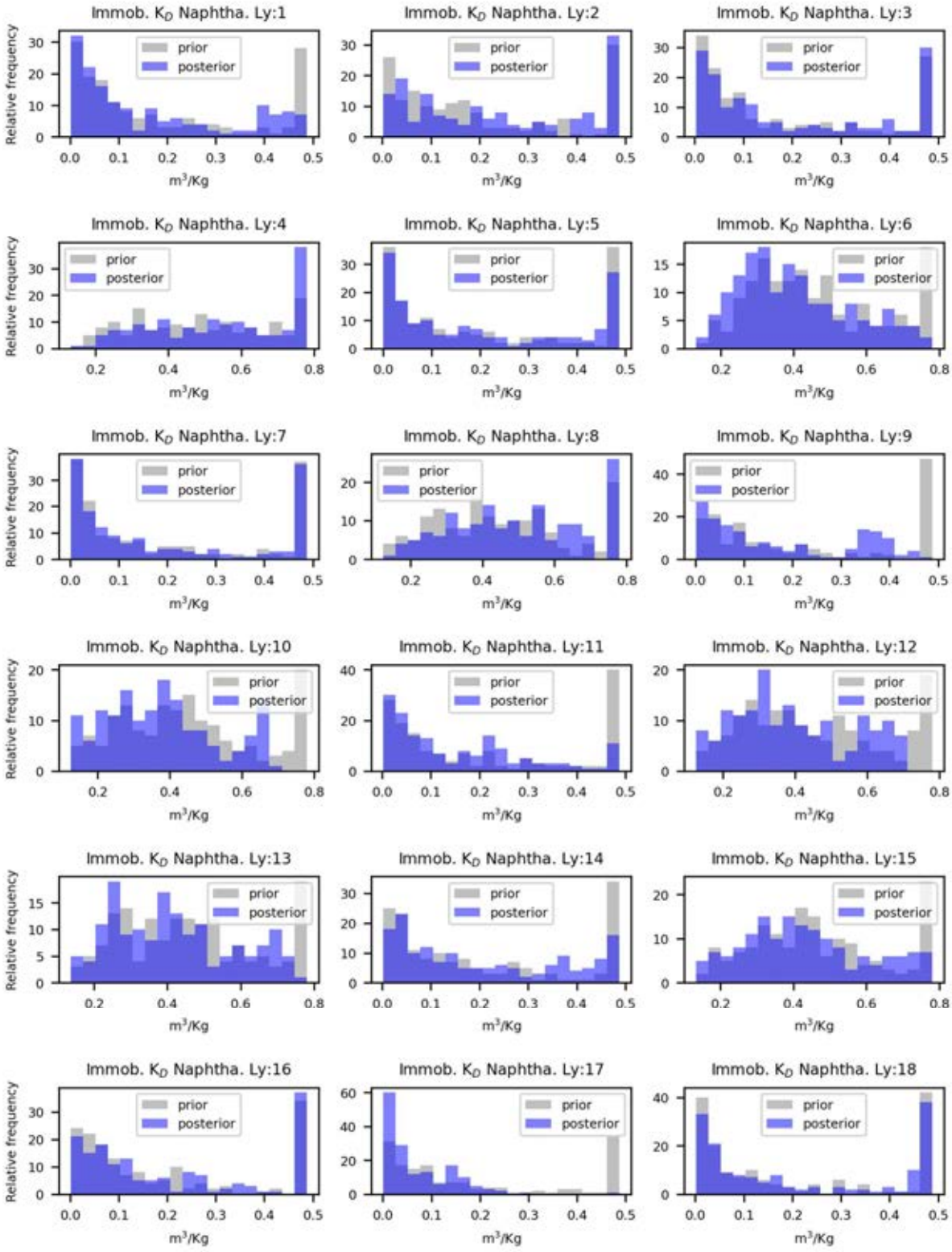
Immob. $K_D$ Naphtha. Ly:1
Immob. $K_D$ Naphtha. Ly:2
Immob. $K_D$ Naphtha. Ly:3
Immob. $K_D$ Naphtha. Ly:4
Immob. $K_D$ Naphtha. Ly:5
Immob. $K_D$ Naphtha. Ly:6
Immob. $K_D$ Naphtha. Ly:7
Immob. $K_D$ Naphtha. Ly:8
Immob. $K_D$ Naphtha. Ly:9
Immob. $K_D$ Naphtha. Ly:10
Immob. $K_D$ Naphtha. Ly:11
Immob. $K_D$ Naphtha. Ly:12
Immob. $K_D$ Naphtha. Ly:13
Immob. $K_D$ Naphtha. Ly:14
Immob. $K_D$ Naphtha. Ly:15
Immob. $K_D$ Naphtha. Ly:16
Immob. $K_D$ Naphtha. Ly:17
Immob. $K_D$ Naphtha. Ly:18
prior
posterior
Relative frequency
$m^3/Kg$

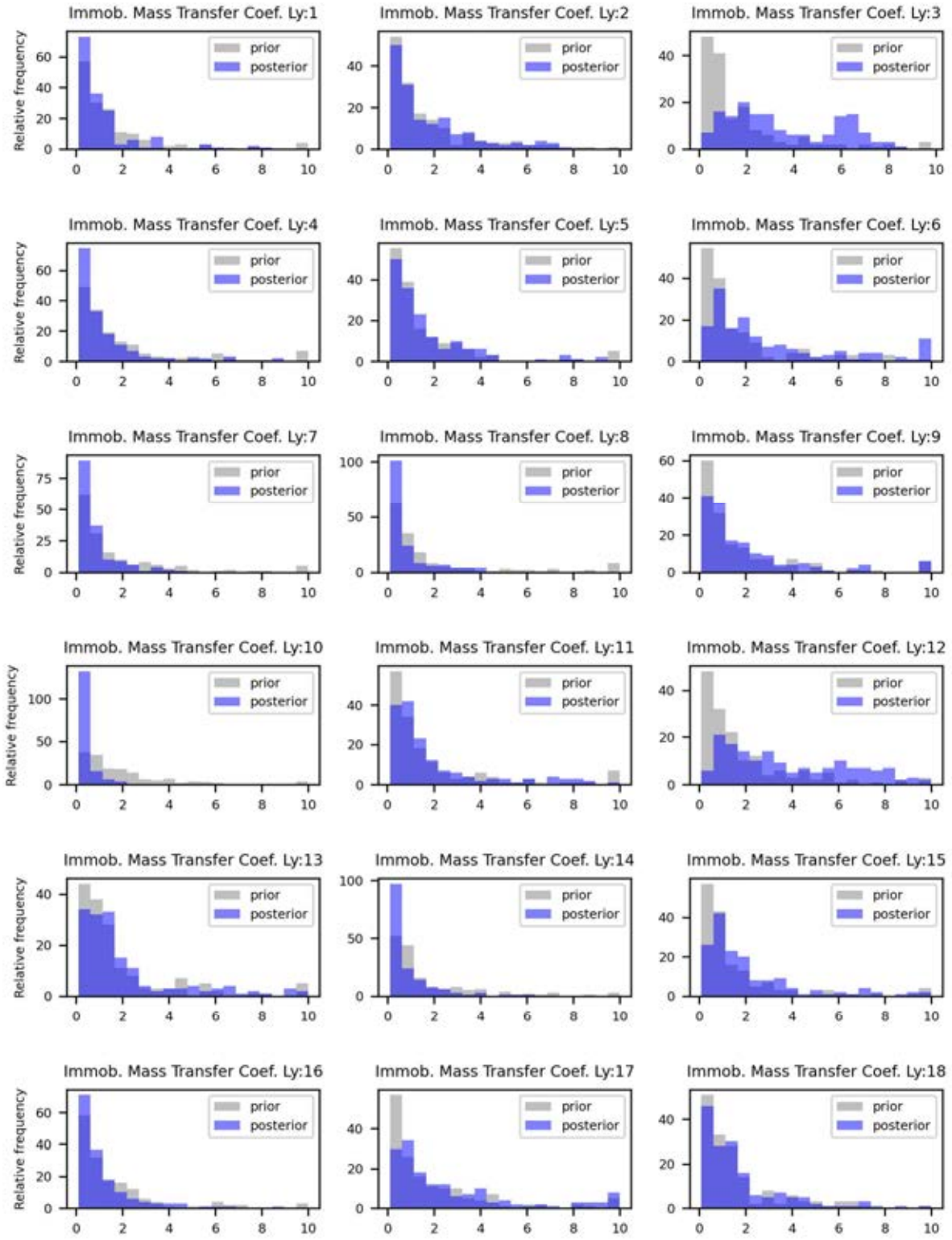
Immob. Mass Transfer Coef. Ly:1
Immob. Mass Transfer Coef. Ly:2
Immob. Mass Transfer Coef. Ly:3
Immob. Mass Transfer Coef. Ly:4
Immob. Mass Transfer Coef. Ly:5
Immob. Mass Transfer Coef. Ly:6
Immob. Mass Transfer Coef. Ly:7
Immob. Mass Transfer Coef. Ly:8
Immob. Mass Transfer Coef. Ly:9
Immob. Mass Transfer Coef. Ly:10
Immob. Mass Transfer Coef. Ly:11
Immob. Mass Transfer Coef. Ly:12
Immob. Mass Transfer Coef. Ly:13
Immob. Mass Transfer Coef. Ly:14
Immob. Mass Transfer Coef. Ly:15
Immob. Mass Transfer Coef. Ly:16
Immob. Mass Transfer Coef. Ly:17
Immob. Mass Transfer Coef. Ly:18
Relative frequency
prior
posterior

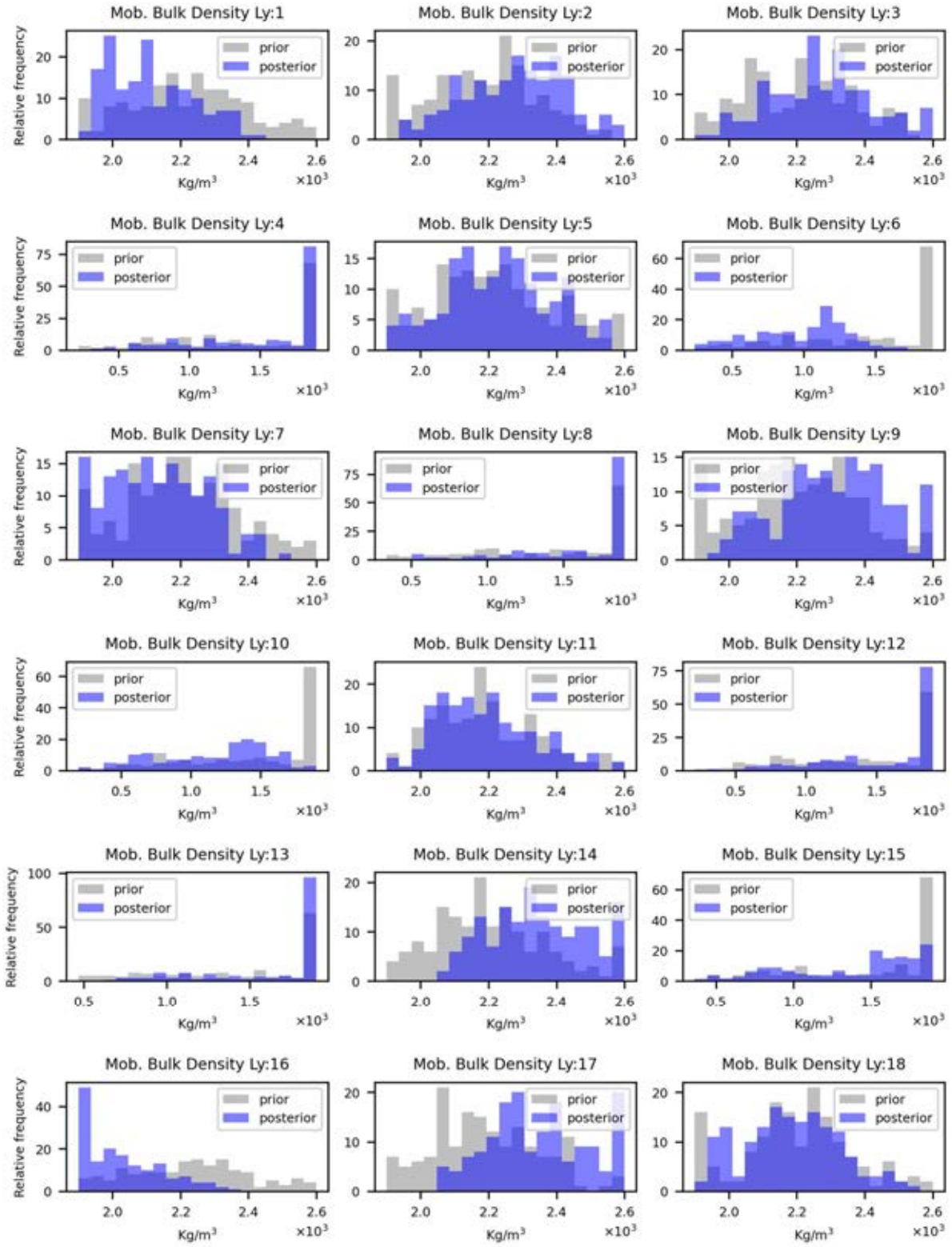
Mob. Bulk Density Ly:1
Mob. Bulk Density Ly:2
Mob. Bulk Density Ly:3
Mob. Bulk Density Ly:4
Mob. Bulk Density Ly:5
Mob. Bulk Density Ly:6
Mob. Bulk Density Ly:7
Mob. Bulk Density Ly:8
Mob. Bulk Density Ly:9
Mob. Bulk Density Ly:10
Mob. Bulk Density Ly:11
Mob. Bulk Density Ly:12
Mob. Bulk Density Ly:13
Mob. Bulk Density Ly:14
Mob. Bulk Density Ly:15
Mob. Bulk Density Ly:16
Mob. Bulk Density Ly:17
Mob. Bulk Density Ly:18
prior
posterior
Relative frequency
Kg/m³
×10³

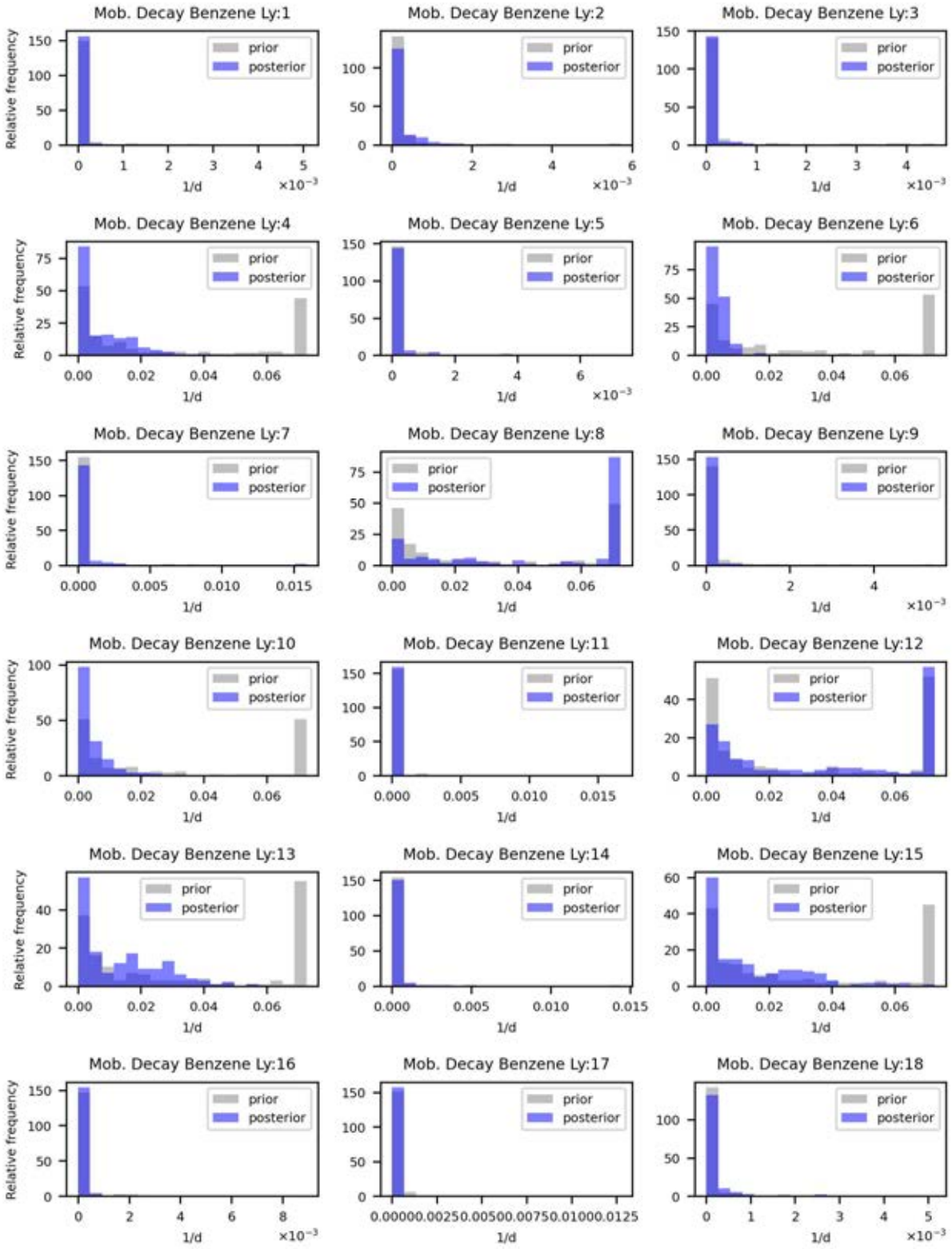
Mob. Decay Benzene Ly:1
Mob. Decay Benzene Ly:2
Mob. Decay Benzene Ly:3
Mob. Decay Benzene Ly:4
Mob. Decay Benzene Ly:5
Mob. Decay Benzene Ly:6
Mob. Decay Benzene Ly:7
Mob. Decay Benzene Ly:8
Mob. Decay Benzene Ly:9
Mob. Decay Benzene Ly:10
Mob. Decay Benzene Ly:11
Mob. Decay Benzene Ly:12
Mob. Decay Benzene Ly:13
Mob. Decay Benzene Ly:14
Mob. Decay Benzene Ly:15
Mob. Decay Benzene Ly:16
Mob. Decay Benzene Ly:17
Mob. Decay Benzene Ly:18
prior
posterior
Relative frequency
1/d
×10⁻³

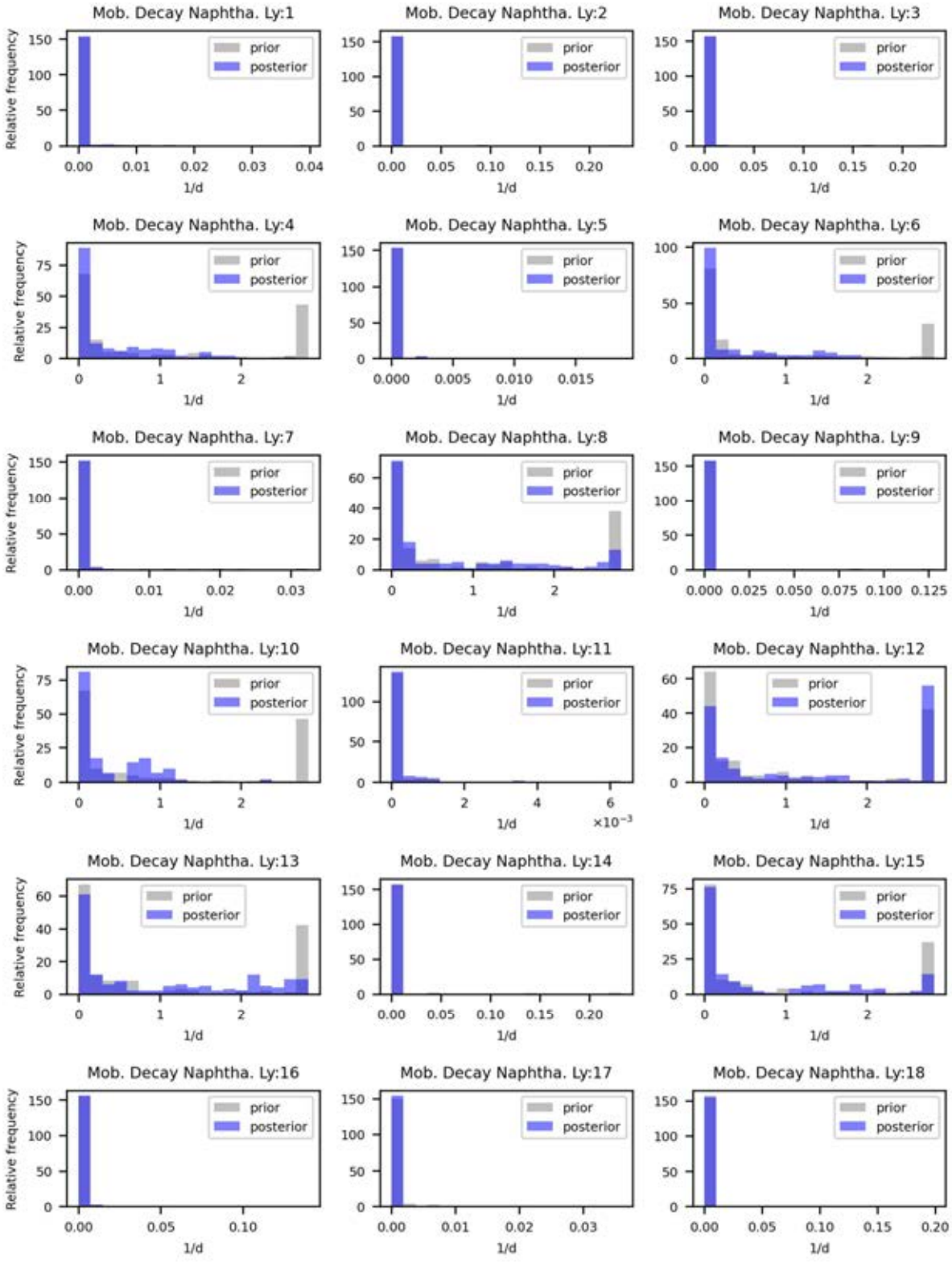
Mob. Decay Naphtha. Ly:1
Mob. Decay Naphtha. Ly:2
Mob. Decay Naphtha. Ly:3
Mob. Decay Naphtha. Ly:4
Mob. Decay Naphtha. Ly:5
Mob. Decay Naphtha. Ly:6
Mob. Decay Naphtha. Ly:7
Mob. Decay Naphtha. Ly:8
Mob. Decay Naphtha. Ly:9
Mob. Decay Naphtha. Ly:10
Mob. Decay Naphtha. Ly:11
Mob. Decay Naphtha. Ly:12
Mob. Decay Naphtha. Ly:13
Mob. Decay Naphtha. Ly:14
Mob. Decay Naphtha. Ly:15
Mob. Decay Naphtha. Ly:16
Mob. Decay Naphtha. Ly:17
Mob. Decay Naphtha. Ly:18
Relative frequency
1/d
prior
posterior
×10⁻³

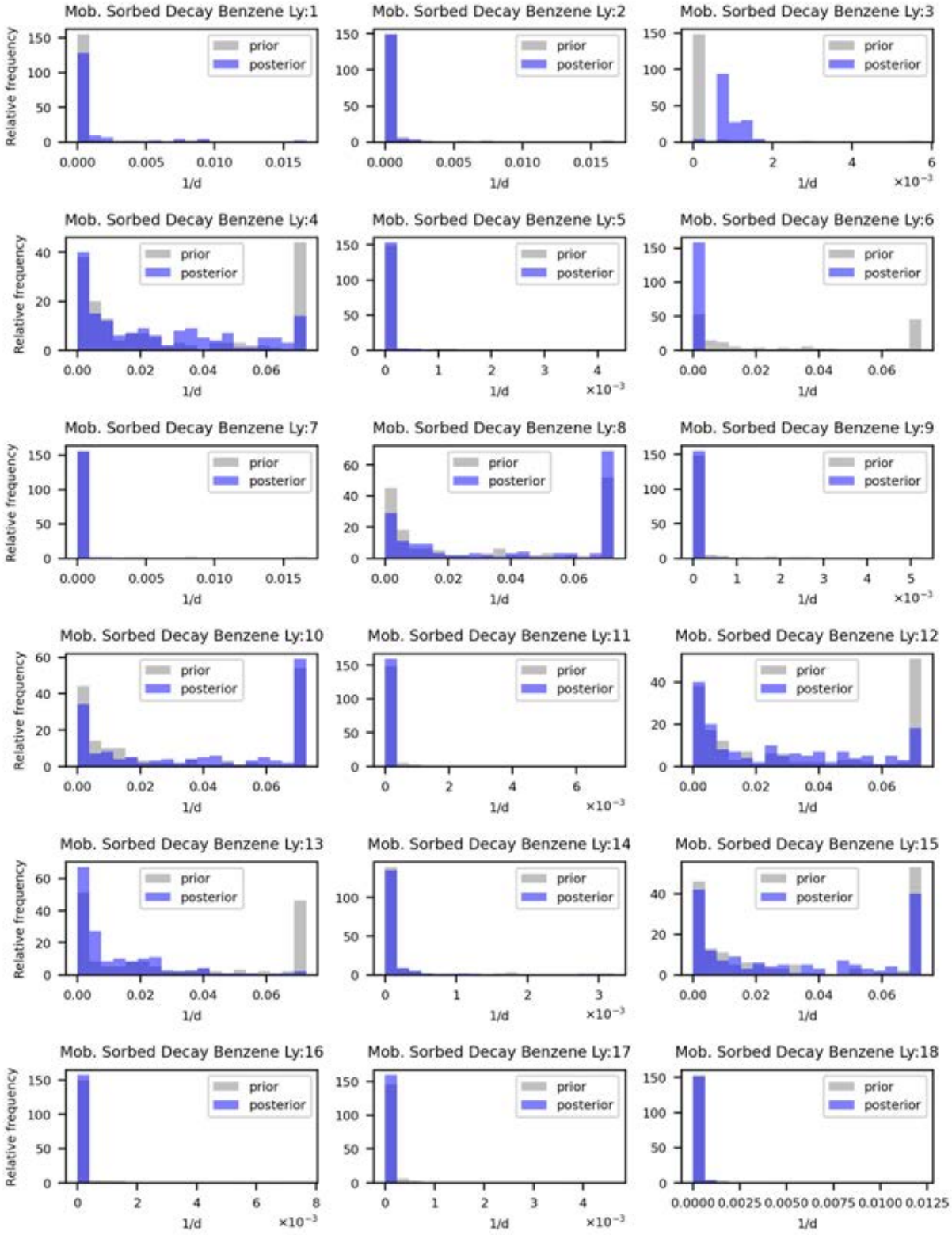
Mob. Sorbed Decay Benzene Ly:1
Mob. Sorbed Decay Benzene Ly:2
Mob. Sorbed Decay Benzene Ly:3
Mob. Sorbed Decay Benzene Ly:4
Mob. Sorbed Decay Benzene Ly:5
Mob. Sorbed Decay Benzene Ly:6
Mob. Sorbed Decay Benzene Ly:7
Mob. Sorbed Decay Benzene Ly:8
Mob. Sorbed Decay Benzene Ly:9
Mob. Sorbed Decay Benzene Ly:10
Mob. Sorbed Decay Benzene Ly:11
Mob. Sorbed Decay Benzene Ly:12
Mob. Sorbed Decay Benzene Ly:13
Mob. Sorbed Decay Benzene Ly:14
Mob. Sorbed Decay Benzene Ly:15
Mob. Sorbed Decay Benzene Ly:16
Mob. Sorbed Decay Benzene Ly:17
Mob. Sorbed Decay Benzene Ly:18
prior
posterior
Relative frequency
1/d
×10⁻³

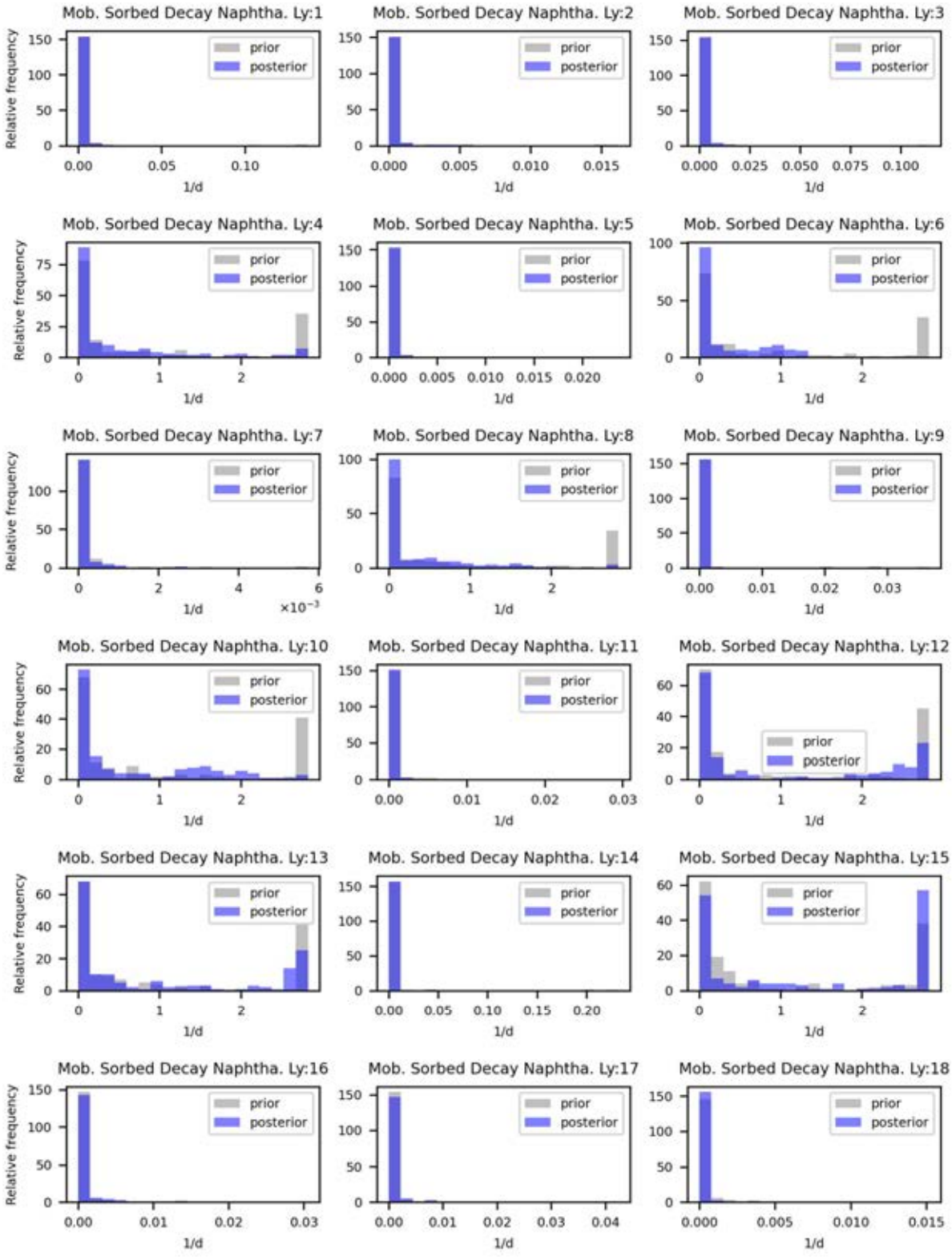
Mob. Sorbed Decay Naphtha. Ly:1
Mob. Sorbed Decay Naphtha. Ly:2
Mob. Sorbed Decay Naphtha. Ly:3
Mob. Sorbed Decay Naphtha. Ly:4
Mob. Sorbed Decay Naphtha. Ly:5
Mob. Sorbed Decay Naphtha. Ly:6
Mob. Sorbed Decay Naphtha. Ly:7
Mob. Sorbed Decay Naphtha. Ly:8
Mob. Sorbed Decay Naphtha. Ly:9
Mob. Sorbed Decay Naphtha. Ly:10
Mob. Sorbed Decay Naphtha. Ly:11
Mob. Sorbed Decay Naphtha. Ly:12
Mob. Sorbed Decay Naphtha. Ly:13
Mob. Sorbed Decay Naphtha. Ly:14
Mob. Sorbed Decay Naphtha. Ly:15
Mob. Sorbed Decay Naphtha. Ly:16
Mob. Sorbed Decay Naphtha. Ly:17
Mob. Sorbed Decay Naphtha. Ly:18
prior
posterior
Relative frequency
1/d
×10⁻³

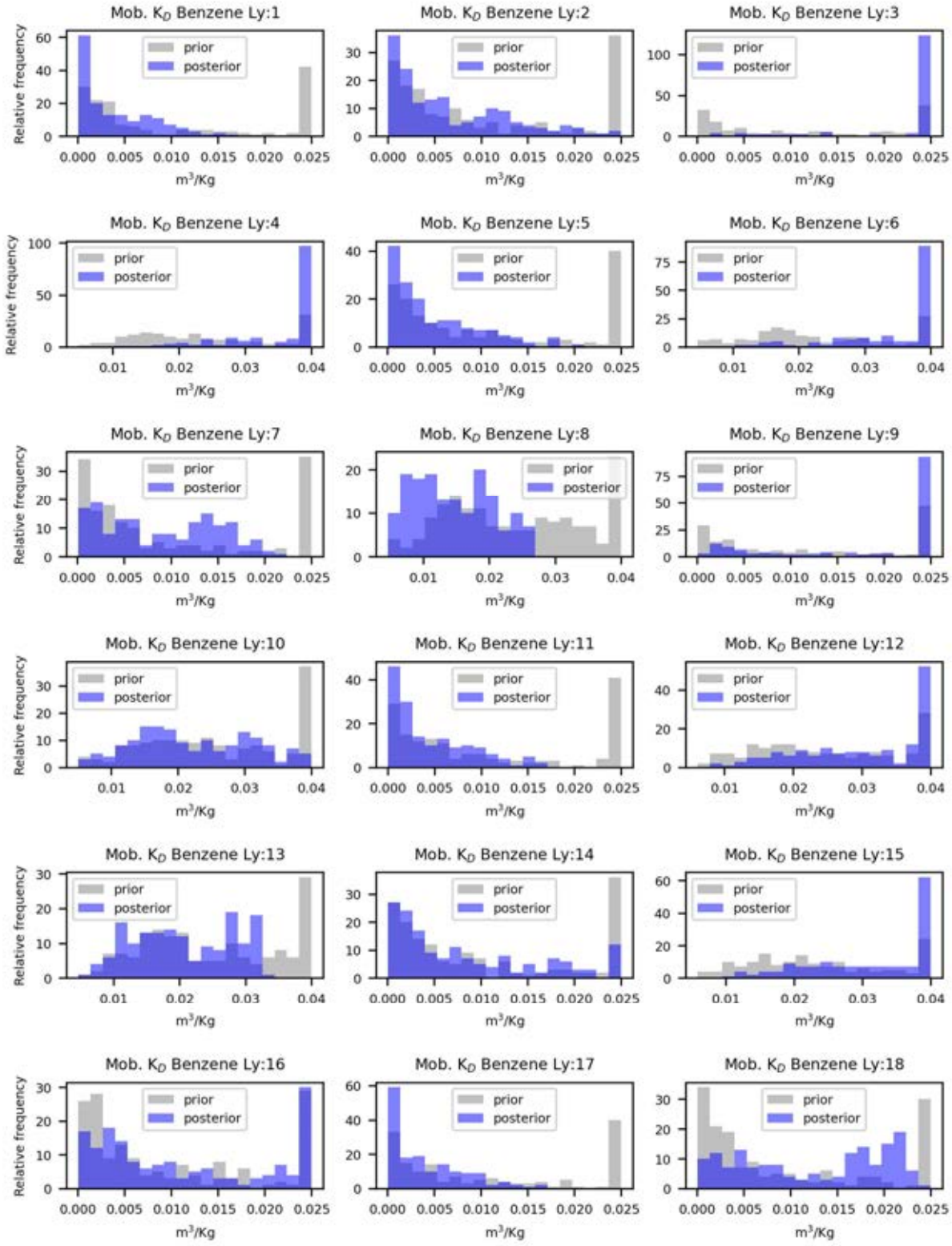
Mob. $K_D$ Benzene Ly:1
Mob. $K_D$ Benzene Ly:2
Mob. $K_D$ Benzene Ly:3
Mob. $K_D$ Benzene Ly:4
Mob. $K_D$ Benzene Ly:5
Mob. $K_D$ Benzene Ly:6
Mob. $K_D$ Benzene Ly:7
Mob. $K_D$ Benzene Ly:8
Mob. $K_D$ Benzene Ly:9
Mob. $K_D$ Benzene Ly:10
Mob. $K_D$ Benzene Ly:11
Mob. $K_D$ Benzene Ly:12
Mob. $K_D$ Benzene Ly:13
Mob. $K_D$ Benzene Ly:14
Mob. $K_D$ Benzene Ly:15
Mob. $K_D$ Benzene Ly:16
Mob. $K_D$ Benzene Ly:17
Mob. $K_D$ Benzene Ly:18
prior
posterior
Relative frequency
$m^3/Kg$

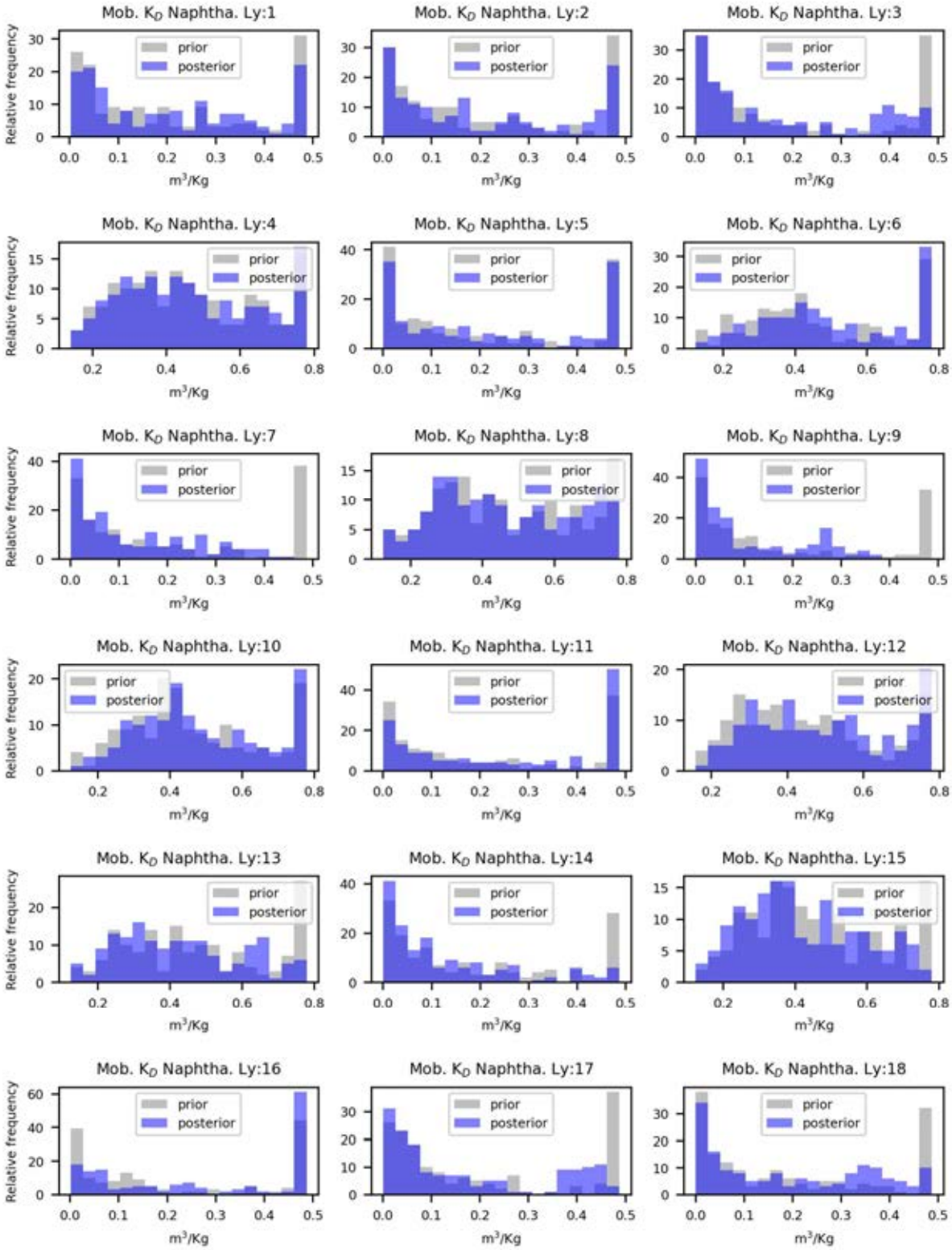
Mob. $K_D$ Naphtha. Ly:1
Mob. $K_D$ Naphtha. Ly:2
Mob. $K_D$ Naphtha. Ly:3
Mob. $K_D$ Naphtha. Ly:4
Mob. $K_D$ Naphtha. Ly:5
Mob. $K_D$ Naphtha. Ly:6
Mob. $K_D$ Naphtha. Ly:7
Mob. $K_D$ Naphtha. Ly:8
Mob. $K_D$ Naphtha. Ly:9
Mob. $K_D$ Naphtha. Ly:10
Mob. $K_D$ Naphtha. Ly:11
Mob. $K_D$ Naphtha. Ly:12
Mob. $K_D$ Naphtha. Ly:13
Mob. $K_D$ Naphtha. Ly:14
Mob. $K_D$ Naphtha. Ly:15
Mob. $K_D$ Naphtha. Ly:16
Mob. $K_D$ Naphtha. Ly:17
Mob. $K_D$ Naphtha. Ly:18
prior
posterior
Relative frequency
$m^3/Kg$

# Appendix L Transport Parameter Group Prior and Posterior Histograms – Source parameters

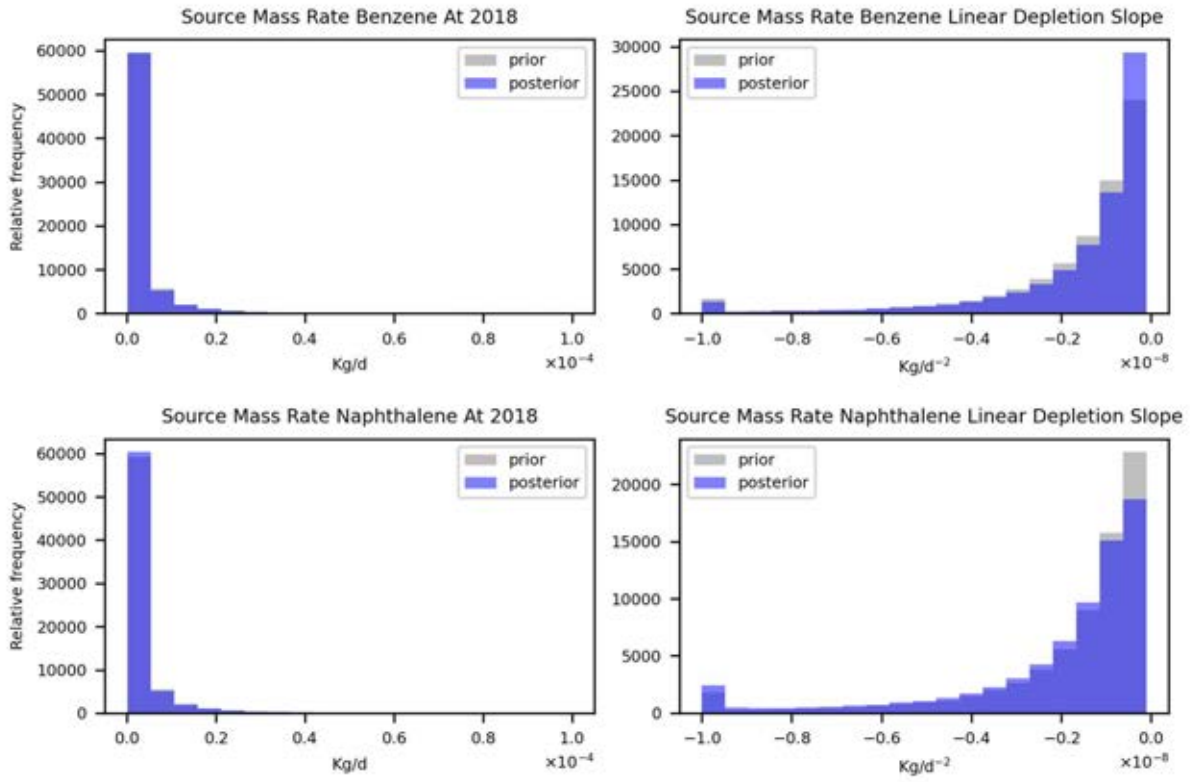
Source Mass Rate Benzene At 2018
prior
posterior
Relative frequency
Kg/d
×10⁻⁴
Source Mass Rate Benzene Linear Depletion Slope
prior
posterior
Kg/d⁻²
×10⁻⁸
Source Mass Rate Naphthalene At 2018
prior
posterior
Relative frequency
Kg/d
×10⁻⁴
Source Mass Rate Naphthalene Linear Depletion Slope
prior
posterior
Kg/d⁻²
×10⁻⁸

# Appendix M Transport Relative Parameter Variance Reduction

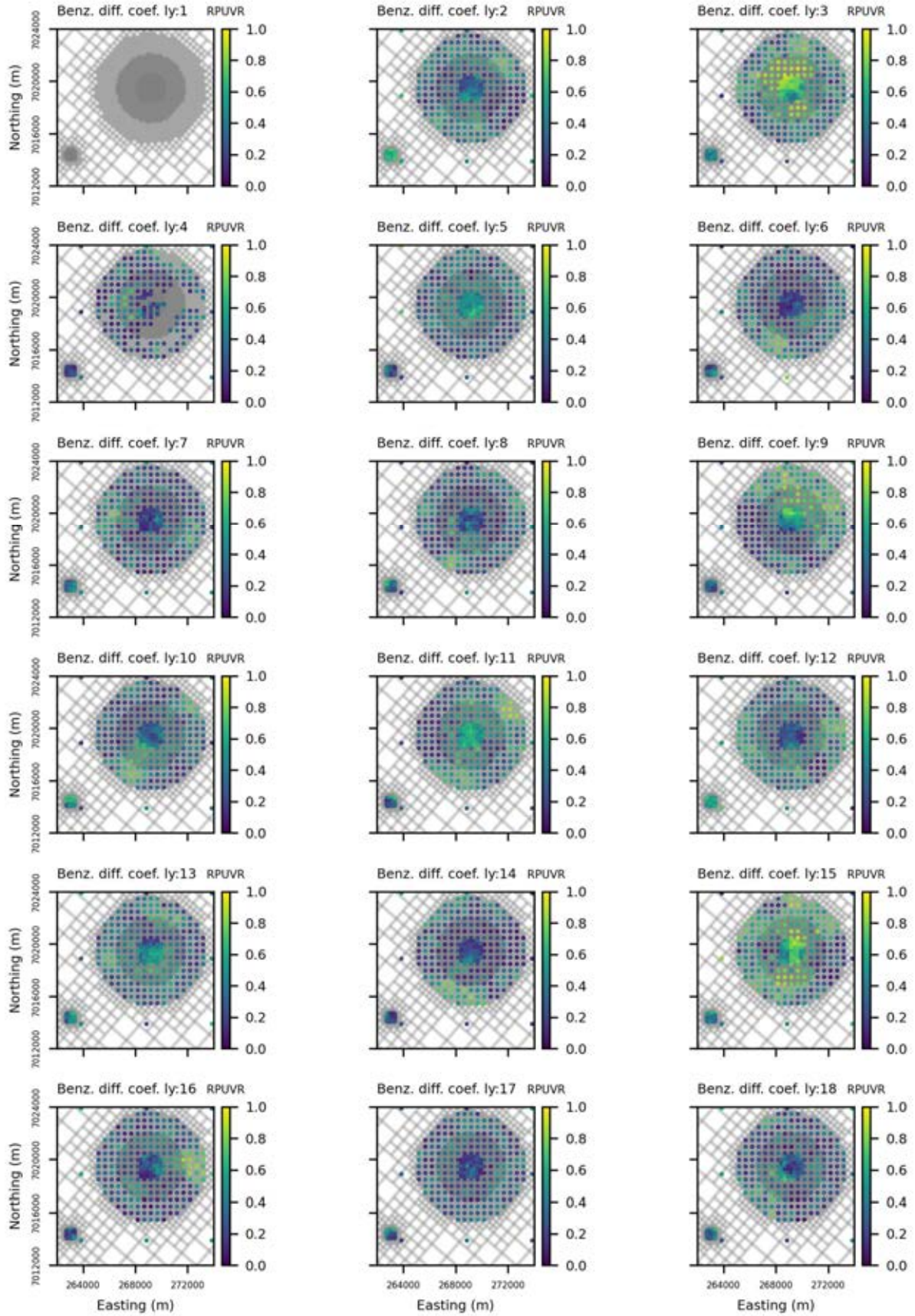
Benz. diff. coef. ly:1 RPUVR
Benz. diff. coef. ly:2 RPUVR
Benz. diff. coef. ly:3 RPUVR
Benz. diff. coef. ly:4 RPUVR
Benz. diff. coef. ly:5 RPUVR
Benz. diff. coef. ly:6 RPUVR
Benz. diff. coef. ly:7 RPUVR
Benz. diff. coef. ly:8 RPUVR
Benz. diff. coef. ly:9 RPUVR
Benz. diff. coef. ly:10 RPUVR
Benz. diff. coef. ly:11 RPUVR
Benz. diff. coef. ly:12 RPUVR
Benz. diff. coef. ly:13 RPUVR
Benz. diff. coef. ly:14 RPUVR
Benz. diff. coef. ly:15 RPUVR
Benz. diff. coef. ly:16 RPUVR
Benz. diff. coef. ly:17 RPUVR
Benz. diff. coef. ly:18 RPUVR
Northing (m)
7024000
7020000
7016000
7012000
1.0
0.8
0.6
0.4
0.2
0.0
264000
268000
272000
Easting (m)

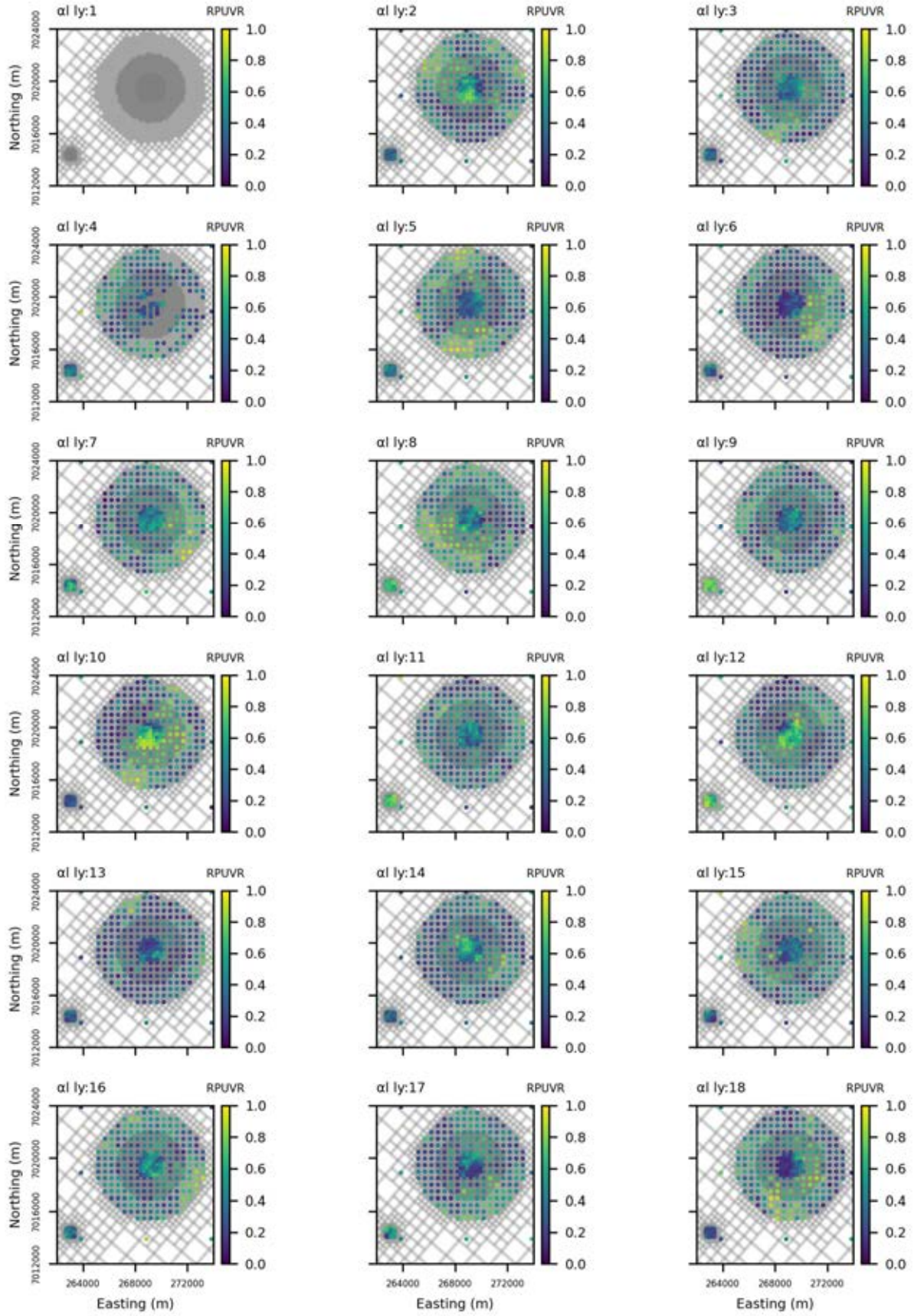
αl ly:1
αl ly:2
αl ly:3
αl ly:4
αl ly:5
αl ly:6
αl ly:7
αl ly:8
αl ly:9
αl ly:10
αl ly:11
αl ly:12
αl ly:13
αl ly:14
αl ly:15
αl ly:16
αl ly:17
αl ly:18
RPUVR
1.0
0.8
0.6
0.4
0.2
0.0
Northing (m)
7024000
7020000
7016000
7012000
264000
268000
272000
Easting (m)

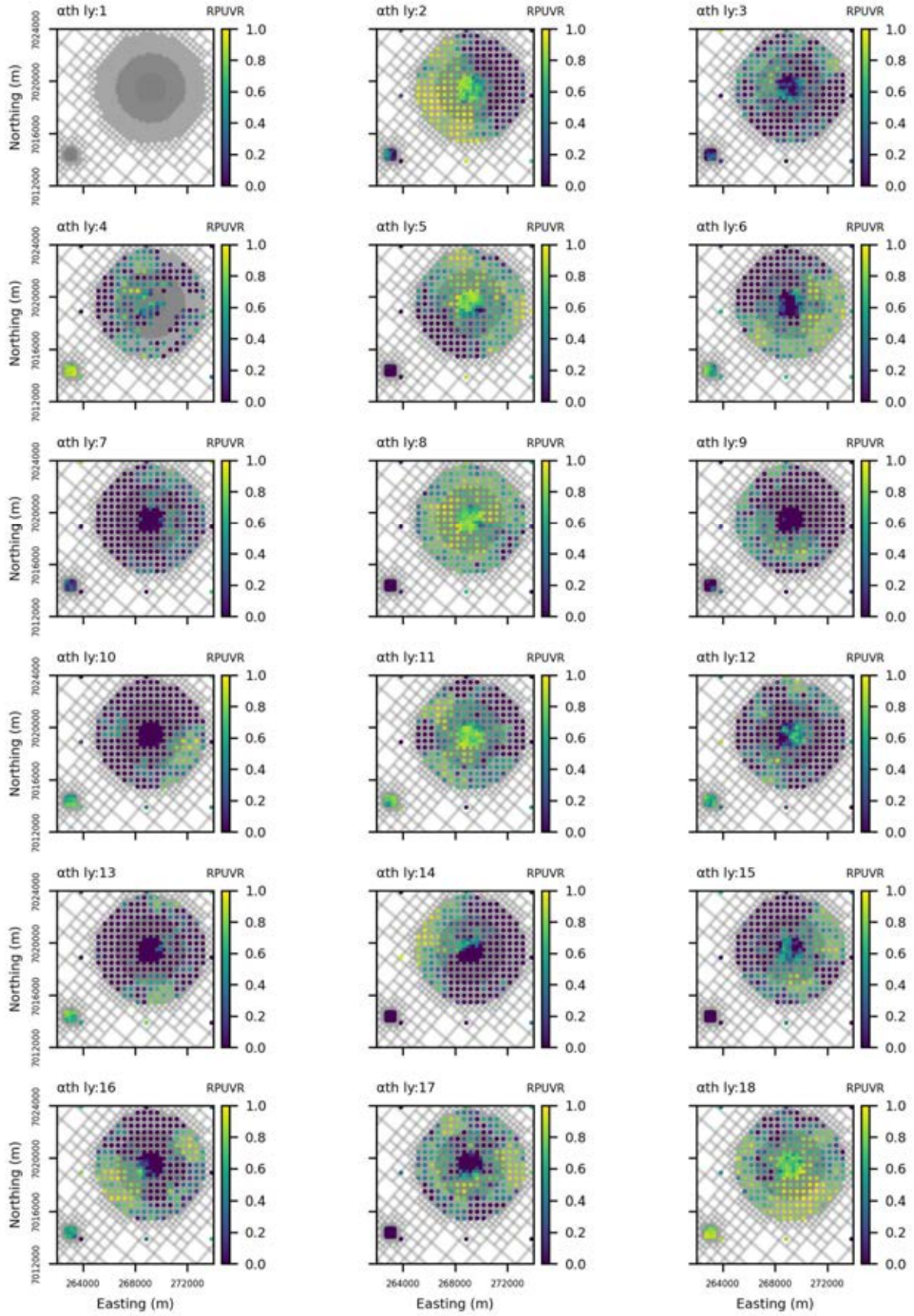
ath ly:1
ath ly:2
ath ly:3
ath ly:4
ath ly:5
ath ly:6
ath ly:7
ath ly:8
ath ly:9
ath ly:10
ath ly:11
ath ly:12
ath ly:13
ath ly:14
ath ly:15
ath ly:16
ath ly:17
ath ly:18
RPUVR
1.0
0.8
0.6
0.4
0.2
0.0
Northing (m)
7024000
7020000
7016000
7012000
264000
268000
272000
Easting (m)

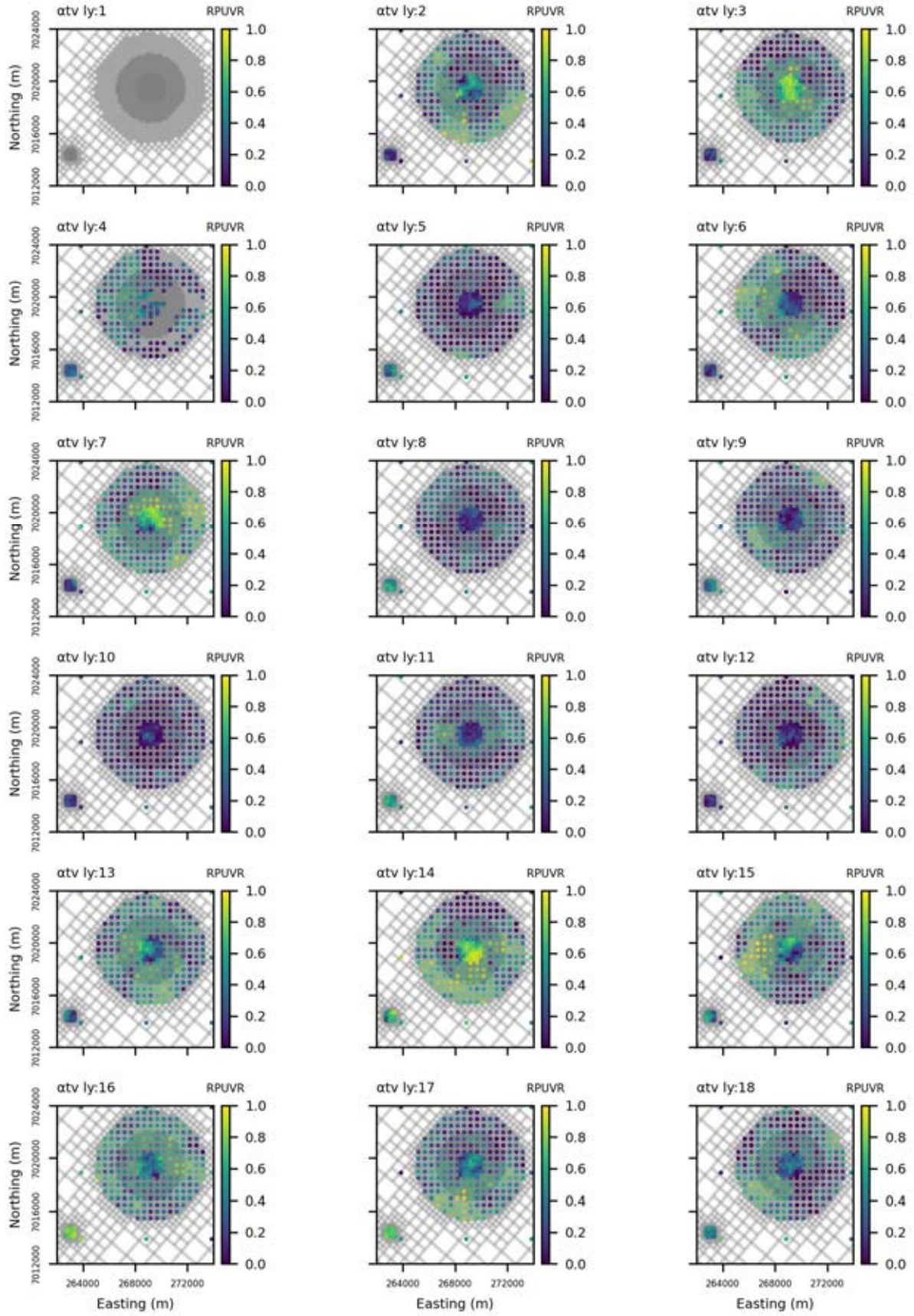
atv ly:1
atv ly:2
atv ly:3
atv ly:4
atv ly:5
atv ly:6
atv ly:7
atv ly:8
atv ly:9
atv ly:10
atv ly:11
atv ly:12
atv ly:13
atv ly:14
atv ly:15
atv ly:16
atv ly:17
atv ly:18
RPUVR
1.0
0.8
0.6
0.4
0.2
0.0
Northing (m)
7024000
7020000
7016000
7012000
264000
268000
272000
Easting (m)

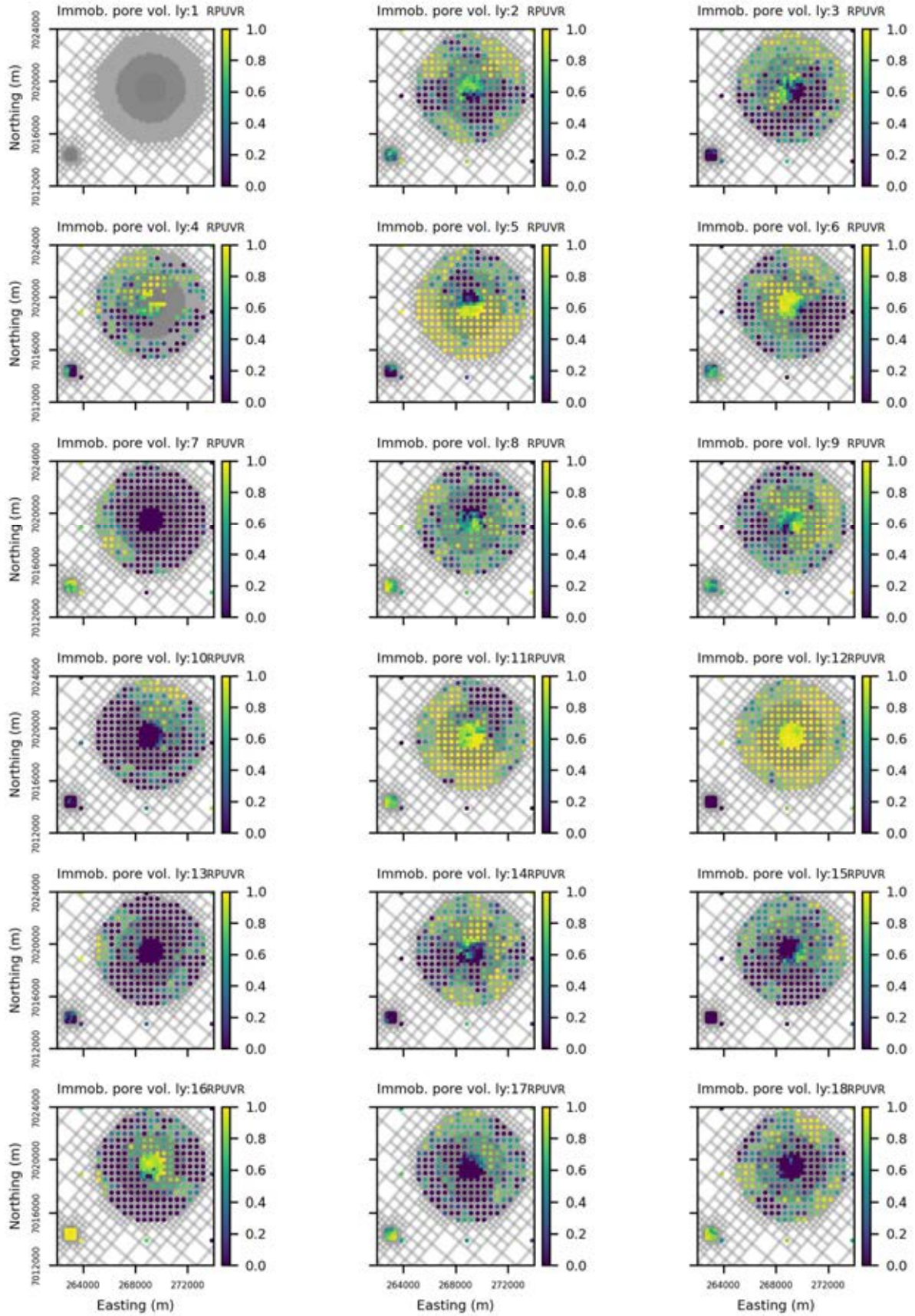
Immob. pore vol. ly:1 RPUVR
Immob. pore vol. ly:2 RPUVR
Immob. pore vol. ly:3 RPUVR
Immob. pore vol. ly:4 RPUVR
Immob. pore vol. ly:5 RPUVR
Immob. pore vol. ly:6 RPUVR
Immob. pore vol. ly:7 RPUVR
Immob. pore vol. ly:8 RPUVR
Immob. pore vol. ly:9 RPUVR
Immob. pore vol. ly:10 RPUVR
Immob. pore vol. ly:11 RPUVR
Immob. pore vol. ly:12 RPUVR
Immob. pore vol. ly:13 RPUVR
Immob. pore vol. ly:14 RPUVR
Immob. pore vol. ly:15 RPUVR
Immob. pore vol. ly:16 RPUVR
Immob. pore vol. ly:17 RPUVR
Immob. pore vol. ly:18 RPUVR
Northing (m)
7012000
7016000
7020000
7024000
1.0
0.8
0.6
0.4
0.2
0.0
264000
268000
272000
Easting (m)

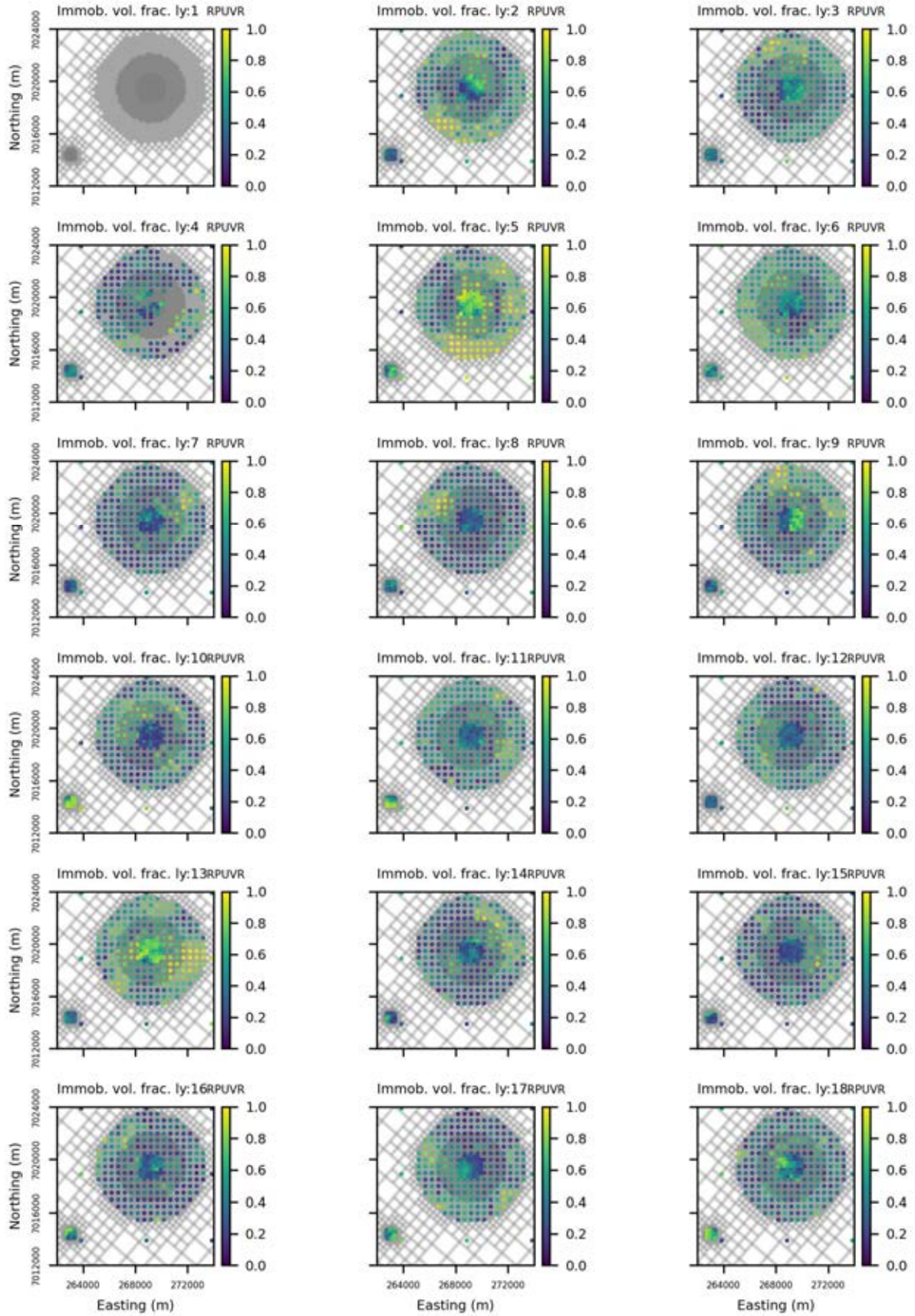
Immob. vol. frac. ly:1 RPUVR
Immob. vol. frac. ly:2 RPUVR
Immob. vol. frac. ly:3 RPUVR
Immob. vol. frac. ly:4 RPUVR
Immob. vol. frac. ly:5 RPUVR
Immob. vol. frac. ly:6 RPUVR
Immob. vol. frac. ly:7 RPUVR
Immob. vol. frac. ly:8 RPUVR
Immob. vol. frac. ly:9 RPUVR
Immob. vol. frac. ly:10 RPUVR
Immob. vol. frac. ly:11 RPUVR
Immob. vol. frac. ly:12 RPUVR
Immob. vol. frac. ly:13 RPUVR
Immob. vol. frac. ly:14 RPUVR
Immob. vol. frac. ly:15 RPUVR
Immob. vol. frac. ly:16 RPUVR
Immob. vol. frac. ly:17 RPUVR
Immob. vol. frac. ly:18 RPUVR
Northing (m)
7012000
7016000
7020000
7024000
Easting (m)
264000
268000
272000
0.0
0.2
0.4
0.6
0.8
1.0

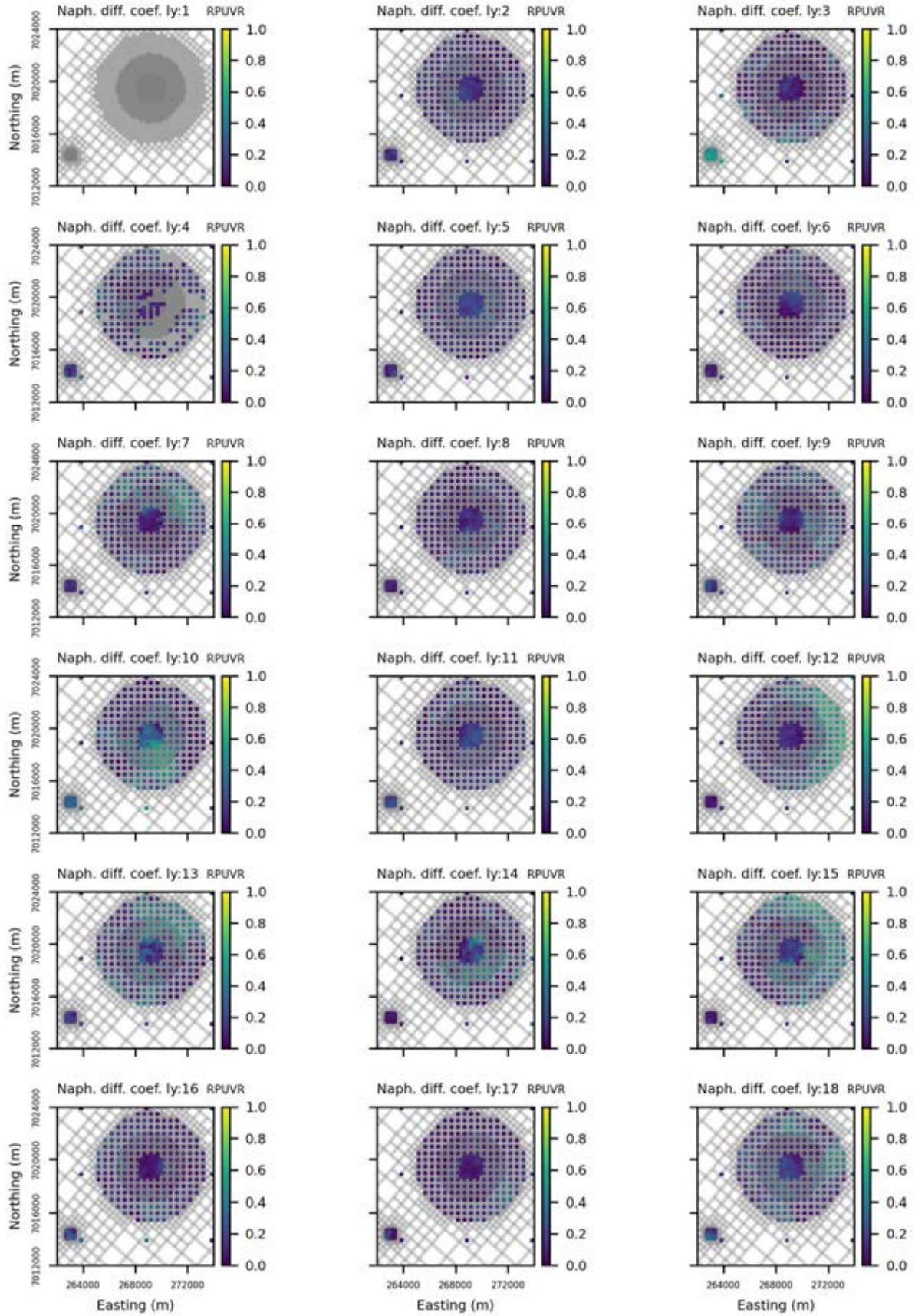
Naph. diff. coef. ly:1 RPUVR
Naph. diff. coef. ly:2 RPUVR
Naph. diff. coef. ly:3 RPUVR
Naph. diff. coef. ly:4 RPUVR
Naph. diff. coef. ly:5 RPUVR
Naph. diff. coef. ly:6 RPUVR
Naph. diff. coef. ly:7 RPUVR
Naph. diff. coef. ly:8 RPUVR
Naph. diff. coef. ly:9 RPUVR
Naph. diff. coef. ly:10 RPUVR
Naph. diff. coef. ly:11 RPUVR
Naph. diff. coef. ly:12 RPUVR
Naph. diff. coef. ly:13 RPUVR
Naph. diff. coef. ly:14 RPUVR
Naph. diff. coef. ly:15 RPUVR
Naph. diff. coef. ly:16 RPUVR
Naph. diff. coef. ly:17 RPUVR
Naph. diff. coef. ly:18 RPUVR
Northing (m)
7024000
7020000
7016000
7012000
1.0
0.8
0.6
0.4
0.2
0.0
264000
268000
272000
Easting (m)

# Appendix N Predicted Mean and Standard Deviation of Benzene Maps at Selected Years for Base Case and PL253 FDP

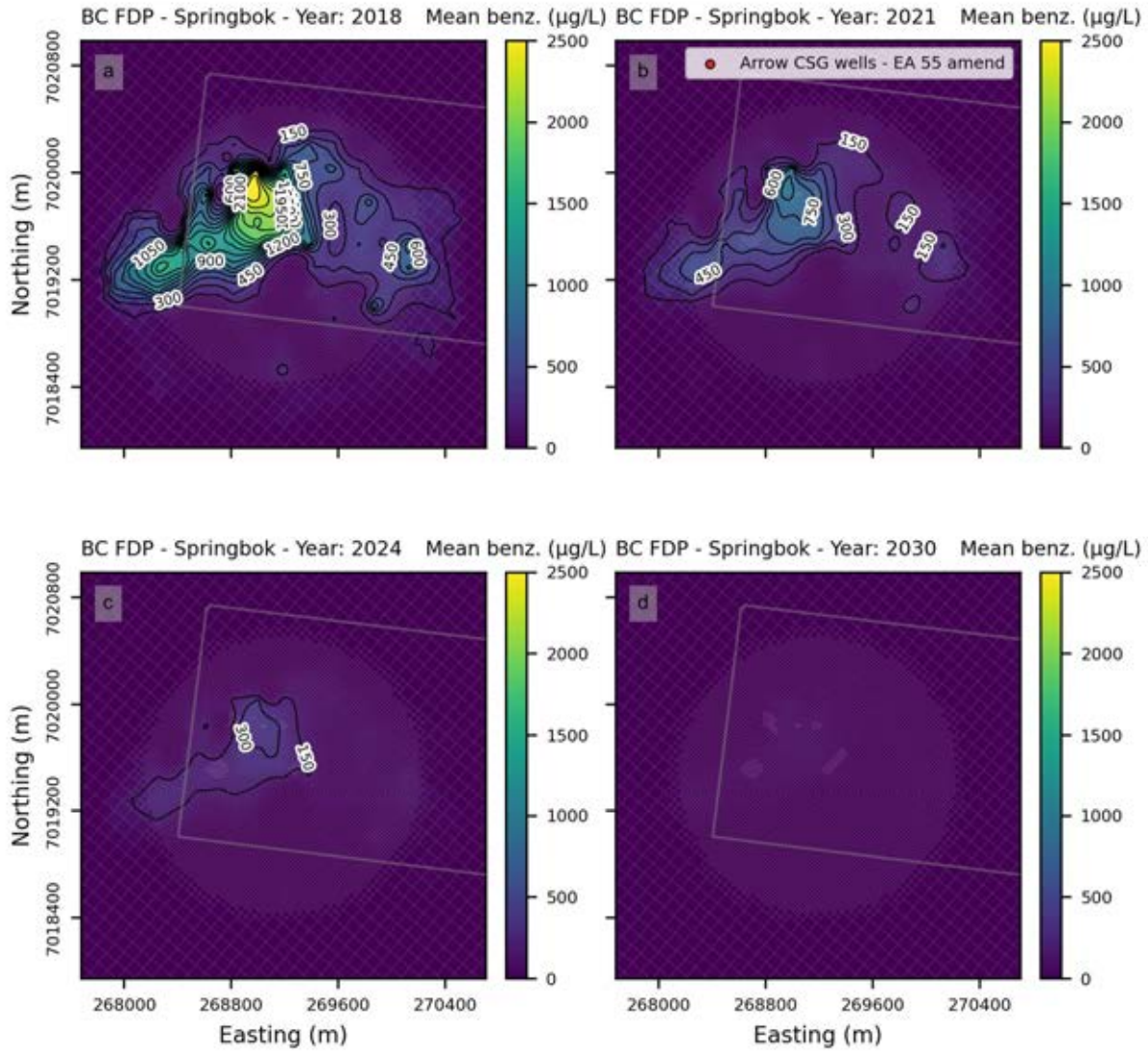


Figure K.1 - Maps showing the mean in benzene concentration for all posterior ensemble realisations (Base Case scenario) in layer 3 (Springbok). Each subplot (a) to (d) displays the years 2018, 2021, 2024, and 2030.

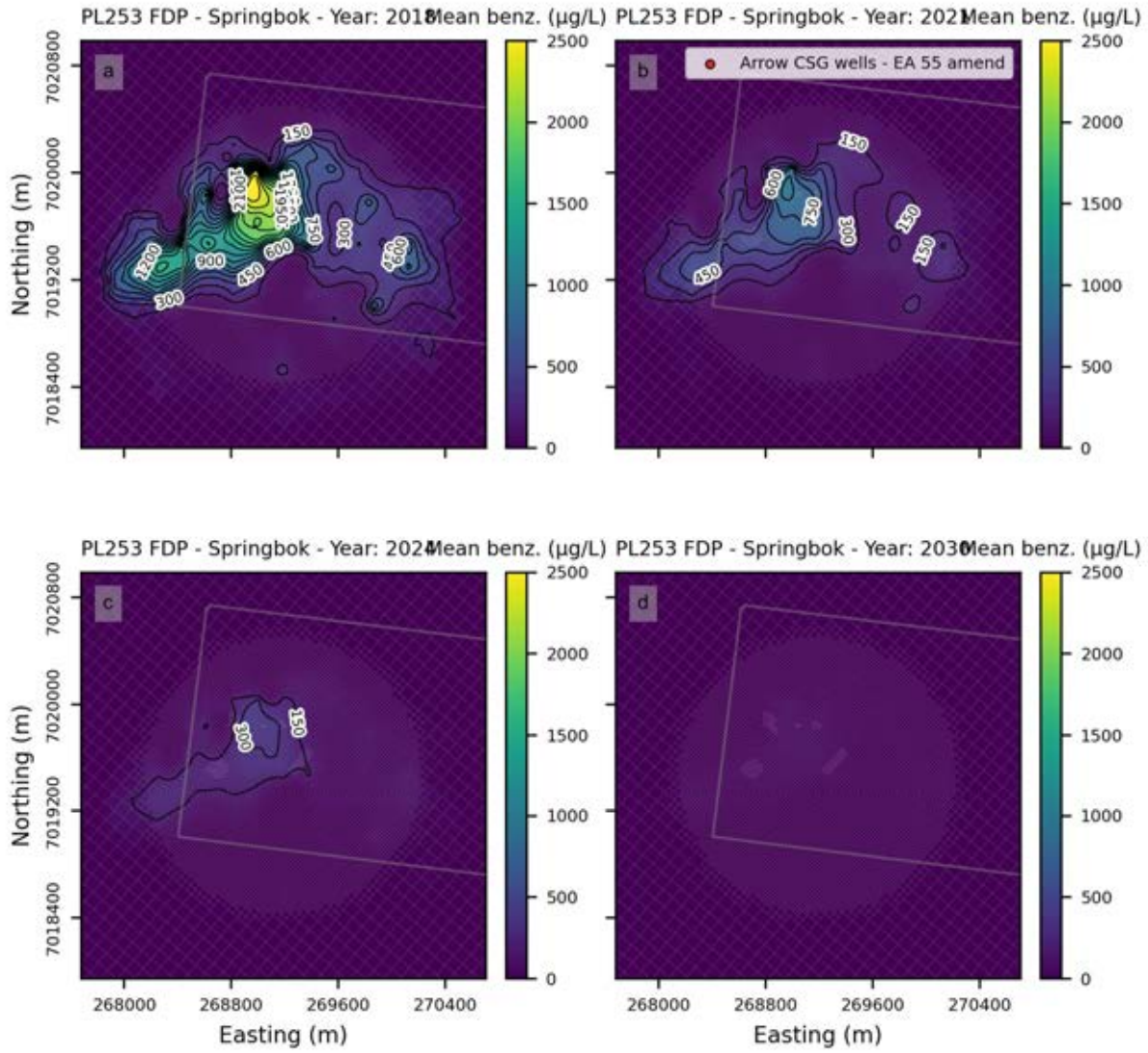


Figure K.2 - Maps showing the mean in benzene concentration for all posterior ensemble realisations (PL253 scenario) in layer 3 (Springbok). Each subplot (a) to (d) displays the years 2018, 2021, 2024, and 2030.

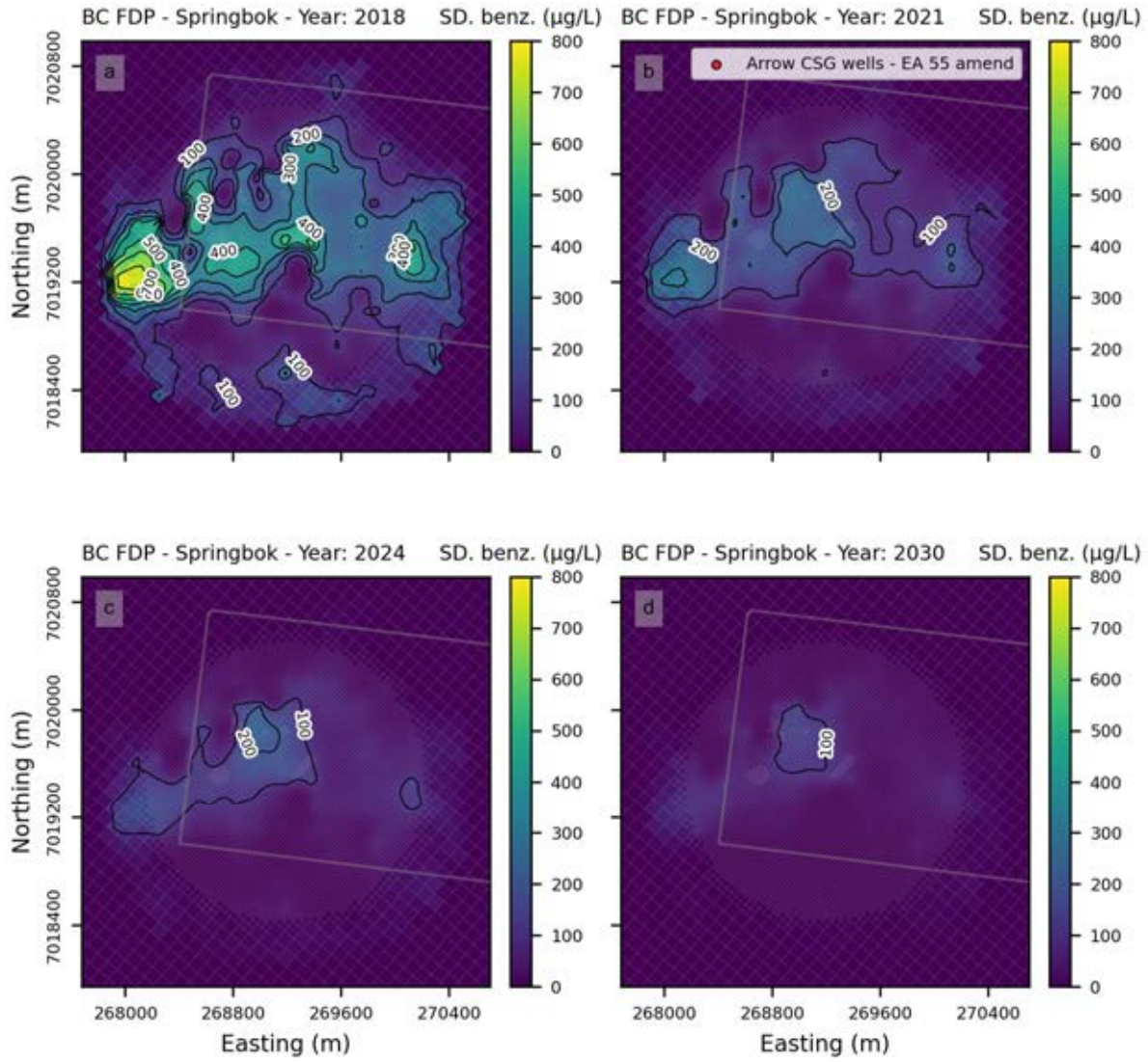


Figure K.3 - Maps showing the standard deviation in benzene concentration for all posterior ensemble realisations (Base Case scenario) in layer 3 (Springbok). Each subplot (a) to (d) displays the years for 2018, 2021, 2024, and 2030.

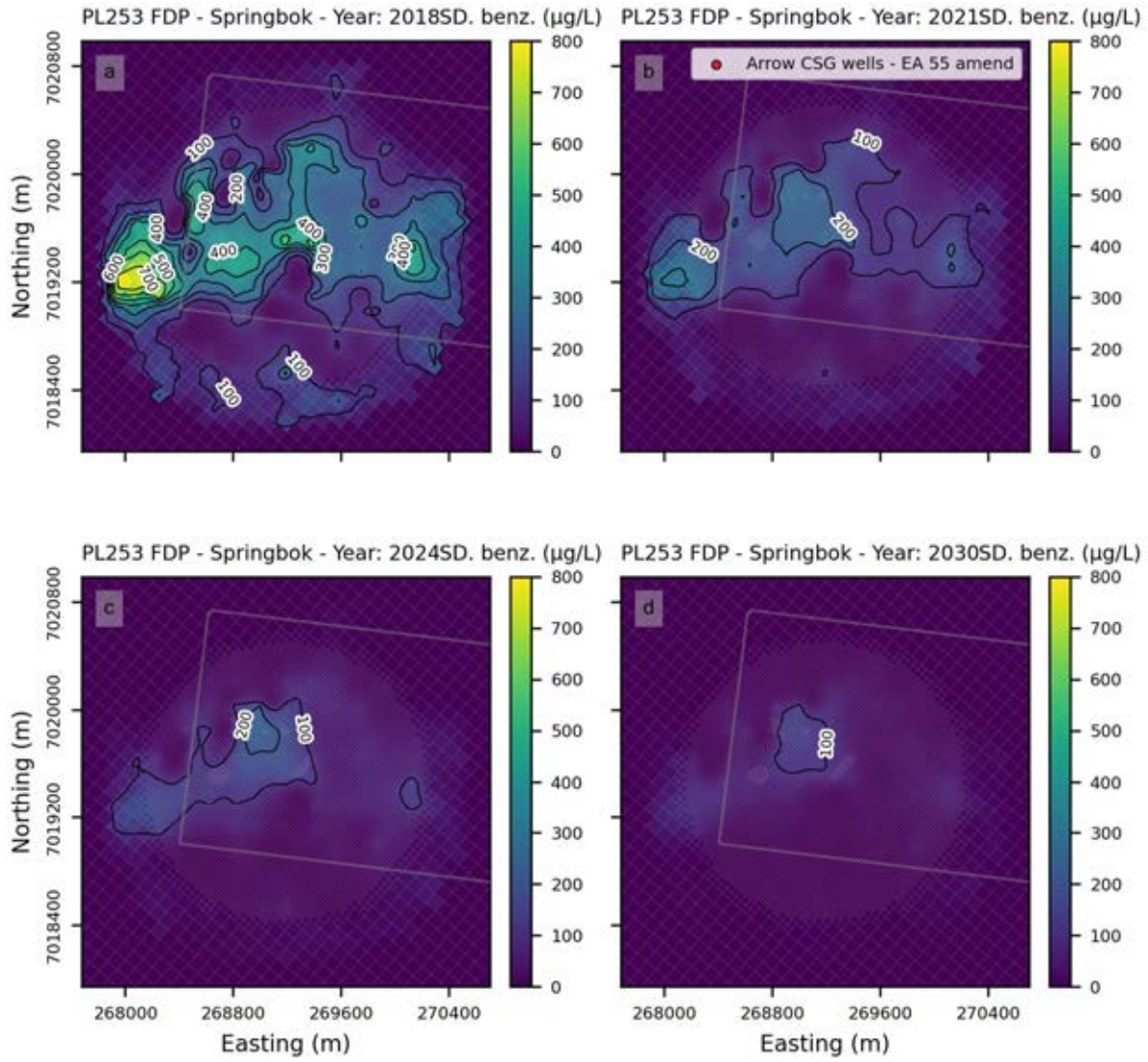


Figure K.4 - Maps showing the standard deviation in benzene concentration for all posterior ensemble realisations (PL253 scenario) in layer 3 (Springbok). Each subplot (a) to (d) displays the years 2018, 2021, 2024, and 2030.

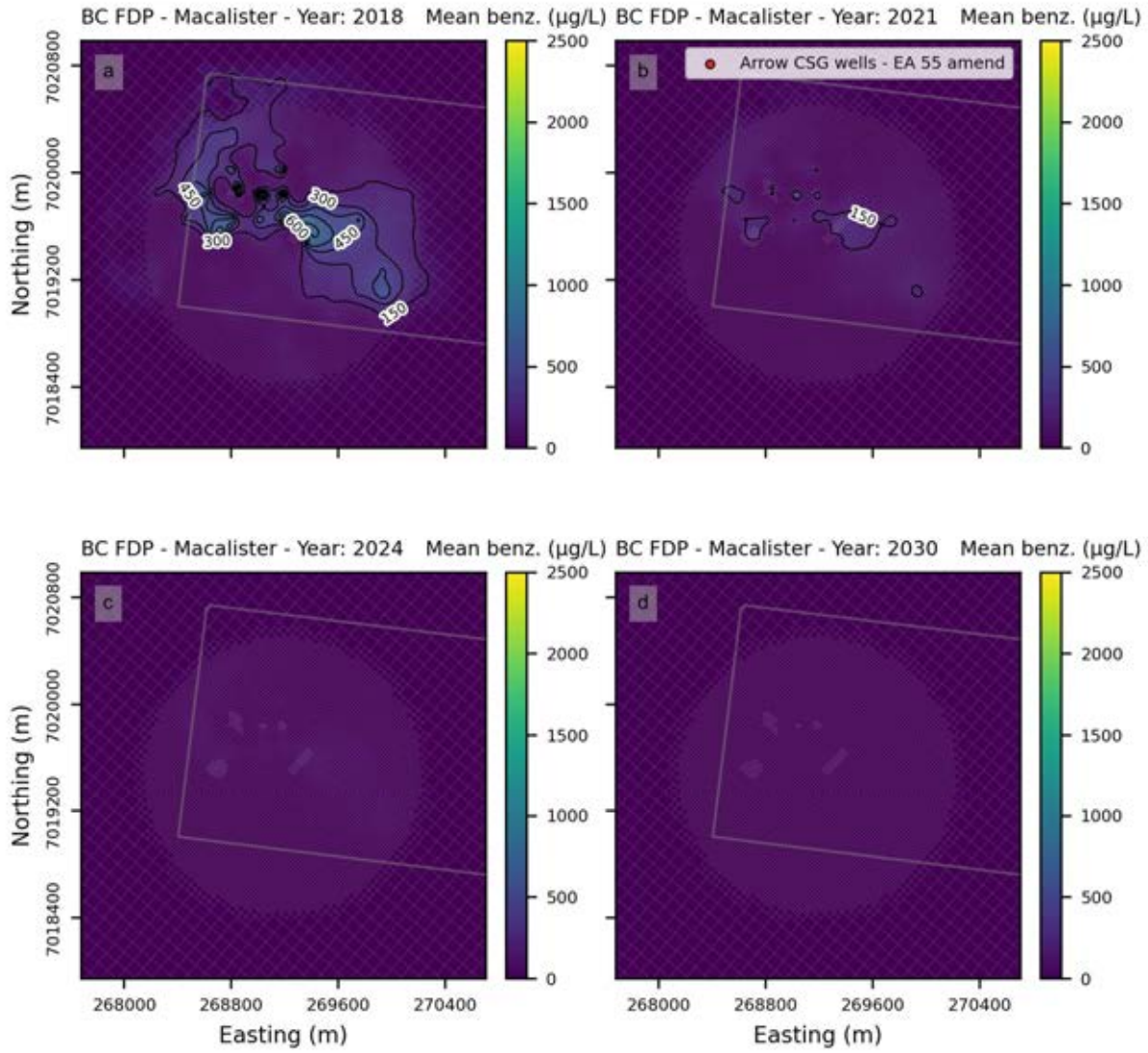


Figure K.5 - Maps showing the mean in benzene concentration for all posterior ensemble realisations (Base Case scenario) in layer 6 (Macalister). Each subplot (a) to (d) displays the years 2018, 2021, 2024, and 2030.

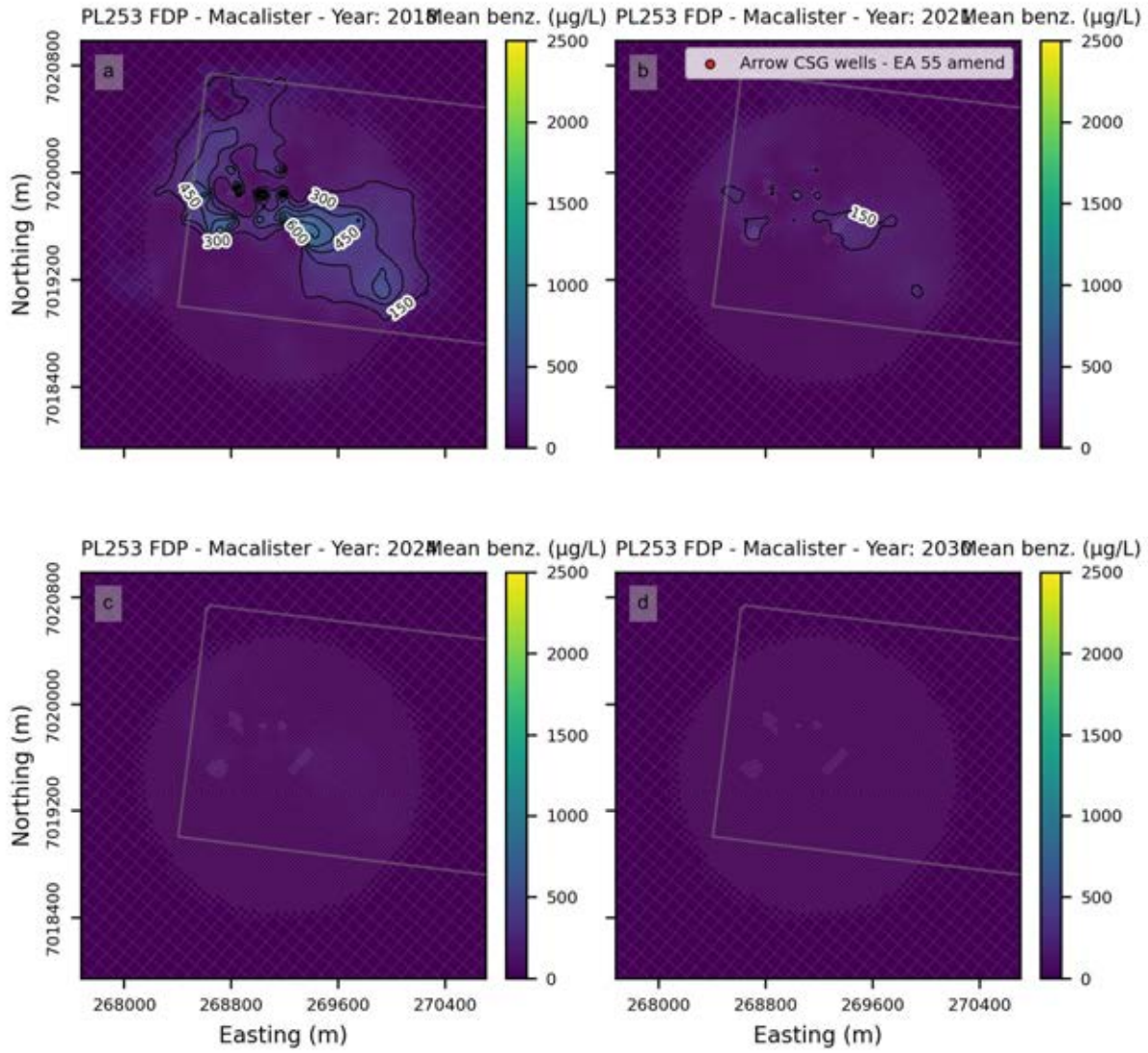


Figure K.6 - Maps showing the mean in benzene concentration for all posterior ensemble realisations (PL253 scenario) in layer 6 (Macalister). Each subplot (a) to (d) displays the years 2018, 2021, 2024, and 2030.

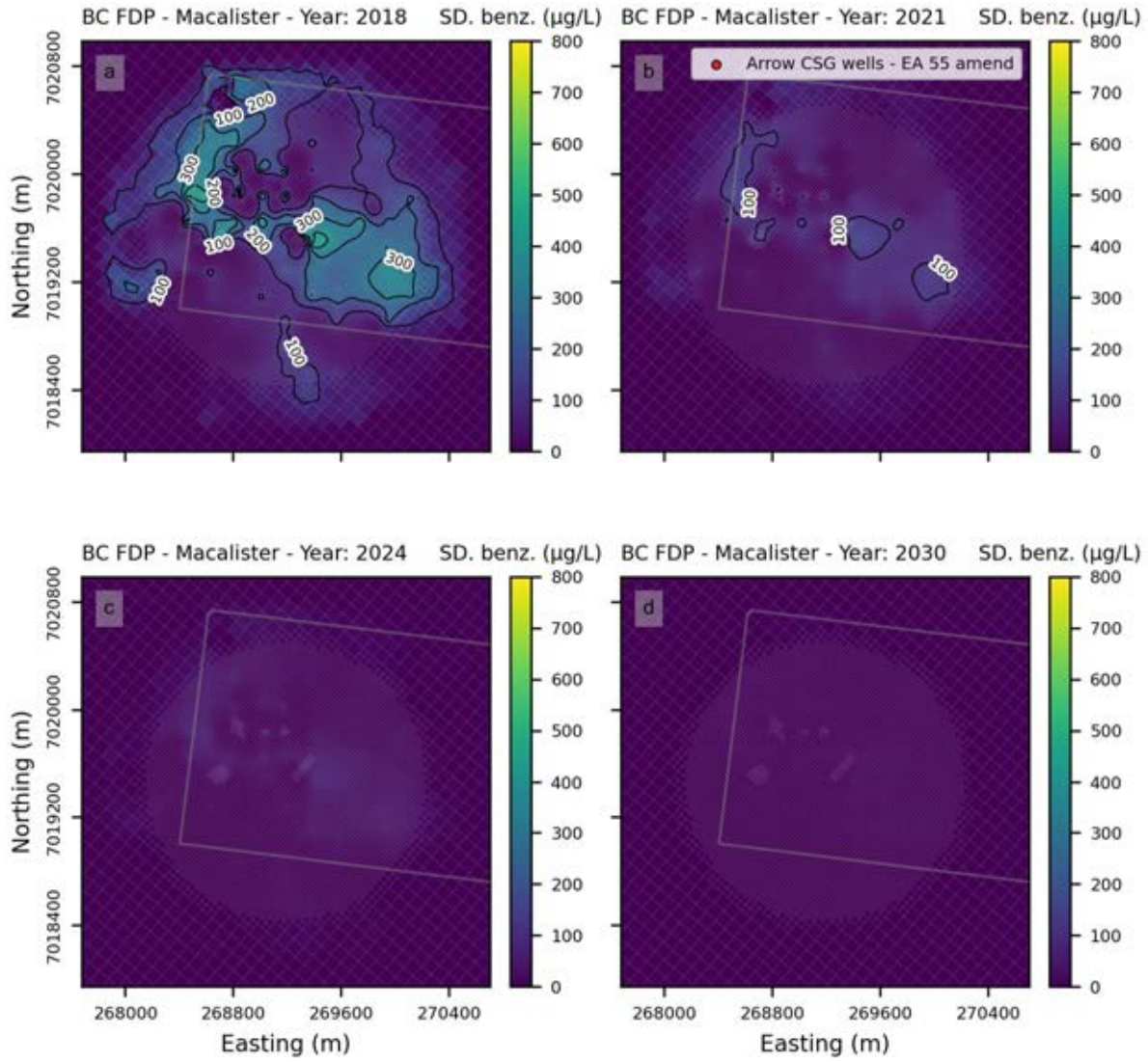


Figure K.7 - Maps showing the standard deviation in benzene concentration for all posterior ensemble realisations (Base Case scenario) in layer 6 (Macalister). Each subplot (a) to (d) displays the years for 2018, 2021, 2024, and 2030.

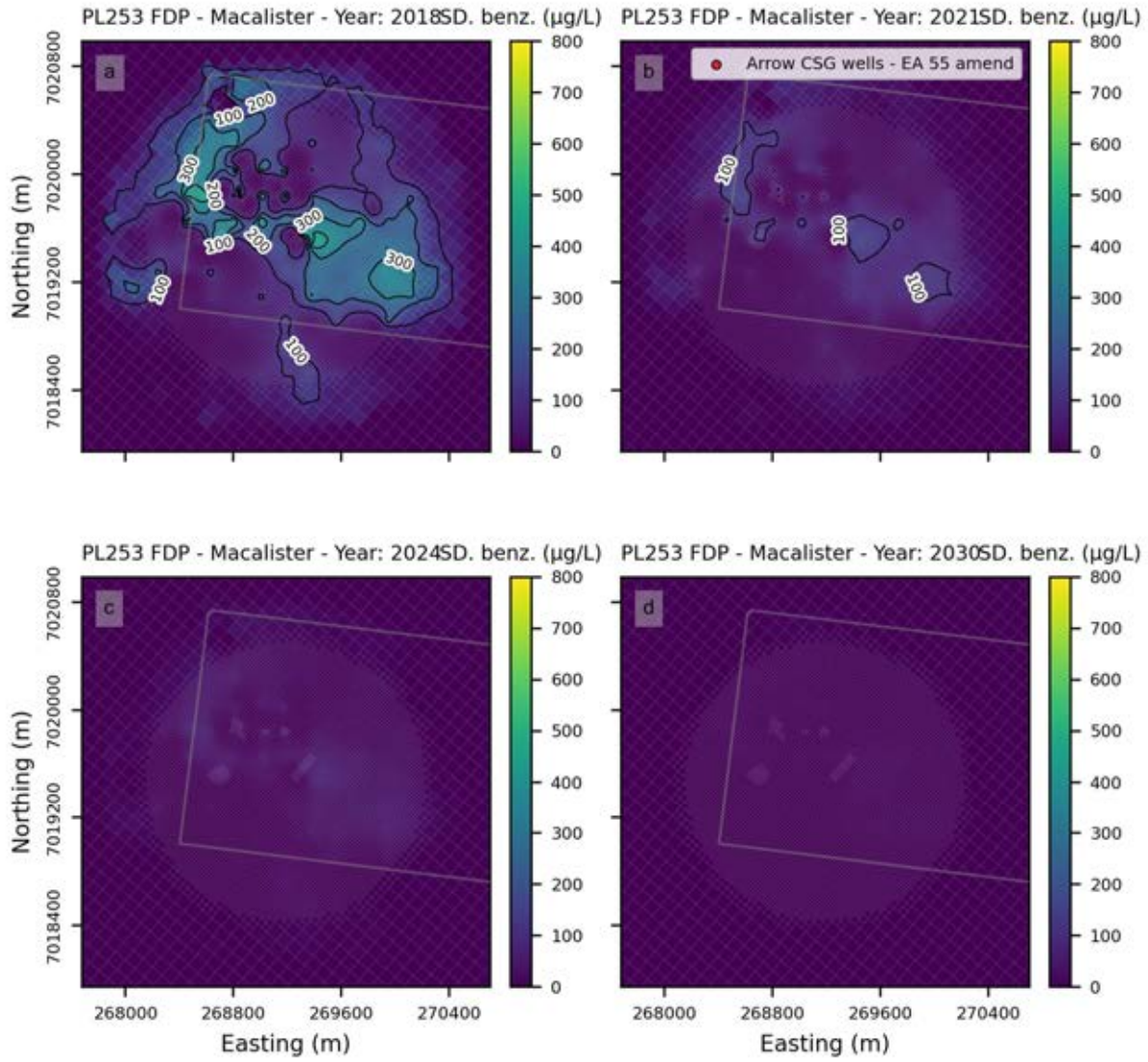


Figure K.8 - Maps showing the standard deviation in benzene concentration for all posterior ensemble realisations (PL253 scenario) in layer 6 (Macalister). Each subplot (a) to (d) displays the years 2018, 2021, 2024, and 2030.

# Appendix O Predicted Mean and Standard Deviation of Naphthalene Maps at Selected Years for Base Case and PL253 FDP

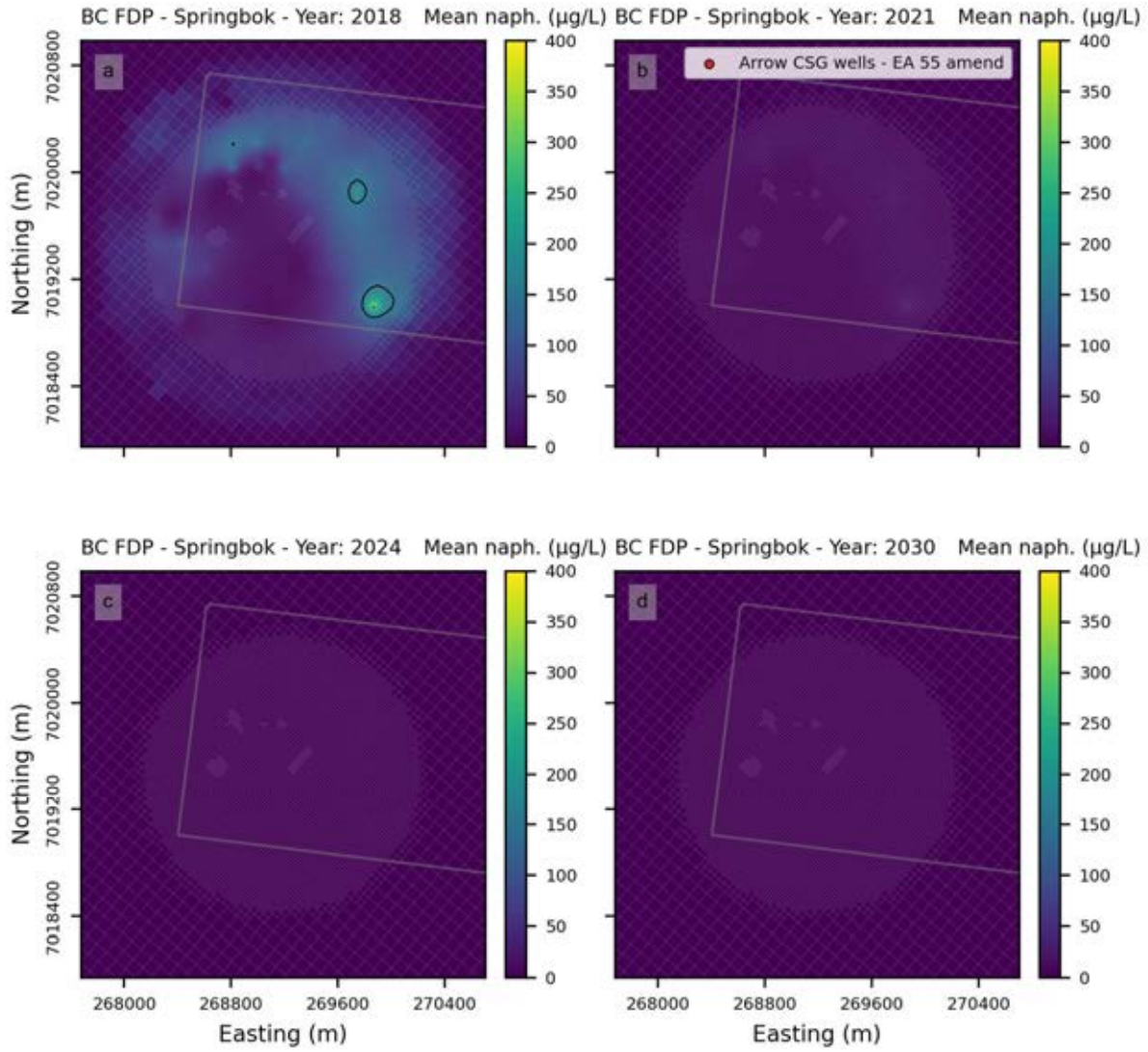


Figure L.1 - Maps showing the mean in naphthalene concentration for all posterior ensemble realisations (Base Case scenario) in layer 3 (Springbok). Each subplot (a) to (d) displays the years 2018, 2021, 2024, and 2030.

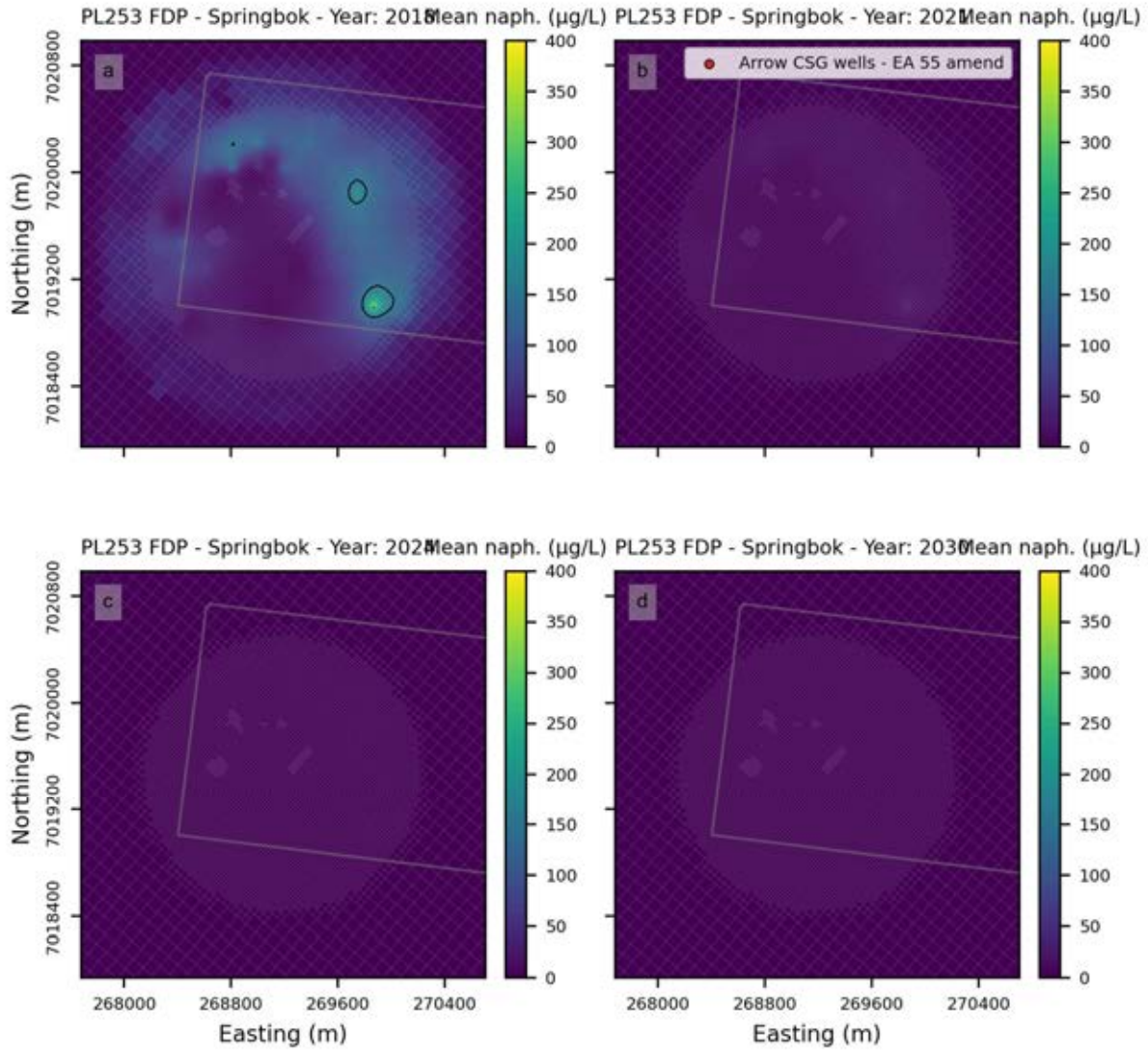


Figure L.2 - Maps showing the mean in naphthalene concentration for all posterior ensemble realisations (PL253 scenario) in layer 3 (Springbok). Each subplot (a) to (d) displays the years 2018, 2021, 2024, and 2030.

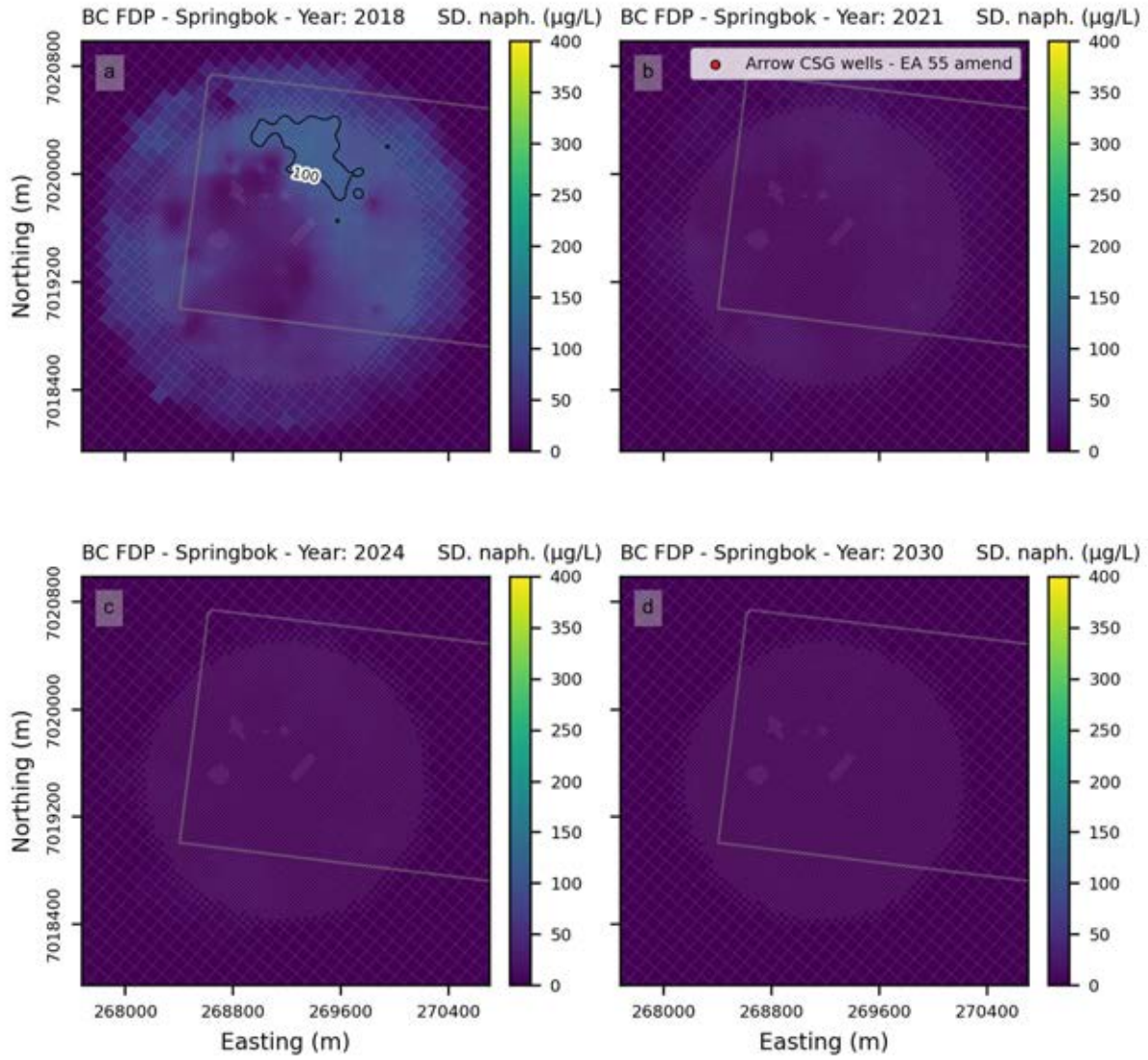


Figure L.3 - Maps showing the standard deviation in naphthalene concentration for all posterior ensemble realisations (Base Case scenario) in layer 3 (Springbok). Each subplot (a) to (d) displays the years for 2018, 2021, 2024, and 2030.

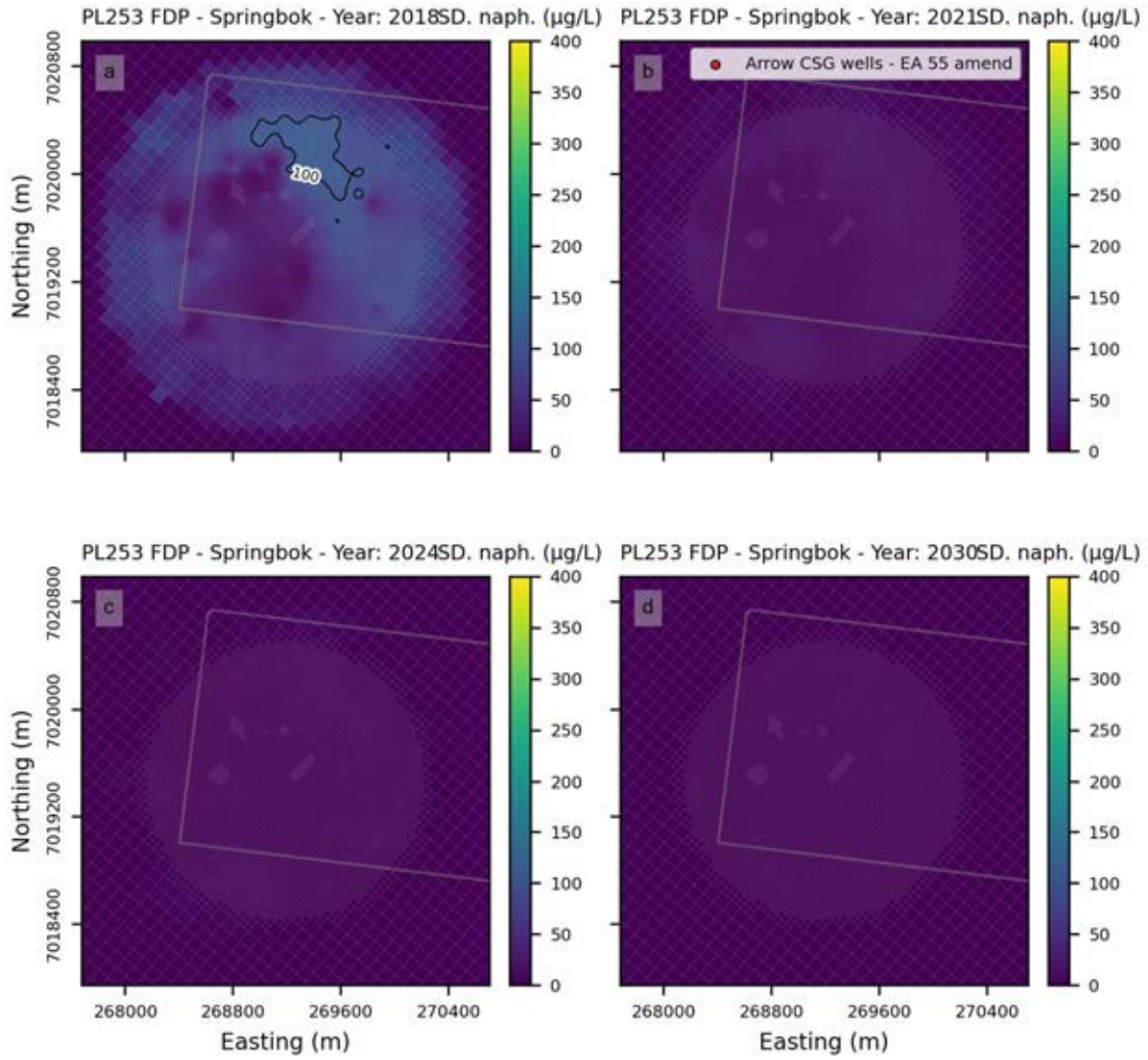


Figure L.4 - Maps showing the standard deviation in naphthalene concentration for all posterior ensemble realisations (PL253 scenario) in layer 3 (Springbok). Each subplot (a) to (d) displays the years 2018, 2021, 2024, and 2030.

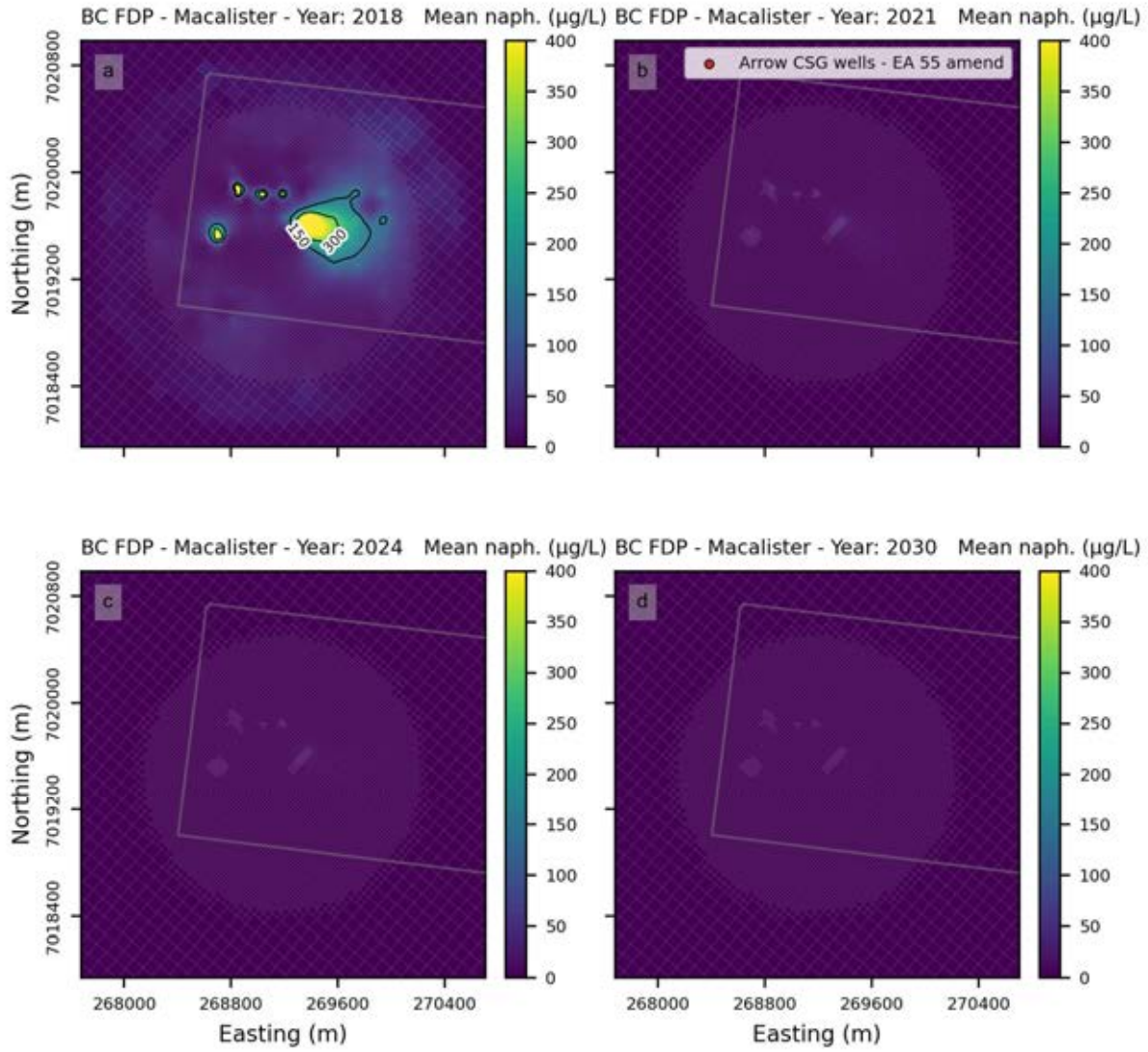


Figure L.5 - Maps showing the mean in naphthalene concentration for all posterior ensemble realisations (Base Case scenario) in layer 6 (Macalister). Each subplot (a) to (d) displays the years 2018, 2021, 2024, and 2030.

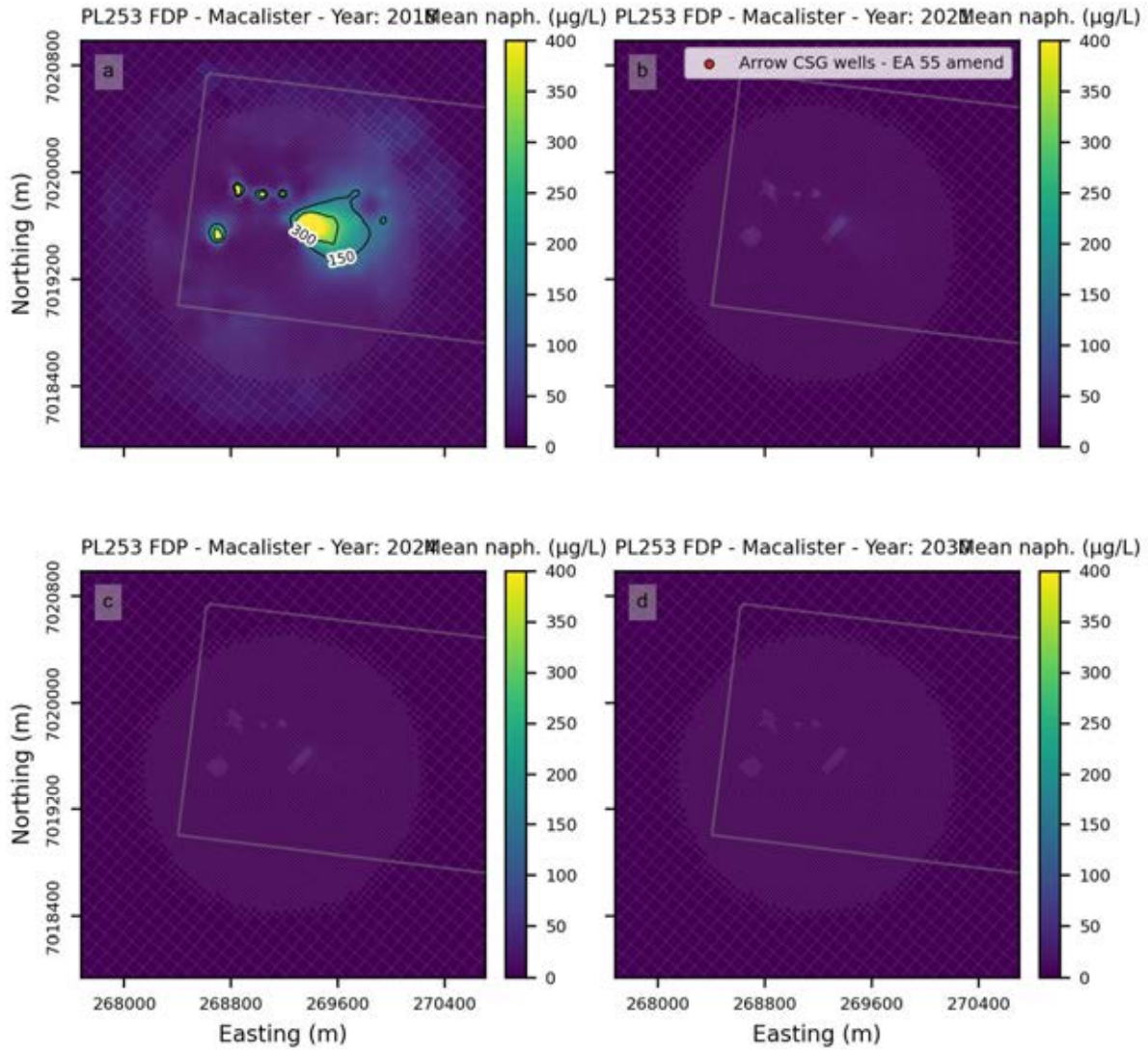


Figure L.6 - Maps showing the mean in naphthalene concentration for all posterior ensemble realisations (PL253 scenario) in layer 6 (Macalister). Each subplot (a) to (d) displays the years 2018, 2021, 2024, and 2030.

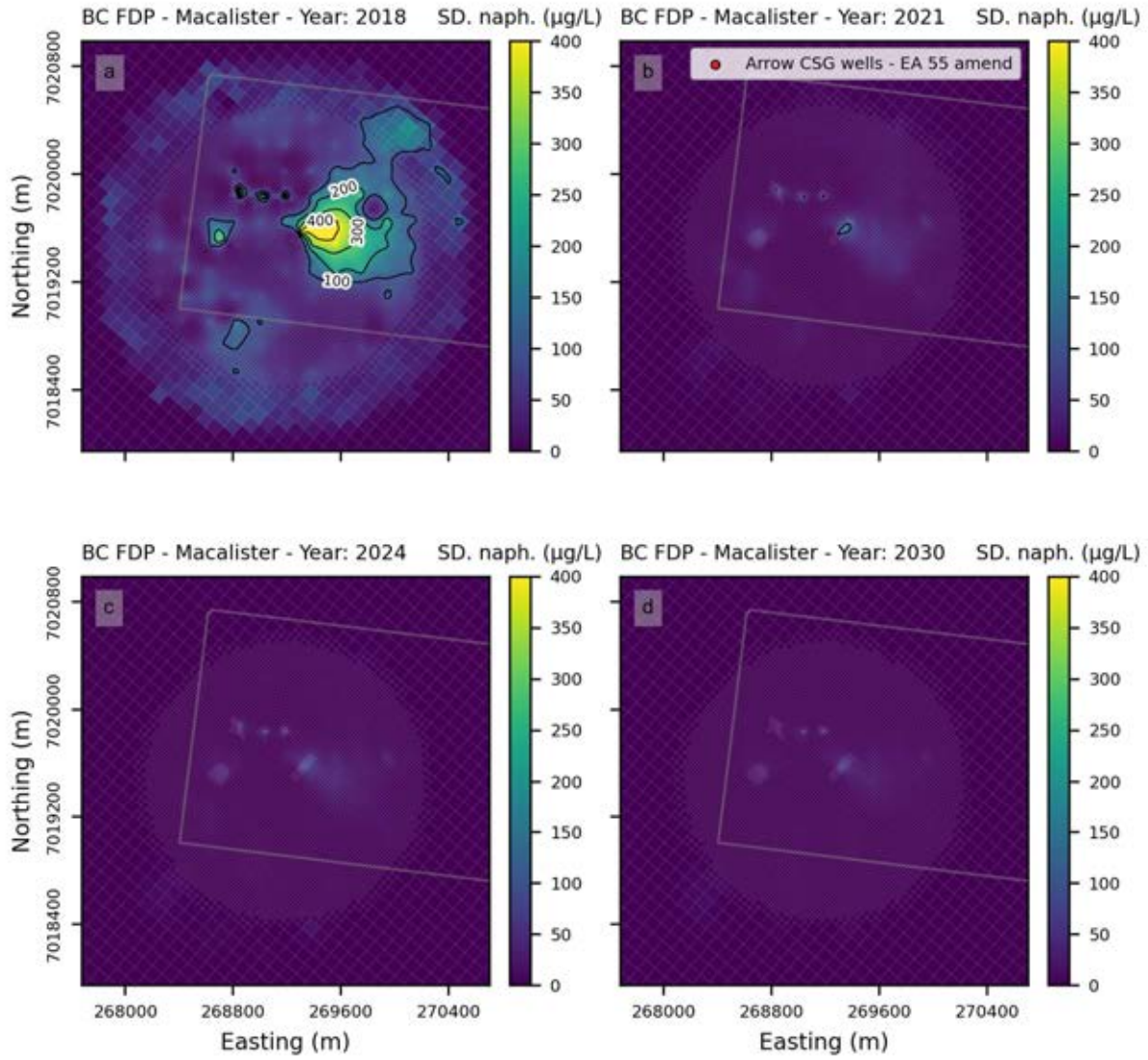


Figure L.7 - Maps showing the standard deviation in naphthalene concentration for all posterior ensemble realisations (Base Case scenario) in layer 6 (Macalister). Each subplot (a) to (d) displays the years for 2018, 2021, 2024, and 2030.

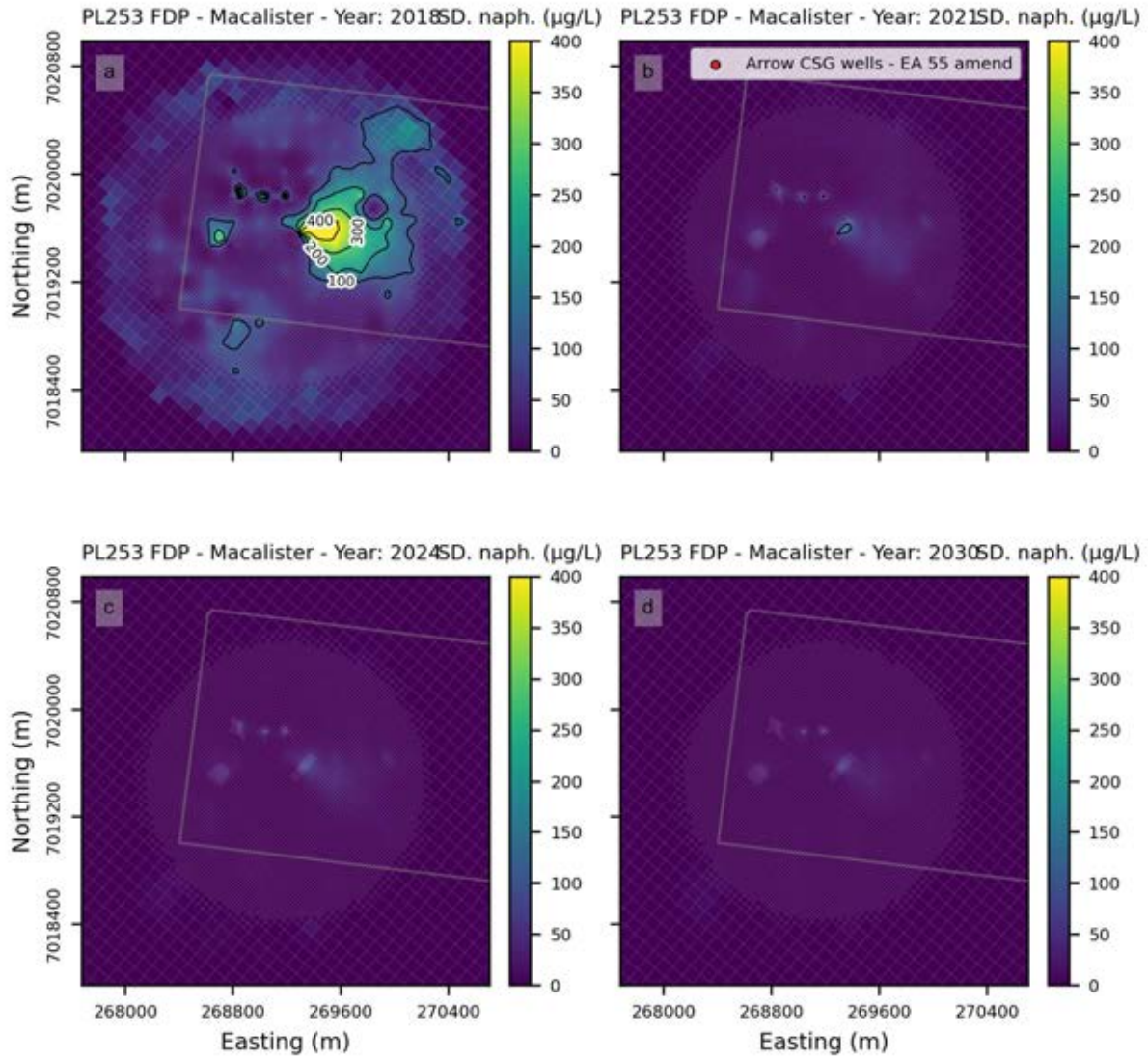


Figure L.8 - Maps showing the standard deviation in naphthalene concentration for all posterior ensemble realisations (PL253 scenario) in layer 6 (Macalister). Each subplot (a) to (d) displays the years 2018, 2021, 2024, and 2030.